NASA Contractor Report 158995

The Noise and Flow Characteristics of Inverted-Profile Coannular Jets

H. K. Tanna, B. J. Tester,
and J. C. Lau

LOCKHEED-GEORGIA COMPANY
Marietta, Georgia 30063

CONTRACT NAS1-15018
FEBRUARY 1979

National Aeronautics and
Space Administration

Langley Research Center
Hampton, Virginia 23665
AC 804 827-3966

NASA Contractor Report 158995

The Noise and Flow Characteristics of Inverted-Profile Coannular Jets

H. K. Tanna, B. J. Tester,
and J. C. Lau

LOCKHEED-GEORGIA COMPANY
Marietta, Georgia 30063

CONTRACT NAS1-15018
FEBRUARY 1979

National Aeronautics and
Space Administration

Langley Research Center
Hampton, Virginia 23665
AC 804 827-3966

FOREWORD

This report was prepared by the Lockheed-Georgia Company, Marietta, Georgia, for the NASA-Langley Research Center, Hampton, Virginia, under Contract NAS1-15018, entitled "Basic Research on Coannular Jet Noise Reduction".

Dr. S. P. Pao was the Technical Monitor for the NASA-Langley Research Center. Lockheed's Program Manager was Dr. H. E. Plumblee, Jr., and Dr. H. K. Tanna was the Principal Investigator.

The authors would like to express their sincere acknowledgements to the following individuals who made significant contributions to the work conducted under this contract: Mr. D. F. Blakney, Mr. W. H. Brown, Mr. R. H. Burrin, Mr. J. Mehta, Dr. P. J. Morris, Dr. M. Salikuddin, Mr. D. M. Smith, Mr. M. C. Whiffen, and Mr. J. C. Wilkins. Finally, gratitude is expressed to Mrs. Barbara C. Reagan for her excellent typing services.

CONTENTS

CONTENTS (Cont'd)

SUMMARY

The work described in this report is conducted to obtain a basic understanding of the noise reduction mechanisms in shock-free inverted-velocity-profile coannular jets. The specific objectives are: (1) To measure the flow properties of coannular jets so as to provide some insight into differences in sound generation between different jets, and (2) To produce a quantitative and scientifically reasonable model for these differences which fits the measured flow and noise data.

The noise characteristics of inverted-profile coannular jets are first measured in the Lockheed anechoic facility, and the effects of "inverted velocity" and "inverted temperature" profiles are isolated for coannular jets having constant total thrust, mass flow rate and exit area.

In order to obtain physical explanations of the measured noise changes, several types of experiments are conducted. These include (1) source location experiments using the "Polar Correlation Technique", (2) mean flow surveys using a combination pressure/temperature probe, and (3) detailed mean flow and turbulence measurements using a two-point four-channel laser velocimeter. The results from these experiments are presented and discussed in detail. From the noise radiation viewpoint, the more important changes in the jet flow characteristics that occur between the inverted-profile coannular jet and the fully-mixed equivalent single jet (i.e. the reference jet) are highlighted.

Finally, the measured variations of coannular jet mixing noise with fan-to-primary velocity ratio (V_f/V_p) and static temperature ratio (T_f/T_p) are interpreted by utilizing the results from the various experimental phases in conjunction with the existing Lockheed single jet noise prediction model. It is shown that at low frequencies, the inverted-profile coannular jet is quieter than the reference jet mainly because in the transition region, the eddy convection velocity, source-region velocity and axial turbulence level of the coannular jet are significantly lower than those of the reference jet. At high frequencies, the measured noise increases can be accurately quantified in terms of the faster outer stream conditions using the currently-understood mechanisms of noise generation, emission, convective amplification and flow-acoustic interactions in single round jets.

1. INTRODUCTION

The noise from coannular jets has been examined experimentally in increasing detail by several investigators ever since the introduction of turbofan engines for aircraft propulsion. In the past three years, as a result of the NASA-funded SCAR (Supersonic Cruise Aircraft Research) programs, it has been noted that coannular jets with "inverted velocity profiles" (i.e. secondary or fan velocity greater than primary or core velocity) provide a significant noise reduction. However, in the majority of these studies, each investigator has adopted his own scheme and criteria for presenting the data and for evaluating the noise benefit offered by coannular jets. Consequently, the existing data on coannular jet noise have not been compared on a universal basis in the past, and this has led to several misconceptions and optimistic projections for noise reductions that can be achieved from coannular jets. Furthermore, when noise reductions do occur, the reasons are not clearly understood. If the inverted profile concept is to be effectively utilized for an aircraft installation, it is crucial to understand what controls the noise generation and how the design can be optimized for minimum jet noise for specified performance criteria.

The overall objective of the present investigation is to obtain a basic understanding of the noise reduction mechanisms in inverted-velocity-profile coannular jets. The specific technical objectives are:

(1) to measure the flow properties of coannular jets so as to provide some insight into differences in sound generation between different jets, and

(2) to produce a quantitative and scientifically reasonable model for these differences which fits the measured flow and noise data.

The total noise field from a coannular jet can be characterized by individual contributions from three noise sources: (i) small-scale turbulent mixing noise, (ii) shock-associated noise, and (iii) noise from large-scale turbulence structure. The relative contribution from each of these three noise sources will depend upon the operating conditions of the two nozzles, the observer angle, and the frequency. For shock-free coannular jets, the observed noise reductions can only be interpreted as reductions in turbulent mixing noise (and/or reductions in noise from large-scale turbulence structure). On the other hand, for shock-containing coannular jets, significant reductions in shock-related noise are believed to occur. Thus, any basic research program must address all three noise sources. Only then can we utilize the resulting understanding and apply optimization criteria to coannular jets at *all* conditions of current and future practical interest.

Although this multiplicity of sources also confronts us in the case of a single jet, the coannular jet is an order of magnitude more complicated owing to the large number of additional parameters (e.g. velocity ratio, temperature ratio, pressure ratio, area ratio, etc.). Hence, the research

program needs to be conducted with a basic philosophy in mind - a philosophy that maintains a proper perspective of all three noise sources as well as all parameter effects, and which is directed toward "isolation of effects." To be more specific, the research program should be based on the following considerations:

(1) Both shock-free and shock-containing coannular flows should be studied systematically, so that the effects of exit velocity profile on shock-associated noise can be isolated as far as possible from profile effects on jet mixing noise.

(2) For the turbulent mixing noise source in particular, source alteration effects should be isolated from the flow-acoustic interaction effects. That is, the theoretical and experimental efforts should be structured in a manner which will isolate, as far as possible , the source "strength" changes from the "shrouding" influence of the surrounding flow field.

(3) The experimental program should be carefully designed, so that only one significant parameter is varied at a time. In particular, the effects of fan-to-primary velocity ratio (V_f/V_p) and static temperature ratio (T_f/T_p) should be quantified independently.

The general approach discussed above has proved to be successful in previous single jet noise research programs conducted at Lockheed. The present study, however, is mainly devoted to noise from inverted-velocity-profile coannular jets under *shock-free* conditions, and therefore detailed conclusions pertaining to the origins of noise reductions (or increases) resulting from velocity profile shaping for *shock-containing* coannular jets are not contained in this report.

An outline of the experimental and some theoretical aspects covered in this report (i) to quantify the noise reductions (or increases) and (ii) to provide physical explanations for the measured noise changes, is given below.

Magnitude and character of noise reductions - An acoustic experimental program was conducted in a unique manner which enables the isolation of "inverted velocity" effects from "inverted temperature" effects for coannular jets having constant thrust, mass flow rate and exit area. The results from these experiments have been analyzed to determine the magnitudes of the noise reductions (or increases), and the angle and frequency regimes over which the noise changes (i.e. reductions or increases) relative to the fully-mixed equivalent single jet are maximum. This part of the investigation is presented in Section 2 of this report.

Location of noise sources - In order to explain the measured noise changes, it is first of all vital to determine the axial locations, within the jet flow, of the noise sources as a function of frequency. The polar correlation technique was used to measure the "apparent" source strength distributions, and these results are presented in Section 3. The results

from these tests were used in the selection of the regions of jet flow for subsequent detailed flow measurements.

Environment surrounding noise sources - In order to study acoustic shielding effects in coannular jets, it is necessary to obtain the mean velocity and mean temperature profiles throughout the jet flow. A combination pressure/temperature probe was used for this purpose, and the results from these extensive surveys are summarized in Section 4.

Strength and character of sources - In order to obtain detailed mean flow and turbulence characteristics for input to the analytical model for coannular jet noise, a laser velocimeter (LV) was used. Single-point LV measurements were used to provide information on turbulence intensity and spectra, mean velocity profiles, etc., whereas two-point measurements yielded quantities such as eddy convection velocity, length scales, etc. These LV results are presented and discussed in Section 5.

Nozzle performance - In evaluating any noise reduction concept or device, the measured noise benefit needs to be assessed against any inherent performance penalty. For coannular jets, the aerodynamic performance of the nozzles can be specified in terms of the "thrust coefficient." Although no direct measurements of nozzle thrust were conducted in the present program, the thrust coefficient was obtained by measuring the flow coefficients and the velocity coefficients of the inner and outer nozzles. These results are discussed in Section 6 of this report.

Model/data correlations - Finally, using the existing theoretical models for turbulent mixing noise from single round jets, a model for the prediction of jet mixing noise from coannular jets was developed, and the results from the various experimental phases discussed above were used to explain the measured noise changes in coannular jets. This part of the investigation is described in Section 7.

Shock-containing coannular jets - As mentioned earlier, although the present program was concentrated on *shock-free* inverted-velocity-profile coannular jets, some measurements were conducted at supercritical conditions. In particular, a series of Schlieren photographs were obtained to provide information on the shock structure (i.e., number of shocks and shock spacing) in coannular jets. These measurements are documented in Appendix 1.

2. ACOUSTIC MEASUREMENTS AND RESULTS

The noise reduction potential of inverted-velocity-profile coannular jets has been examined extensively in two recent studies (refs. 2.1 and 2.2) funded by NASA. Although a large amount of useful acoustic data was acquired in these programs, it is perhaps fair to say that the test programs were not designed to isolate the various effects *explicitly*, as mentioned in the Introduction (Section 1). Furthermore, the noise benefit of IVP coannular jets was initially assessed by comparing the coannular jet noise levels with the corresponding "synthesized" jet noise levels, and it was only relatively recently that some selected results were reexamined to assess the noise reductions with respect to the corresponding "fully-mixed equivalent single jets." Consequently, it was decided that an independent set of acoustic results is required in the present program to complement the jet flow measurements, which will be discussed in the subsequent sections of this report. This acoustic test program, the facilities used, and the results from these experiments are described in the present section.

2.1 TEST PROGRAM

Due to the large number of absolute parameters (e.g. velocity, temperature, area, etc.) as well as parameter ratios involved in characterizing coannular jet noise, the noise reduction can be (and has been) examined and quantified in a number of different ways. In the earlier studies on normal-velocity-profile coannular jets (fan-to-primary velocity ratio $V_f/V_p < 1$), the coannular jet noise levels were almost always compared with the noise levels from the primary jet alone. In some of the more recent studies on inverted-velocity-profile coannular jets (i.e. $V_f/V_p > 1$), the noise reduction has been assessed in most part by either (i) comparing coannular jet noise levels with synthesized noise levels, or (ii) comparing coannular jet noise levels to the $V_f/V_p = 1$ case for fixed fan velocity V_f. The "synthesized" method has no physical rationale, whereas the other two schemes are at best misleading.

In order to evaluate the noise benefit, it is desirable to have a means of comparing different coannular jet noise levels which takes realistic account of the aircraft propulsion design constraints. Significant parameters in this context include nozzle gross thrust, mass flow rate, total enthalpy change, and exit area. A constant-thrust comparison is obviously essential; which other two parameters should be kept constant is to some extent arbitrary. Area and mass flow rate have been chosen in the present investigation, but the choice is not regarded as final. As a basis for quantifying the noise reductions, therefore, we use the *fully-mixed equivalent (FMEQ) jet*, defined as having a uniform exit profile and the same exit area, mass flow rate and thrust as the actual coannular jets. Comparisons on this basis indicates where particular coannular configurations hold promise of useful noise reductions in an actual propulsion application.

Table 2.1 Coannular jet - subcritical (shock-free) test conditions for constant thrust and mass flow rate.

$T_f/T_p \rightarrow$	1.00				1.75				2.00			
V_f/V_p	ξ_p	T_{tp}/T_o	ξ_f	T_{tf}/T_o	ξ_p	T_{tp}/T_o	ξ_f	T_{tf}/T_o	ξ_p	T_{tp}/T_o	ξ_f	T_{tf}/T_o
1.00	① 1.455	2.126	1.455	2.126	⑤ 1.575	1.775	1.306	2.945	⑨ 1.601	1.717	1.275	3.218
1.35	② 1.325	2.024	1.643	2.152	⑥ 1.446	1.697	1.467	2.982	⑩ 1.476	1.644	1.428	3.257
1.55	③ 1.270	1.950	1.731	2.131	⑦ 1.385	1.635	1.553	2.956	⑪ 1.415	1.585	1.511	3.230
1.75	④ 1.226	1.877	1.806	2.096	⑧ 1.333	1.569	1.630	2.909	⑫ 1.361	1.522	1.587	3.180

The numbers in circles refer to Test Point (TP) numbers.

A matrix of shock-free test conditions was therefore designed which not only satisfies the constant thrust, mass flow rate and area requirements discussed above, but also enables the isolation of "inverted velocity" effects from "inverted temperature" effects for coannular jets. This test matrix, consisting of twelve Test Points (TP), is shown in Table 2.1. It can be seen that along each of the three columns of the matrix, the static temperature ratio at the nozzle exit (T_f/T_p) is held constant while the velocity ratio (V_f/V_p) is varied from 1.00 to 1.75. Conversely, along each row of the matrix, the effects of T_f/T_p can be examined for a fixed value of V_f/V_p. Two more comments regarding this test plan are worth noting. First, it should be recognized that although the velocity and temperature *ratios* V_f/V_p, T_f/T_p are kept constant, the *absolute values* of velocity and temperature (V, T) for the two streams vary from one test point to another. Second, Test Point 1 ($V_f/V_p = 1$, $T_f/T_p = 1$) represents the fully-mixed equivalent jet corresponding to the remaining eleven test conditions, and it is therefore referred to as the "reference jet" in the rest of this report. In this manner, the noise measurements at any test point can be compared directly with the reference jet noise levels to determine the noise benefit within the performance criteria discussed earlier.

In addition to these subcritical test conditions, two supercritical jet operating conditions were selected. These conditions, identified as TP's 13 and 14, are defined in Table 2.2. They are not related in any way to the subcritical test points. They were selected purely on the basis that significant noise reductions have been observed at these conditions in previous studies - TP 13 was selected from reference 2.1 and TP 14 was selected from reference 2.3.

Table 2.2 Coannular jet - supercritical (shock-containing) test conditions.

TP	ξ_p	ξ_f	T_{tp}	T_{tf}	V_f/V_p	T_f/T_p
13	1.51	2.46	728°K	978°K	1.66	1.26
14	2.02	3.04	294°K	728°K	1.95	2.47

2.2 FACILITIES AND DATA ACQUISITION

The acoustic experiments were conducted in the Lockheed anechoic facility which has been used extensively in the past to conduct single jet noise measurements. In 1977, the existing single jet rig was modified to enable measurements of noise from dual-flow jets. This modified facility, and the calibration tests which were conducted following the modifications, are described fully in reference 2.4. The salient features of the facility are summarized below.

The anechoic chamber provides a free-field environment at all frequencies above 200 Hz, and incorporates a specially-designed exhaust collector/muffler which (i) provides adequate quantities of jet entrainment air, (ii) distributes this entrainment air symmetrically around the jet axis, and (iii) keeps the air flow circulation velocities in the room to a minimum.

The air supply for the primary and secondary jets originates from the main compressor which provides up to 9 kg/sec of clean dry air at 2.07×10^6 N/m^2. This air is heated by a propane burner to approximately 1100°K. Downstream of the burner, the primary and secondary air supplies are controlled independently and each has a hot and cold valve so that any desired jet operating conditions can be achieved within the pressure and temperature limitations of the system. Each air stream is then directed through a set of diffuser and muffler to minimize internal noise levels. The primary flow then passes through banks of electric heaters so that the primary plenum temperature may be raised to ~1350°K. The two streams finally enter their respective plenums which are located upstream of the coannular nozzle section.

Special attention has been paid to flow conditioning. Downstream of the mufflers, the flow area to nozzle exit area is maintained greater than 36:1 up to the nozzle inlet. This ensures that no additional noise or turbulence is generated, since the flow velocities are very low.

In order to ensure that the relative axial positions of the exit planes of the two nozzles do not vary, a special expansion coupling has been incorporated in the primary ductwork, with a corresponding spacer in the secondary ductwork. It provides for expansion or contraction of the inner duct relative to the outer duct of ±4 mm from center which is adequate for the thermal expansion associated with the likely temperature differentials between primary and secondary flows.

Finally, in order to maintain concentricity of the two nozzles at all times, a special spoked nozzle attachment flange is included.

Coannular Nozzle Configuration

The coannular nozzle that was used *throughout* this investigation is shown in Figure 1.1. The nozzles have been carefully designed to give minimum boundary layer thickness and flow streamlines parallel to the jet axis at the exit. The specifications of the nozzle configuration are as follows:

Diameter of primary nozzle	$D_p = 4.996$ cm
Diameter of fan nozzle	$D_f = 6.797$ cm
Primary nozzle lip thickness	$t_p = 0.0508$ cm
Fan nozzle lip thickness	$t_f = 0.0508$ cm
Primary nozzle wall thickness *at fan nozzle exit plane*	$= 0.127$ cm
Primary nozzle extension beyond fan nozzle exit plane	$L = 0.4\ D_p$
Radius ratio	$r_p/r_f = 0.735$
Area ratio	$A_f/A_p = 0.747$
Equivalent nozzle diameter	$D_{eq} = 6.603$ cm

Data Acquisition

The acoustic measurements were conducted on a polar arc of radius 3.66 m (12 feet). Ten 6.35 mm (1/4-inch) B&K microphones Type 4135 (combined with preamplifiers Type 2619) were positioned from 20° to 110° to the downstream jet axis at intervals of 10°. The sound pressure levels were analyzed "on line" on a General Radio one-third octave band analyzer over the frequency range from 200 Hz to 80 KHz, and the results were recorded on an incremental tape recorder. The recorded levels were subsequently processed on a digital computer using a data reduction program which applies microphone frequency response corrections and atmospheric attenuation corrections (ref. 2.5), and computes overall sound pressure levels over the frequency range 200 Hz - 80 KHz. All sound pressure and sound power results presented in the following subsection are *lossless* (i.e., with zero atmospheric attenuation).

2.3 RESULTS AND DISCUSSION

2.3.1 Sound Pressure Level Results

The effects of fan-to-primary velocity ratio (V_f/V_p) on 1/3-octave SPL spectra at various angles to the jet exhaust are shown in Figure 2.2, where the static temperature ratio (T_f/T_p) is held constant at unity. Hence, "inverted velocity" effects are examined *explicitly* in this figure. At and around 90° to the jet axis, a quick look at Figure 2.2(d) indicates that there is little change in noise levels at low frequencies. However, a closer examination of these low-frequency SPL's reveals that for frequencies less than approximately 4 KHz, there is a slight, but fairly consistent reduction in level of the order of 1 to 2 dB as V_f/V_p is increased from 1.00 to 1.75. In contrast, at frequencies above approximately 4 KHz, the noise levels increase systematically as V_f/V_p increases, and at $V_f/V_p = 1.75$, the levels increase by as much as 6-7 dB.

The magnitudes of these noise reductions at low frequencies and noise increases at high frequencies do not change significantly as the observer moves from $\theta = 90°$ to $\theta = 50°$ (where θ is the microphone angle relative to the jet *exhaust*). At $\theta = 30°$ [Figure 2.2(a)], however, these noise level changes are greatly enhanced; the maximum noise reductions (which occur between 1 and 2 KHz) at low frequencies are now ~8 dB, and the maximum noise increases at high frequencies are ~9 dB. The net result is that the reference jet ($V_f/V_p = 1$) spectrum, which has the characteristic peaky shape of a single jet noise spectrum at $\theta = 30°$, has changed progressively to a double-peaked shape as V_f/V_p is increased from 1.00 to 1.75. (The minor peak around f = 63 KHz in most of the spectra is tentatively attributed to the noise generated by the wake of the primary nozzle lip.)

The corresponding spectral results at $T_f/T_p = 1.75$ and 2.00 are shown in Figures 2.3 and 2.4, respectively. The effects of V_f/V_p at these two temperature ratios are qualitatively very similar to the effects discussed above for the $T_f/T_p = 1.00$ case. The two minor quantitative differences worth noting are (i) at $\theta = 90°$, velocity ratio has virtually no effect on the low frequency

noise levels for the $T_f/T_p = 2.00$ case [see Figure 2.4(d)], and (ii) at $\theta = 30°$, the high-frequency noise increases are as much as 13 dB for the $T_f/T_p = 2.00$ case [see Figure 2.4(a)] compared to ~9 dB for the $T_f/T_p = 1.00$ case [Figure 2.2(a)] discussed above.

The effects of fan-to-primary static temperature ratio (T_f/T_p) on 1/3-octave SPL spectra at several angles are shown in Figures 2.5 and 2.6, where the velocity ratio (V_f/V_p) is held constant at 1.00 and 1.55, respectively. That is, the temperature ratio effects are examined independently here. Unlike velocity ratio, temperature ratio does not appear to be a significant parameter in coannular jet noise, and "inverted velocity" effects are much more powerful than "inverted temperature" effects. For a fixed velocity ratio, the only noticeable effect of temperature ratio (relative to the $T_f/T_p = 1.00$ case) is that it provides a small reduction in high-frequency noise levels at small angles to the jet axis, as shown in Figures 2.5(a) and 2.6(a).

The overall sound pressure levels of jet mixing noise for all test conditions defined in Table 2.1 are plotted on a relative basis in Figure 2.7, where the difference ΔOASPL between the inverted profile coannular jet OASPL (i.e. $V_f/V_p > 1$ and/or $T_f/T_p > 1$) and the flat profile reference jet OASPL (i.e. $V_f/V_p = 1$ and $T_f/T_p = 1$) is plotted against V_f/V_p at several angles. That is, a positive ΔOASPL indicates a noise increase, whereas a negative ΔOASPL indicates a noise reduction relative to the fully-mixed equivalent single jet. At large angles to the jet axis ($\theta = 70°$, 90°, and 110°), the noise levels increase as the velocity ratio increases. This is due to the increase in the high-frequency noise levels observed earlier in the spectral results. At $\theta = 50°$, this trend in ΔOASPL begins to reverse, and at $\theta = 30°$, the OASPL's decrease as V_f/V_p increases. It indicates that the low-frequency noise reductions at this angle are more powerful than the high-frequency noise increases, thus resulting into a net decrease in the overall sound pressure levels. The maximum reduction in OASPL is about 4 dB, and this occurs over a range of V_f/V_p from 1.4 to 1.8. Finally, at most V_f/V_p values, the ΔOASPL's for the three values of T_f/T_p are nominally within 1 dB of each other, thus indicating once again that temperature ratio is not a significant parameter in controlling the noise reduction (or increase) in coannular jets.

2.3.2 Sound Power Level Results

The polar sound pressure level results (lossless data) were used to compute the corresponding sound power levels at all test points, using conventional procedures.

The variation of sound power level spectrum with velocity ratio (V_f/V_p) is shown in Figure 2.8 for a constant value of temperature ratio ($T_f/T_p = 1.00$). For the reference jet ($V_f/V_p = 1$), the PWL spectrum has a single peak at 1.25 KHz, and the levels on either side of the peak drop off rapidly in a manner consistent with single jet noise characteristics. As the velocity ratio increases, the peak level drops, and the high-frequency levels increase significantly. The cross-over frequency remains constant at about 4 KHz for the velocity ratios considered in these experiments.

The effect of temperature ratio (T_f/T_p) on PWL spectrum is shown explicitly in Figure 2.9, where the velocity ratio is kept constant at unity. As observed previously in the SPL results, inverted temperature has little effect on turbulent mixing noise from a coannular jet, except at the high-frequency end where the radiated sound energy decreases slightly when T_f/T_p is increased from 1.00 to 2.00.

The overall sound power levels for all subcritical test points were calculated by adding the 1/3-octave band PWL's, and the results are presented in Figure 2.10 on a relative basis, in a manner similar to the OASPL plot of Figure 2.7. The figure shows that inverted-velocity profile coannular jets at subcritical conditions do radiate less acoustic energy compared to that radiated from a fully-mixed equivalent single jet at identical thrust, mass flow rate and exit area; however, this reduction is rather small (of the order of 2 dB) on the decibel scale.

2.3.3 Perceived Noise Level (PNL) Results

The model-scale acoustic data presented above were finally transformed to larger-scale conditions using standard scaling procedures for jet noise. Although a scale factor of 20 would have been more appropriate to obtain results for a full-scale engine suitable for AST application, such a large scale factor would reduce the maximum frequency of 80 KHz in the model scale to 4 KHz in the full scale, which is rather low. A scale factor of ten was, therefore, used for this purpose, and this resulted into the following specifications for the larger-scale configuration:

Equivalent nozzle diameter = 0.66 m (26 in.)
Total exit area = 0.3425 m^2 (3.69 ft^2)
Total thrust = 26490 Newtons (5950 pounds)
Total mass flow rate = 73.5 kg/sec (162 pounds/sec).

The lossless larger-scale data were then subjected to atmospheric attenuation corrections for standard FAA day (25°C, 70% relative humidity), and static PNL's in PNdB were calculated for three sideline distances of 61 m (200 ft.), 244 m (800 ft.), and 649 m (2128 ft.).

The variation of (static) *peak* PNL with velocity ratio and temperature ratio for the twelve subcritical test points specified in Table 2.1 is shown in Figure 2.11. Once again, the PNdB levels for the coannular jet are plotted relative to the reference jet level (which is shown by the broken line) at each sideline distance considered. It can be seen that although the inverted-velocity-profile coannular jet radiates less acoustic energy compared to the fully-mixed equivalent single jet, the coannular jet becomes subjectively noisier as the velocity ratio V_f/V_p is increased. This result is a direct consequence of the high-frequency noise increase in IVP coannular jets, which is weighted higher in the standard PNL calculation procedures. For the same reason, the magnitudes of the PNdB increases fall as the sideline distance increases, due to the increasing atmospheric attenuation of sound with distance at these higher frequencies. Eventually, at very large sideline distances, the higher frequencies would be attenuated to such an extent that the low-frequency noise reductions would begin to increase the PNL's, and a reduction in PNdB with V_f/V_p can be expected to occur.

Finally, for the sake of completeness, the SPL spectra for the two supercritical test points (i.e., TP's 13 and 14 defined in Table 2.2) are presented in Figures 2.12 and 2.13, respectively.

2.4 CONCLUSIONS

The noise characteristics of inverted-velocity-profile coannular jets operated at subcritical pressure ratios have been measured in the Lockheed anechoic facility using a coannular nozzle configuration of fan-to-primary area ratio $A_f/A_p = 0.747$ and equivalent nozzle diameter $D_{eq} = 6.6$ cm. The test program was designed to isolate the "inverted velocity" effects from the "inverted temperature" effects for coannular jets *having constant thrust, mass flow rate and exit area*. The fully-mixed equivalent single jet velocity (or specific thrust) for each point in the test matrix was 365 m/sec (1200 ft/sec). Although this value is not in the optimum range for coannular jet noise reduction, it was chosen mainly for the purpose of studying trends in jet aerodynamics.

The results from the acoustic experiments have been analyzed to determine the magnitudes of the noise reductions (or increases), and the angle and frequency regimes over which the noise changes (i.e. reductions or increases) relative to the fully-mixed equivalent single jet are maximum. At high frequencies, the noise levels increase as the fan-to-primary velocity ratio (V_f/V_p) increases. At low frequencies, however, the coannular jet is quieter at small angles to the jet exhaust. The effect of inverted temperature profile is insignificant compared to the effect of inverted velocity profile.

For the area ratio of 0.75 and at the fully-mixed equivalent single jet velocity of 365 m/sec considered in the present experiments, the total acoustic energy radiated by the coannular jet is approximately 2 dB lower than that radiated by the reference jet. The present results are consistent with the coannular jet noise data obtained previously by other investigators (refs. 2.1 and 2.2). At other area ratios and especially for higher equivalent jet velocities, larger noise reductions have been observed in these previous studies.

In the present investigation, only the turbulent mixing noise component of the total noise from coannular jets is examined. For coannular jets operated at supercritical conditions, significant noise reductions have been observed by other investigators even at the higher frequencies. However, a systematic study is required to quantify these shock noise reductions explicitly.

Finally, it must be recognized that even at subcritical (i.e. shock-free) jet operating conditions, the inverted-velocity-profile concept offers an excellent opportunity to suppress the *low-frequency* jet mixing noise component which has hitherto been very difficult to achieve. Taken together with the lined ejector technology to suppress the high-frequency noise components (which are generated close to the nozzle exit), this low-frequency noise benefit can in principle be exploited in a specific practical application.

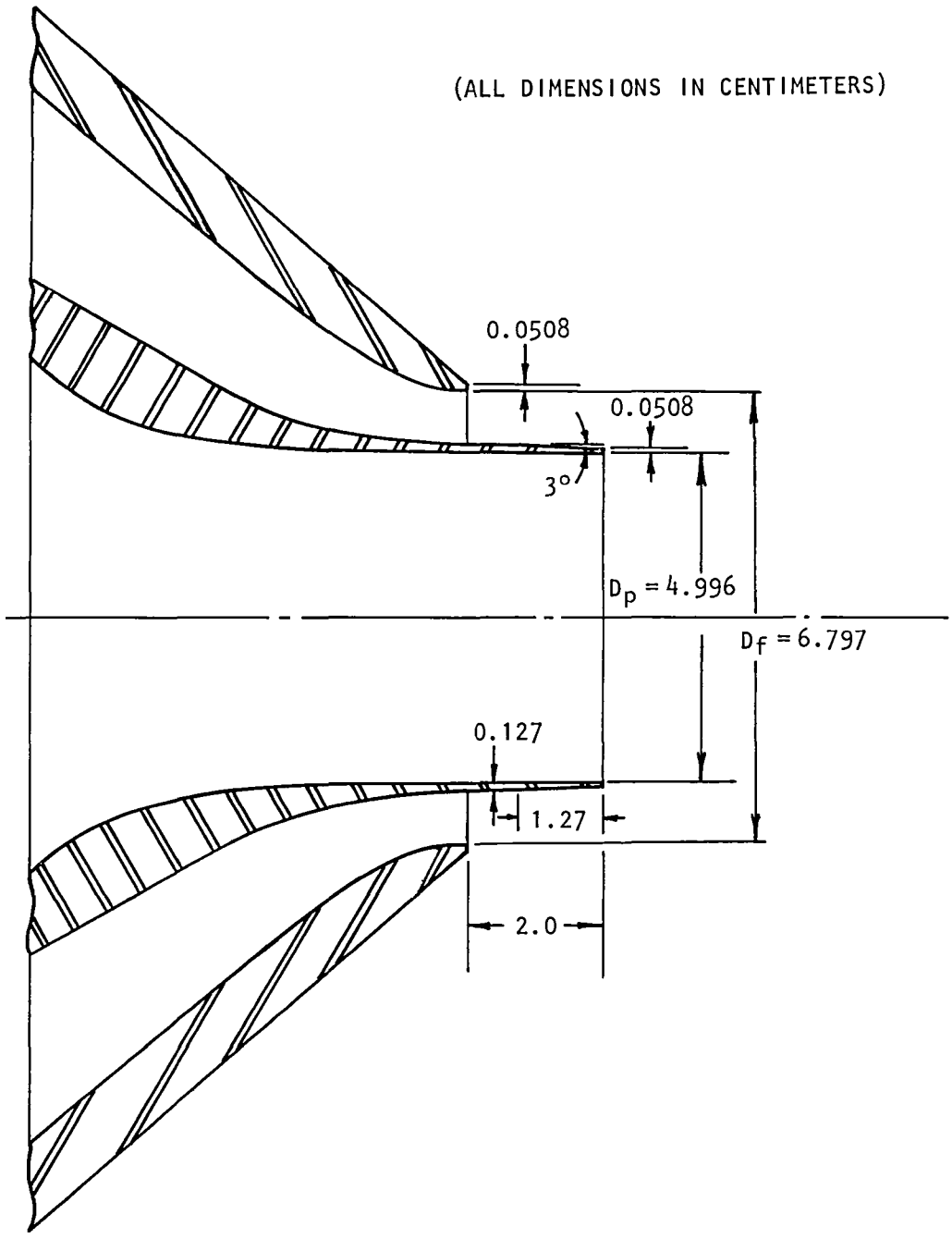

Figure 2.1 Coannular nozzle configuration.

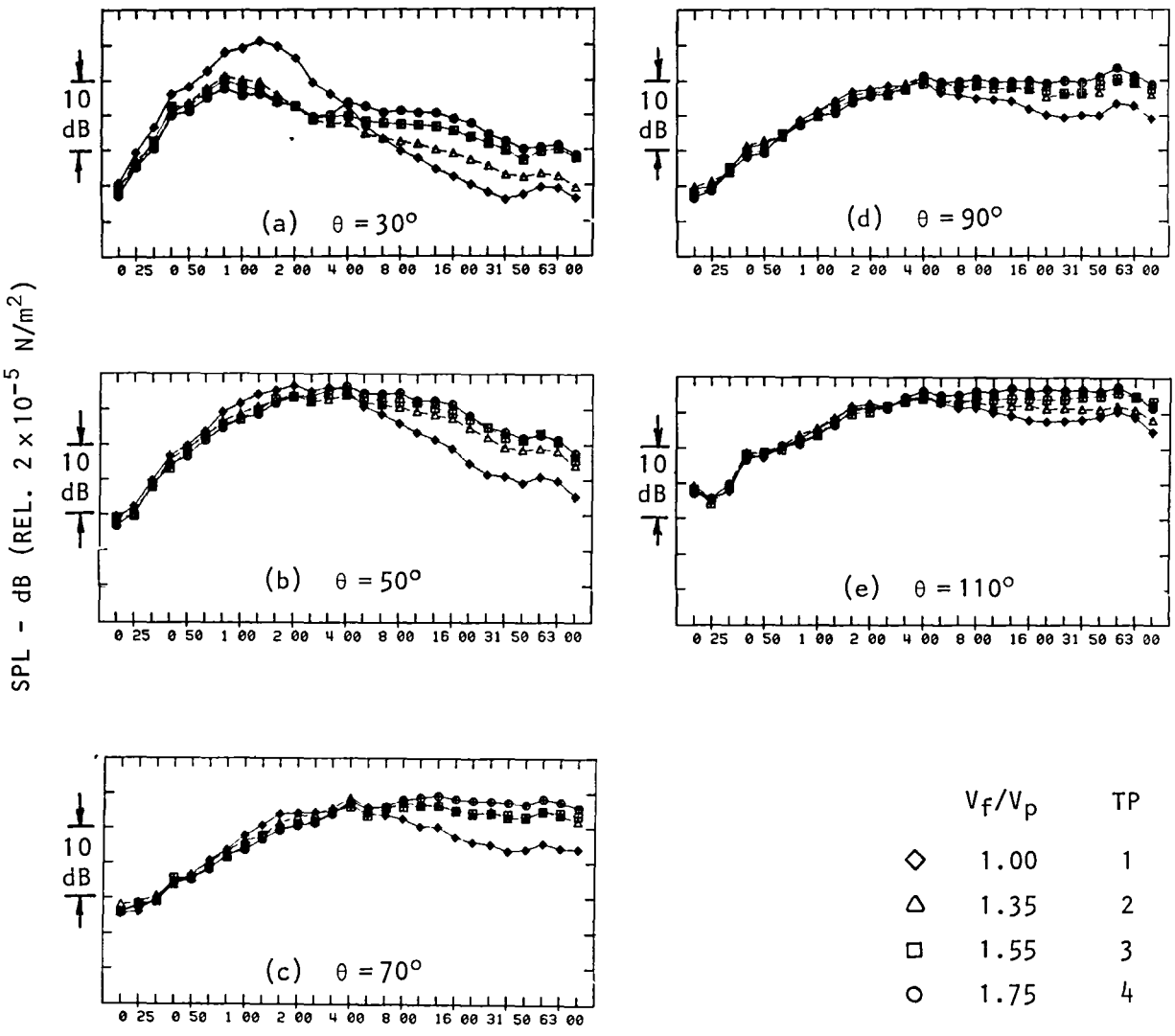

Figure 2.2 Variation of SPL spectra with V_f/V_p for constant $T_f/T_p = 1.00$.

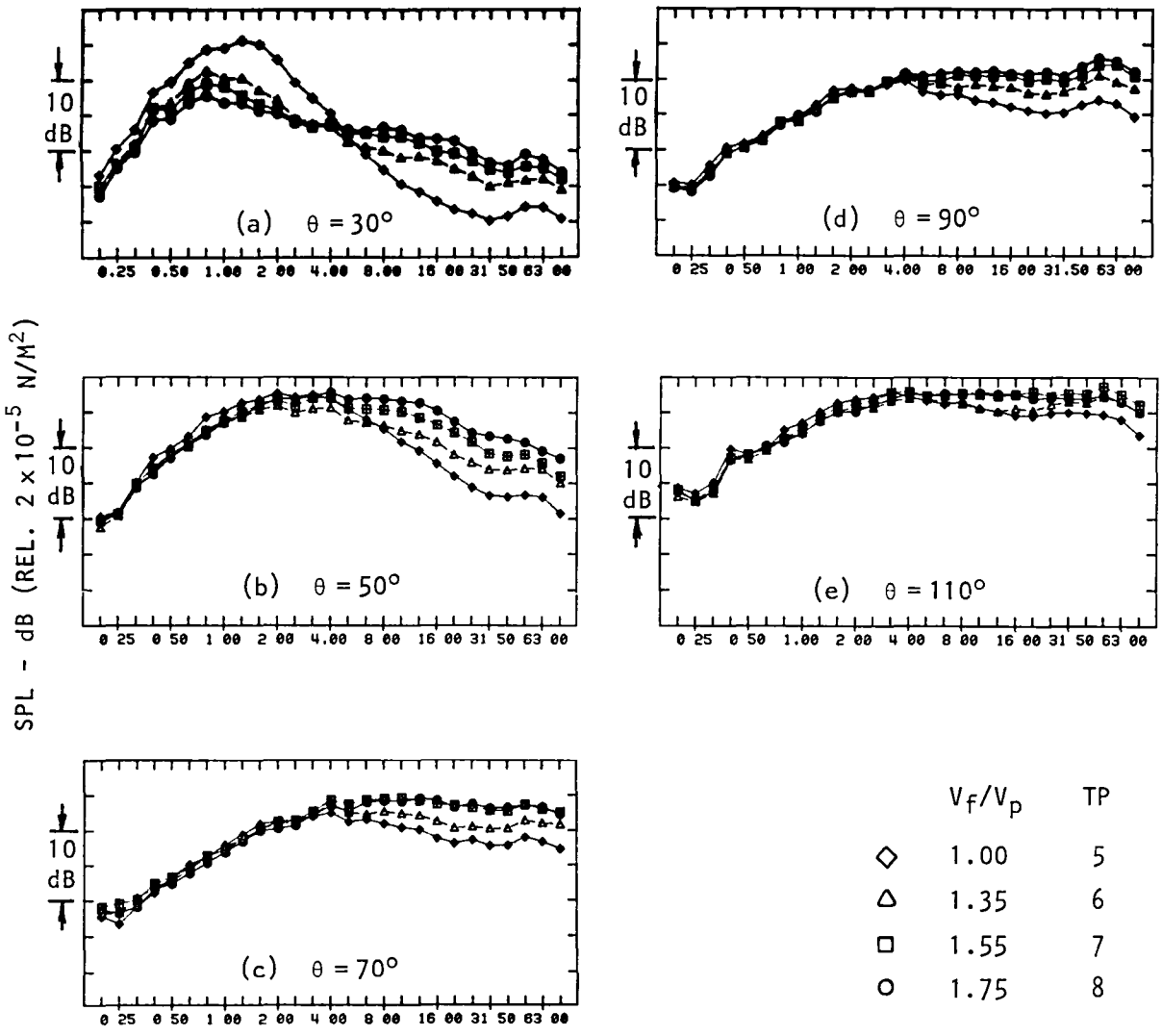

Figure 2.3 Variation of SPL spectra with V_f/V_p for constant $T_f/T_p = 1.75$.

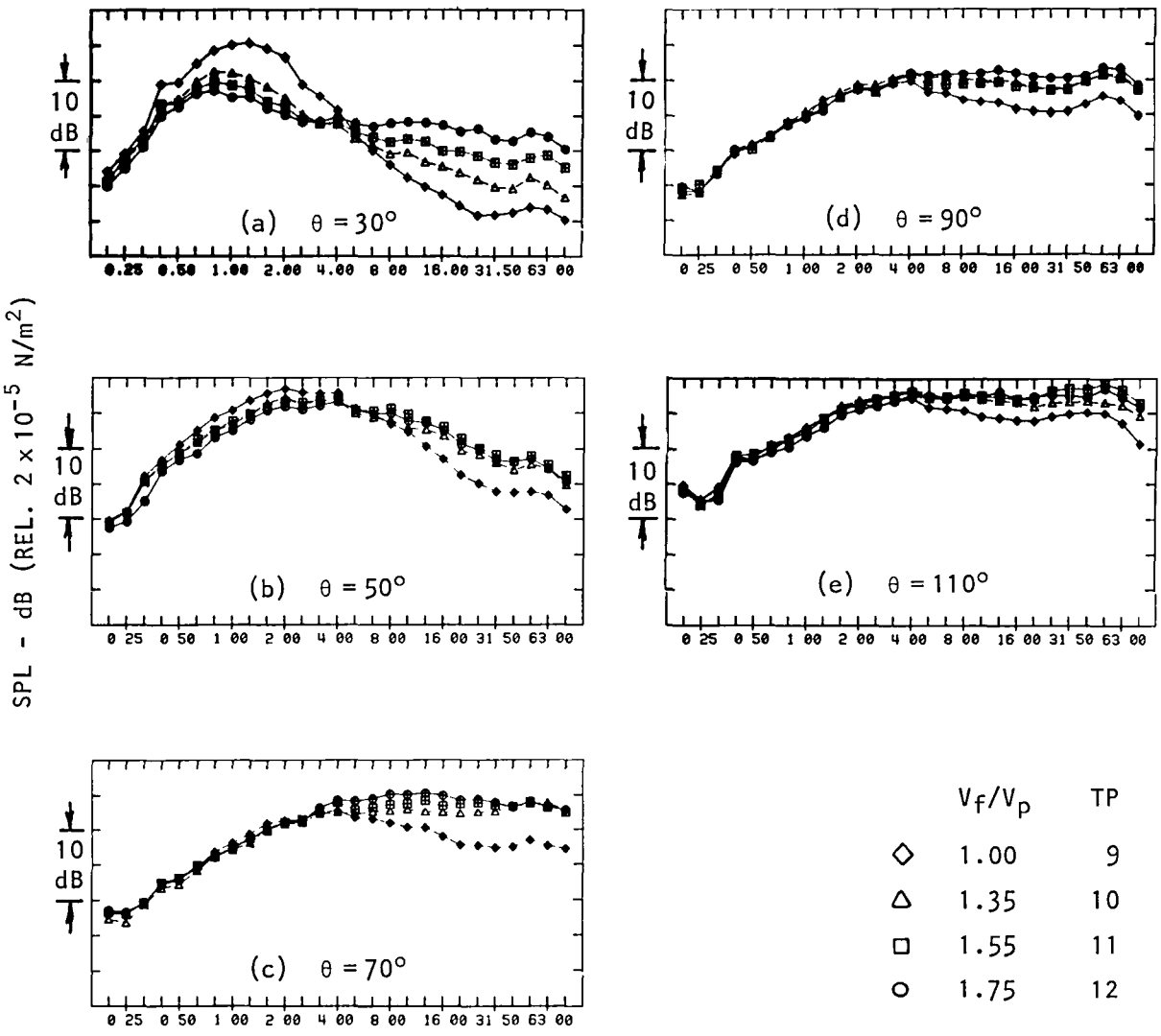

Figure 2.4 Variation of SPL spectra with V_f/V_p for constant $T_f/T_p = 2.00$.

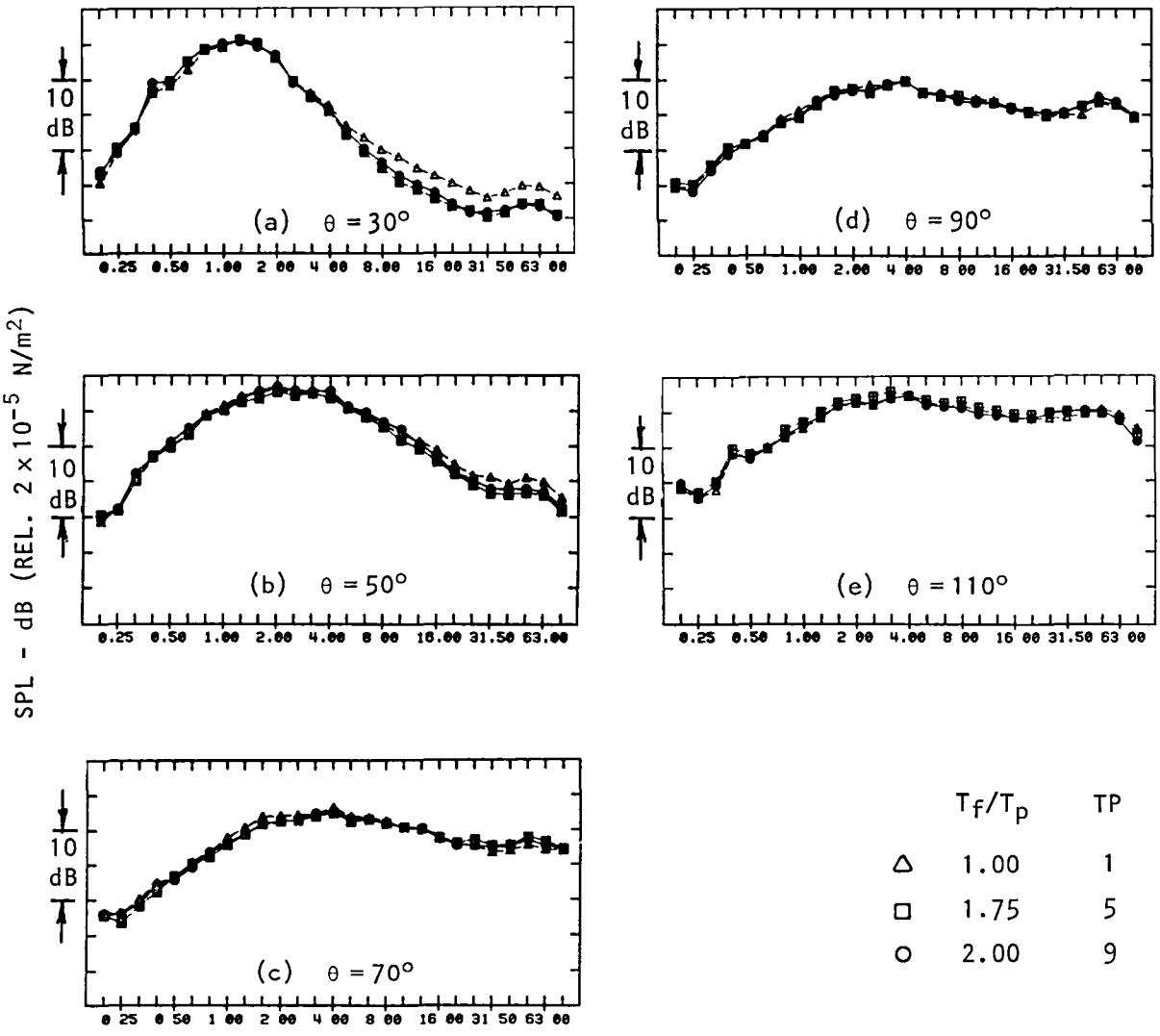

Figure 2.5 Variation of SPL spectra with T_f/T_p for constant $V_f/V_p = 1.00$.

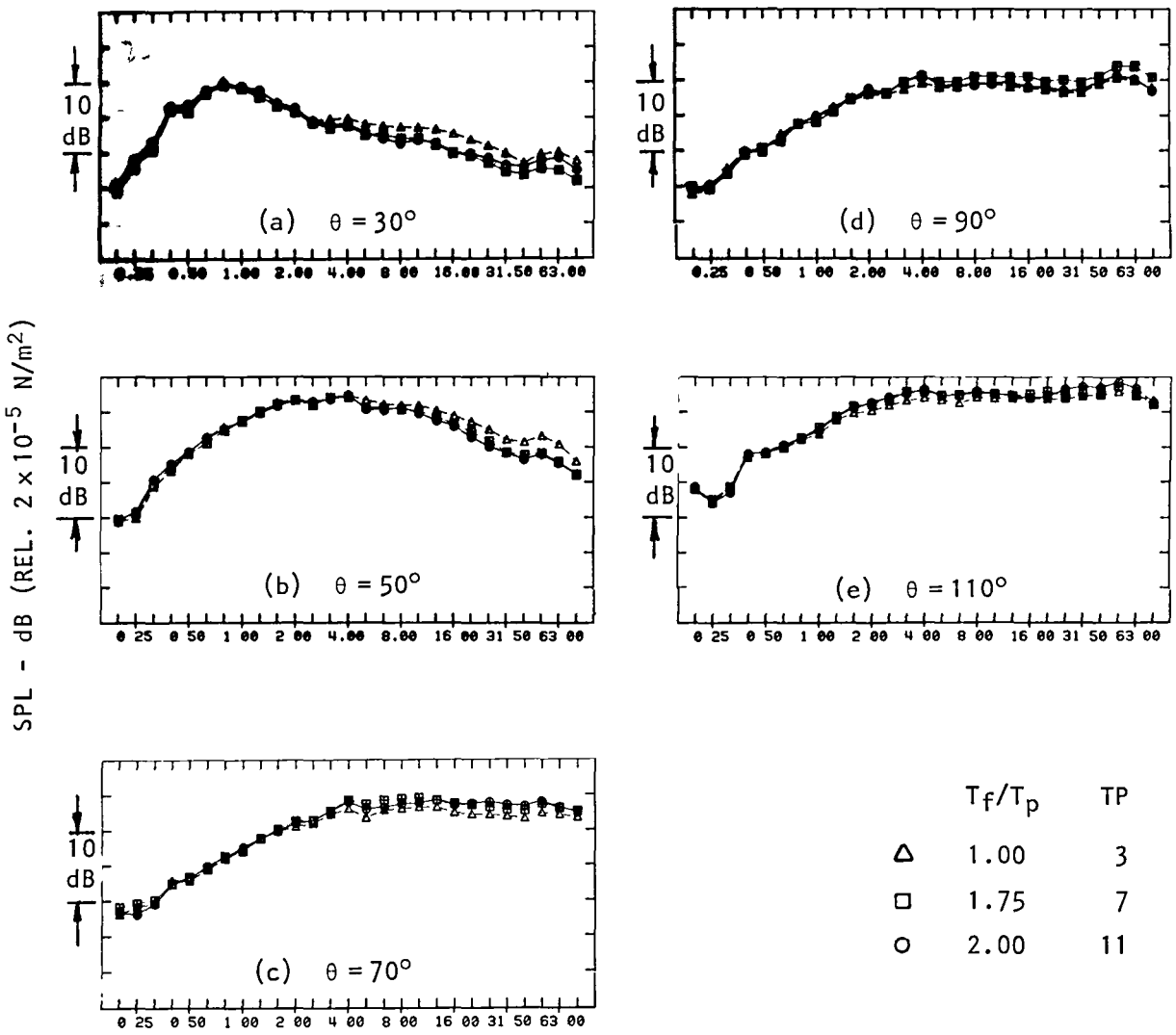

Figure 2.6 Variation of SPL spectra with T_f/T_p for constant $V_f/V_p = 1.55$.

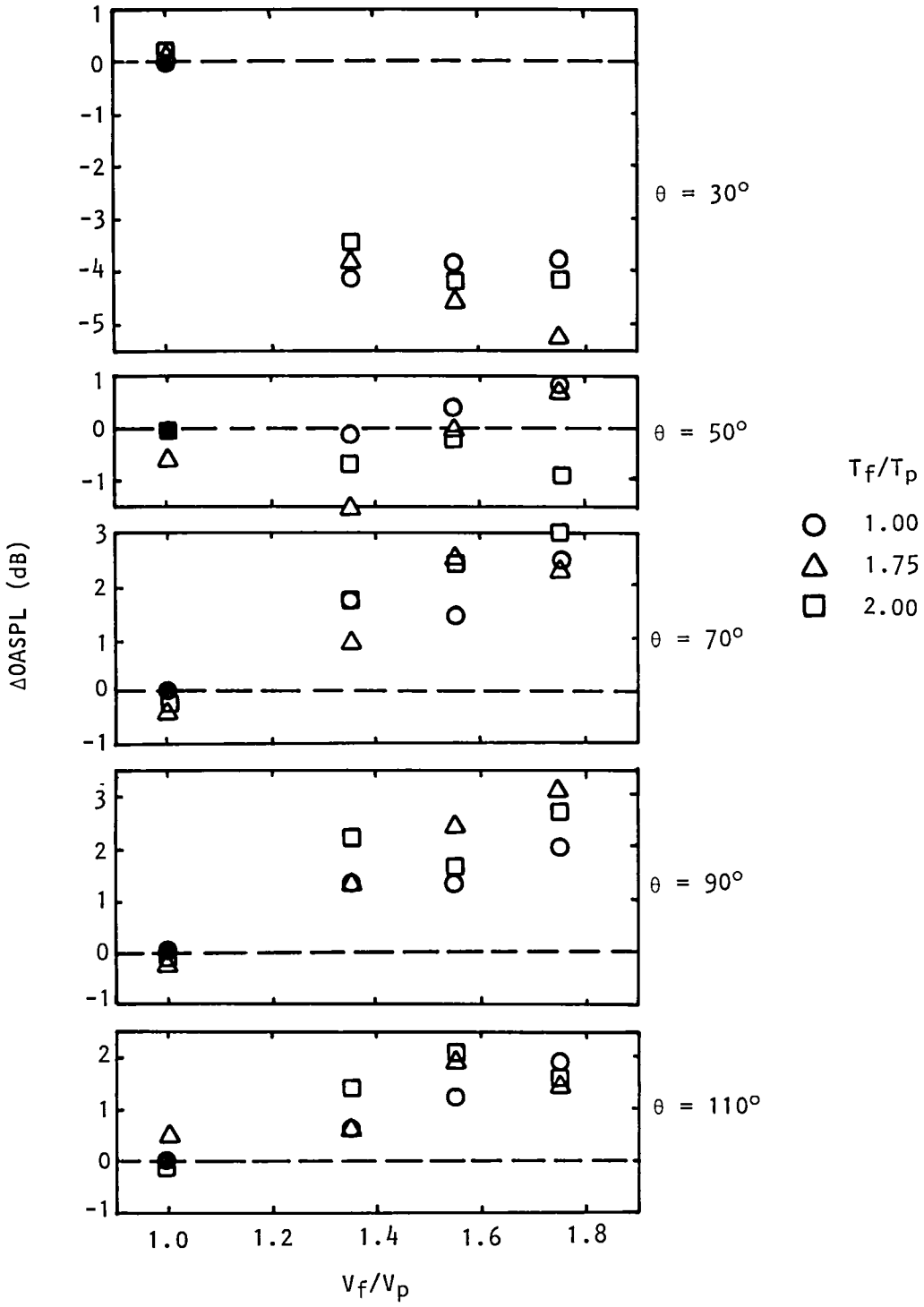

$$\Delta OASPL\ (V_f/V_p,\ T_f/T_p) = OASPL\ (V_f/V_p,\ T_f/T_p) - OASPL\ (V_f/V_p = 1,\ T_f/T_p = 1)$$

Figure 2.7 Variation of ΔOASPL with V_f/V_p and T_f/T_p.

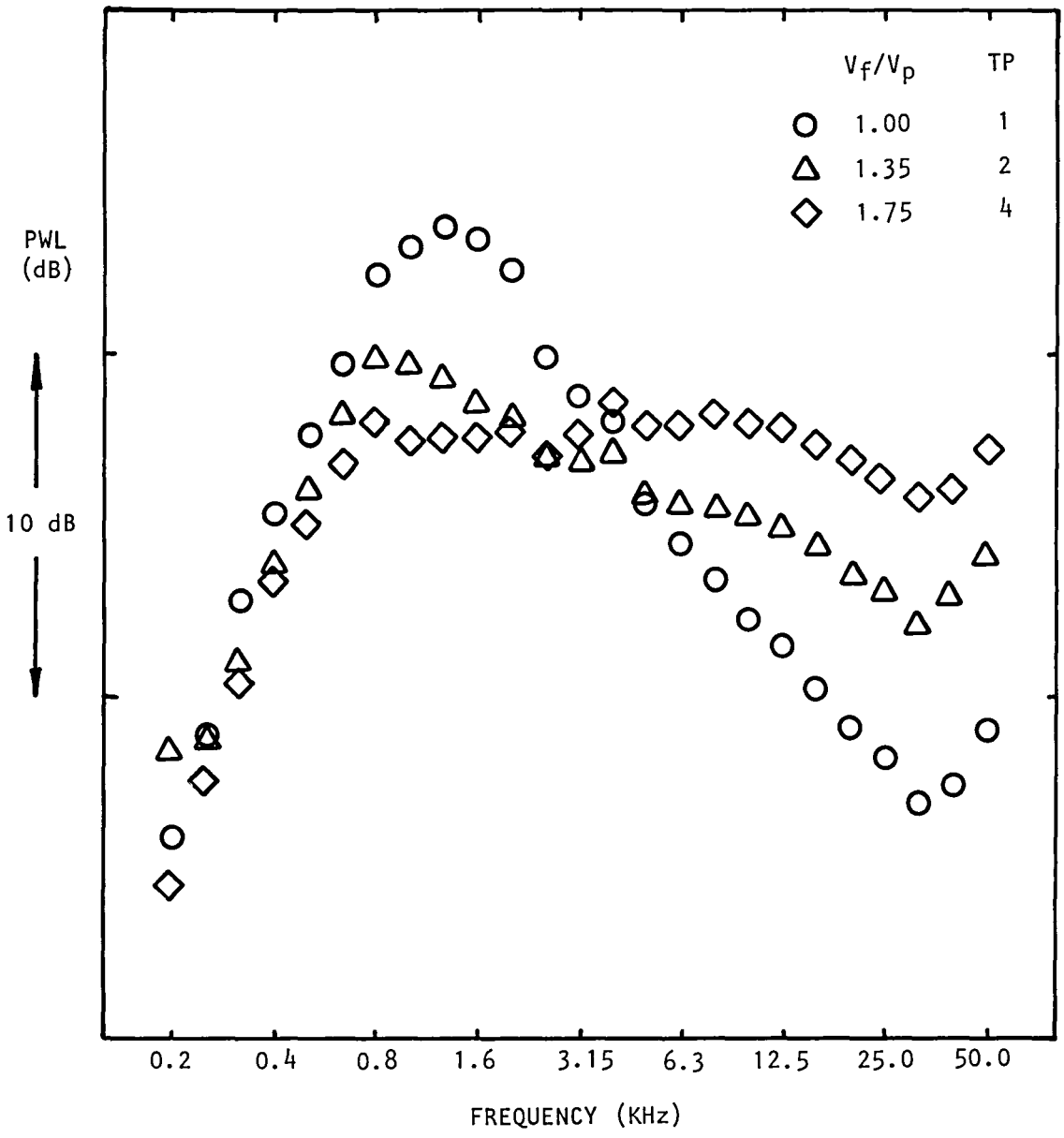

Figure 2.8 Variation of PWL spectrum with V_f/V_p for constant $T_f/T_p = 1.00$.

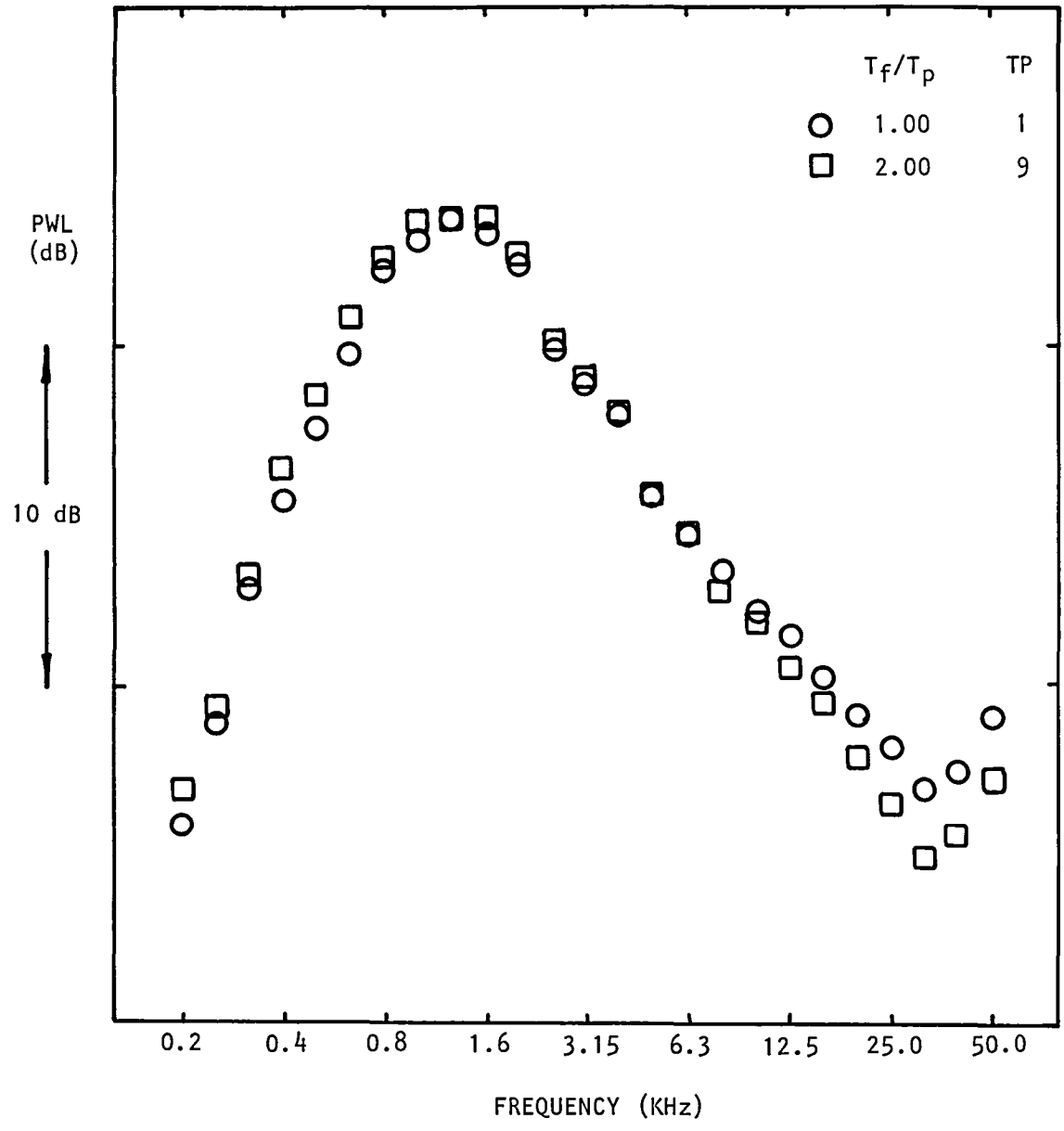

Figure 2.9 Variation of PWL spectrum with T_f/T_p for constant $V_f/V_p = 1.00$.

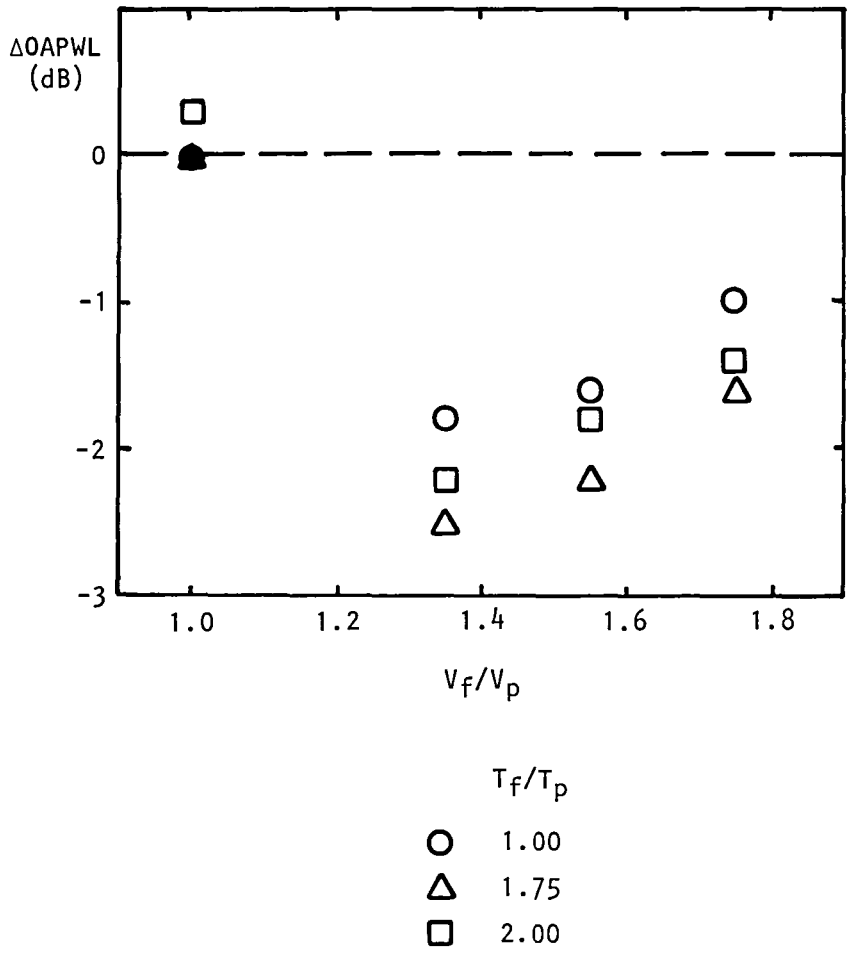

$$\Delta OAPWL\ (V_f/V_p,\ T_f/T_p) = OAPWL\ (V_f/V_p,\ T_f/T_p) - OAPWL\ (V_f/V_p = 1,\ T_f/T_p = 1)$$

Figure 2.10 Variation of ΔOAPWL with V_f/V_p and T_f/T_p.

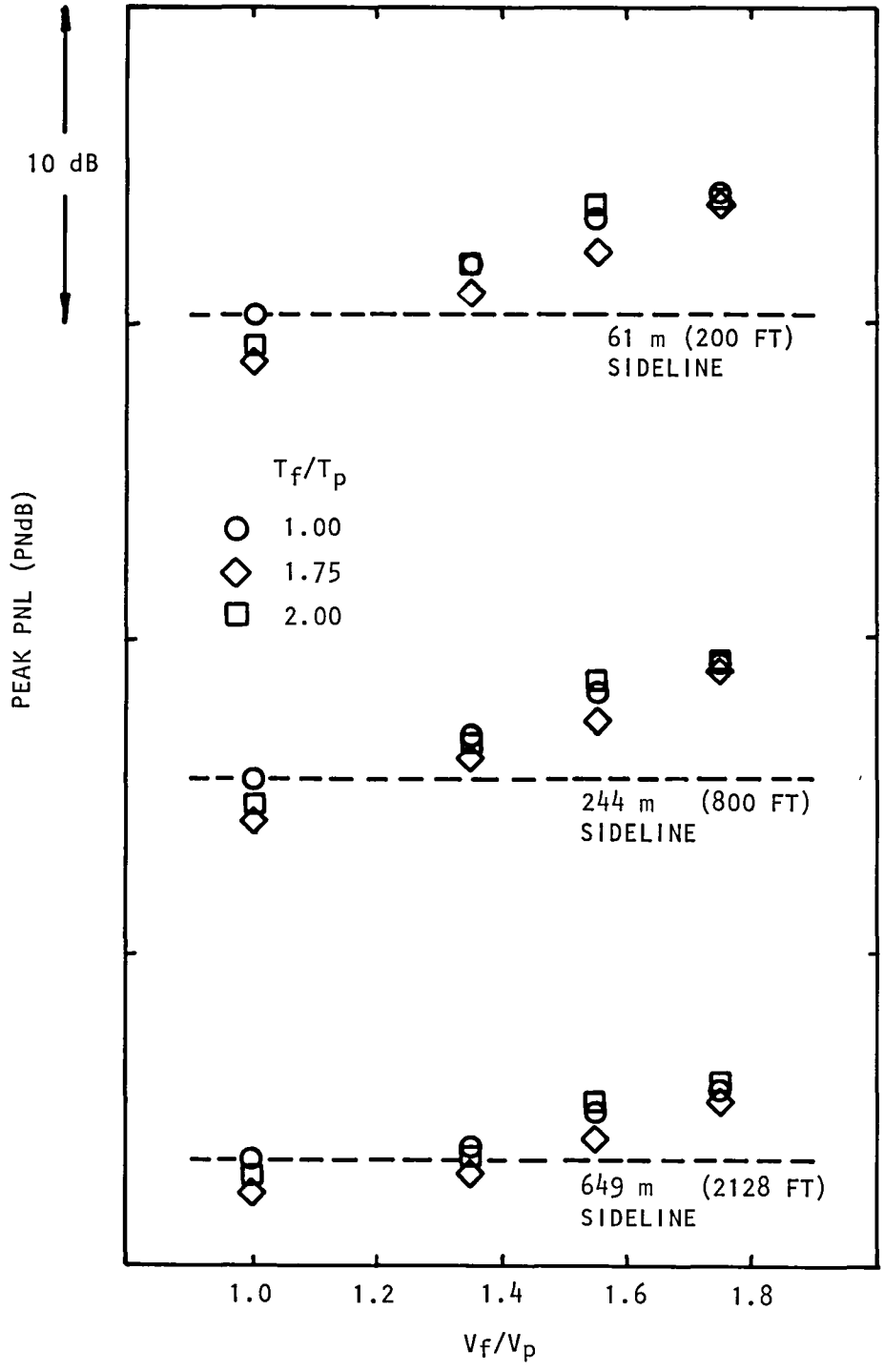

Figure 2.11 Variation of static peak PNL with V_f/V_p and T_f/T_p at several sideline distances.

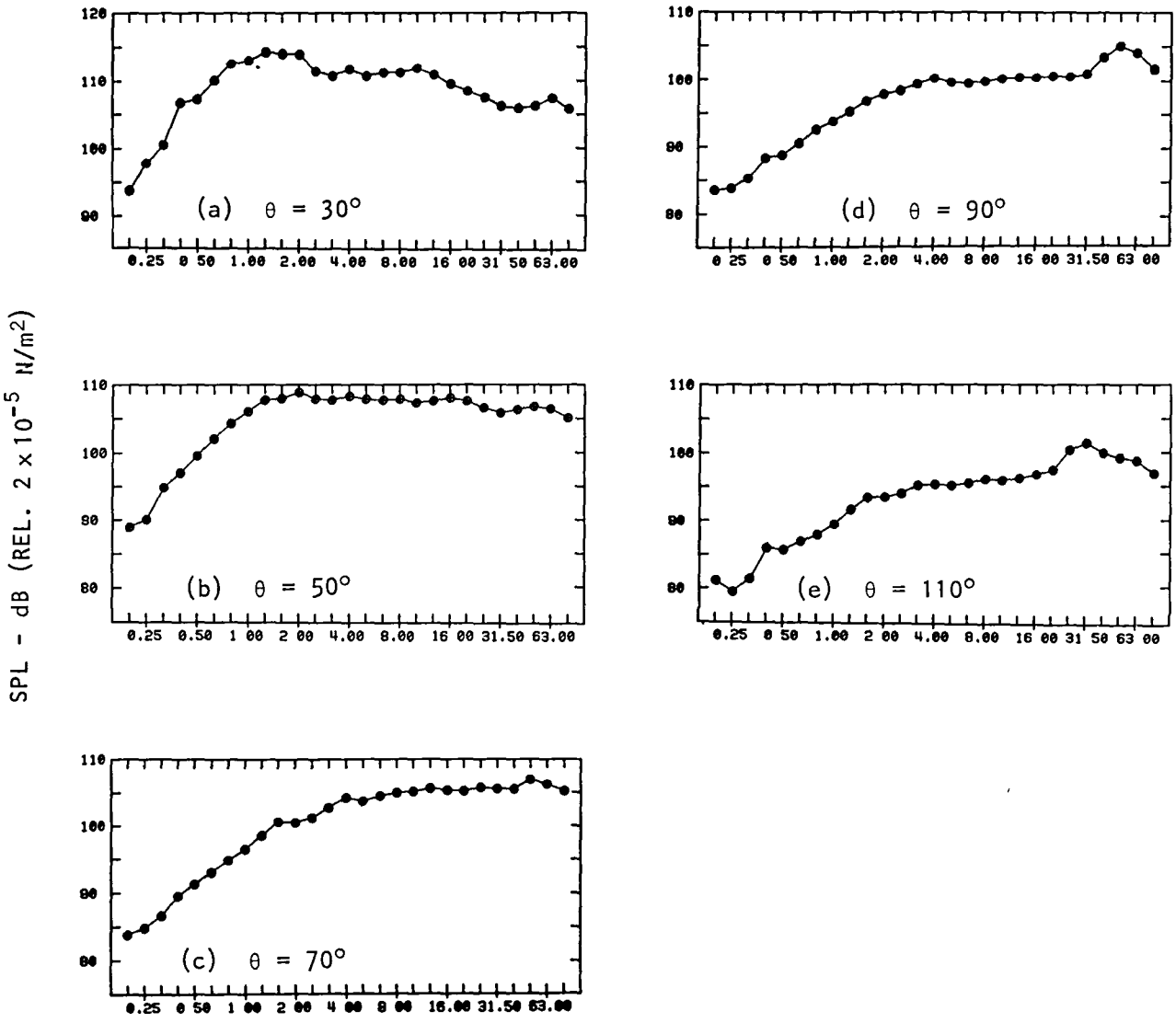

Figure 2.12 SPL spectra for TP 13.

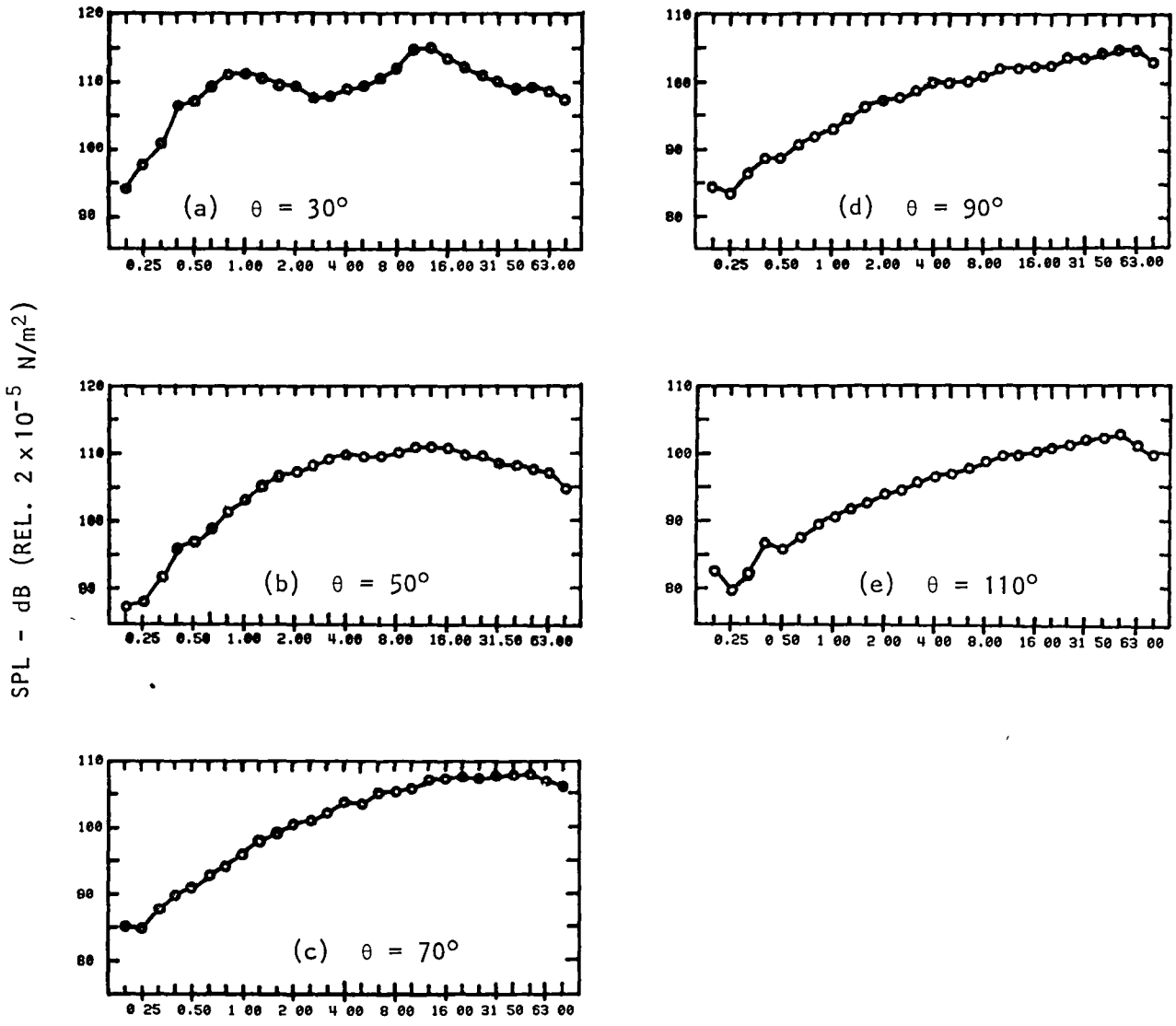

Figure 2.13 SPL spectra for TP 14.

3. SOURCE LOCATION MEASUREMENTS AND RESULTS

Axial distributions of the mixing noise source(s) in the coannular jet flow at all test points specified in Tables 2.1 and 2.2 of the previous section have been derived from far-field, *two-point* measured acoustic data (obtained in the Lockheed anechoic facility) with the so-called Polar Correlation Technique (ref. 3.1). Although "source image" information of this kind is limited in accuracy by various factors (as discussed in refs. 3.1 and 3.2), it is reasonable to assume that, within a given frequency band, the axial peak is a reliable indication of the dominant noise-generation location in the jet flow. This information is used, for example, to calculate convective amplification alteration effects from LV measurements of the convection velocity (Section 5), that is, LV measurements† at axial locations determined by the peaks in the axial source distributions.

Within their inherent resolution limitations, the source image results also provide a measure of the axial extent of the source distribution and, potentially, the results can display more than one peak if individual source regions are sufficiently well separated on a wavelength scale. No solid evidence of this phenomenon has been found in the present results, however.

Images of the axial source distributions can be constructed, in principle, for different observer or "reference" angles to the jet axis, but in most results published to date, with the exception of those in reference 3.3, the reference angle is 90° to the jet axis. In the present investigation also, the results are confined to this reference angle; although measurements *were* taken to provide the necessary data for the calculation of source images as viewed from a reference angle of 20°, recording difficulties prevented the data from being analyzed. This information may have been particularly useful since the maximum noise reductions from shock-free coannular jets are found to be at small angles to the (downstream) jet axis.

3.1 DATA ACQUISITION

The two-point data for source distribution calculations were acquired simultaneously with a fixed microphone array on a polar arc, of radius 3.048 m (10 feet), centered at the intersection of the jet axis and the *primary* nozzle exit plane. The output from each microphone, after signal conditioning was recorded on one of the three multi-channel tape recorders (Honeywell 7600, Ampex FR1300 and an Ampex Loop Machine) at a tape speed of 1.524 m/sec (60 inches/sec).

†*Or interpolations of the measured data.*

In order to "calibrate out" any phase† differences between channels (on playback) caused by differences in (1) transducer response (i.e. the microphone "button"), (2) signal conditioning (e.g. cathode follower cable, Sanborn amplifiers), and (3) tape recording, the following phase calibration procedure was adopted.

The non-identical phase response of each microphone "button" was measured by inserting two microphones into a small enclosure excited by an acoustic source of broadband noise. One of these microphones was used simply to provide a phase reference; the other microphone and signal conditioning channel was used to obtain a relative phase measurement, over the frequency range from 60 Hz to 30.66 KHz in steps of 60 Hz, for each of the microphone buttons to be calibrated. The difference between each "button phase" and the 90°-reference "button phase" was denoted by ψ_b.

The non-identical phase response of each signal conditioning and tape recording channel combined - relative to that of the 90°-reference channel - was measured by recording the signal generated by a voltage applied to the cathode follower. The phase of the transfer function of that voltage and the output voltage on playback was measured and the difference between this phase and that of the 90°-reference channel was denoted by ψ_c. The sum of ψ_c and ψ_b (the "button" calibration phase) was denoted by ψ. This total calibration phase at each frequency (60 Hz to 30.66 KHz in steps of 60 Hz) and for each microphone channel was stored on a computer file for future use in calibrating any phase values obtained from the recorded data, as described below.

In order to minimize any phase differences between channels caused by microphone radial position errors (i.e. propagation time differences between the center of array and microphone), adjustments were made to each microphone position as follows. The same phase calibration procedure was adopted as described above, except in this case the tape recorders were not included, that is, a total, relative calibration phase, ψ', was obtained for each microphone button and signal conditioning channel only (at selected frequencies). The 90° reference microphone was positioned at a fixed radius with all the other microphones positioned on the polar measurement arc at nominally the same radius (3.048 m) and with a broadband-noise "point" source positioned at the center of the arc (the coannular nozzles were removed for this purpose). The phase of the cross spectrum of each microphone channel with that of the 90° reference channel was displayed and compared with the calibration phase ψ' at three frequencies (3, 6 and 9 KHz). Differences at these frequencies were then minimized by moving the microphone radially inwards or outwards. Since the phase error caused by propagation time differences should be simply proportional to frequency, this procedure was judged to be adequate, except perhaps for very high frequencies (>>10 KHz).

---

†*Phase in the statistical sense, e.g. phase of the cross spectrum.*

Table 3.1 Source location measured SPL's at reference angle (90°) (60 Hz constant bandwidth).

				FREQUENCY (Hz)						
Test Point	Run No.	V_f/V_p	T_f/T_p	300	600	1200	2460	4980	9960	19980
1	4	1.00	1.00	83.1	85.1	87.3	86.3	81.3	77.6	72.6
2	3	1.35	1.00	82.7	84.9	86.8	85.8	81.4	79.1	74.4
3	2	1.55	1.00	81.8	84.2	85.8	84.8	80.9	79.2	74.6
4	1	1.75	1.00	81.4	83.6	85.3	85.0	81.7	80.3	75.7
5	8	1.00	1.75	82.3	83.9	86.2	85.5	81.1	76.2	71.7
6	7	1.35	1.75	82.3	83.8	86.3	85.9	81.7	78.4	74.4
7	6	1.55	1.75	83.3	85.2	87.2	86.9	83.4	80.4	76.5
8	5	1.75	1.75	82.2	84.2	86.3	86.3	82.8	80.8	76.8
9	16	1.00	2.00	82.7	84.2	86.4	85.9	81.9	76.5	71.9
10	15	1.35	2.00	82.2	83.7	85.8	85.7	82.3	78.4	74.0
11	14	1.55	2.00	--	--	--	--	--	--	--
12	13	1.75	2.00	80.8	82.8	84.9	84.8	81.3	79.5	75.3
--	11	$V_p/a_o = 0.90$	$T_p/T_o = 0.84$	77.4	79.8	81.9	81.7	77.4	74.7	69.8
--	12	$V_p/a_o = 1.04$	$T_p/T_o = 1.91$	77.8	80.6	84.0	84.3	80.6	79.5	74.1
14	9	1.95	2.47	91.4	93.2	95.7	96.2	94.6	91.8	86.6
13	10	1.66	1.26	89.9	91.6	93.7	93.9	90.5	91.4	88.2
13	17*	1.66	1.26	90.2	92.5	93.7	93.9	92.3	90.1	86.5

**Repeat of Run Number 10.*

Noise data were recorded at the twelve subcritical test points described in the previous section (Table 2.1), at two test points with the fan stream turned off and at two supercritical test points (defined in Table 2.2) which are not discussed further in this section, but the results are included in Appendix 2 for completeness. The test points, with corresponding run numbers, are listed in Table 3.1, showing the coannular fan/primary velocity and temperature ratios (V_f/V_p, T_f/T_p) and the measured sound pressure levels at the 90° reference angle, for the several center frequencies that were selected for analysis.

3.2 DATA ANALYSIS: COHERENCE AND PHASE

The amplitude and phase information required by the Polar Correlation Technique was obtained with a Spectral Dynamics SD360 Analyzer at a constant bandwidth of 60 Hz. The amplitude information in the form of the coherence function, γ^2, did not require any calibration corrections. The quantity actually used in the source distribution calculations, $(\gamma^2)^{\frac{1}{2}}$, is illustrated in Figure 3.1 at the selected test frequencies and is referred to as the "Coherence." At low frequencies (300 Hz, 600 Hz) the coherence decays slowly with microphone separation angle; measurements were taken (and utilized) up to 69° but this last data-point is excluded in this and other figures for presentation purposes. At higher frequencies the coherence decays more rapidly until at the highest frequency (~20 KHz) the coherence is less than 10% at a separation of 4° in this example. The maximum separation or "aperture" was maintained at the values shown below in Table 3.2 for purposes of data analysis and presentation. In most cases, this involved a very minor truncation of the data. It should be noted that the results of Figure 3.1 are referred to by "Test Number" in the figure; *this is the same as the "Run Number"* and therefore, referring to Table 3.1, corresponds in this case to Test *Point* Number 4.

Table 3.2 Constant aperture angle selected for each test frequency.

Frequency (Hz)	300	600	1200	2460	4980	9960	19980
α_{max} (deg.)	68.96	68.96	68.96	68.96	19.47	13.49	9.59

The phase information required for the source distribution calculations is the phase of the cross-spectral density. From this phase – obtained with the SD360 also – the calibration phase, ψ, (see previous Section 3.1) was subtracted to obtain the "true phase," which is illustrated in Figure 3.2. The comments on the coherence results of Figure 3.1 apply here as well; it should also be noted that, as in the previous figure, the data points are connected by straight lines, but this gives a slightly misleading impression with the phase data. That is, the large excursions in phase angle from

+180° to -180° are not real changes but simply result from re-defining the continuous phase function to lie in the interval (-180°, 180°), by subtracting multiples of 2π.

The coherence and phase data at all other test conditions are given in Appendix 2.

3.3 RESULTS AND DISCUSSION

The coherence and phase data have been utilized according to the theory of reference 3.1 to compute the axial source distribution at each test frequency for all the test conditions listed in Table 3.1. The main objective here is to investigate the influence of coannular jet velocity and temperature ratio V_f/V_p, T_f/T_p on the axial peak location and shape of the source distribution.

The effect of velocity ratio V_f/V_p for $T_f/T_p = 1$ is shown in Figure 3.3. At each frequency the solid curve is the axial source distribution of the reference jet ($V_f/V_p = 1$). Corresponding distributions at the three different velocity ratios $V_f/V_p = 1.35$, 1.55 and 1.75 tend to be similar (to one another) in many instances and are noticeably different from the reference case; the best example of this is the set of distributions at 1200 Hz in Figure 3.3(c). The axial peak location and shape is virtually the same in all three cases but the peak of the reference distribution is located slightly further downstream and also it is a rather wider distribution. It is of interest to note that the peak level for $V_f/V_p = 1.35$ is higher than that of the reference level, but Table 3.1 shows that the coannular SPL (86.8 dB) is in fact lower (by 1/2 dB) than the reference SPL (87.3). Thus, the narrower source distribution in the coannular jet more than compensates for its higher peak level, yielding a smaller area "under the curve," i.e. a lower radiated SPL.

At *higher* frequencies, e.g. 9.96 KHz in Figure 3.3(f), the increase in noise level with increasing velocity ratio is quite evident although again the coannular source distributions are narrower than the reference distribution. However, at this frequency and the highest test frequency [19.98 KHz in Figure 3.3(g)], the results are becoming irregular, probably due to measurement, calibration and analysis errors in the phase data, and interpretation of the results is not straightforward.

Results showing the effect of velocity ratio (V_f/V_p) at the other temperature ratios ($T_f/T_p = 1.75$, 2.00) are given in Appendix 2 and have many features in common with the unit temperature ratio case discussed above.

The effect of temperature ratio at a given velocity ratio is illustrated in Figure 3.4. In these comparisons the velocity ratio is held constant, $V_f/V_p = 1.75$ – the highest velocity ratio – and the temperature ratio takes three values, $T_f/T_p = 1.00$, 1.75, and 2.00. As before, the

coannular jet distributions appear to be similar to one another in shape and peak position. At and above the frequency of 1200 Hz in Figures 3.4(c) through 3.4(f), the peak level at the intermediate temperature ratio $T_f/T_p = 1.75$ is consistently higher than that of the other two temperature ratios. However, this cannot be attributed to any specific reason, since the single-point acoustic data presented in Section 2 indicates that the 90° sound pressure levels are virtually unaffected by temperature ratio at these conditions.

Results at other velocity ratios are given in Appendix 2.

The principle conclusion to be drawn from these source distribution measurements is that the axial peak source location is quite insensitive to the velocity and temperature ratio of coannular jet flows, especially at low-to-medium frequencies. This is a particularly useful result for our modelling of low-frequency coannular jet noise reductions (relative to the case $V_f/V_p = T_f/T_p = 1$) in which measured mean velocity and turbulence data at each axial station are associated with a particular radiation frequency. Once that relation is established, it will be assumed that it is unaffected by the variation of coannular velocity and temperature ratio at the different shock-free test points under investigation.

In earlier work (ref. 3.3), an empirical relation between radiated frequency or Strouhal number, $S = fD/V_J$ and axial position, x_s, in the form

$$x_s/D = \{0.057S + 0.021S^2\}^{-\frac{1}{2}} \qquad (3\text{-}1)$$

was adopted, which is based on the source location data of Grosche (ref. 3.4) and Laufer et al. (ref. 3.5) for a single jet of diameter D and velocity V_J. This is probably a somewhat oversimplified relation in that the jet exit velocity and temperature can also influence the source distribution as the results of reference 3.3 demonstrate, although these are possibly second-order effects. However, to ensure that these effects are taken into account, the *present* axial peak location measurements are plotted *versus* Strouhal number in Figure 3.5 for comparison with the earlier Grosche/Laufer empirical curve. Results are given for the reference case ($V_f/V_p = T_f/T_p = 1$, $V_f/a_o = 1.042$, $T_f/T_o = 1.920$, $D_{eq} = 6.6$ cm) and also for the primary jet alone at two conditions labelled Run Numbers 11 and 12 in Table 3.1 (11: $V_p/a_o = 0.90$, $T_p/T_o = 0.84$; 12: $V_p/a_o = 1.04$, $T_p/T_o = 1.91$; $D_p = 4.996$ cm).

Except at the lowest Strouhal number the primary-jet-alone results (Run No. 11) for a nearly isothermal jet agree quite closely with the Grosche/Laufer curve but the effect of heating the jet to $T_p/T_o = 1.91$ at a slightly higher velocity (Run No. 12) is quite dramatic. The lower Strouhal number peaks lie much closer to the nozzle exit plane and this trend persists virtually throughout the range of Strouhal numbers. The results of real interest – from the coannular reference jet – reverse this trend, particularly at the medium-to-high Strouhal numbers, and agree much more closely with Equation (3-1) even though the two jet streams are at almost identical conditions to that of Run No. 12 (primary jet alone). At low Strouhal numbers, however, Equation (3-1) still overpredicts the distance of the peak from the nozzle. By simply multiplying the coefficient 0.057 in Equation (3-1) by a factor of two viz.

$$x_s/D_{eq} = \{0.114S + 0.021S^2\}^{-\frac{1}{2}} \qquad (3\text{-}2)$$

(since this coefficient controls the low-Strouhal number behavior), an alternative curve-fit is obtained which agrees better with the results of Run No. 12 and the reference jet, as shown in Figure 3.5. However, there is always a degree of uncertainty at low Strouhal numbers concerning the precise location of the peak, because the *real* peak lies somewhere between the measured value and the axial position of the distribution *centroid* (ref. 3.6).

Thus, measurements of mean flow and turbulence properties at a particular axial station can be associated only with a *band* of Strouhal numbers - of the order of one octave in width for small values of S - and Equations (3-1) and (3-2) can perhaps be regarded as providing an indication of the upper and lower limits of this band (or rather the inverse of those equations).

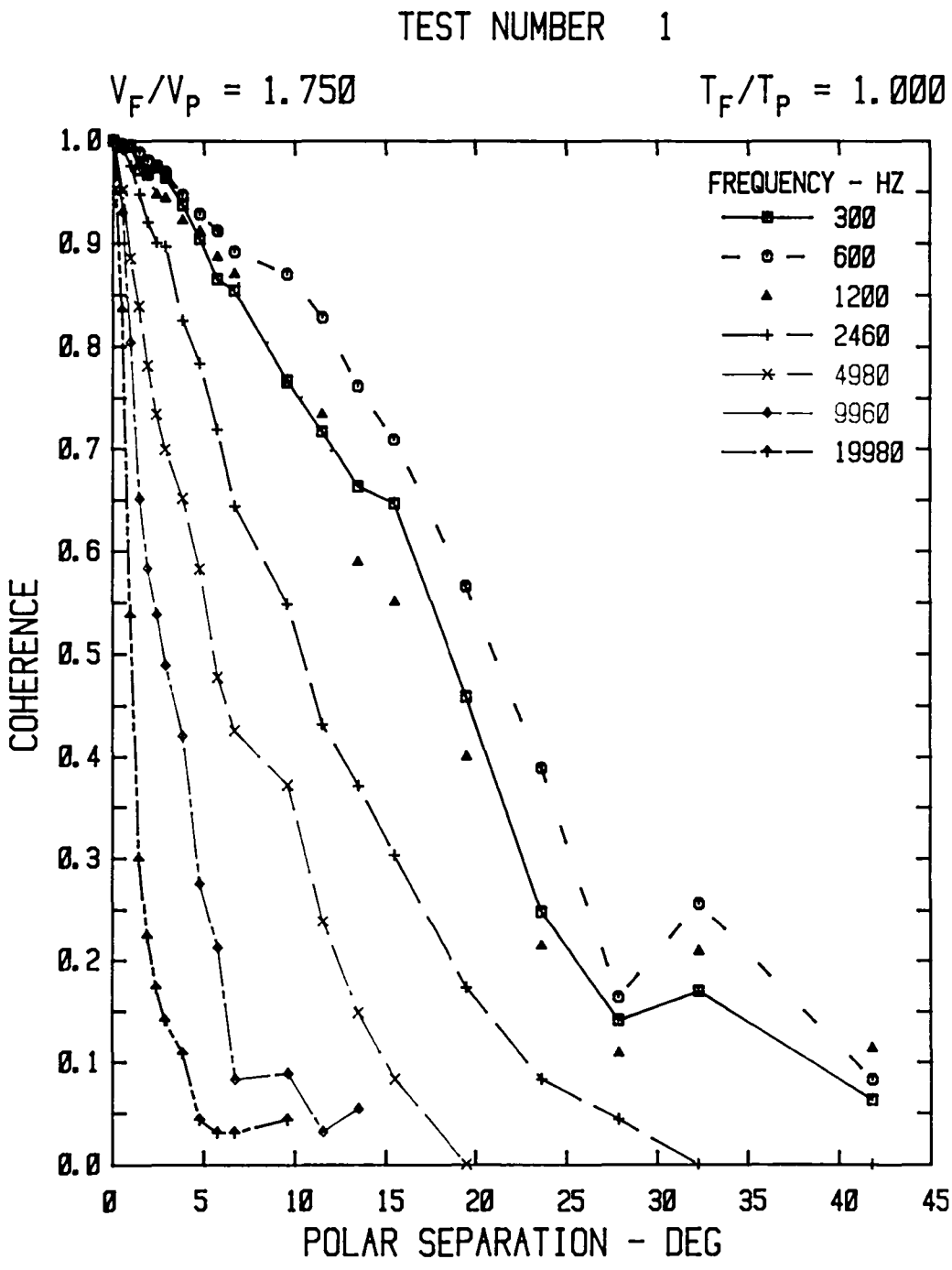

Figure 3.1 - Typical coherence plot from source location measurements.

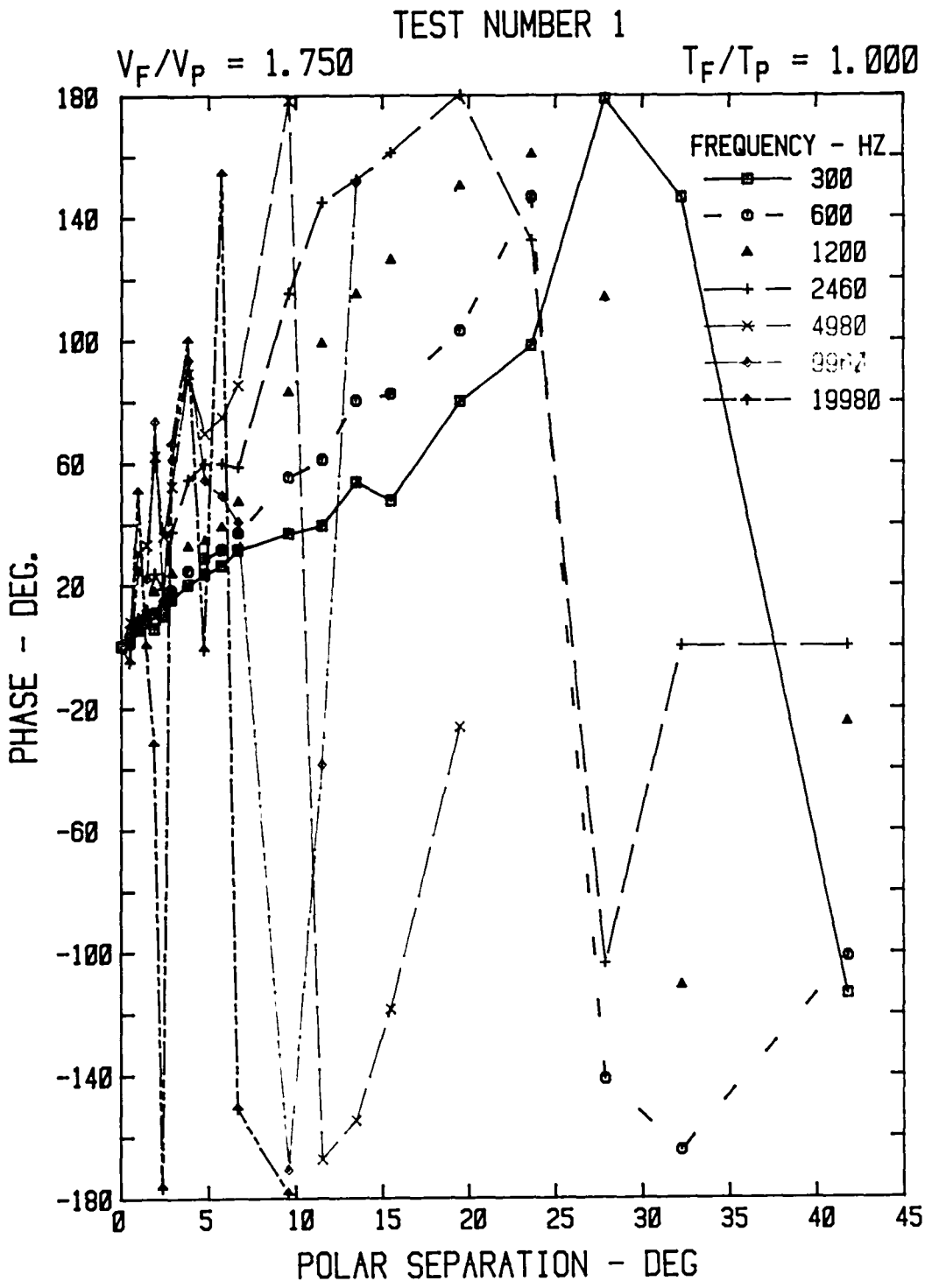

Figure 3.2 Typical phase plot from source location measurements.

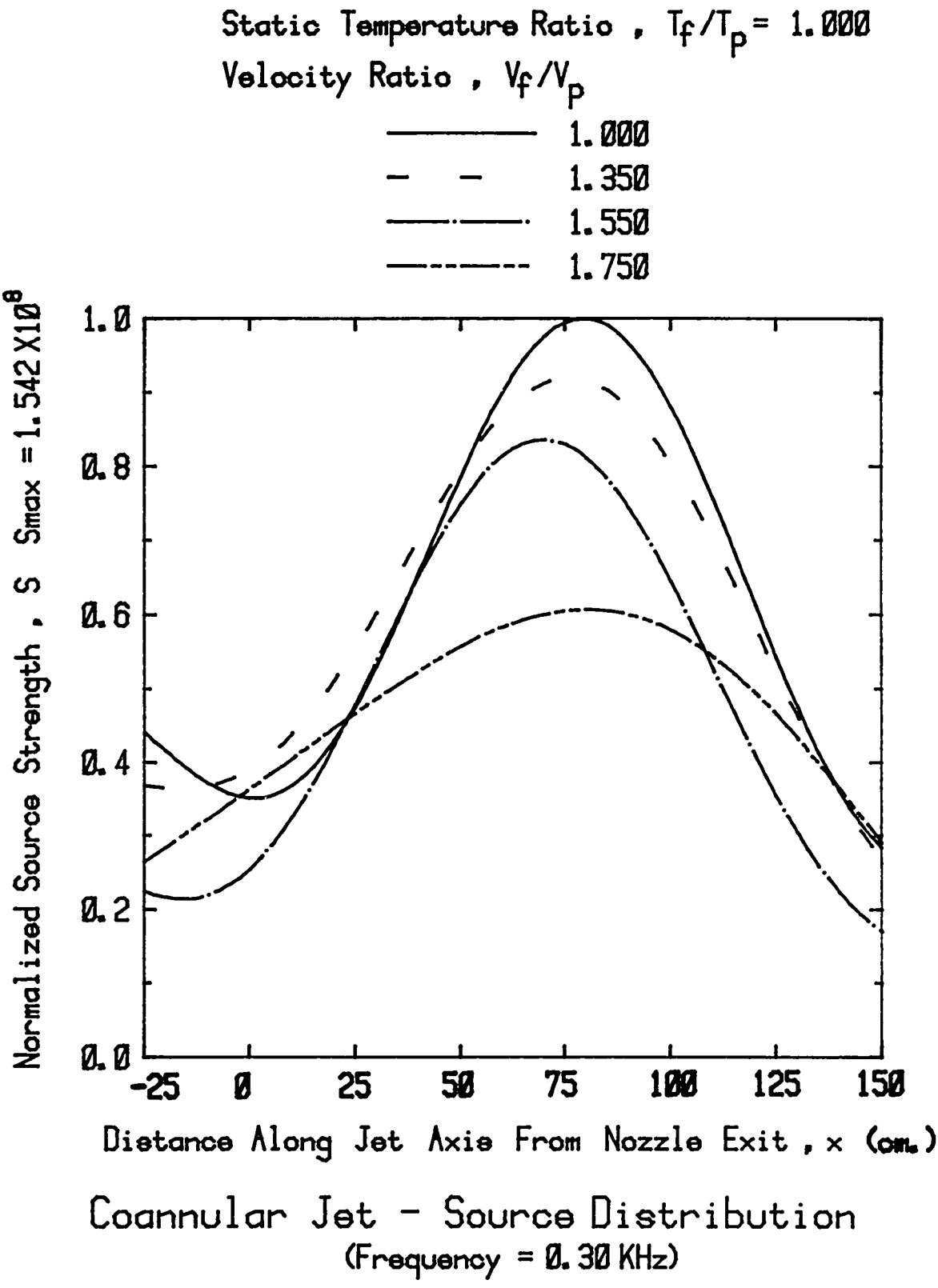

Figure 3.3(a) Effect of V_f/V_p on source distribution.

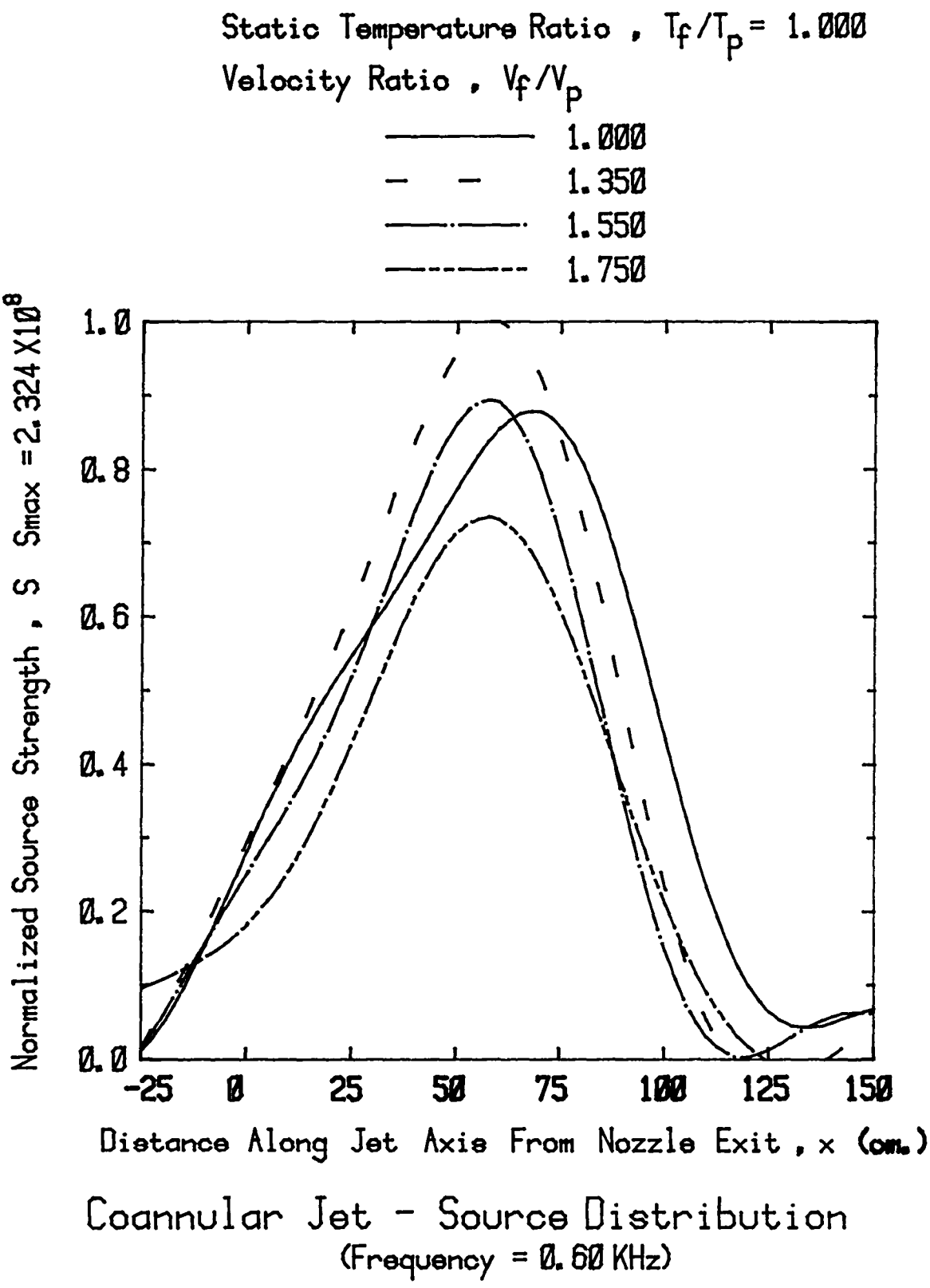

Figure 3.3(b) Effect of V_f/V_p on source distribution.

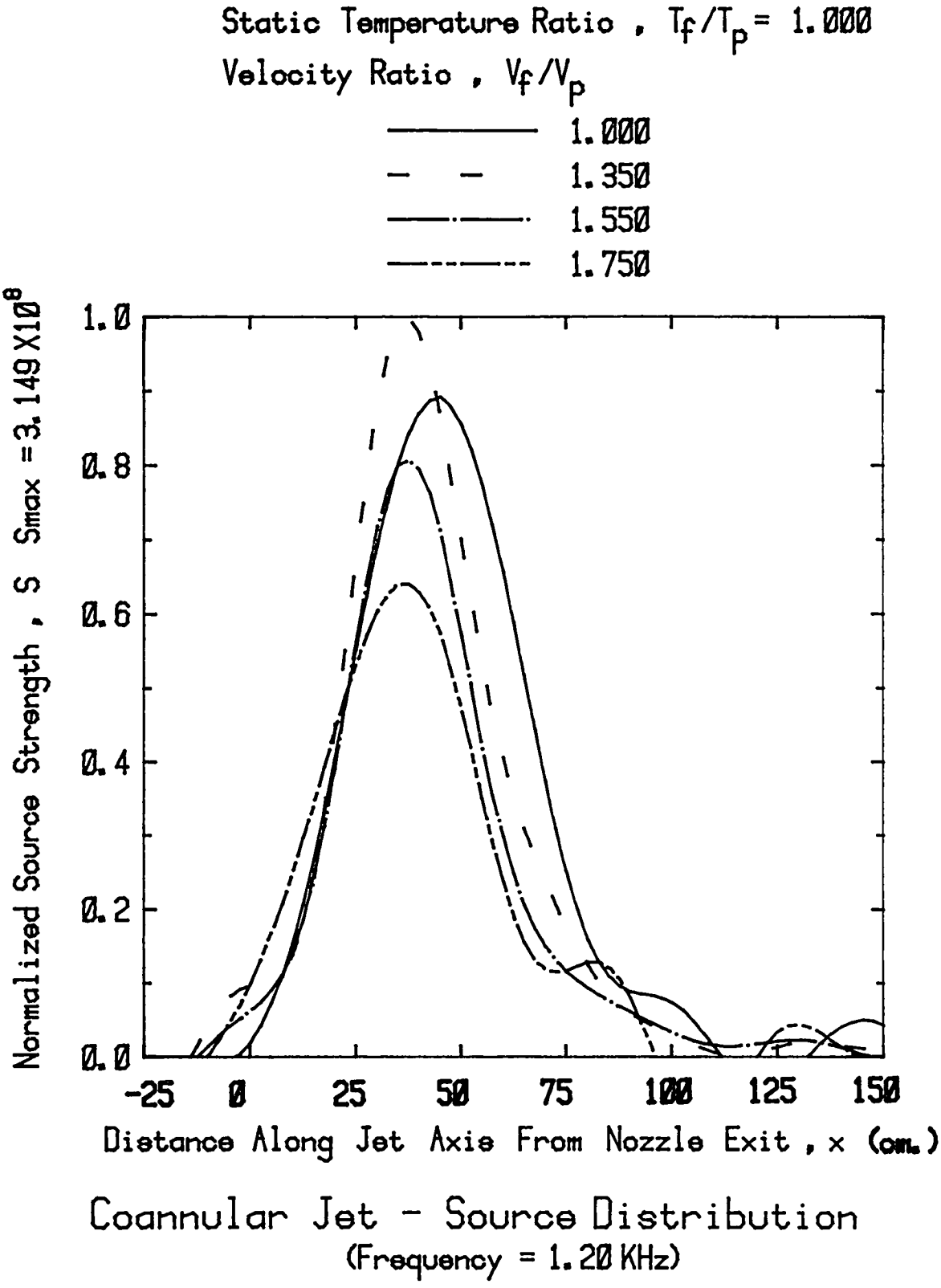

Figure 3.3(c) Effect of V_f/V_p on source distribution.

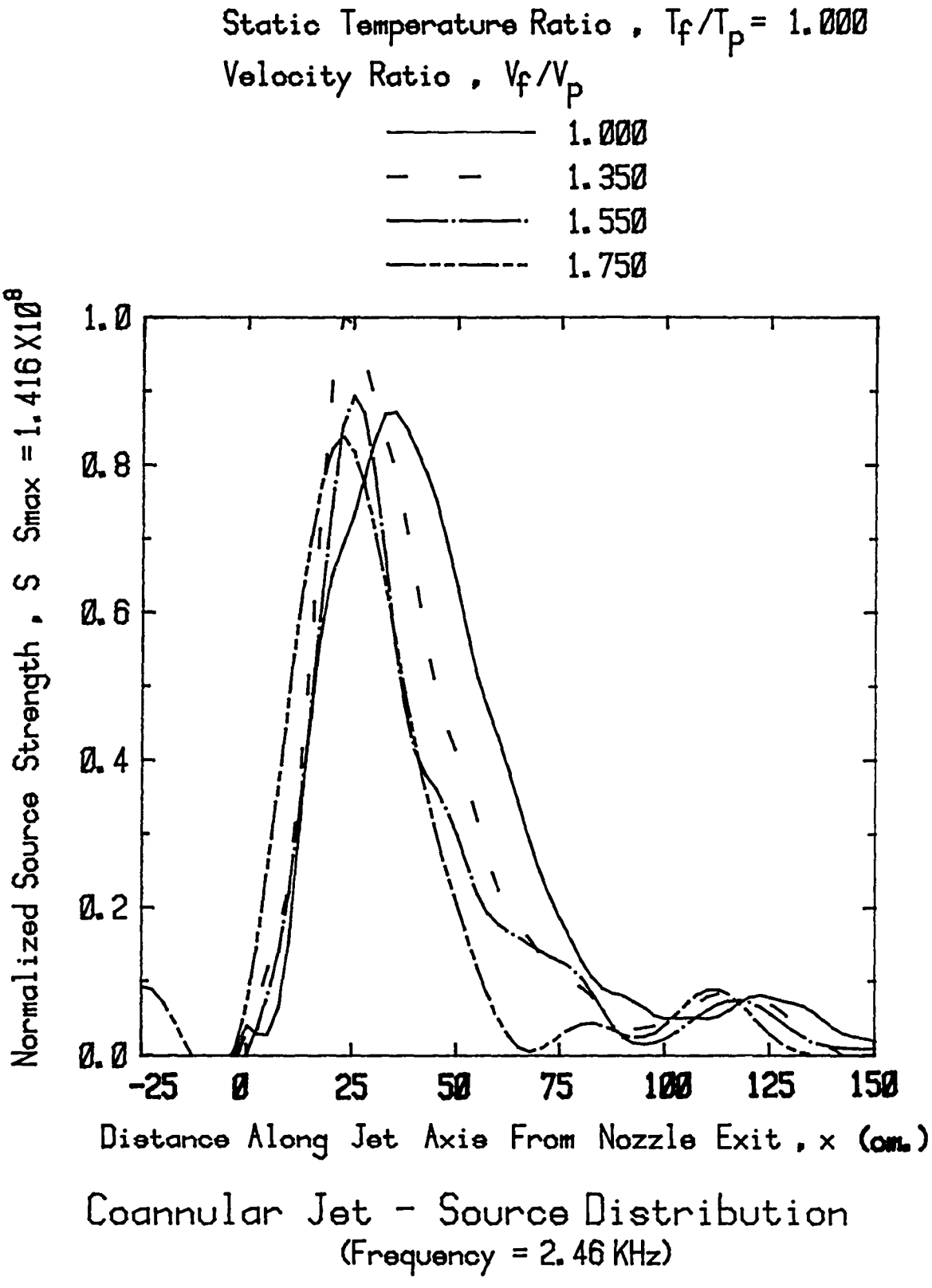

Figure 3.3(d) Effect of V_f/V_p on source distribution.

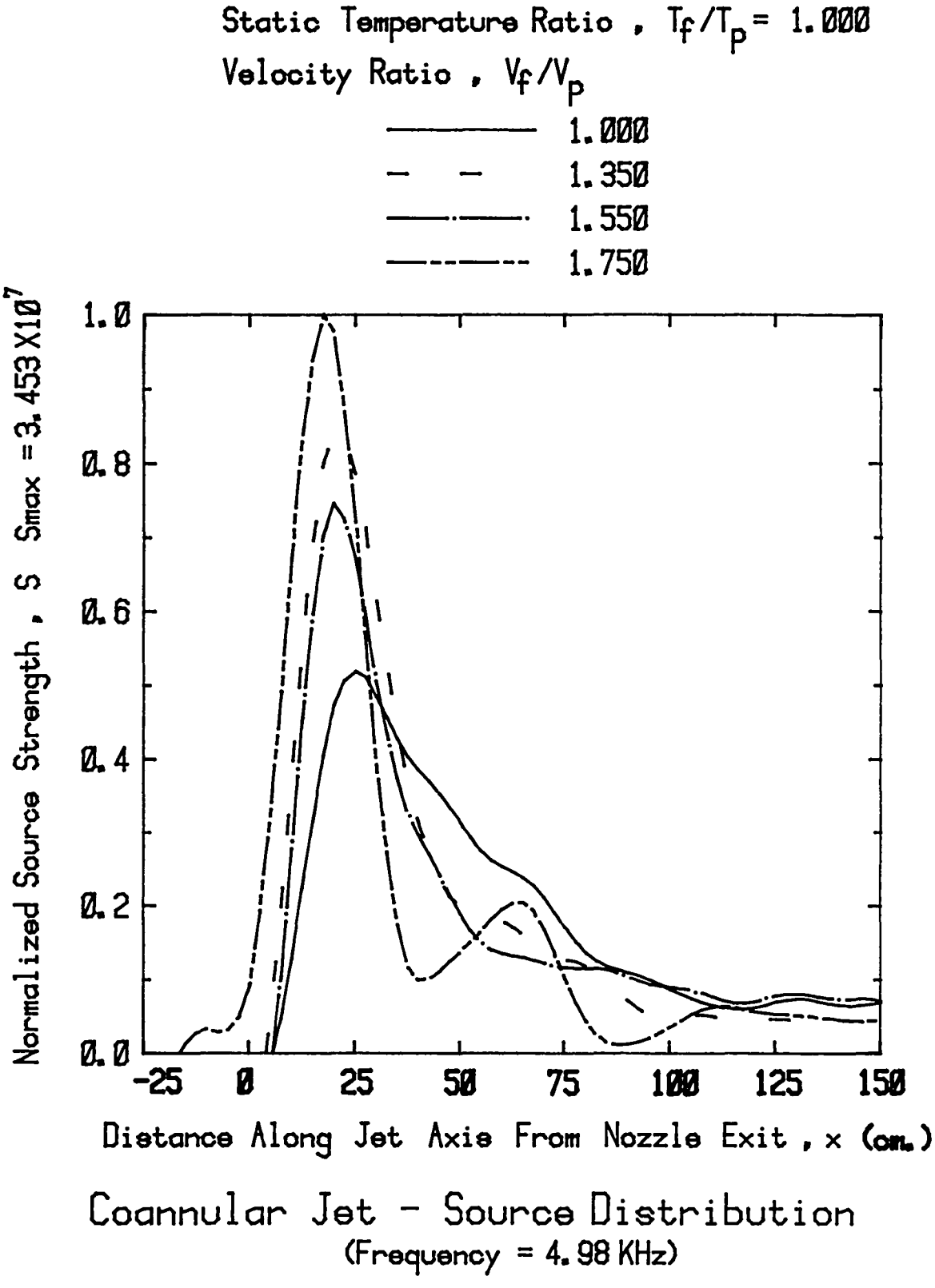

Figure 3.3(e) Effect of V_f/V_p on source distribution.

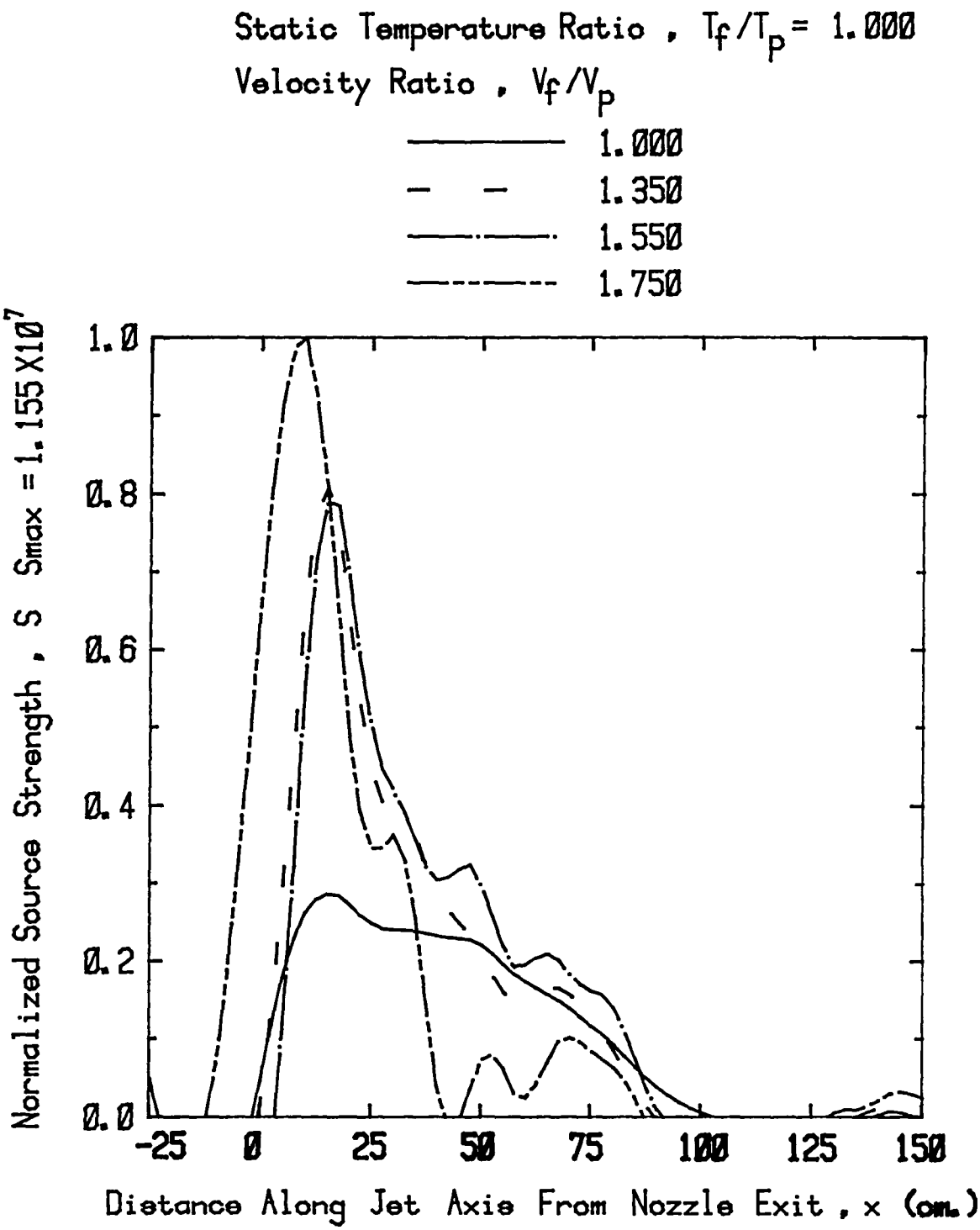

Figure 3.3(f) Effect of V_f/V_p on source distribution.

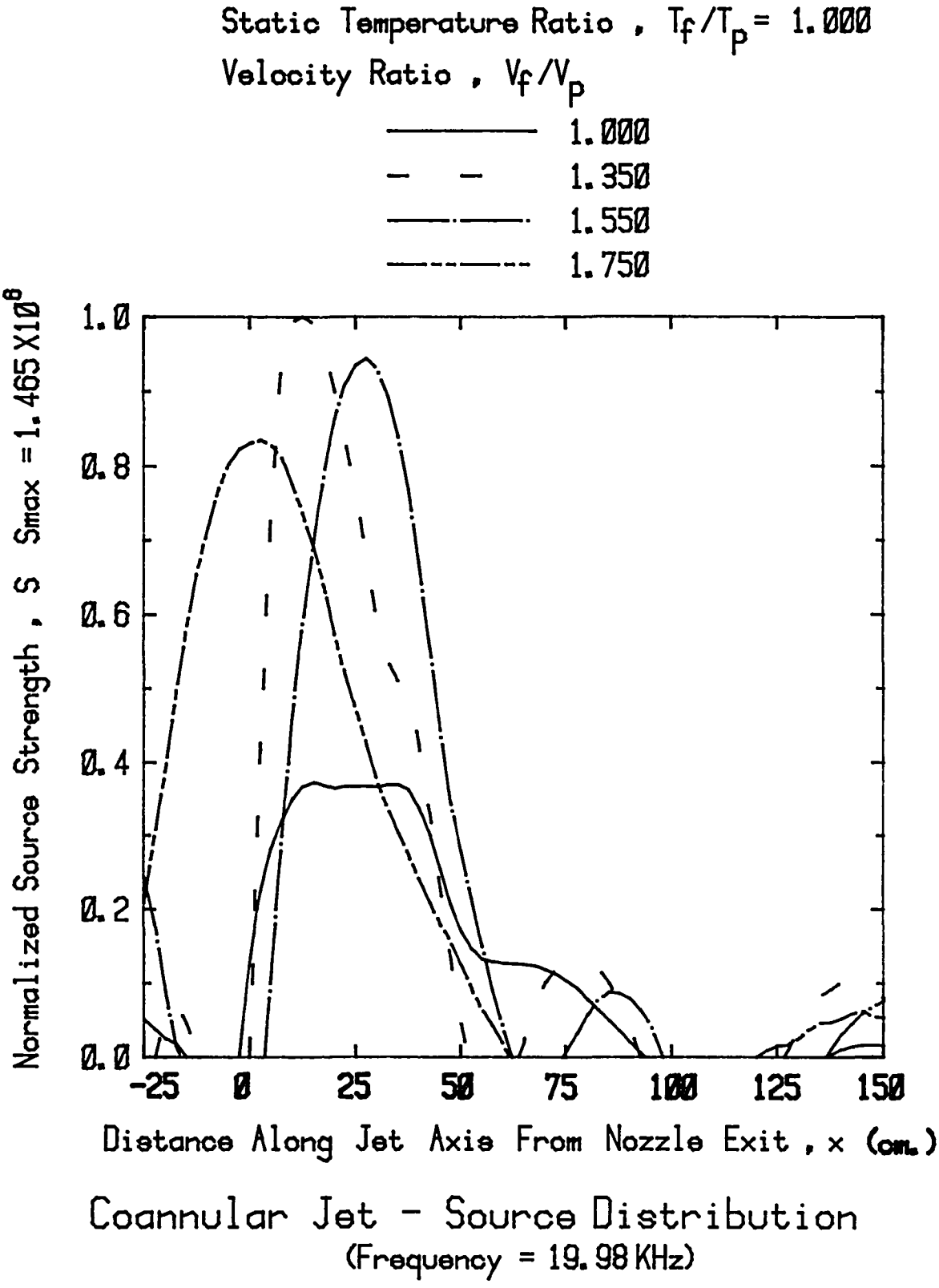

Figure 3.3(g) Effect of V_f/V_p on source distribution.

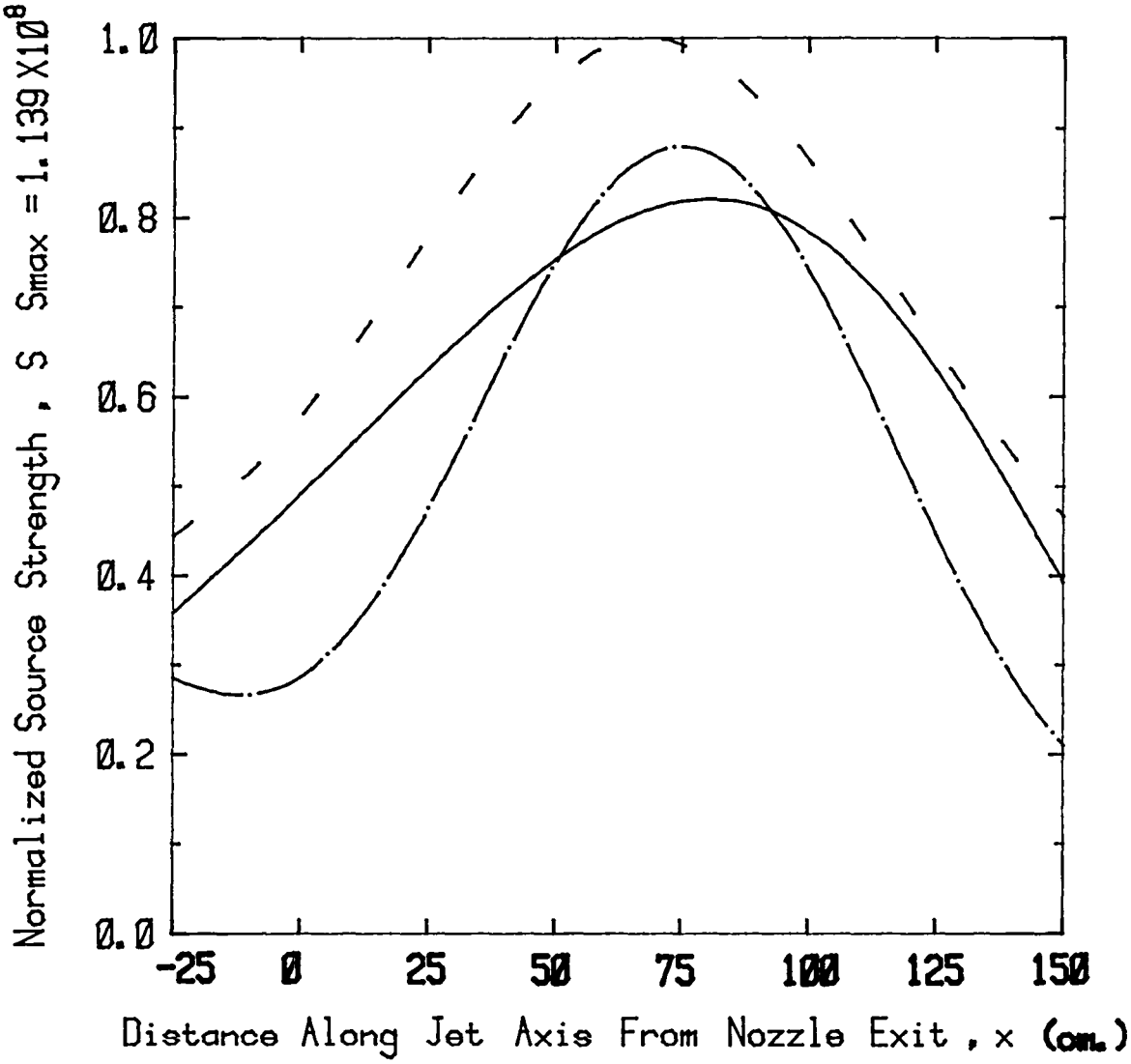

Figure 3.4(a) Effect of T_f/T_p on source distribution.

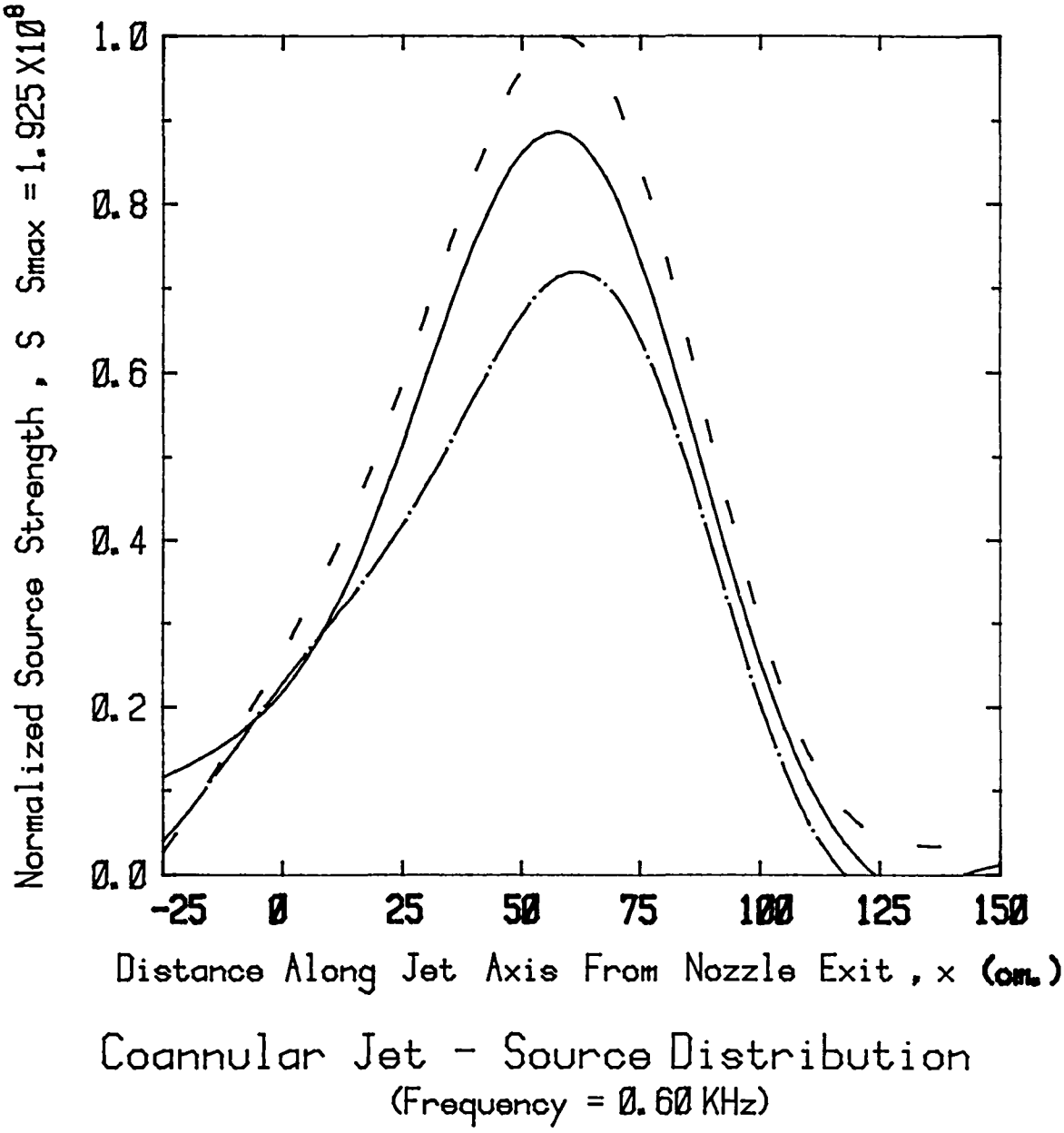

Figure 3.4(b) Effect of T_f/T_p on source distribution.

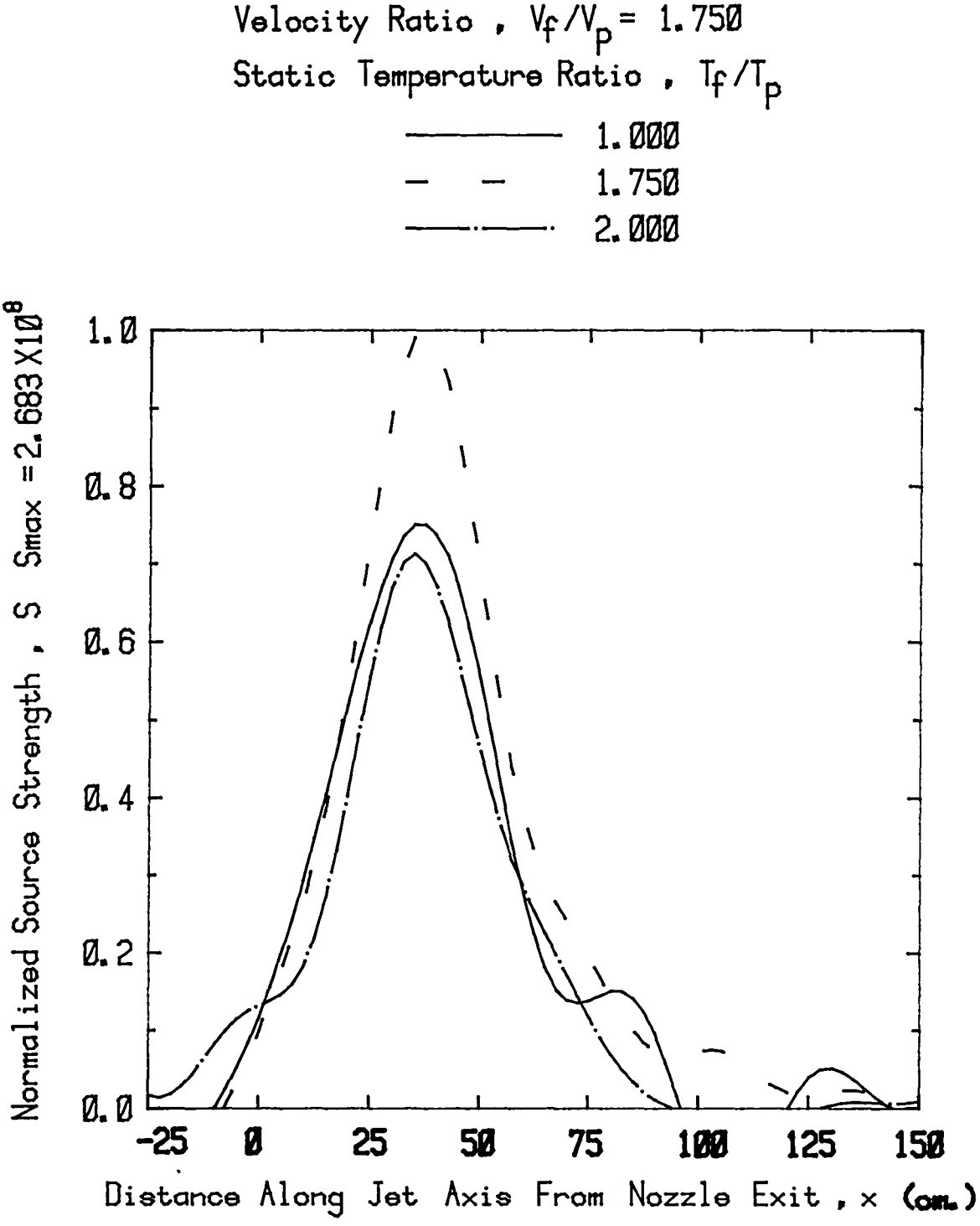

Figure 3.4(c) Effect of T_f/T_p on source distribution.

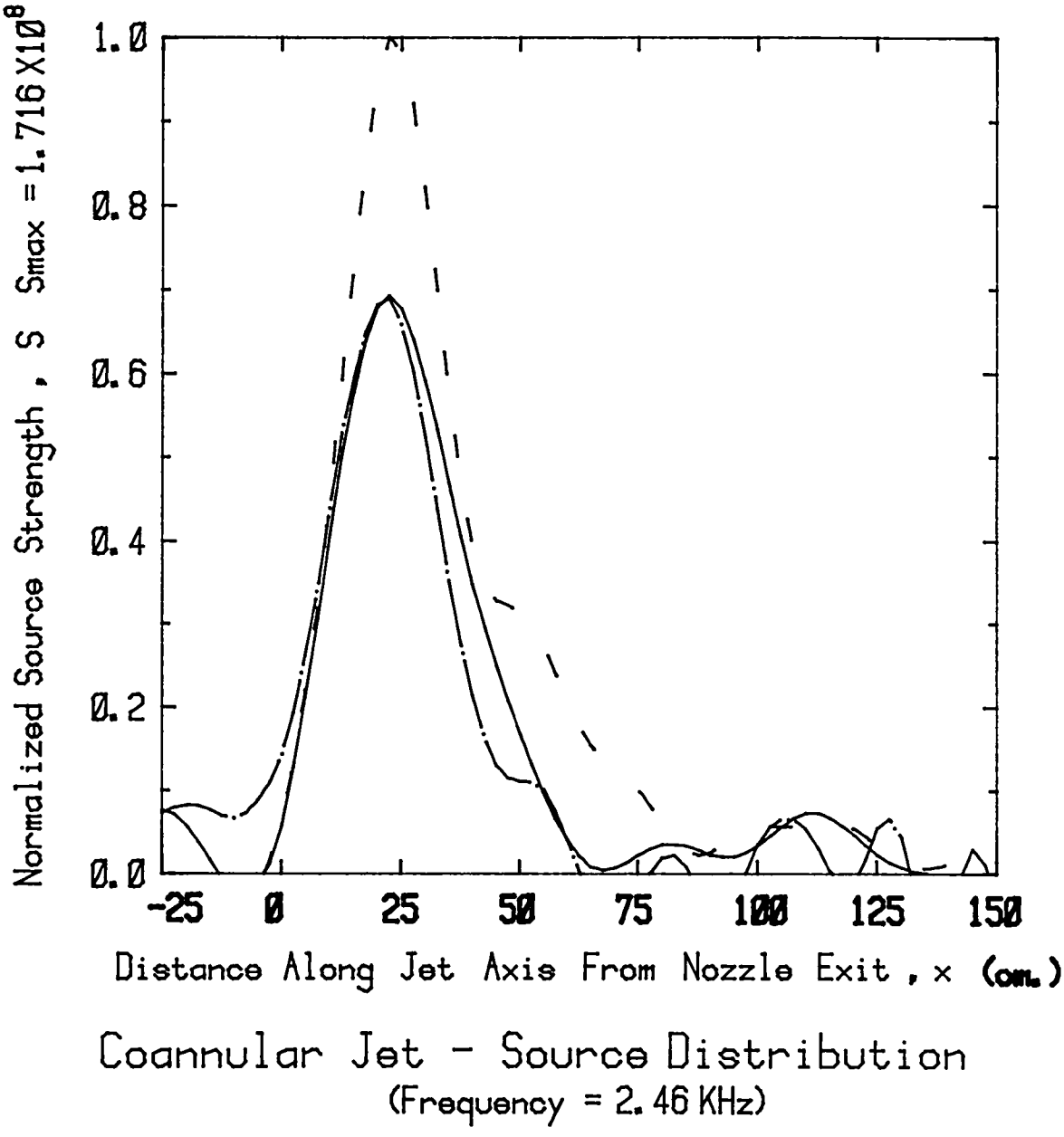

Figure 3.4(d) Effect of T_f/T_p on source distribution.

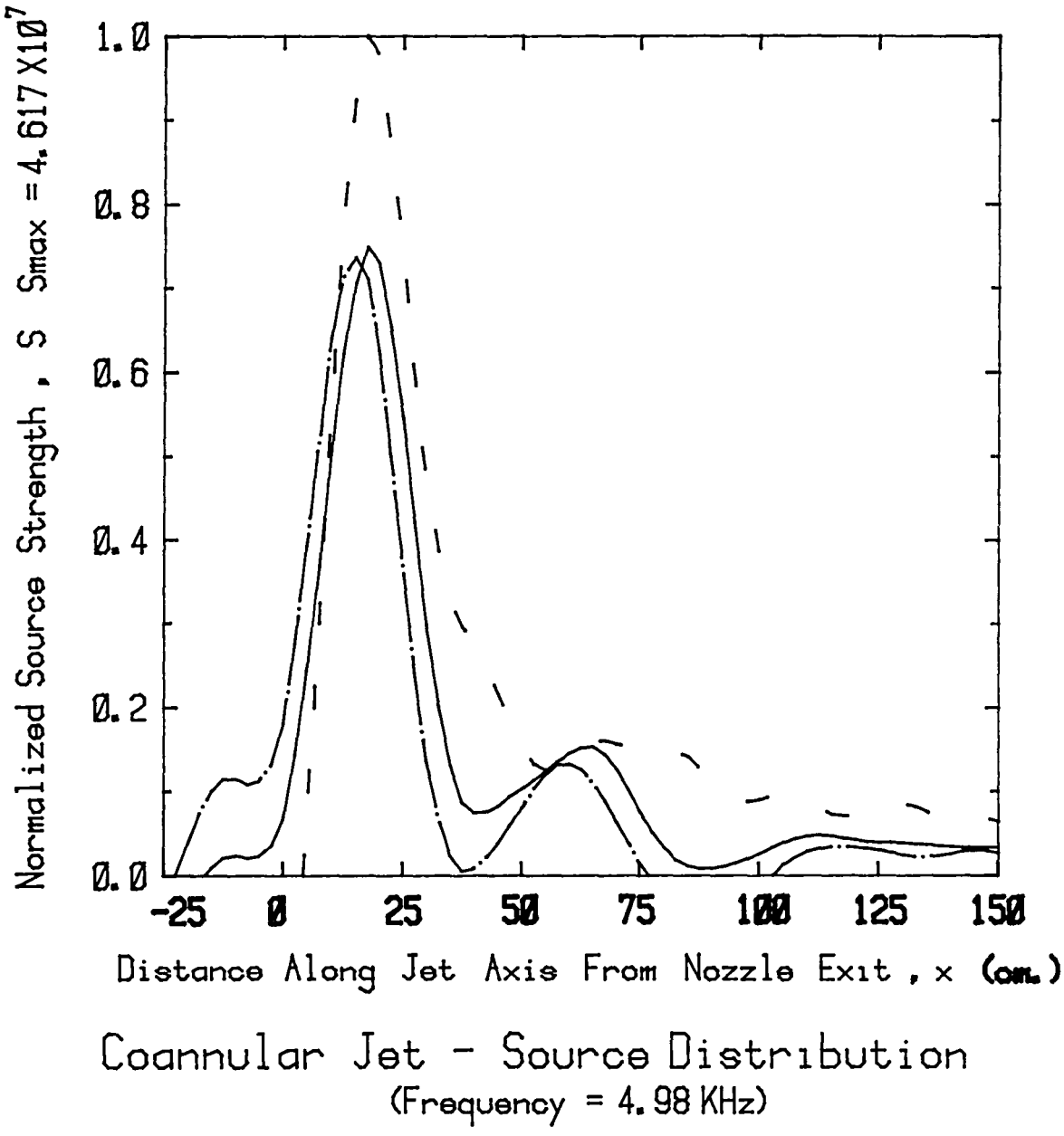

Figure 3.4(e) Effect of T_f/T_p on source distribution.

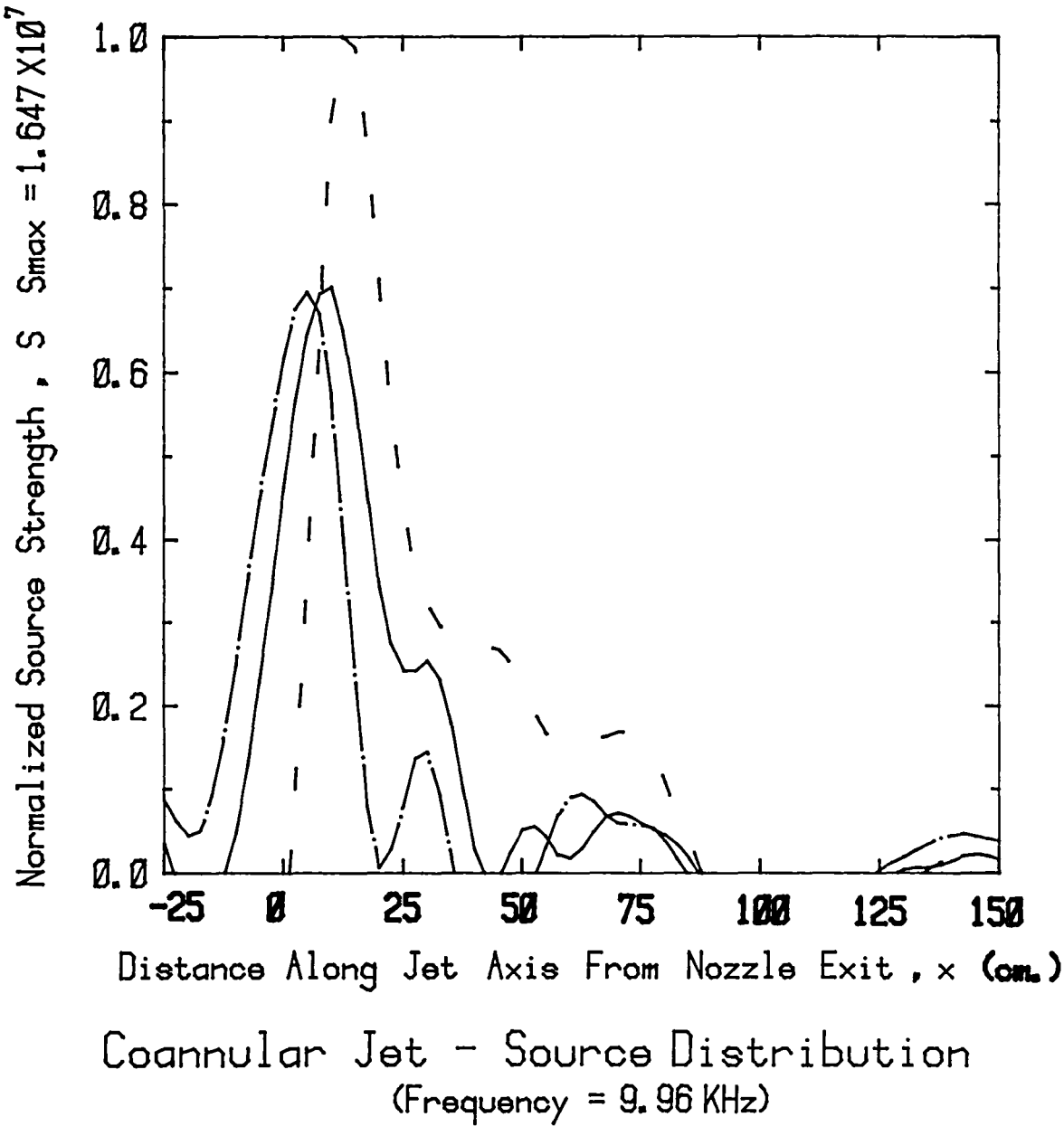

Figure 3.4(f) Effect of T_f/T_p on source distribution.

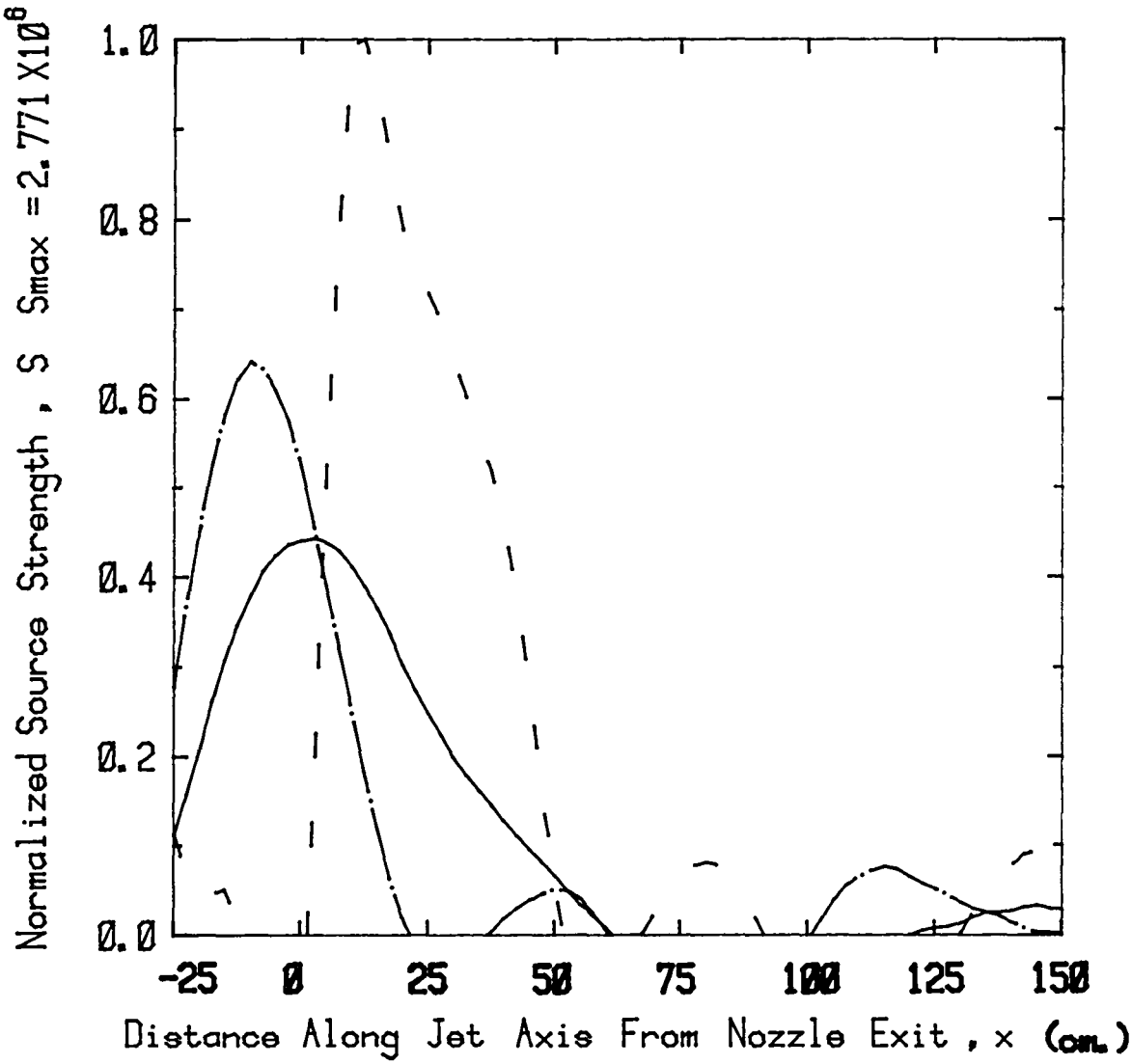

Figure 3.4(g) Effect of T_f/T_p on source distribution.

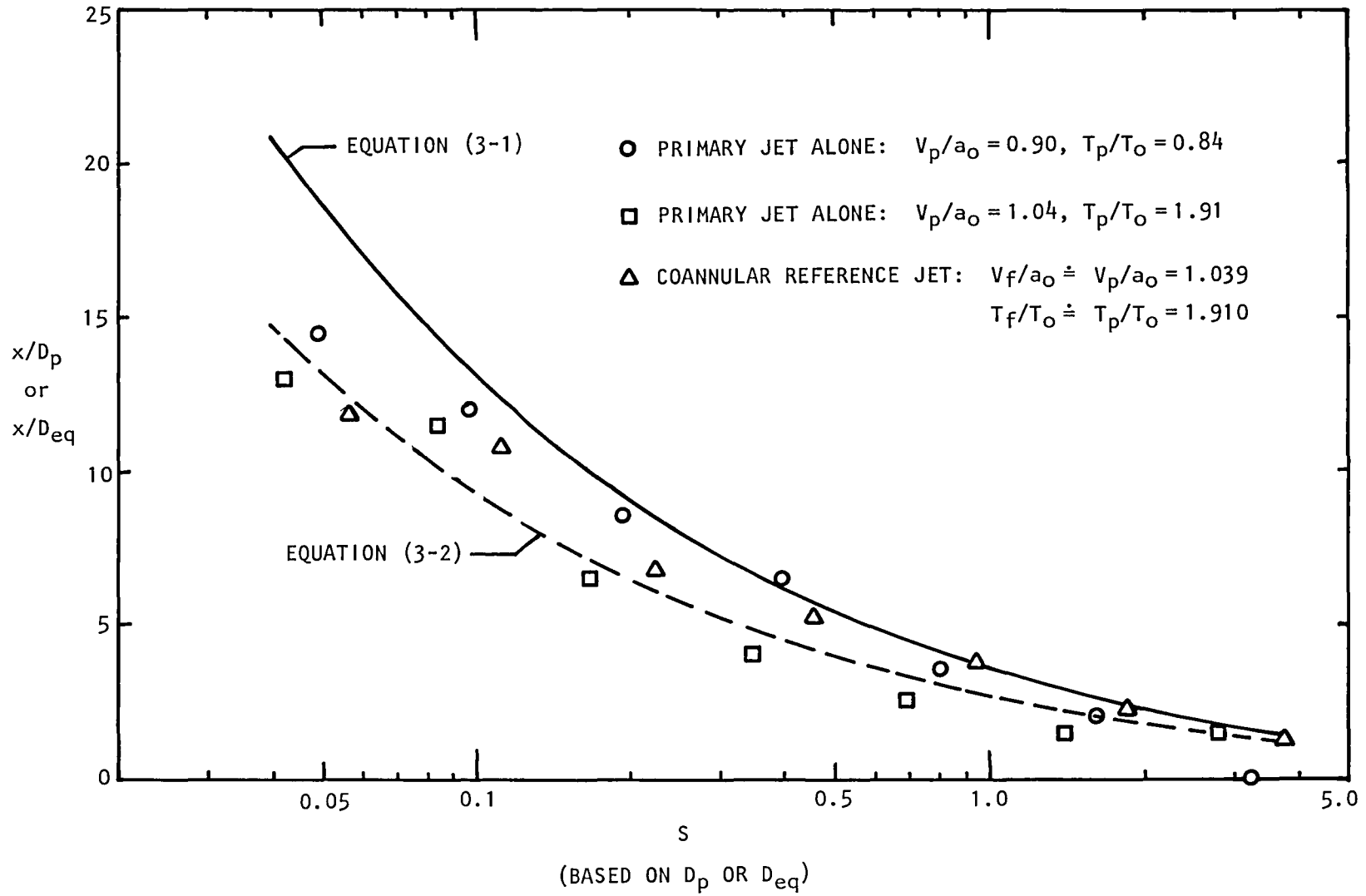

Figure 3.5 Axial source location as a function of Strouhal number (based on D_p or D_{eq}).

4. MEAN FLOW SURVEYS AND RESULTS

The mean flow characteristics of coannular jets were measured by using a conventional 3.2 mm (1/8-inch) diameter pitot-static probe with integral thermocouple. The experiments, which were all conducted with the coannular nozzle configuration described in Section 2, were performed in the coannular flow turbulence facility described in Section 5. The jet flow was mapped in detail from the nozzle exit planes to approximately twenty equivalent nozzle diameters. The measured total pressure, static pressure, and total temperature profiles at all axial stations were used to generate radial profiles of mean velocity, Mach number, total temperature and static temperature, as well as contours of these parameters.

4.1 DATA ACQUISITION AND REDUCTION

The pressure and temperature data acquisition system is shown in Figure 4.1. Essential features of the system are (1) computer control of test conditions, and (2) conditional sampling of test data.

The MAC computer, in response to keyboard entry, (i) controls the hot and cold valves which supply air to the two nozzles, (ii) positions the probe at specified coordinates, (iii) acquires the requested quantity of data when test conditions are within specified limits, (iv) performs initial data reduction, (v) outputs results to the CRT and the line printer, and (vi) outputs the raw data on digital tape for subsequent processing. Subsequent processing , by another MAC computer, includes more rigorous data reduction and the generation of plotted output.

One of the problems encountered with the pressure/temperature combination probe was that the thermal response of the probe was rather slow. It was thought that the response rate and total temperature recovery could be improved by isolating the thermocouple junction within the total pressure cavity of the probe. Attempts to accomplish those improvements were marginally successful in lower temperature flows and catastrophic at higher temperatures. The major problems were the large-size of the thermocouple wire, the inability to provide a vented total temperature environment for the junction, and the lack of an adequate joining technique to reassemble the modified probe. In practice, the modified probe failed at the braze joints as did one similar unmodified probe. Ultimately, an unmodified probe was used, and the traversing rate and direction were selected to compensate for the poor response rate of the probe.

The data acquisition procedure used for these experiments can be summarized as follows. At the beginning of each run, the test conditions (i.e. total pressure and total temperature for the primary and secondary streams) were input to the MAC computer from the keyboard. The MAC computer controlled the hot and cold valves such that the desired test conditions were attained and maintained. When the test conditions were achieved, the probe was moved to the center of the nozzle exit plane, and the jet reference conditions were recorded. The probe was then moved, under computer control,

to the starting point of the first axial location at which a radial traverse was to be conducted. The probe was paused at this point until it came to thermal equilibrium with its environment at that location. Then, 1000 data points were read and averaged, and the probe was stepped to the next radial measurement location. After completing one radial traverse, the probe was moved to the starting point of the next traverse (i.e. the next axial station) and, again, paused before initiating the traverse.

Computation of Mach number, static temperature and velocity:

Using the measured values of total pressure (p_t), static pressure (p), and total temperature (T_t), the corresponding values of Mach number (M), static temperature (T) and velocity (V) were computed by using the standard compressible flow relationships. For subsonic flows, the relevant relationships are as follows:

Mach number (M):

$$\frac{P_t}{p} = \left(1 + \frac{\gamma-1}{2} M^2\right)^{\frac{\gamma}{\gamma-1}} \tag{4-1}$$

Static temperature (T):

$$\frac{T}{T_t} = \left(1 + \frac{\gamma-1}{2} M^2\right)^{-1} \tag{4-2}$$

Velocity (V):

$$V = M\sqrt{\gamma RT} \tag{4-3}$$

(where R is the characteristic gas constant).

The specific heat ratio γ in the above equations is a function of temperature. In computing these parameters, the value of γ was assumed to be 1.4 in a first approximation. The local Mach number and static temperature were then determined, and the new value of γ corresponding to this static temperature was obtained. The process was repeated until the value of γ remained constant with succeeding iterations.

4.2 TYPICAL RESULTS

The experimental program was mainly concentrated on shock-free coannular jets, and complete mean flow surveys were conducted for test points (TP) 1 through 8 defined in Table 2.1 of Section 2. In addition, measurements were conducted with the primary jet operated alone, and attempts were also made to acquire data for the two shock-containing conditions defined in Table 2.2. However, for the shock-containing cases, several problems, mainly associated

with the measurement of static pressure in supersonic flows, were encountered, and therefore results pertaining to these cases are not included in this report.

The data acquired from these surveys are documented fully in Appendix 3, where individual radial profiles of mean velocity, Mach number, total temperature, and static temperature at several axial stations (ranging from the nozzle exit plane to approximately 20 equivalent nozzle diameters) are presented systematically for all test points. In the present section, typical results are shown in Figures 4.2 through 4.8 to highlight the effects of velocity ratio V_f/V_p and temperature ratio T_f/T_p on mean velocity and static temperature profiles at various axial locations. Most of these composite plots are self-explanatory.

Effects of velocity ratio V_f/V_p:

The effect of V_f/V_p on mean velocity variation along jet centerline is shown in Figure 4.2 where the temperature ratio is held constant at unity. This plot is perhaps one of the most important plots obtained from these experiments, and it will be used in Section 7 to explain the low-frequency noise reductions at small angles to the jet exhaust. The centerline mean velocity in inverted-velocity-profile coannular jets is always lower than that of the reference jet (i.e. $V_f/V_p = 1$), and this reduction is maintained (at least qualitatively) all the way from the nozzle exit plane to the fully-mixed region. The corresponding radial profiles of mean velocity at several axial locations are shown in Figures 4.3(a) through (e). The reduction in mean velocity with V_f/V_p on and around the jet centerline ($r = 0$) can be seen here as well.

The effect of V_f/V_p on static temperature profiles at various axial locations is shown in Figures 4.4 and 4.5 for T_f/T_p of 1.00 and 1.75, respectively. It should be remembered that T_f/T_p is the static temperature ratio *at the nozzle exit plane*. Furthermore, although this temperature *ratio* is kept constant as V_f/V_p is varied, the *absolute values* of temperature (T_f, T_p) do not remain constant as V_f/V_p is increased. This variation in absolute values of temperature is imposed by the requirement that the total thrust and mass flow rate remain constant for all test points.

Effects of temperature ratio T_f/T_p:

The effect of T_f/T_p on mean velocity variation along jet centerline is shown in Figure 4.6 where the velocity ratio is held constant at unity. The centerline velocity for $T_f/T_p = 1.00$ decays faster than the centerline velocity decay for $T_f/T_p = 1.75$. The corresponding radial profiles of mean velocity at three axial stations are shown in Figures 4.7(a) through (c), and the behavior on and around the jet centerline ($r = 0$) is consistent with the centerline velocity decays shown in Figure 4.6. In these two figures also, it should be noted that V_f/V_p is the velocity ratio *at the nozzle exit plane*, and although this velocity *ratio* is kept constant as T_f/T_p is varied, the *absolute values* of velocity (V_f, V_p) do not remain constant as T_f/T_p is increased. The velocities have turned out to be nearly identical in this case purely by coincidence.

Finally, the effect of T_f/T_p on static temperature profiles at three values of x/D_{eq} is shown in Figures 4.8(a) through (c) where V_f/V_p is held constant at unity.

Some of the mean flow results presented in this section will be referred to in Section 7 of this report where the measured noise changes in coannular jets will be interpreted in terms of the changes in mean flow and turbulence characteristics in such jets.

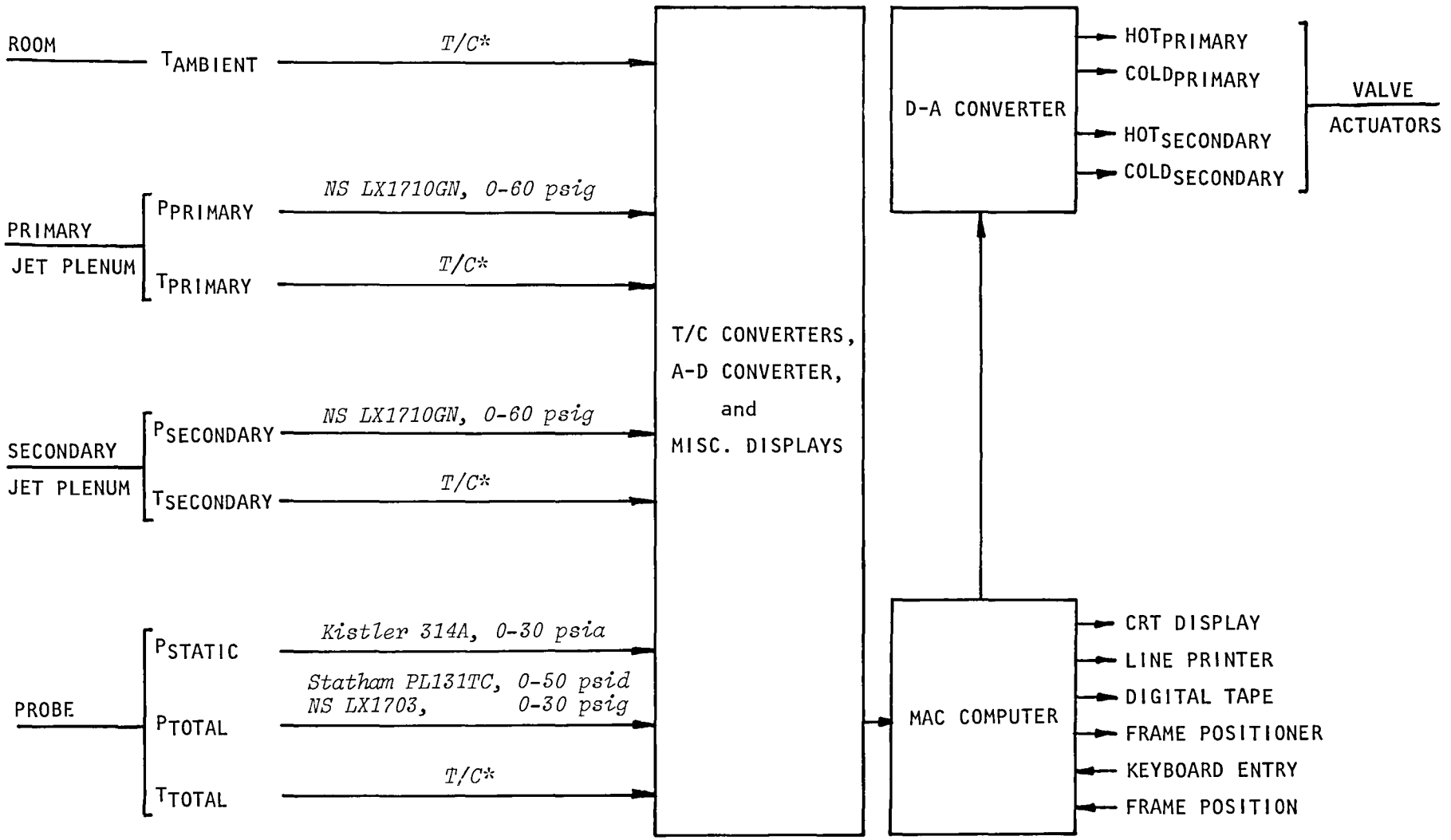

*T/C = Iron Constantan Thermocouples.

Figure 4.1 Pressure/Temperature Data Acquisition System Schematic.

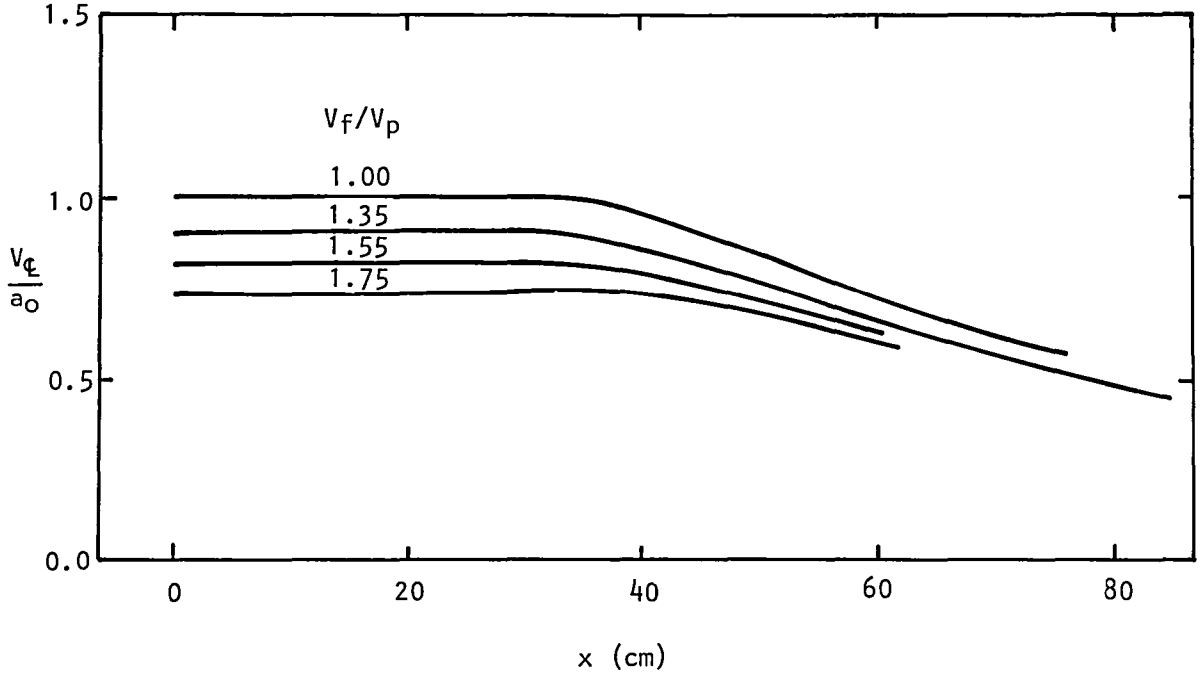

Figure 4.2 Effect of V_f/V_p on mean velocity decay along jet centerline; $T_f/T_p = 1$.

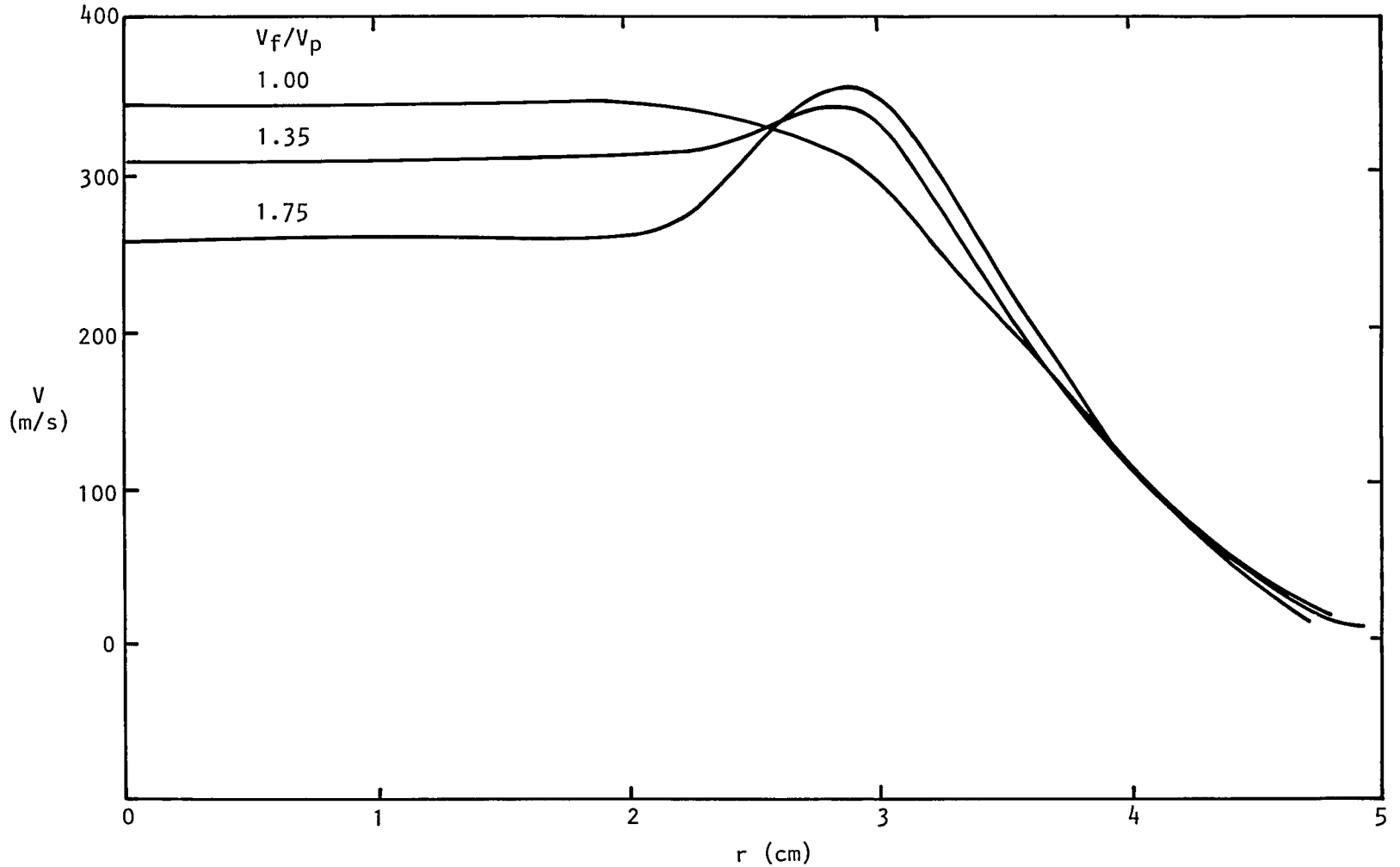

Figure 4.3(a) Effect of V_f/V_p on mean velocity profiles at $x/D_{eq} = 1.51$; $T_f/T_p = 1$.

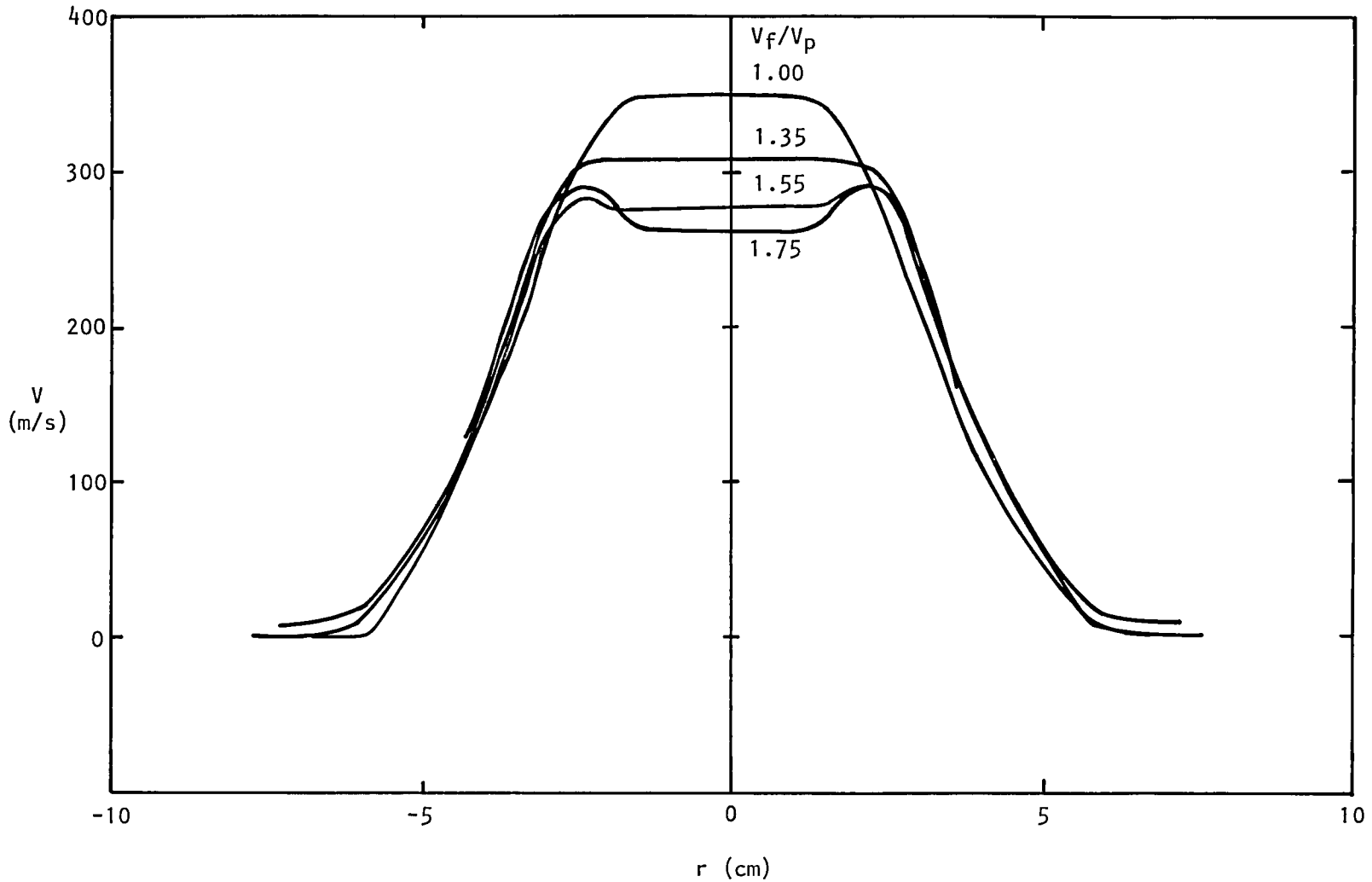

Figure 4.3(b) Effect of V_f/V_p on mean velocity profiles at $x/D_{eq} = 3.03$; $T_f/T_p = 1$.

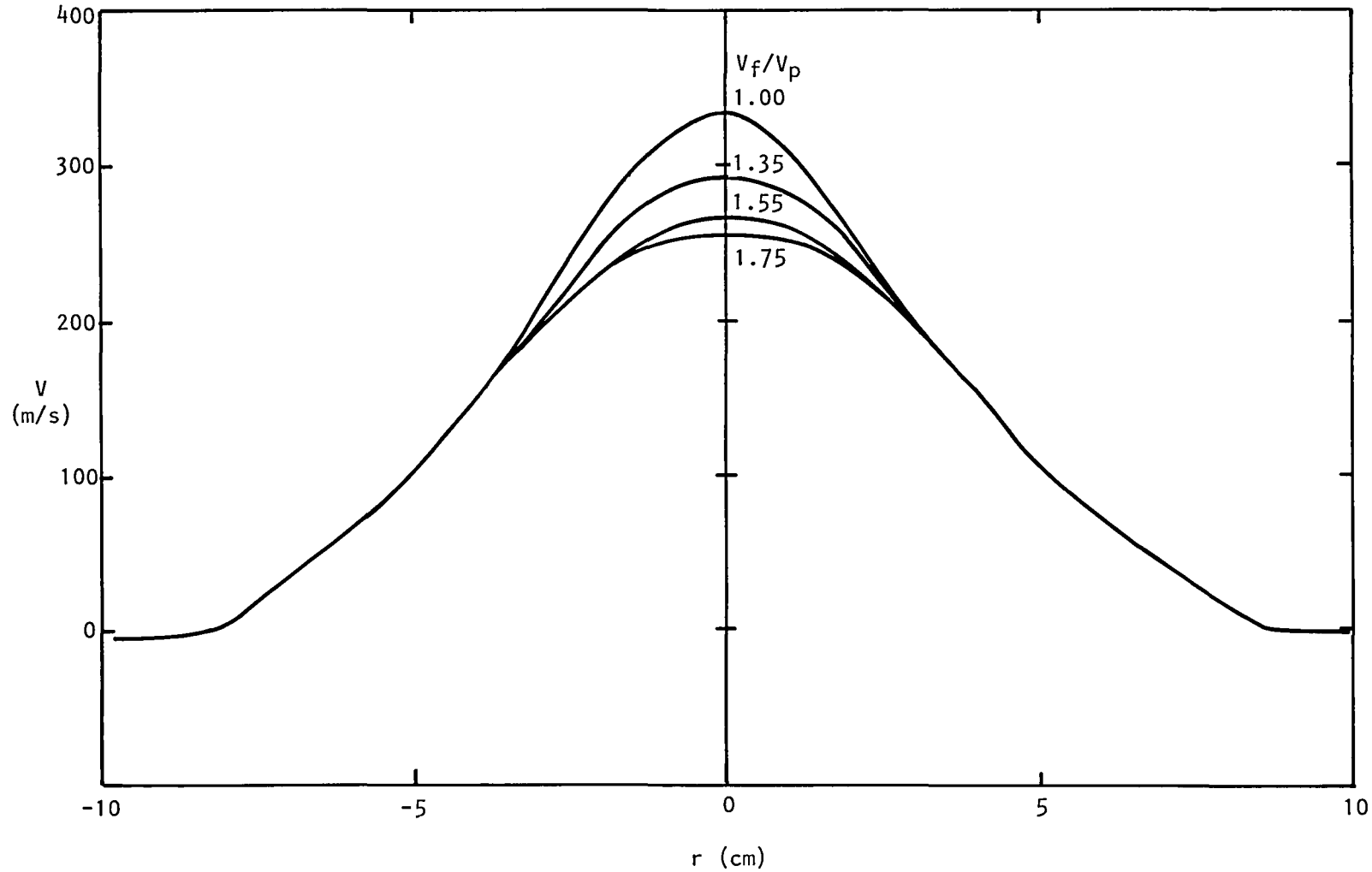

Figure 4.3(c) Effect of V_f/V_p on mean velocity profiles at $x/D_{eq} = 6.06$; $T_f/T_p = 1$.

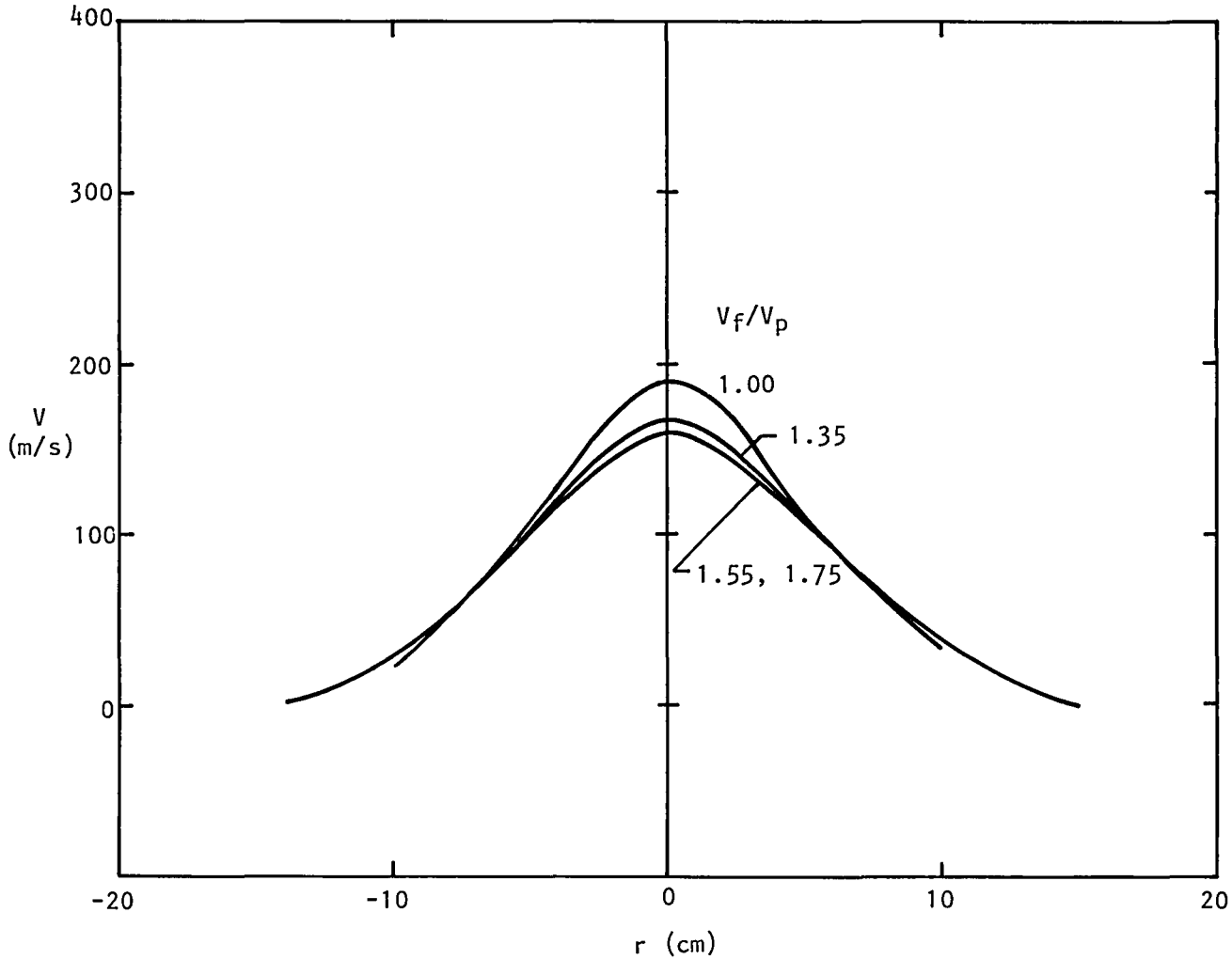

Figure 4.3(d) Effect of V_f/V_p on mean velocity profiles at $x/D_{eq} = 12.12$; $T_f/T_p = 1$.

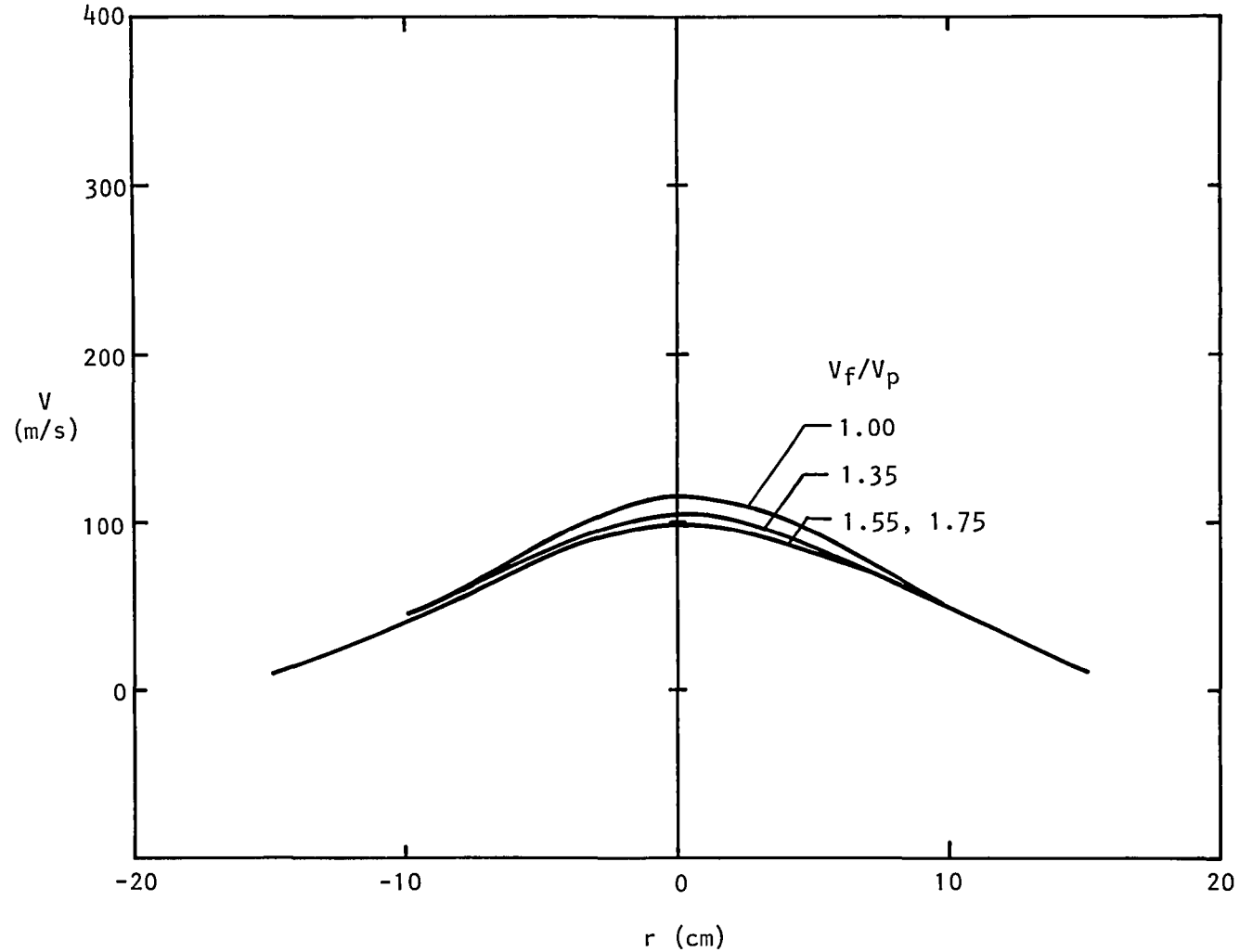

Figure 4.3(e) Effect of V_f/V_p on mean velocity profiles at $x/D_{eq} = 18.17$; $T_f/T_p = 1$.

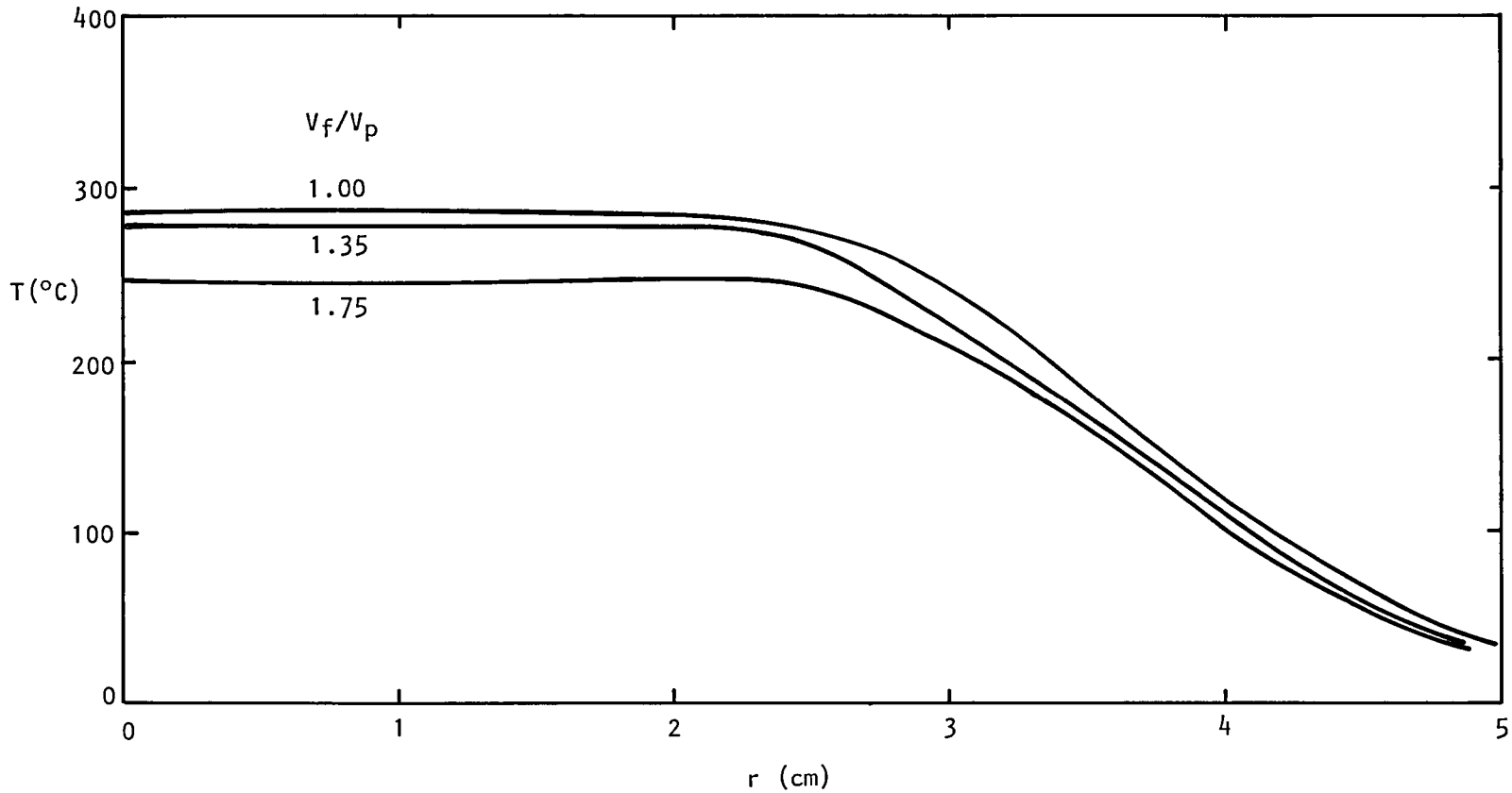

Figure 4.4(a) Effect of V_f/V_p on static temperature profiles at $x/D_{eq} = 1.51$; $T_f/T_p = 1$.

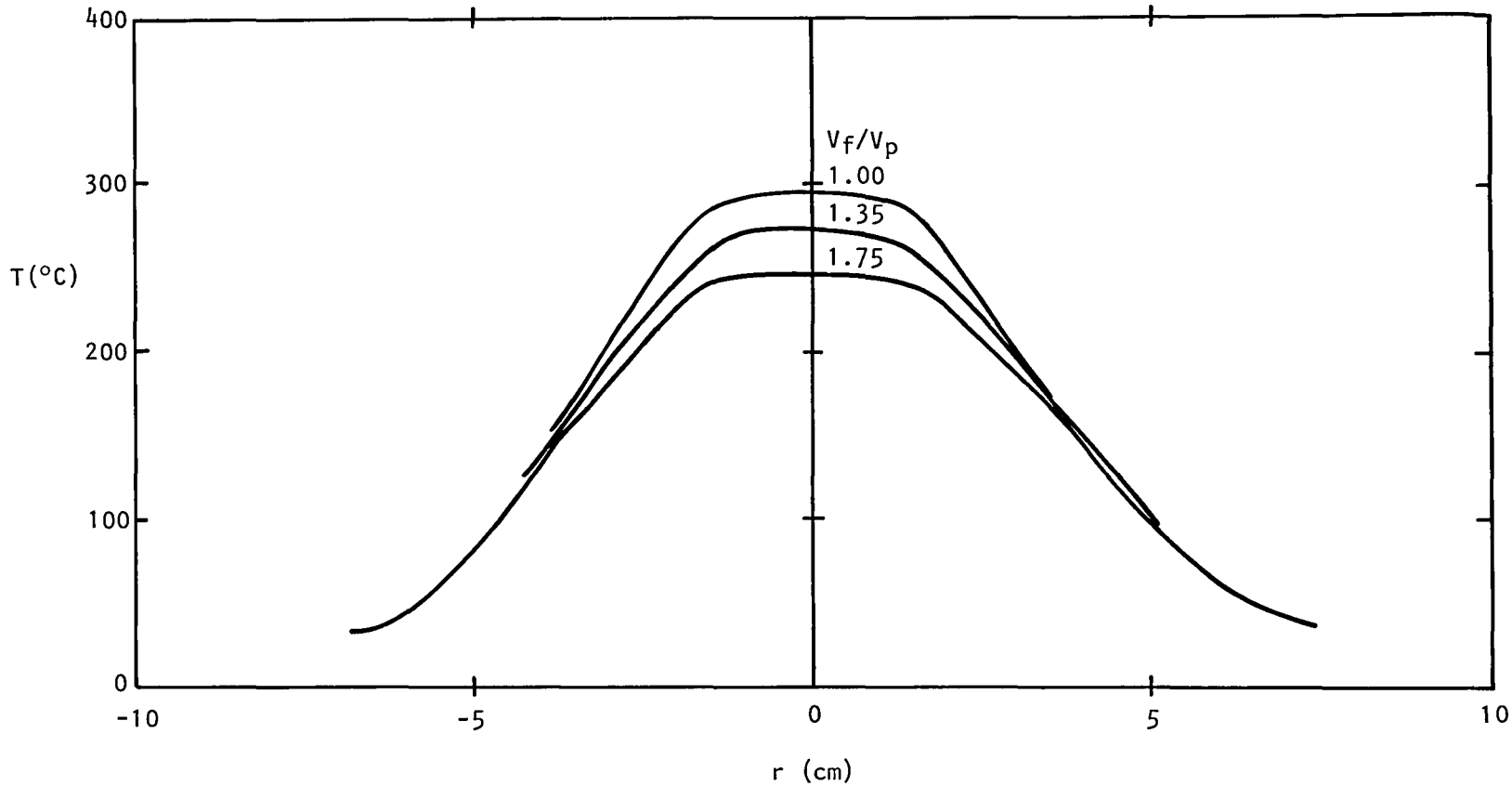

Figure 4.4(b) Effect of V_f/V_p on static temperature profiles at $x/D_{eq} = 3.03$; $T_f/T_p = 1$.

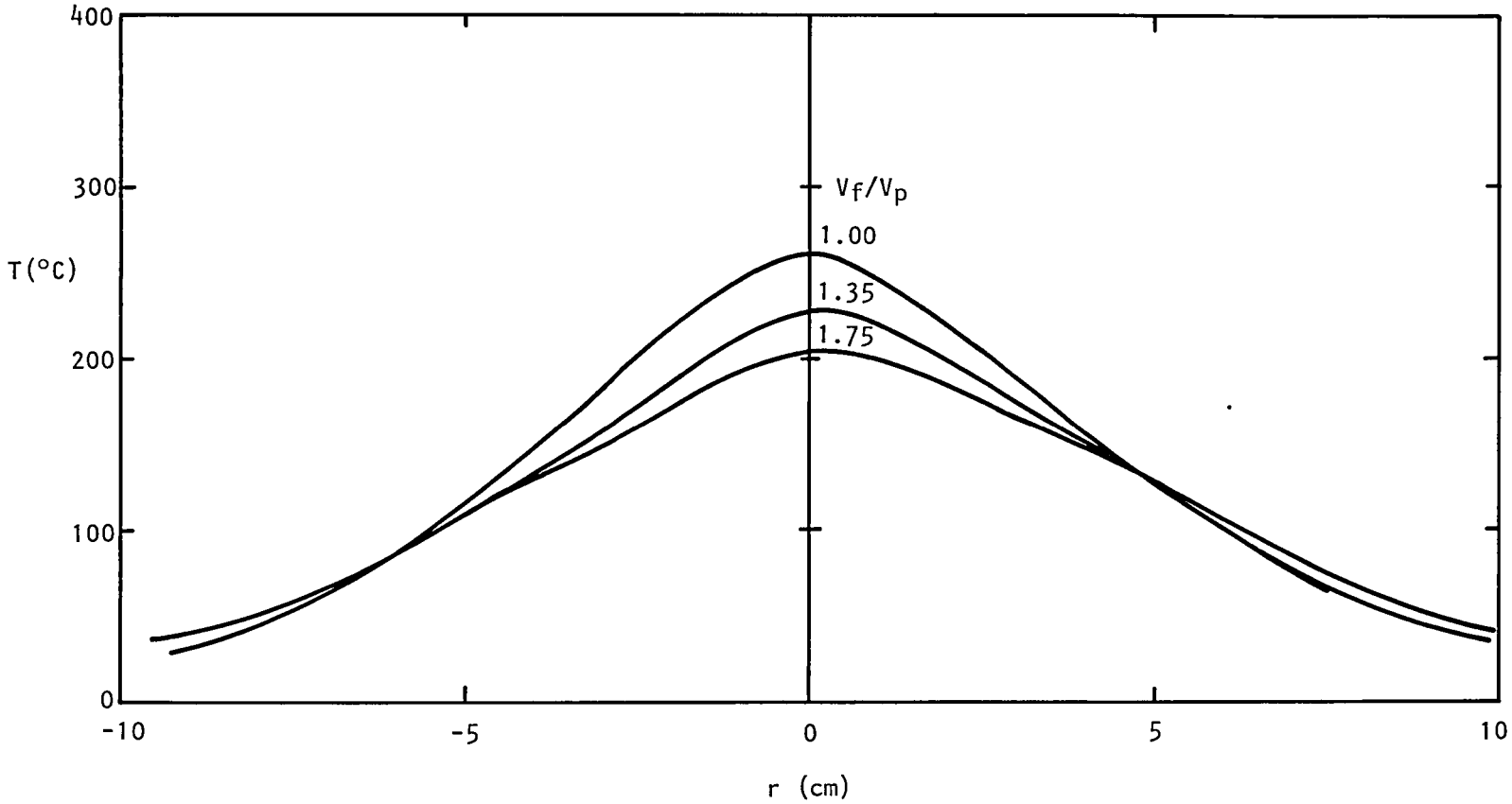

Figure 4.4(c) Effect of V_f/V_p on static temperature profiles at $x/D_{eq} = 6.06$; $T_f/T_p = 1$.

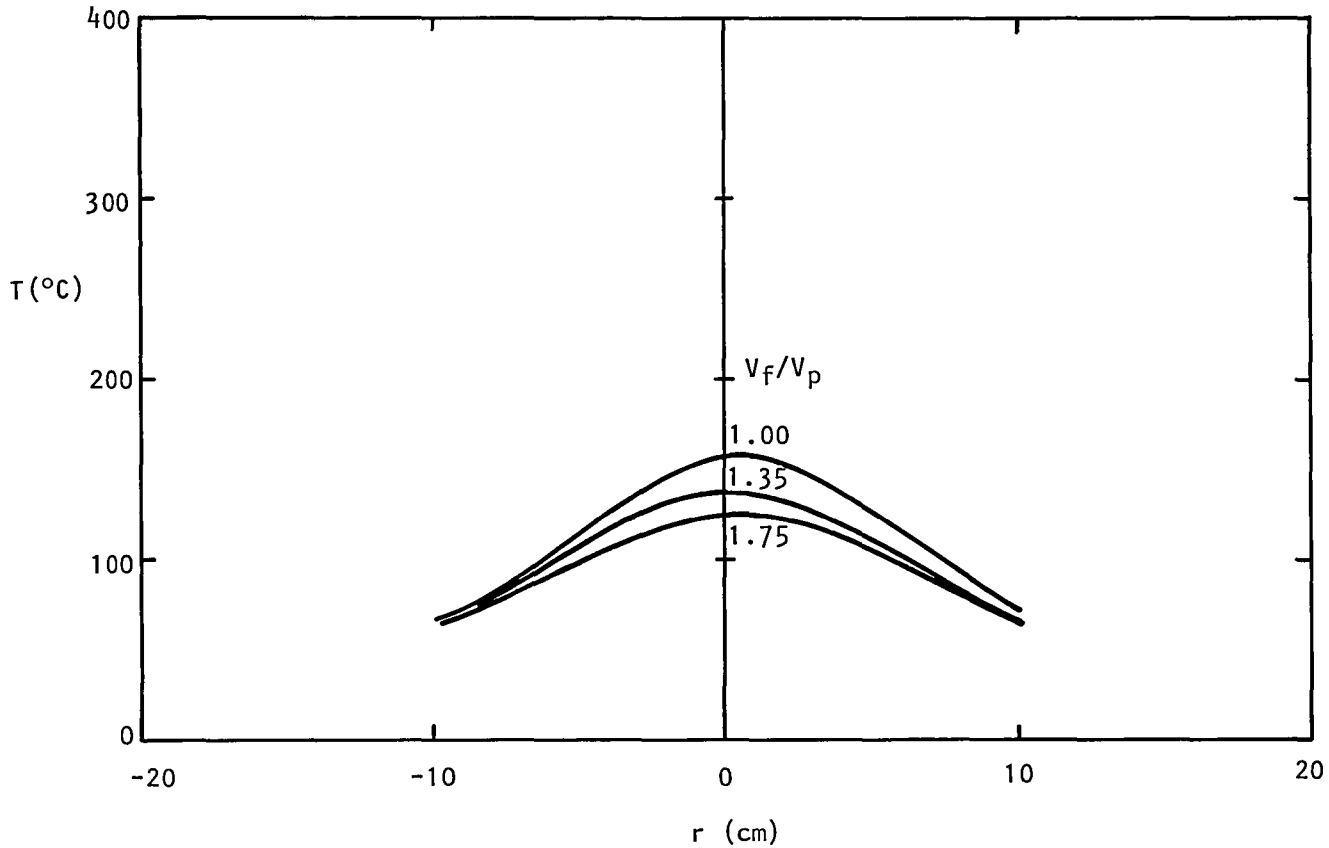

Figure 4.4(d) Effect of V_f/V_p on static temperature profiles at $x/D_{eq} = 12.12$; $T_f/T_p = 1$.

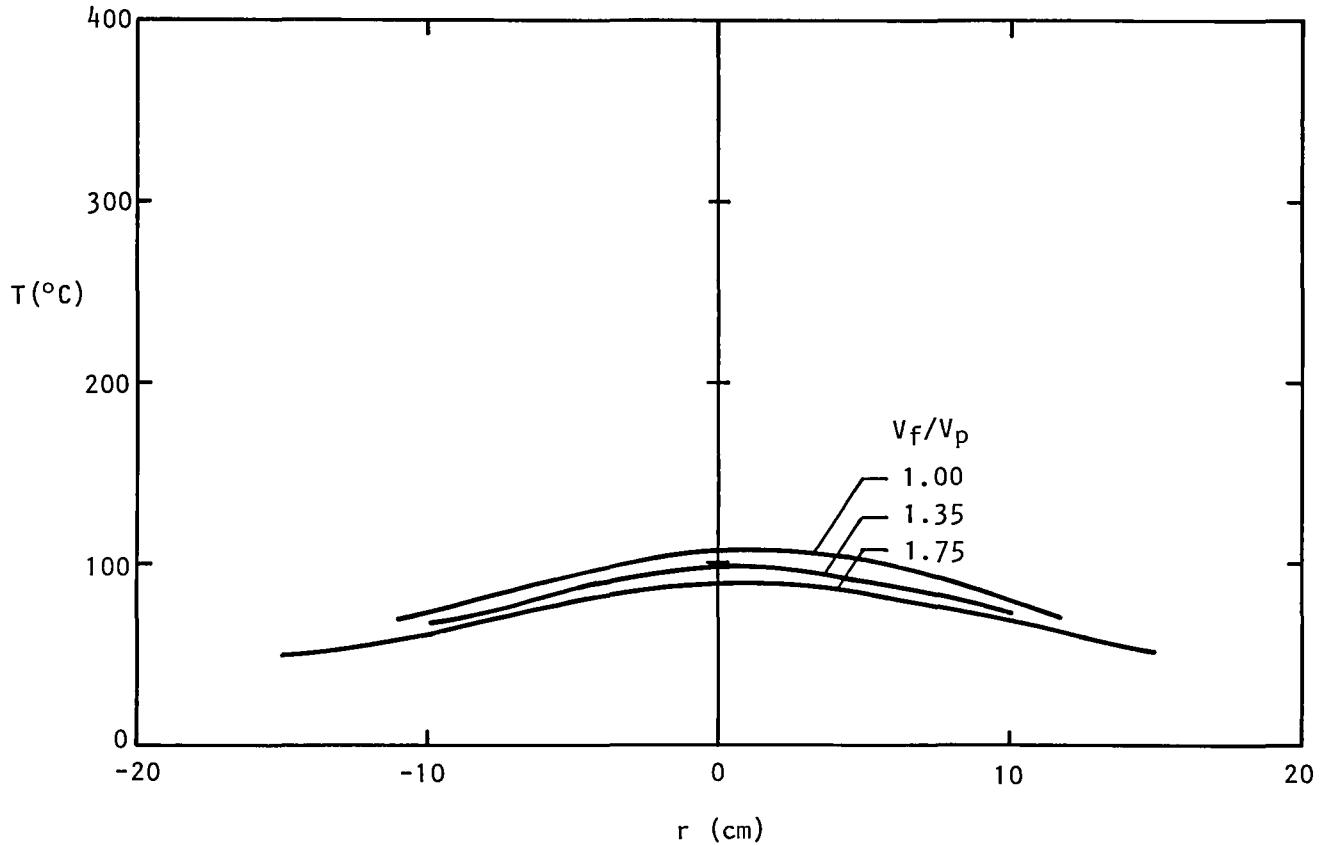

Figure 4.4(e) Effect of V_f/V_p on static temperature profiles at $x/D_{eq} = 18.17$; $T_f/T_p = 1$.

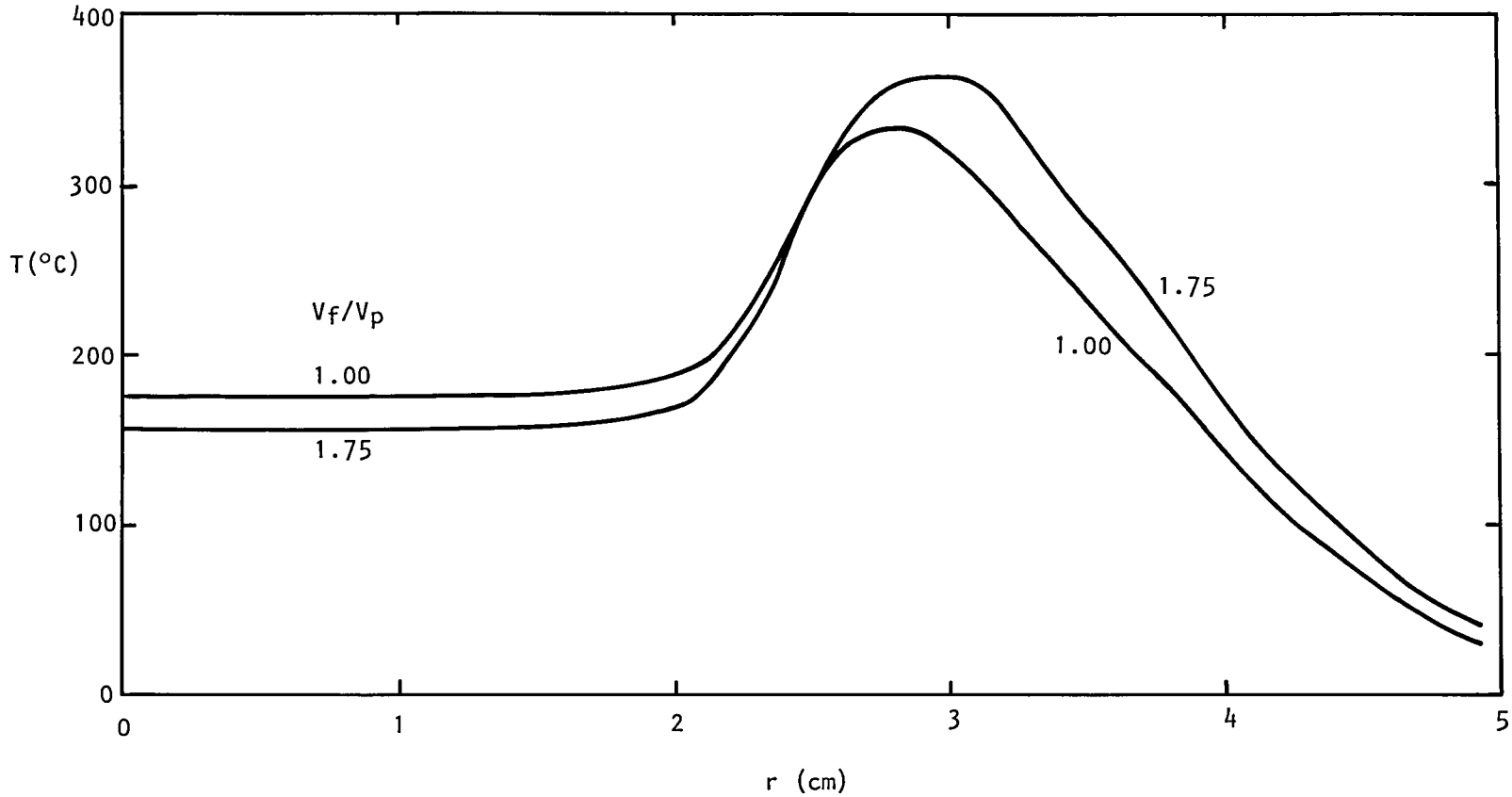

Figure 4.5 (a) Effect of V_f/V_p on static temperature profiles at $x/D_{eq} = 1.51$; $T_f/T_p = 1.75$.

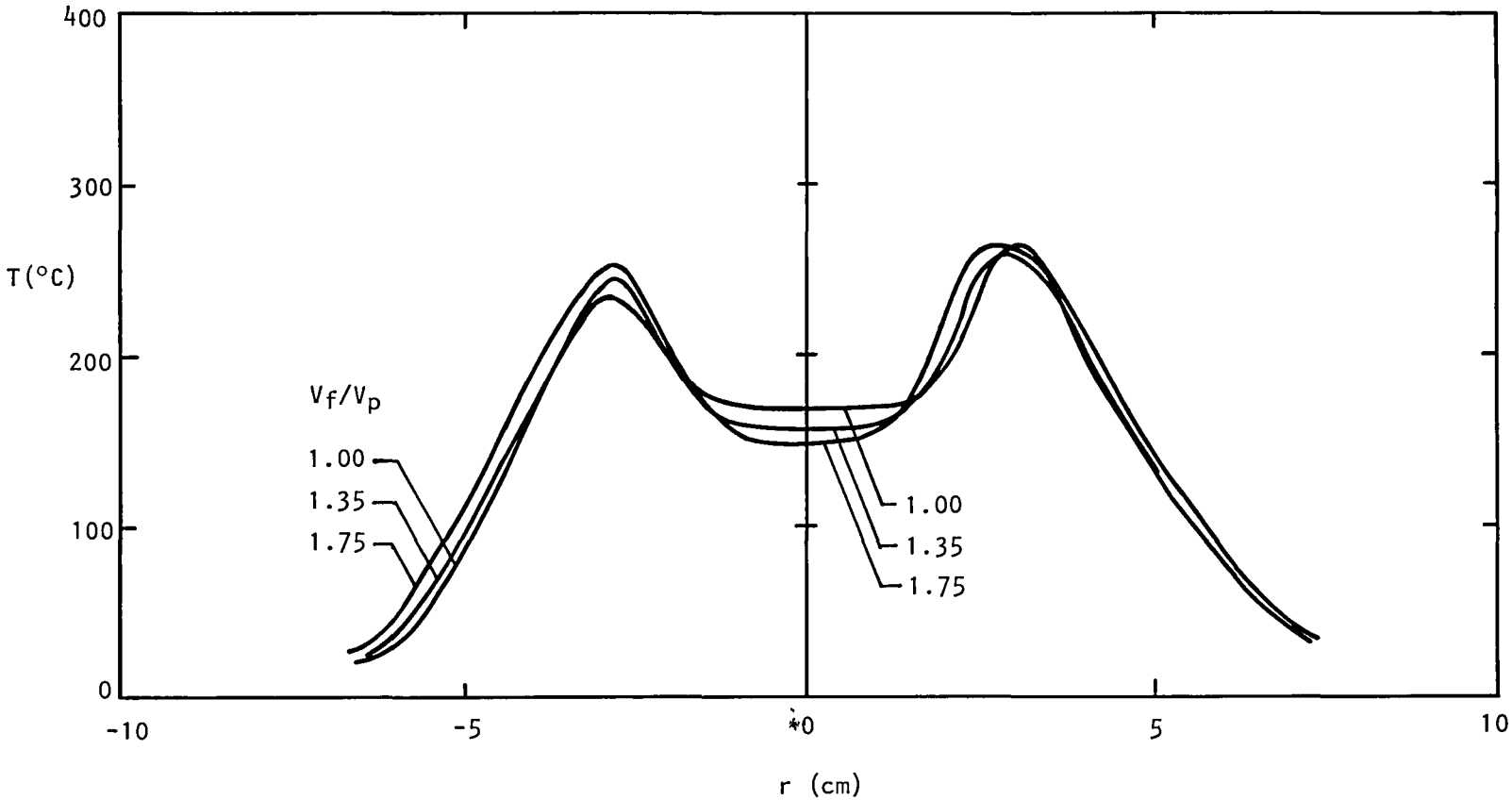

Figure 4.5(b) Effect of V_f/V_p on static temperature profiles at $x/D_{eq} = 3.03$; $T_f/T_p = 1.75$.

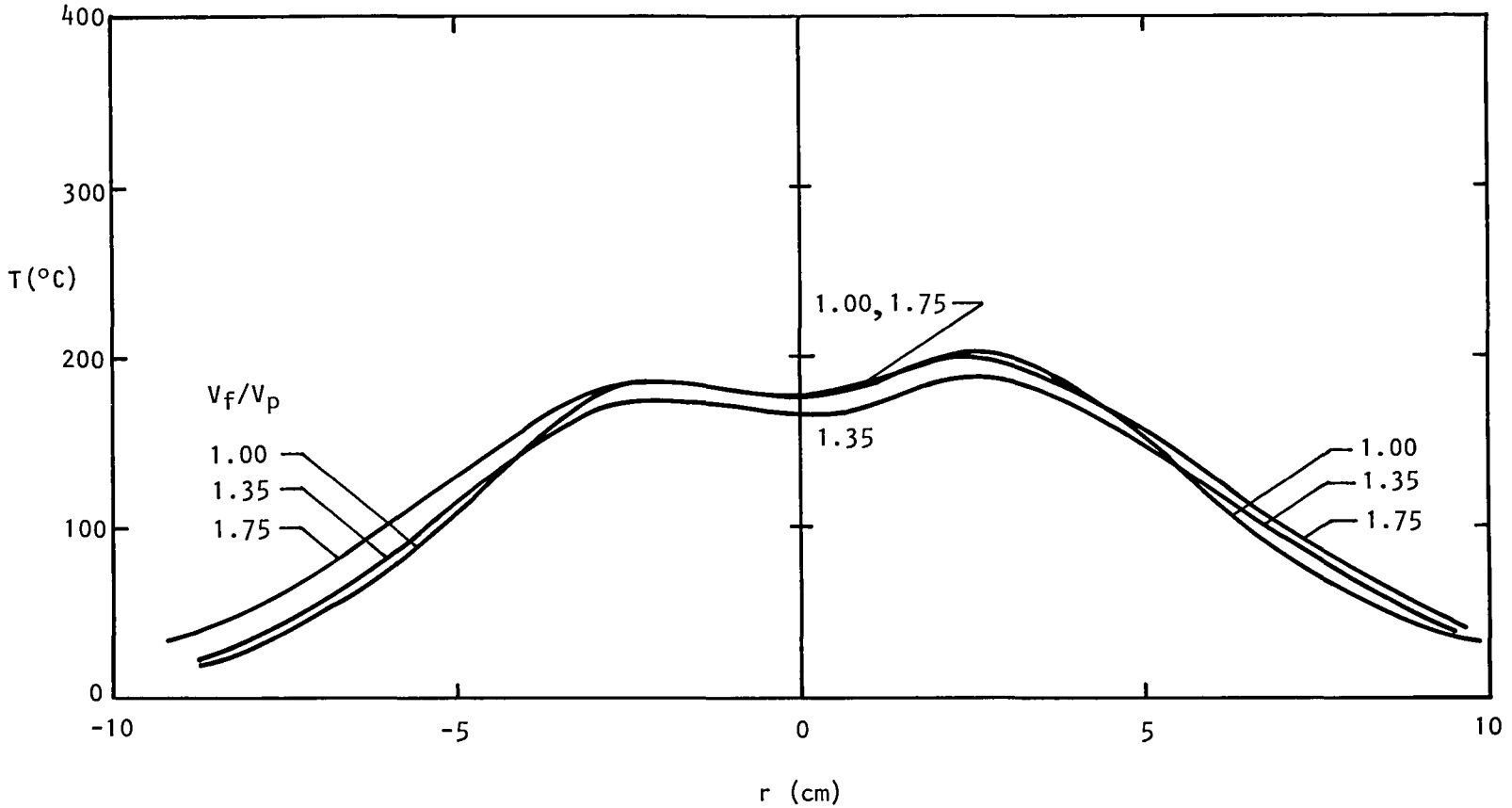

Figure 4.5(c) Effect of V_f/V_p on static temperature profiles at $x/D_{eq} = 6.06$; $T_f/T_p = 1.75$.

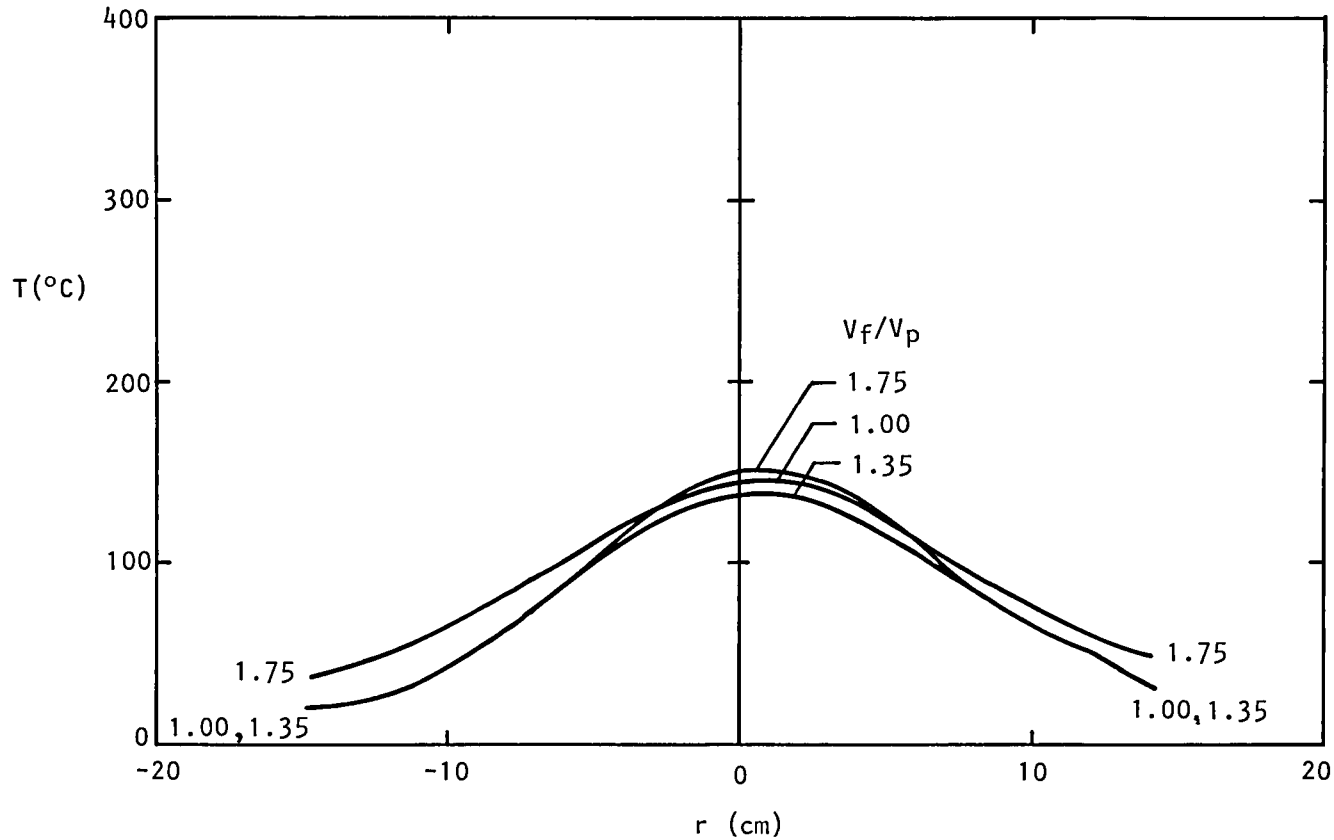

Figure 4.5(d) Effect of V_f/V_p on static temperature profiles at $x/D_{eq} = 12.12$; $T_f/T_p = 1.75$.

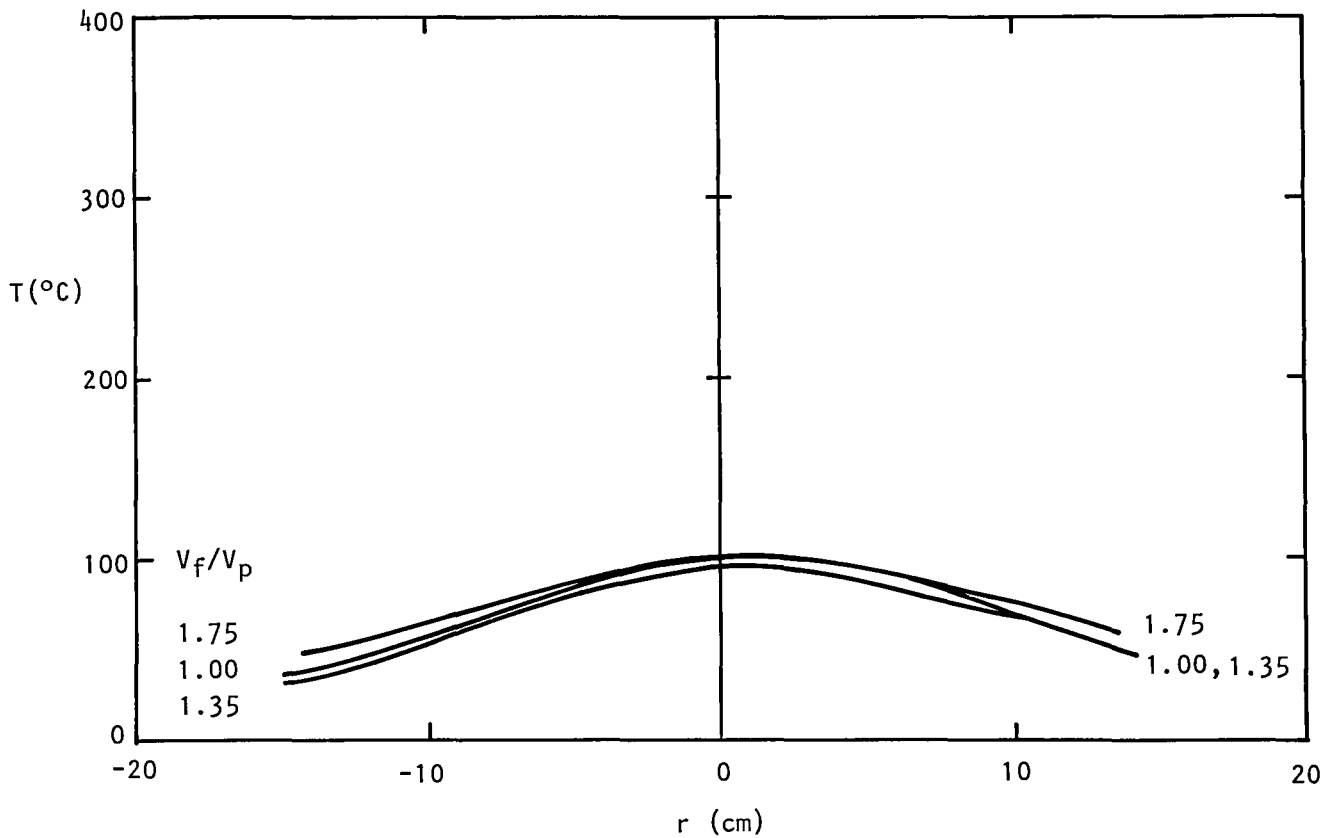

Figure 4.5(e) Effect of V_f/V_p on static temperature profiles at $x/D_{eq} = 18.17$; $T_f/T_p = 1.75$.

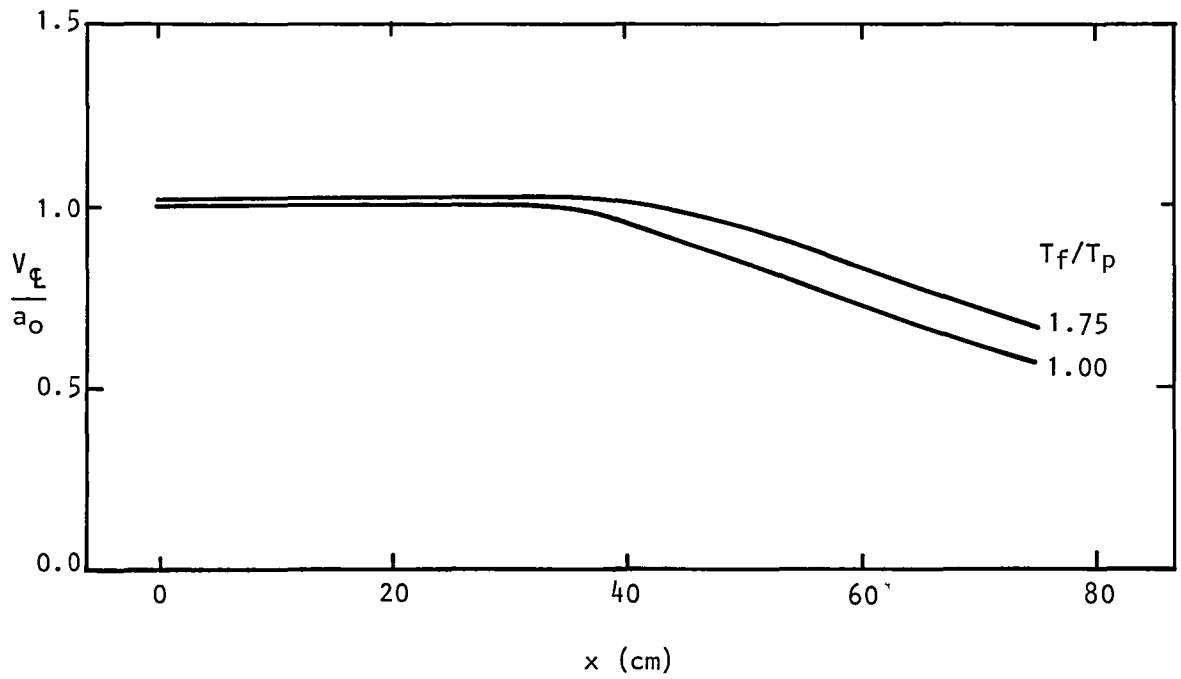

Figure 4.6 Effect of T_f/T_p on mean velocity decay along jet centerline; $V_f/V_p = 1$.

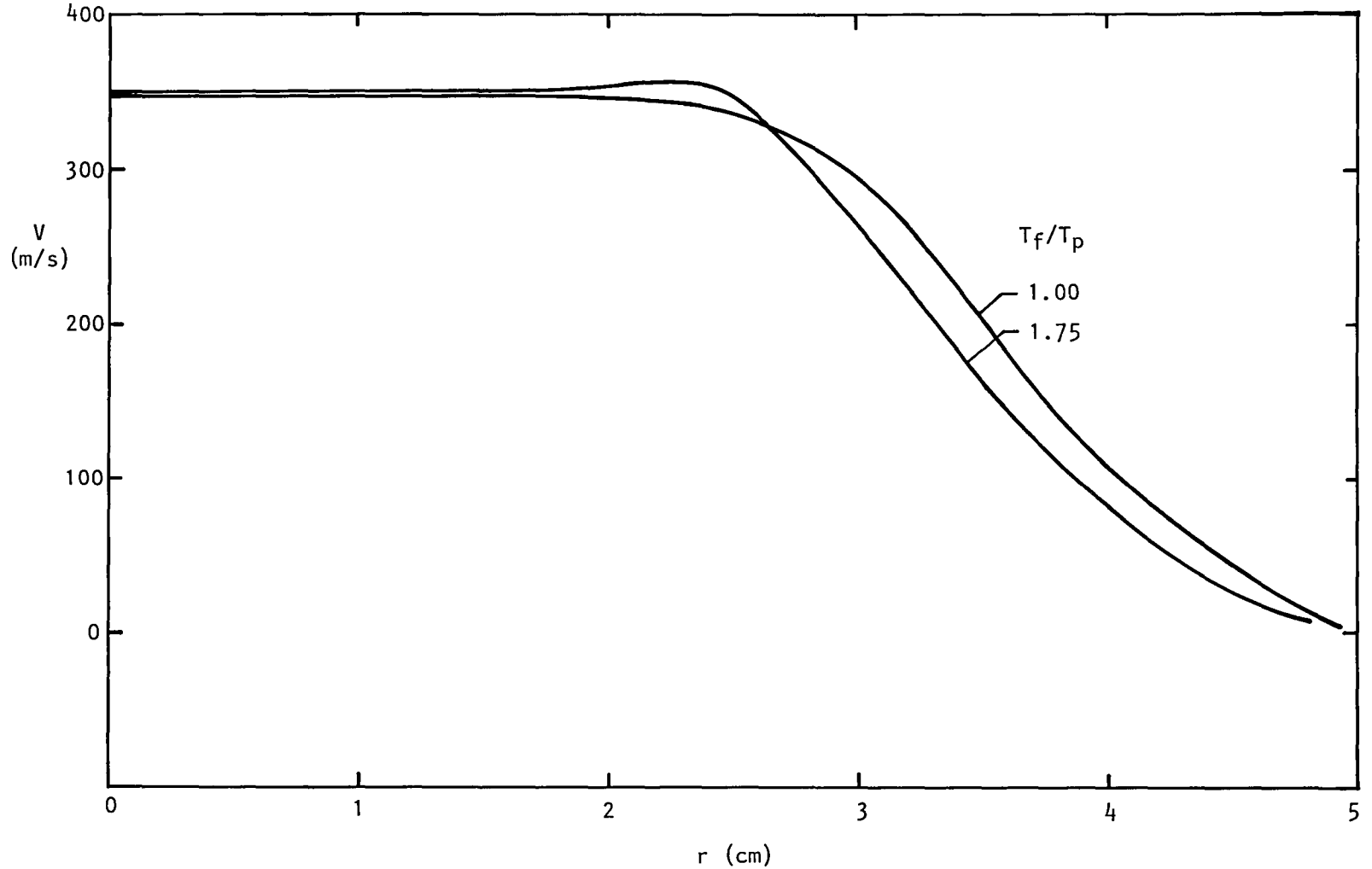

Figure 4.7(a) Effect of T_f/T_p on mean velocity profiles at $x/D_{eq} = 1.51$, $V_f/V_p = 1$.

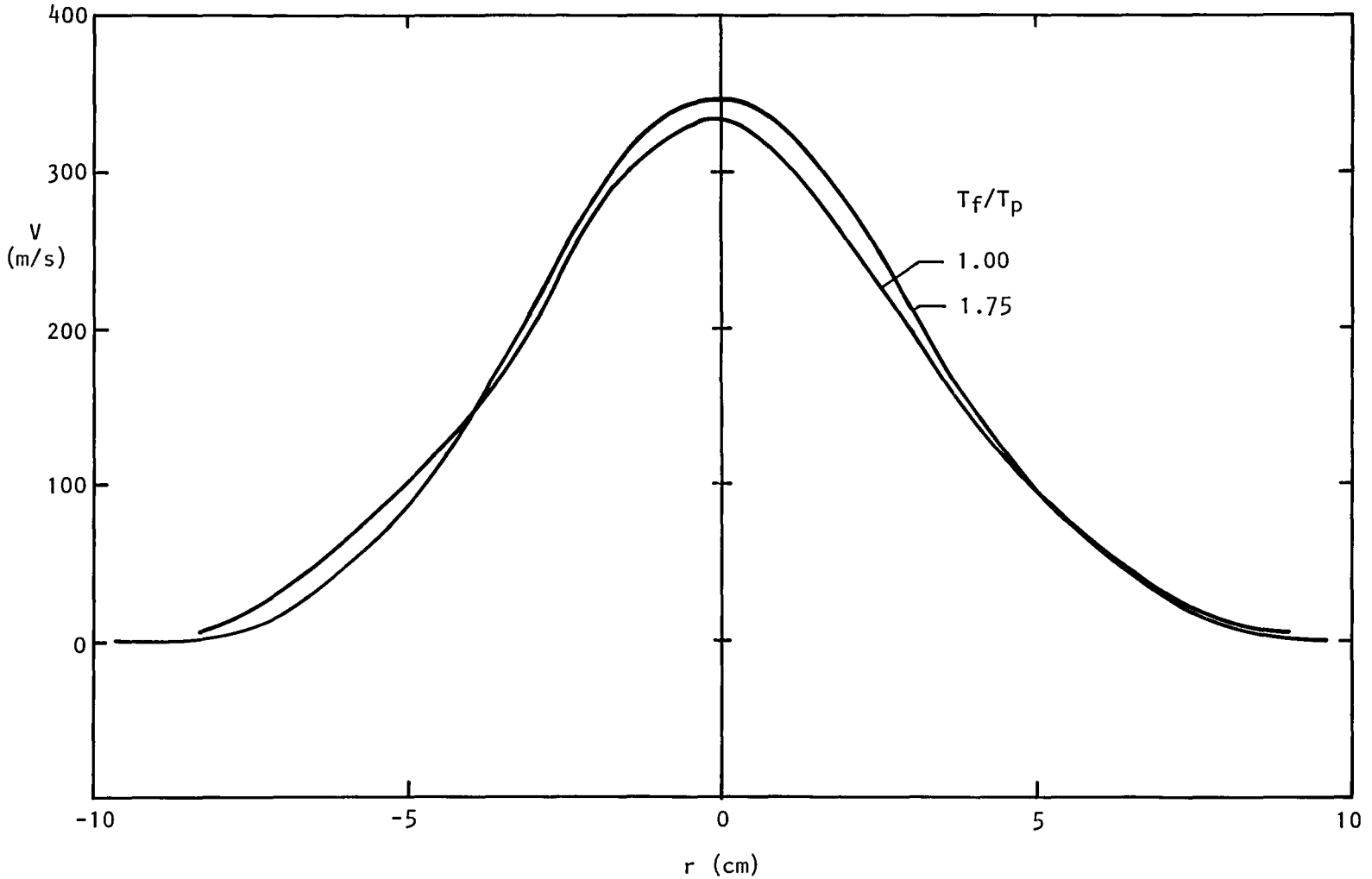

Figure 4.7(b) Effect of T_f/T_p on mean velocity profiles at $x/D_{eq} = 6.06$; $V_f/V_p = 1$.

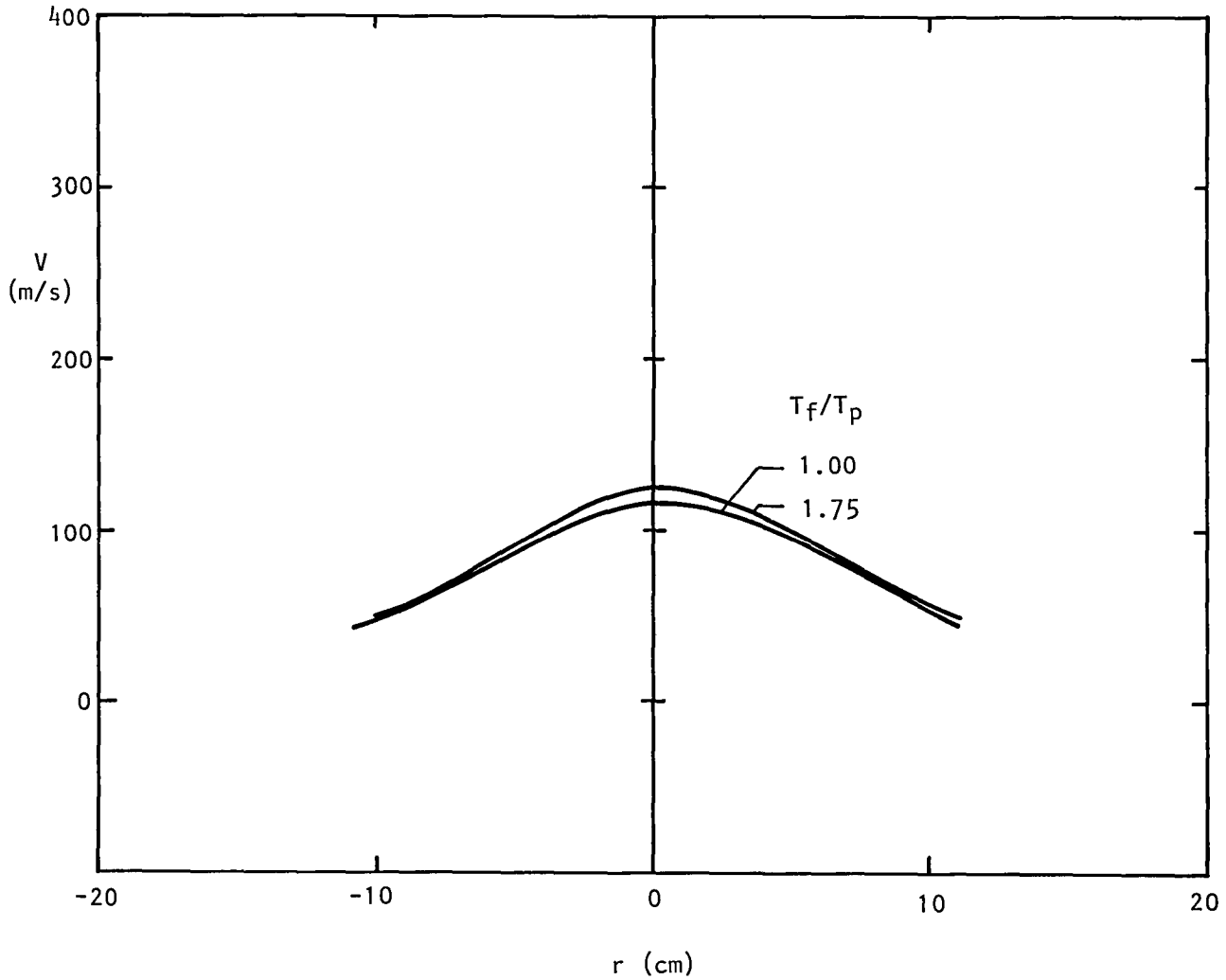

Figure 4.7(c) Effect of T_f/T_p on mean velocity profiles at $x/D_{eq} = 18.17$; $V_f/V_p = 1$.

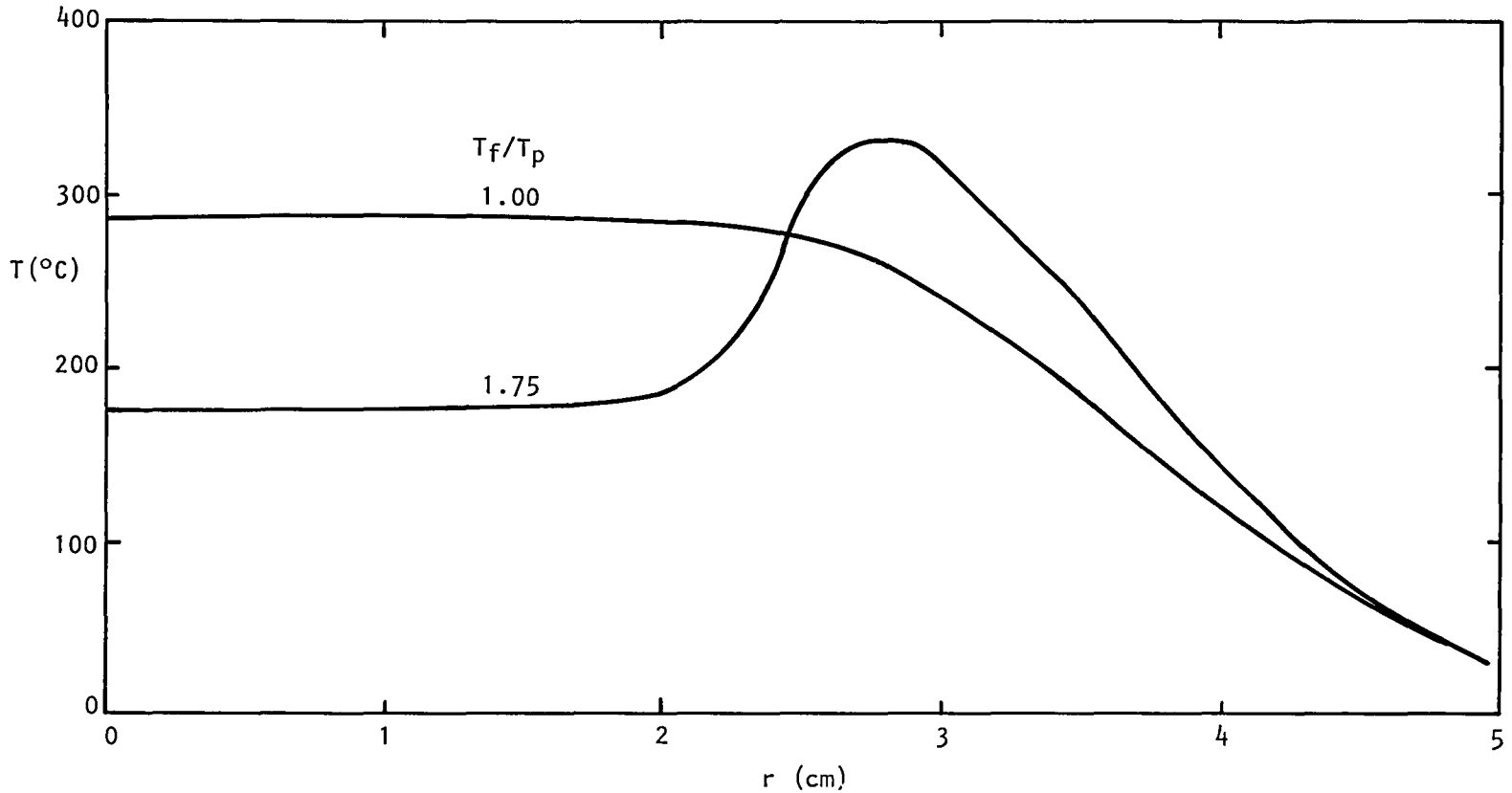

Figure 4.8(a) Effect of T_f/T_p on static temperature profiles at $x/D_{eq} = 1.51$; $V_f/V_p = 1$.

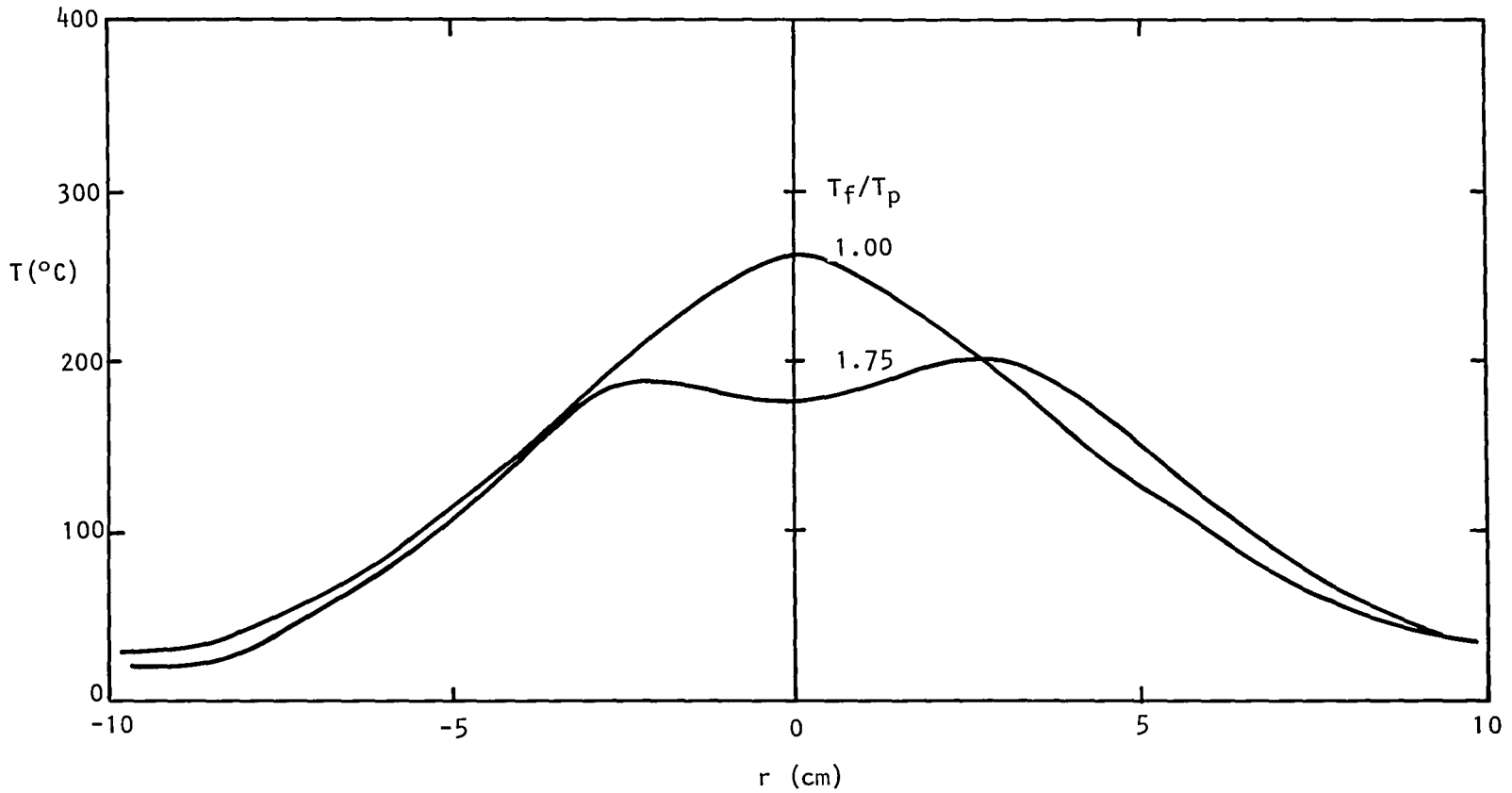

Figure 4.8(b) Effect of T_f/T_p on static temperature profiles at $x/D_{eq} = 6.06$; $V_f/V_p = 1$.

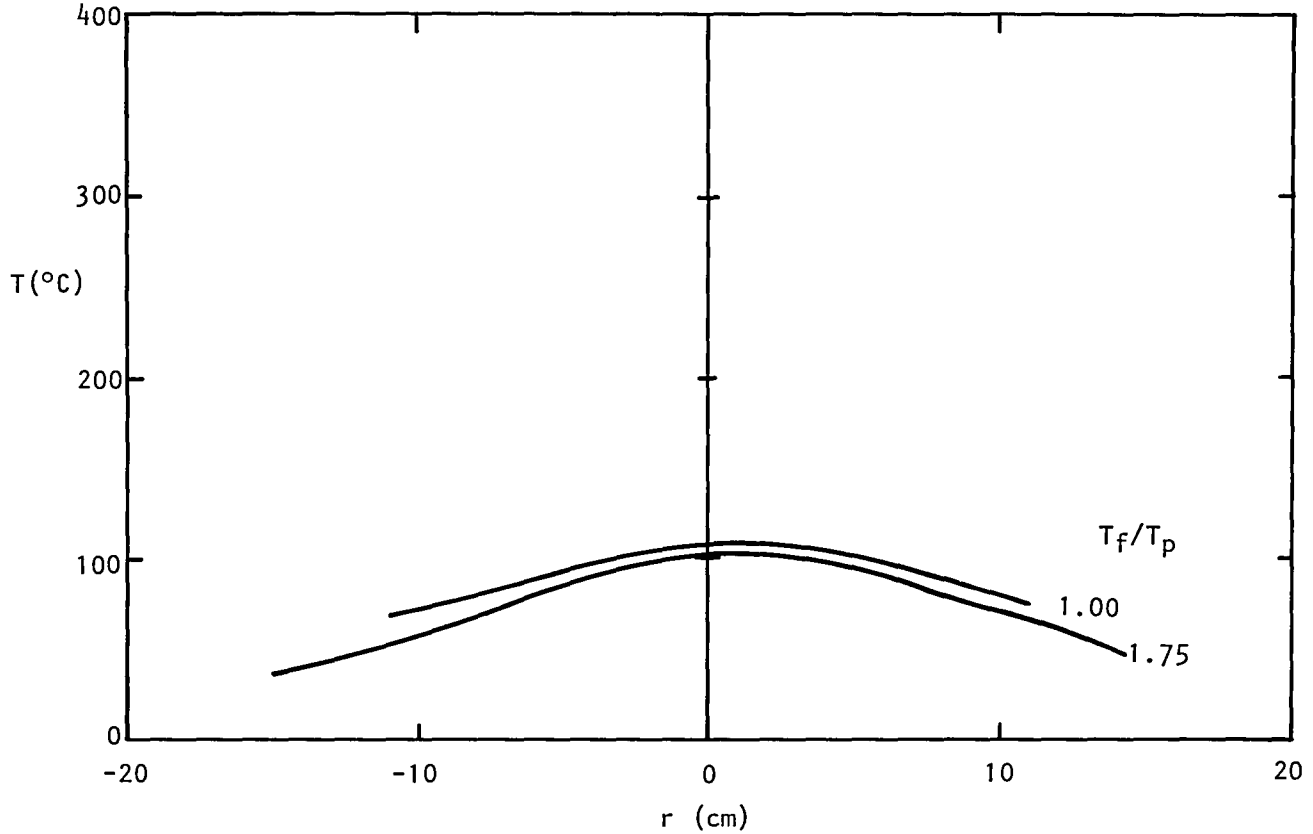

Figure 4.8(c) Effect of T_f/T_p on static temperature profiles at $x/D_{eq} = 18.17$; $V_f/V_p = 1$.

5. LASER VELOCIMETER MEASUREMENTS AND RESULTS

5.1 INTRODUCTION

In addition to the pressure and temperature surveys described in the previous section, jet flow measurements have been conducted using a two-point four-channel laser velocimeter. These LV experiments are also conducted to provide detailed jet flow information which can be used to explain the changes in the noise characteristics of coannular jets operated under inverted-velocity-profile conditions

Coannular flows have been investigated before by Willis and Glassman (ref. 5.1); Chigier and Beer (ref. 5.2); Williams, Ali and Anderson (ref. 5.3), Durão and Whitelaw (ref. 5.4), and more recently by Ko and Kwan (ref. 5.5). Others have also studied flows of jets emitting into a co-flowing stream [e.g. Forstall and Shapiro (ref. 5.6), Antonia and Bilger (ref. 5.7), and Morris (ref. 5.8)]. Together, they provide useful insights into the effects of an external flow field surrounding a single primary jet. Most of these works however are concerned with cases where the external flow has a lower speed than the primary jet. Durão and Whitelaw, and Chigier and Beer considered the case of an inverted velocity profile, but the primary jet of the former issued from a long pipe and therefore the mean velocity profile at the exit was not flat. Moreover, the arrangements of the jets in those two studies were such that there was essentially a thick lip in the primary nozzle. It is expected that a large wake would form, and it would affect the mixing process downstream in a manner different from that formed downstream of a thin-lipped nozzle.

In the present study, the primary nozzle lip is very thin, and the nozzles are contoured so that the flow issues from both the primary and annular nozzles in a direction which is parallel to the jet axis. In addition, the exit plane of the secondary nozzle is displaced a little upstream of the exit plane of the primary nozzle. Thus, the exit boundary layer on the outer side of the primary nozzle lip is expected to be different from that which would result when the nozzles are coplanar as in most of these earlier studies.

The major difference between the present experiments and the earlier studies, however, is that the annular jet velocity in the present study is equal to or greater than the primary jet velocity. Moreover, the magnitudes of the velocities involved (stemming from the higher Mach numbers and temperatures) are generally significantly higher than those investigated earlier.

5.1.1 Test Plan

The general experimental program plan for this contract was described in section 2, where the detailed implications of the test conditions selected were also discussed. The matrix of subcritical test points (TP) 1 through 12 given in Table 2.1 (Section 2) has been designed to provide constant thrust and mass flow rate at each test point. In addition, two supercritical test

points (TP's 13 and 14 defined in Table 2.2 of Section 2) were selected purely on the basis that significant noise reductions have been observed at these two conditions in previous studies on coannular jet noise. These two supercritical test points are not related to each other or to the twelve subcritical test points.

The test plan for the LV measurements is an abridged version of the general test plan because of the greater effort involved in making LV measurements. Thus, only a representative set of test points is selected on the basis of trends observed in the pressure/temperature surveys (Section 4) and the acoustic measurements (Section 2). The test conditions originally chosen for the LV measurements are given in Table 5.1. The four subcritical conditions (i.e. TP's 1, 2, 4, and 9) represent the minimum number of cases necessary to allow meaningful trends to be revealed.

Table 5.1 Test conditions for laser velocimeter measurements.

			PRIMARY		FAN	
Test Point (TP)	V_f/V_p	T_f/T_p	M_p	T_p/T_o	M_f	T_f/T_o
1	1.00	1.00	0.752	1.91	0.752	1.91
2	1.35	1.00	0.647	1.87	0.873	1.87
4	1.75	1.00	0.548	1.77	0.959	1.77
9	1.00	2.00	0.849	1.50	0.600	3.00
13	1.66	1.26	0.790	2.19	1.211*	2.76
14	1.95	2.47	1.055*	0.83	1.367*	2.07

**Mach number for an equivalent fully-expanded jet.*

In the course of the preliminary measurements and initial efforts to correlate the noise data with the flow data, it became clear that the jet flow field at each subcritical test point needed to be surveyed in greater detail than had originally been intended. Due to that expanded effort in the subcritical regime, there was no time left to study the second supercritical test case (i.e. TP 14).

The measurements were performed in two parts. Firstly, measurements were made at individual points in the flow and displays of mean velocity and turbulence intensity distributions were obtained. Since velocities in two orthogonal directions are obtained simultaneously, a map of axial and radial velocity distributions in the flow field were obtained in one sweep. In the second part, two-point cross-correlation measurements were obtained, and from these the length scale of turbulence and the convection speed were deduced.

5.1.2 The Use of the Laser Velocimeter

The reason for using a laser velocimeter for this part of the study is that the Mach numbers and temperatures of the jets are relatively high and this precludes the use of a hot-wire anemometer which has hitherto played a dominant role in turbulence research and in our present understanding of the flow structure in low-speed jets.

The laser velocimeter is an instrument of recent development, and various efforts have been made to quantify its capabilities as an instrument for turbulence research. Its main advantage is that no external probe is inserted into the flow. Thus, it is not subject to breakage under severe flow conditions such as those encountered in the present study. Moreover, the absence of an external probe in the flow region ensures that the measurements are truly those of the "undisturbed" flow field. An added advantage is that when an LV is provided with frequency shifting in one of the beams, it is possible to determine the direction of each instantaneous velocity vector without ambiguity. This capability is not available with hot-wire anemometers and is an important feature when measurements have to be made within regions where reversed flows are suspected.

Hot-wire anemometers actually measure mass flow rate, and at low enough Mach numbers ($M < 0.3$) where density effects may be neglected, they give directly a measure of the velocity. However, at high Mach numbers or where the temperature variations are large, the interpretation of hot-wire results becomes a problem. The LV on the other hand measures the velocity of the flow uniquely and is therefore not subjected to such limitations.

Independent studies have been conducted by Barnett and Giel (ref. 5.9) and Lau, Morris and Fisher (ref. 5.10) to assess the capabilities of the laser velocimeter, by comparing laser velocimeter and hot-wire measurements in unheated single jets at very low Mach numbers. The measurements included spectra and higher statistical moments (skewness and kurtosis) of the fluctuating signals, and demonstrated that the laser velocimeter in the present form has practically all the capabilities of the hot-wire. One exception is that it cannot, in its present form, be used dependably for conditionally sampled measurements, but is is conceivable that this may also become possible with further development of the instrument.

The mean velocities obtained with the laser velocimeter and the hot-wire were of comparable magnitudes and the spectra of velocity fluctuations exhibited the same appearance. In particular, the peaks of the spectra obtained in the potential core of the jet occurred at the same Strouhal number. The laser velocimeter results of turbulence intensity were, however, systematically higher than the corresponding hot-wire results on the inner part of the jet even after all known corrections had been applied to both the results. The discrepancy was almost uniform from the jet axis to the lip line and a percentage error of about 14% of the hot-wire results was measured in the region of maximum intensity. Effort is being made to resolve this error and it is now believed [Whiffen, Lau and Smith (ref. 5.11)] that the inherent "shot noise" from the photomultiplier tube may have contributed to the error in the LV turbulence intensity results.

5.1.3 Layout of Present Section

The results are presented in two subsections. The first subsection (Section 5.3) deals with single-point measurements made at different locations in the jet and consists of measurements of the mean velocities, turbulence intensities and their characteristics in the axial and radial directions. The effects of varying test conditions (i.e. V_f/V_p and T_f/T_p) on their distributions are studied in detail. In the second subsection (Section 5.4), two-point cross-correlation data are discussed. These results include measurements of the convection velocity and length scale of turbulence at various points in the flow field. These are also studied with respect to changes in the jet conditions. However, before presenting and discussing the data, the equipment is described in Section 5.2 below.

5.2 EQUIPMENT AND TECHNIQUES

5.2.1 Air Supply

Figure 5.1 shows a schematic view of the air system. Dry air is supplied from a plant air compressor facility at $2MN/m^2$. Upstream of the nozzle and the jet plenum, the air line divides into two branches. One branch goes to the sudden expansion burner where the air is heated by burning propane. The other continues downstream and subsequently connects with the outlet from the burner. The desired plenum pressure and temperature for each jet are achieved by an appropriate control of the two streams (hot and cold) of air. The valves for this facility are computer controlled, and they are duplicated in such a way that air at any desired pressure and temperature may be supplied independently to the two plenums.

Figure 5.2 shows a photograph of the jet rig. The coannular jet nozzles and their arrangement are identical to those used for the noise measurements and have been discussed in Section 2.

5.2.2 Laser Velocimeter and Ancillary Equipment

The physical features of the laser velocimeter have been described earlier (refs. 5.8 and 5.10). It consists essentially of a transmitting optical system (Figure 5.3) which sends out two pairs (one green and the other blue) of coherent laser beams which intersect at the measurement point in the jet. The beams are oriented in such a way that the two sets of fringes formed at the measurement volume are normal to each other. Thus, velocities in two orthogonal directions are obtained. The fringes are made to move within the measurement volume by means of frequency shifting induced with an acousto-optical transducer (Bragg cell).

The alternating light scattered by the individual particles of aluminum oxide powder seeded in the flow is detected by the receiving optical system placed at about 30° to the transmitting beams. Color separators, which allow separation of the green and blue light detected at the measurement volume, are placed in the receiving optical system across the path of the scattered

light. The alternating green and blue light signals are then converted into alternating voltages by photomultiplier tubes (PMT) and these voltages are processed in the electronic processor. Validation circuits are incorporated in the processor to ensure that the signals are the signals arising out of the passage of single seeding particles, and the validated signals are analyzed by a digital computer to give results on mean velocity, turbulence level and covariance of the velocity components. The raw data on instantaneous velocities may also be recorded on magnetic tape for subsequent analysis to give results on spectra and auto- and cross-correlations.

A set of the transmitting and receiving optics is mounted securely on each of the two traversing frames shown in Figure 5.3. The measurement volumes are therefore fixed relative to their respective frames and their positioning is accomplished by moving the frames. The frames are mounted on a large platform which is free to move axially. They are also arranged so that the downstream frame may move relative to the other frame, and each frame has transverse motion in two orthogonal directions. By the use of absolute positioning encoders, the location of the measurement volume can be determined to an accuracy of better than 0.1 mm. The frame movement is controlled by the computer and is fully automated.

5.3 SINGLE-POINT RESULTS

5.3.1 Subcritical Flow

5.3.1.1 Radial distributions

(a) Mean Velocity. Figure 5.4 shows the radial distributions of the axial mean velocity for Test Point 1. The different curves are for different axial stations of the jet. In this case, the primary and secondary jets have identical conditions, and the composite jet is expected to behave much like a single jet except for the effects of the lip of the primary nozzle and the boundary layers built up on the inside and outside surfaces of the nozzle. At $x/D_{eq} = 0.5$ (D_{eq} being the diameter of the equivalent nozzle), the distribution shows a dip along the lip line of the primary nozzle demonstrating these effects. But from $x/D_{eq} = 2$, the effects of the primary nozzle lip are no longer evident. Figure 5.5 shows distributions for Test Point 9, and the distributions have the same appearance as those of Figure 5.4.

Figures 5.6 and 5.7 show radial distributions of the axial mean velocity for Test Points 2 and 4, respectively. The mean velocities are normalized by the primary jet exit velocity V_p in Figures 5.6(a) and 5.7(a) and by the fan or annular jet exit velocity V_f in Figures 5.6(b) and 5.7(b). The development of the composite jet displays very similar characteristics to those exhibited by the results of Williams et al. (ref. 5.3) even though the present jet has an inverted velocity profile. Initially, the primary and secondary shear layers are separated from each other by the annular potential core. With distance downstream, each layer increases in its spread and finally merges with the other layer causing a termination of the annular potential core. At greater distances downstream, the two shear layers apparently become more

deeply infused into each other, and in the present case of an inverted velocity profile, the maximum velocity in the annular region falls. The process continues until the velocity peak in the annular region disappears. This occurs for Test Points 2 and 4 at about $x/D_{eq} = 3$ and 4, respectively. At these stations, the primary potential core is still present.

The extent of the present measurements does not allow the length of the annular potential core to be determined exactly. However, there are indications from measurements along the $r/D_{eq} = 0.42$ line to suggest that the annular potential core length may increase with increasing fan-to-primary velocity ratio (V_f/V_p). It is possible therefore that there is a connection between the length of the annular potential core and the distance at which the inverted profile disappears.

Figures 5.6 and 5.7 also indicate that the annular flow tends to bend towards the jet centerline with increasing axial distance from the nozzle. This is evident in the movement of the peak in the inverted velocity profile. The results of Williams et al. (ref. 5.3), K_o and Kwan (ref. 5.5), and Durão and Whitelaw (ref. 5.4) also indicate this tendency for the annular flow to bend towards the jet axis.

It is observed that for both test cases, the primary potential core behaves like a single jet in that there is a region of constant velocity which gradually diminishes in radial extent with increasing axial distance from the nozzle. This apparently is not necessarily true for all coannular flows. Durão and Whitelaw's results suggest that the velocity in the "core region" may under certain circumstances be lifted up by the annular flow as the axial distance is increased, and the trend is especially evident in their results for the case where the annular velocity is about 4.35 times the primary velocity.

Figures 5.8(a) through (d) show distributions of the unnormalized mean velocity at four axial stations. A comparison is made between the distributions under varying jet exit conditions. This would be equivalent to comparing the distributions when the velocities are normalized by a constant value (e.g. by the equivalent jet exit velocity V_{eq}). Close to the jet centerline, the curves differ substantially from one test to another, and this difference is more marked close to the nozzle exit. At large radial distances ($r/D_{eq} > 0.6$) all curves tend to converge for the test cases considered. It would appear therefore that changing the initial primary and secondary jet conditions does not substantially affect the flow field in the outer part of the jet. At large distances from the nozzle, this situation extends even to the inner region.

One of the characteristics of mean velocity distributions of single jets is that the distributions exhibit similarity behavior. For example, when the distributions are plotted in terms of V/V_J and $\eta^* = (r - r_{0.5})/x$, V_J being the jet exit velocity and $r_{0.5}$ the radius of the half velocity point, they collapse onto one curve (refs. 5.10, 5.12). Ko and Kwan (ref. 5.5) also reported reasonably good collapse of the data for coannular jets.

Figures 5.9 and 5.10 show such plots for Test Points 1 and 9, and good collapse of the data is achieved. Results for an equivalent single jet of corresponding Mach number and temperature conditions are reconstructed from a universal curve obtained previously (ref. 5.12) and are also shown. There is generally good agreement at $\eta^* > 0$ and around $\eta^* = 0$. At $\eta^* < 0$, however, the present results are a little higher. It appears therefore that the existence of an inner primary nozzle lip inside a jet merely alters the profile on the inner side of the jet.

Figures 5.11 and 5.12 show similar plots for Test Points 2 and 4, respectively. The mean velocities are normalized by (a) the primary jet exit velocity (V_p), (b) the secondary jet exit velocity (V_f), and (c) the jet exit velocity of the equivalent single jet (V_{eq}).

Normalizing by V_p results in a systematic scatter of the data. With increasing distance from the nozzle, the distributions become more spread out, and the slopes generally smaller. The same trends are observed in the results obtained by normalizing with V_{eq}.

The results tend to collapse better when normalized by V_f especially those of Test Point 2. In the region around $\eta^* > 0$, the data at the different axial stations may be seen to collapse onto one curve. This suggests that the secondary shear layer preserves its similarity to some degree in spite of the growing influence from the primary shear layer as the axial distance is increased. Closer to the primary flow region ($\eta^* < 0$), the effect of the primary flow is increasingly felt, and the curve for each succeeding axial position peels off from its preceding curve at a greater radius. The depression in the velocity is due to the lower primary flow velocity. It appears therefore that the outer shear layer of the fan stream is attempting to preserve some degree of similarity like that of a single jet.

For a detailed study of the development of the primary shear layer, a more intensive set of measurements would need to be conducted in the initial region of the jet. The present results however give a good general view of the developments. Figure 5.13 shows the distributions of the mean velocity in the primary shear layer of the coannular jet at Test Point 4. The ordinate is expressed in terms of $(V-V_p)/(V_f-V_p)$ and the abscissa in terms of $\eta^{*\prime}=(r-r'_{0.5})/x$ where $r'_{0.5}$ is the location of $(V-V_p)/(V_f-V_p) = 0.5$. The figure shows reasonable collapse of the data and would agree with Ko and Kwan's findings (ref. 5.5). The spreading rate in the inner shear layer is apparently somewhat less than that of the outer shear layer. However, it should be pointed out that because of the sparsity of the data and the inaccuracies which accrue from taking differences of large numbers, the present results are not necessarily conclusive.

(b) Turbulence. Figures 5.14(a), (b), and (c) show radial distributions of the axial and radial turbulence intensities and the covariance $\overline{u'v'}/V_f^2$, respectively for Test Point 1. At $x/D_{eq} = 0.5$, a second peak appears in the distribution. This is due to the presence of the lip of the primary nozzle. By $x/D_{eq} = 2.0$, however, the effects of the lip are not noticeable anymore. The peak axial turbulence intensity around $x/D_{eq} = 2$ to 4 is in the region of 17% to 18% and would agree with the results from a single jet (ref. 5.12). The peak radial turbulence intensity is (as for the single jet) about 2/3 to 3/4 of the axial turbulence intensity. The covariance is also of comparable size.

Figures 5.15(a), (b) and (c) show the same distributions for Test Point 9. The peak values generally are about 10% higher than for Test Point 1, but the relationships between the peak values of $\tilde{u}/V_f$, $\tilde{v}/V_f$, and $\overline{u'v'}/V_f^2$ are the same.

Similar distributions for Test Points 2 and 4 are shown in Figures 5.16 and 5.17, respectively. It is significant that except for $x/D_{eq} = 0.2$, the intensity distributions show only one distinct peak, even where an independent primary shear layer still exists [e.g. compare Figures 5.7 and 5.17(a)]. Moreover, the peak is located in the secondary shear layer suggesting that the maximum turbulence intensity in a coannular jet is mainly associated with the secondary shear layer. This is why the normalized velocities in these curves are expressed in terms of the annular jet exit velocity V_f. The peak axial turbulence intensity for the two test cases is about 19% at $x/D_{eq} = 2.0$, which compares well with results of Test Points 1 and 9. The ratio of the peak radial-to-axial turbulence intensities tends to be a little lower.

With single jets, it is possible to reduce all radial distributions of the turbulence intensities to one curve by plotting the results in terms of $\tilde{u}/\tilde{u}_p$ and η^* (ref. 5.12). The quantity $\tilde{u}_p$ is the peak turbulence intensity and η^* is the radial position parameter defined earlier. Figure 5.18 shows the turbulence intensity results for Test Point 9 plotted in this manner. The data points lie within a narrow band as was observed for single jets (ref. 5.12). Test Point 1 results are not shown, but they have essentially the same characteristics.

Results from a single jet of nearly comparable exit conditions ($M_J = 0.7$, $T_J/T_o = 2.32$) are also drawn in Figure 5.18. The distributions appear to be a little broader than for Test Point 9, but the general behavior and appearance of the curves are similar.

The results for Test Points 2 and 4 (not presented here) show a large scatter, and the location of the peaks deviate substantially from each other and from $\eta^* = 0$. This situation is found to be more pronounced in TP 4 ($V_f/V_p = 1.75$) than in TP 2 ($V_f/V_p = 1.35$). It suggests strongly that the peak turbulence intensity location and the half-velocity point are not necessarily coincident, and the greater the inversion of the velocity profile, the greater is the separation of these two points.

Figures 19(a) and (b) show how the peak turbulence levels $\tilde{u}_p$ and $\tilde{v}_p$ vary with axial distance. The levels have not been normalized so that they appear in terms of m/s. This has the same effect as normalizing the levels by a factor which is common to all the test cases. For Test Points 1 and 9 ($V_f/V_p = 1.00$ in both cases), the levels change very little between $x/D_{eq} = 3$ and $x/D_{eq} = 11$. Downstream of that, however, the levels fall rather rapidly. This is especially true of the $\tilde{u}$ data and is reminiscent of single jet results (ref. 5.12). The data of Test Points 2 and 4 (inverted velocity profile in both cases) show a steady fall in level after the initial rise between the nozzle exit and $x/D_{eq} = 2$. There is therefore a difference in the way the peak turbulence level changes axially depending on whether there is an inversion of the velocity profile or not.

(c) Spectra. Figures 5.20(a) to (f) show a representative set of spectra obtained at various points in the jet and under different test conditions. The distributions have been expressed in terms relative to the exit velocity of the coannular jet (V_f). The curves corresponding to positions in the potential core of the jet tend to exhibit a narrow band peak. Otherwise, they start off by being flat for a range of low frequencies but fall off at varying high frequencies. The frequency at which each curve starts to fall depends on the measurement point in the jet and the jet exit conditions. Following the fall, the curves may be seen in some cases to develop a series of spikes. These spikes are in general about 15 dB lower than the maximum intensity and are caused by the velocity sampling rate being insufficiently high. Figures 5.21(a) to (d) show the variation of this frequency with axial position, for Test Points 1, 2, 4 and 9, respectively, and it is evident in all cases that the magnitude of this frequency decreases with axial distance from the nozzle. Results from the centerline are also shown and they represent the frequencies at which the peaks occur. These also show the frequency to fall with axial distance.

5.3.1.2 Centerline distributions

Figure 5.22 shows the centerline distribution of the mean axial velocity. The mean velocity has not been normalized so that the curves show essentially the effects of changing the exit velocity profile (i.e. V_f/V_p) for coannular jets of the same equivalent single jet exit velocity.

For each of the test points, the velocity remains essentially constant in the initial region. There appears no tendency, even where the annular flow is much higher than the primary flow (i.e. for TP's 2 and 4), for the mean velocity on the centerline to be raised gradually by the higher annular flow. This differs from the results of Durão and Whitelaw (ref. 5.4) which indicate a climb in the centerline velocity for some distance from the nozzle before the velocity decay finally sets in. It is believed that these differences arise because Durão and Whitelaw's primary jet originates from a developed pipe flow. Moreover, the lip of their primary nozzle is substantially thicker and their annular region is much larger.

The initial rate of decay in the centerline velocity decreases with increasing exit velocity ratio (V_f/V_p). Therefore, although some curves begin at lower speeds, they all ultimately merge at some downstream position. Downstream of this point, the decay appears to be uniform and the curves fall at about the same rate.

Figure 5.23 shows the mean velocities normalized by the primary jet exit velocity for the respective test point. The results of Test Points 1 and 2 collapse on one curve in the region up to $x/D_{eq} = 12$. Downstream of that, the TP 2 curve peels off and rises above the TP 1 curve. This suggests a lifting of the centerline velocity by the higher annular flow with the effect becoming noticeable only after $x/D_{eq} = 12$.

Comparing next the results of Test Points 2 and 4, it may be seen that the curve for TP 4 lies downstream of that for TP 2. It has been found in single jets that the curves for centerline distributions move upstream when the jet Mach number is decreased (ref. 5.12). However, studies of jets with a co-flowing stream around them also show (e.g. refs. 5.6 and 5.8) that increasing the co-flowing stream velocity (for a fixed single jet velocity) causes the distributions to move *downstream*. Therefore, in changing from TP 2 to TP 4, two counteracting effects are brought into play, and it would seem that the downstream movement is greater. [In view of the temperature ratios involved, temperature effects are not expected to play a significant role (ref. 5.12).]

Similarly, it may be reasoned that the agreement between TP's 1 and 2 suggests that the upstream shift is identically offset by the downstream shift.

The curve for Test Point 9 is downstream of that for Test Point 1 and would reflect the higher primary jet Mach number in the former case. Witze (ref. 5.13) has shown, on the basis of Kleinstein's derivation (ref. 5.14) and data available on single jets, that the axial mean velocity distribution along the jet centerline may be represented by the equation:

$$V_a/V_J = 1 - \exp\{1/\chi\} = 1 - \exp\{\alpha/(1 - x/x_c)\} \qquad (5\text{-}1)$$

for $x > x_c$. The parameters α and x_c are determined from experimental results of V_a/V_J vs x/D by plotting $\chi = 1/\{\ln(1 - V_a/V_J)\}$ against x/D. The x-intercept of the straight line passing through the data points thus defines the potential length (x_c). This technique proved very successful in analyzing previous data on single jets (ref. 5.12).

Witze's formulation would not generally apply to coannular flows where two shear layers are involved and are liable to interact. However, the jets for Test Points 1 and 9 are essentially single jets with the exception of the wake of the primary lip. In view of this, Witze's formulation is used with the data of Test Points 1 and 9, and the plot of χ vs x/D is shown in Figure 5.24. Straight lines may be drawn through the data to give potential core lengths of 5.9 D_{eq} and 6.3 D_{eq}, respectively.

For Test Points 2 and 4, it is necessary to return to Figure 5.23. In these cases, the potential core lengths are estimated to be 6.0 D_{eq} and 6.4 D_{eq}, respectively.

Another interesting result which emerged from the study of single jets is that the centerline distributions tend to collapse on one universal curve when the axial distance is normalized by x_c. Figure 5.25 shows the present results plotted in this manner. For x/x_c up to about 2, the data for the different test points are reasonably close, but further downstream, they tend to diverge. The universal curve from single jet results is also shown and it would seem that the rate of decay of the mean velocity is slower for single jets.

Figure 5.26 shows the variation of $(x_c)/(x_c)_{\lambda=0}$ with the velocity ratio ($\lambda = V_f/V_p$). The results of other investigations for various values of λ and area ratio ($\beta = A_f/A_p$) are also shown. It appears that the potential core length ratio generally increases with β and λ.

The axial distribution of the axial mean velocity along the $r/D_{eq} = 0.42$ line is shown in Figure 5.27 for Test Points 2 and 4. The curve for TP 2 begins to fall off before that for TP 4. This suggests the presence of a longer annular potential cone for TP 4 than for TP 2. This trend would be in agreement with Ko and Kwan's results (ref. 5.5) but be in disagreement with the observation made by Williams et al. (ref. 5.3).

Figures 5.28 and 5.29 show respectively the variation of the axial and radial turbulence intensities along the centerline. The intensities are normalized by the respective peak values and the axial distance by the potential core length. The results do not agree very well upstream of the peak, but at the peak and downstream the data for the different test points fall very close to each other. It is interesting that the peak turbulence intensity in all cases is located at about $x/x_c \doteq 1.7$, suggesting that the location of the peaks is dependent purely on the potential core length.

The magnitudes of the peak turbulence levels are tabulated in Table 5.2. It appears that increasing the velocity ratio of the inverted profile has the effect of reducing the peak turbulence level on the jet centerline.

Table 5.2 Peak turbulence levels on the centerline.

Test Point	$\tilde{u}_{ap}$ (m/s)	$\tilde{v}_{ap}$ (m/s)
1	55.0	34.2
2	53.9	30.8
4	43.2	28.0
9	57.3	41.0

5.3.2 Supercritical Flow

The aim of the measurements described in this subsection is to study the flow characteristics when either one or both jets are at supercritical conditions. Since the nozzles have not been contoured to give fully-expanded supersonic flows, shock waves are expected to form close to the exit. The intention is to concentrate the effort on jets having conditions for which noise measurements have been acquired in previous studies and which are known to give optimum noise reductions. Two test cases were originally selected for these measurements, but due to the expansion of the subcritical flow study program, only Test Point 13 could be considered.

Figures 5.30(a) and (b) show radial distributions of the mean axial velocity at six axial stations. In Figure 5.30(a) the velocity is normalized by V_p and in Figure 5.30(b) by V_f. The annular flow is supercritical in this case and has an equivalent exit Mach number of 1.21. The distributions are smooth and display essentially the same characteristics as those observed earlier for Test Points 2 and 4. The higher velocity in the annular region may clearly be seen in the curves at the first four stations and there is no evidence of the effects of shock waves in the distributions. As before, the high velocity is soon suppressed and the annular flow becomes a part of the integrated shear layer by about $x/D_{eq} = 6.0$. It is suspected that the good reproduction of the trends of subcritical flow is due to the supercritical over-pressure being relatively low and the shock waves being weak to begin with. At more severe supercritical conditions, where the shock waves are much stronger, the situation would conceivably be very different.

Figure 31 shows radial distributions of the axial turbulence intensity. At $x/D_{eq} = 0.5$, two peaks may be seen indicating the two shear layers of the jet. By $x/D_{eq} = 2.0$, however, except for a small kink in the distribution, the inner peak has all but disappeared. It shows once again that the secondary shear layer is the more dominant one. The peak intensity rises to about 18% at around $x/D_{eq} = 2.0$ which is comparable to the earlier results for subcritical flows.

Figure 5.32 shows the centerline distribution of the axial mean velocity. It suggests a potential core length of about 8 D_{eq}.

5.4 TWO-POINT CORRELATION RESULTS

Space-time cross-correlation results were obtained for Test Points 1, 4 and 13. These results provide information on integral length scales and convection velocities of the velocity fluctuations.

Figure 5.33 shows a family of correlation curves obtained on the jet centerline with varying separations (ξ) of the two measurement points. The abscissa is the time delay (τ) expressed in μs, and the ordinate is the cross-correlation coefficient (R_{11}) which is defined for the more general case by:

$$R_{ij}(\vec{\xi},\tau) = \frac{\overline{u'_{iA}(\vec{x};t) \cdot u'_{jB}(\vec{x}+\vec{\xi};\ t+\tau)}}{\tilde{u}_{iA} \cdot \tilde{u}_{jB}} \qquad (5\text{-}2)$$

where the bar and tilde denote respectively the time-averaged mean and rms values of the velocity fluctuations. The subscripts i and j refer to the directions of the velocity components being correlated and A and B the locations of the two measurement points separated by $\vec{\xi}$.

To prevent confusion, only two of the curves are fully drawn. These are typical of the curves shown and are reminiscent of those obtained in the potential core of single jets (ref. 5.15 to 5.17). The curves have a damped-sinusoidal appearance and as the separation of the measurement points is increased the curves and their respective peaks move to progressively greater time delays. The magnitudes of the peaks also fall with increasing separation, the rate of fall being more rapid at small separations.

The movement of the curves depicts a convection phenomenon and the convection velocity of the fluctuations may be determined by plotting the separation against the corresponding time delay for maximum correlation and determining the gradient of the straight line. This is shown typically in Figure 5.34.

The convection velocity V_c determined at various points in the flow is shown in Figures 5.35 and 5.36. The corresponding mean velocity distributions at the axial stations are also shown. At axial stations close to the nozzle, the value of V_c on the jet axis is significantly lower than the local mean velocity. As the mixing region is entered, the difference becomes smaller. This is similar to observations in a single jet reported by Bradshaw et al. (ref. 5.16), Davies (ref. 5.17) and in reference 5.15.

The difference in the velocities on the jet centerline is attributed to the fluctuations on the centerline being manifestations arising from flow events within the mixing region and therefore would convect with the mean velocity of these flow events (ref. 5.18). On this basis, it could be reasoned from the results at $x/D_{eq} = 2$ and 4 [Figures 5.36(a) and (b)] for example, that these events are located at r/D_{eq} of between 0.5 and 0.58, which is within the secondary shear layer. This is consistent with the earlier suggestion that the secondary shear layer is dominant.

Figure 5.37 shows the variation of the convection velocity along the jet centerline for varying jet conditions. The curve for a single jet at Mach 0.9 and static temperature ratio (T_J/T_o) of 2.32 is also shown. It lies close to the curve for Test Point 1, and above the curve for Test Point 4. The difference between the results of Test Points 1 and 4 is large at small distances from the nozzle, but reduces as the distance is increased. It is conceivable that at a distance far enough downstream, the two curves would merge. All the curves seem to exhibit the same character. They rise in the initial region, reaching a peak between $x/D_{eq} \doteq 3$ and 8 and subsequently fall. The results for Test Point 13 are also shown and are higher than the others. They suggest also a tendency for the convection velocity to rise with x in the initial region.

Figure 5.38 shows the axial distributions of the convection velocity for Test Point 4 at $r/D_{eq} = 0$, 0.288, and 0.515. The radial positions correspond to points located (a) on the jet axis, (b) within the primary shear layer, and (c) within the secondary shear layer. In the primary shear layer, the convection velocity does not change substantially with axial distance. In the secondary shear layer, however, the convection velocity tends to drop off rapidly even in the region close to the nozzle.

The family of cross-correlation curves in Figure 5.38 also allows the integral length scale to be determined. Values of R_{ij} at $\tau = 0$ are extracted from these curves and plotted in terms of the separation between the measurement points (ξ) as shown in Figure 5.39. For the particular case shown, the curve has a damped sinusoidal appearance. This is typical of results obtained in the potential core of the jet. In the mixing region, the curves tend to fall continuously and asymptote to zero. The integral length scale is in general given by:

$$L_k = \int_0^\infty R_{ij}\ (\xi;\ \tau = 0)\ d\xi_k$$

However, where the curve oscillates as in Figure 5.39, the integral is only taken up to the first zero crossing.

Figure 5.40 shows the variation of the length scale with axial distance within the two mixing regions, and the results are not significantly different. For comparison, the results from a single jet are also shown. These are for a jet at a Mach number of 0.9 and jet to ambient temperature ratio of 2.32 (ref. 5.15).

The variation of the integral length scale with axial distance measured along the jet centerline is shown for different test conditions in Figure 5.41. The results for Test Points 1 and 4 are quite close to each other, and tend to be lower than those for a single jet. The length scale for Test Point 13 could only be obtained at one point due to the limitation of time and is larger than that for subcritical jets.

5.5 CONCLUSIONS

The present set of laser velocimeter measurements has confirmed many of the earlier observations made with regard to coannular or coaxial jets. It has also shed new light on the behavior of such jets when the exit velocity of the secondary or annular jet is greater than that of the primary jet. A unique feature of the present measurements is that the test conditions for the primary and secondary jets are such that the total mass flow rate and thrust of the composite jet remain constant from one test point to another. Thus, although the Mach number and temperature of the primary and secondary jets may vary (resulting in different ratios of the fan to primary velocity), there is still a common denominator between the different test cases.

Listed below are some of the more salient observations for the coannular nozzle configuration (area ratio $A_f/A_p = 0.75$) used in the present experiments:

(1) The radial distributions of the mean axial velocity (unnormalized) at a given axial station differ in general appearance depending on the velocity ratio of the jet (Figure 5.8). The difference is more pronounced at stations close to the nozzle. However, all the curves tend to merge at $r/D_{eq} > 0.6$.

(2) At a given velocity ratio (e.g. Figure 5.6), the peak in the mean velocity distributions (located in the annular flow region) does not persist very far downstream, and disappears before the termination of the primary potential core. For $V_f/V_p = 1.35$ and 1.75 the peak disappears at about 3 D_{eq} and 4 D_{eq}, respectively, for a primary potential core length of about 6 D_{eq}.

(3) The normalized mean velocity profiles of the secondary shear layer do not exhibit similarity characteristics when there is an inverted exit velocity profile. Normalization of the mean velocity by V_f [e.g. Figure 4.11(b)] produces reasonable collapse of the data at $\eta^* \geq 0$, but there are substantial deviations at $\eta^* \leq 0$. It appears that low velocity flow in the primary region tends to depress the velocities in the inner side of the outer jet and in this way causes the radial distributions of the mean velocity to deviate gradually from establishing similarity.

(4) At axial stations very close to the nozzle, the radial distributions of the turbulence intensity exhibit two peaks representing the two shear layers in the jet. However, the inner peak very quickly becomes submerged within the outer peak which is associated with the outer shear layer, and by $x/D_{eq} = 2.0$, there is little evidence of the inner peak. The peak axial turbulence intensity is of the order of 18% of V_f, which is comparable to that of single jets, and is about 4/3 to 3/2 times larger than the radial turbulence intensity, thus concurring with single jet results.

(5) The predominance of the secondary shear layer is also displayed in the convection velocity measurements. These measurements made along the jet centerline suggest that the fluctuations detected there are caused by events occurring in the outer shear layer (Figure 5.36).

(6) Centerline distributions of the mean velocity (V_a) tend to collapse for at least two potential core lengths downstream when plotted in terms of V_a/V_p and x/x_c, x_c being the potential core length. This is true even for the case where the annular exit velocity is 1.75 times that of the primary.

(7) The potential core length is apparently a function of the velocity ratio and the area ratio.

(8) The turbulence intensity on the centerline peaks a little upstream of $x/x_c = 2.0$.

(9) Spectra of the fluctuating velocity are obtained at selected points in the flow field under varying jet exit conditions. In the potential core, they show a narrow-band peak, and the peak frequency falls with axial distance. The fall becomes more rapid near the nozzle.

(10) Convection velocities obtained at various points in the jet flow field reveal the same kind of distribution relative to the mean velocity as has been observed in single jets.

(11) The integral length scale increases linearly with axial distance. The trend conforms with single jet results.

(12) Only one test case is studied in which either one or both of the jets is supercritical. For this case, the annular jet plenum pressure is 2.46 of the ambient value. The mean velocity (Figure 5.30) and turbulence intensity (Figure 5.31) distributions are found to possess the same character as those for the subcritical cases (i.e. Points 2 and 4). The peak turbulence intensity rises to about 18% as for the subcritical cases. It appears therefore that at the plenum pressure considered, the shock waves are weak enough to begin with so that their presence cannot be detected in the results. Conceivably, at higher plenum pressures, the situation would be quite different.

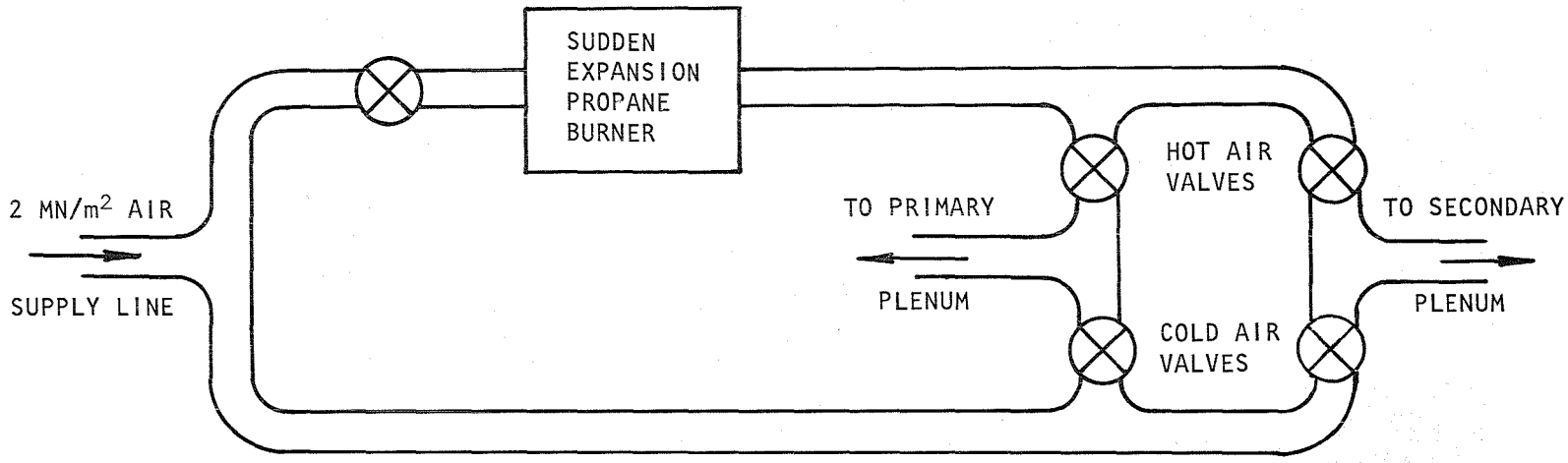

Figure 5.1 Schematic view of air system.

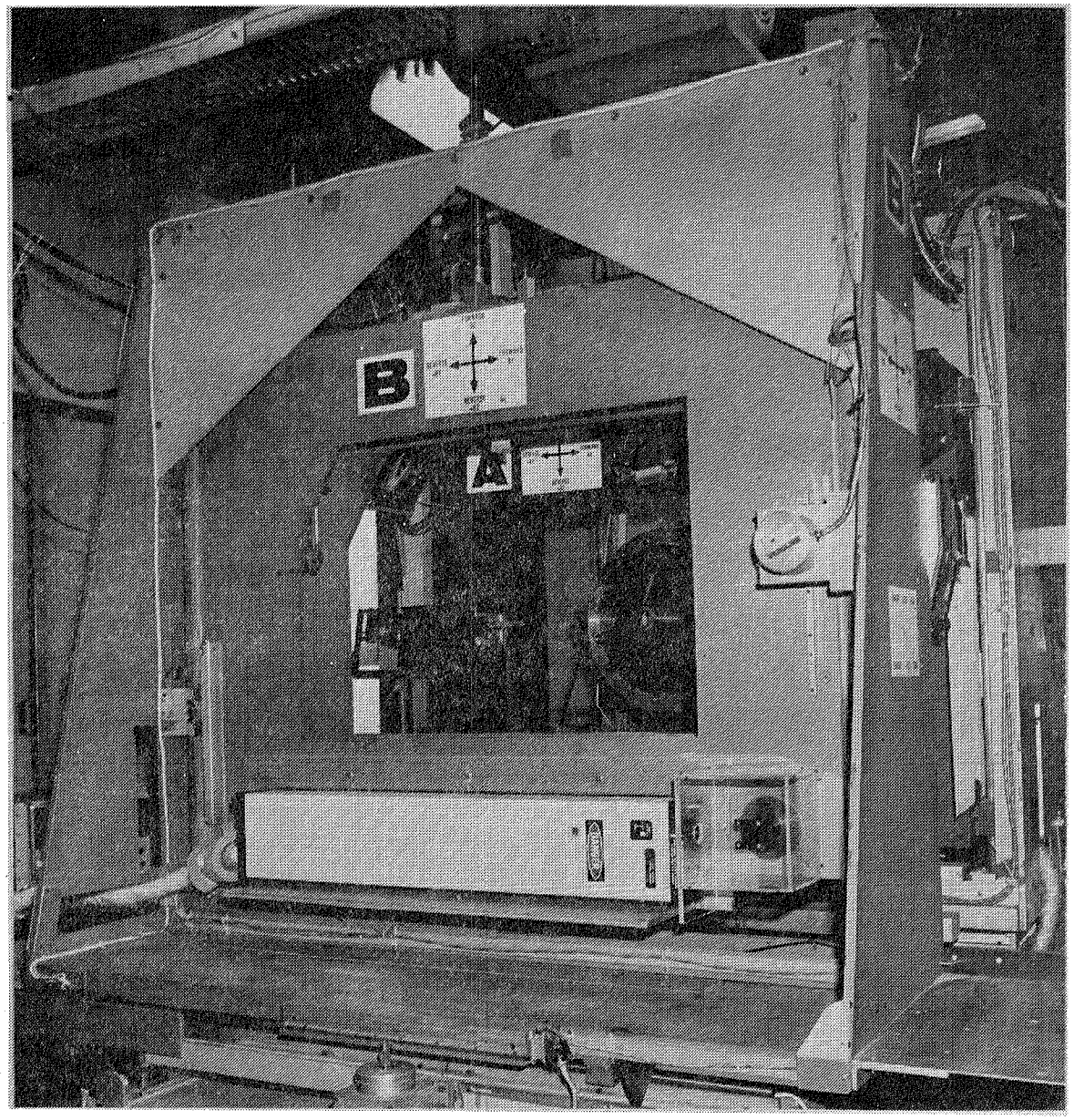

Figure 5.2 Photograph of the coannular jet rig and the traversing gear.

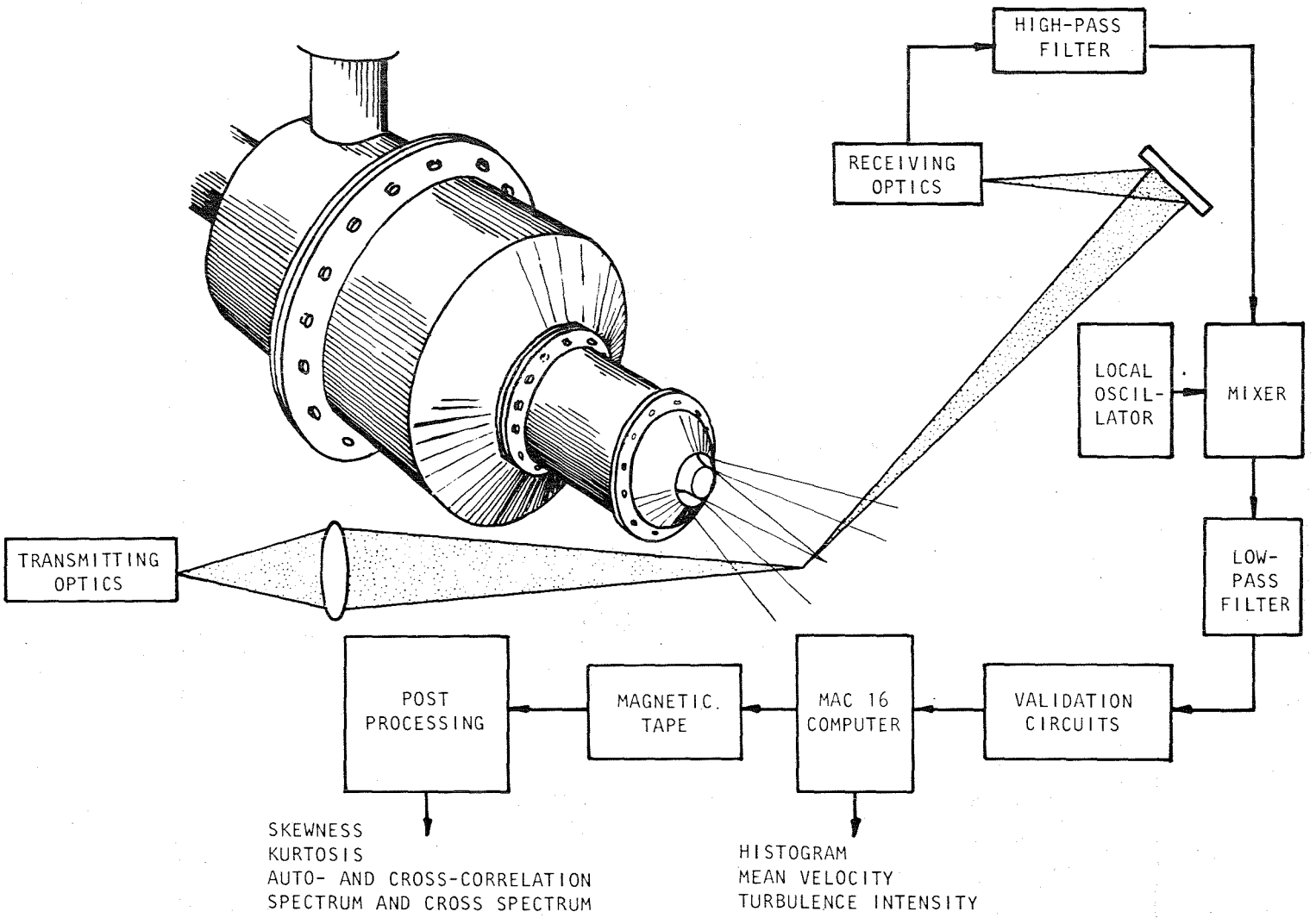

Figure 5.3 Schematic View of the Laser Velocimeter Arrangement.

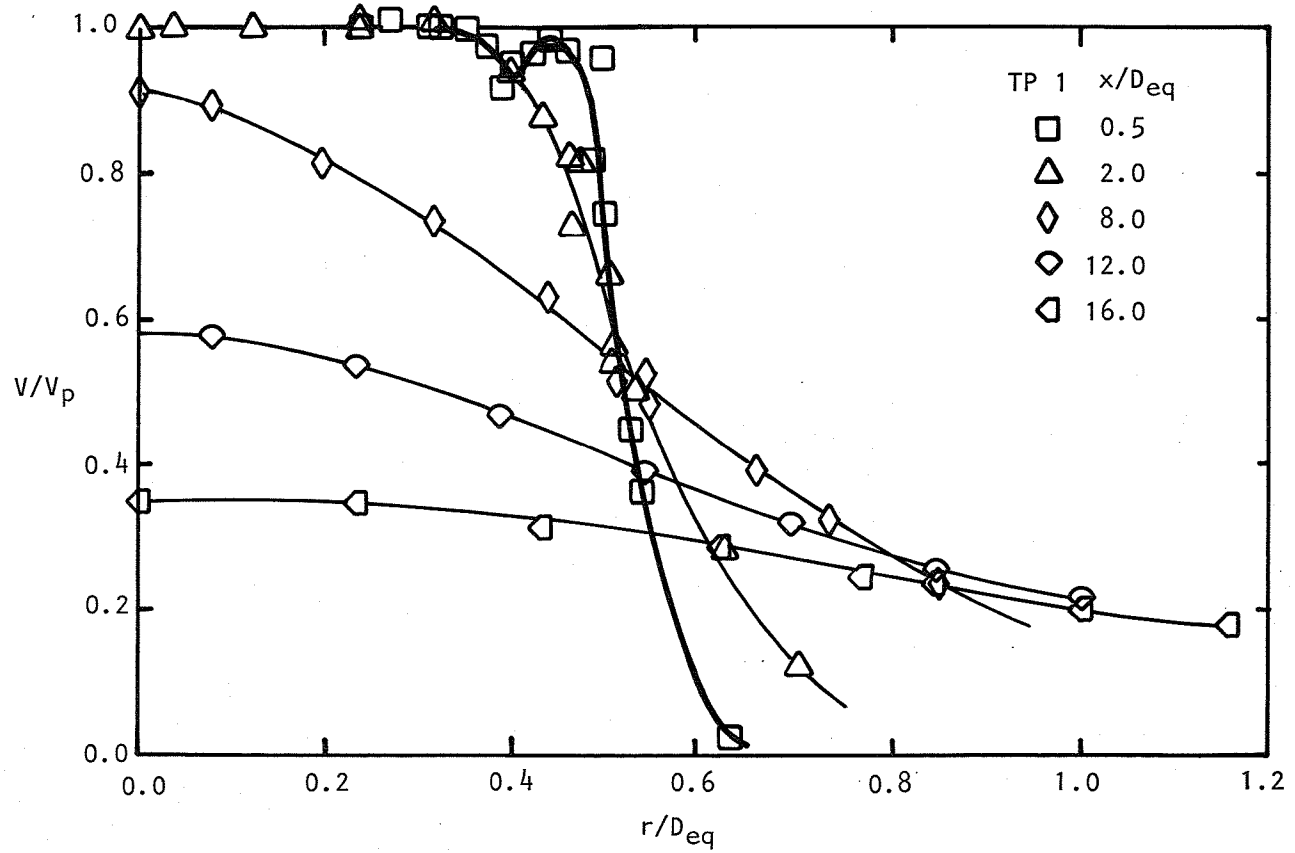

Figure 5.4 Radial distribution of V/V_p for TP 1: $V_f/V_p = 1.00$, $T_f/T_p = 1.00$.

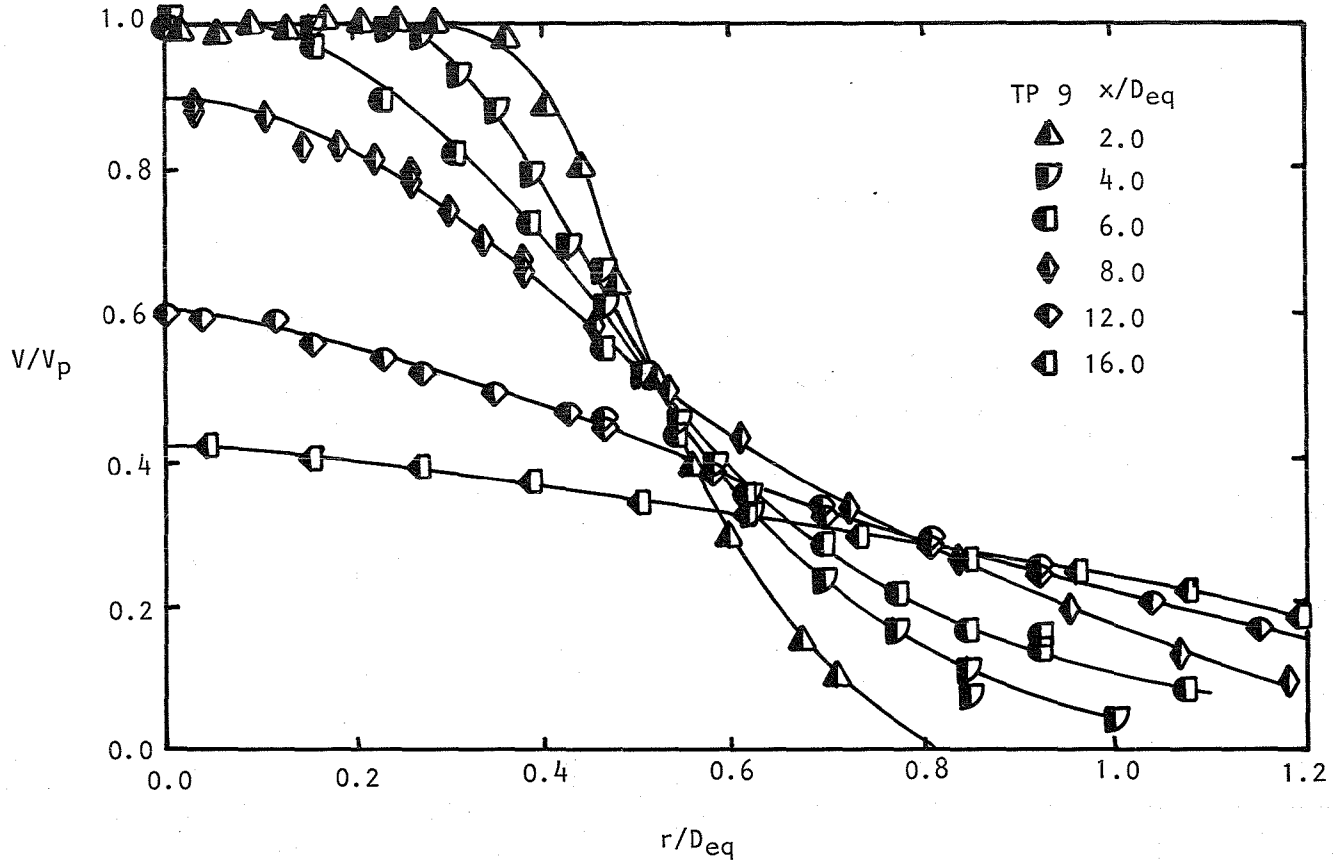

Figure 5.5 Radial distribution of V/V_p for TP 9: $V_f/V_p = 1.00$, $T_f/T_p = 2.00$.

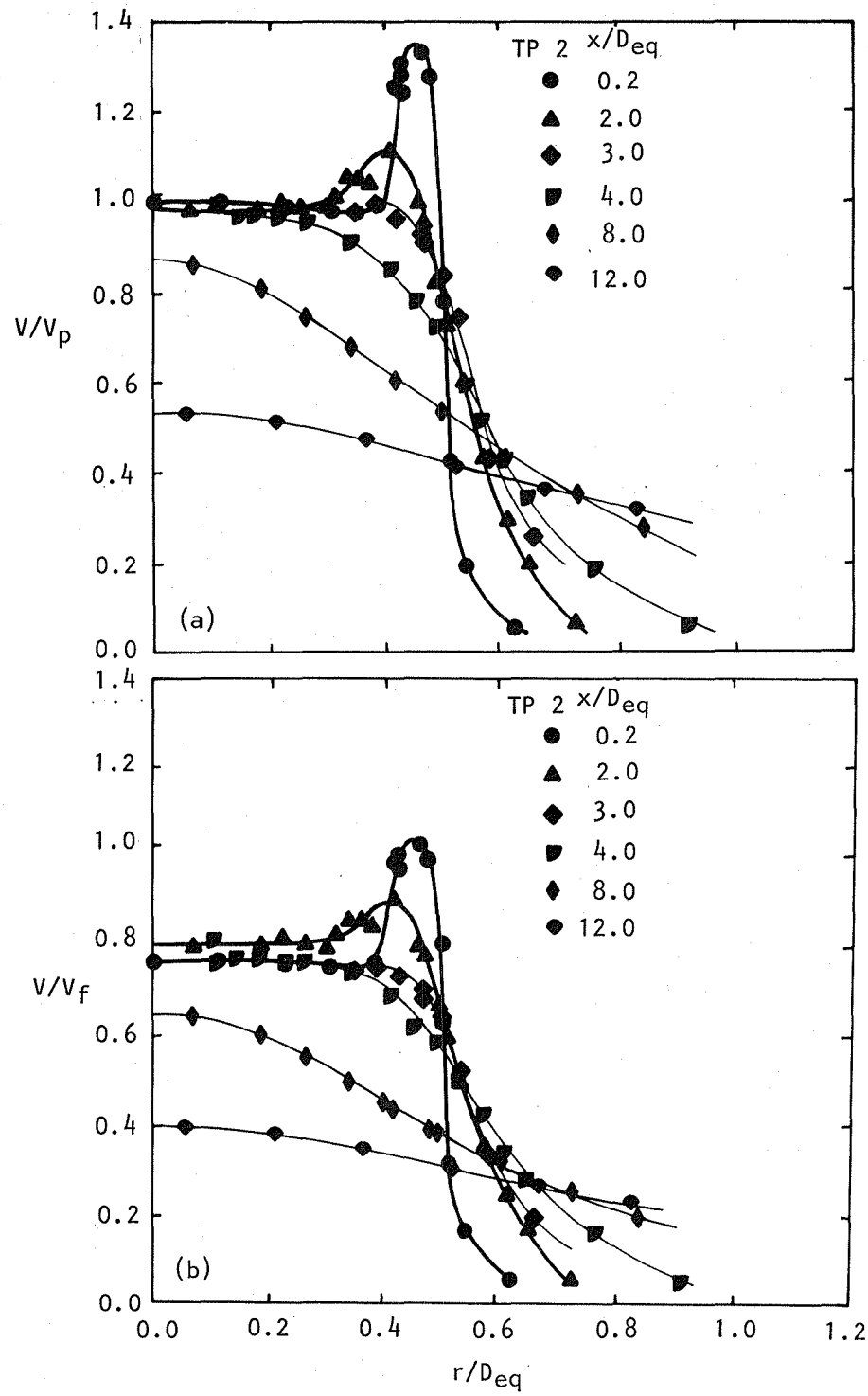

Figure 5.6 Radial distribution of (a) V/V_p, (b) V/V_f for TP 2: $V_f/V_p = 1.35$, $T_f/T_p = 1.00$.

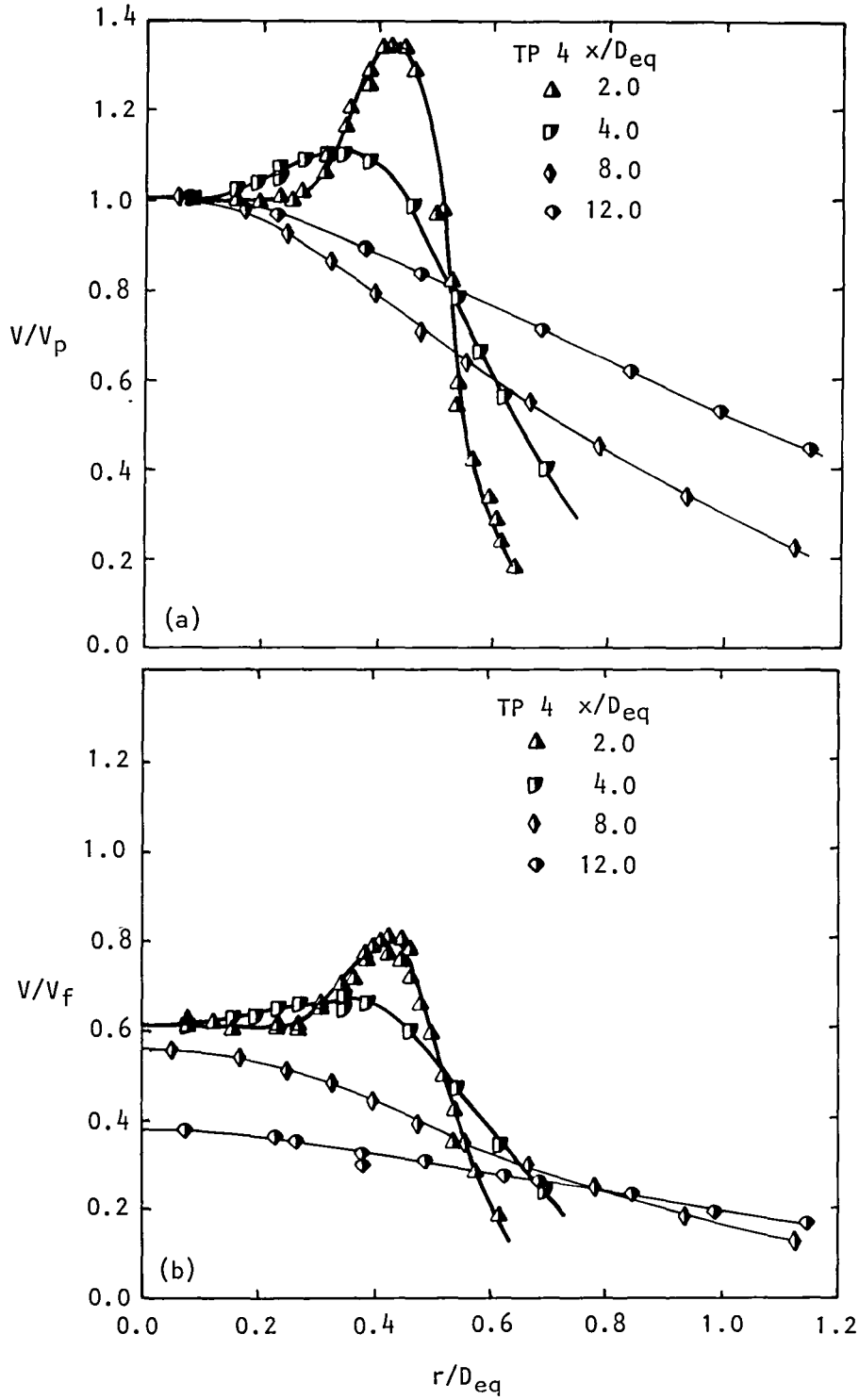

Figure 5.7 Radial distribution of (a) V/V_p, (b) V/V_f for TP 4: $V_f/V_p = 1.75$, $T_f/T_p = 1.00$.

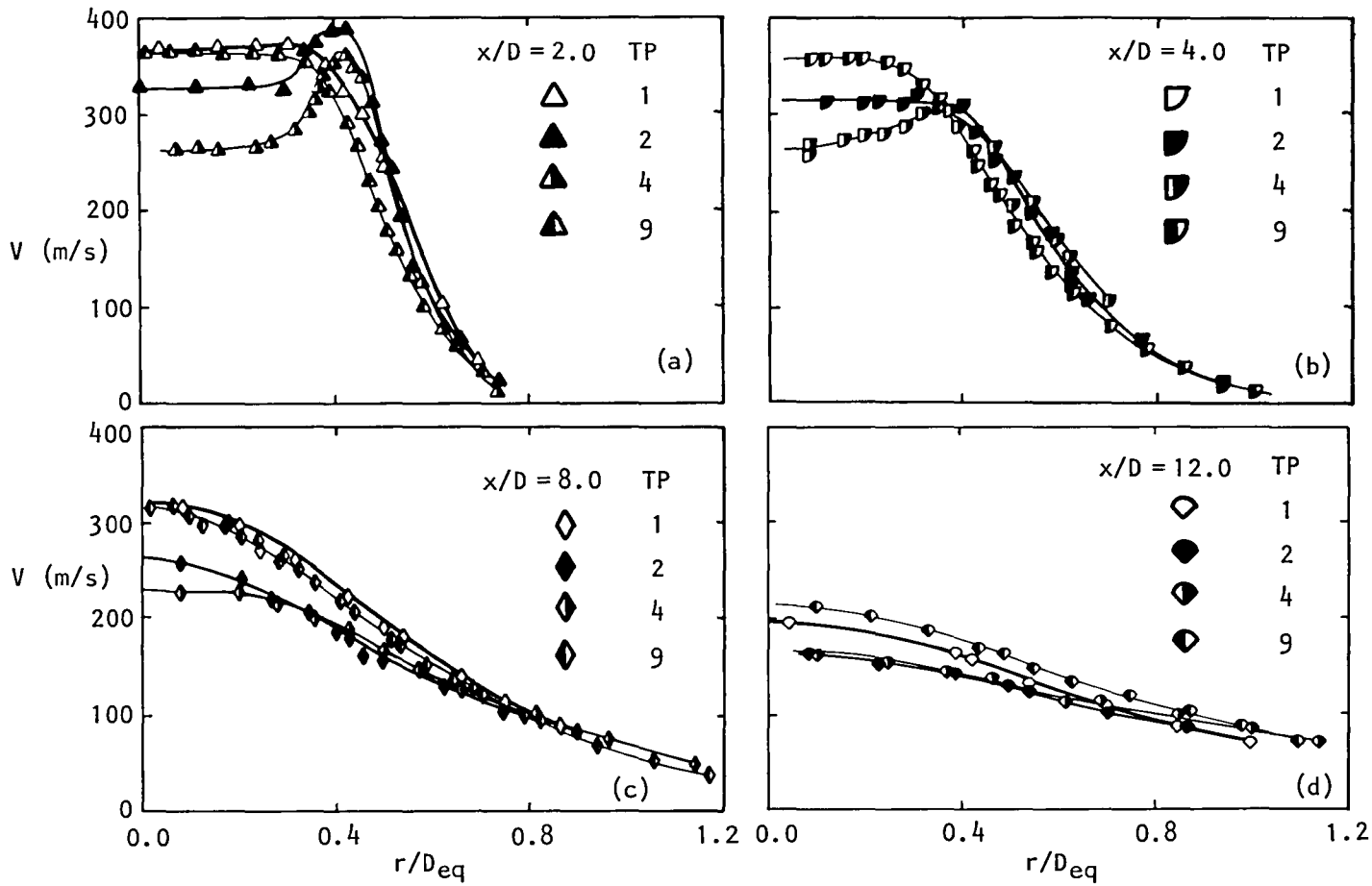

Figure 5.8 Radial distribution of V (m/s).

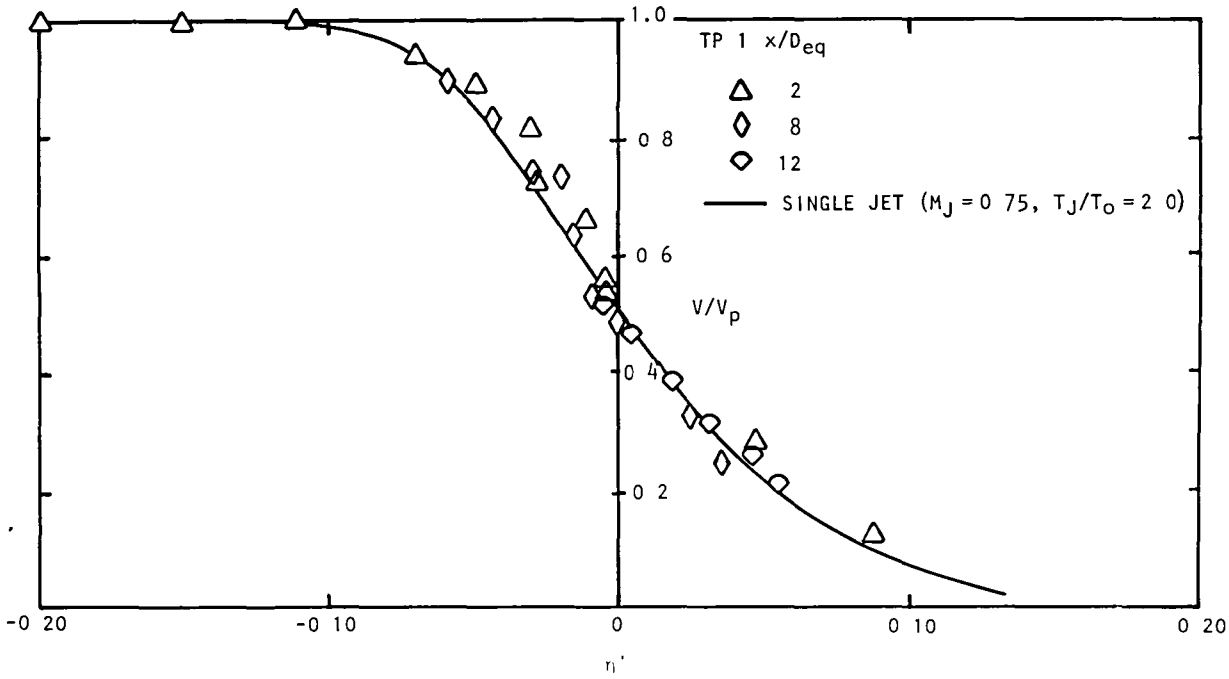

Figure 5.9 V/V_p vs η^*. TP 1: $V_f/V_p = 1.00$, $T_f/T_p = 1.00$.

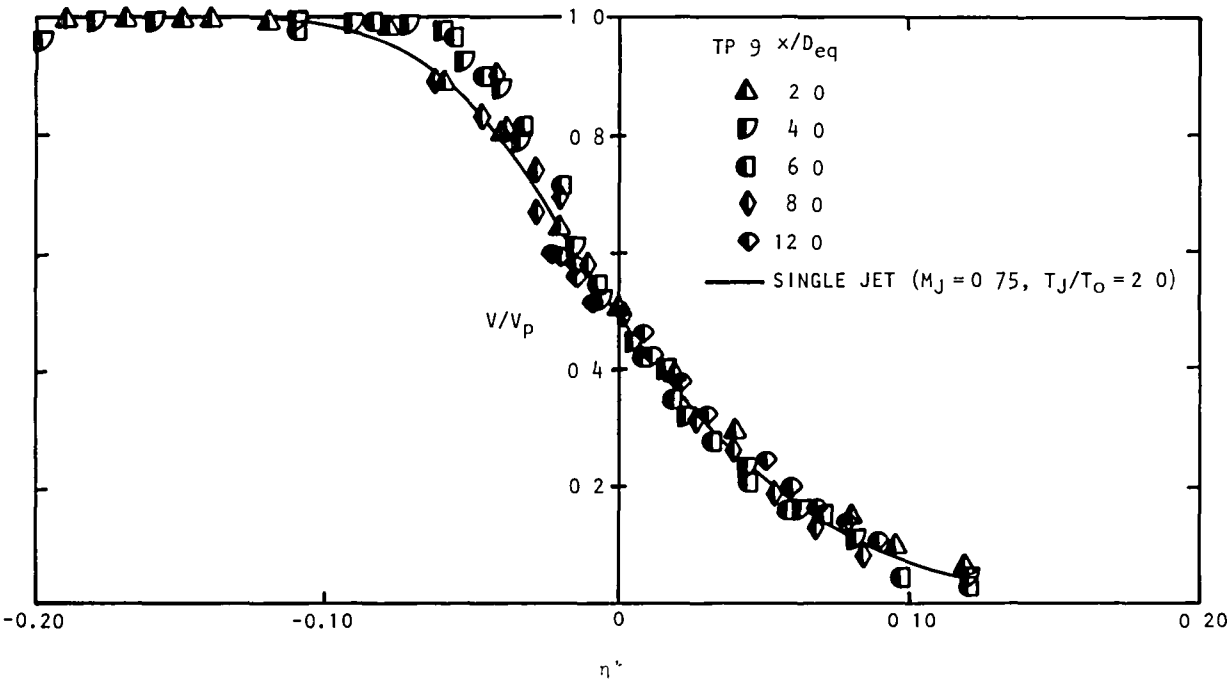

Figure 5.10 V/V_p vs η^*. TP 9: $V_f/V_p = 1.00$, $T_f/T_p = 2.00$.

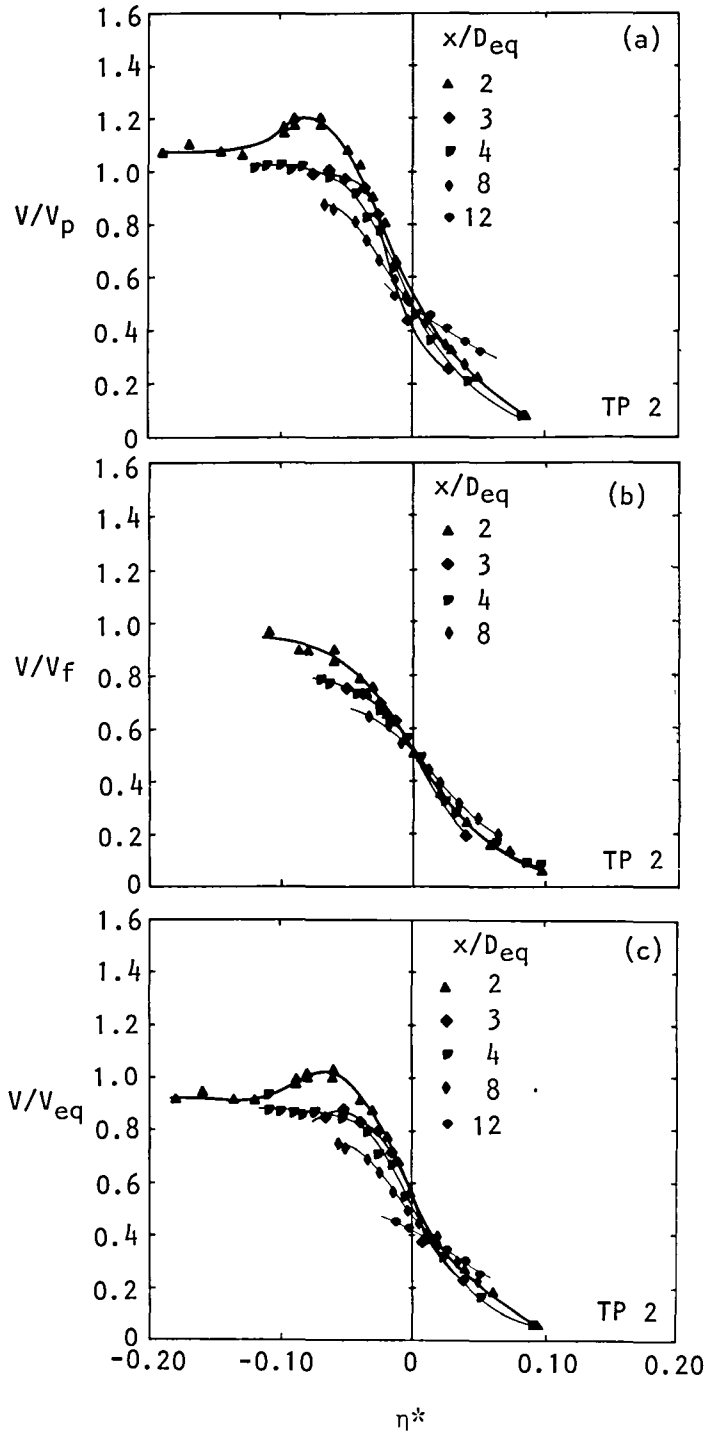

Figure 5.11 (a) V/V_p vs η^*, (b) V/V_f vs η^*, and (c) V/V_{eq} vs η^* for TP 2: $V_f/V_p = 1.35$, $T_f/T_p = 1.00$.

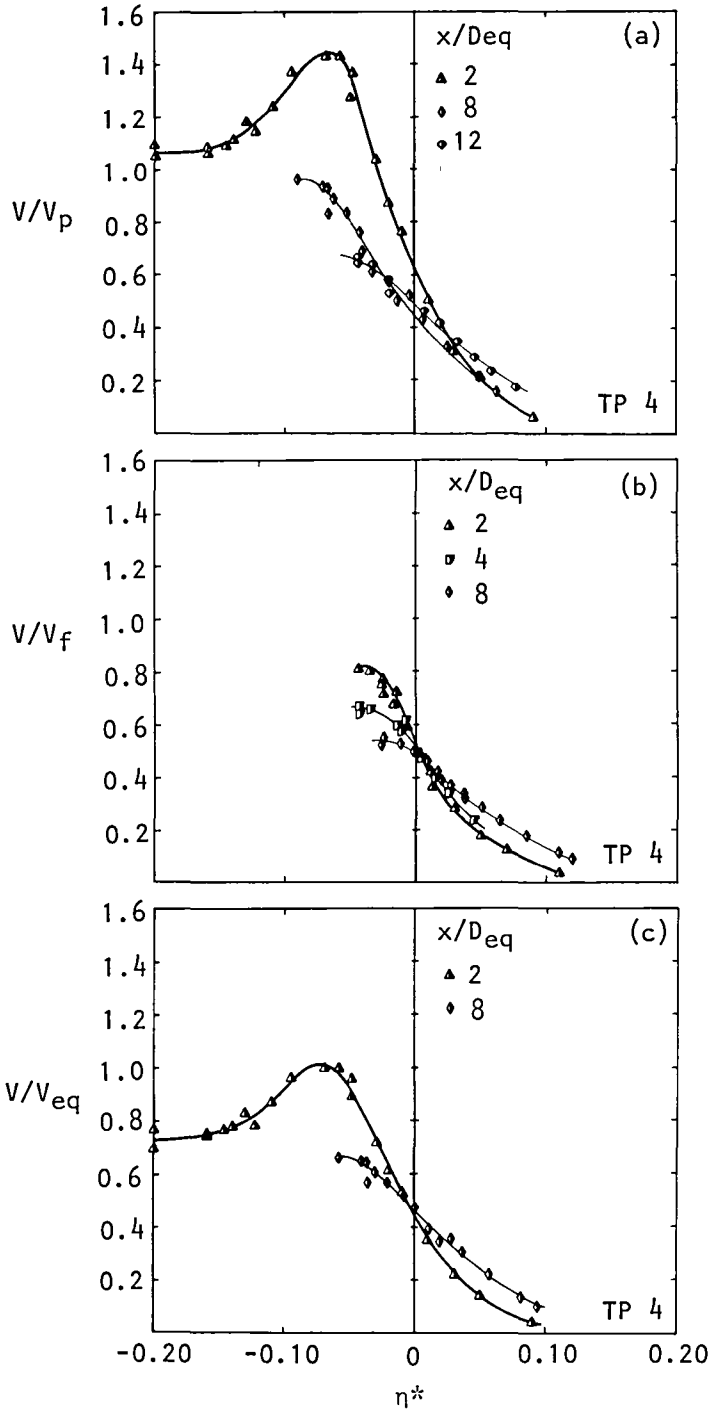

Figure 5.12 (a) V/V_p vs η^*, (b) V/V_f vs η^*, and (c) V/V_{eq} vs η^* for TP 4: $V_f/V_p = 1.75$, $T_f/T_p = 1.00$.

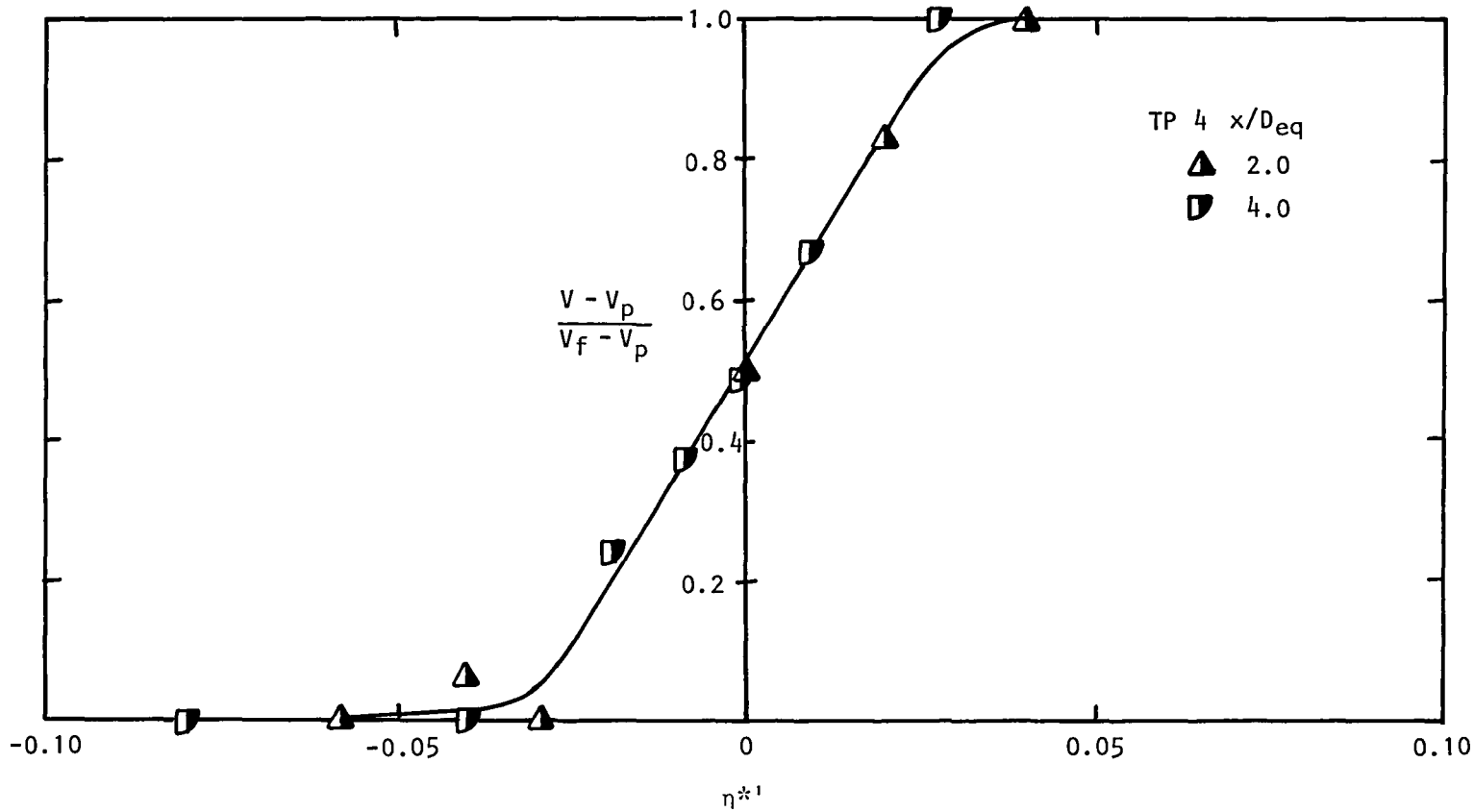

Figure 5.13 Normalized radial distribution of axial mean velocity in primary shear layer for TP 4: $V_f/V_p = 1.75$, $T_f/T_p = 1.00$.

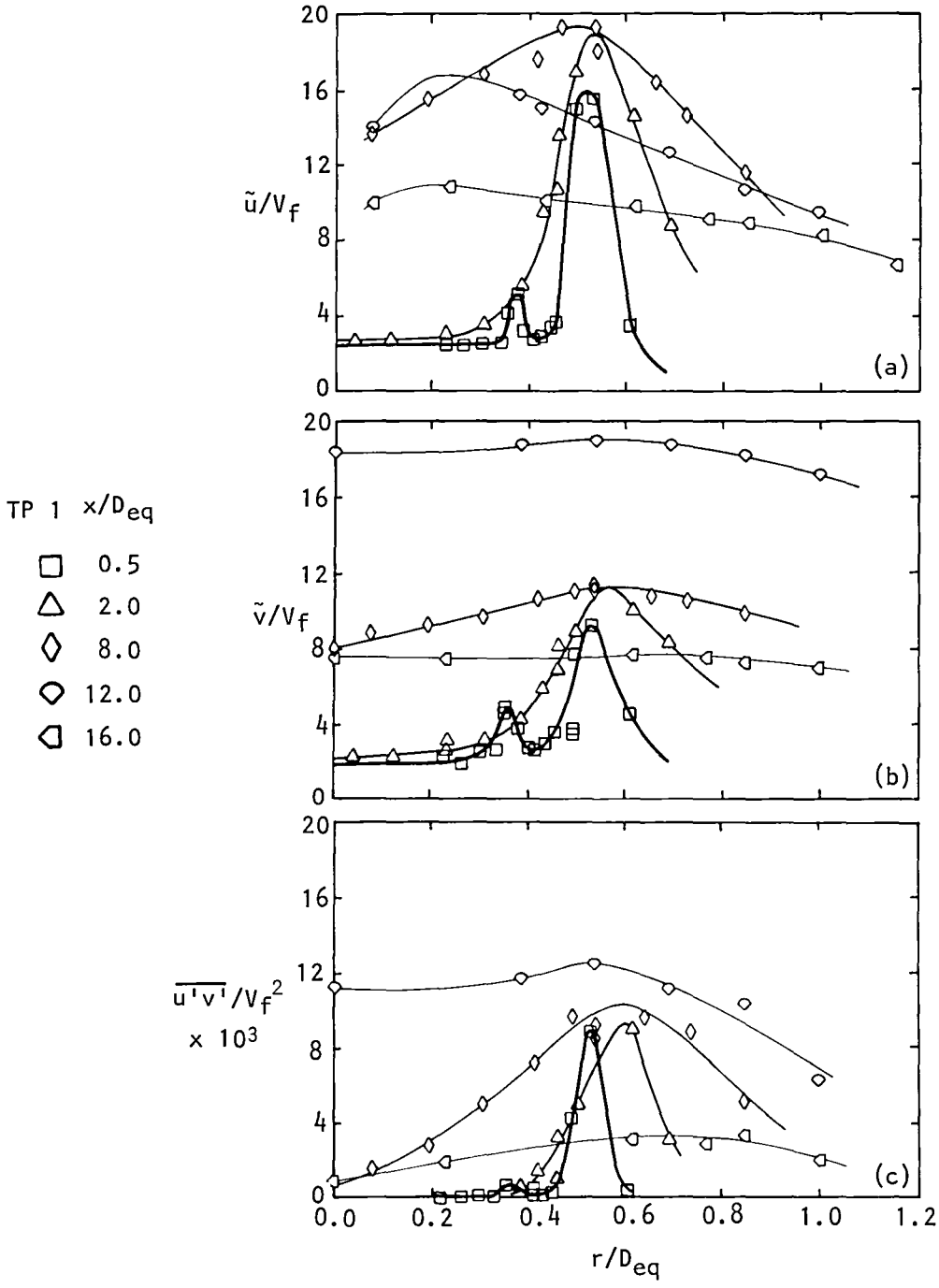

Figure 5.14(a) Radial distribution of $\tilde{u}/V_f$

(b) Radial distribution of $\tilde{v}/V_f$

(c) Radial distribution of $\overline{u'v'}/V_f^2$

for TP 1: $V_f/V_p = 1.00$, $T_f/T_p = 1.00$.

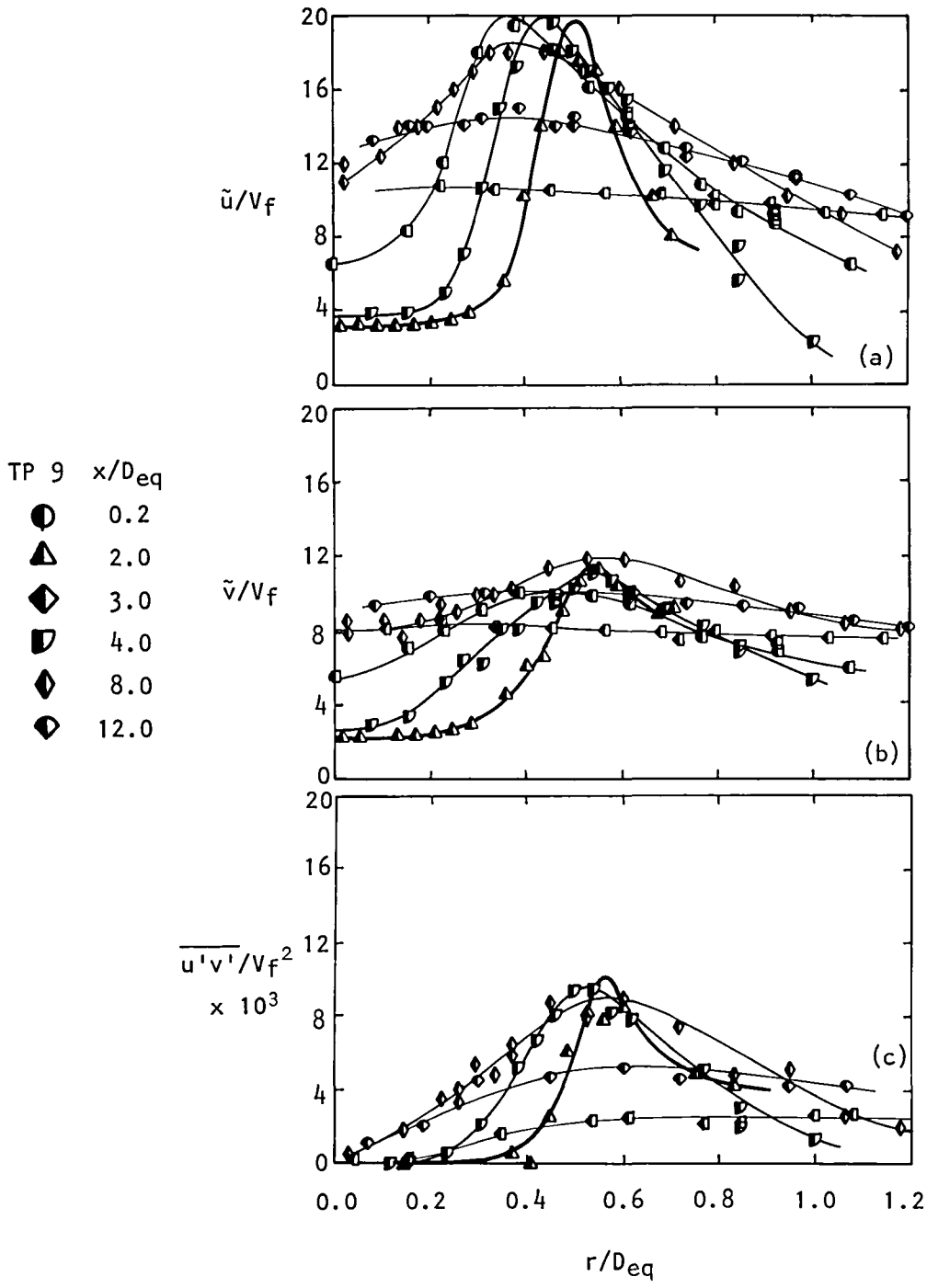

Figure 5.15(a) Radial distribution of $\tilde{u}/V_f$

(b) Radial distribution of $\tilde{v}/V_f$

(c) Radial distribution for $\overline{u'v'}/V_f^2$

for TP 9: $V_f/V_p = 1.00$, $T_f/T_p = 2.00$.

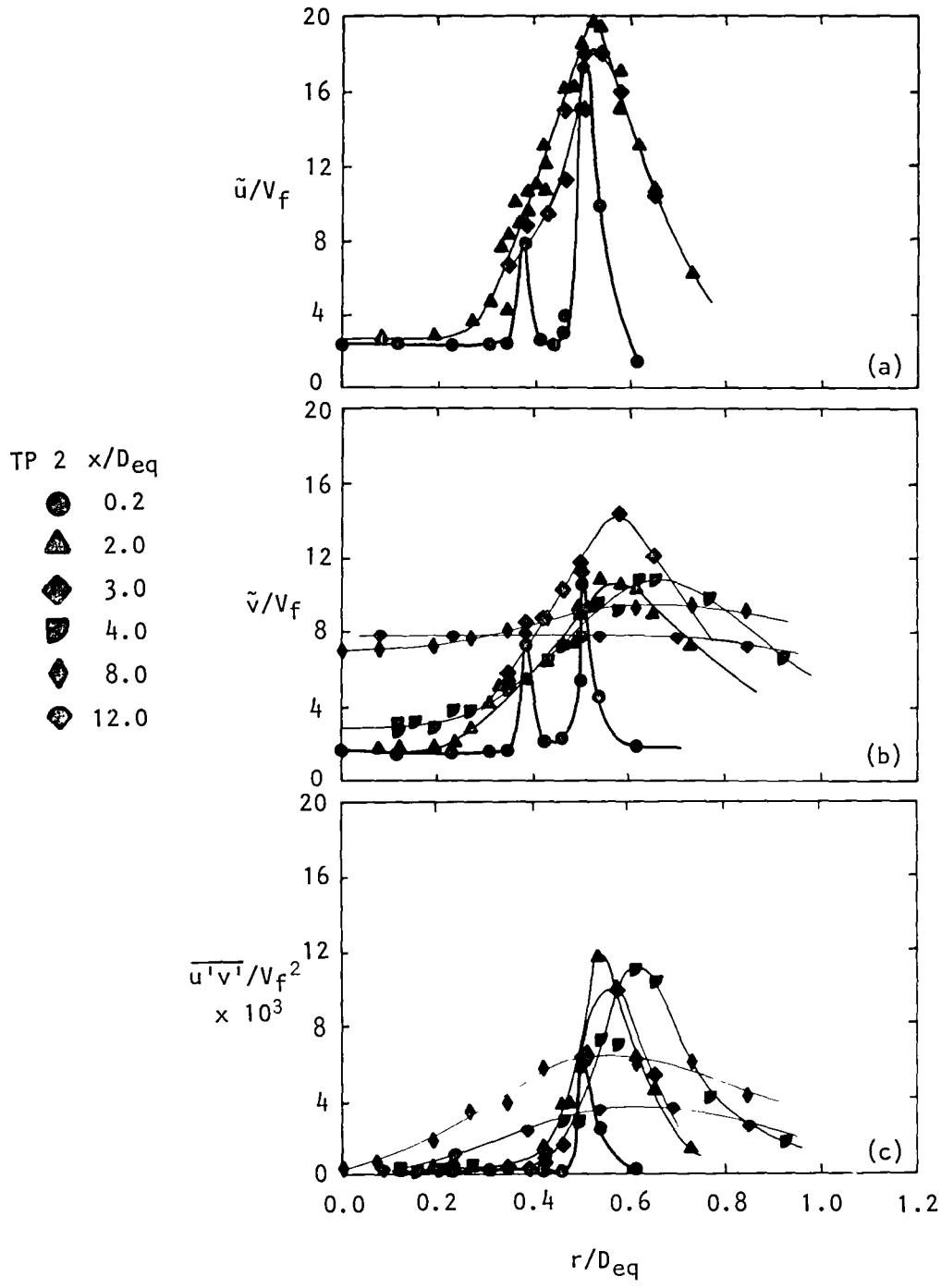

Figure 5.16(a) Radial distribution for $\tilde{u}/V_f$

(b) Radial distribution for $\tilde{v}/V_f$

(c) Radial distribution for $\overline{u'v'}/V_f^2$

for TP 2: $V_f/V_p = 1.35$, $T_f/T_p = 1.00$.

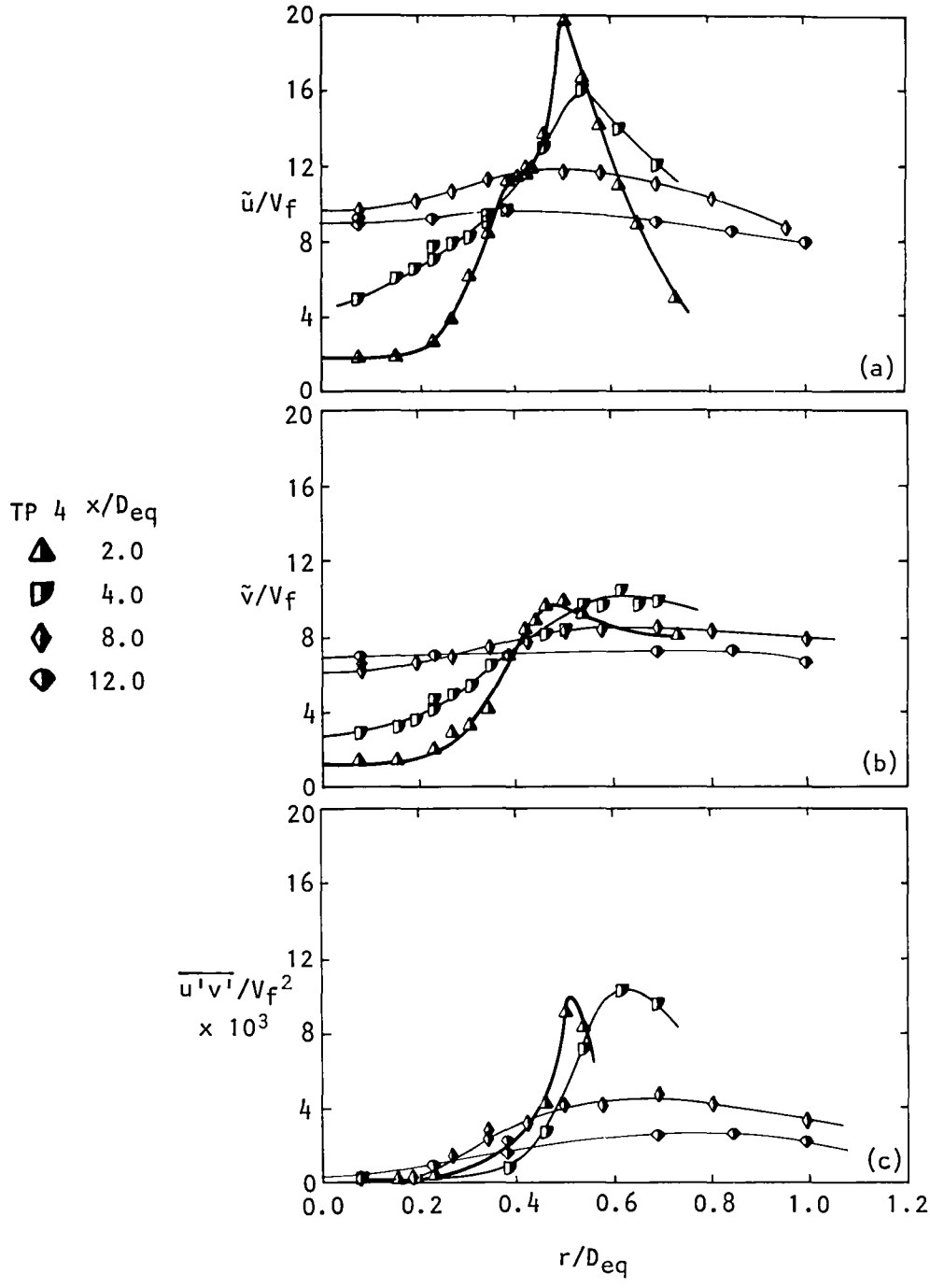

Figure 5.17(a) Radial distribution for $\tilde{u}/V_f$

(b) Radial distribution for $\tilde{v}/V_f$

(c) Radial distribution for $\overline{u'v'}/V_f$

for TP 4: $V_f/V_p = 1.75$, $T_f/T_p = 1.00$.

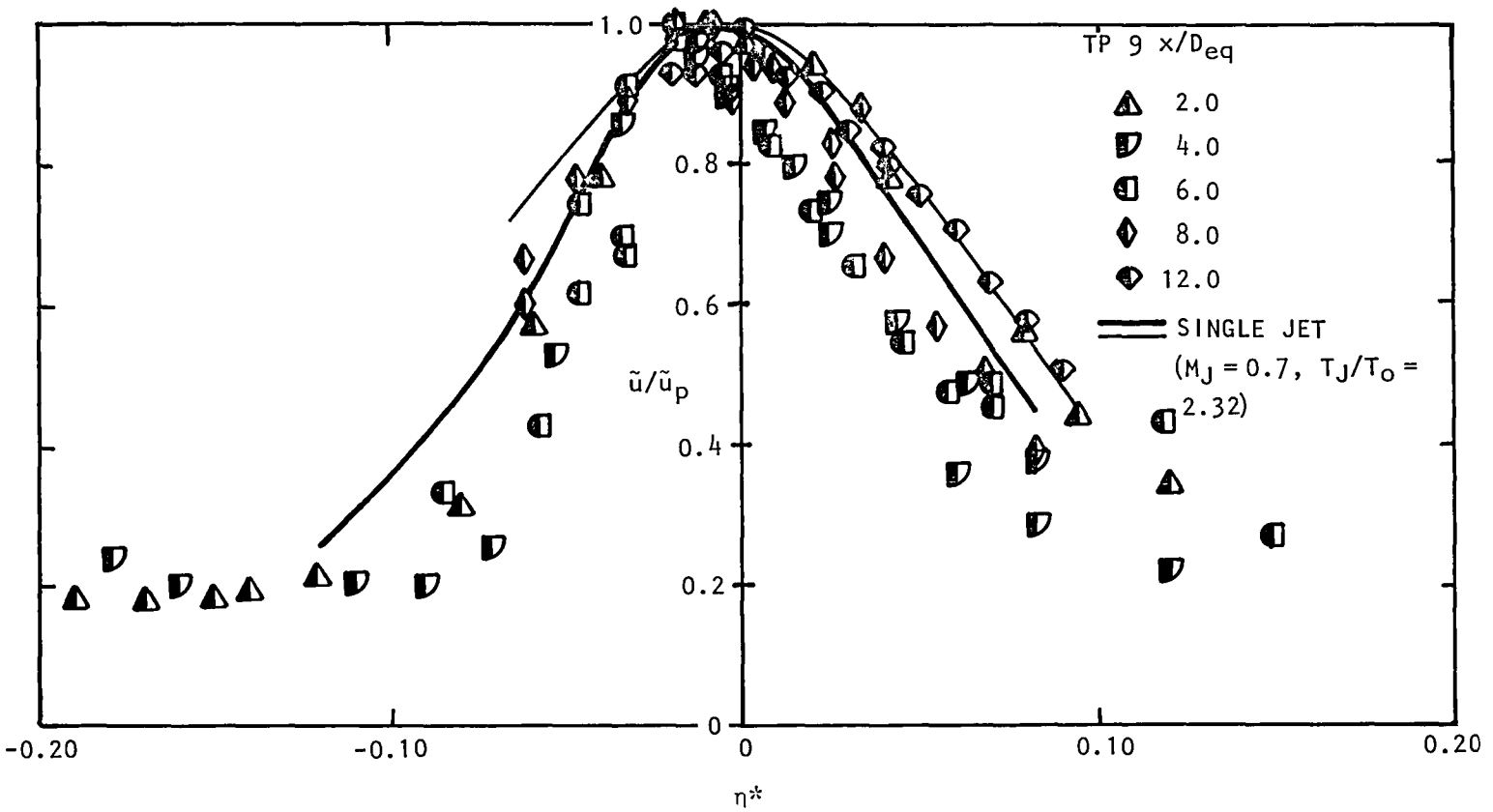

Figure 5.18 Normalized radial distribution of $\tilde{u}/\tilde{u}_p$ for TP 9: $V_f/V_p = 1.00$, $T_f/T_p = 2.00$.

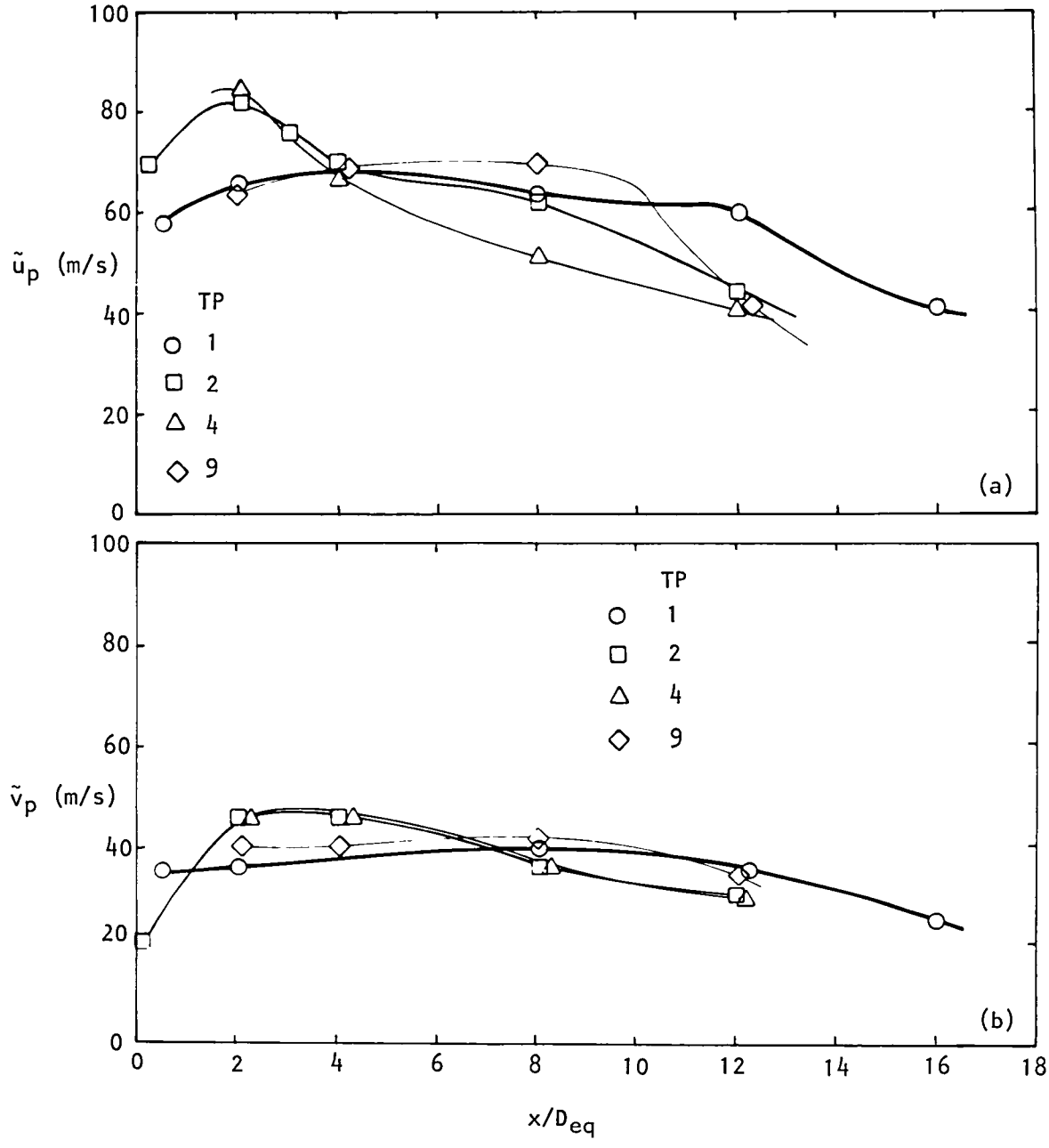

Figure 5.19 Axial distributions of the peak turbulence levels: (a) $\tilde{u}_p$, (b) $\tilde{v}_p$.

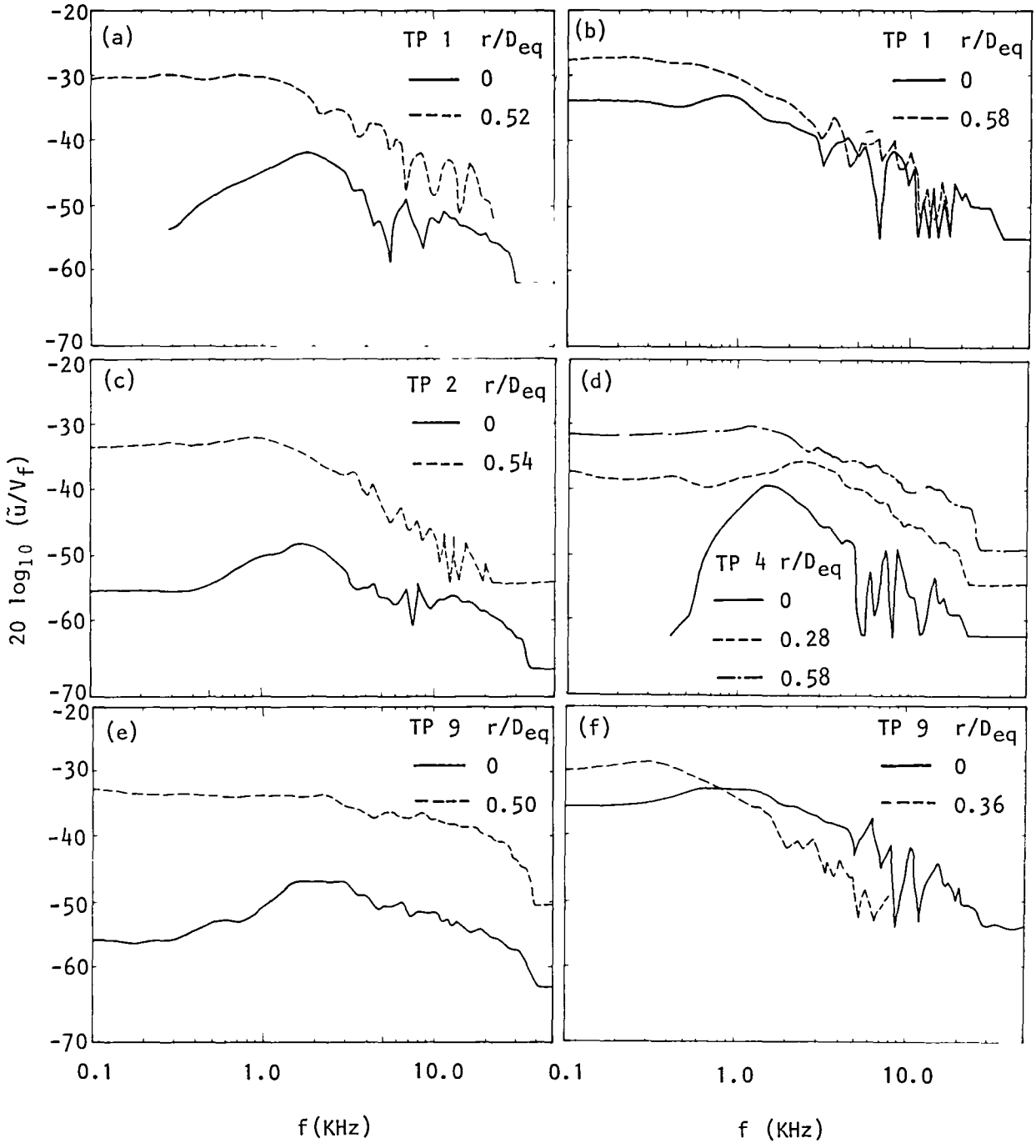

	TP	x/Deq
(a)	1	4.0
(b)	1	8.0
(c)	2	4.0
(d)	4	4.0
(e)	9	4.0
(f)	9	12.0

Figure 5.20 Spectra of u'-signals.

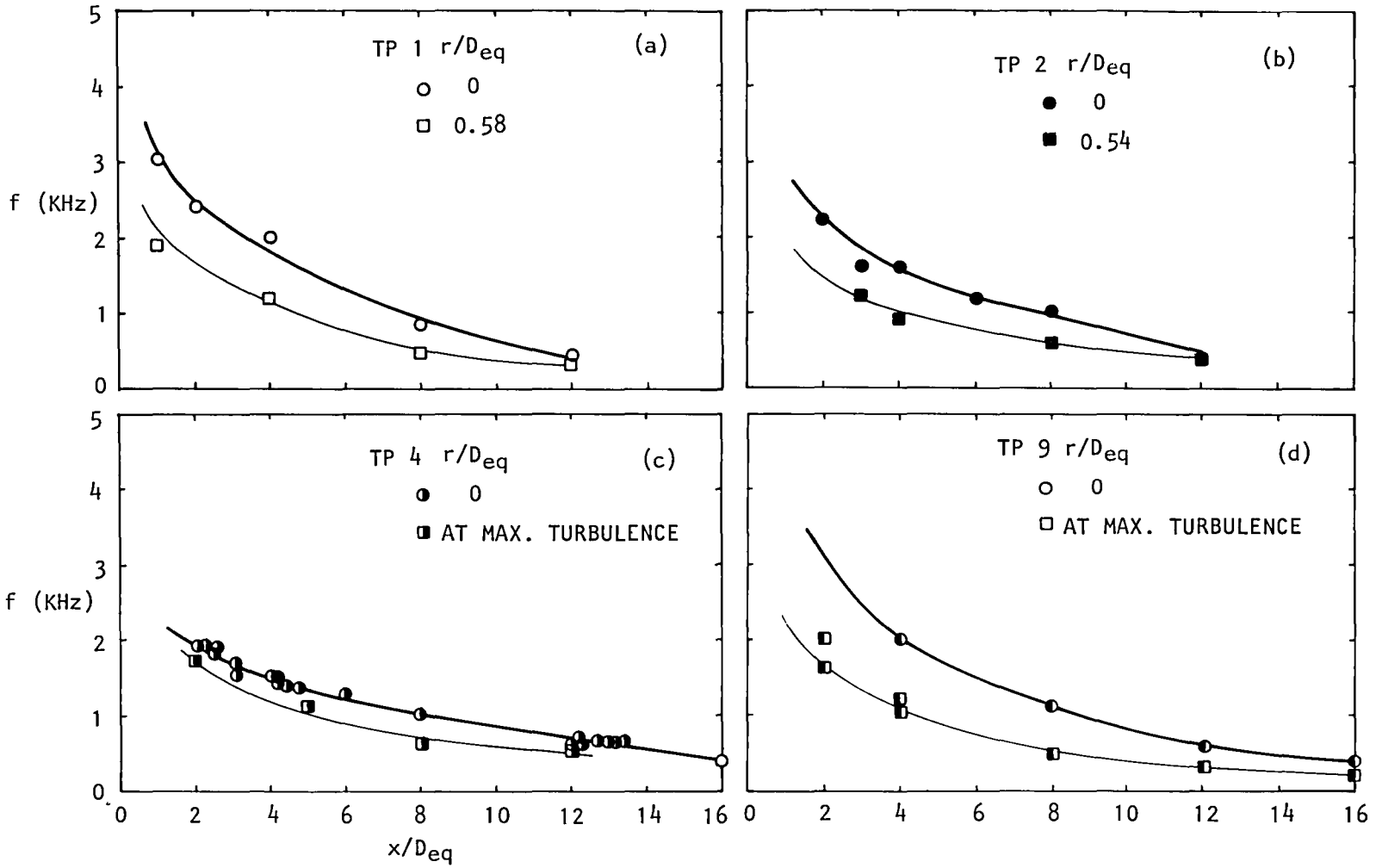

Figure 5.21 Axial distribution of characteristic frequency:
(a) TP 1, (b) TP 2, (c) TP 4, (d) TP 9.

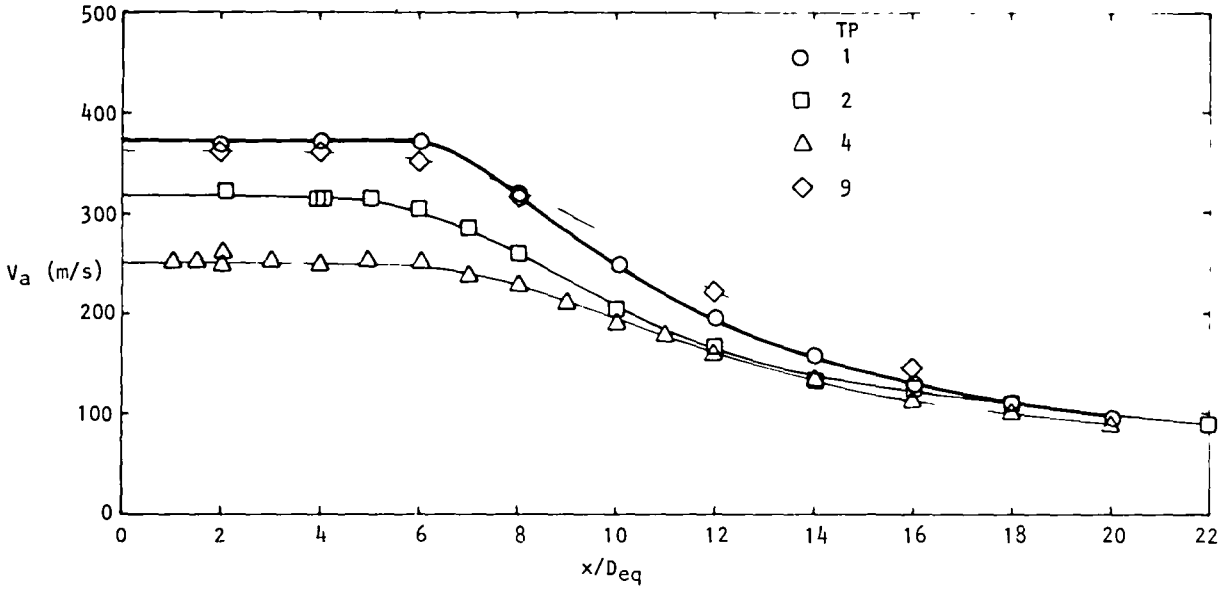

Figure 5.22 Axial distribution of centerline mean velocity V_a.

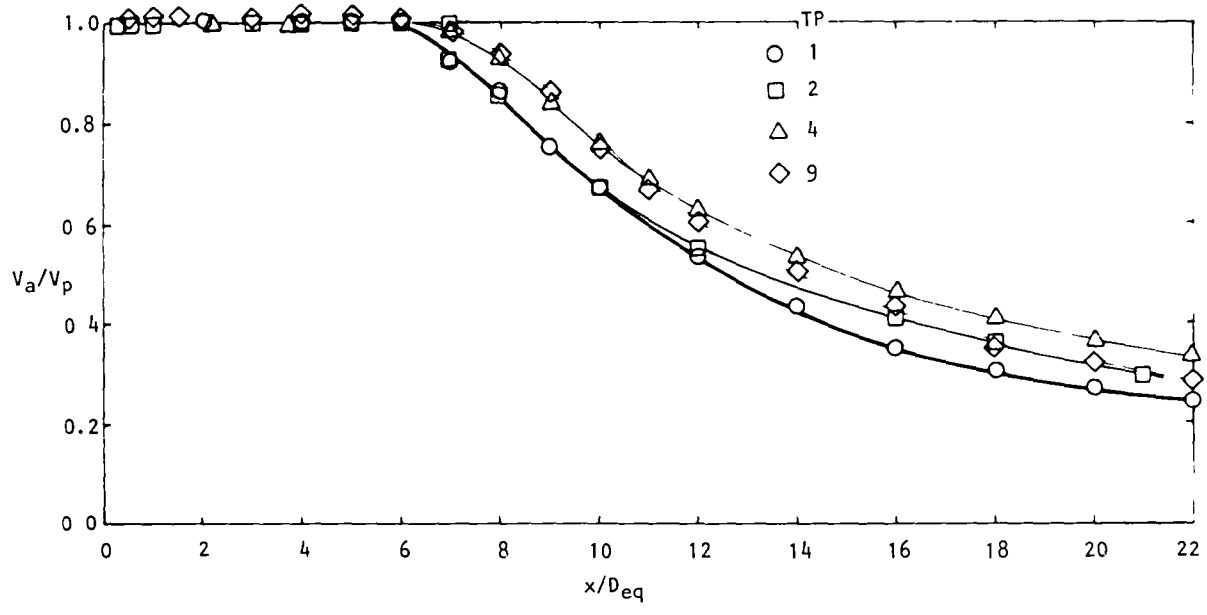

Figure 5.23 Centerline distribution of V_a/V_p.

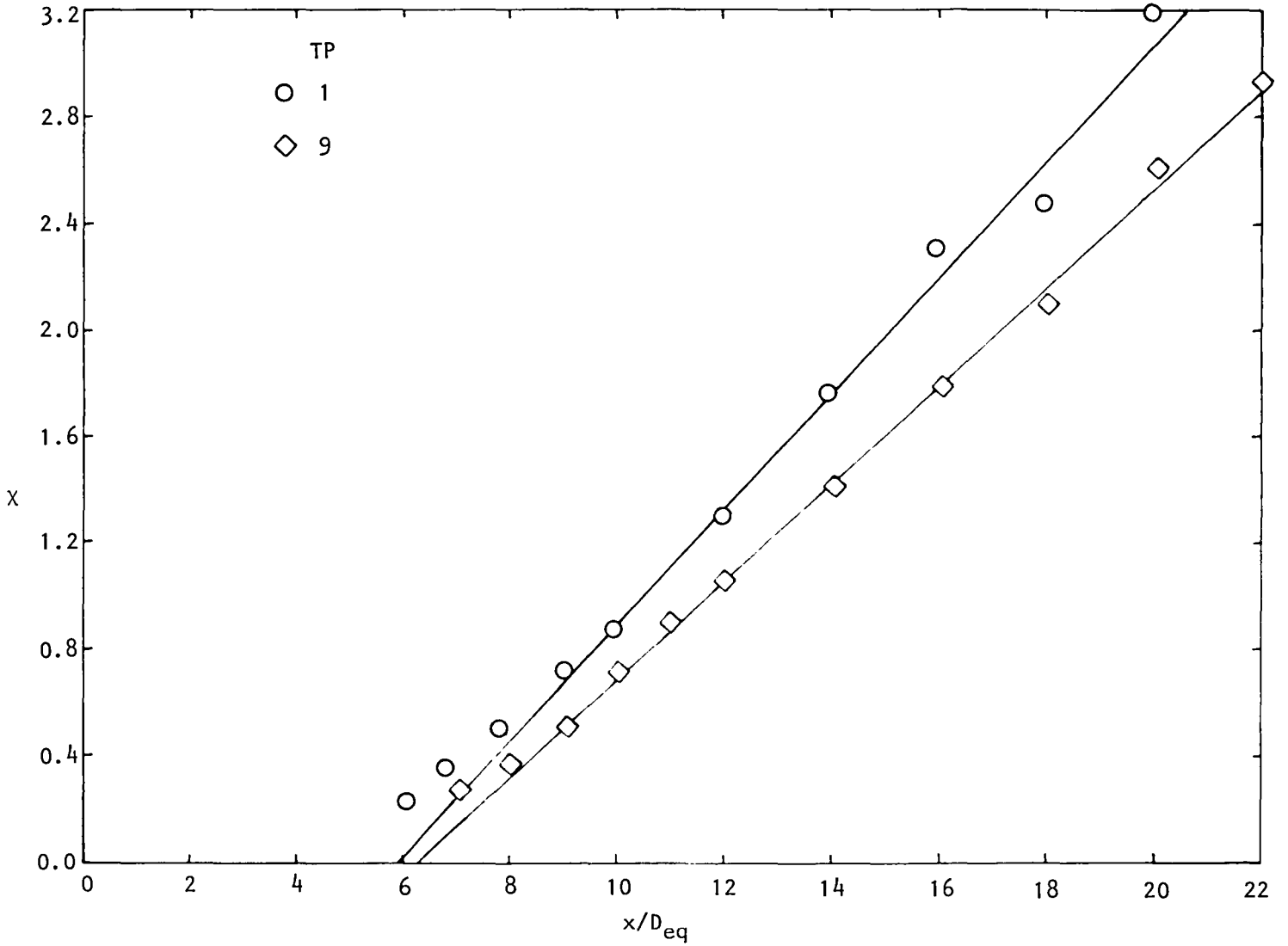

Figure 5.24 χ vs x/D_{eq}.

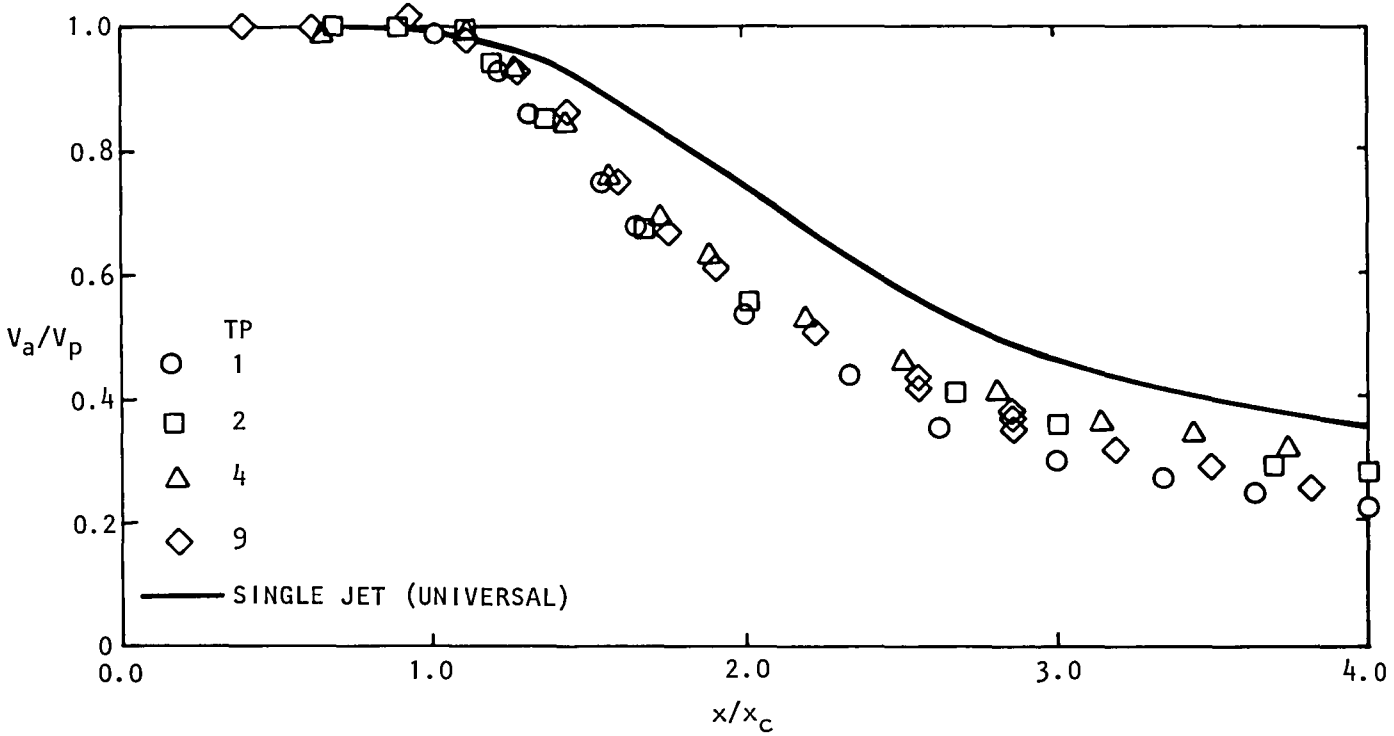

Figure 5.25 V_a/V_p vs x/x_c.

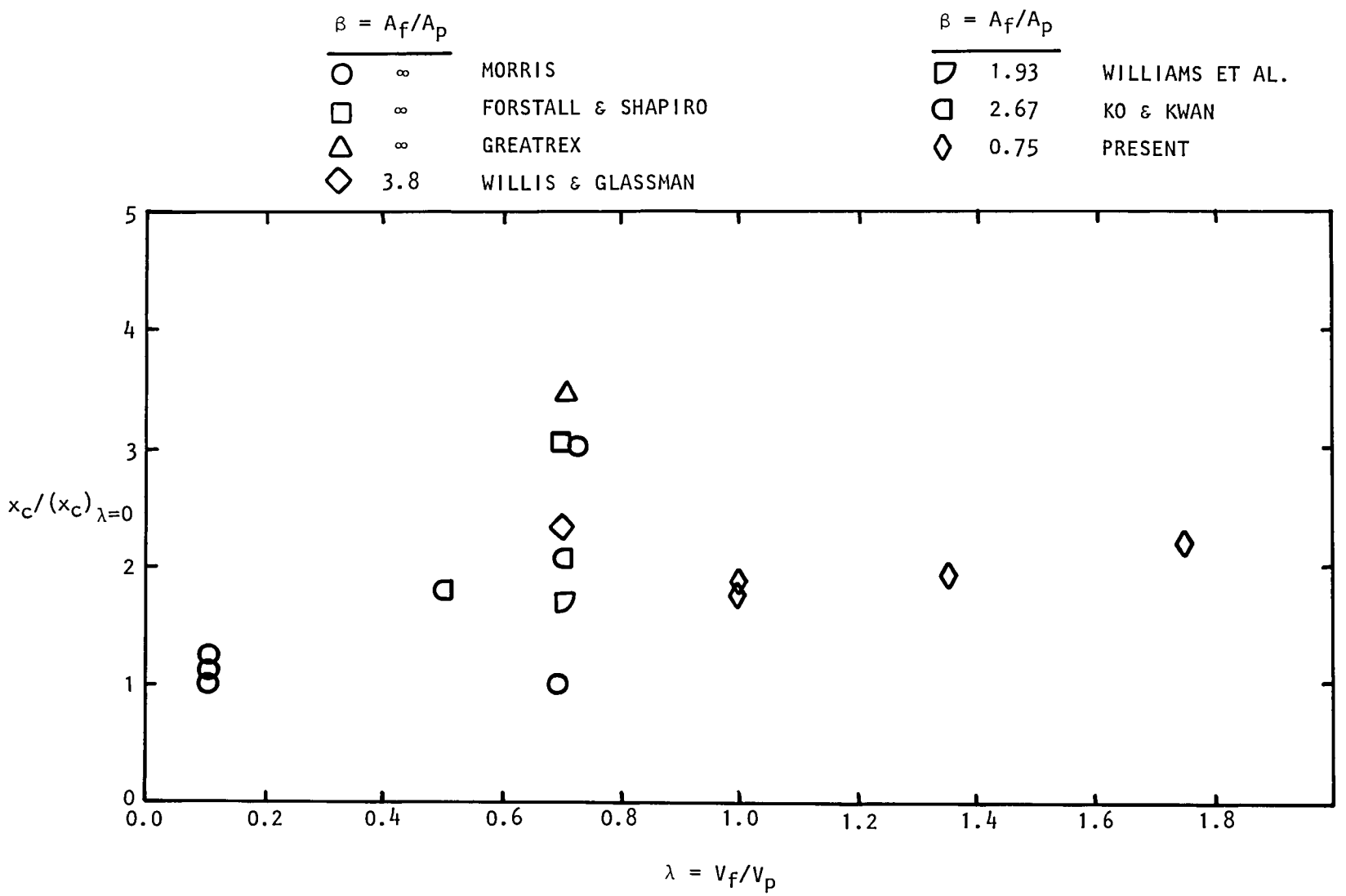

Figure 5.26 Variation of potential core length.

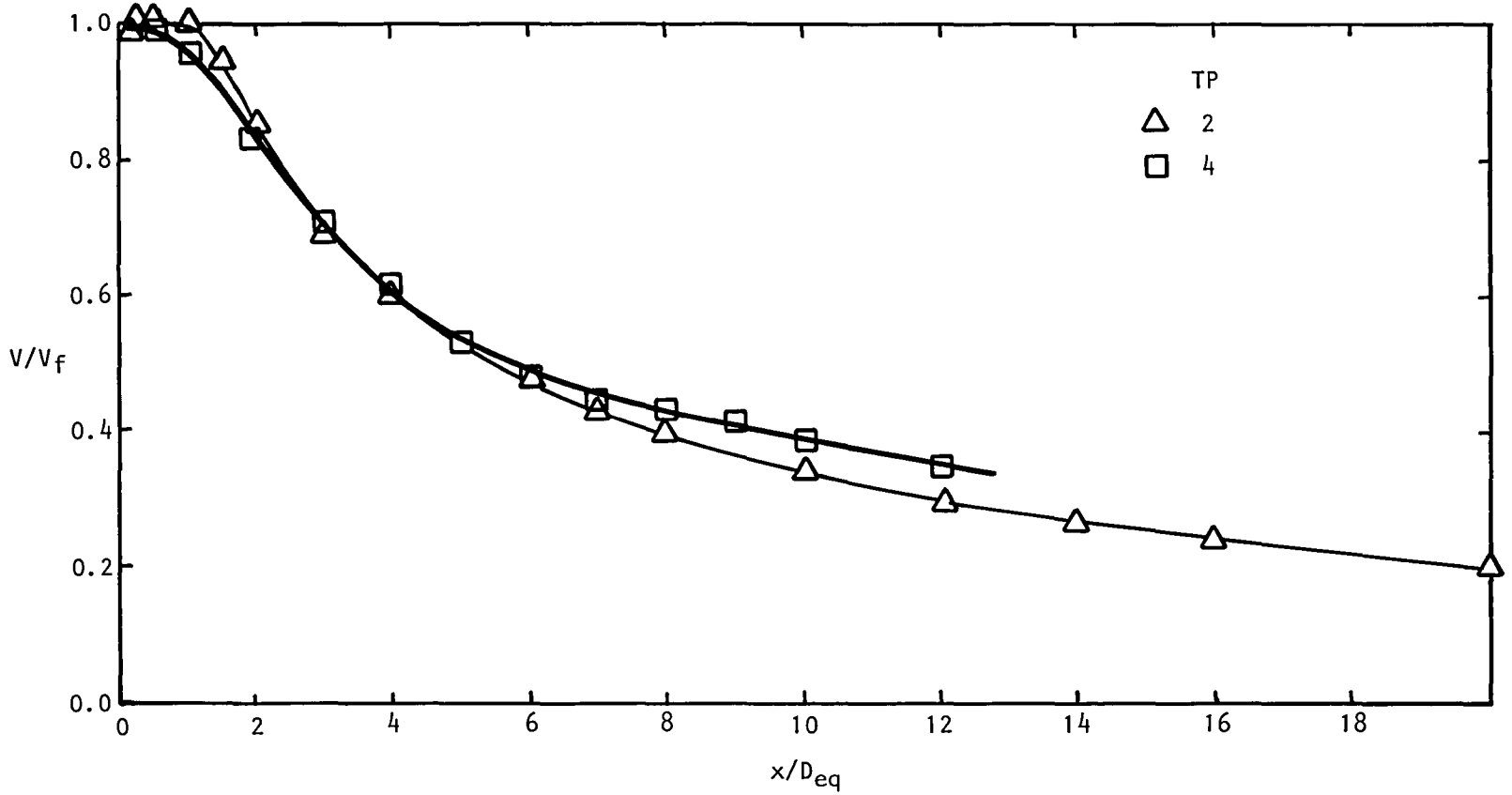

Figure 5.27 Axial distribution of V/V_f along $r/D_{eq} = 0.42$ line.

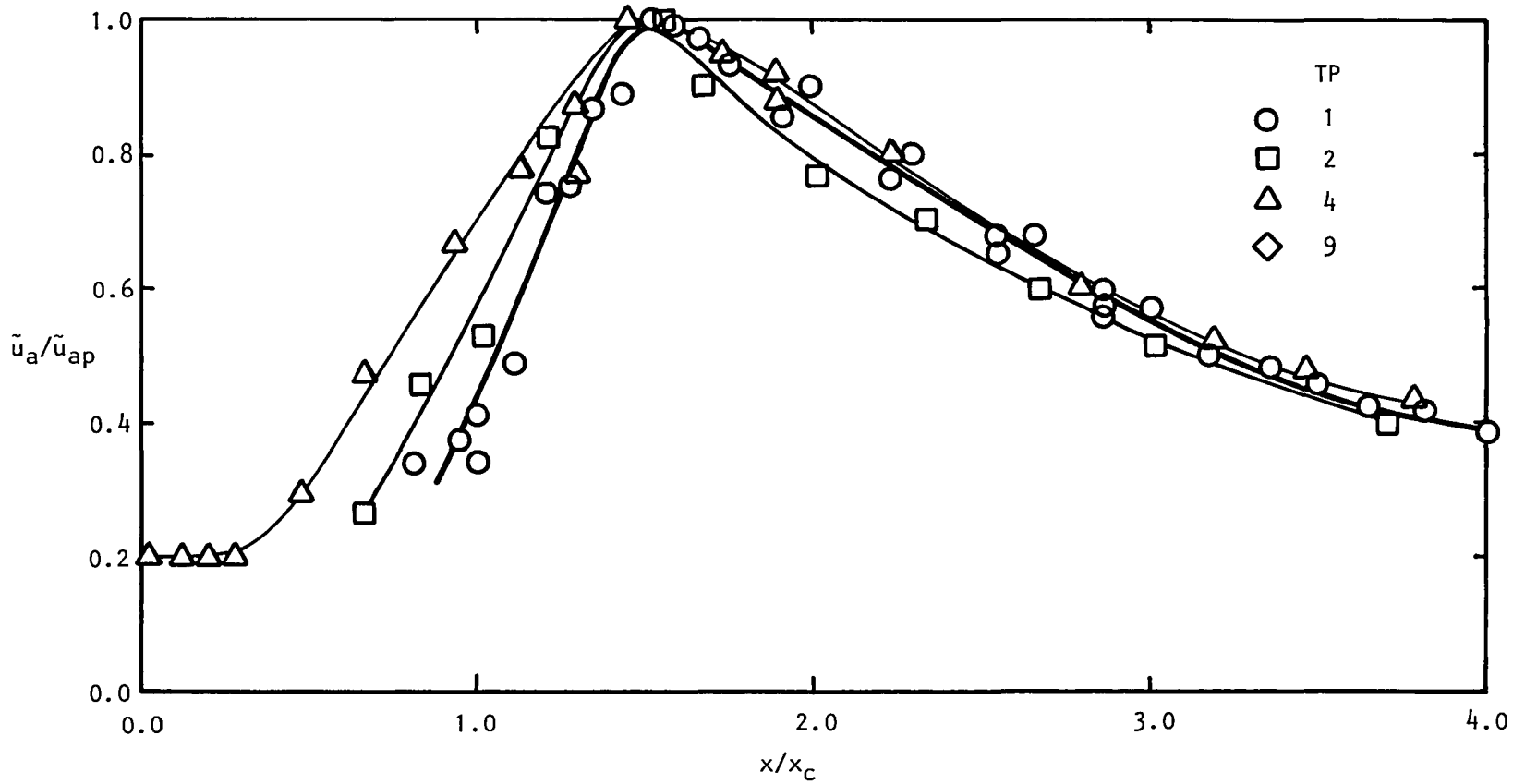

Figure 5.28 Axial distribution of axial turbulence intensity on centerline ($\tilde{u}_a/\tilde{u}_{ap}$).

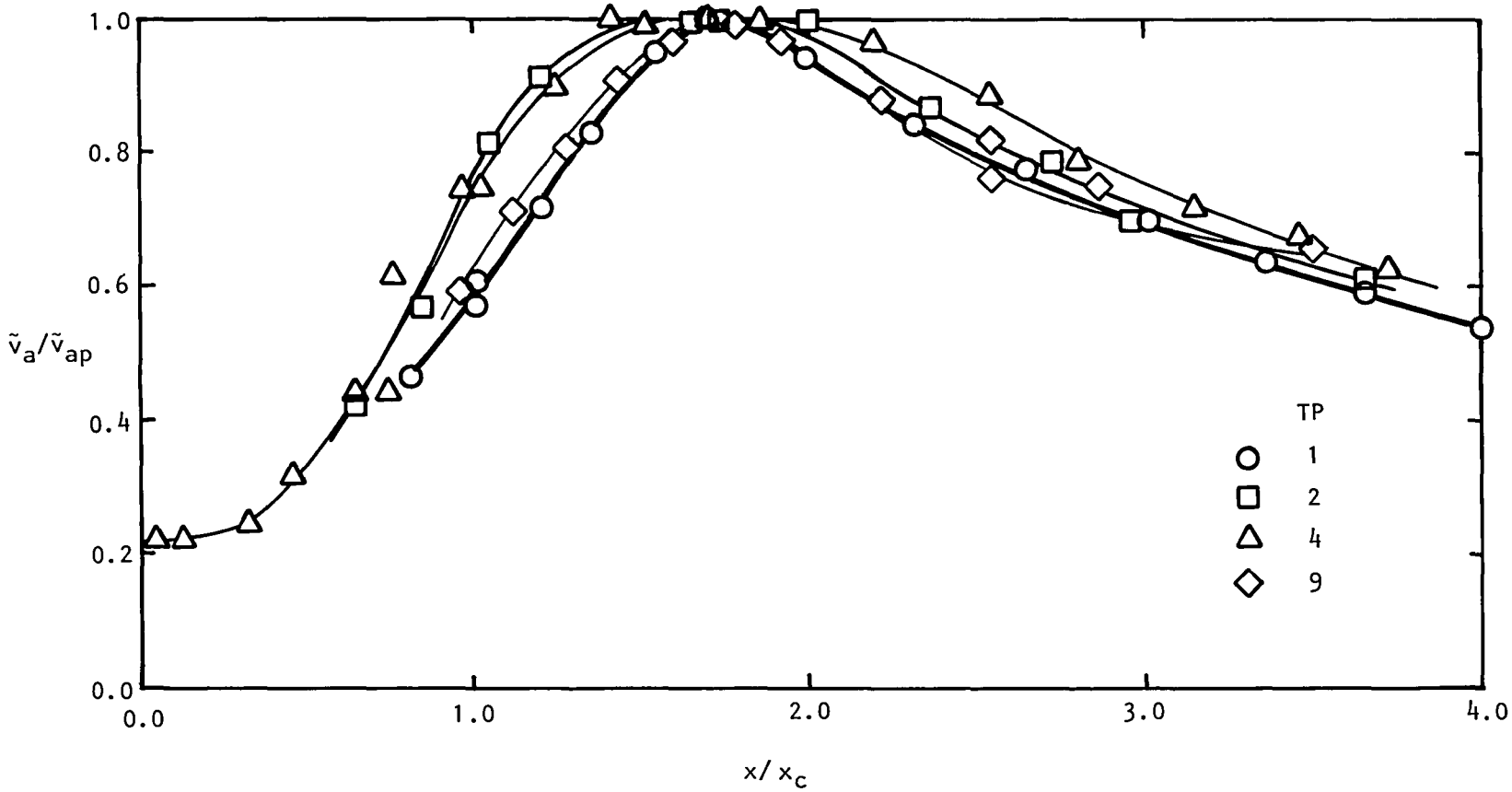

Figure 5.29 Axial distribution of radial turbulence intensity on centerline ($\tilde{v}_a/\tilde{v}_{ap}$).

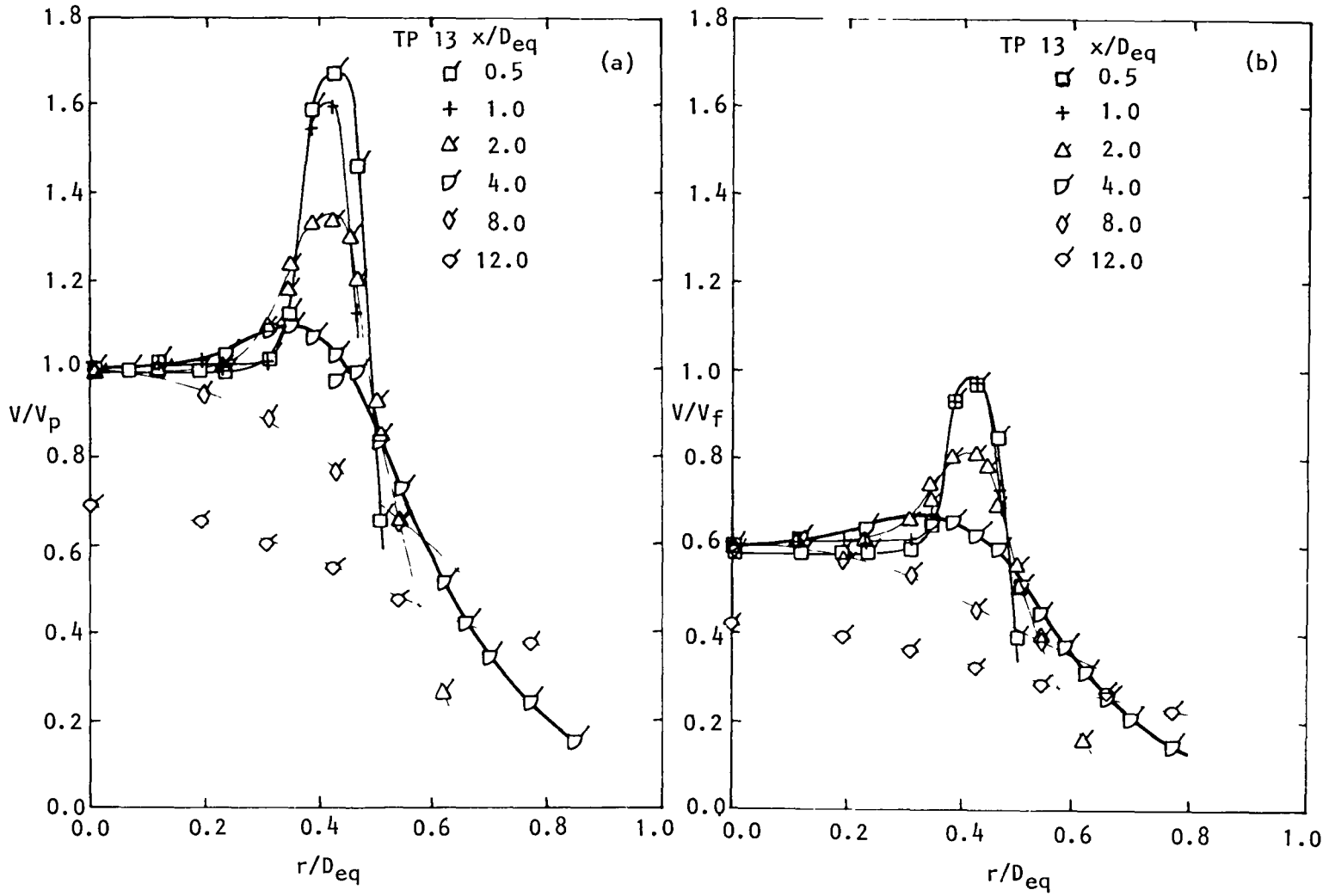

Figure 5.30 Radial distribution of (a) V/V_p and (b) V/V_f for TP 13: $V_f/V_p = 1.66$.

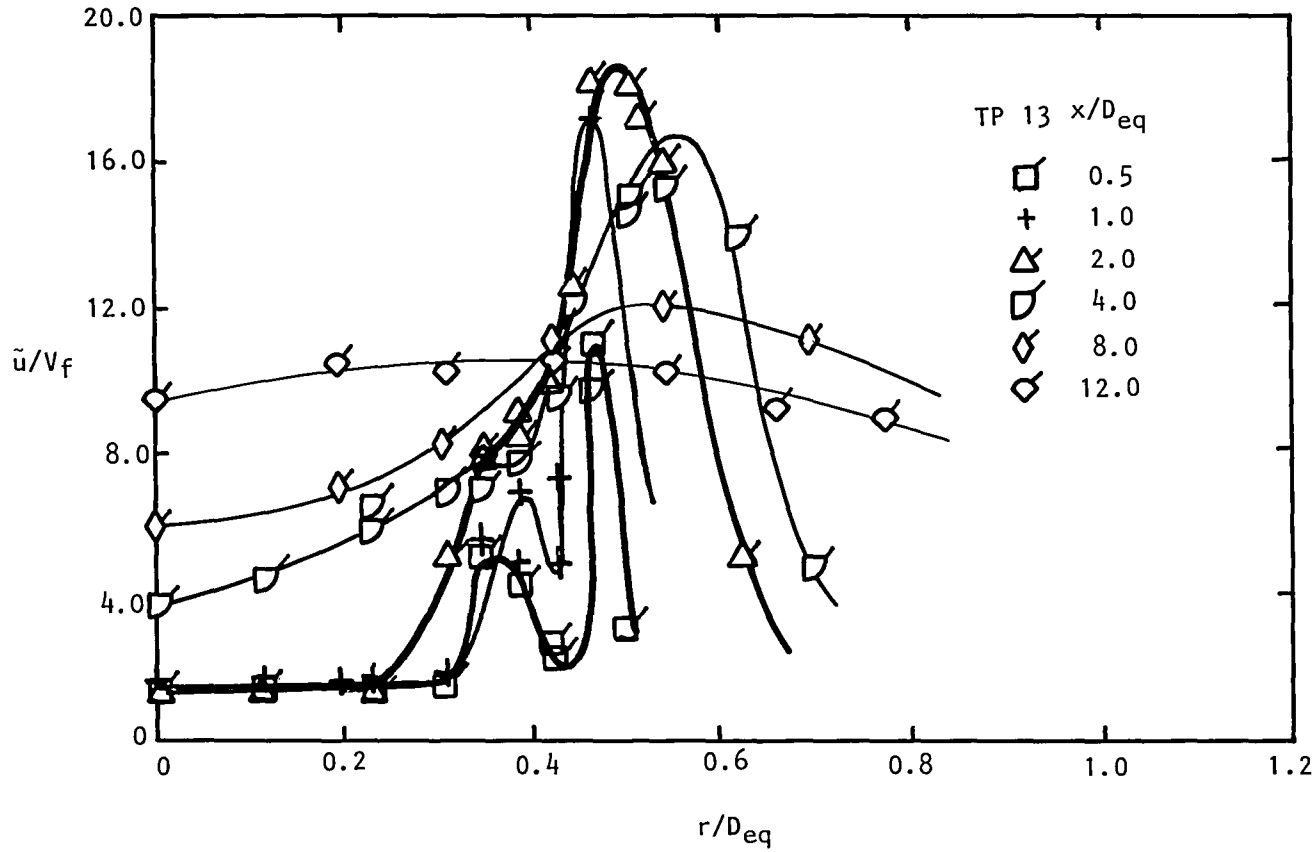

Figure 5.31 Radial distribution of $\tilde{u}/V_f$ for TP 13: $V_f/V_p = 1.66$.

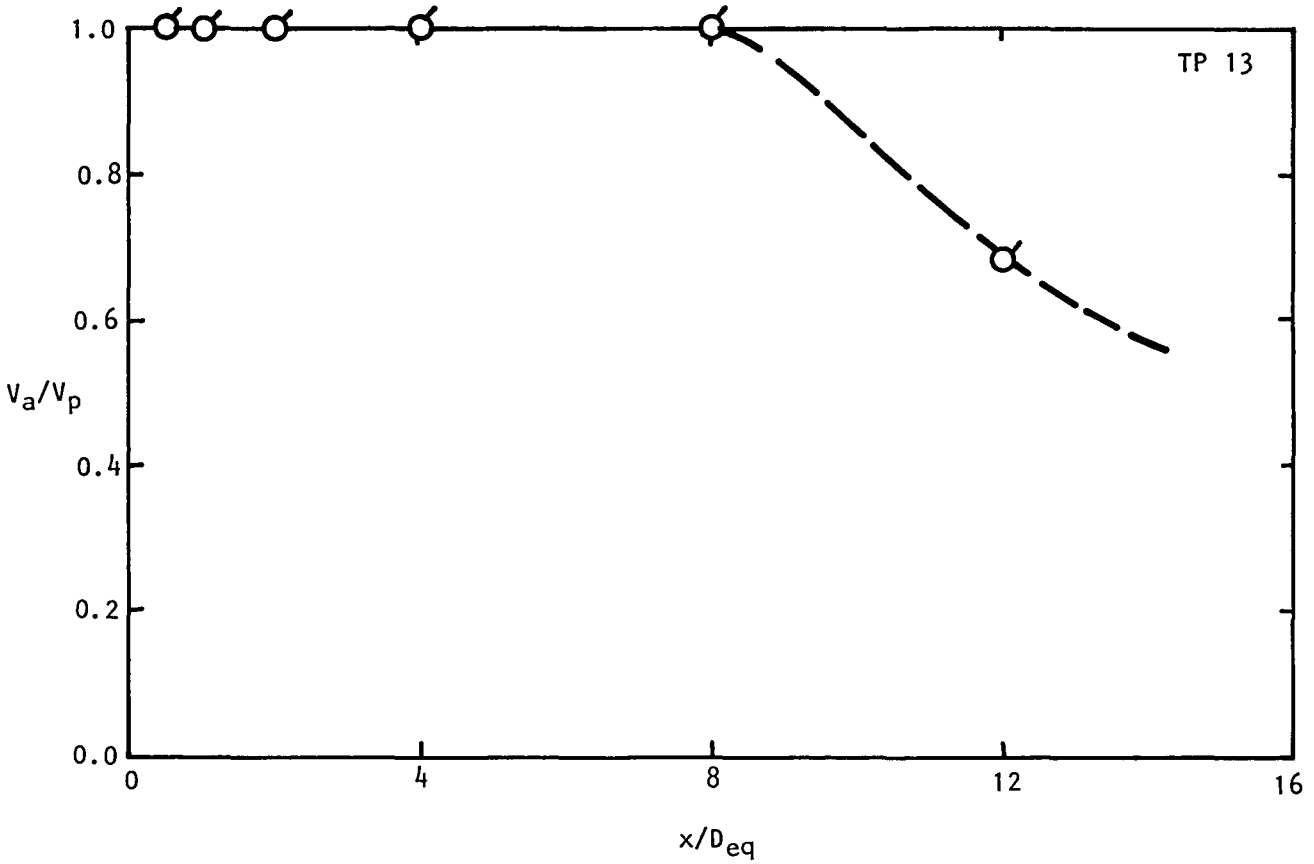

Figure 5.32 Centerline distribution of V_a/V_p for TP 13: $V_f/V_p = 1.66$.

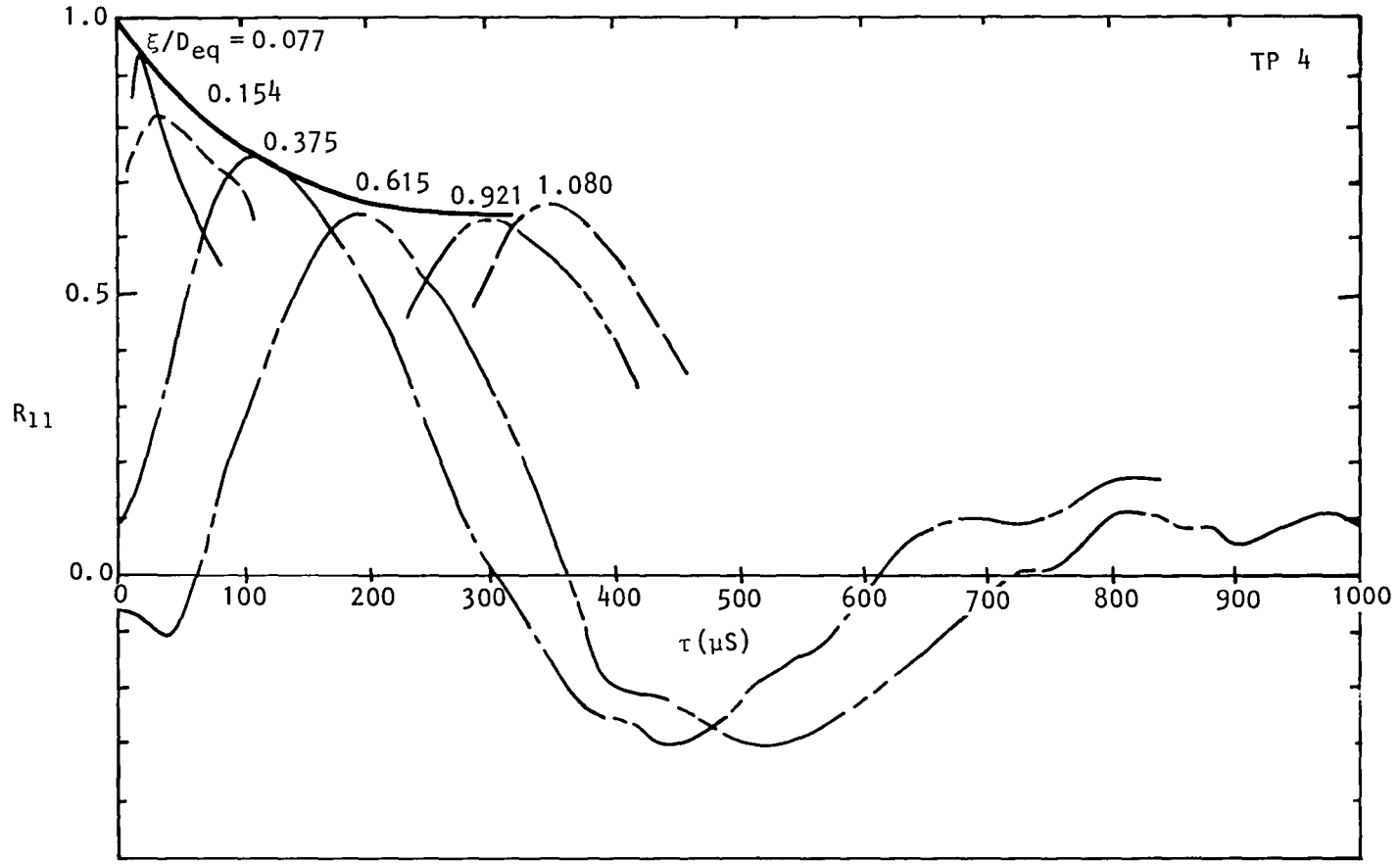

Figure 5.33 Distribution of cross-correlation coefficient.
(TP 4, $x/D_{eq} = 4$, $r/D_{eq} = 0$)

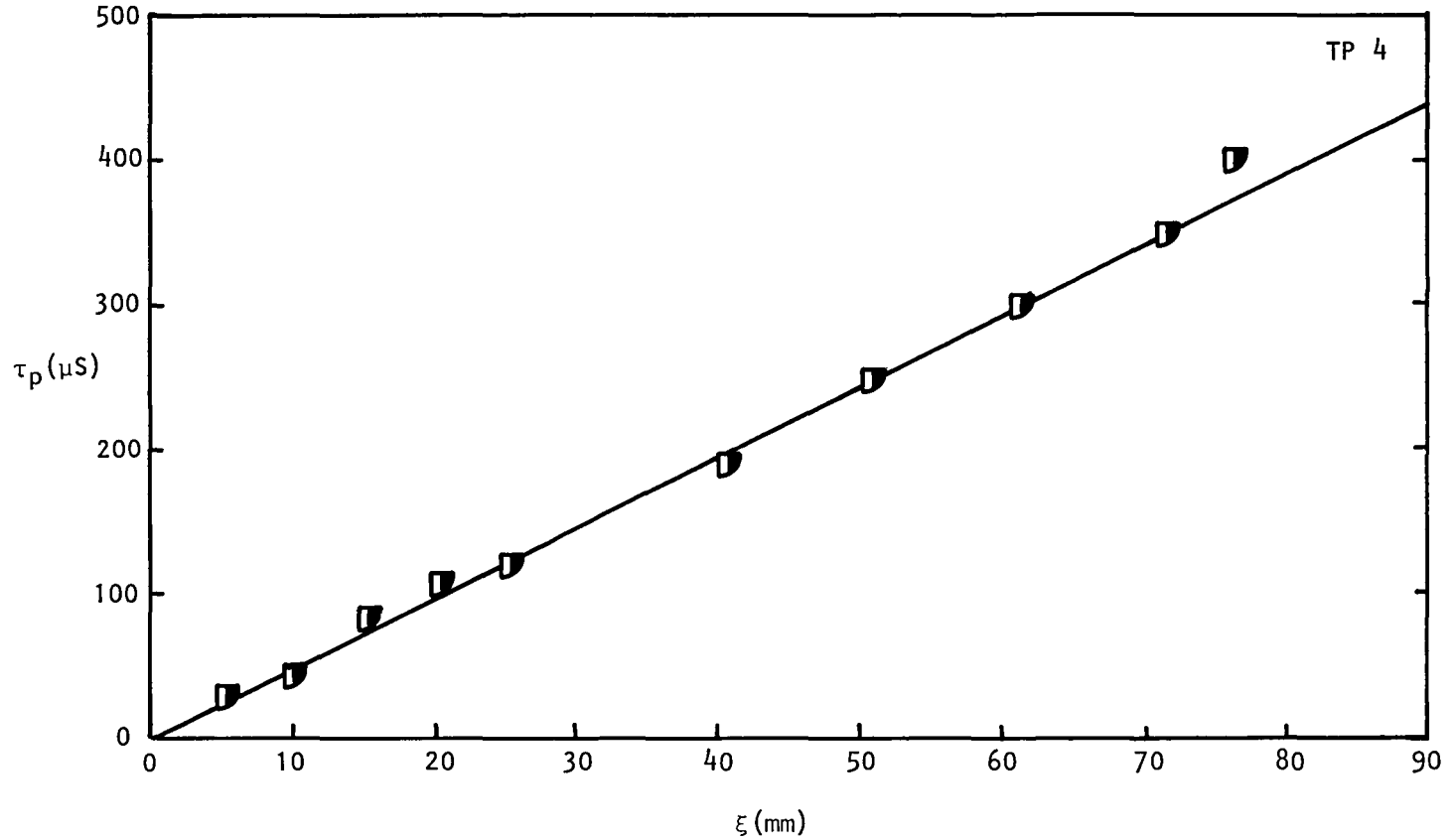

Figure 5.34 Peak time delay τ_p vs separation ξ. (TP 4, $x/D_{eq} = 4$, $r/D_{eq} = 0$).

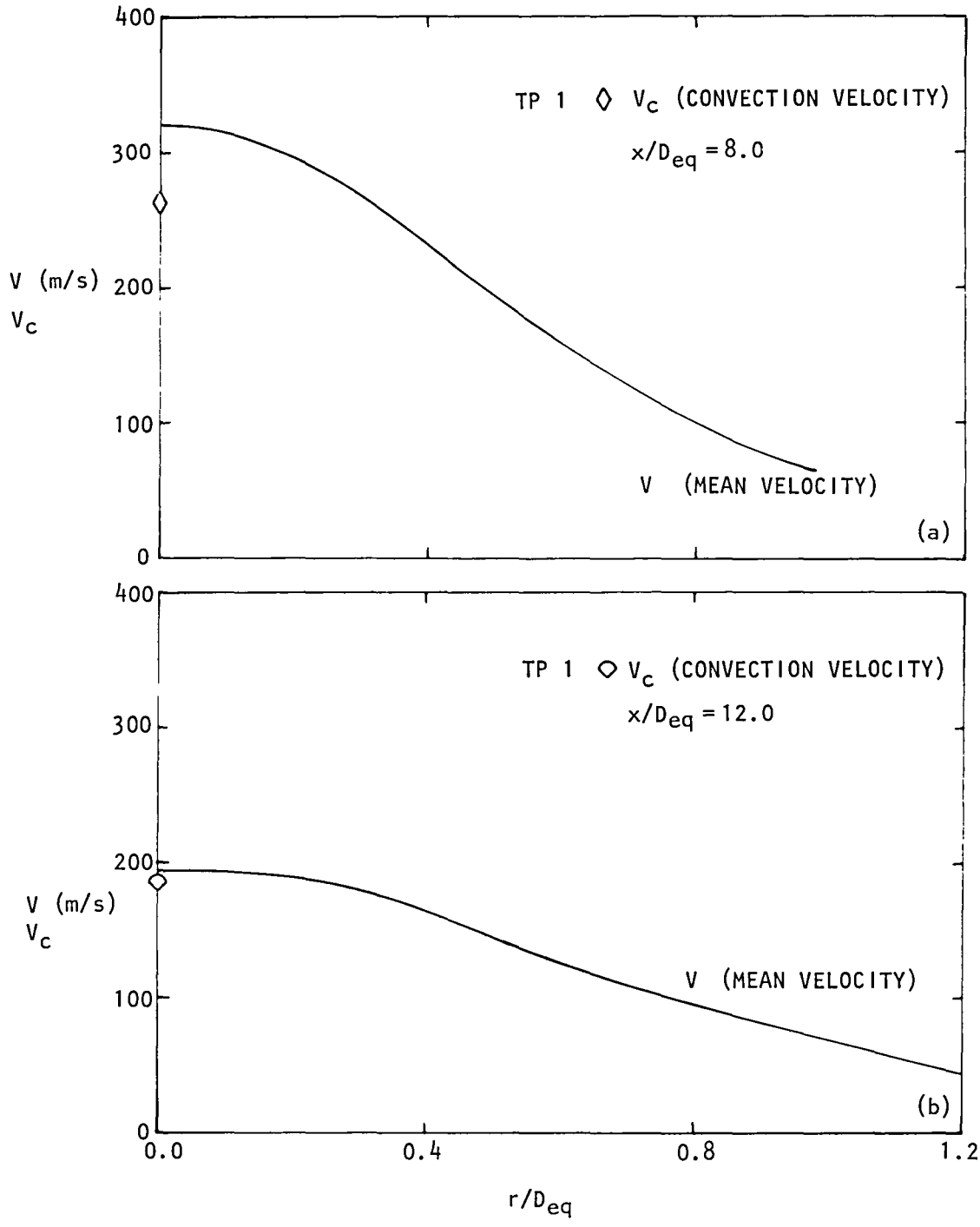

Figure 5.35 Comparison between V_c and V (Test Point 1). x/D_{eq}: (a) 8.0, (b) 12.0.

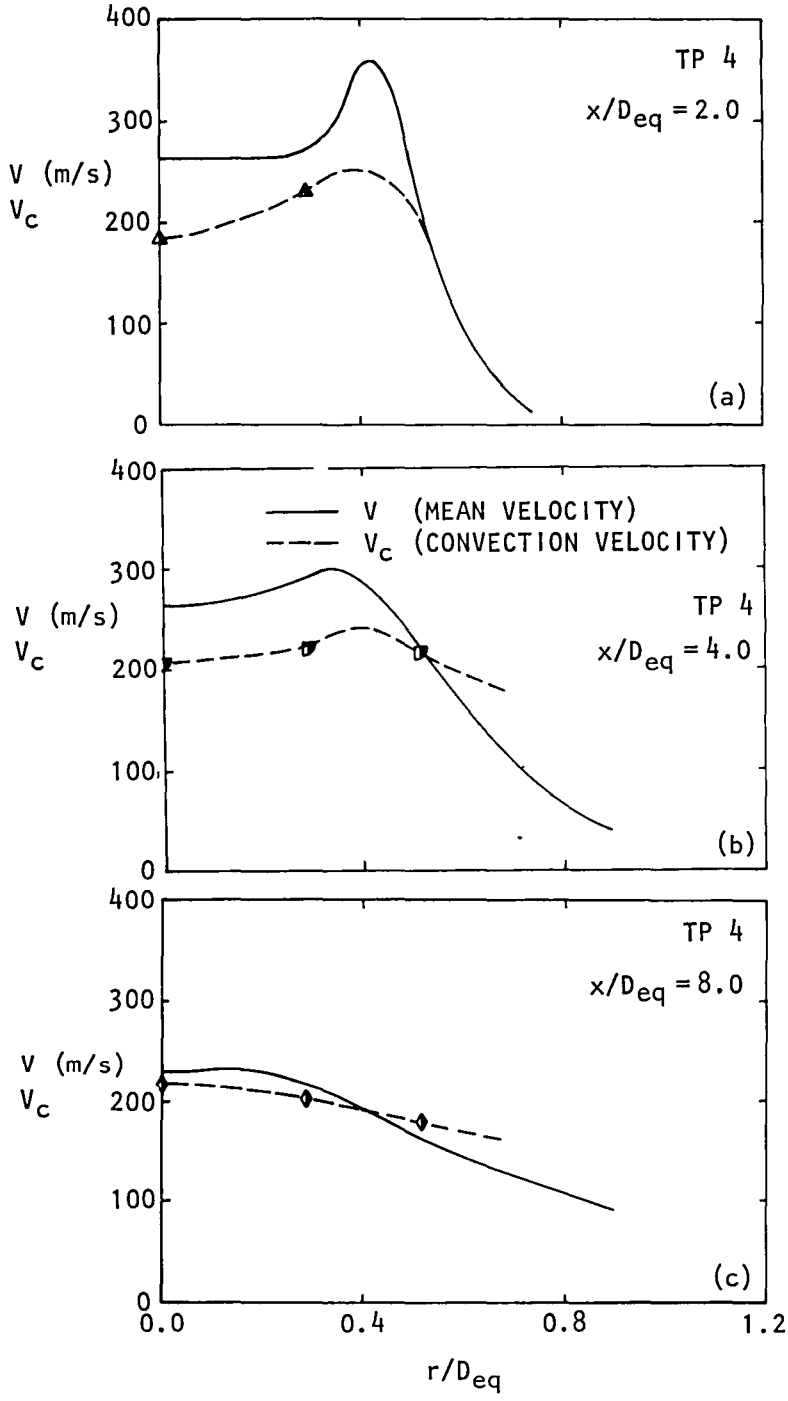

Figure 5.36 Comparison between V_c and V (Test Point 4). x/D_{eq}: (a) 2.0, (b) 4.0, (c) 8.0.

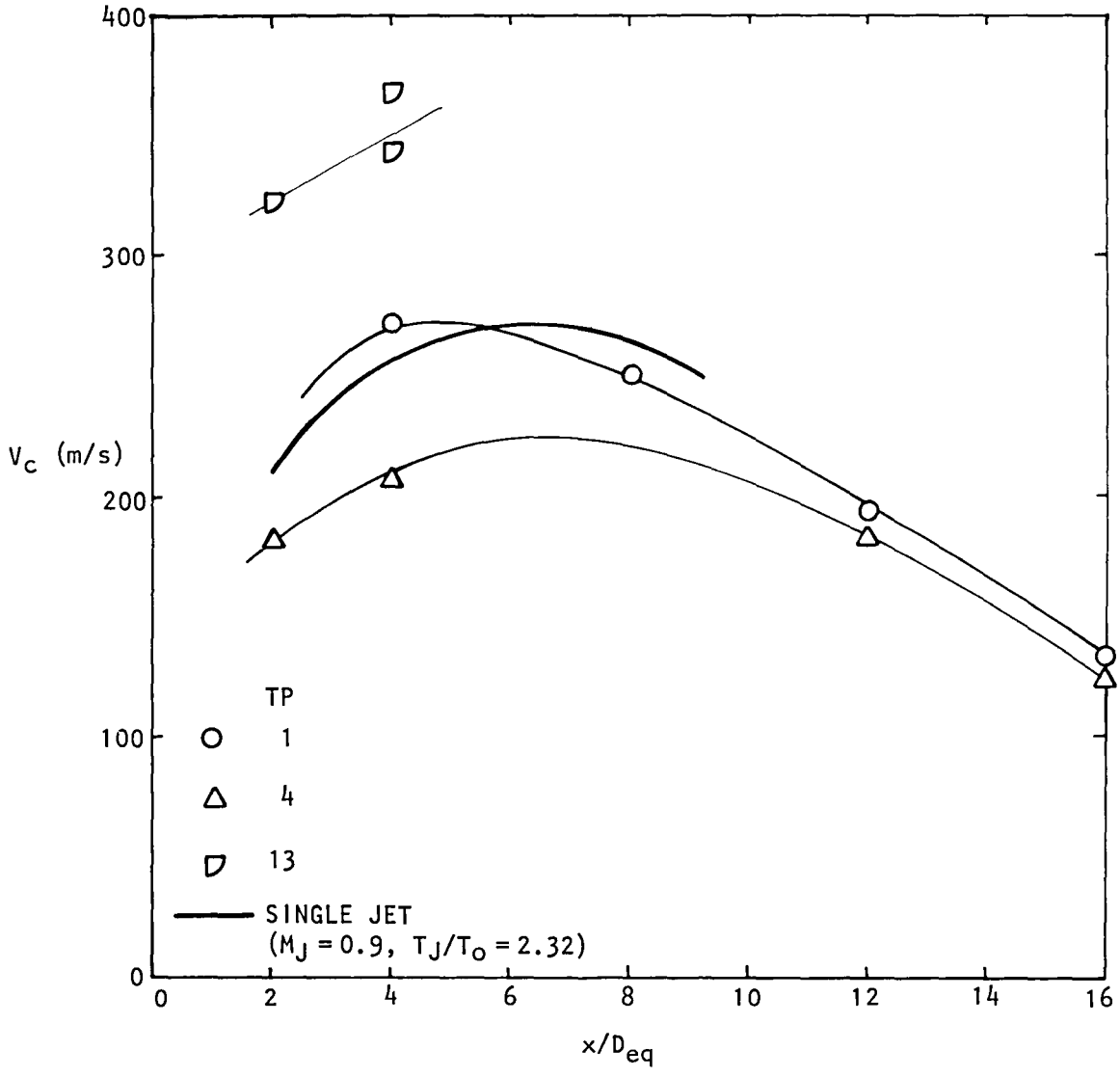

Figure 5.37 Axial distribution of V_c ($r/D_{eq} = 0$).

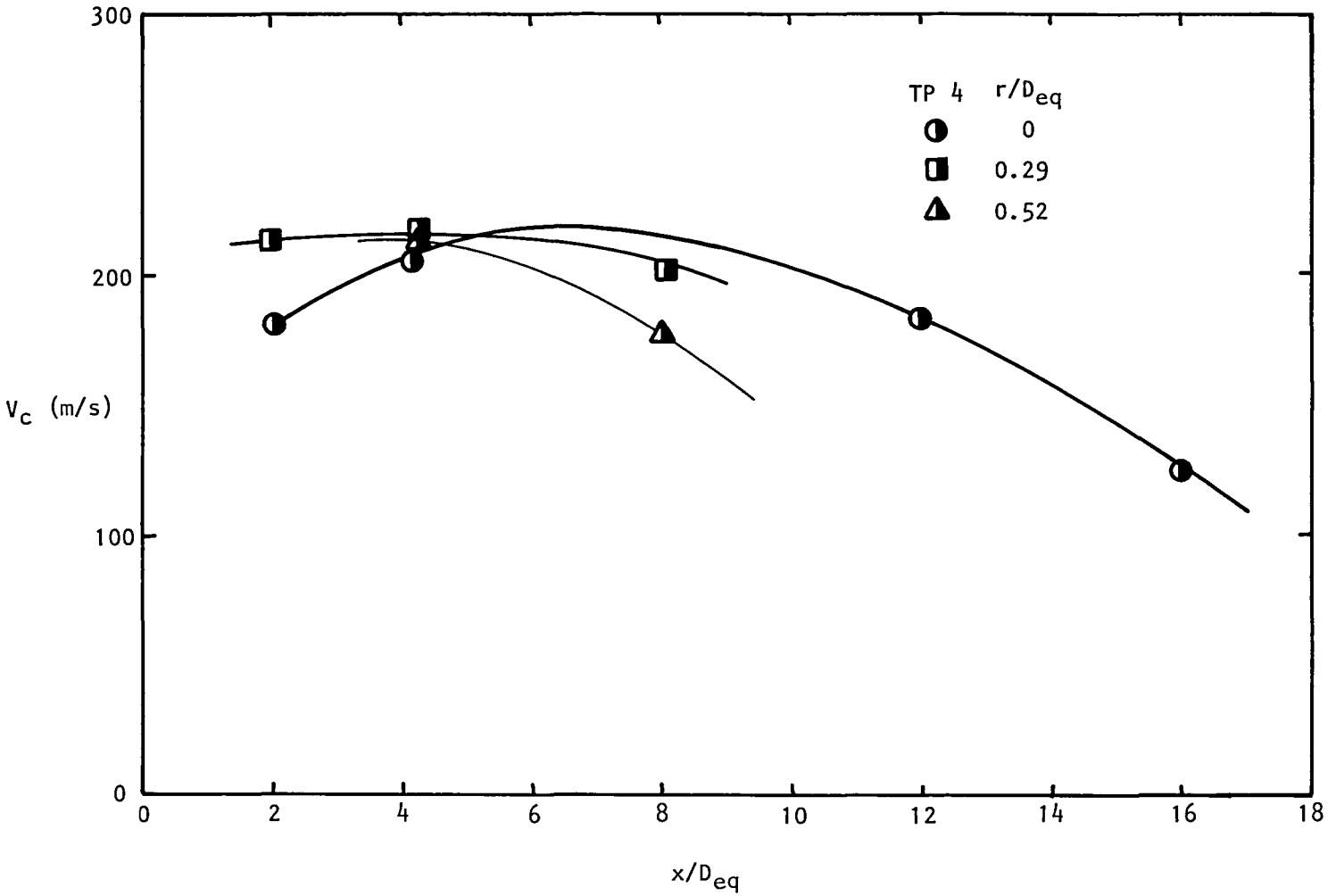

Figure 5.38 Axial distribution of V_c (Test Point 4).

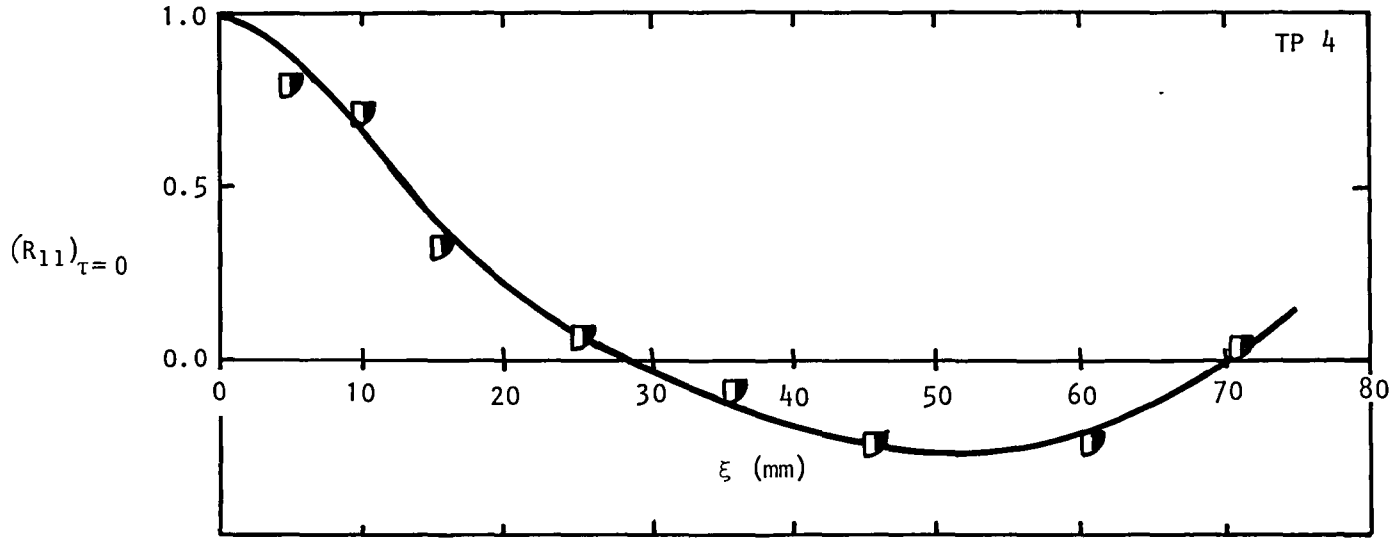

Figure 5.39 Space correlation (Test Point 4, $x/D_{eq} = 4$, $r/D_{eq} = 0$).

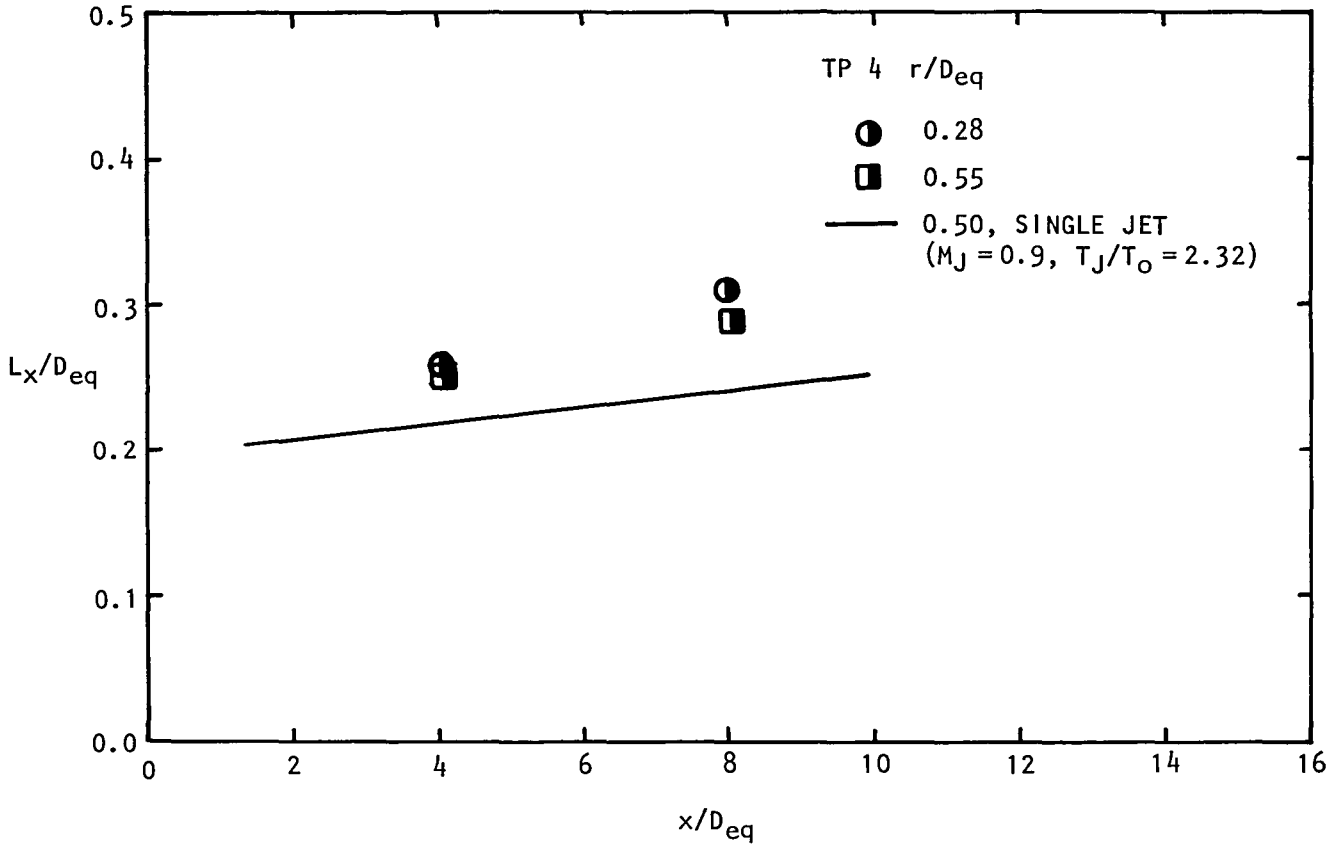

Figure 5.40 Axial distribution of length scale (Test Point 4).

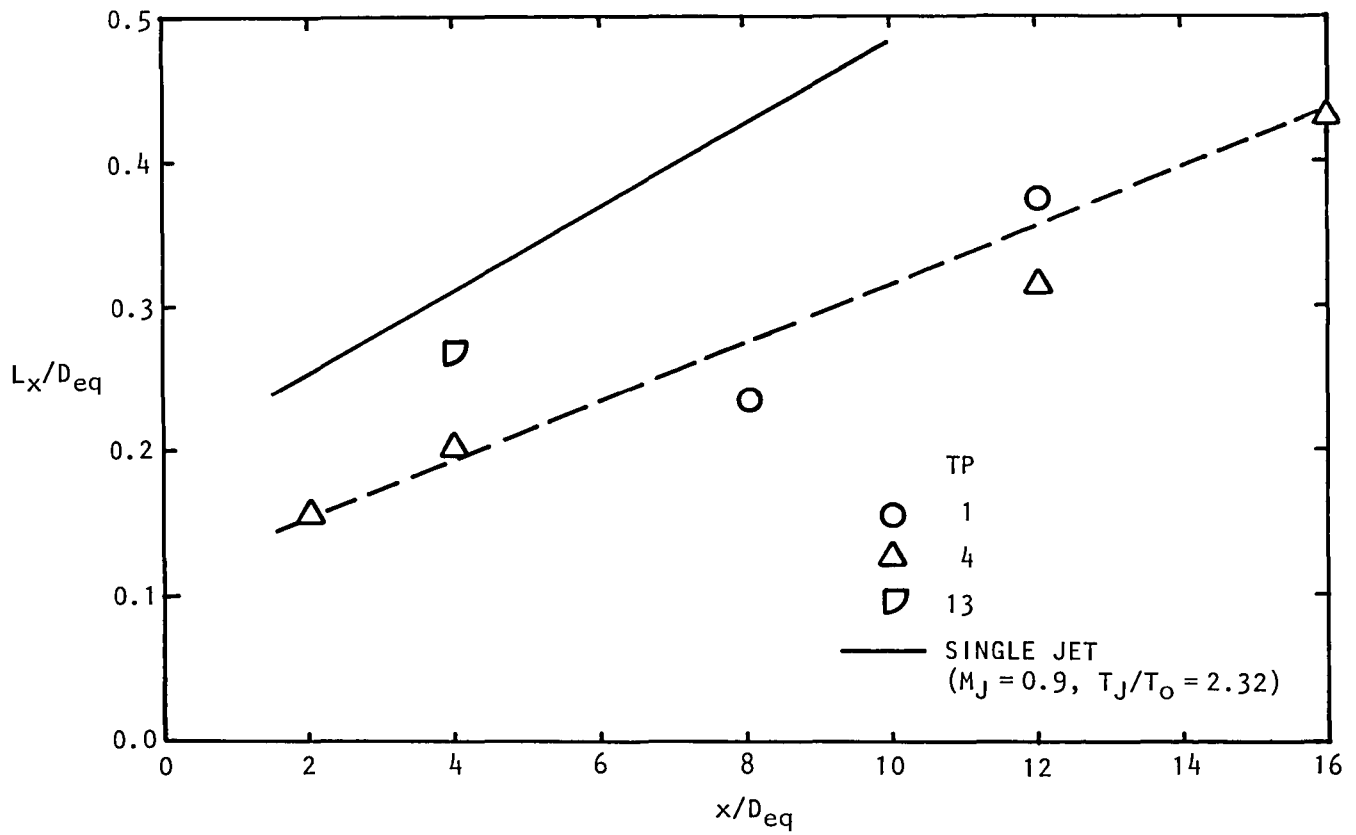

Figure 5.41 Axial distribution of length scale ($r/D_{eq} = 0$).

6. NOZZLE PERFORMANCE TESTS AND RESULTS

In order to evaluate the aerodynamic performance of the coannular nozzle configuration used throughout this investigation, the mass flow coefficients ($C_{m,p}$, $C_{m,f}$) and velocity coefficients ($C_{v,p}$, $C_{v,f}$) of the primary and fan streams were determined. The flow coefficient C_m is defined as the ratio of measured mass flow rate to ideal mass flow rate,

$$C_m = \dot{m}_{measured}/\dot{m}_{ideal}, \tag{6-1}$$

and the velocity coefficient is defined as the measured area-weighted mean exit velocity divided by the ideal nozzle exit velocity,

$$C_v = \frac{\frac{1}{A}\int_A V_{measured}\, dA}{V_{ideal}}. \tag{6-2}$$

The thrust coefficient (C_g) was subsequently calculated as the product of the mass flow and velocity coefficients.

Experiments were conducted at two test conditions:

Test Point (TP) 1: $V_f/V_p = 1.00$, $T_f/T_p = 1.00$

Test Point (TP) 4: $V_f/V_p = 1.75$, $T_f/T_p = 1.00$.

6.1 FLOW COEFFICIENT

The mass flow rates were measured in both the primary and secondary air supply ducts using thin plate orifices. The ductwork of the two supply lines was made as similar as possible with regard to positioning of valves, elbows and T-junctions, etc., so that identical orifice plates could be used. Based on the most stringent requirements with regard to proximity of valves, etc., the maximum allowable ratio of orifice diameter to pipe diameter, d/D, was 0.65. Three pairs of orifice plates were used with d/D = 0.65, 0.60 and 0.55.

The differential pressure measurements across the orifice plates were employed to compute the mass flow rates using the standard ASME flow measurement procedures given in reference 6.1.

The ideal mass flow rate was calculated by using the expression

$$\dot{m}_{ideal} = \rho AV$$

$$= PAM\gamma^{\frac{1}{2}} (RT)^{-\frac{1}{2}} \qquad (6\text{-}3)$$

where
P = nozzle static pressure,
A = nozzle exit area,
M = Mach number,
γ = specific heat ratio,
R = characteristic gas constant, and
T = static temperature.

For each test point, several runs were conducted and the results were arithmetically averaged. The *average* values of measured and ideal mass flow rates, and the corresponding flow coefficients are given in Table 6.1.

Table 6.1 Nozzle flow coefficients.

TP		$\dot{m}_{measured}$ (kg/s)	$\dot{m}_{ideal}$ (kg/s)	Flow Coefficient C_m
1	PRIMARY FAN	0.3979 0.2969	0.4020 0.2985	0.990 0.995
4	PRIMARY FAN	0.2794 0.4043	0.2941 0.3932	0.950 1.028

The above results for TP 4 show the primary flow coefficient to be somewhat less than expected and the fan flow coefficient to be slightly greater than unity which at first sight seems to be physically impossible. Consideration of the possible reasons for these results suggests that there could be a flow leakage from one duct to the other, as explained below.

In order to allow for the differential expansion between the primary and fan ducts in the test rig, a labyrinth-type expansion joint has been incorporated. This type was chosen over the more conventional "bellows" unit since geometric and space limitations dictated that only a very short unit could be tolerated. This type of joint would allow a small amount of leakage from one duct to the other if the pressure difference between them is high.

For TP 4, the fan flow pressure is almost four times that of the primary whereas the pressures are the same for TP 1. Taking an average of the primary

and fan flow coefficients for TP 4 yields a coefficient of 0.989, which is consistent with both the primary and fan coefficients for TP 1.

Therefore, on average, the flow coefficients for both the primary and fan nozzles do not differ significantly, and are of the order of 0.99.

6.2 VELOCITY COEFFICIENT

In order to determine the velocity coefficients, the mean velocity profiles at the nozzle exit planes should ideally be measured. However, due to the light reflection from the nozzle surfaces, attempts to conduct laser velocimeter measurements at or very close to the nozzle exit planes were not very successful. A pitot probe was therefore used instead, and the Mach number profiles at the exit planes of the primary and fan nozzles were determined by measuring the total pressure profiles. The resulting Mach number coefficient would give the velocity coefficient if the exit temperature in the actual situation is the same as the exit temperature in the ideal case. The pitot probe was traversed automatically in the radial direction, and the pressure was recorded (on magnetic tape) at a sufficient number of radial positions to allow an accurate profile to be established for subsequent integration to obtain an area-weighted average Mach number.

The ideal Mach number was calculated by using the standard relationship

$$M = \left[\frac{2}{\gamma-1}\left\{(\xi)^{\frac{\gamma-1}{\gamma}} - 1\right\}\right]^{\frac{1}{2}}, \qquad (6\text{-}4)$$

where ξ is the nozzle pressure ratio.

The velocity coefficient results are given in Table 6.2. Due to some tape recording difficulties, all of the primary nozzle data for TP 1 could not be retrieved; however, since the primary nozzle operating conditions for TP 1 are not very different from those for TP 4, the velocity coefficient result for TP 4 can be taken to be a good indication of the velocity coefficient for TP 1.

6.3 THRUST COEFFICIENT

Based on the velocity and flow coefficient measurements, the thrust coefficients for both the primary and fan nozzles, computed as the products of flow and velocity coefficients, are of the order of 0.985.

Table 6.2 Nozzle velocity coefficients.

TP		$\frac{1}{A}\int_A M_{measured}\, dA$	M_{ideal}	Velocity Coefficient C_v
1	PRIMARY	--	--	--
	FAN	0.7427	0.7481	0.993
4	PRIMARY	0.5084	0.5093	0.998
	FAN	0.9456	0.9541	0.991

7. MODEL/DATA COMPARISONS

In this section the coannular jet mixing noise measurements presented in Section 2 are interpreted with the aid of the source location results (Section 3), the jet flow measurements (Sections 4 and 5), and *two* single-jet models of the inverted-profile coannular jet. The mixing noise spectra of the single-jet models, which are used to separately model low- and high-frequency coannular jet mixing noise, are calculated with the Lockheed jet noise prediction program. The main objective of this work is to understand the variation of coannular jet mixing noise with velocity ratio (V_f/V_p) and temperature ratio (T_f/T_p). Absolute noise spectrum predictions are not attempted here; instead, the *changes* in noise levels relative to the reference jet noise levels (i.e. the noise reductions at low frequencies and the noise increases at high frequencies) are calculated and compared with measured noise changes. The reference jet is defined here as the condition where the jet streams of the coannular jet have the same exit velocity and the same exit static temperature ($V_f/V_p = 1$, $T_f/T_p = 1$).

7.1 SINGLE JET MODEL OF COANNULAR JET AT LOW AND HIGH FREQUENCIES

7.1.1 Low-Frequency Single-Jet Model

The source location measurements on coannular jets, presented in Section 3 indicate, as in the case of a single jet, that the low-frequency noise is generated at a considerable distance downstream of the coannular nozzle exit planes. The probe measurements of the mean velocity and the static temperature profiles presented in Section 4 also show that the two streams of the coannular flow mix quite rapidly and resemble single jet profiles not far downstream of the primary potential core. It follows that at *low frequencies*, calculation methods for convective amplification, acoustic-mean flow interaction effects, etc., in a single round jet may be used to interpret and predict the variation of these effects with velocity and temperature ratio (V_f/V_p, T_f/T_p) in a coannular jet.

Although it can be argued that the effects of mean flow on the emission and radiation of sound are governed by *local* properties of the flow, the Lockheed mixing noise prediction method for the single round jet has been developed to calculate noise levels at all frequencies based on nozzle *exit* conditions alone, i.e. jet exit velocity V_J, exit static temperature T_J, and nozzle diameter D_J. (It is emphasized, however, that the method *does* incorporate effects such as the mean velocity decay along the jet axis.) In order to use this prediction method, therefore, it is necessary to calculate the single-jet exit conditions (D_J, V_J, T_J) which would give rise to the *same* mean flow conditions far downstream of the nozzle exit plane as those found in the coannular jet. The calculation method is described below.

The single-jet conditions (D_J, V_J, T_J) required for prediction purposes are given in Table 7.1. These have been calculated by (see Figure 7.1):

Table 7.1 Coannular and corresponding single jet exit conditions
[$P_o = 98112.4$ N/m^2 (14.23 psia), $D_J = 6.807$ cm (2.68 in.)]

TP	Run No.	V_f/V_p	T_f/T_p	V_p/a_o	V_f/a_o	T_p/T_o	T_f/T_o	T_o (°K)	V_J/a_o	T_J/T_o
1	26	1.00	1.00	1.039	1.042	1.910	1.920	301.7	1.040	1.914
2	25	1.35	1.00	0.885	1.199	1.873	1.884	303.1	1.040	1.876
3	24	1.55	1.00	0.806	1.250	1.838	1.838	303.4	1.032	1.832
4	23	1.75	1.00	0.730	1.282	1.778	1.782	304.3	1.019	1.772
5	22	1.00	1.75	1.043	1.045	1.565	2.759	304.6	1.044	1.955
6	21	1.35	1.75	0.924	1.251	1.532	2.709	304.3	1.068	2.012
7	20	1.55	1.75	0.851	1.329	1.483	2.639	305.1	1.069	1.998
8	19	1.75	1.75	0.785	1.382	1.440	2.554	305.1	1.065	1.972
9	18	1.00	2.00	1.047	1.042	1.518	3.030	304.9	1.045	1.969
10	17	1.35	2.00	0.933	1.262	1.476	2.980	304.9	1.074	2.044
11	16	1.55	2.00	0.865	1.352	1.433	2.928	305.3	1.081	2.051
12	15	1.75	2.00	0.800	1.416	1.391	2.850	305.7	1.081	2.042

COANNULAR JET SINGLE JET

(1) equating the total nozzle exit area of the coannular nozzle, $A_p + A_f$, with the single-jet exit area, A_J; (2) defining (for this purpose) the flow conditions as *uniform* over the single-jet exit area and over each nozzle of the coannular jet; (3) equating the *thrust* (axial momentum efflux) and *energy output* (stagnation enthalpy efflux relative to the ambient state) of the coannular nozzle with that of the single jet.

The single jet is defined in this way for the following reasons. To a reasonable approximation† the axial momentum efflux and the stagnation enthalpy efflux (both relative to that of the ambient fluid) are independent of distance along the jet axis. Therefore, at distances sufficiently far downstream from the coannular nozzle where the flow profiles are approximately identical to those of a single jet of the same total exit area, the absolute mean velocities and temperatures must be roughly the same as those of a single jet of the same thrust and energy output. Hence, the convective amplification effects, acoustic-mean flow interactions, etc., in the coannular jet should be the same as in this single jet.

This concept can be extended to include intermediate regions of the coannular jet flow which have the "monotonic" profiles of a single jet (i.e. profiles similar in character to single jet profiles) but significant differences in shape (particularly near the centerline) relative to that of the reference jet, as shown for example in Figure 4.3(c), ($x/D_{eq} = 6.06$). This reduction in mean velocity - with increasing velocity ratio - in the velocity of the jet axis will be associated with a reduction in both the "source region" velocity, V_s, and the eddy convection velocity, V_c. Thus, acoustic-mean flow interaction effects will be calculated here with the single-jet conditions as given in Table 7.1, but with appropriate modifications to the "source region" velocity, V_s, as determined from the mean velocity measurements.

There is a risk of confusing the single-jet conditions defined above with those of the reference jet. There *is* a considerable degree of similarity between the two; in fact, the single-jet exit velocity, V_J, is essentially the same as the reference jet exit velocity, V_{eq}, that being nominally the same for all test points (since the mass flow and thrust are nominally the same). Therefore, measured differences in the mean *velocity* fields of the coannular and reference jets can be interpreted as departures of the coannular jet from its single-jet asymptote which, in turn will yield changes in calculated noise levels (at low frequencies).

On the other hand, when temperature profiles are compared as in Figure 4.4(c) ($T_f/T_p = 1$, $x/D_{eq} = 6.06$), differences *are* to be expected as V_f/V_p is increased, because the calculated single-jet temperature (see Table 7.1) is changing also. For this reason, no attempt has been made to utilize the static temperature data to interpret noise level changes for the case $T_f/T_p = 1$, which is the only case considered in detail here at low frequencies.

---

†*Neglecting effects of viscous stresses, heat conduction, axial Reynolds stresses, axial turbulent energy transport and the radial mean velocity component; resulting errors are of the order of axial turbulence intensity squared, or less.*

It is of interest to note that in the case $T_f/T_p = 1.75$, Table 7.1 shows that the single-jet exit temperature *is* almost a constant as V_f/V_p is varied over the test points 5, 6, 7 and 8. The static temperature radial profile measurements at the axial stations $x/D_{eq} = 6.06$, 12.12 and 18.17 in Figures 4.5(c) - 4.5(e) therefore lie much closer together than those of Figures 4.4(c) - 4.4(e) where the single-jet temperature is varying significantly with V_f/V_p.

To summarize thus far, the mixing noise *reductions* exhibited by the coannular jet at *low frequencies* (i.e. relative to the reference noise levels of Test Point 1) will be interpreted by using the difference between calculated noise levels obtained with the Lockheed prediction method for a single jet. The single-jet conditions for each test point, given in Table 7.1, are calculated by defining the single jet to have the same nozzle exit area, thrust and energy output as the coannular jet. For each test point, the difference between the *measured* coannular 1/3-octave noise level and that of the reference jet, Δ_m, (at the same center-frequency and angle) will be compared with the *calculated* difference, Δ_c. A reasonable agreement between Δ_m and Δ_c would indicate that the dominant coannular noise reduction mechanisms had been interpreted correctly.

Naturally, if the single-jet exit velocity and static temperature corresponding to a given coannular test point are approximately the same as those of the reference jet (e.g. Test Point 12 in Table 7.1), then the calculated difference, Δ_c, will be negligible. It is the departure of coannular flow velocity profiles from the reference profiles, together with changes in the coannular jet turbulence structure, that will be utilized to modify the single-jet input parameters and hence modify the single-jet noise level predictions.

The changes in the turbulence structure to be considered include (a) the eddy convection velocity, (b) the radial maximum of the turbulence level in the radial directon, and (c) the same quantity but in the axial direction. The convection velocity is an optional input parameter to the Lockheed unified jet noise (UNIJET) prediction program (ref. 3.3). The radial turbulence level can be related to the "master spectra", while the axial turbulence level is closely associated with the anisotropy coefficients, all of which are optional inputs to this prediction program.

7.1.2 High-Frequency Single-Jet Model

At high frequencies, it is reasonable to assume, and the source location data presented in Section 3 largely confirm this, that the sound is generated essentially within the cylindrical shear layers close to the coannular nozzle. Furthermore, preliminary calculations have shown that only the outer shear layer needs be considered from the noise viewpoint, principally because the mean velocity difference (V_f) across this layer is considerably larger than that across the inner layer ($V_f - V_p$). It follows that a single-jet model can be used to interpret *high-frequency* coannular jet noise variations with velocity and temperature ratio.

Thus, the outer shear-layer noise has been calculated with the Lockheed UNIJET prediction program (ref. 3.3) with the assumption that the annulus height, h, is equivalent to the jet "diameter". In other words, the annular jet cross-section is visualized as the cross-section of a circular jet for the purposes of noise calculation. To obtain valid estimates of the *absolute* noise levels, the predicted intensity is multiplied by a factor D_f/h to allow for the larger volume of turbulent flow in the annular jet.

The noise levels of the reference jet have been calculated with D_f as the jet diameter† and these have been subtracted from the high-frequency coannular noise levels calculated with the fan stream conditions (V_f, T_f) listed in Table 7.1, together with the annulus height h = 0.90 cm (0.35 inches) for the jet diameter, as explained above.

Unlike the low-frequency case, no flow or source alteration effects have been incorporated in these calculations, other than the obvious ones that result from increases in fan-stream velocity, V_f, (since V_f increases with V_f/V_p at constant fully-mixed equivalent conditions) and changes in the fan-stream temperature, T_f. Noise level changes calculated in this way are compared with the measured changes at a selected number of test points in Section 7.3.

7.2 LOW-FREQUENCY NOISE REDUCTIONS

In the following two subsections, measurements of the mean and fluctuating components of the flow velocity in coannular jets are compared with measurements at the same axial station in the reference jet. Relative changes are then incorporated in the appropriate parameters of the Lockheed single-jet noise prediction method to yield a calculated noise level difference; this is compared with the measured difference at a selected number of test points.

7.2.1 Mean Velocity and Convection Velocity Alteration Effects

The measured mean velocity profiles displayed in Figures 4.3(c) through 4.3(e) (x/D_{eq} = 6.06, 12.12 and 18.17) exhibit a marked *reduction* in velocity at and near the jet axis as the coannular jet velocity ratio (V_f/V_p) is increased. The fractional decrease on the jet axis for each velocity ratio will be applied directly to the "source-region" velocity parameter, V_s, of the Lockheed prediction method. In this prediction method (based on high-frequency Lilley equation solutions), the parameter V_s controls the acoustic-mean-flow interactions between the mean velocity profile and the processes of sound emission and propagation in the jet flow. The modified values of V_s for the case V_f/V_p = 1.75 are given in Table 7.2 together with the original values used in the prediction method. In order to obtain these values at each modified Strouhal number (as required by the prediction method), the

---

†*That is, neglecting the primary nozzle lip thickness.*

Table 7.2 Original and modified values of the source-region velocity, V_S

Strouhal Number S_m	x_S/D_{eq}	Original V_S/V_J	Reduction Factor (%)	Modified V_S/V_J
0.0316	16.6	0.32	93.4	0.30
0.040	14.8	0.36	90.4	0.33
0.050	13.2	0.40	87.8	0.35
0.063	11.7	0.44	85.3	0.38
0.080	10.4	0.47	83.2	0.39
0.100	9.3	0.50	81.4	0.41
0.125	8.3	0.52	79.7	0.41
0.160	7.3	0.54	78.1	0.42
0.200	6.5	0.56	76.7	0.43
0.250	5.8	0.57	75.6	0.43
0.316	5.1	0.58	74.4	0.43
0.400	4.5	0.585	73.4	0.43
0.500	4.0	0.59	72.6	0.43

relation between axial peak position and Strouhal number given by Equation (3-2) has been utilized. Also, the measured velocity data have been interpolated to obtain estimates of the reduction in centerline velocity at the axial stations which correspond to the standard modified Strouhal numbers [i.e. according to Equation (3-2)].

These parameter modifications could be utilized to obtain a set of calculated noise level differences; but first, it is preferable to incorporate the other modification, that of *convection* velocity alteration. The eddy convection velocity, V_c, is obtained from the measured space-time correlation functions of the turbulent velocity components, as described in Section 5, and is not necessarily identical to the source region velocity V_S. However, as might be expected from the mean velocity data, the convection velocity obtained from centerline correlation measurements *does* reduce, as indicated in Figure 5.37. In this figure, the convection velocity results from Test Point 4 are compared with those of Test Point 1 (reference jet) at different axial stations. Although the trend is clear in these results, it is preferable to obtain quantitative estimates of the convection velocity reductions from the mean velocity data acquired with the probe, since these are available at more closely spaced axial positions along the jet. Thus, the fractional changes applied to the source region velocity, V_S, as in Table 7.2, will be applied to the eddy convection velocity as well, the assumption being that V_c is proportional to the centerline mean velocity. Although this is not completely borne out by the LV measurements, it is reasonably well supported in the important region between six and twelve equivalent diameters downstream of the

primary nozzle. The modified convection velocity for Test Point 4 ($V_f/V_p = 1.75$) is given in Table 7.3. The *original* values for the convection velocity are considerably higher than the measurements indicate; this is a problem associated primarily with the use of *high-frequency* Lilley equation solutions in the prediction method, as discussed in reference 3.3. It is for this reason that fractional changes are applied, instead of relating absolute measured values to the input parameters of the prediction method.

Table 7.3 Original and modified values of the eddy convection velocity, V_c

Strouhal Number S_m	x_s/D_{eq}	Original V_c/V_J	Reduction Factor (%)	Modified V_c/V_J
0.0316	16.6	1.00	93.4	0.93
0.040	14.8	1.00	90.4	0.90
0.050	13.2	1.00	87.8	0.88
0.063	11.7	1.00	85.3	0.85
0.080	10.4	1.00	83.2	0.83
0.100	9.3	1.00	81.4	0.81
0.125	8.3	1.00	79.7	0.80
0.160	7.3	1.00	78.1	0.78
0.200	6.5	0.90	76.7	0.69
0.250	5.8	0.80	75.6	0.60
0.316	5.1	0.73	74.4	0.54
0.400	4.5	0.68	73.4	0.50
0.500	4.0	0.65	72.6	0.47

With these modified values of V_s and V_c, the 1/3-octave spectrum levels at each observer angle (θ) were calculated with the Lockheed UNIJET program (ref. 3.3) at Test Point 4 using the single-jet conditions given in Table 7.1. Then the calculations were repeated at the same frequencies and angles for Test Point 1 – but with the original values of V_s and V_c – and these levels were subtracted from those of Test Point 4 to form the calculated difference, Δ_c. The measured and calculated noise level differences at the observer angle of 30° are compared in Figure 7.2 over the frequency range where the noise levels are reduced. This angle was chosen because here the *measured* coannular noise reductions are the largest, reaching 8 dB at 1.6 KHz. The maximum *calculated* noise reduction is not as large, just under 6 dB, and occurs approximately one 1/3-octave band higher (2 KHz) than the measured value. Considering all the assumptions and approximations involved, the agreement is quite encouraging. Furthermore, only two of the prediction parameters have been modified so far: two more are considered below in Section 7.2.2.

To summarize, the reduced mixing noise levels radiated by a coannular jet ($V_f/V_p = 1.75$) - relative to the reference jet ($V_f/V_p = 1.00$) — at small angles and low frequencies can be partly explained by the *lower* centerline convection velocities and mean velocities found in the coannular jet downstream of the potential cores. Through the well-established mechanism of convective amplification and with a recently developed model of acoustic-mean flow interactions, nearly two-thirds of the noise level reduction can be explained by these reduced velocities.

7.2.2 Turbulence Level Alteration Effects

The laser velocimeter measurements of peak turbulence levels described in Section 5 can be utilized to aid the interpretation of low-frequency coannular jet noise reductions in a straightforward way provided it is assumed that the turbulence structure is otherwise unaltered. For example, there are changes in the radial distribution of the turbulence level as the velocity ratio is varied and no attempt has been made to evaluate the effects of this and other changes (e.g. changes in length scales), although we would judge these to be small effects in most cases.

The variation of the radial maximum of the *radial* turbulence level with distance downstream is shown in Figure 5.19(b) for Test Points 1, 2 and 4 (corresponding to the velocity ratios $V_f/V_p = 1.00$, 1.35 and 1.75). The square of this quantity is the quadrupole source strength responsible for radiation at 90° to the jet axis (assuming the azimuthal turbulence levels to be similar). Clearly, at the axial stations $x/D_{eq} = 8$ and 12, there are distinct reductions of approximately 10% and 17%, respectively, when the velocity ratio, V_f/V_p, is increased from 1.00 to 1.75. These changes should yield† reductions of 1.8 dB and 3.3 dB in the noise radiated from the source regions at $x/D_{eq} = 8$ and 12, respectively. The *measured* noise levels at $\theta = 90°$ *do* appear to reduce slightly, for example, by 1.8 dB at 1250 Hz [see Figure 2.2(d)] which according to the source location data of Section 3 is radiated from around six equivalent diameters downstream of the primary nozzle exit plane. However, there is some scatter in the noise level differences, and since the LV data is limited to those two axial stations, further data interpretation along these lines is probably not worthwhile.

The variation of the radial maximum of the axial turbulence level with distance downstream is shown in Figure 5.19(a) for each Test Point (1, 2, and 4). The levels exhibit a more pronounced reduction as V_f/V_p is increased. Specifically, a 20% reduction at $x/D_{eq} = 8$ and a 28% reduction at $x/D_{eq} = 12$ is observed as V_f/V_p is increased from 1.00 to 1.75. Again, since these results are limited to two axial stations, the effect of this reduction is calculated only approximately and at one frequency corresponding to the modified Strouhal number, $S_m = 0.1$.

---

†*Assuming the noise intensity is proportional to the fourth power of the turbulence level.*

According to the prediction method, the quadrupole anisotropy coefficient C_q takes the value 2.3 at $S_m = 0.1$, corresponding approximately to a typical axial turbulence level 35% above the transverse level. A reduction of 28% in the axial turbulence level yields a modified value for $C_q = -0.11$. This then yields a predicted noise *reduction* of 3.1 dB at the observer angle $\theta = 30°$. This reduction, when combined with the predicted noise reductions due to source region and convection velocity alteration (shown in Figure 7.2) would give comparable noise reductions to the measured values.

To summarize, the pressure probe measurements of mean velocity and the LV measurements of turbulence levels in the coannular jet have revealed significant changes in the flow structure as V_f/V_p is increased. When these changes are incorporated in the Lockheed mixing noise prediction method (UNIJET), the calculated low-frequency noise reductions at one particular angle (i.e. the angle at which the noise reductions are maximum) are comparable to the measured noise reductions. From this, it is tentatively concluded that the inverted profile coannular jet is quieter than the reference jet at low frequencies and small angles principally because in the transition region the eddy convection velocity, source-region velocity and axial turbulence level of the coannular jet ($V_f/V_p > 1$) are significantly lower than those of the reference jet ($V_f/V_p = 1$, $T_f/T_p = 1$).

7.3 HIGH-FREQUENCY NOISE INCREASES

The noise radiated by the *outer* shear layer of the coannular jet has been calculated at each test point, with the Lockheed UNIJET prediction program, on the basis of the high-frequency single-jet model described in Section 7.1.2. In this section the *changes* in *calculated* noise levels are compared with *measured* changes, the reference cases being respectively the calculated and measured noise levels of Test Point 1, as in the low-frequency comparisons presented above. All the comparisons that follow are in the form of a "difference spectrum" covering the frequency range 200 Hz - 40 KHz; a positive difference means that the coannular noise level is higher than that of the reference case, while negative differences indicate that the coannular jet is quieter than the reference case ($V_f/V_p = 1$, $T_f/T_p = 1$). It must be recognized, however, that the comparison between measured and calculated noise changes considered here is strictly valid only at the high frequencies, which are generated in the premerged region of the coannular jet flow. At intermediate frequencies, where sound is generated in the transition region, the single-jet model used here cannot adequately represent the real situation.

First, we consider changes in noise level at the observer angle $\theta = 90°$. Here the noise levels should be essentially independent of convective amplification effects and acoustic-mean velocity interactions, but *are* influenced by the flow temperature, in the source region, according to the Lilley equation prediction model. However, the fan-stream exit temperature does not vary greatly with velocity ratio (V_f/V_p) at a fixed value of the temperature ratio (T_f/T_p), and thus the effect of V_f/V_p at $\theta = 90°$ can be interpreted approximately as turbulence-source alteration effects. Measured and calculated difference spectra at $\theta = 90°$ are compared in Figure 7.3 for $T_f/T_p = 2$ at the three coannular velocity ratios (the case $V_f/V_p = 1$ is omitted here - since differences are negligible - but can be found in Figure 7.9). The agreement

is quite good at the highest frequencies, the measured noise levels increasing by up to 5½ dB and the maximum calculated value by 7 dB.

Similar results are obtained at the test points where $T_f/T_p = 1$, as shown in Figure 7.4. Clearly, the coannular jet noise source strength at high frequencies is changing with fan exit velocity in a way that can be closely predicted by this single-jet calculation method. At lower frequencies, the calculated and measured differences diverge quite rapidly which indicates that the single-jet model is valid, as expected, only in the high-frequency limit and cannot be used on its own to predict coannular jet noise much below a frequency of 20 KHz for the present configuration. However, when translated to frequencies at full scale, this may still represent a useful upper frequency range.

At observer angles other than 90°, the effects of convective amplification and acoustic-mean flow interactions are important, particularly at small angles to the downstream jet axis. Measured and calculated results at the different velocity ratios for $T_f/T_p = 1$ are displayed at the observer angles of 70°, 50° and 30° in Figures 7.5, 7.6 and 7.7, respectively. Again the measured increase in high-frequency noise as V_f/V_p is increased appears to be matched quite well by the calculated results. At the smallest angle ($\theta = 30°$, Figure 7.7), the agreement is good down to 10 KHz, except at the lowest velocity ratio, and the maximum noise increase of 8-9 dB in the frequency range 12.5 - 25 KHz is predicted almost exactly by the single-jet model calculations.

Unfortunately, the agreement is not as good at the same angle when the temperature ratio is elevated to $T_f/T_p = 2$, as shown in Figure 7.8. Although the maximum noise increase is predicted quite well, the frequency at which it occurs is predicted to be about one octave lower than the measured value. No explanation can be offered for that discrepancy at this time.

The effect of temperature ratio when V_f/V_p is held constant at unity is shown at different observer angles in Figure 7.9; except at the smallest angle, there are no significant measured changes in noise levels. The calculated changes are also almost negligible at large angles. At the two smallest angles, the agreement between measured and calculated high-frequency noise *reductions* is reasonably good.

In general the single-jet model calculations appear to reproduce the variation of measured coannular jet high-frequency noise levels with V_f/V_p, T_f/T_p quite well. It can therefore be concluded that the mechanisms of noise generation, emission, convection and acoustic-mean flow interactions in the inverted profile coannular jet *at high frequencies* are essentially the same as those in a single jet. It follows that at these subjectively important frequencies (at full scale) the single-jet model could be used to predict coannular jet noise and, perhaps, in conjunction with the *low frequency* single-jet model described in previous sections, it could form the basis for a general prediction scheme for coannular jet noise.

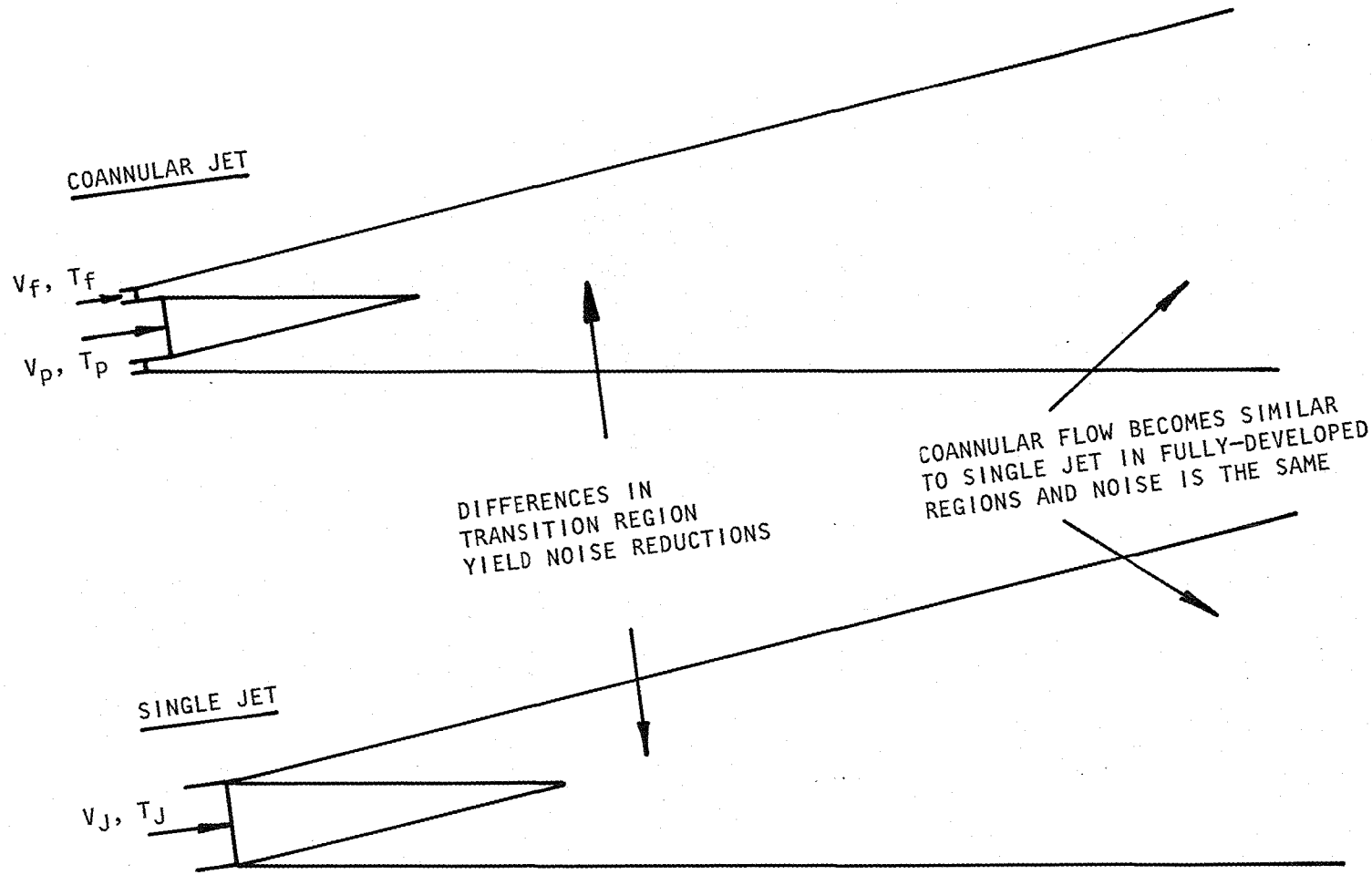

Figure 7.1 Low-frequency single-jet model of coannular jet.

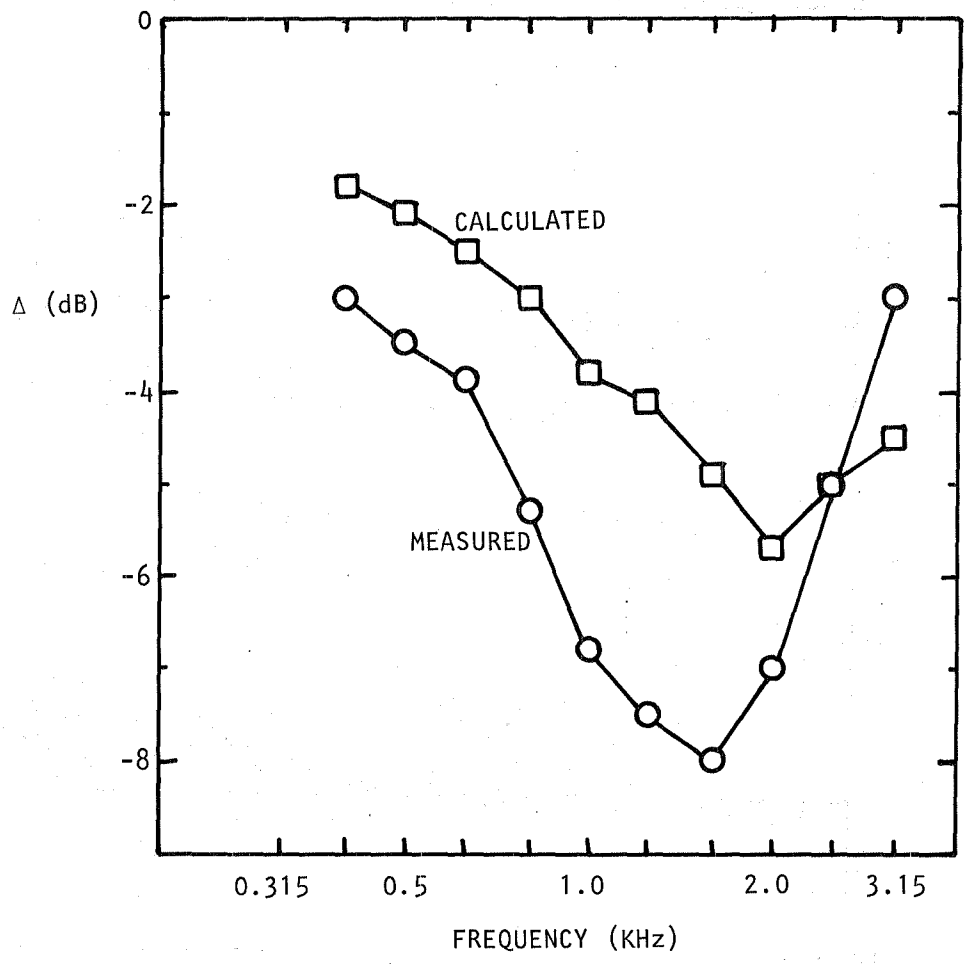

$\theta = 30°$

$V_f/V_p = 1.75$

$T_f/T_p = 1.00$

Figure 7.2 Measured and calculated coannular jet mixing noise reductions at low frequencies.

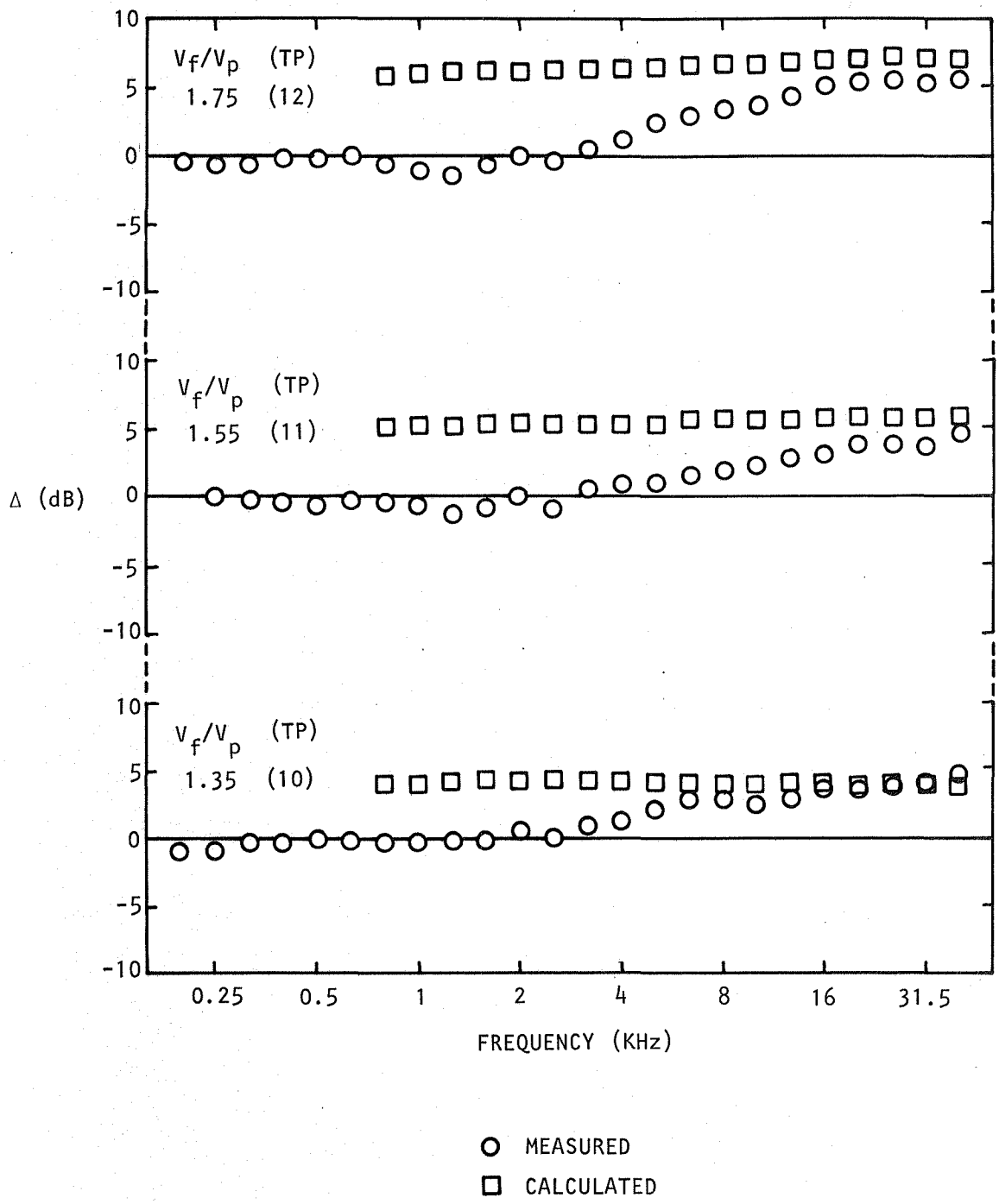

Figure 7.3 Measured and calculated difference spectra at different velocity ratios; $\theta = 90°$, $T_f/T_p = 2$.

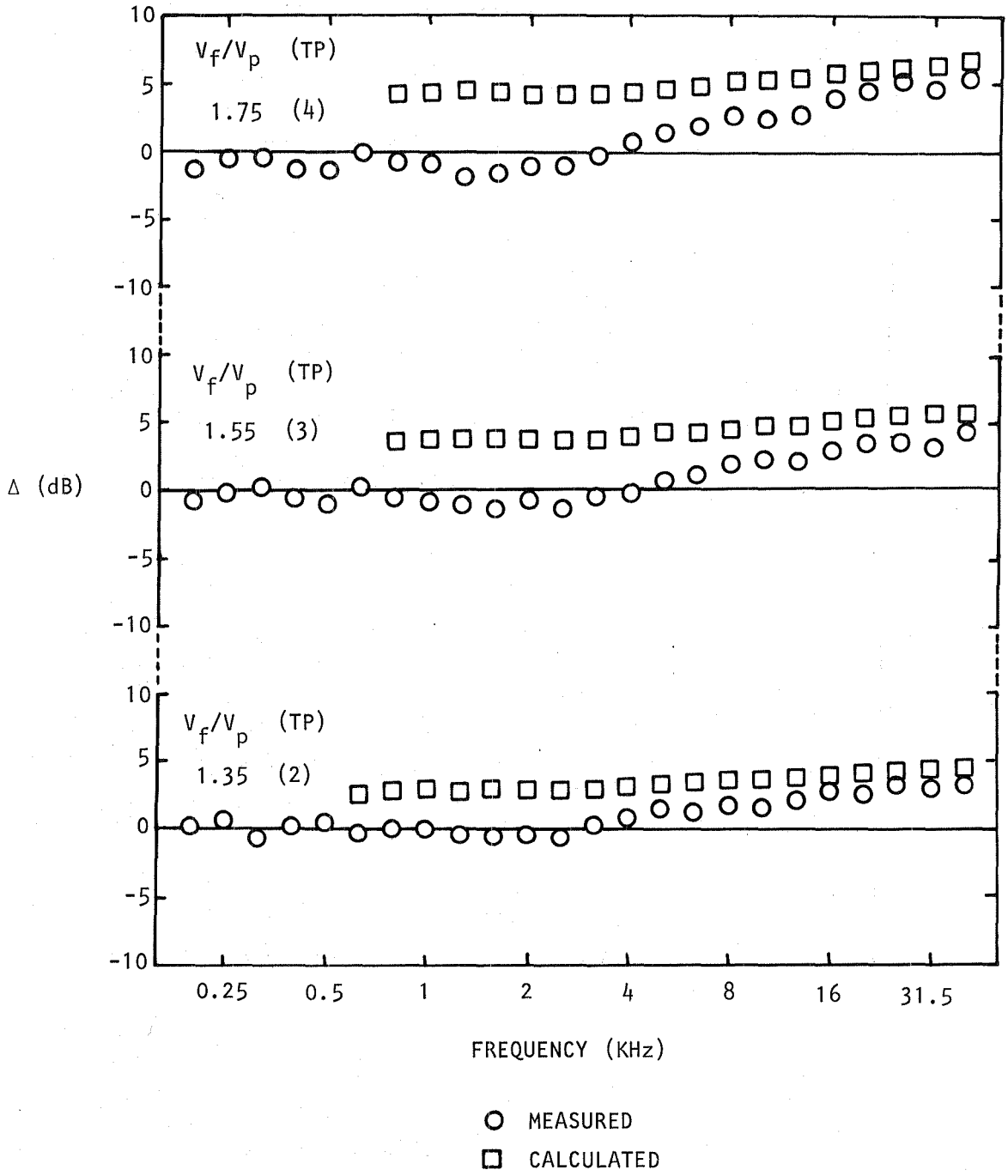

Figure 7.4 Measured and calculated difference spectra at different velocity ratios; $\theta = 90°$, $T_f/T_p = 1$.

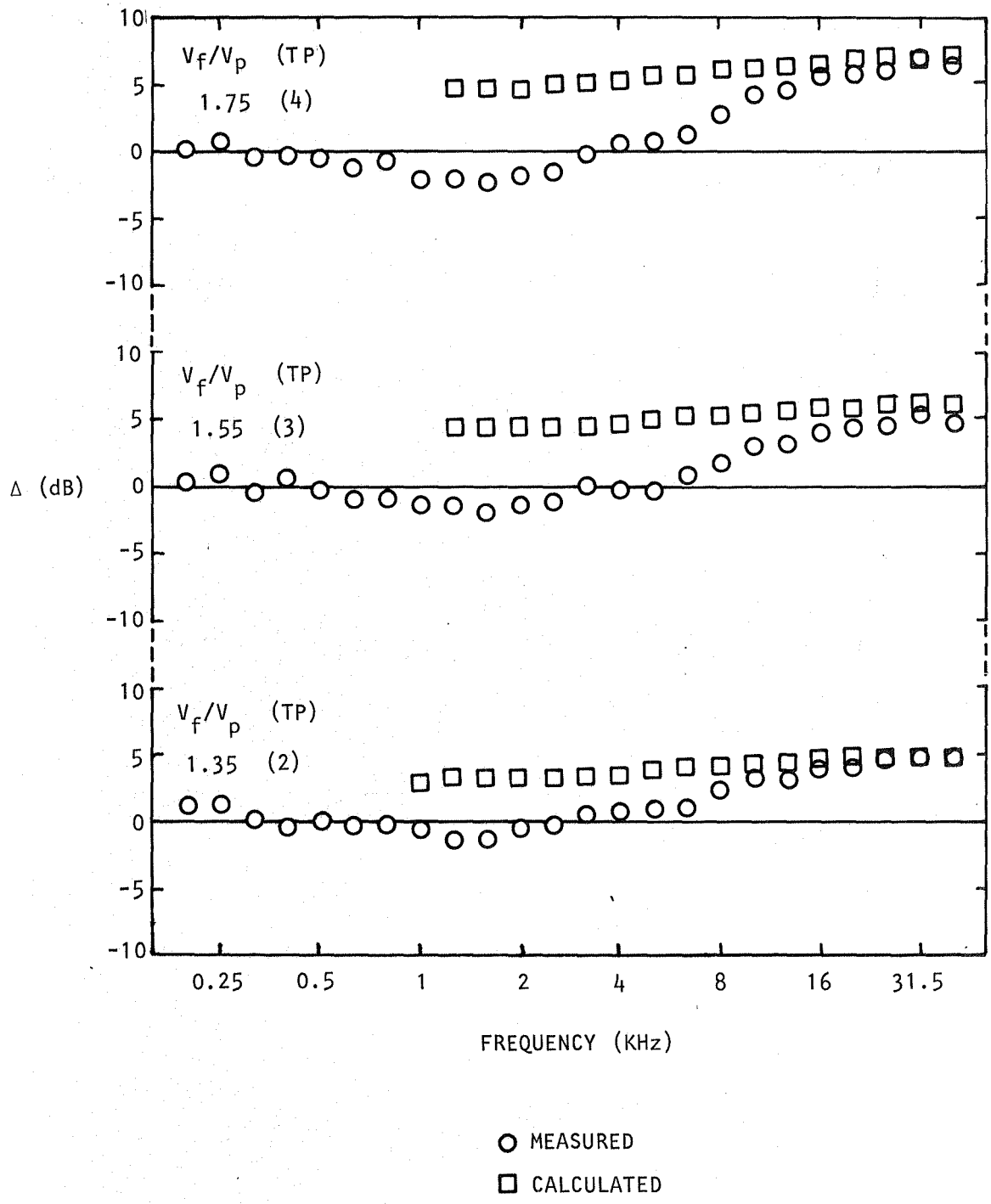

Figure 7.5 Measured and calculated difference spectra at different velocity ratios; $\theta = 70°$, $T_f/T_p = 1$.

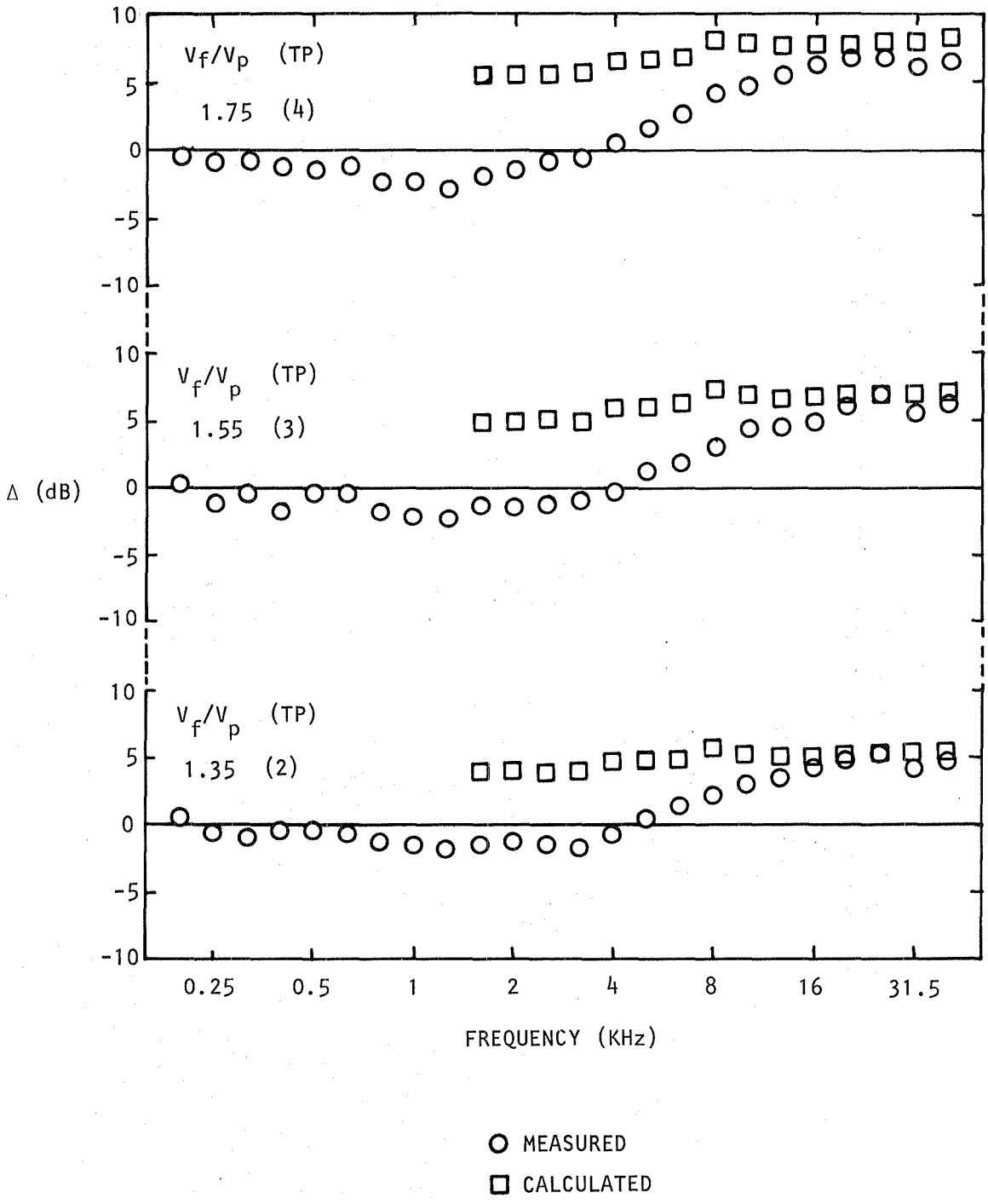

Figure 7.6 Measured and calculated difference spectra at different velocity ratios; $\theta = 50°$, $T_f/T_p = 1$.

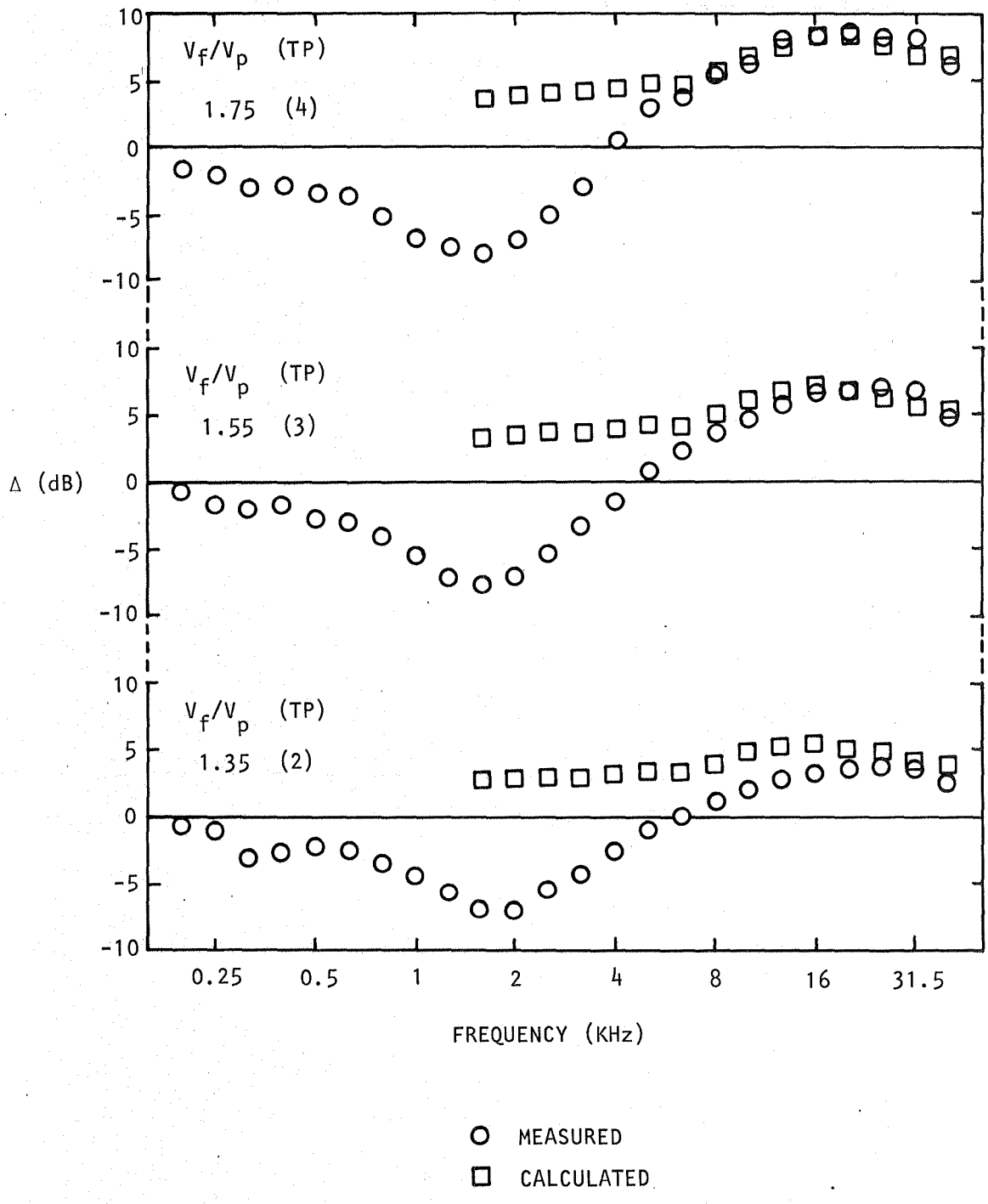

Figure 7.7 Measured and calculated difference spectra at different velocity ratios; $\theta = 30°$, $T_f/T_p = 1$.

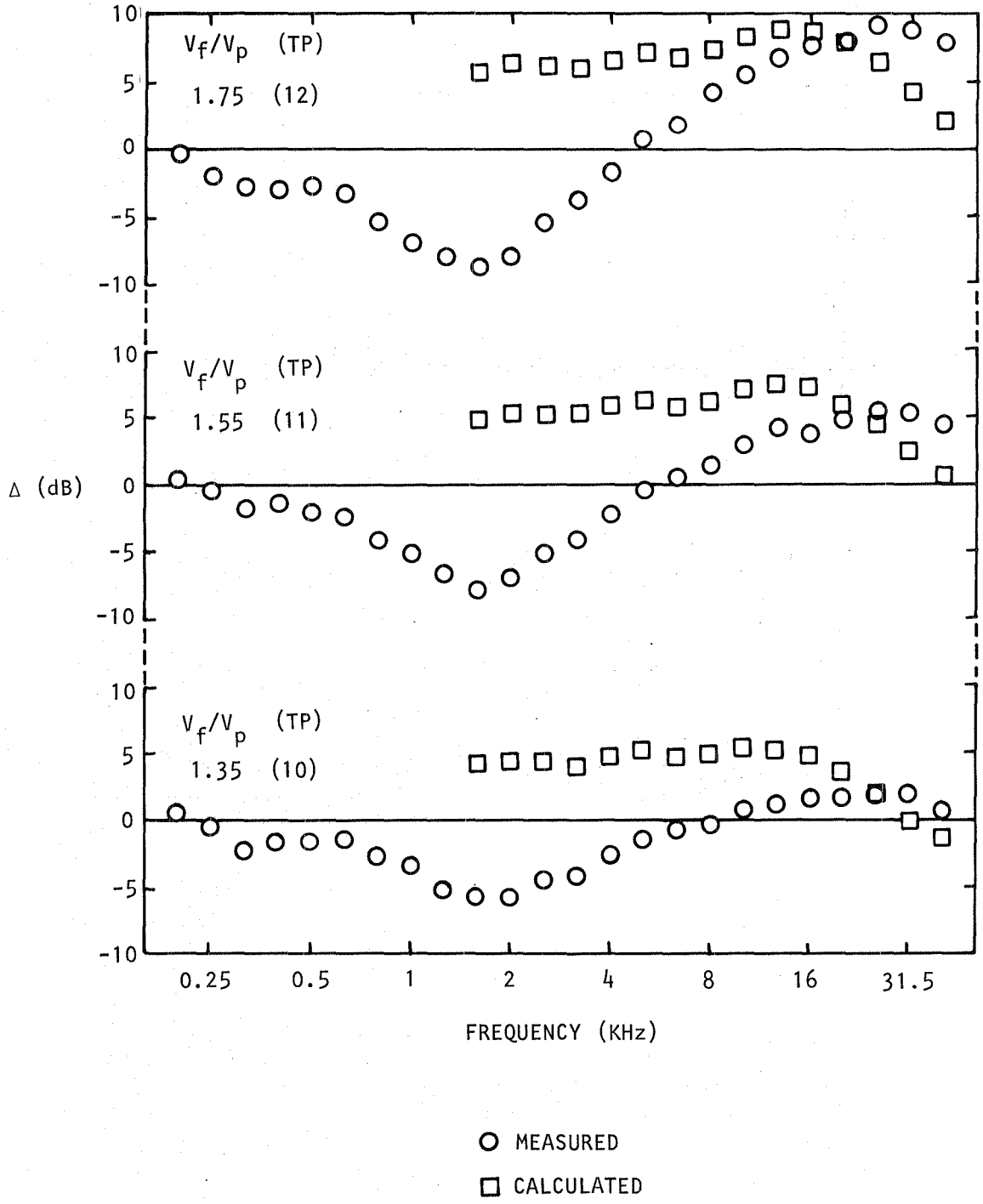

Figure 7.8 Measured and calculated difference spectra at different velocity ratios; $\theta = 30°$, $T_f/T_p = 2$.

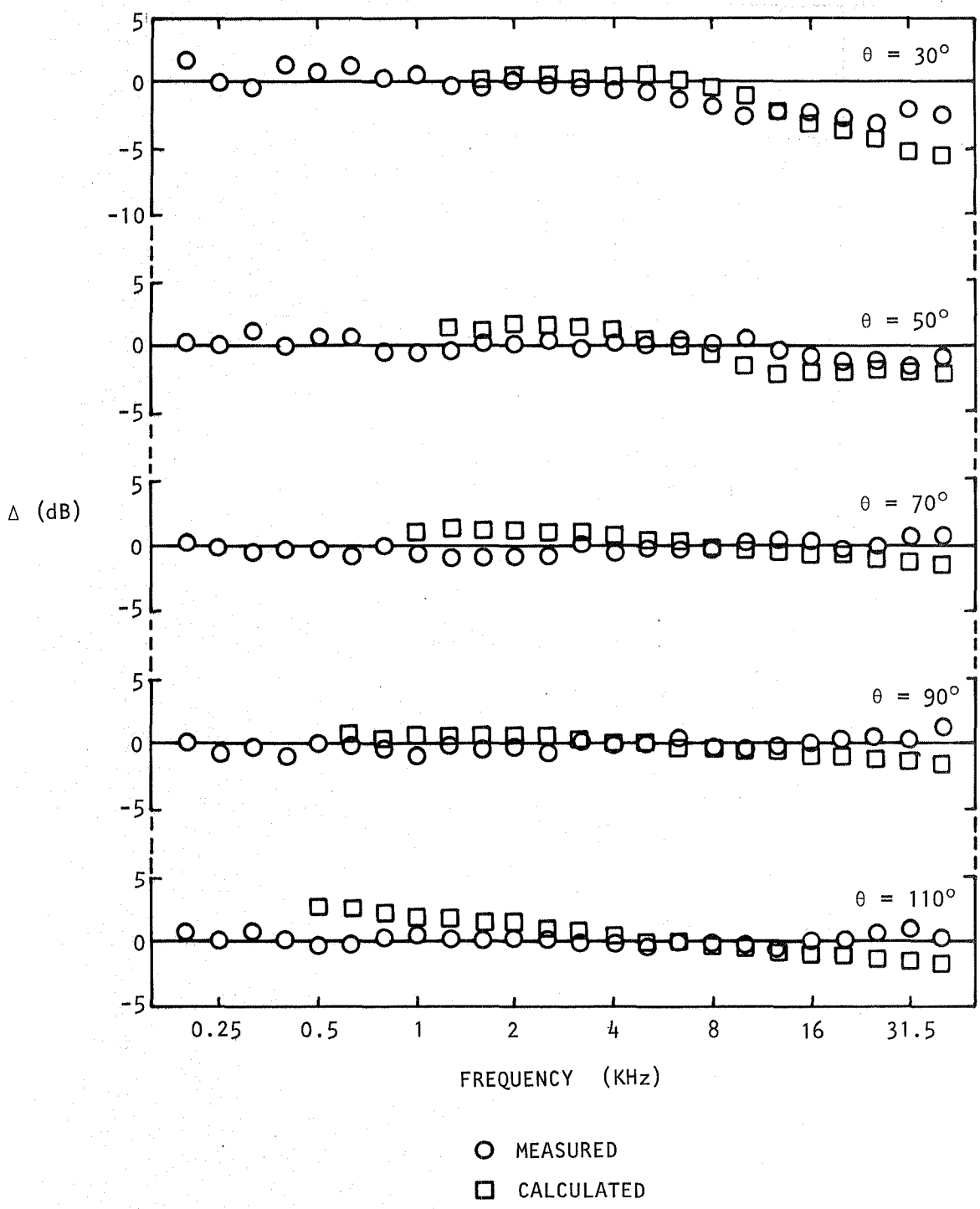

Figure 7.9 Measured and calculated difference spectra at different observer angles; $V_f/V_p = 1$, $T_f/T_p = 2$ (TP 9).

8. CONCLUSIONS

The overall objective of the present investigation was to obtain a basic understanding of the noise reduction mechanisms in inverted-velocity-profile coannular jets. The specific technical objectives were:

(1) To measure the flow properties of coannular jets so as to provide some insight into differences in sound generation between different jets, and

(2) To produce a quantitative and scientifically reasonable model for these differences which fits the measured flow and noise data.

A summary of the work conducted to achieve these objectives and the main conclusions are given below. The present study was mainly devoted to *subcritical* coannular jets, and therefore detailed conclusions pertaining to the origins of noise reductions (or increases) resulting from velocity profile shaping for *shock-containing* coannular jets are *not* contained here.

Magnitude and Character of Noise Reductions

The noise characteristics of inverted-velocity-profile coannular jets operated at subcritical pressure ratios have been measured in the Lockheed anechoic facility using a "primary-extended" coannular nozzle configuration of fan-to-primary area ratio $A_f/A_p = 0.747$ and equivalent nozzle diameter $D_{eq} = 6.6$ cm. The test program was designed to isolate the "inverted velocity" effects from the "inverted temperature" effects for coannular jets *having constant thrust, mass flow rate and exit area.* The fully-mixed equivalent single jet velocity (or specific thrust) for each point in the test matrix was 365 m/sec (1200 ft/sec). Although this value is not in the optimum range for coannular jet noise reduction, it was chosen mainly for the purpose of studying trends in jet aerodynamics.

The results from the acoustic experiments have been analyzed to determine the magnitudes of the noise reductions (or increases) and the angle and frequency regimes over which the noise changes (i.e. reductions or increases) relative to the fully-mixed equivalent single jet are maximum. At high frequencies, the noise levels increase as the fan-to-primary velocity ratio (V_f/V_p) increases. At low frequencies, however, the coannular jet is quieter at small angles to the jet exhaust. The effect of inverted temperature profile is insignificant compared to the effect of inverted velocity profile.

For the area ratio of 0.75 and at the fully-mixed equivalent single jet velocity of 365 m/sec considered in the present experiments, the total acoustic energy radiated by the coannular jet is approximately 2 dB lower

than that radiated by the reference jet. The present results are consistent with the coannular jet noise data obtained previously by P&WA and G.E. At other area ratios and especially for higher equivalent jet velocities, larger noise reductions have been observed in these previous studies.

Location of Noise Sources

In order to obtain a physical understanding of the measured noise changes, it was first of all necessary to determine the axial locations, within the jet flow, of the noise sources as a function of frequency. The "polar correlation technique" has been used to measure the "apparent" source strength distributions, and the influence of coannular jet velocity and temperature ratio V_f/V_p, T_f/T_p on the axial peak location and shape of the source distribution has been investigated.

The axial peak source location is quite insensitive to the velocity and temperature ratios of coannular flows especially at low-to-medium frequencies, where the noise reductions (relative to the fully-mixed equivalent single jet) are maximum. This is a particularly useful result for modelling the low-frequency noise reductions, in which once a particular radiation frequency is associated with a particular axial station, this relationship can be assumed to be unaffected by the variation of velocity and temperature ratio in coannular jets.

Mean Flow Surveys

In order to study the acoustic shielding effects in coannular jets, it was necessary to obtain the mean velocity and mean temperature profiles throughout the jet flow. A pitot-static probe with integral thermocouple has been used for this purpose, and the jet flow has been mapped in detail from the nozzle exit planes to approximately twenty equivalent nozzle diameters.

The most important result from these tests is that the mean velocity on and around the jet centerline in inverted-velocity-profile coannular jets is always lower than that of the reference jet (i.e. $V_f/V_p = 1$), and this reduction is maintained (at least qualitatively) all the way from the nozzle exit plane to the fully-mixed region.

Laser Velocimeter Measurements

In order to obtain detailed mean flow and turbulence characteristics for input to the analytical model for coannular jet noise, a two-point four-channel laser velocimeter has been used. Single-point LV measurements were conducted to provide information on turbulence intensity and spectra, mean velocity distributions, etc., whereas two-point measurements yielded quantities such as eddy convection velocity, length scales, etc.

Specific conclusions pertaining to the variation of coannular jet flow structure with velocity ratio (V_f/V_p) and temperature ratio (T_f/T_p) were given at the end of Section 5, and therefore they are not repeated here. For the purpose of modelling the low-frequency noise reductions, three features are worth noting: When flow measurements for the inverted-velocity-profile coannular jet are compared with the flow measurements for the reference jet (at constant total thrust, mass flow rate and exit area), it is found that (1) the mean velocity on and around the jet centerline in the coannular jet is lower than that in the reference jet (as noted earlier in the probe surveys); (2) the centerline eddy convection velocities (absolute values) in the coannular case are lower than the convection velocities in the reference case; and (3) in the transition region, the peak turbulence levels (i.e. the absolute values of the peaks in the radial distributions of both the axial and radial components of turbulence at fixed axial stations) in the coannular jet are lower than the corresponding peak turbulence levels in the reference jet.

Nozzle Performance

The aerodynamic performance of the coannular nozzle configuration used throughout this investigation has been evaluated. For both the primary and fan nozzles, the mass flow coefficients are of the order of 0.99, and the velocity coefficients are greater than 0.99. The thrust coefficients, computed as the products of flow and velocity coefficients, are of the order of 0.985.

Model/Data Comparisons

The measured variations of coannular jet mixing noise with velocity ratio (V_f/V_p) and temperature ratio (T_f/T_p) have been interpreted with the aid of the source location results and the jet flow measurements. In particular, the noise reductions at low frequencies and the noise increases at high frequencies (relative to the reference jet noise levels) have been modelled separately with the Lockheed single jet noise prediction program, and the calculated noise changes have been compared with the measured noise changes.

At low frequencies and small angles to the jet exhaust, the inverted-profile coannular jet is quieter than the fully-mixed equivalent single jet (i.e. the reference jet with $V_f/V_p = 1$, $T_f/T_p = 1$) principally because in the transition region, the eddy convection velocity, source-region velocity and axial turbulence level of the coannular jet ($V_f/V_p > 1$) are significantly lower than those of the reference jet.

At high frequencies, where the sound is generated in the pre-merged region, the noise contribution from the inner shear layer is negligible compared to the noise radiated from the faster outer shear layer. The variation in noise levels with V_f/V_p and T_f/T_p at these higher frequencies can be quantified quite accurately in terms of the secondary or fan flow conditions only. It can therefore be concluded that the mechanisms of noise generation,

emission, convective amplification and acoustic-mean flow interactions in the inverted-profile coannular jet *at high frequencies* are essentially the same as those in a single jet.

Shock-Containing Coannular Jets

Finally, although the present program has been concentrated on shock-free coannular jets, some measurements have been conducted at supercritical conditions. In particular, a large number of Schlieren photographs have been taken to observe the variation of shock structure in coannular jets as a function of fan and primary pressure ratio combinations.

The optical measurements indicate that for a fixed supercritical fan pressure ratio ξ_f, the shock structure of the outer flow undergoes a sudden change when the primary pressure ratio ξ_p becomes just supercritical. This phenomenon, which was previously identified by Dosanjh and his co-workers at Syracuse University, needs to be explored in depth in future studies, and further work is also required to understand any noise benefit which might be associated with these "sudden" changes in the shock structure.

APPENDIX I

SCHLIEREN MEASUREMENTS

The optical measurements were conducted to observe the variation of shock structure in coannular jets as a function of fan and primary pressure ratio combinations (ξ_f, ξ_p). The Schlieren system used for these optical measurements is shown schematically in Figure A1.1. The double-pass optical path begins with a light source consisting of a slit illuminated by a mercury arc, and ends with a camera. The 40.64 cm diameter flat mirror directs the source beam through the test section (i.e. the jet flow) to the parabolic mirror, and the return beam to the knife edge and camera. The slit light source and the knife edge are oriented to obtain maximum sensitivity in the flow direction. Adverse double-imaging effects inherent in double-pass arrangements are minimized by keeping the two passes through the test section as parallel as possible and by having the double image in the direction normal to the flow, so that no ambiguity in shock positions results from double imaging. The photographs were taken on Polaroid Type 55 P/N film, which provides a quick look at the results and permanent negatives. Most of the photographs were taken with a 1/25-second shutter speed; however, some of the earlier, low-pressure runs were conducted with a 1/50-second shutter speed.

The Schlieren measurements were conducted at *three series* of test conditions, giving a total of 42 photographs. In each series, the primary stream total temperature (T_{tp}), the fan stream total temperature (T_{tf}), and the fan stream pressure ratio (ξ_f) were kept constant, and the primary stream pressure ratio (ξ_p) was varied over an extensive range. The nominal values of the constant parameters are as follows:

	T_{tp} (°K)	T_{tf} (°K)	ξ_f	ξ_p
Series 1	294	728	2.93	1.00 → 4.49
Series 2	728	294	2.93	1.00 → 3.48
Series 3	728	978	2.37	1.00 → 3.53

In series 1, the fan flow is heated while the primary flow is unheated; in series 2, the primary flow is heated while the fan flow is unheated; finally, in series 3, both streams are heated.

The exact jet operating conditions for the three series of experiments are given in detail in Tables A1.1 to A1.3, respectively. The corresponding Schlieren photographs of shock-containing coannular jets are shown in Figures A1.2 to A1.4.

In each series of photographs, the variation in shock structure with increasing primary nozzle pressure ratio is qualitatively similar and most revealing. For $\xi_p = 1$ (first photograph in each series), there is no flow

exhausting from the primary nozzle; the annular flow exhausting from the fan nozzle contains a number of clearly identifiable, "donut-shaped" shock cells which rapidly decrease in diameter with downstream distance due to the convergence of the annular flow towards the jet centerline. As soon as the primary flow is turned on, these shock cells remain essentially constant in size, and up to 10 or 12, almost regularly spaced shock cells can now be identified. As ξ_p is increased further, there is not a significant change in the overall "donut-shaped" shock structure, until ξ_p becomes greater than the critical pressure ratio. As soon as ξ_p is increased to approximately 1.9, a drastic change in the shock structure occurs. At this point, the closely-spaced shock structure observed in all cases for $\xi_p \lesssim 1.9$ is largely destroyed, and it is replaced by only one or two shock cells close to the nozzle exits. As ξ_p is now increased to values well in excess of 1.9, the shock cells in the supercritical primary stream become more and more evident, and increase in spacing as ξ_p increases. At the highest value of ξ_p (last photograph in each series), the total shock structure consists of one or two shocks close to the nozzle exit from the fan stream and three or four widely-spaced shock cells in the primary stream.

Although this description of the observed changes in shock structure in inverted-velocity-profile coannular jets is greatly oversimplified, the Schlieren measurements do indicate a sudden change in the shock structure of the outer flow when the inner flow becomes supercritical. This phenomenon needs to be explored in depth in future studies. Based on these observations, it is also tempting to infer that the broadband shock-associated noise from coannular jets will be greatly reduced at and near the conditions at which this sudden change in the fan flow shock pattern occurs. However, acoustic measurements to support this are not available at the present time, and these should be conducted in a future research program.

Finally, it is pointed out that the "sudden" changes in shock structure observed in the present measurements are by no means the first time that these observations are made. Dosanjh and his co-workers at Syracuse University have conducted similar optical studies for several years. However, in their earlier work, it is emphasized that an "optimum" ratio of pressure ratios (ξ_f/ξ_p) is required to obtain this change in the shock structure. In contrast, the present experiments indicate that it is only the primary nozzle pressure ratio that controls this effect, and regardless of fan pressure ratio ξ_f, the shock structure is greatly modified when ξ_p becomes just supercritical.

FIGURE NUMBER	$P_o \times 10^{-5}$ (N/m^2)	P_o (PSI)	T_o (°K)	T_{tp} (°K)	T_{tf} (°K)	$P_{tf} \times 10^{-5}$ (N/m^2)	P_{tf} (PSIG)	$P_{tp} \times 10^{-5}$ (N/m^2)	P_{tp} (PSIG)	ξ_f	ξ_p
A1.2(a)	0.976	14.16	307	294	728	1.888	27.39	0.000	0.00	2.93	1.000
(b)	0.976	14.16	311	294	728	1.888	27.39	0.381	5.53	2.93	1.391
(c)	0.976	14.16	311	294	728	1.888	27.39	0.580	8.41	2.93	1.594
(d)	0.976	14.16	309	294	728	1.888	27.39	0.758	10.99	2.93	1.776
(e)	0.976	14.16	308	294	728	1.888	27.39	0.778	11.28	2.93	1.797
(f)	0.982	14.24	300	299	725	1.902	27.59	0.837	12.14	2.94	1.853
(g)	0.982	14.24	300	300	724	1.915	27.78	0.949	13.77	2.95	1.967
(h)	0.982	14.24	300	299	726	1.895	27.49	1.028	14.91	2.93	2.047
(i)	0.976	14.16	308	294	728	1.888	27.39	1.142	16.57	2.93	2.170
(j)	0.976	14.16	307	294	728	1.888	27.39	1.398	20.27	2.93	2.431
(k)	0.976	14.16	310	294	728	1.888	27.39	1.588	23.03	2.93	2.626
(l)	0.976	14.16	308	294	728	1.888	27.39	1.905	27.63	2.93	2.951
(m)	0.976	14.16	306	294	728	1.888	27.39	2.095	30.39	2.93	3.146
(n)	0.976	14.16	309	294	728	1.888	27.39	2.286	33.15	2.93	3.341
(o)	0.976	14.16	305	294	728	1.888	27.39	3.409	49.45	2.93	4.492

Table A1.1 Coannular jet – test conditions for Schlieren measurements (series 1)

FIGURE NUMBER	$P_o \times 10^{-5}$ (N/m^2)	P_o (PSI)	T_o (°K)	T_{tp} (°K)	T_{tf} (°K)	$P_{tf} \times 10^{-5}$ (N/m^2)	P_{tf} (PSIG)	$P_{tp} \times 10^{-5}$ (N/m^2)	P_{tp} (PSIG)	ξ_f	ξ_p
A1.3(a)	0.978	14.19	302	728	293	1.889	27.40	0.000	0.00	2.93	1.000
(b)	0.978	14.19	302	728	298	1.895	27.49	0.382	5.54	2.94	1.390
(c)	0.978	14.19	305	722	300	1.882	27.30	0.580	8.41	2.92	1.593
(d)	0.978	14.19	307	727	300	1.876	27.21	0.791	11.47	2.92	1.808
(e)	0.978	14.19	307	732	300	1.869	27.11	0.963	13.96	2.91	1.984
(f)	0.978	14.19	310	719	299	1.856	26.92	1.153	16.73	2.90	2.179
(g)	0.978	14.19	313	736	299	1.876	27.21	1.404	20.36	2.92	2.435
(h)	0.978	14.19	312	720	293	1.869	27.11	1.569	22.75	2.91	2.603
(i)	0.978	14.19	315	724	294	1.850	26.83	1.911	27.72	2.89	2.953
(j)	0.978	14.19	314	721	294	1.922	27.87	2.135	30.97	2.96	3.183
(k)	0.978	14.19	316	713	295	1.863	27.02	2.294	33.27	2.90	3.345
(l)	0.978	14.19	320	703	295	1.889	27.40	2.426	35.18	2.93	3.479

Table A1.2 Coannular jet - test conditions for Schlieren measurements (series 2)

FIGURE NUMBER	$P_o \times 10^{-5}$ (N/m^2)	P_o (PSIG)	T_o (°K)	T_{tp} (°K)	T_{tf} (°K)	$P_{tf} \times 10^{-5}$ (N/m^2)	P_{tf} (PSIG)	$P_{tp} \times 10^{-5}$ (N/m^2)	P_{tp} (PSIG)	ξ_f	ξ_p
A1.4(a)	0.976	14.16	326	728	978	1.353	19.62	0.000	0.00	2.39	1.000
(b)	0.978	14.18	326	724	987	1.327	19.24	0.389	5.64	2.36	1.398
(c)	0.978	14.19	326	728	980	1.333	19.34	0.382	5.54	2.36	1.390
(d)	0.978	14.18	326	728	978	1.352	19.62	0.415	6.02	2.38	1.425
(e)	0.978	14.19	327	721	971	1.360	19.72	0.494	7.17	2.39	1.505
(f)	0.978	14.19	327	724	965	1.405	20.38	0.593	8.60	2.44	1.606
(g)	0.978	14.19	327	725	973	1.320	19.15	0.745	10.80	2.35	1.761
(h)	0.978	14.19	332	722	969	1.373	19.91	0.936	13.58	2.40	1.957
(i)	0.978	14.19	333	729	976	1.340	19.43	1.173	17.02	2.37	2.199
(j)	0.978	14.19	327	714	974	1.360	19.72	1.424	20.65	2.39	2.455
(k)	0.978	14.19	331	719	972	1.327	19.24	1.622	23.52	2.36	2.658
(l)	0.978	14.19	330	717	971	1.366	19.81	1.938	28.11	2.40	2.981
(m)	0.978	14.19	325	726	978	1.313	19.05	2.083	30.21	2.34	3.129
(n)	0.978	14.19	326	728	978	1.354	19.64	2.290	33.22	2.38	3.341
(o)	0.978	14.19	333	739	975	1.313	19.05	2.472	35.85	2.34	3.526

Table A1.3 Coannular jet - test conditions for Schlieren measurements (series 3)

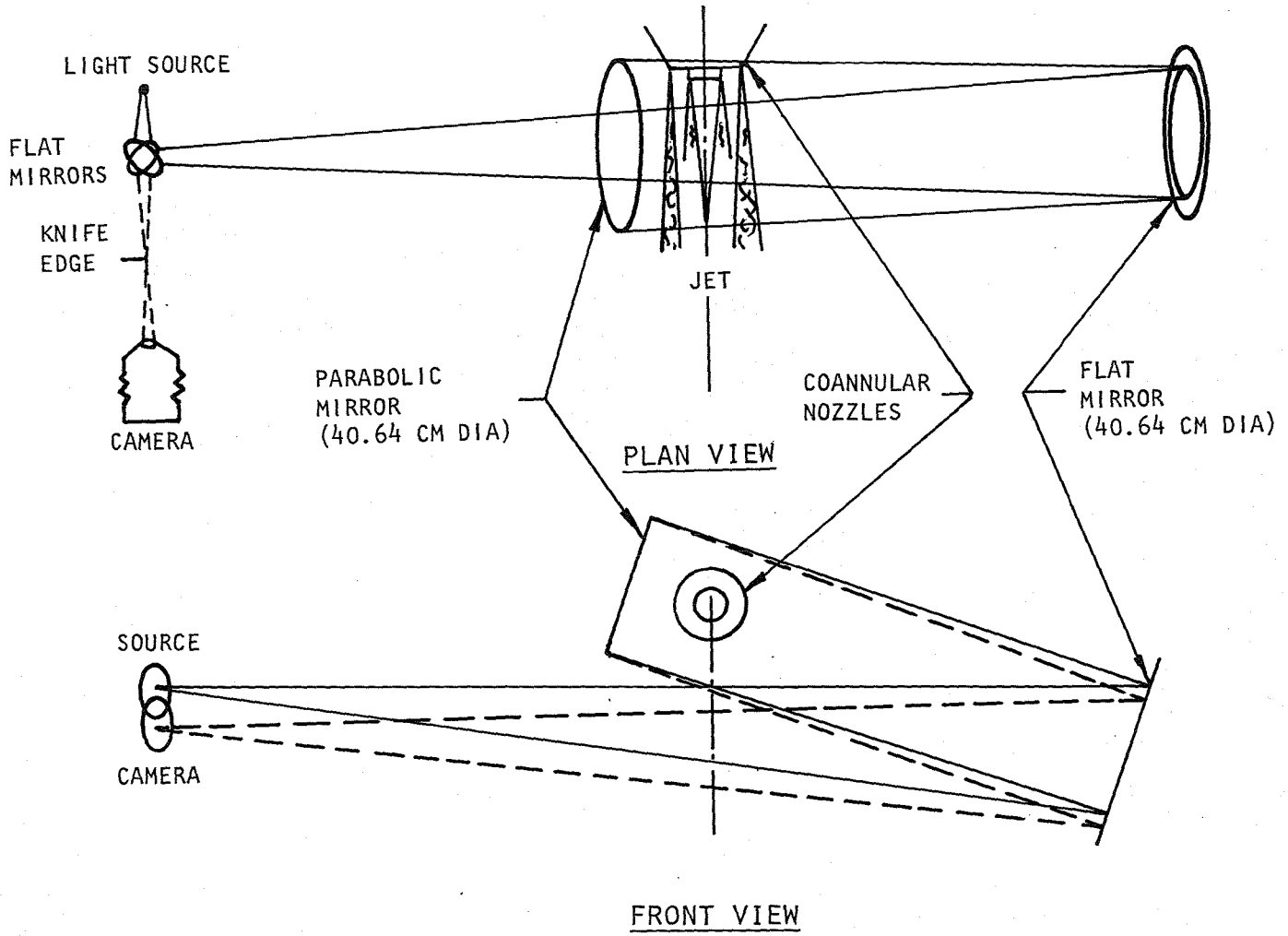

Figure A1.1 Schlieren System Schematic.

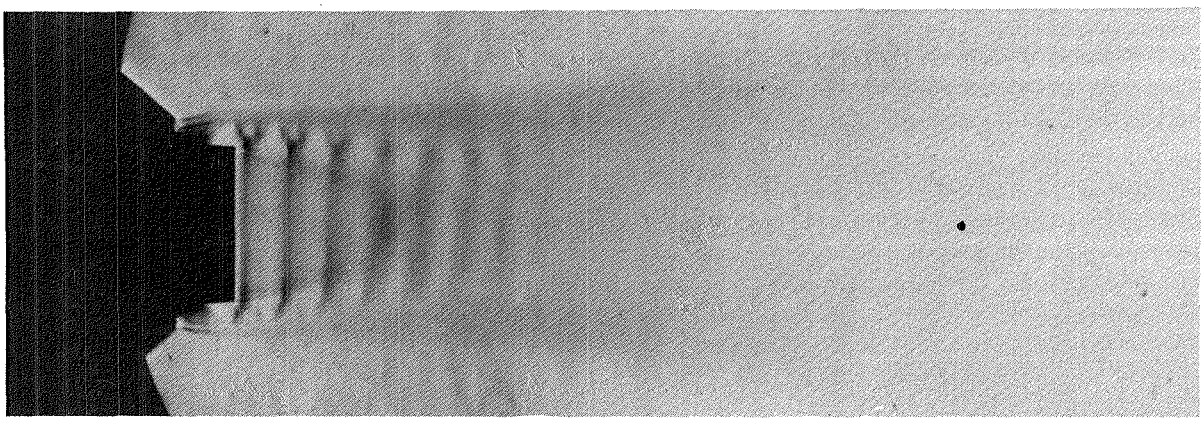

(a) $\xi_p = 1.000$

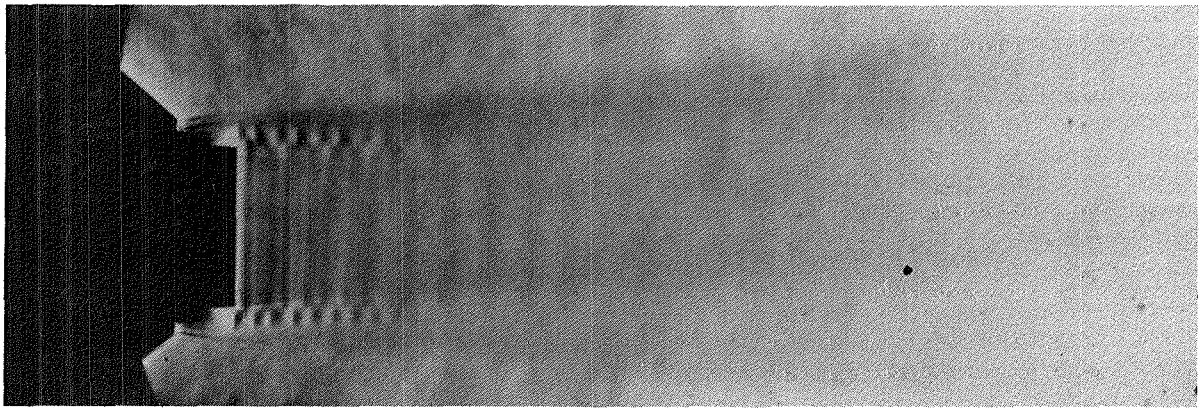

(b) $\xi_p = 1.391$

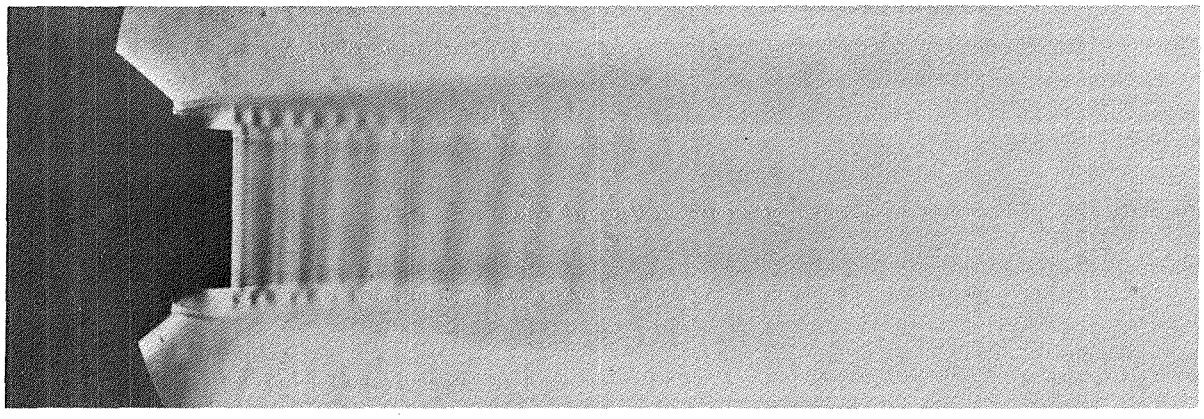

(c) $\xi_p = 1.594$

Figure A1.2 Coannular jet — Schlieren photographs
Series 1 : $\xi_f = 2.93$, $T_{tp} = 294$ °K, $T_{tf} = 728$ °K.

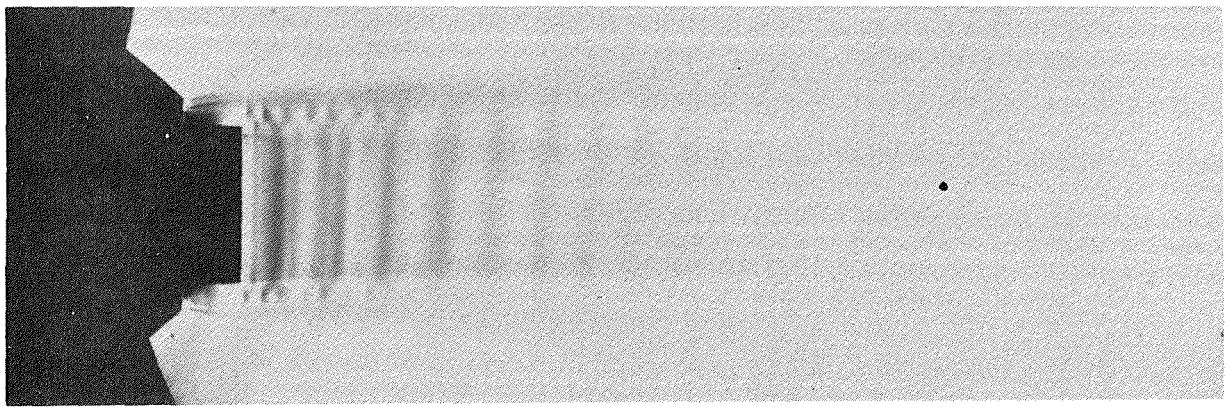

(d) $\xi_p = 1.776$

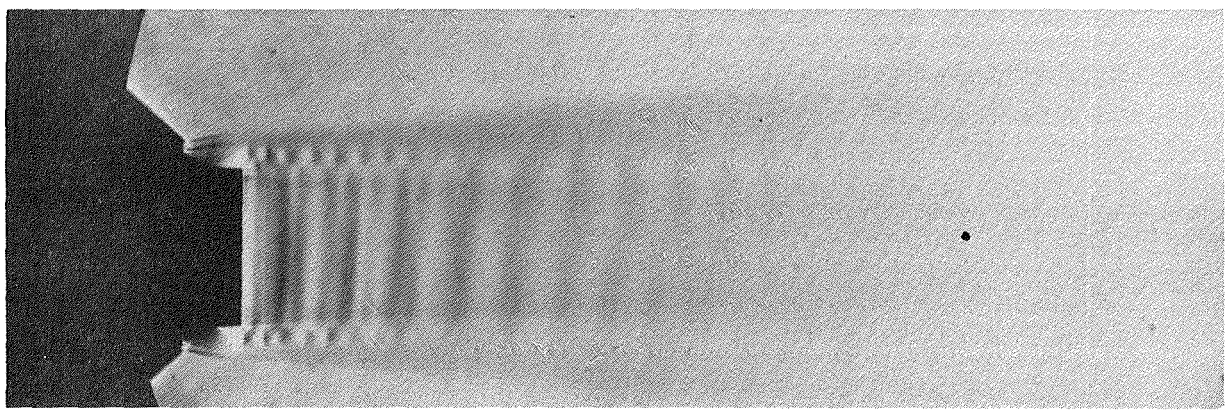

(e) $\xi_p = 1.797$

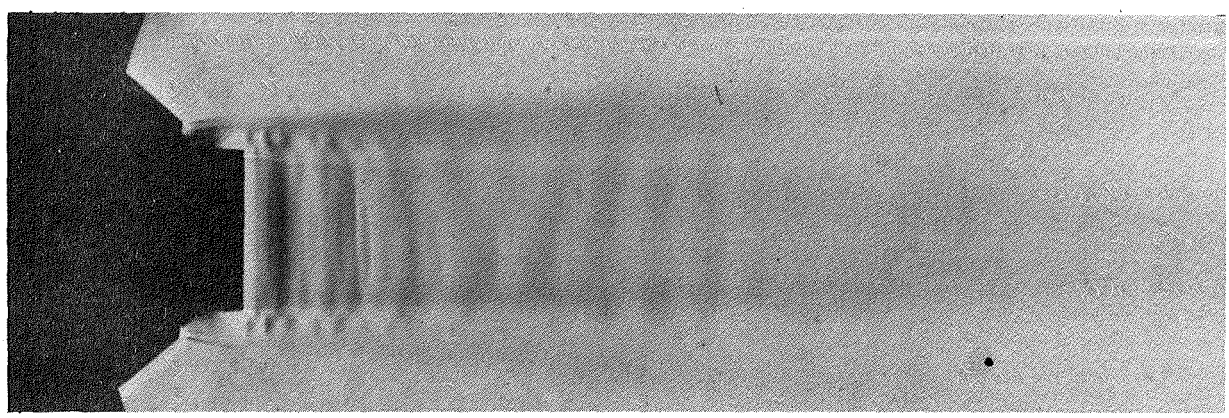

(f) $\xi_p = 1.853$

Figure A1.2 (Continued).

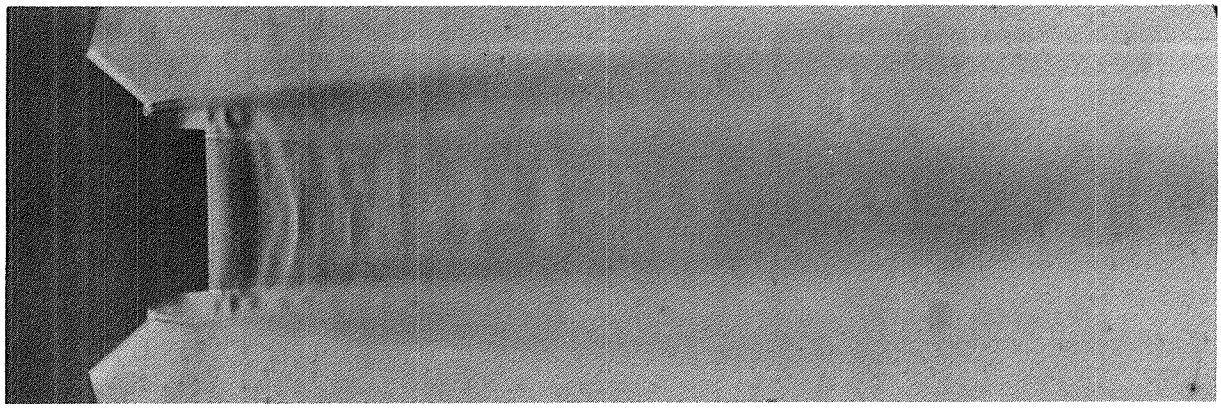

(g) $\xi_p = 1.967$

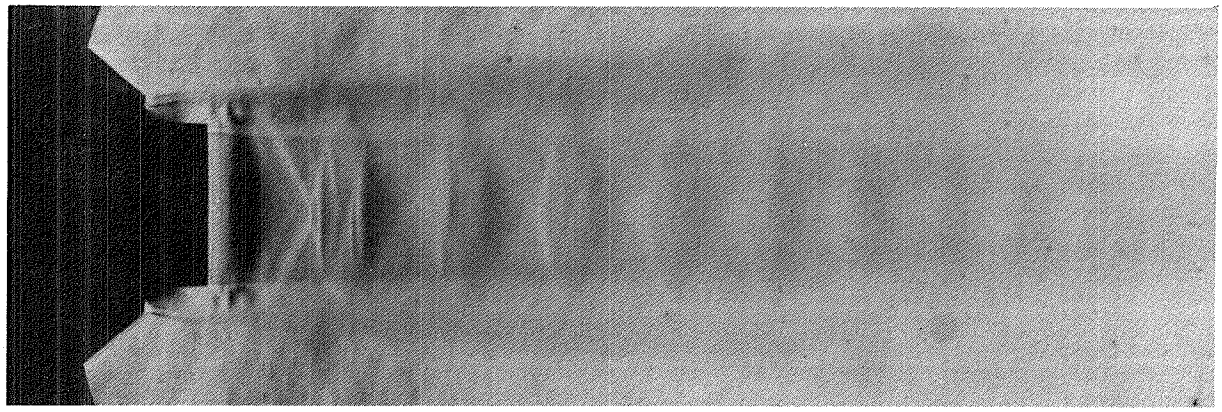

(h) $\xi_p = 2.047$

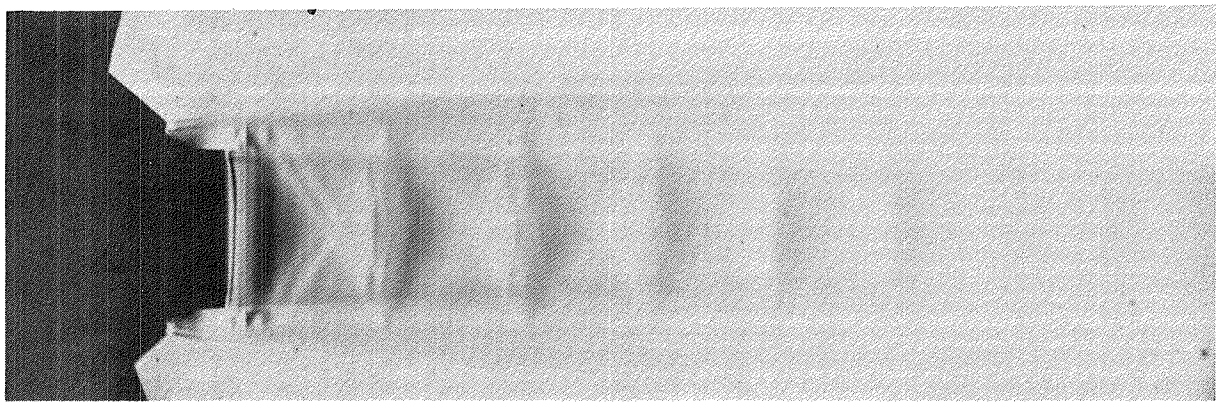

(i) $\xi_p = 2.170$

Figure A1.2 (Continued).

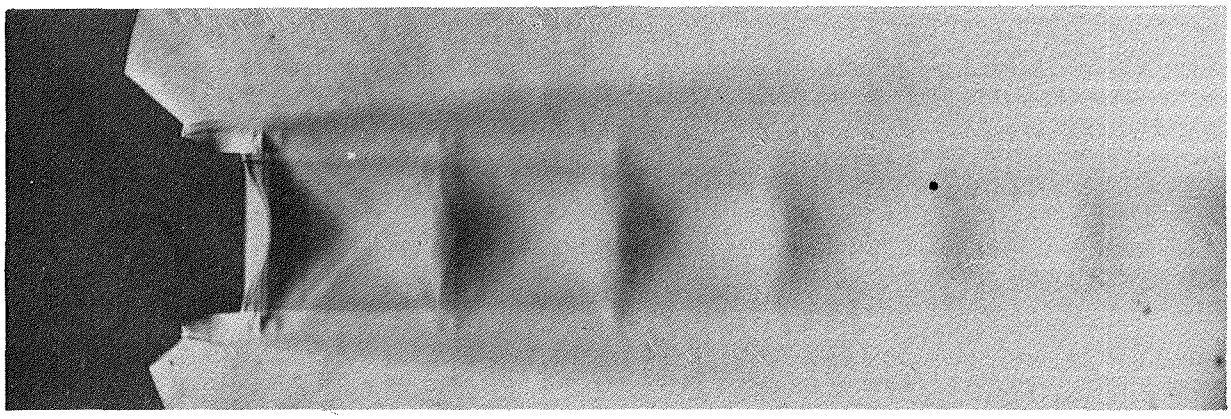

(j) $\xi_p = 2.431$

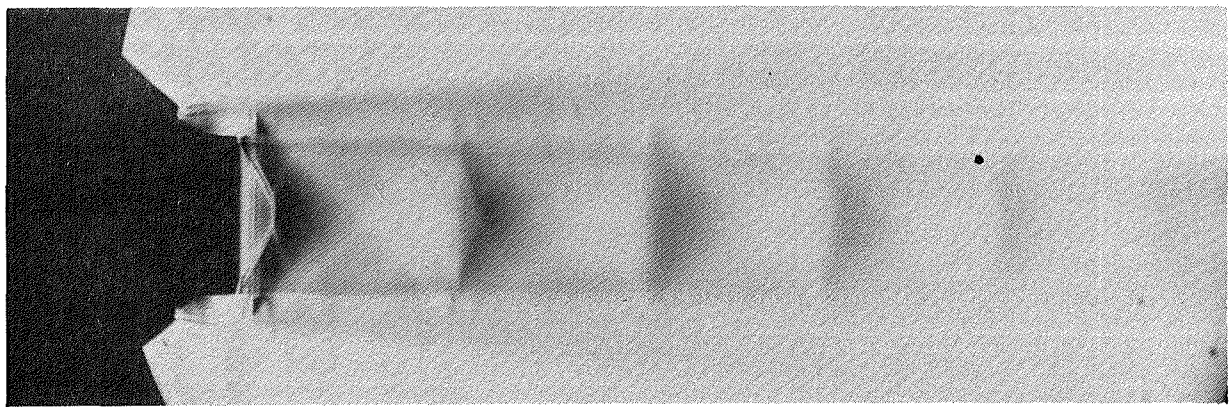

(k) $\xi_p = 2.626$

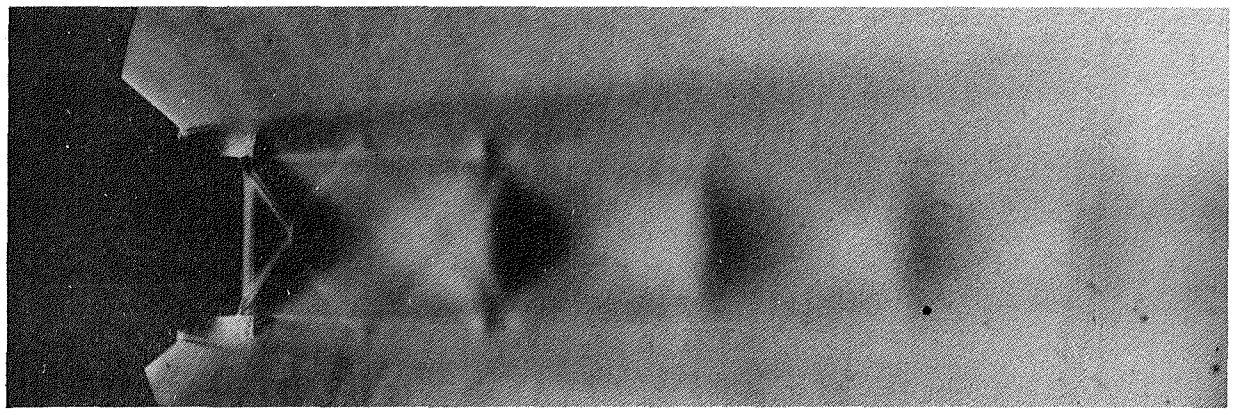

(ℓ) $\xi_p = 2.951$

Figure A1.2 (Continued).

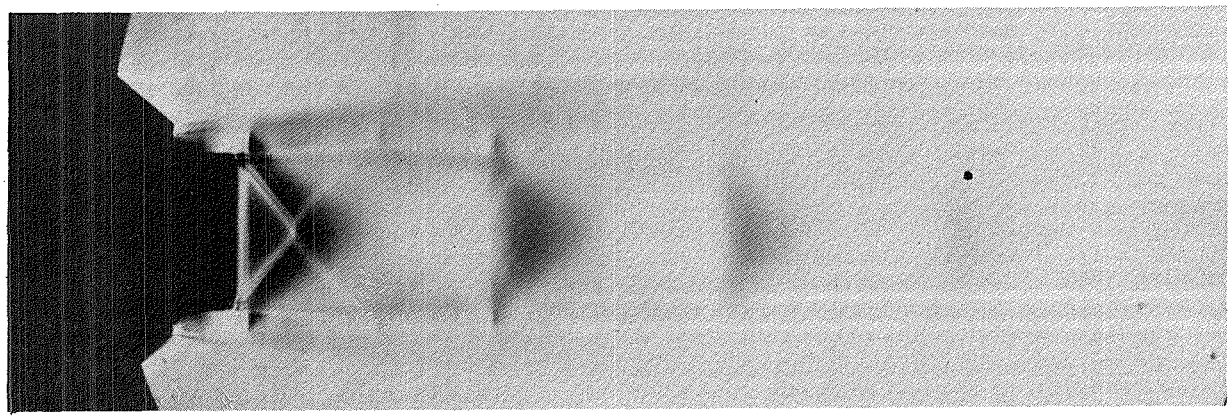

(m) $\xi_p = 3.146$

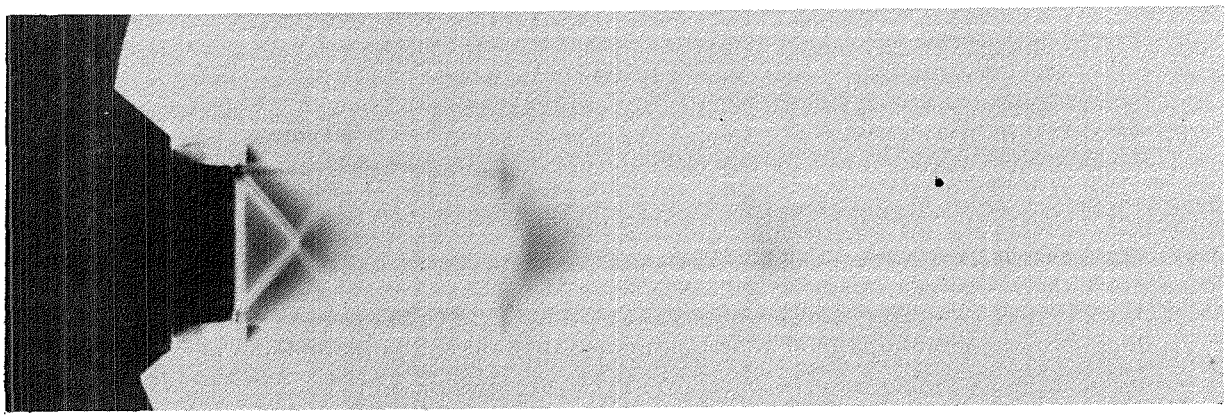

(n) $\xi_p = 3.341$

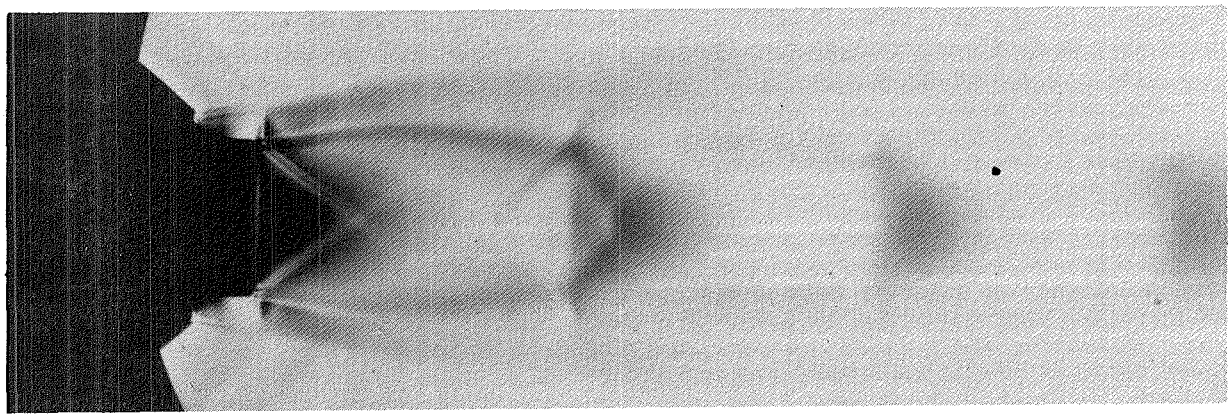

(o) $\xi_p = 4.492$

Figure A1.2 (Concluded).

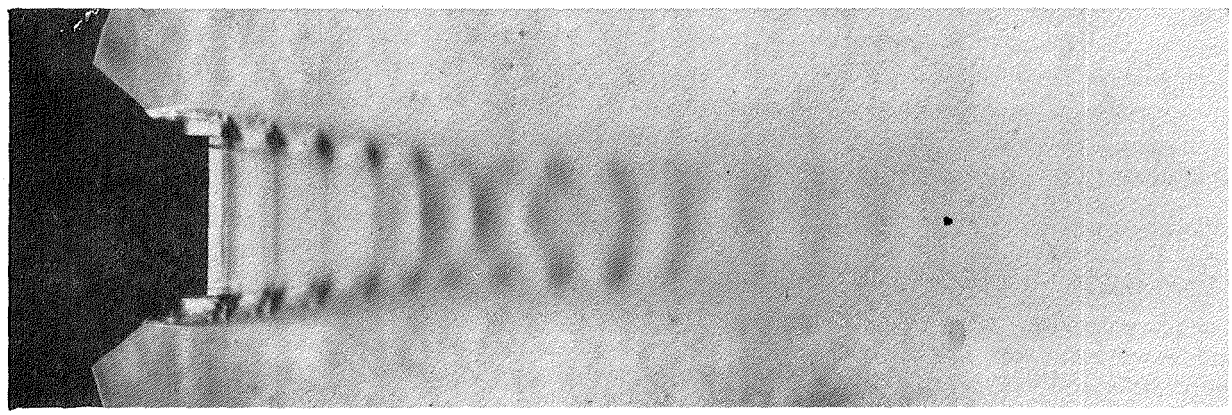

(a) $\xi_p = 1.000$

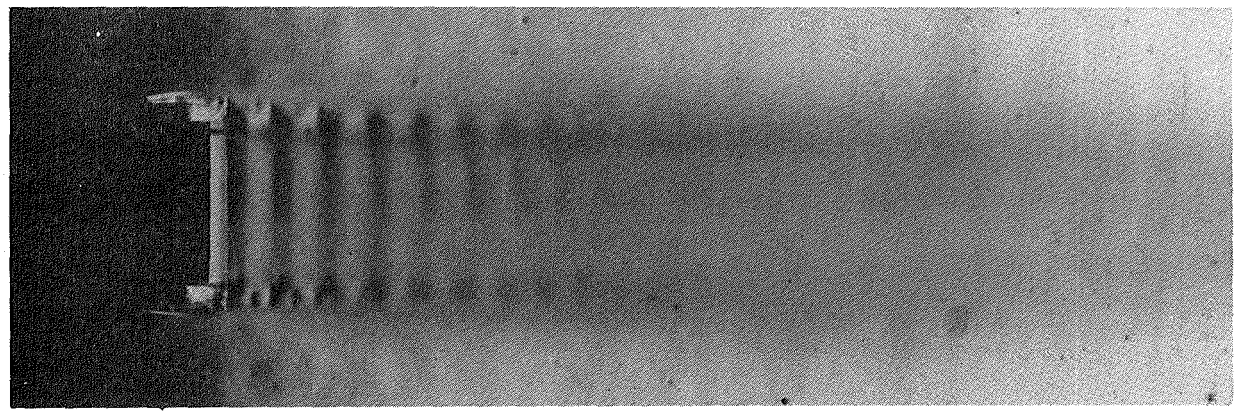

(b) $\xi_p = 1.390$

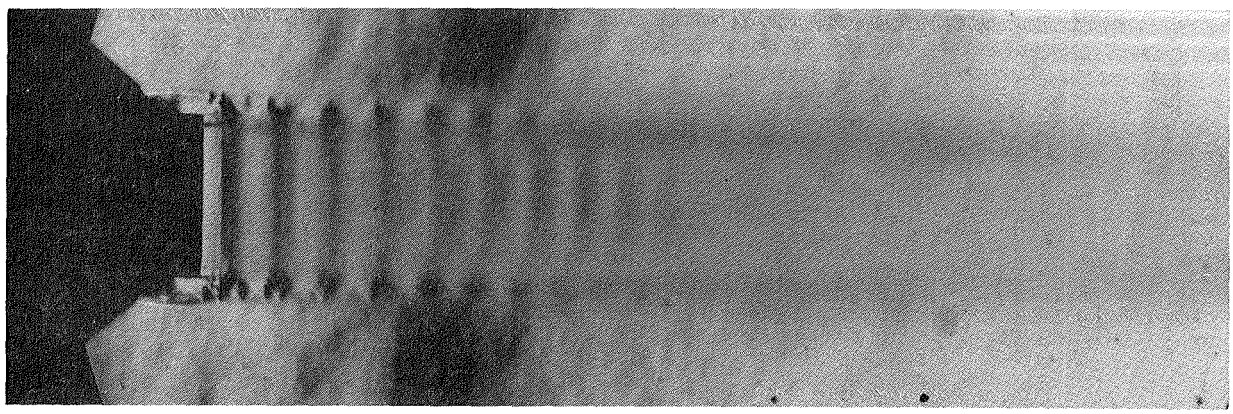

(c) $\xi_p = 1.593$

Figure A1.3 Coannular jet — Schlieren photographs.
Series 2 : $\xi_f = 2.93$, $T_{tp} = 728\ ^{\circ}K$, $T_{tf} = 294\ ^{\circ}K$.

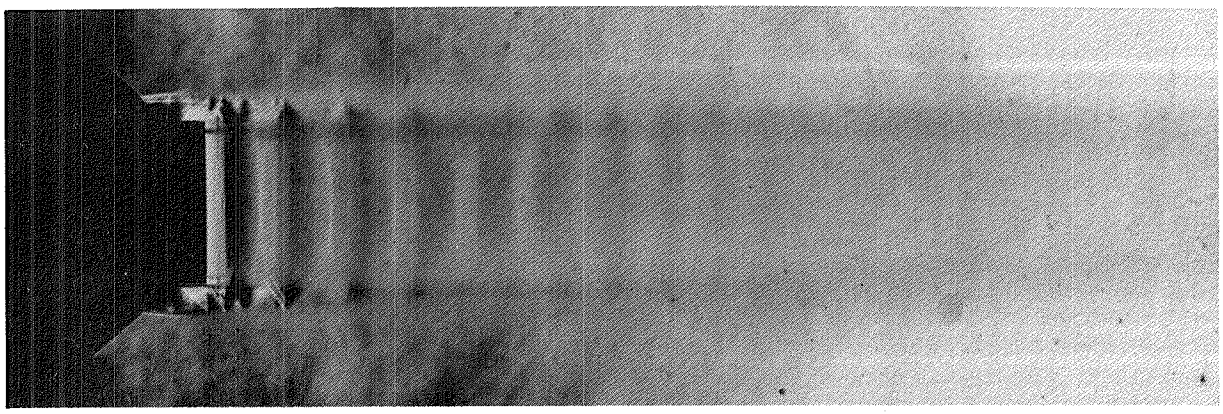

(d) $\xi_p = 1.808$

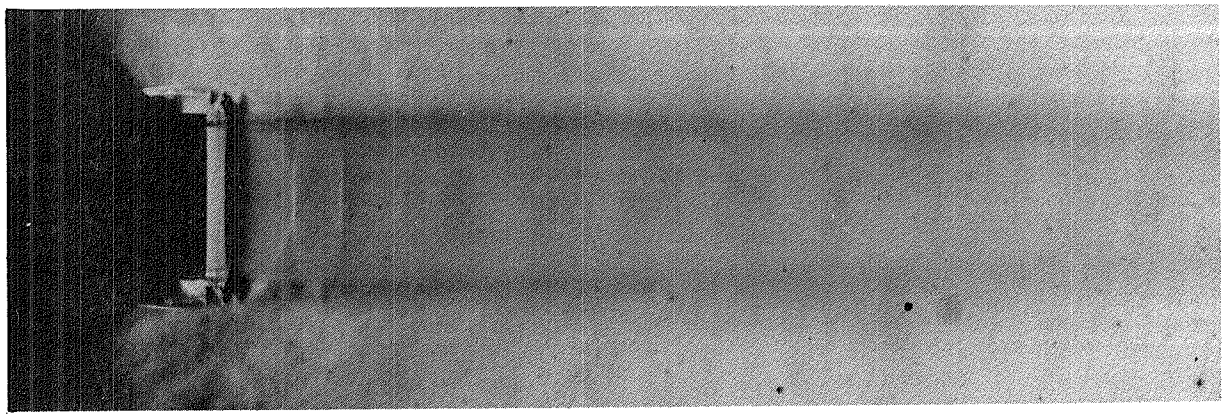

(e) $\xi_p = 1.984$

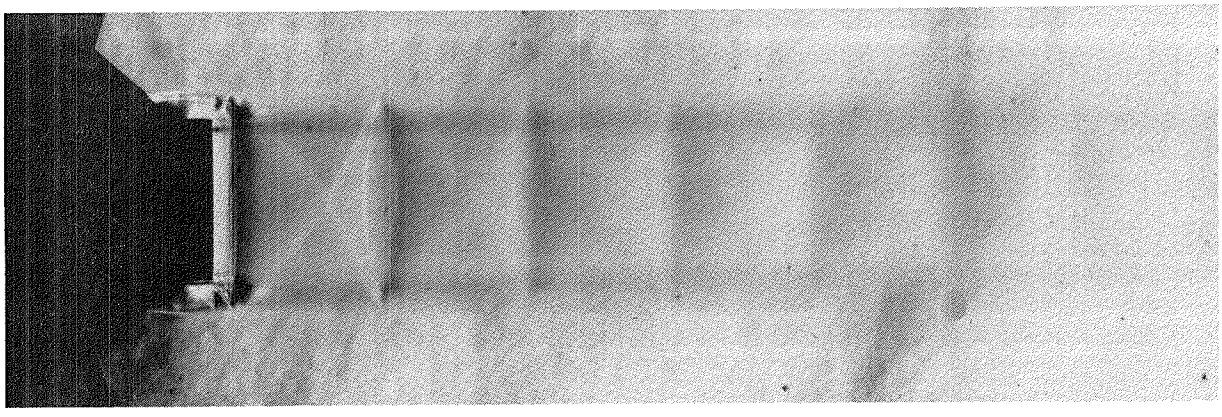

(f) $\xi_p = 2.179$

Figure A1.3 (Continued).

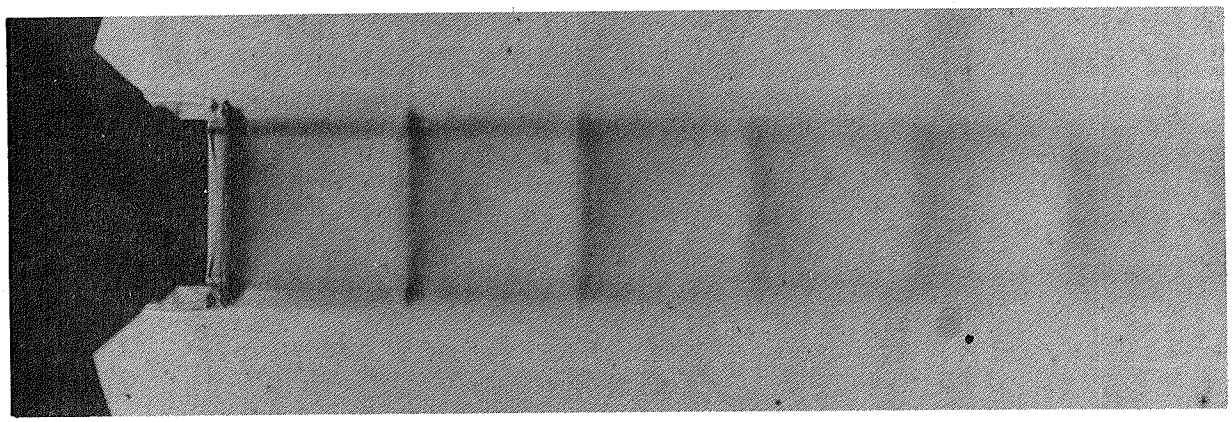

(g) $\xi_p = 2.435$

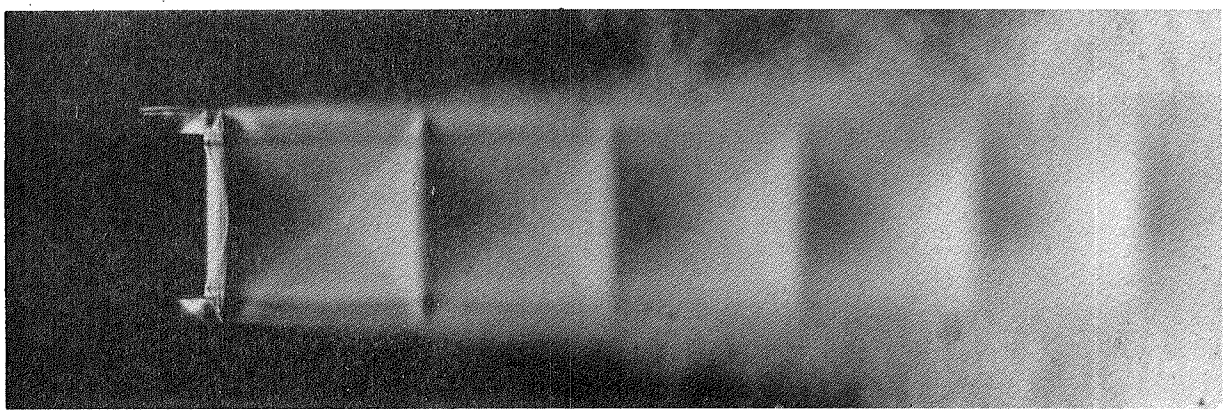

(h) $\xi_p = 2.603$

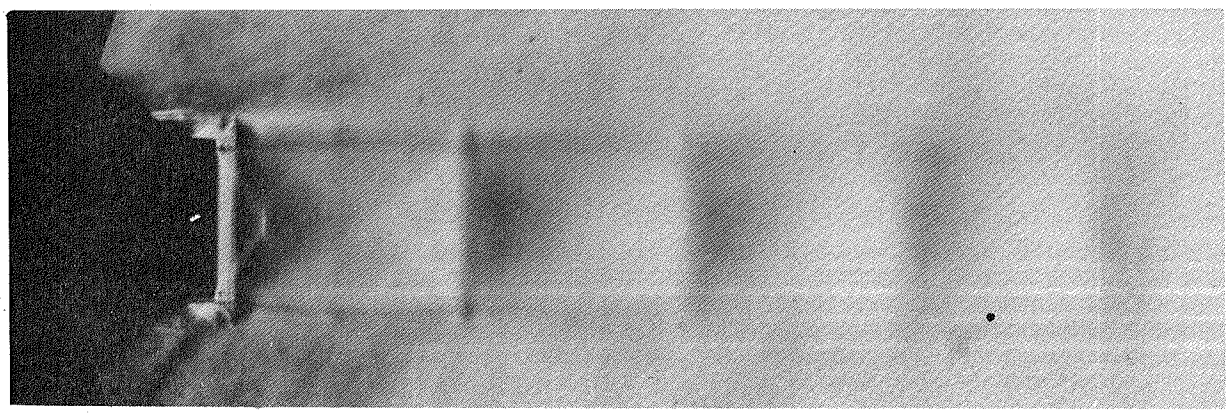

(i) $\xi_p = 2.953$

Figure A1.3 (Continued).

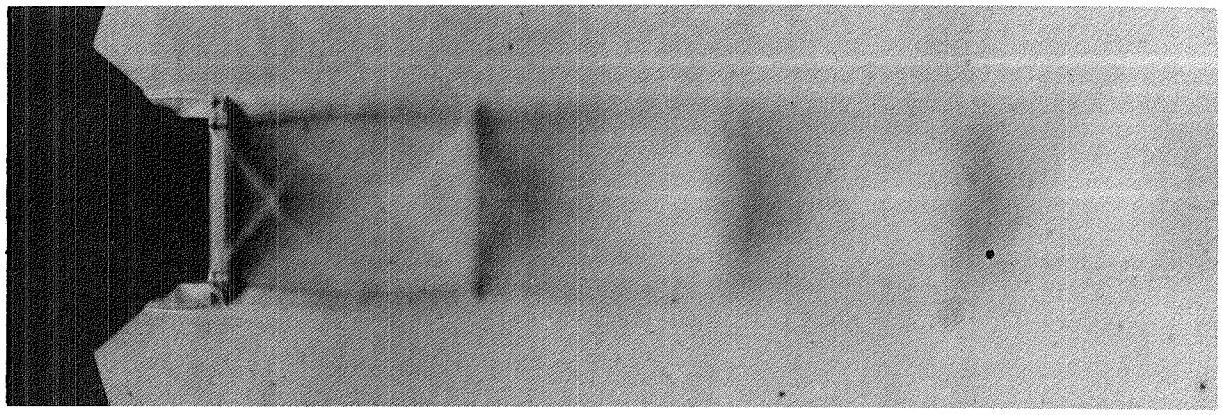

(j) $\xi_p = 3.183$

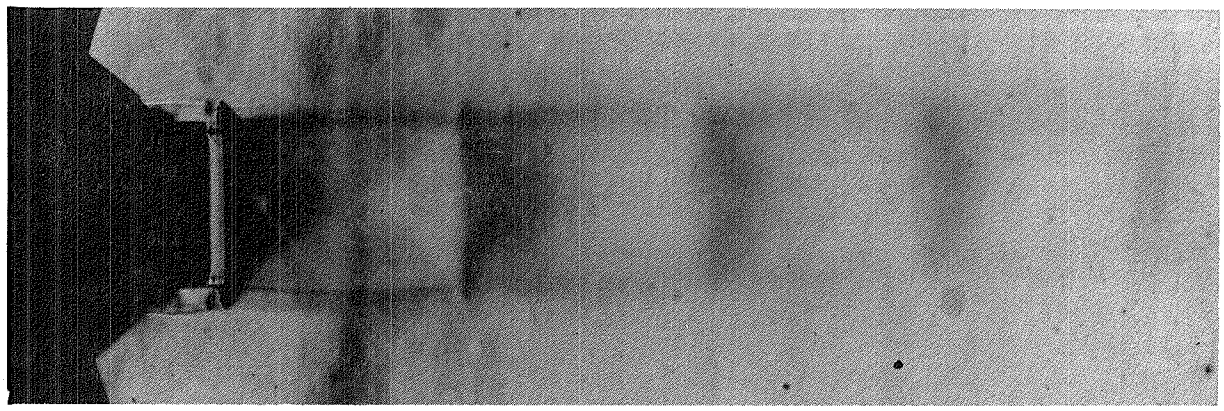

(k) $\xi_p = 3.345$

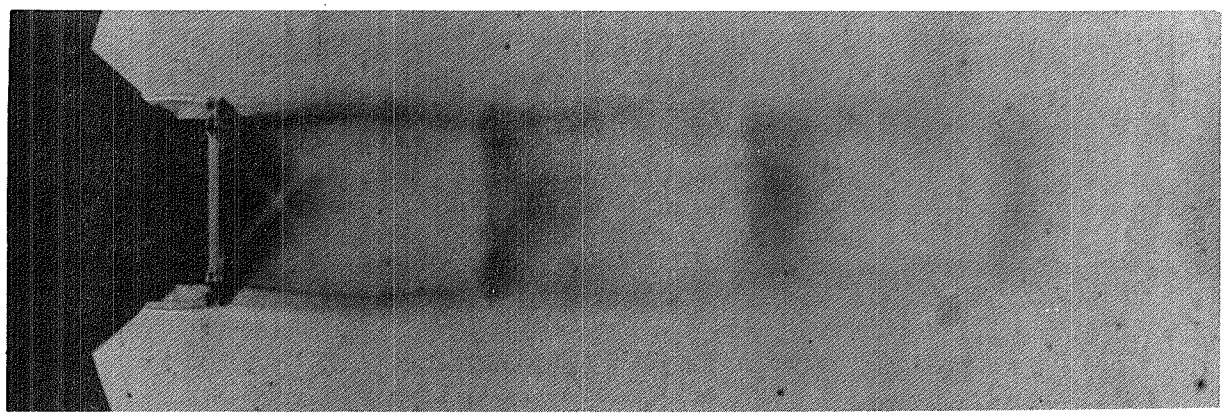

(ℓ) $\xi_p = 3.479$

Figure A1.3 (Concluded).

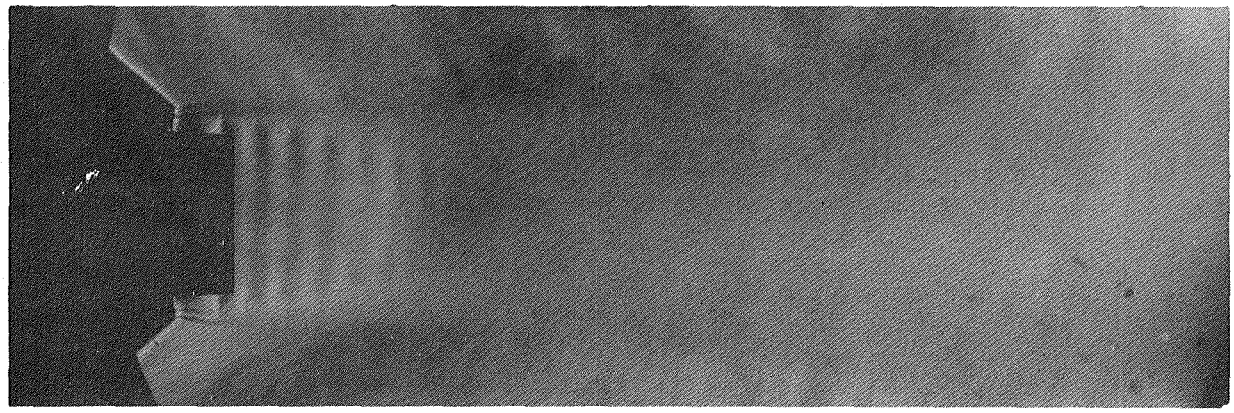

(a) $\xi_p = 1.000$

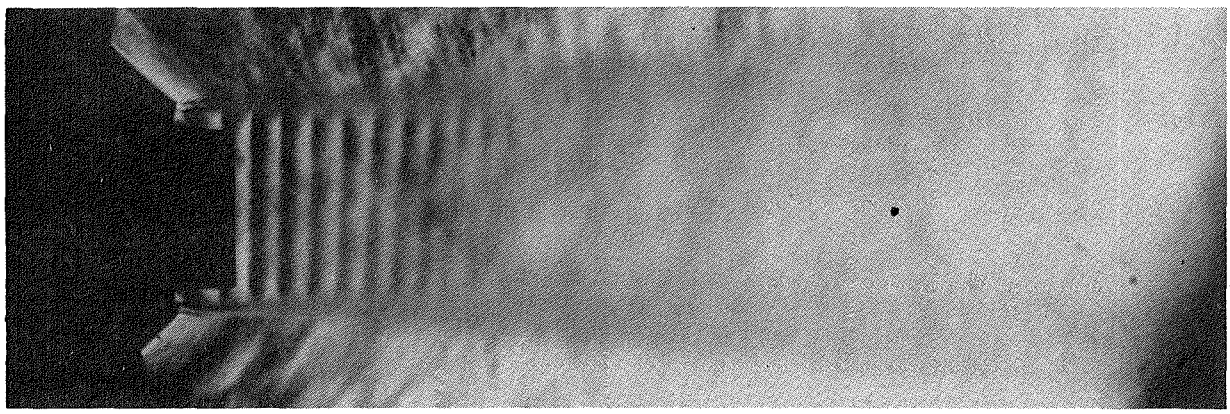

(b) $\xi_p = 1.398$

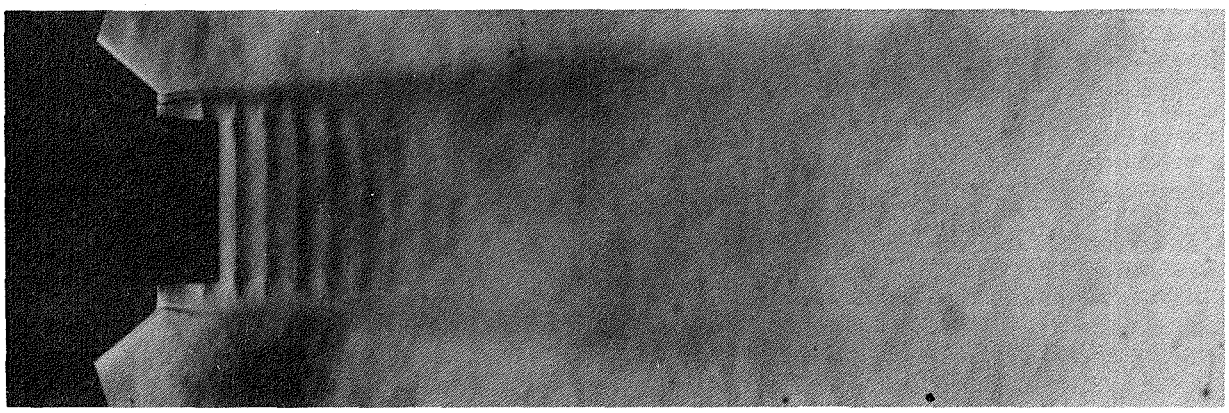

(c) $\xi_p = 1.390$

Figure A1.4 Coannular jet — Schlieren photographs.
Series 3 : $\xi_f = 2.37$, $T_{tp} = 728\ ^\circ K$, $T_{tf} = 978\ ^\circ K$.

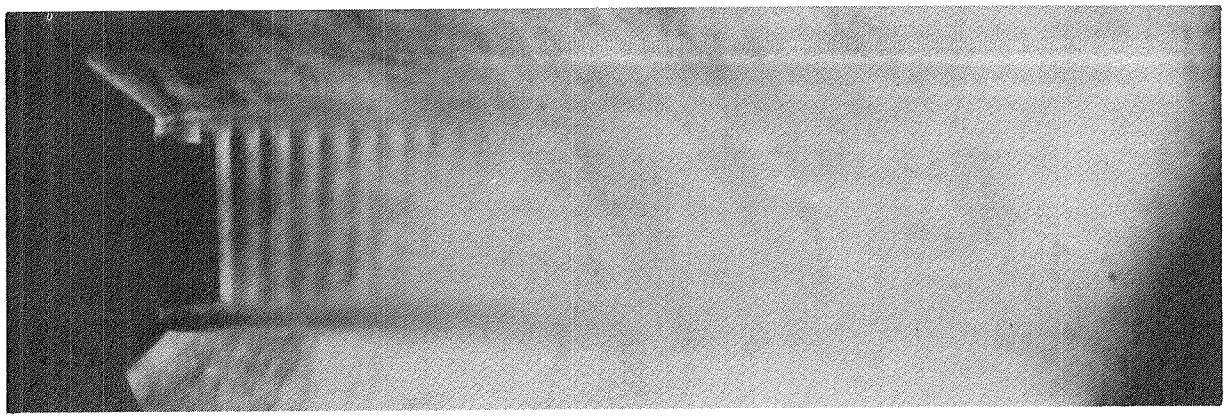

(d) $\xi_p = 1.425$

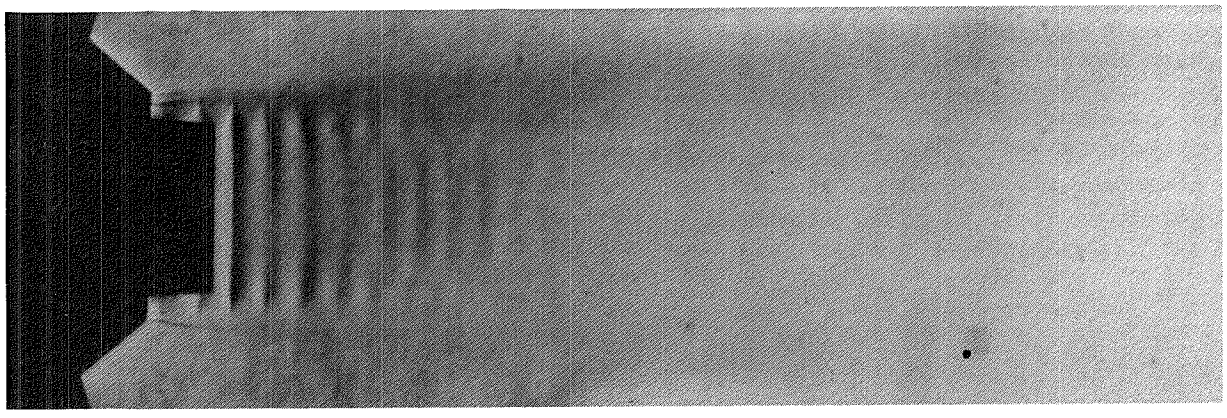

(e) $\xi_p = 1.505$

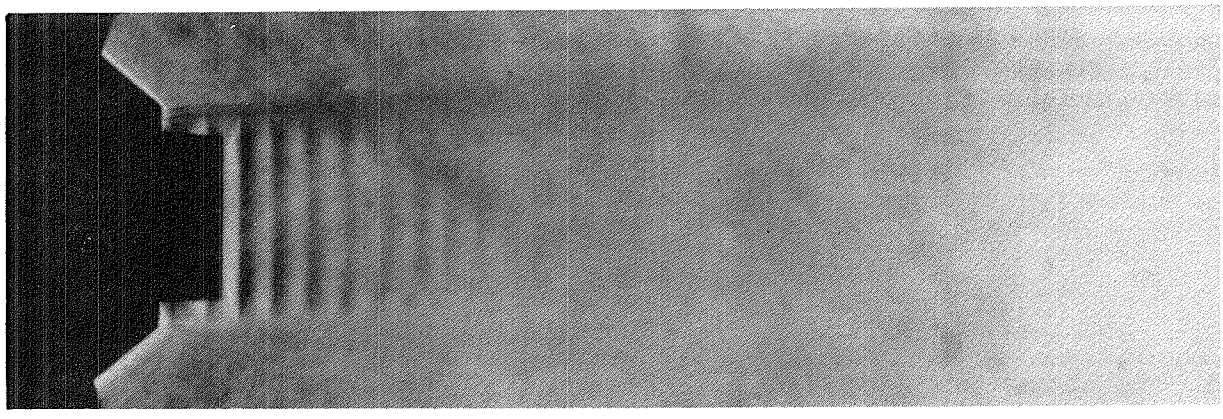

(f) $\xi_p = 1.606$

Figure A1.4 (Continued).

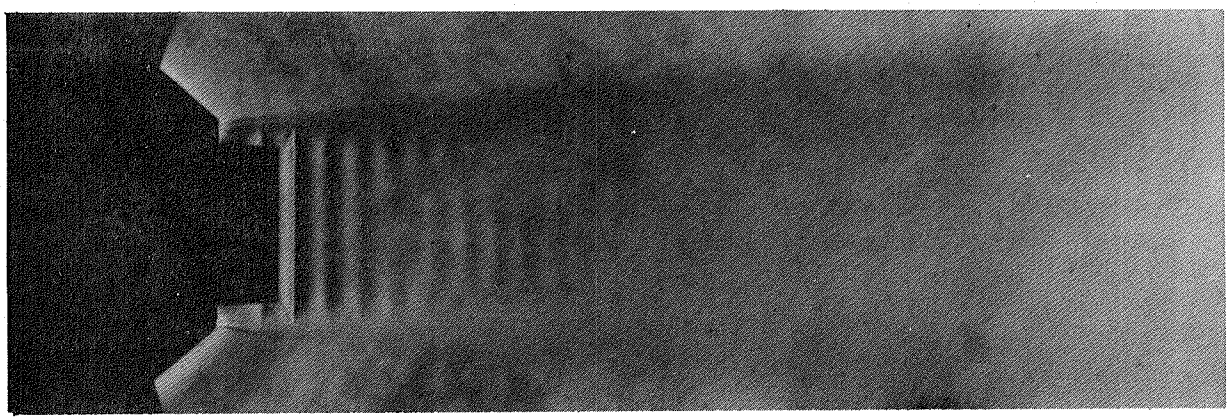

(g) $\xi_p = 1.761$

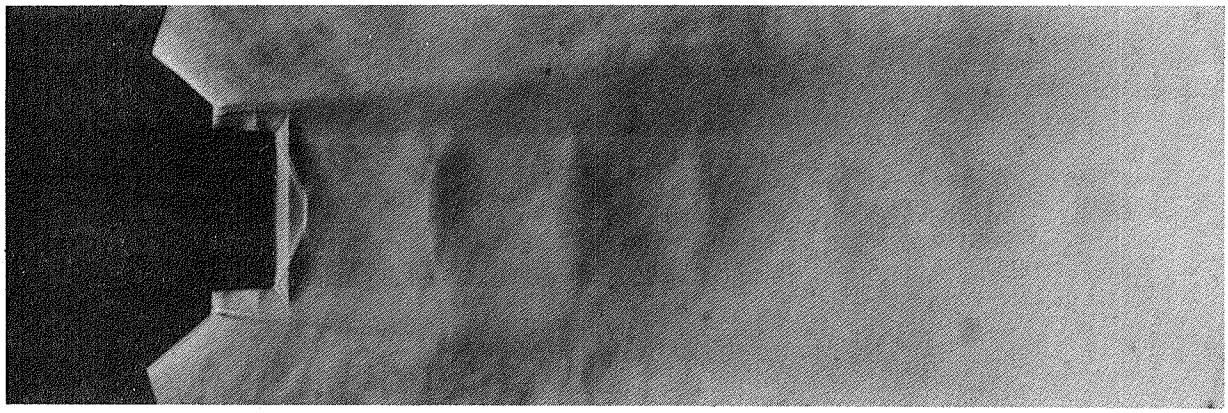

(h) $\xi_p = 1.957$

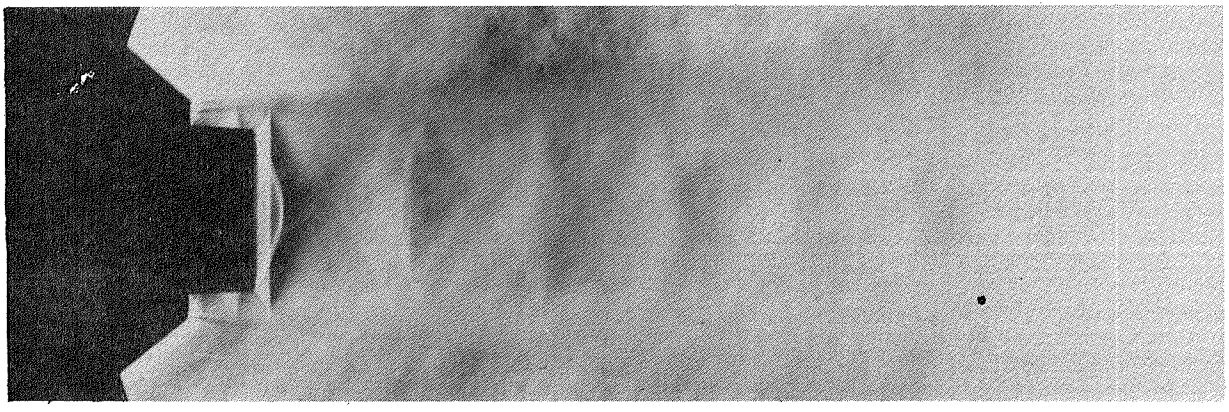

(i) $\xi_p = 2.199$

Figure A1.4 (Continued).

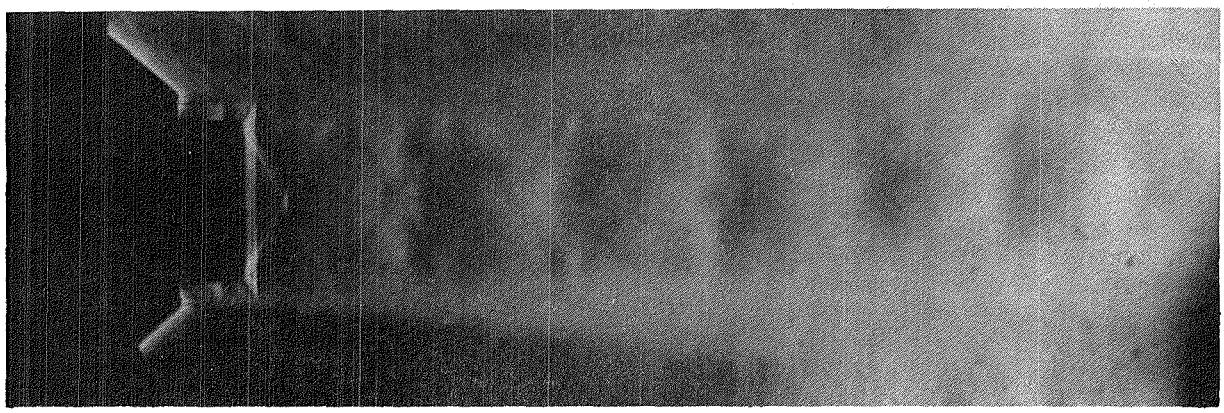

(j) $\xi_p = 2.455$

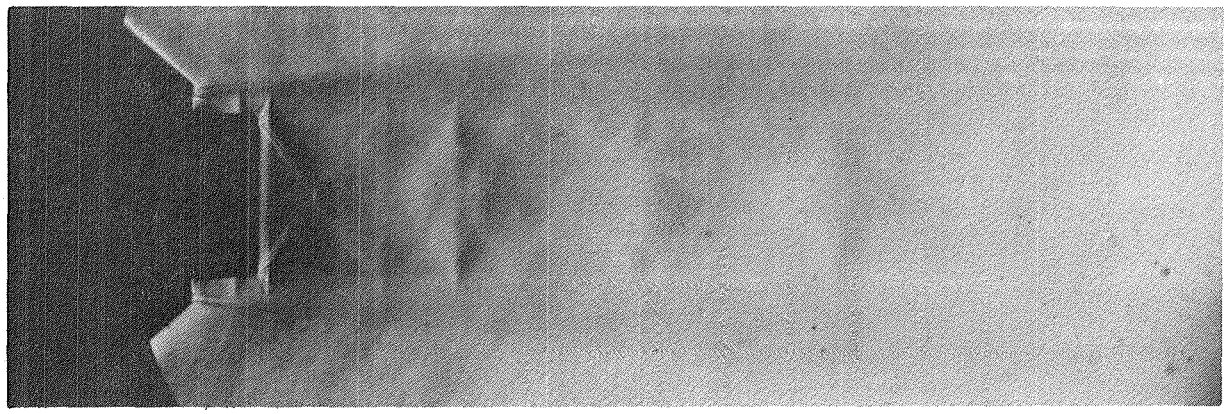

(k) $\xi_p = 2.658$

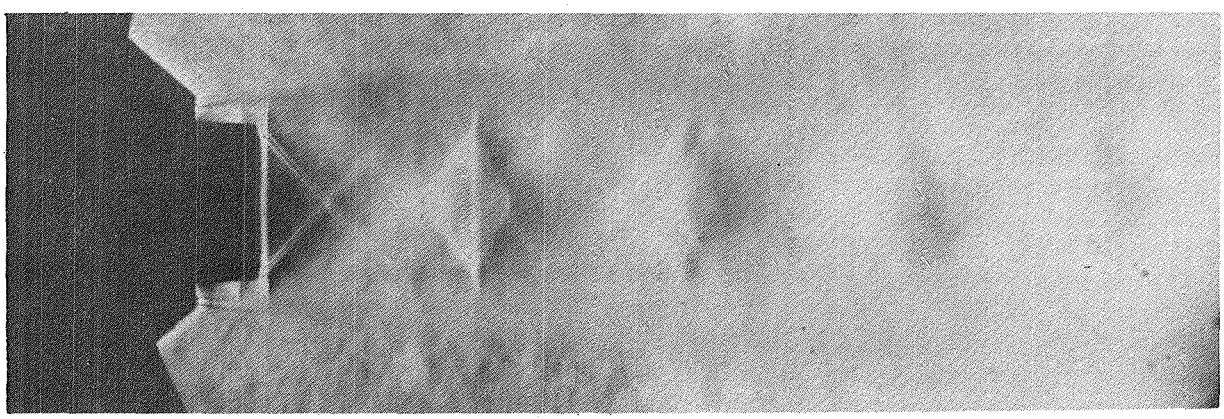

(ℓ) $\xi_p = 2.981$

Figure A1.4 (Continued).

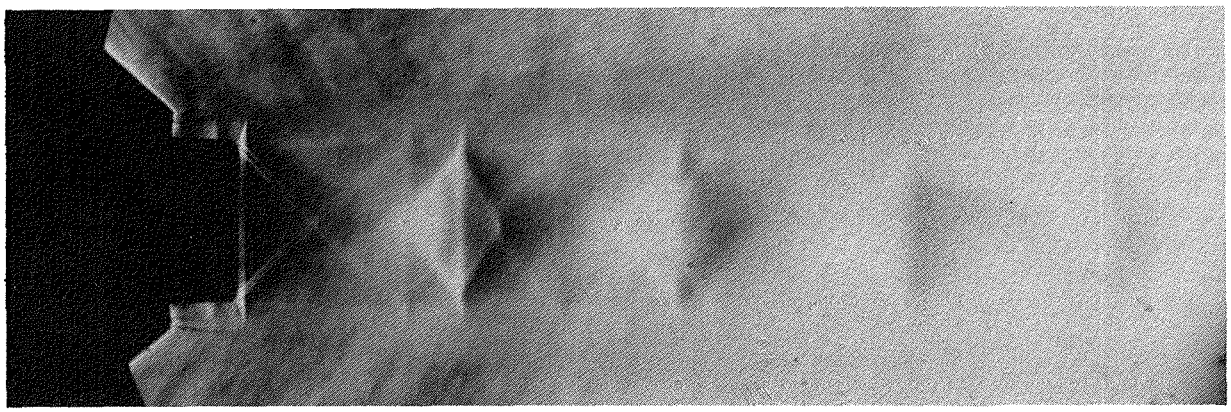

(m) $\xi_p = 3.129$

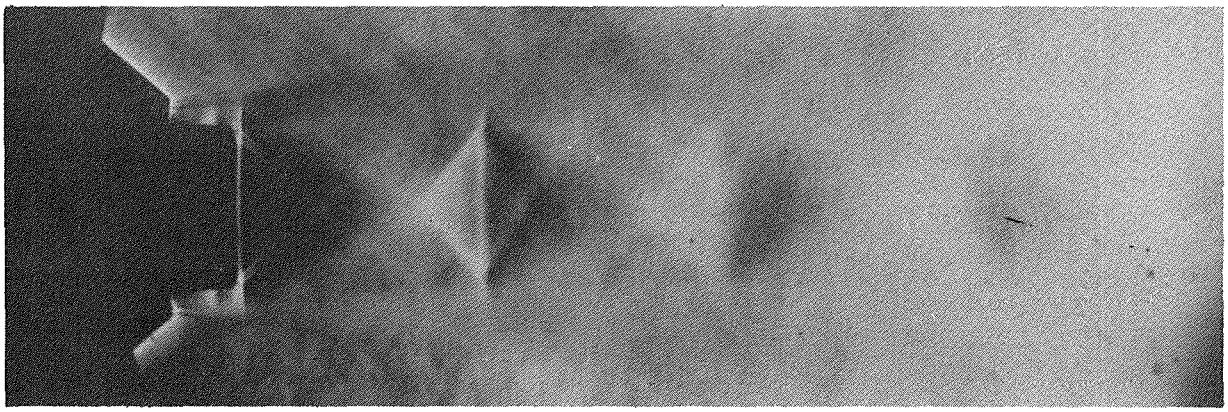

(n) $\xi_p = 3.341$

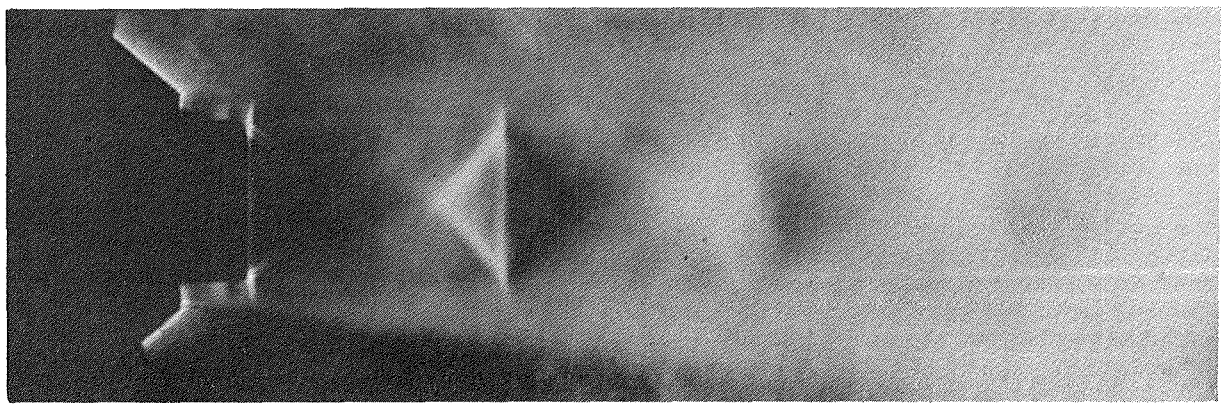

(o) $\xi_p = 3.526$

Figure A1.4 (Concluded).

APPENDIX 2
SOURCE LOCATION DATA

This appendix contains all the source location data acquired under this contract, and the corresponding axial source distributions with the exception of the source distribution results that appear in the main text. The table below indicates where results for each test point may be found. Figures A2.1 through A2.16 contain the measured and calibrated coherence and phase data; the remaining figures compare the calculated axial source distributions at different coannular velocity and temperature ratios, with the exception of Figures A2.22 through A2.26 which contain individual results. In the title of Figures A2.11, A2.12, A2.24, and A2.25 (primary stream only), the velocity and temperature ratios (V_f/V_p, T_f/T_p) quoted should be interpreted, respectively, as V_p/a_o, T_p/T_o.

Table A2.1 Figure index for source location data

Figure Number	Test/Run No.	Test Point No.	Comments
A2.1(a), (b)	1	4	Coherence, Phase
A2.2(a), (b)	2	3	
A2.3(a), (b)	3	2	
A2.4(a), (b)	4	1	
A2.5(a), (b)	5	8	
A2.6(a), (b)	6	7	
A2.7(a), (b)	7	6	
A2.8(a), (b)	8	5	
A2.9(a), (b)	9	14	
A2.10(a), (b)	10	13	
A2.11(a), (b)	11	--	
A2.12(a), (b)	12	--	
A2.13(a), (b)	13	12	
A2.14(a), (b)	15	10	
A2.15(a), (b)	16	9	
A2.16(a), (b)	17	13	
A2.17(a) - (g)	--	5, 6, 7, 8	V_f/V_p varied, $T_f/T_p = 1.75$
A2.18(a) - (g)	--	9, 10, 11, 12	V_f/V_p varied, $T_f/T_p = 2.00$
A2.19(a) - (g)	--	1, 5, 9	T_f/T_p varied, $V_f/V_p = 1.00$
A2.20(a) - (g)	--	2, 6, 10	T_f/T_p varied, $V_f/V_p = 1.35$
A2.21(a) - (g)	--	3, 7, 11	T_f/T_p varied, $V_f/V_p = 1.55$
A2.22(a) - (g)	9	14	Supercritical condition
A2.23(a) - (g)	10	13	Supercritical condition
A2.24(a) - (g)	11	--	Primary stream only (cold)
A2.25(a) - (g)	12	--	Primary stream only (hot)
A2.26(a) - (g)	17	13	Repeat of Run No. 10

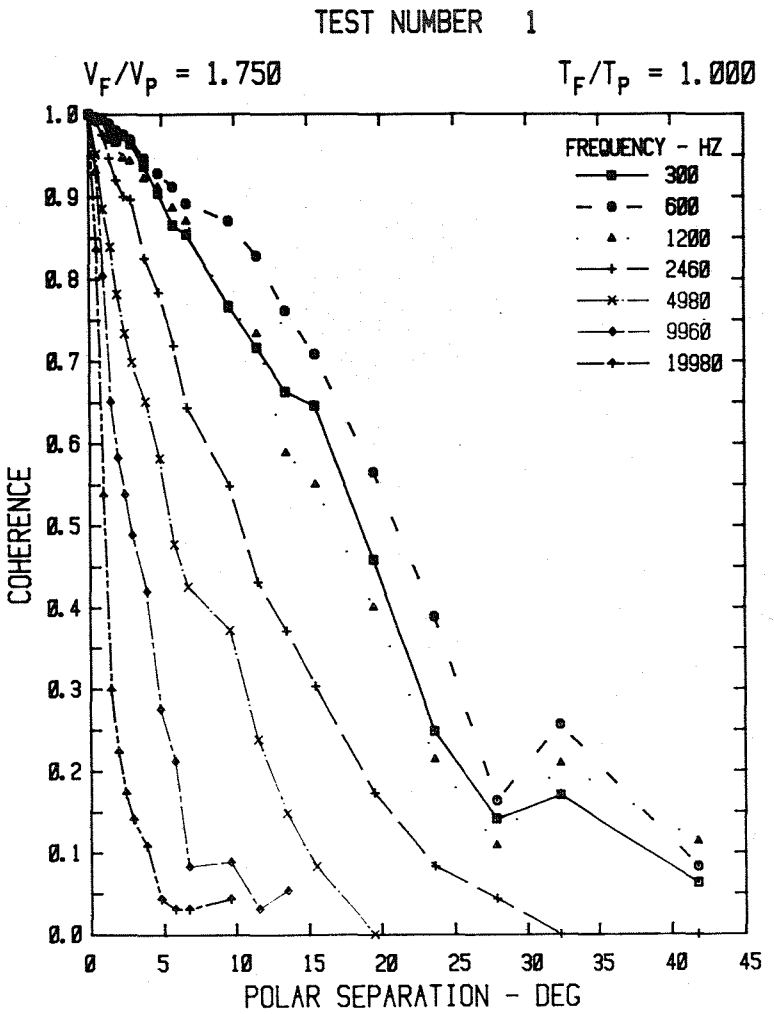

Figure A2.1(a)

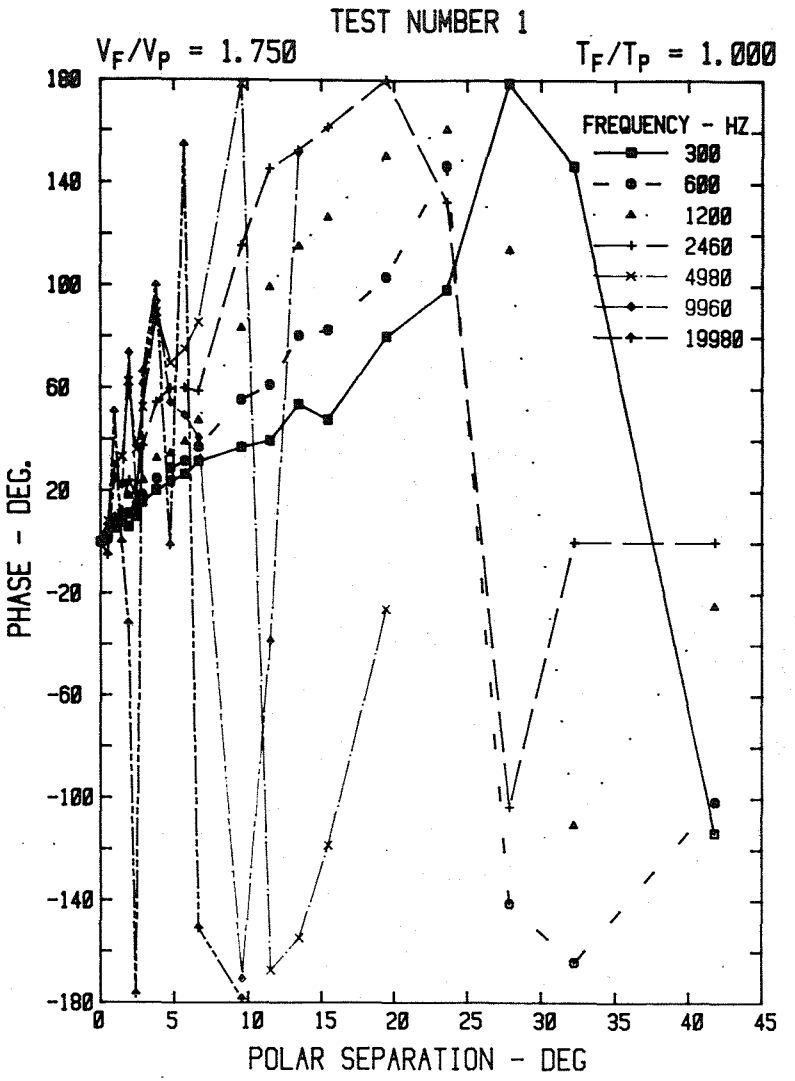

Figure A2.1(b)

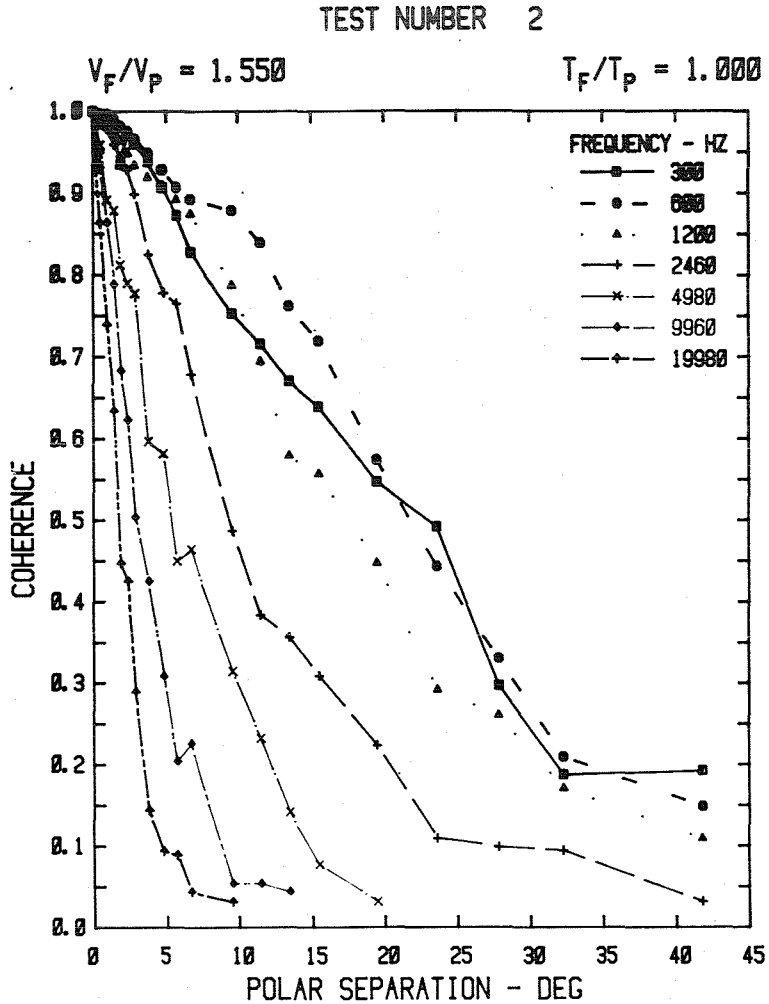

Figure A2.2(a)

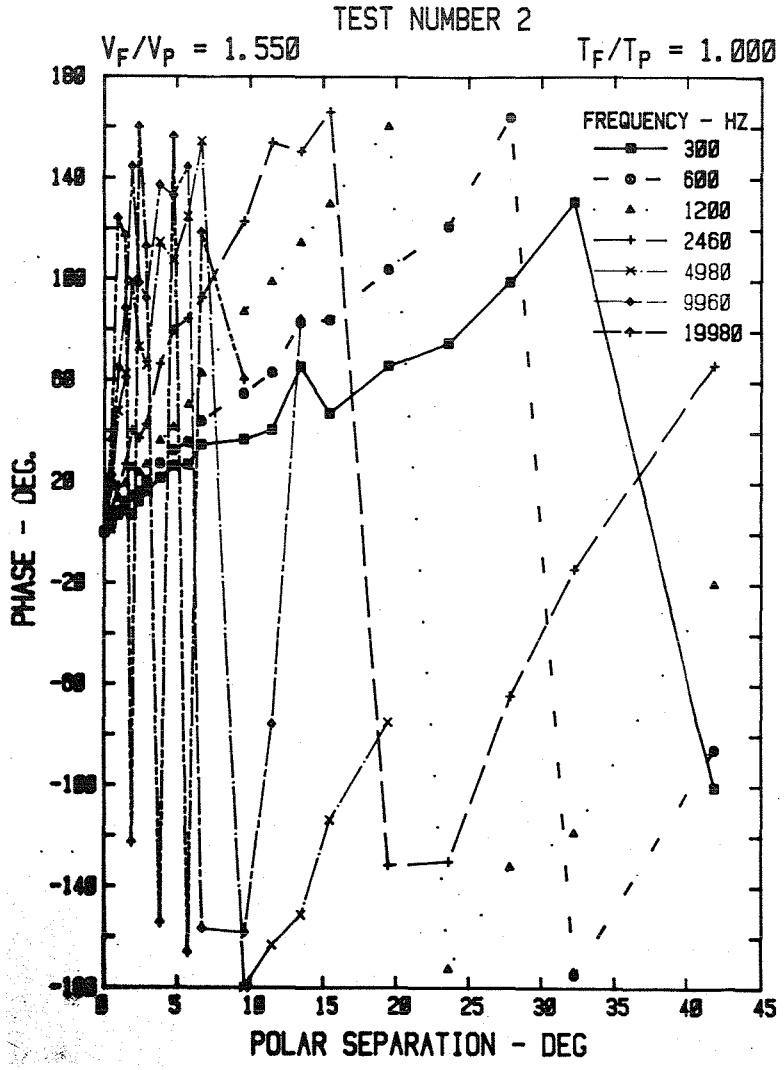

Figure A2.2(b)

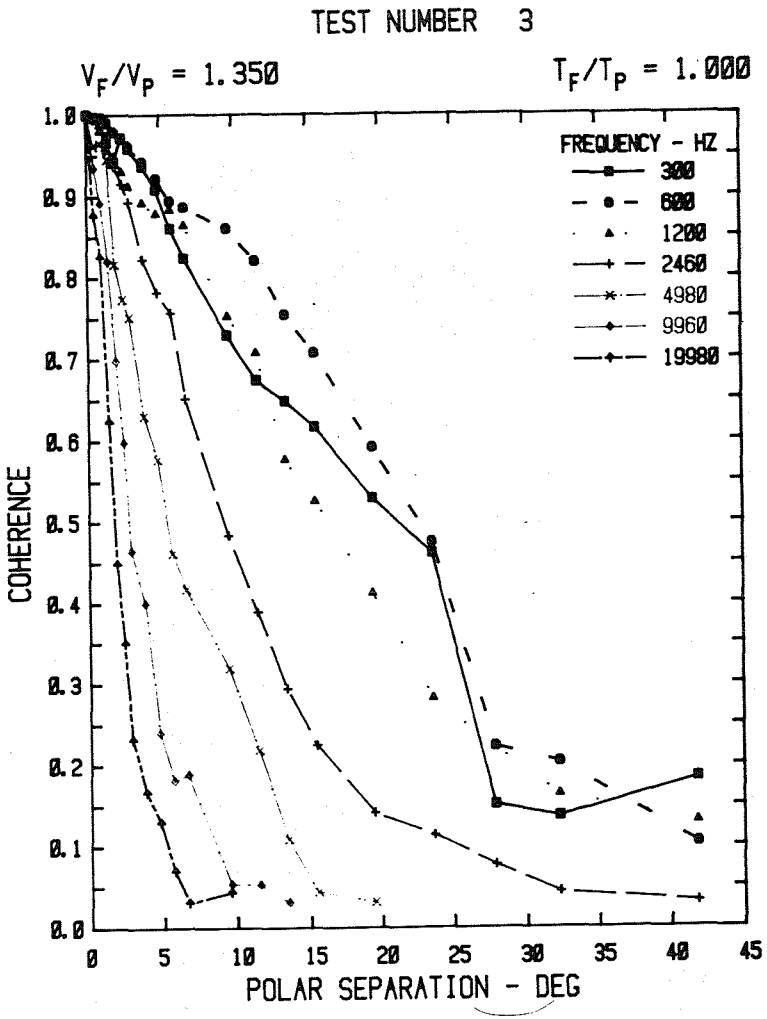

Figure A2.3(a)

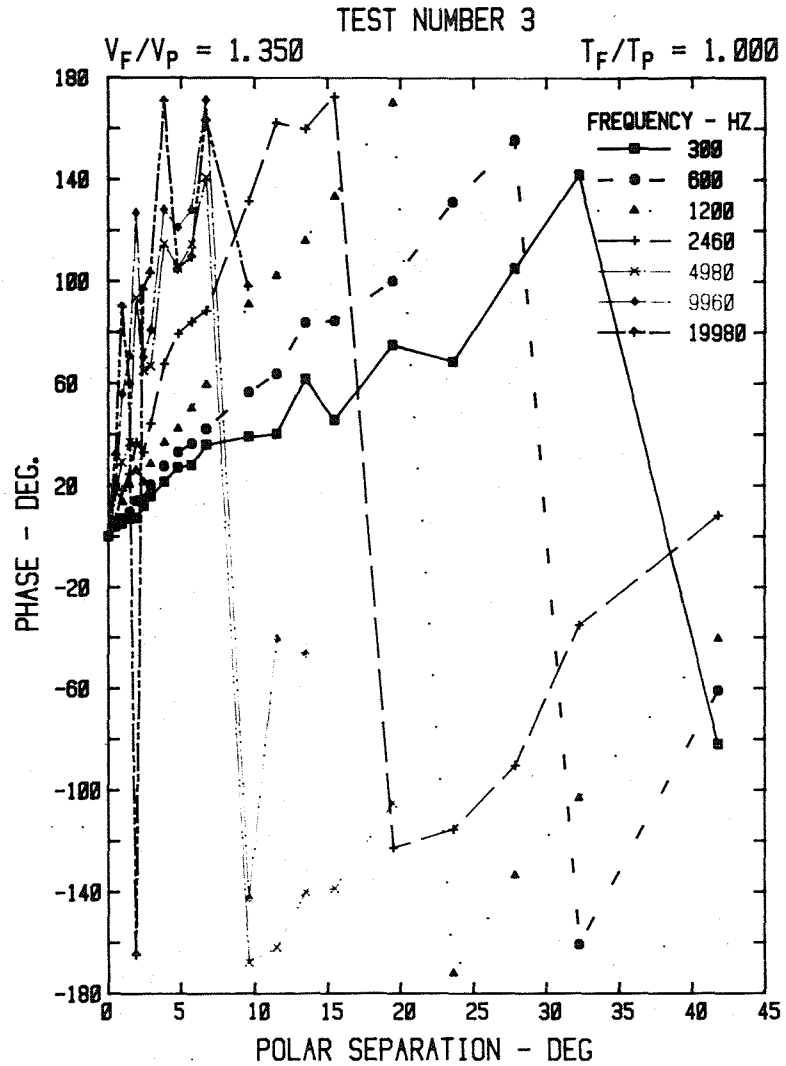

Figure A2.3(b)

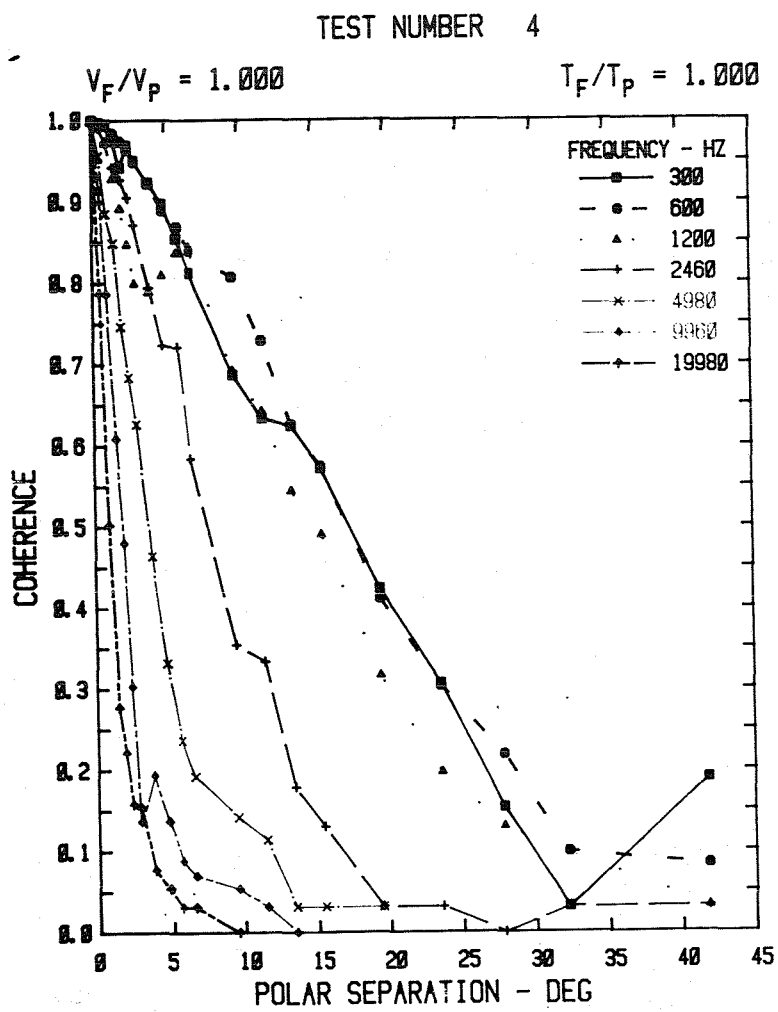

Figure A2.4(a)

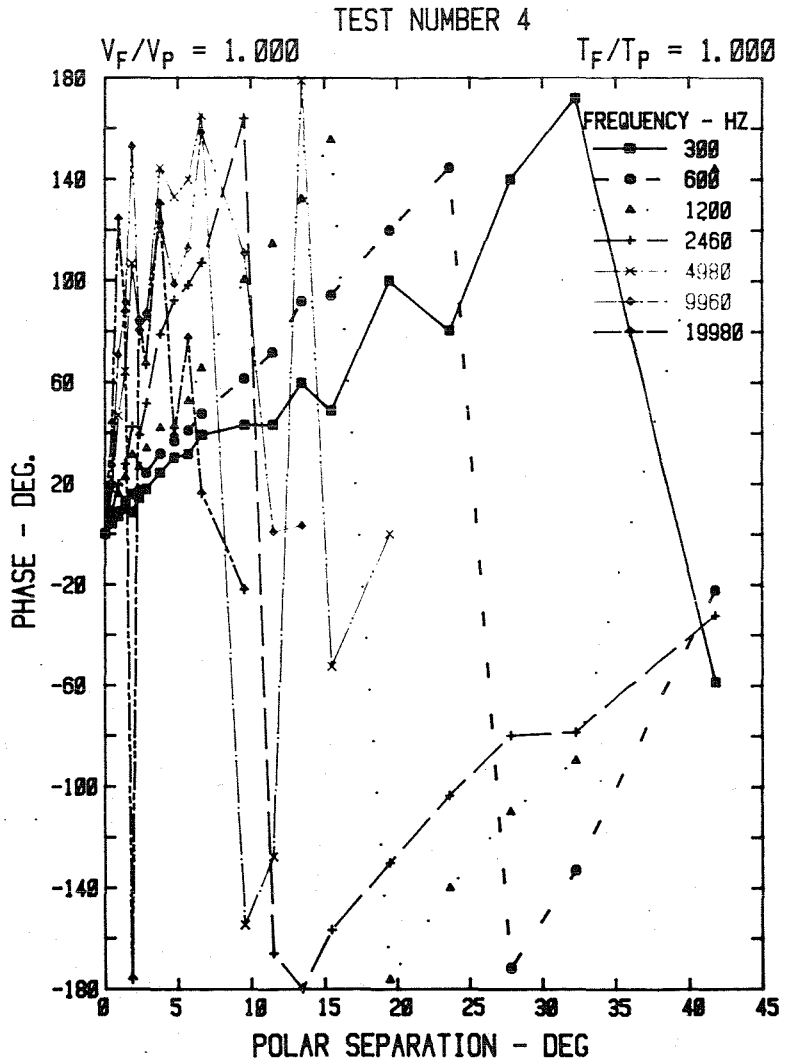

Figure A2.4(b)

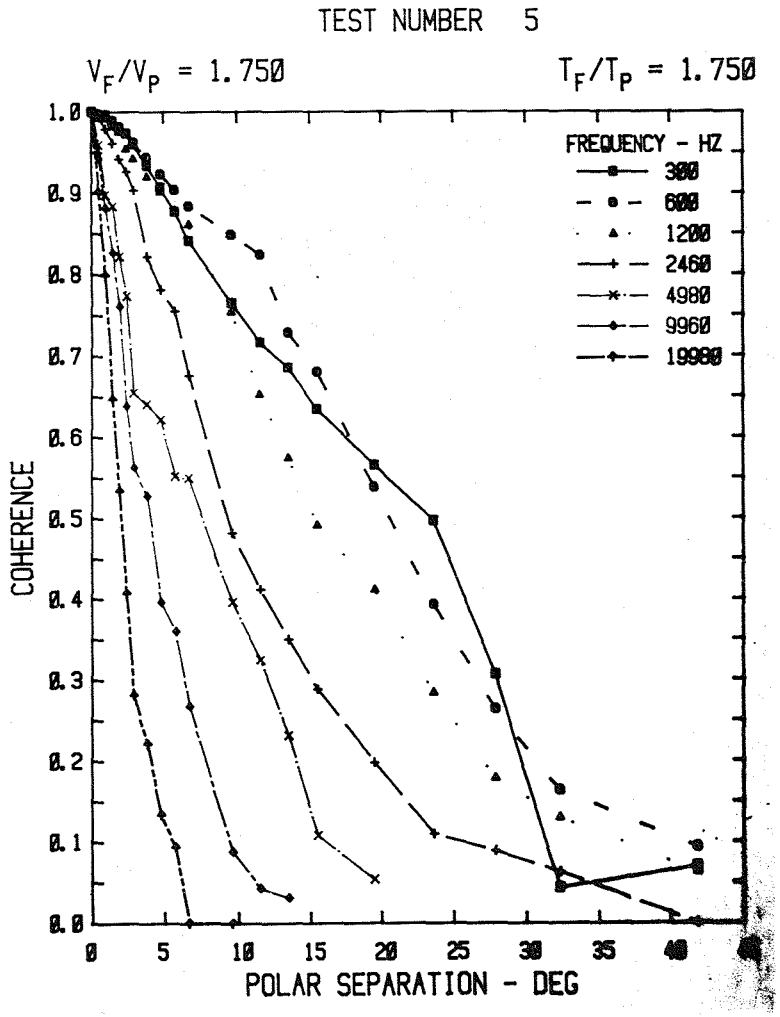

Figure A2.5(a)

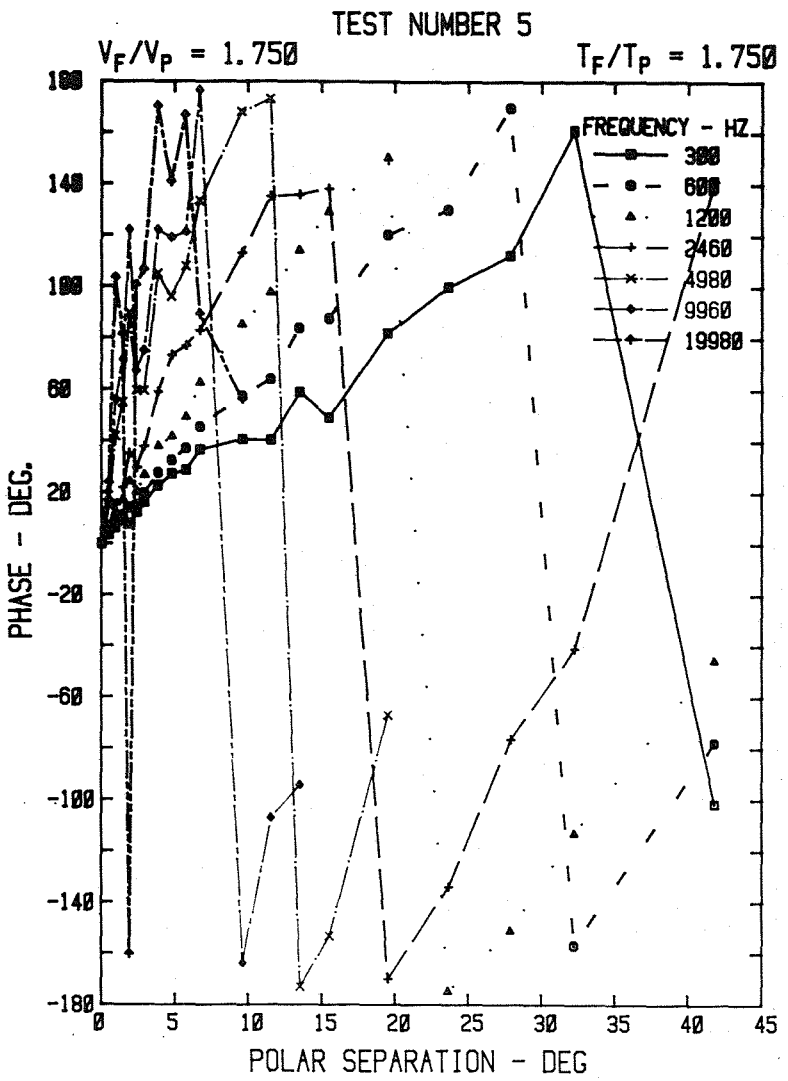

Figure A2.5(b)

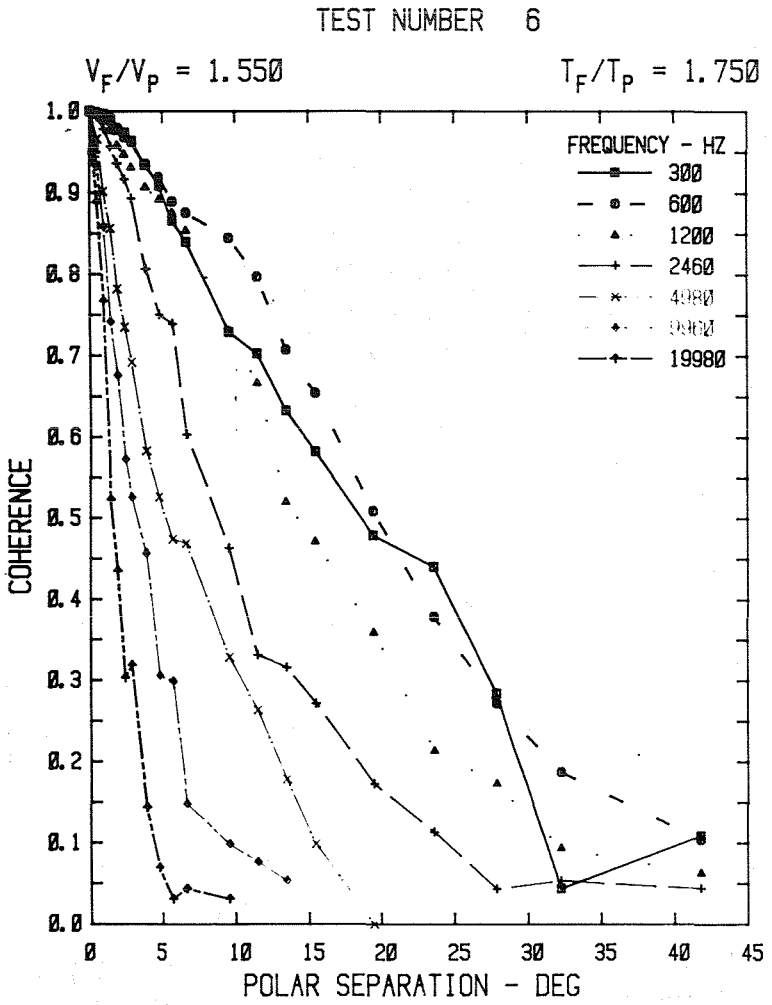

Figure A2.6(a)

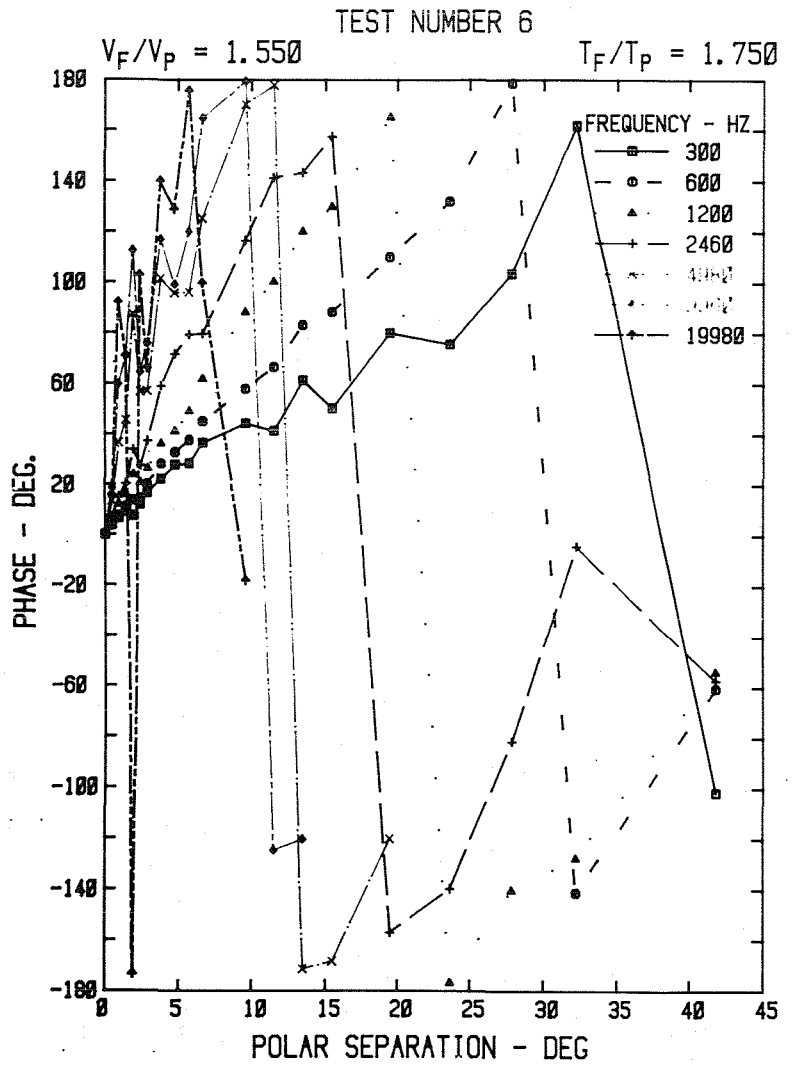

Figure A2.6(b)

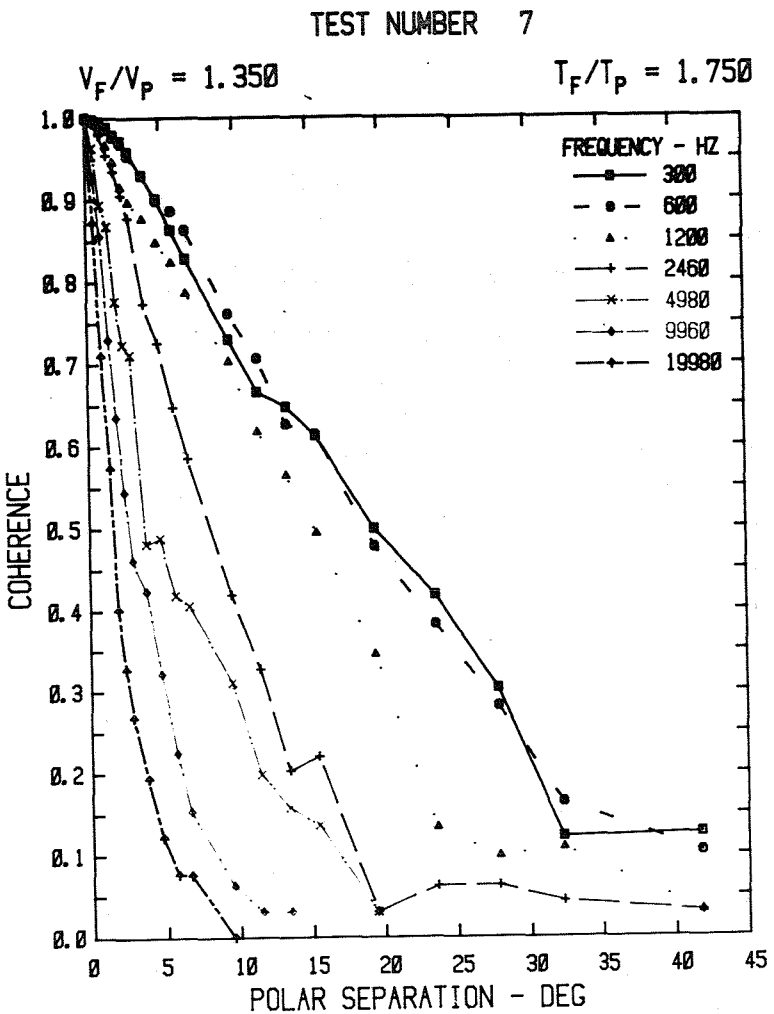

Figure A2.7(a)

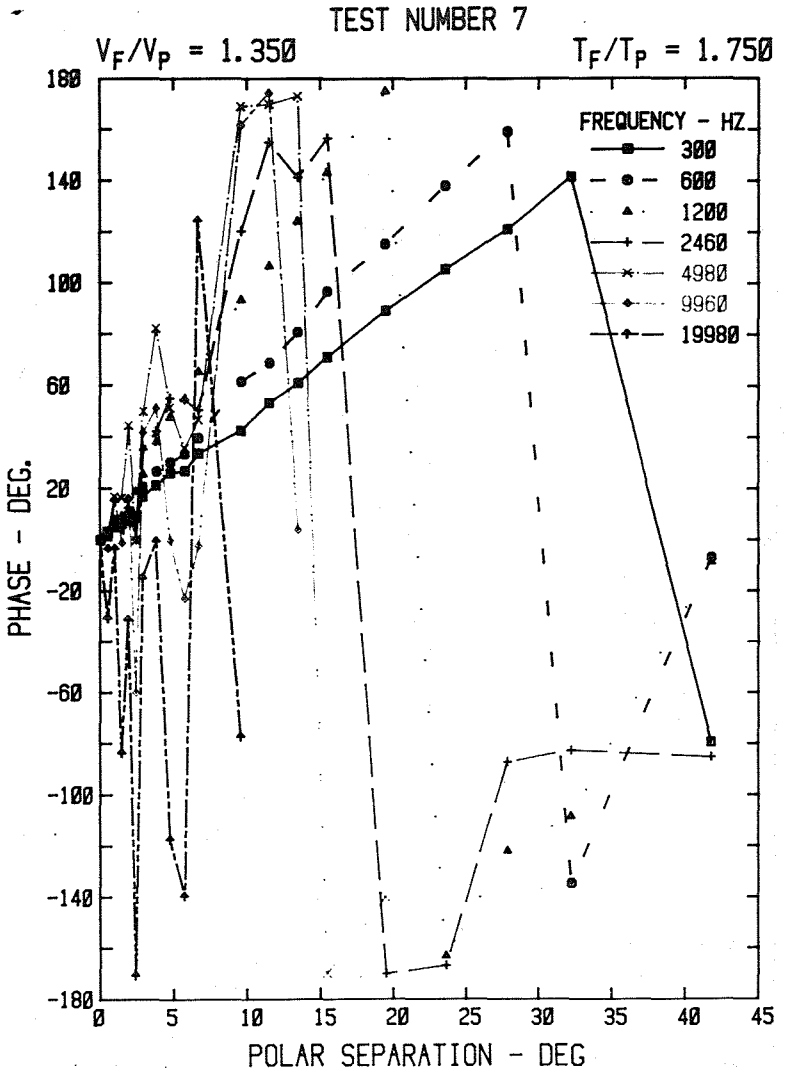

Figure A2.7(b)

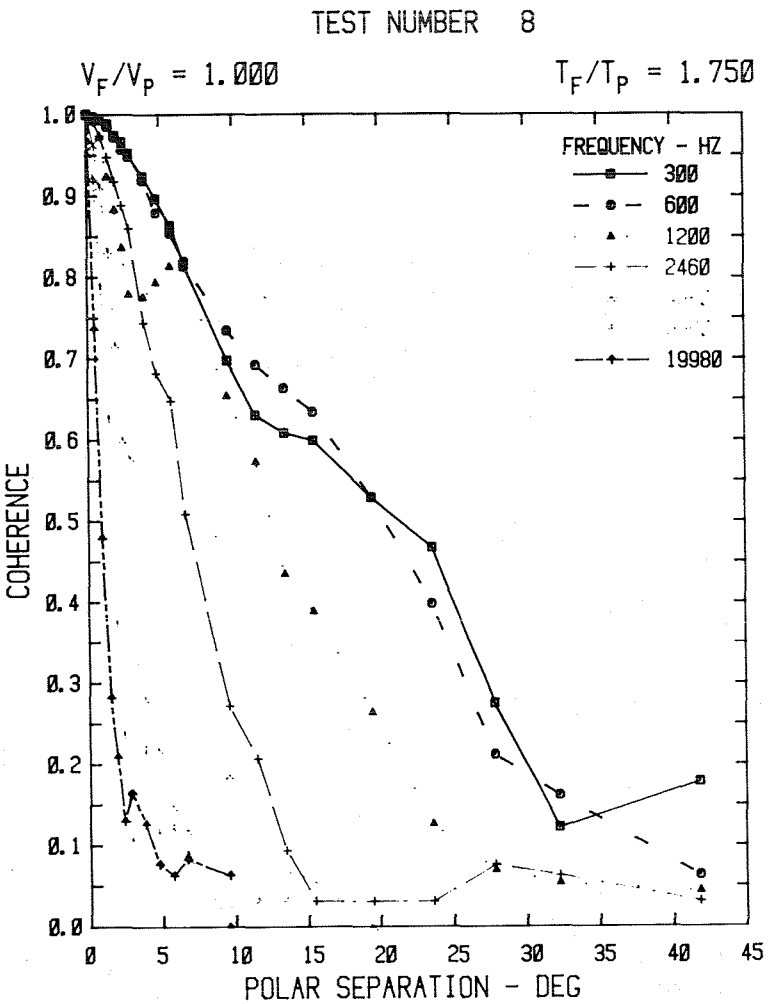

Figure A2.8(a)

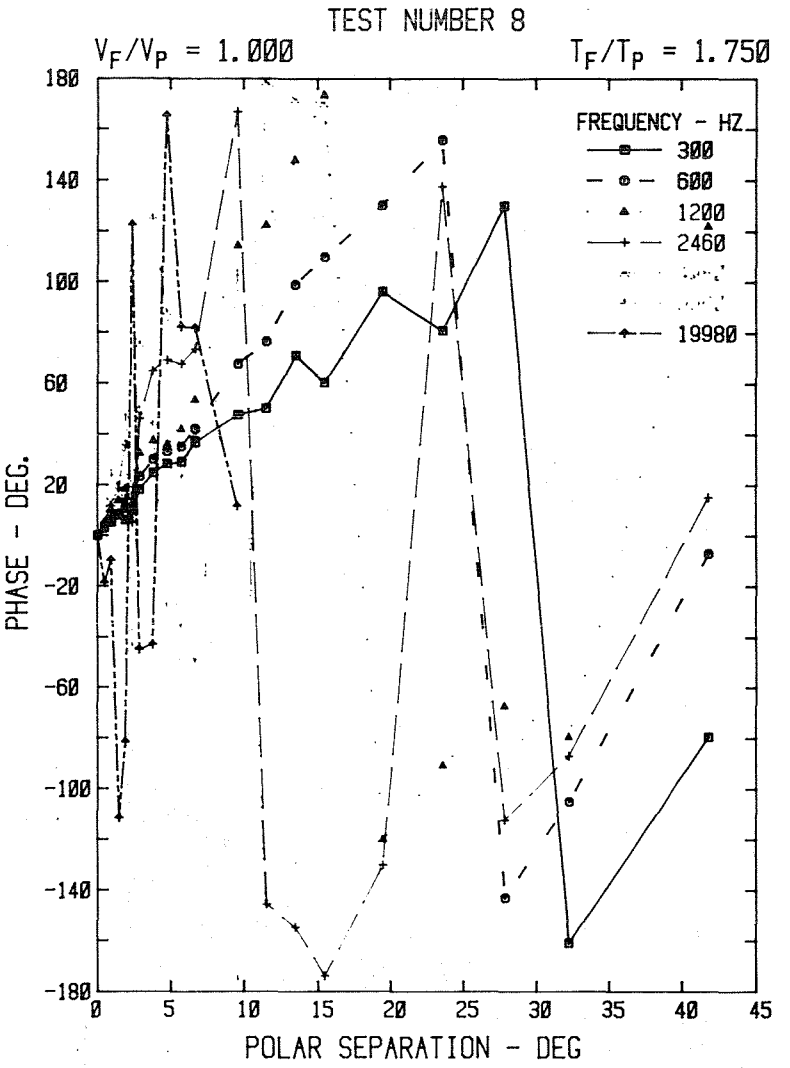

Figure A2.8(b)

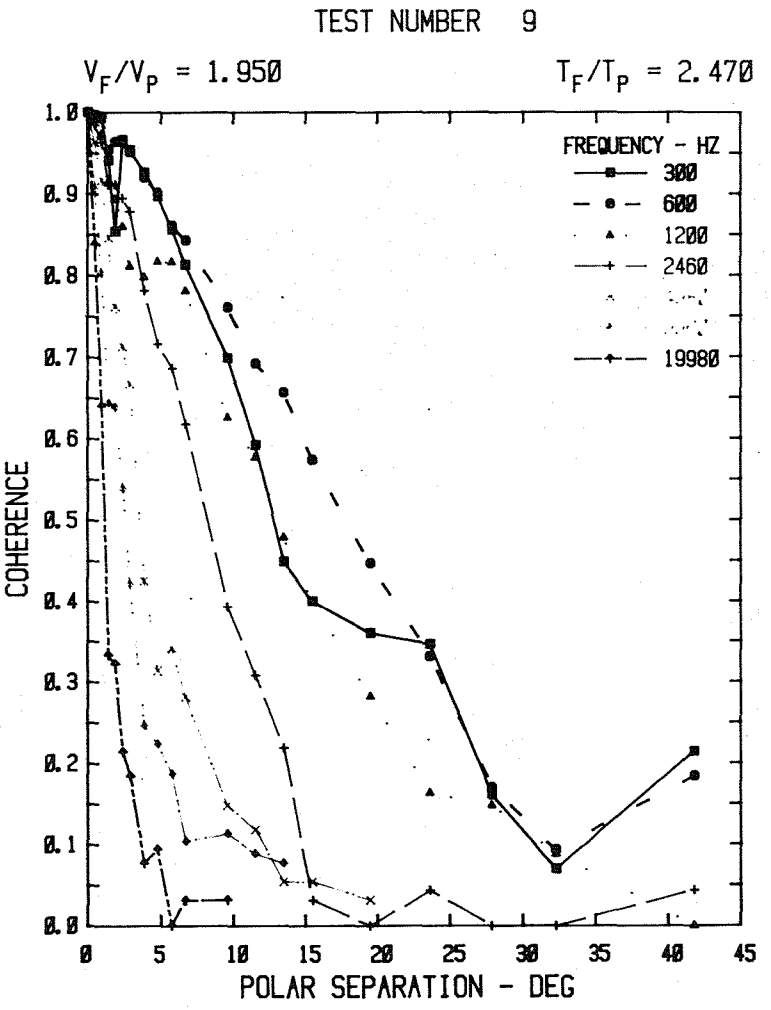

Figure A2.9(a)

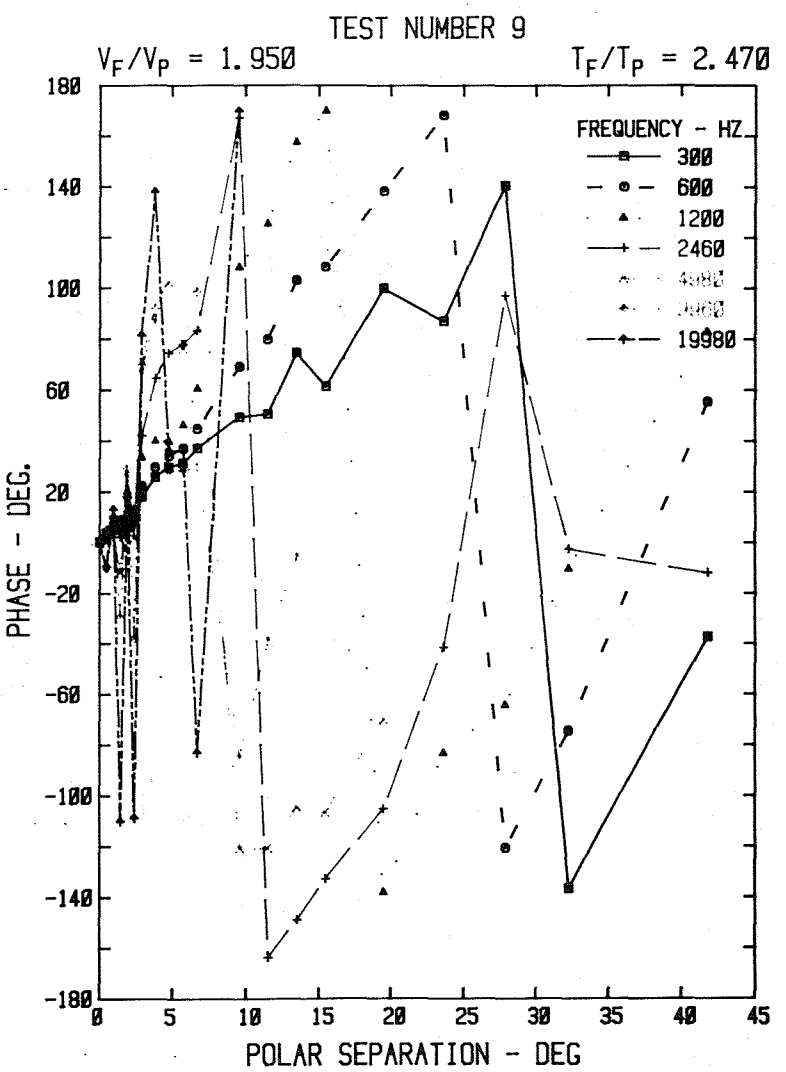

Figure A2.9(b)

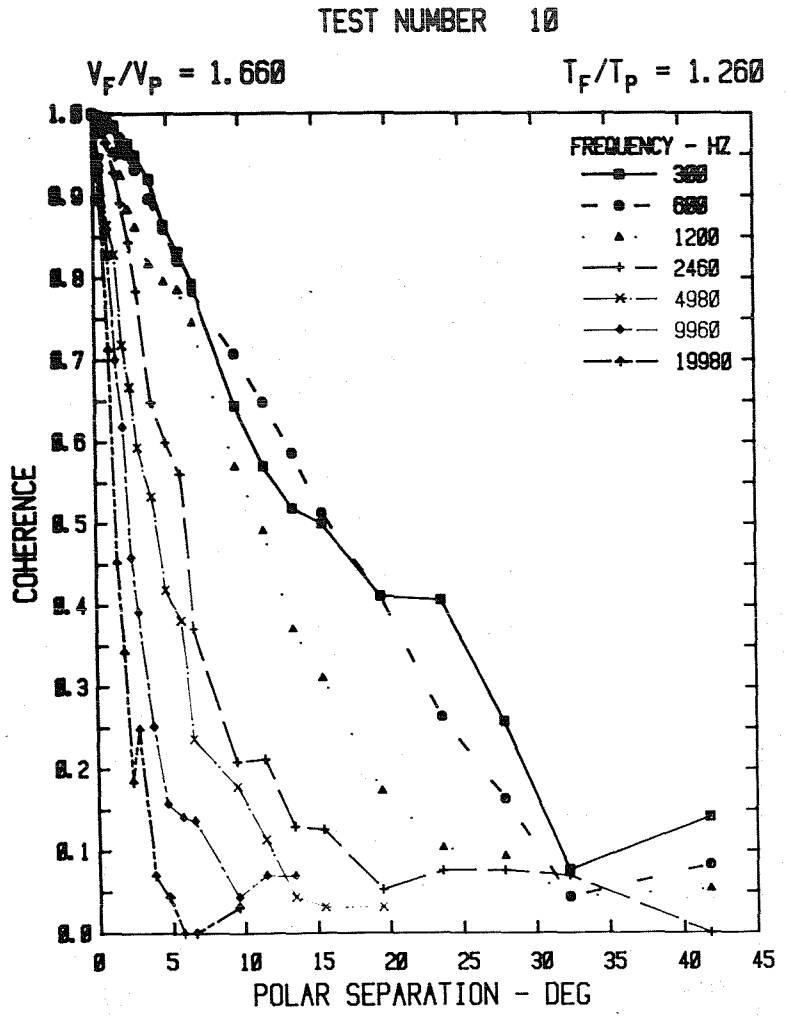

Figure A2.10(a)

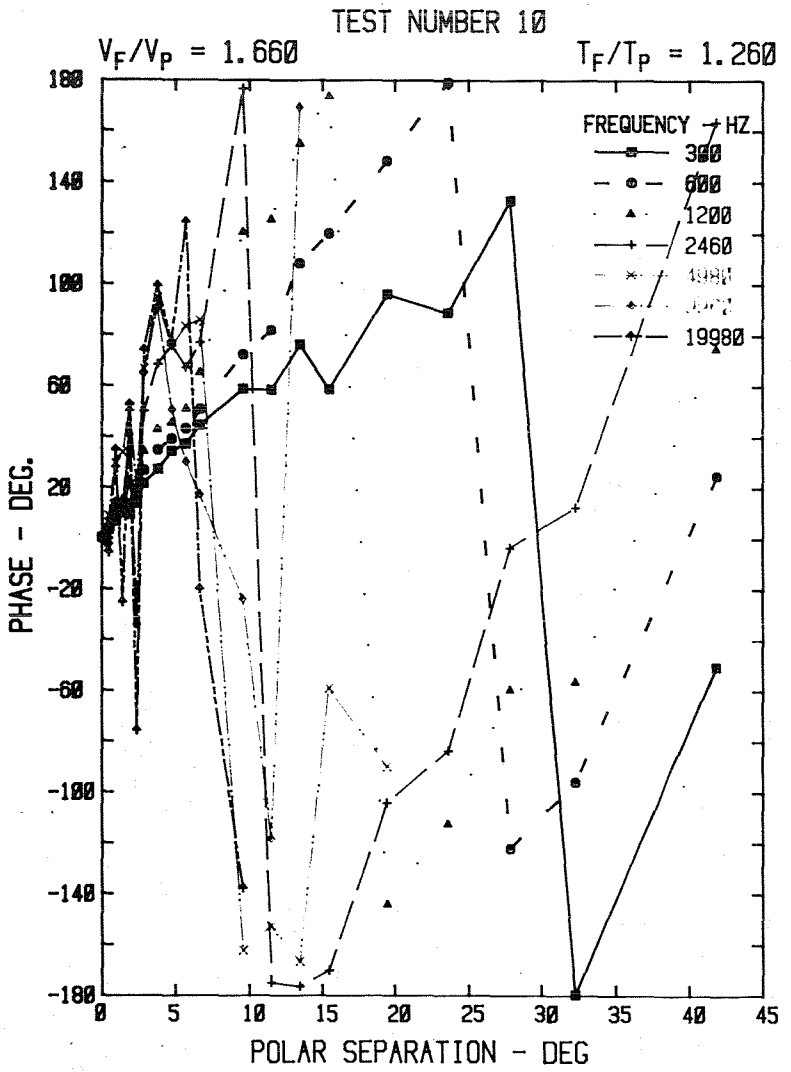

Figure A2.10(b)

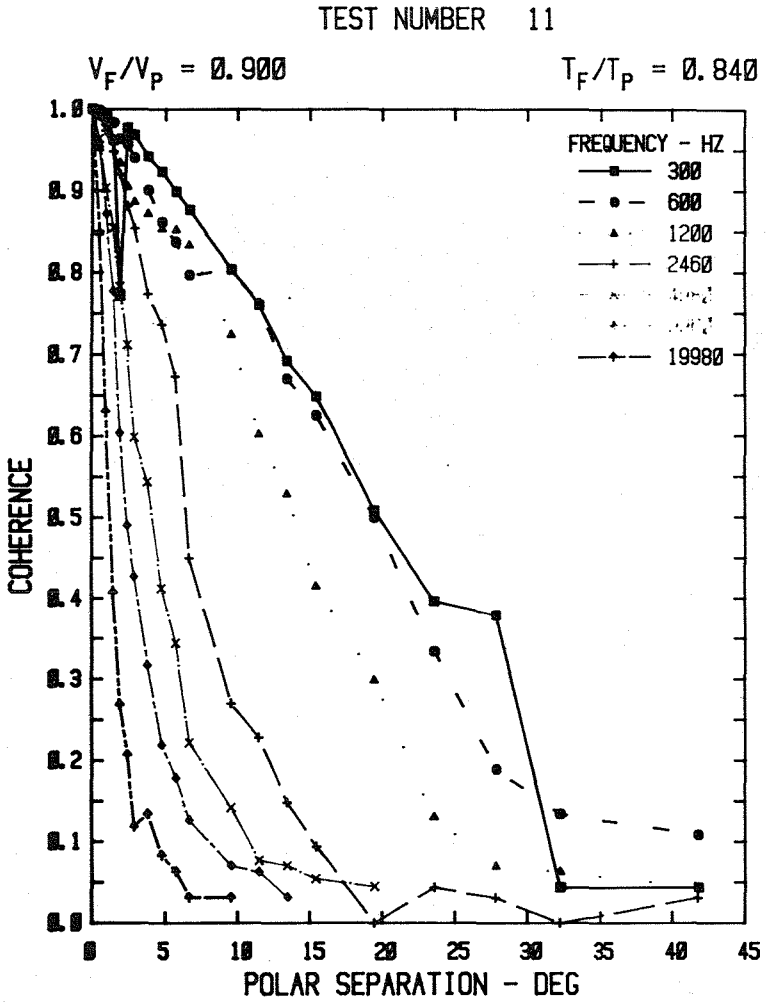

Figure A2.11(a)

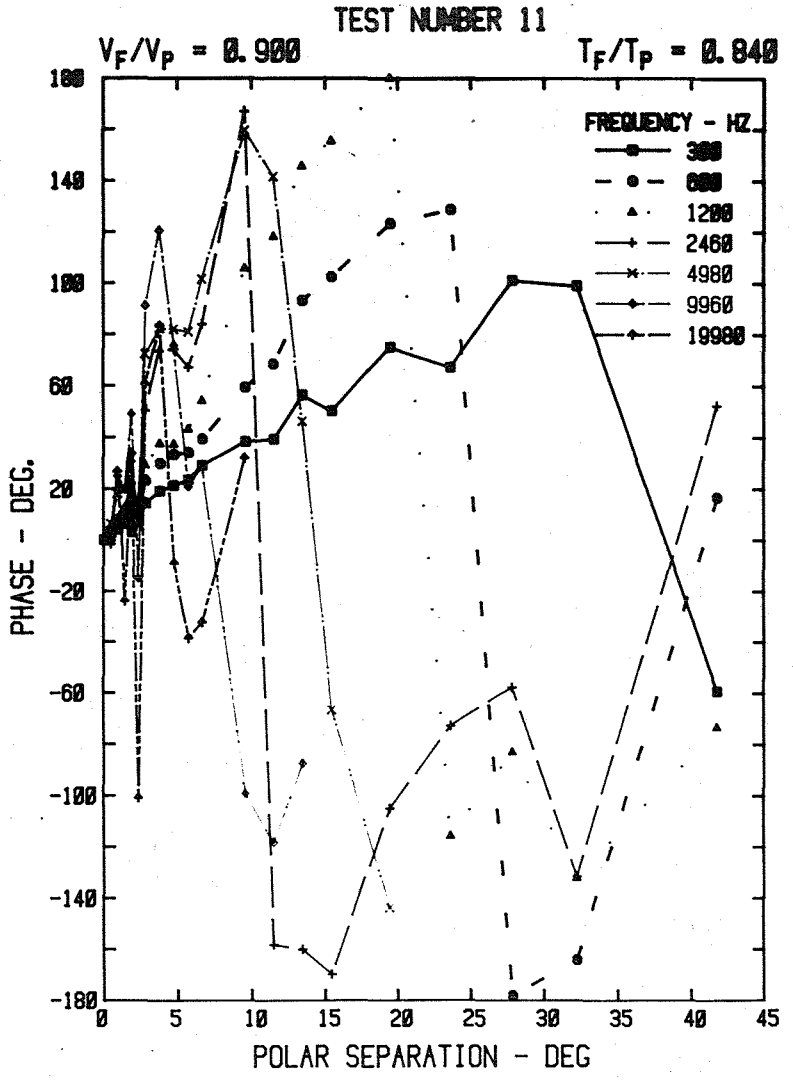

Figure A2.11(b)

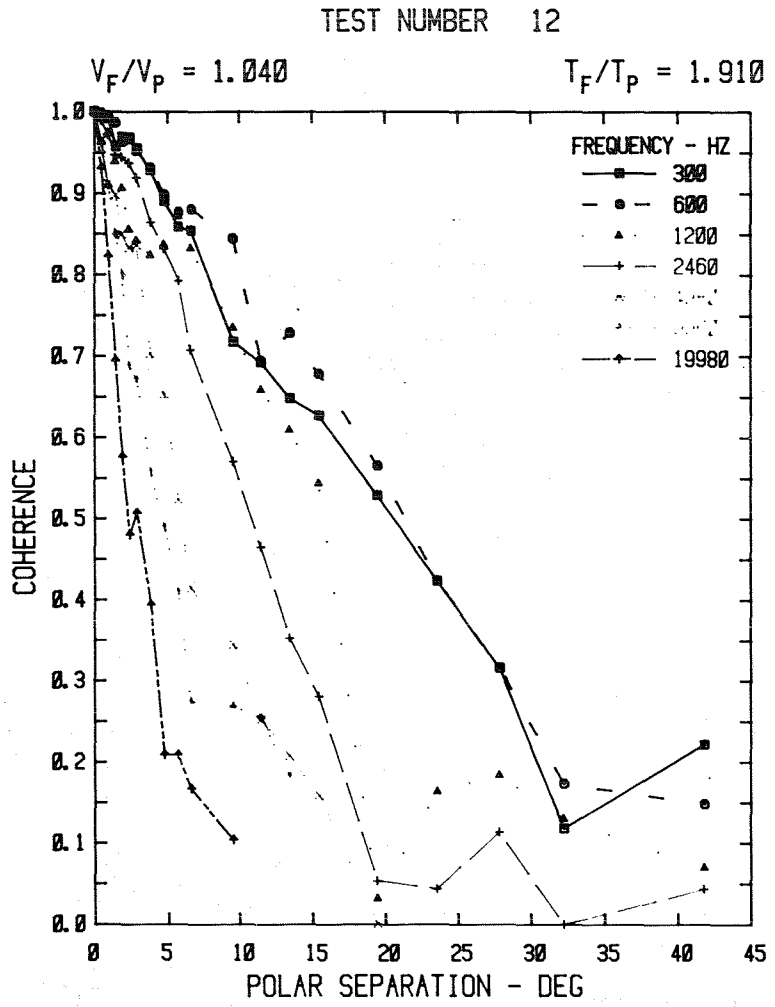

Figure A2.12(a)

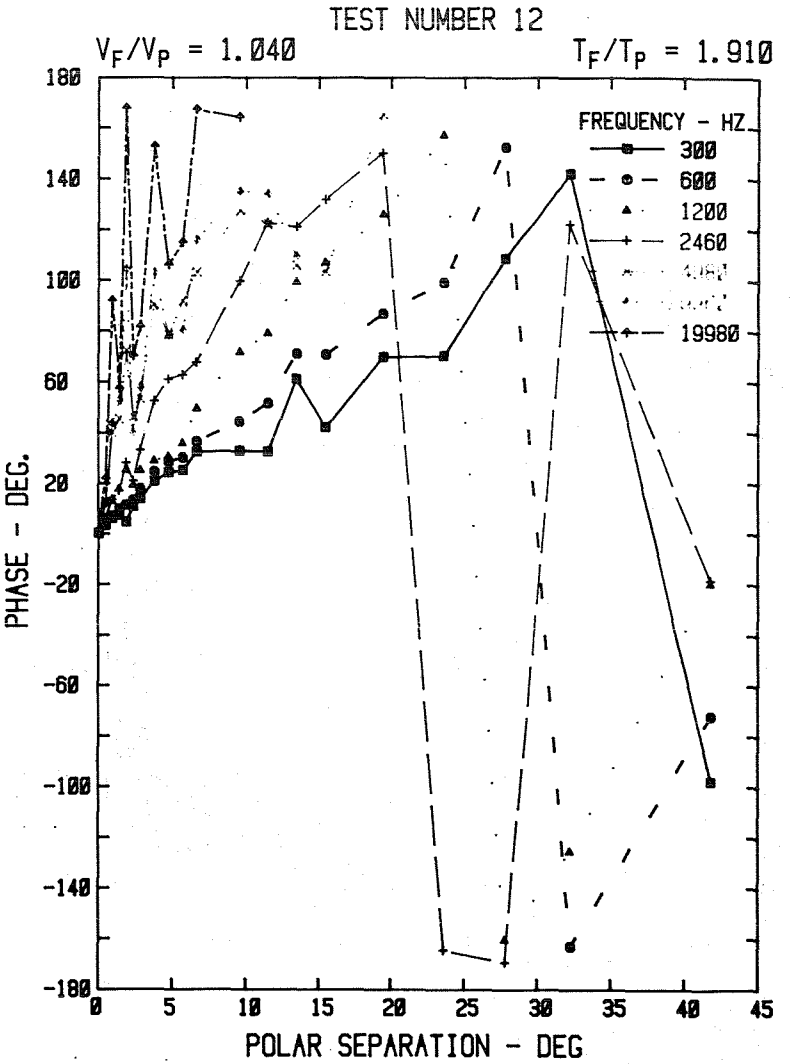

Figure A2.12(b)

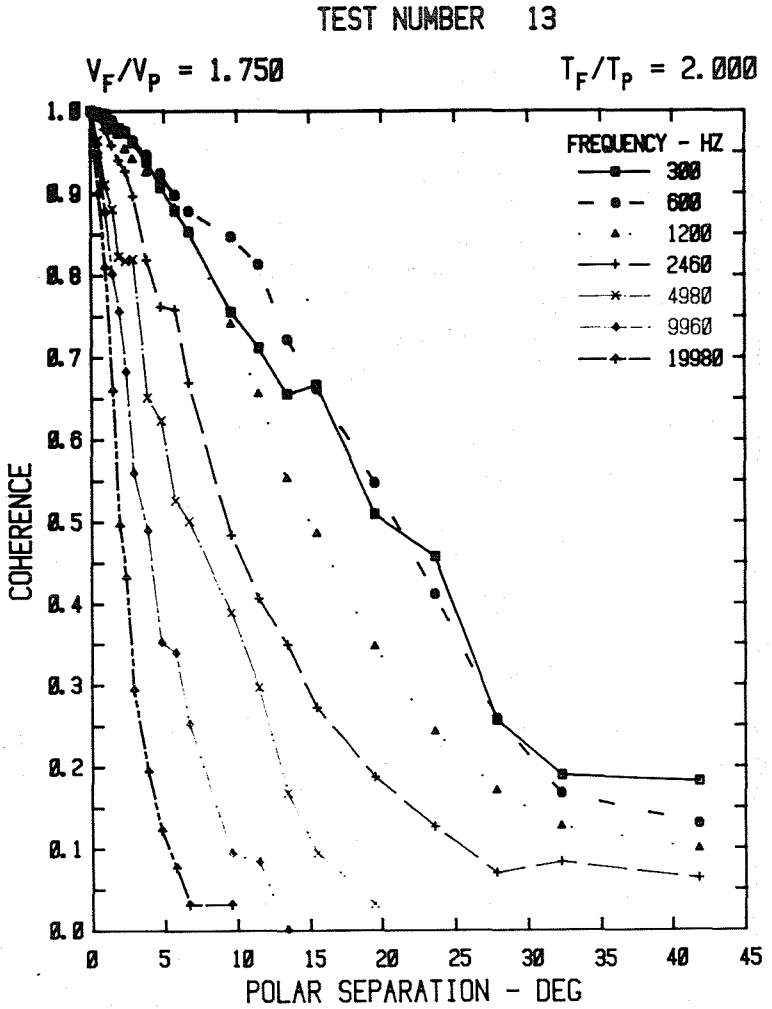

Figure A2.13(a)

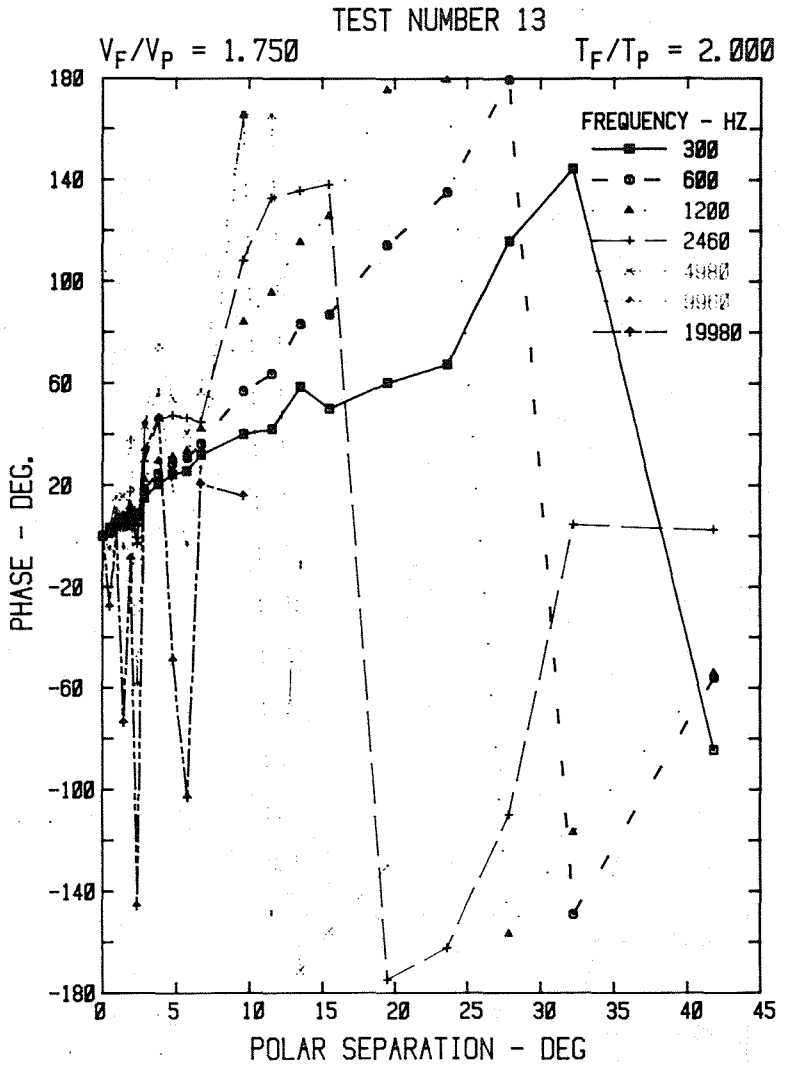

Figure A2.13(b)

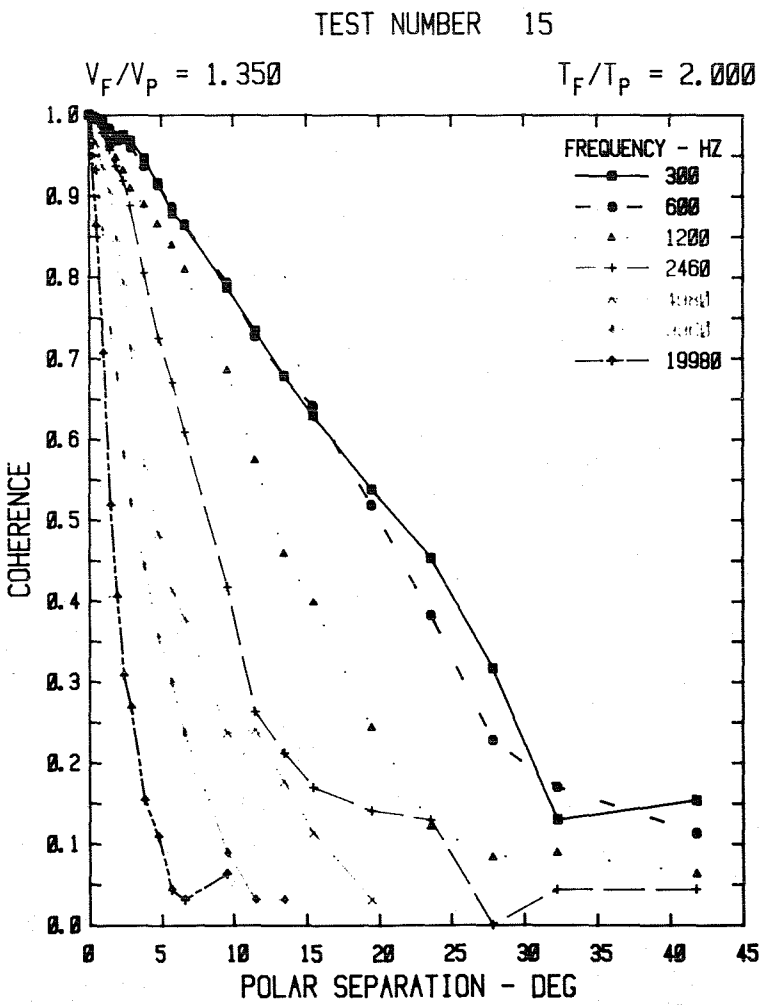

Figure A2.14(a)

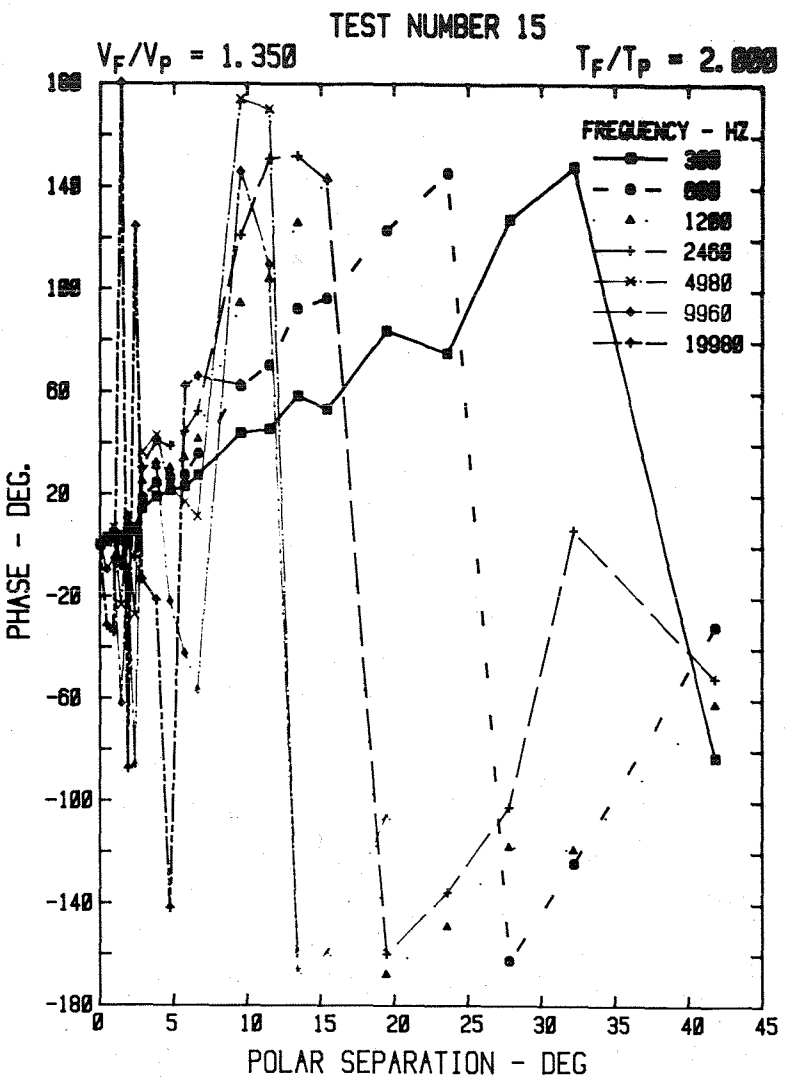

Figure A2.14(b)

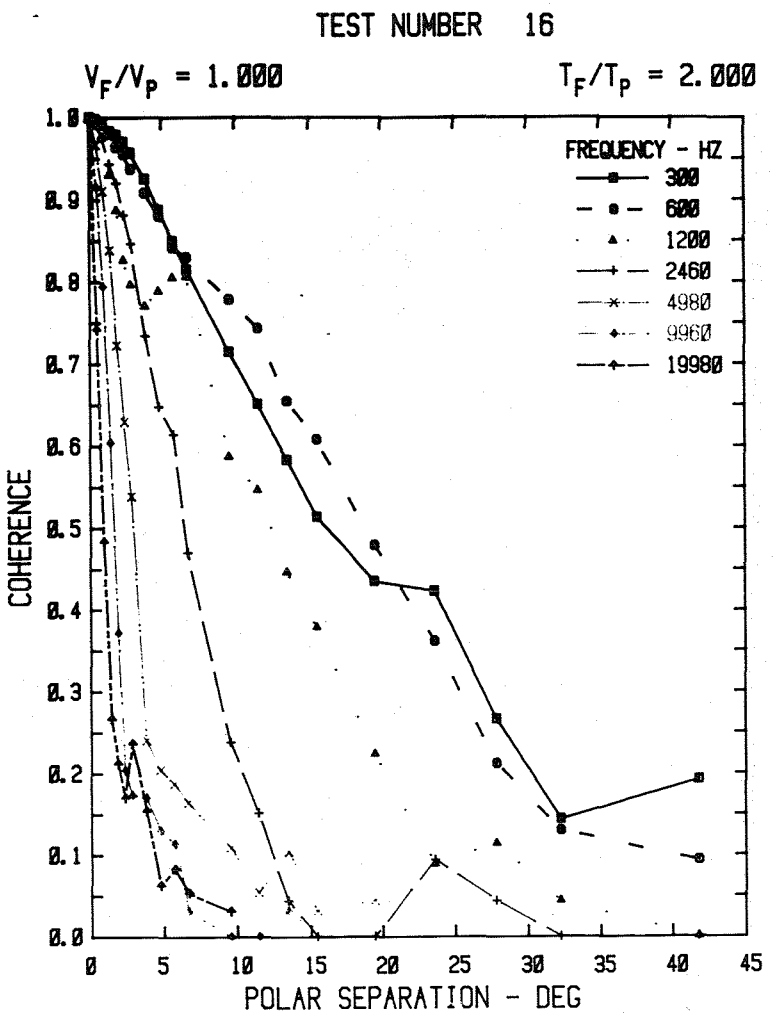

Figure A2.15(a)

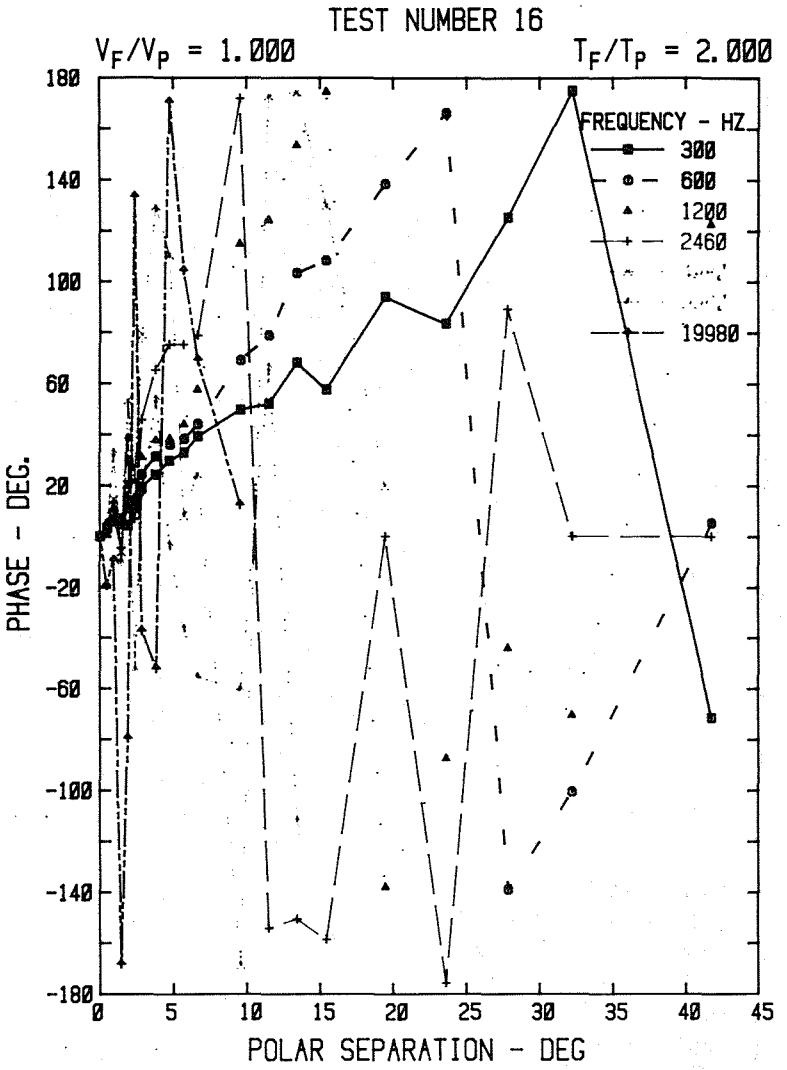

Figure A2.15(b)

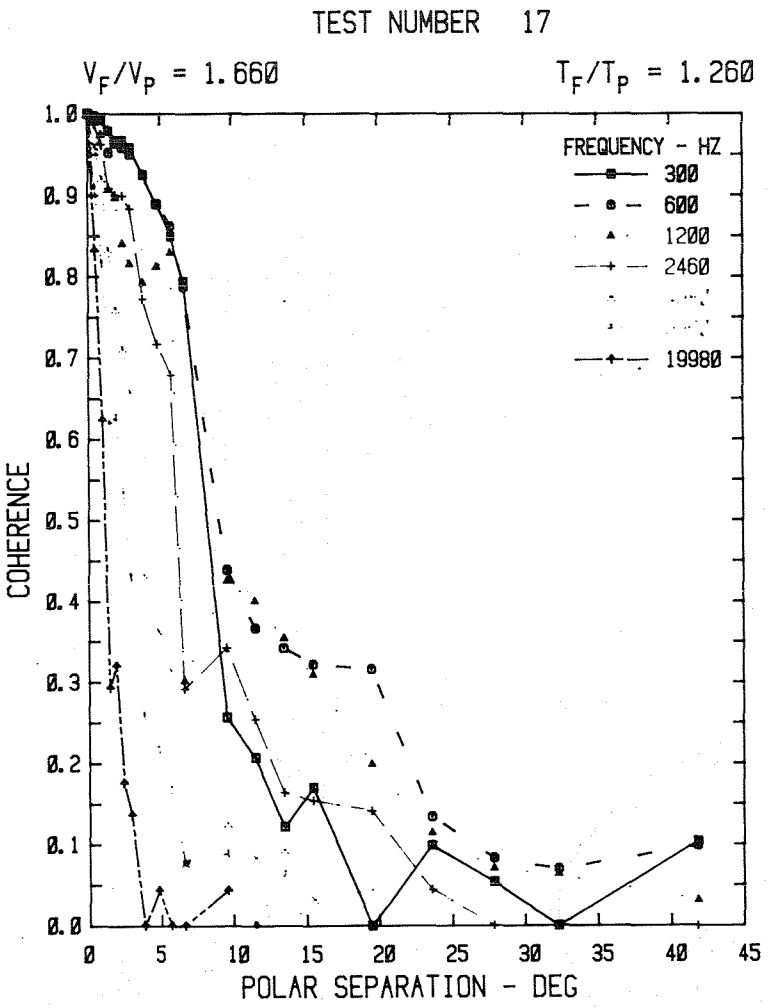

Figure A2.16(a)

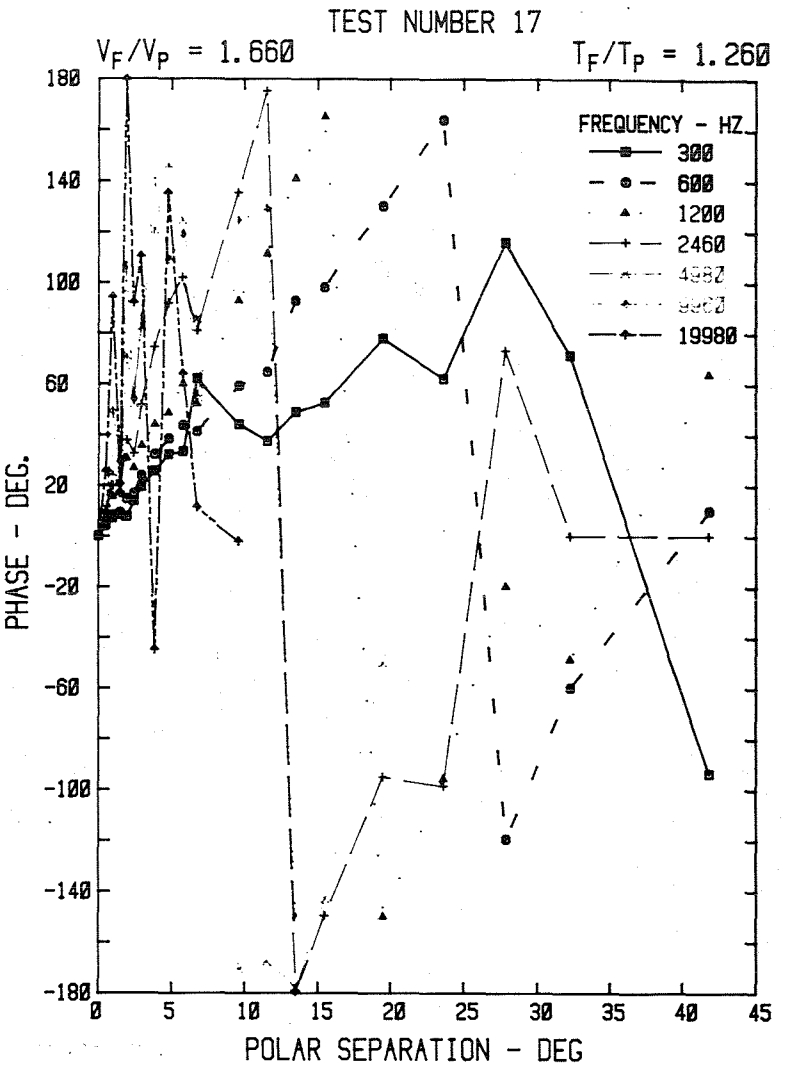

Figure A2.16(b)

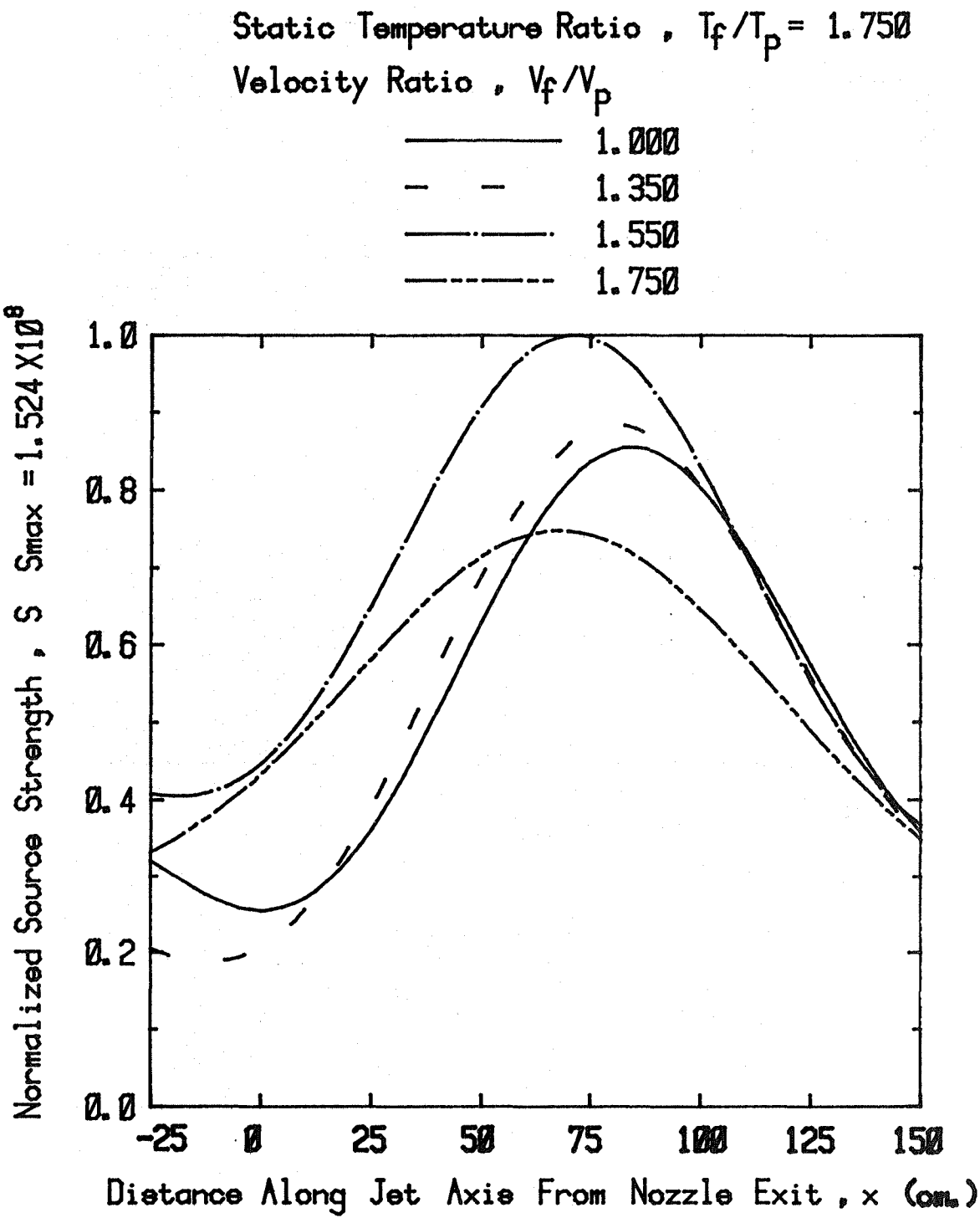

Coannular Jet - Source Distribution
(Frequency = 0.30 KHz)

Figure A2.17(a)

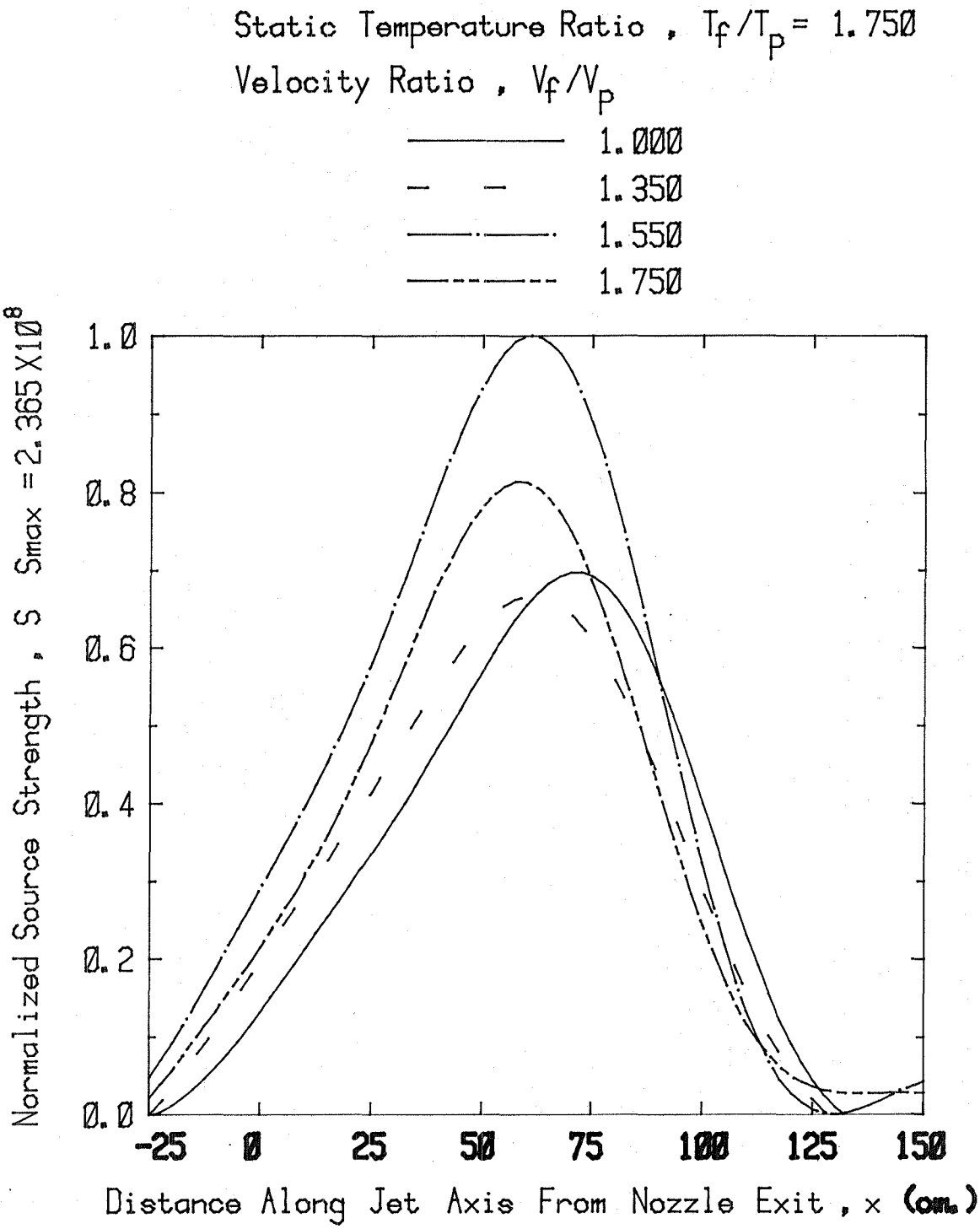

Coannular Jet - Source Distribution
(Frequency = 0.60 KHz)

Figure A2.17(b)

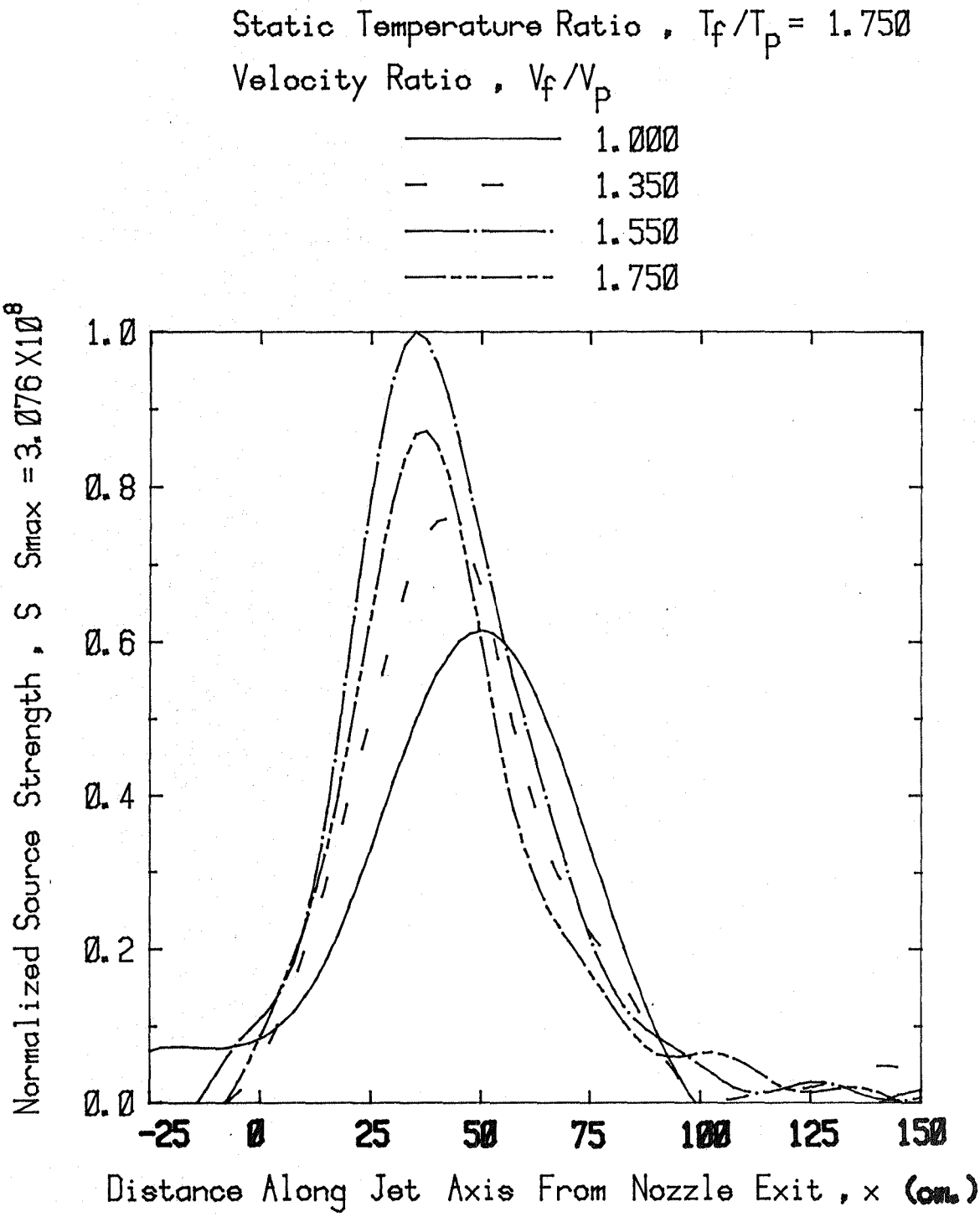

Coannular Jet - Source Distribution
(Frequency = 1.20 KHz)

Figure A2.17(c)

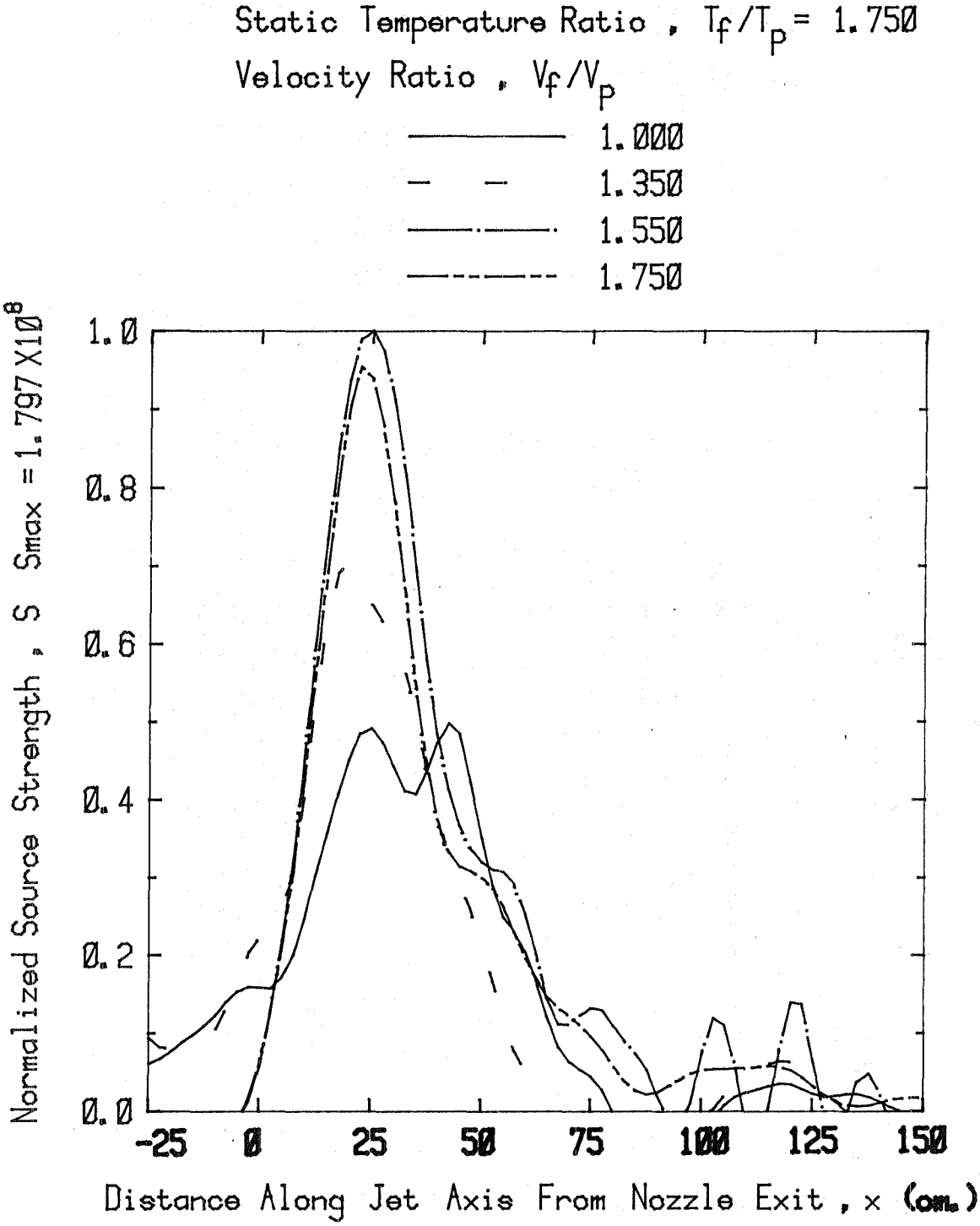

Coannular Jet - Source Distribution
(Frequency = 2.46 KHz)

Figure A2.17(d)

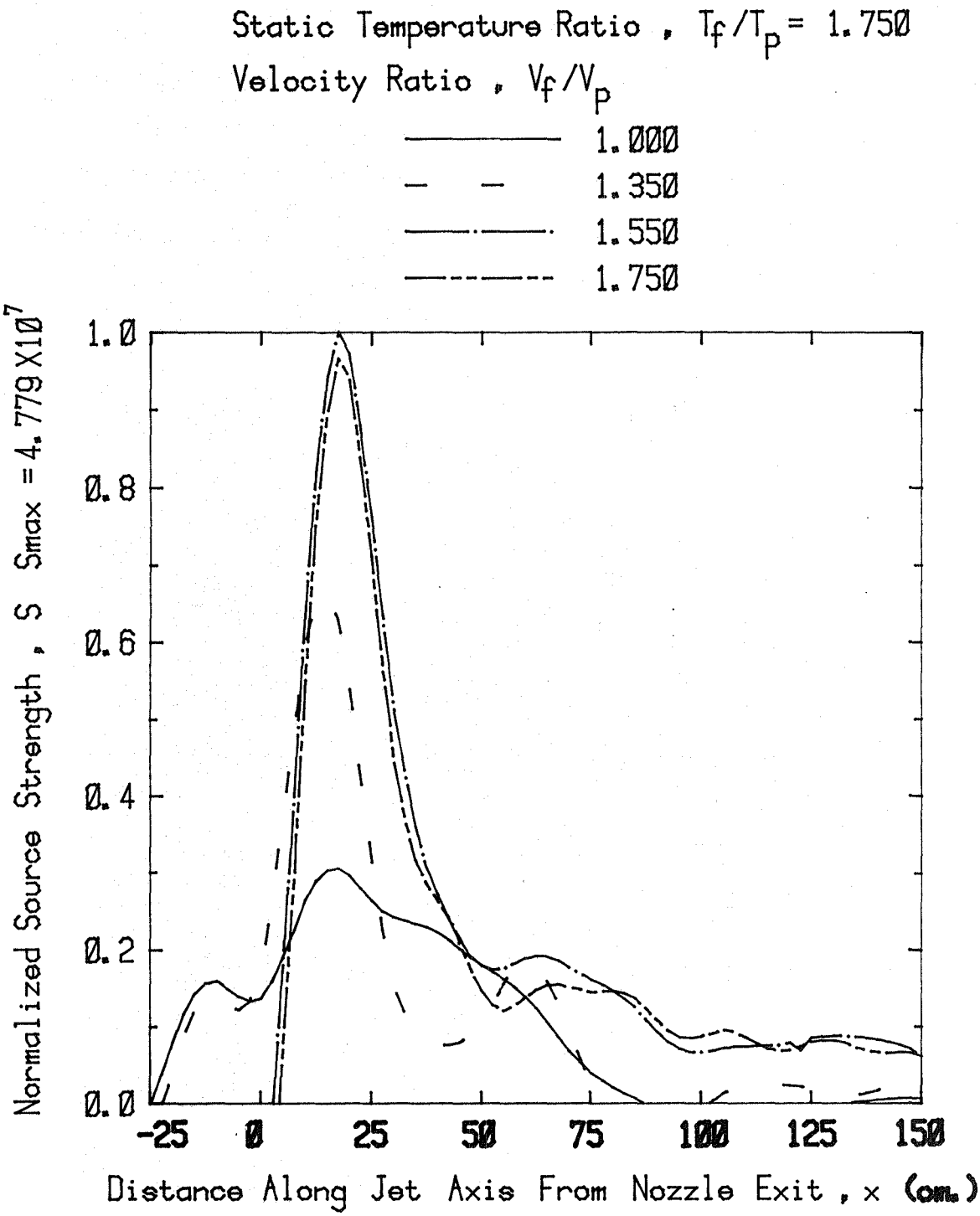

Coannular Jet - Source Distribution
(Frequency = 4.98 KHz)

Figure A2.17(e)

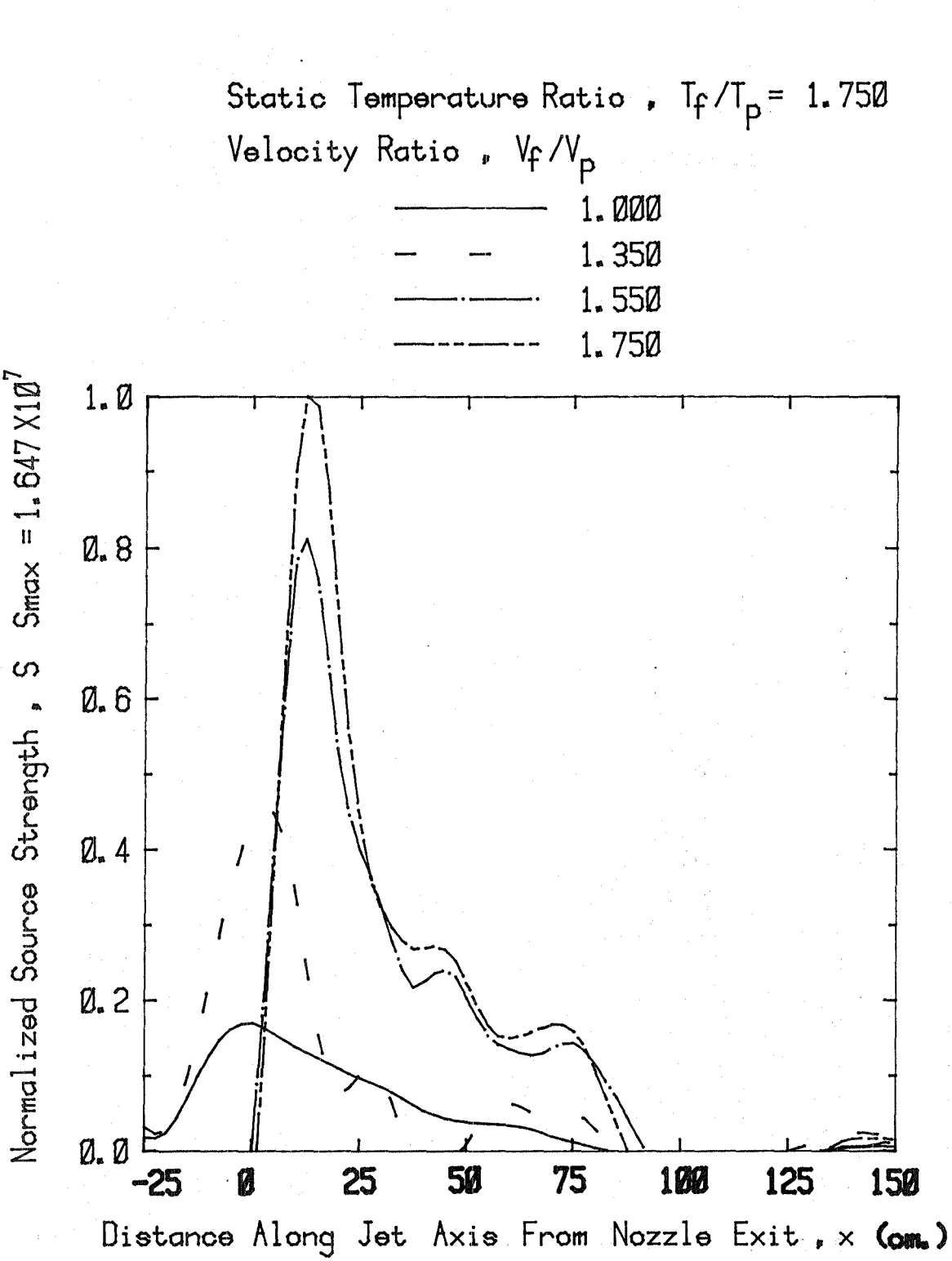

Coannular Jet - Source Distribution
(Frequency = 9.96 KHz)

Figure A2.17(f)

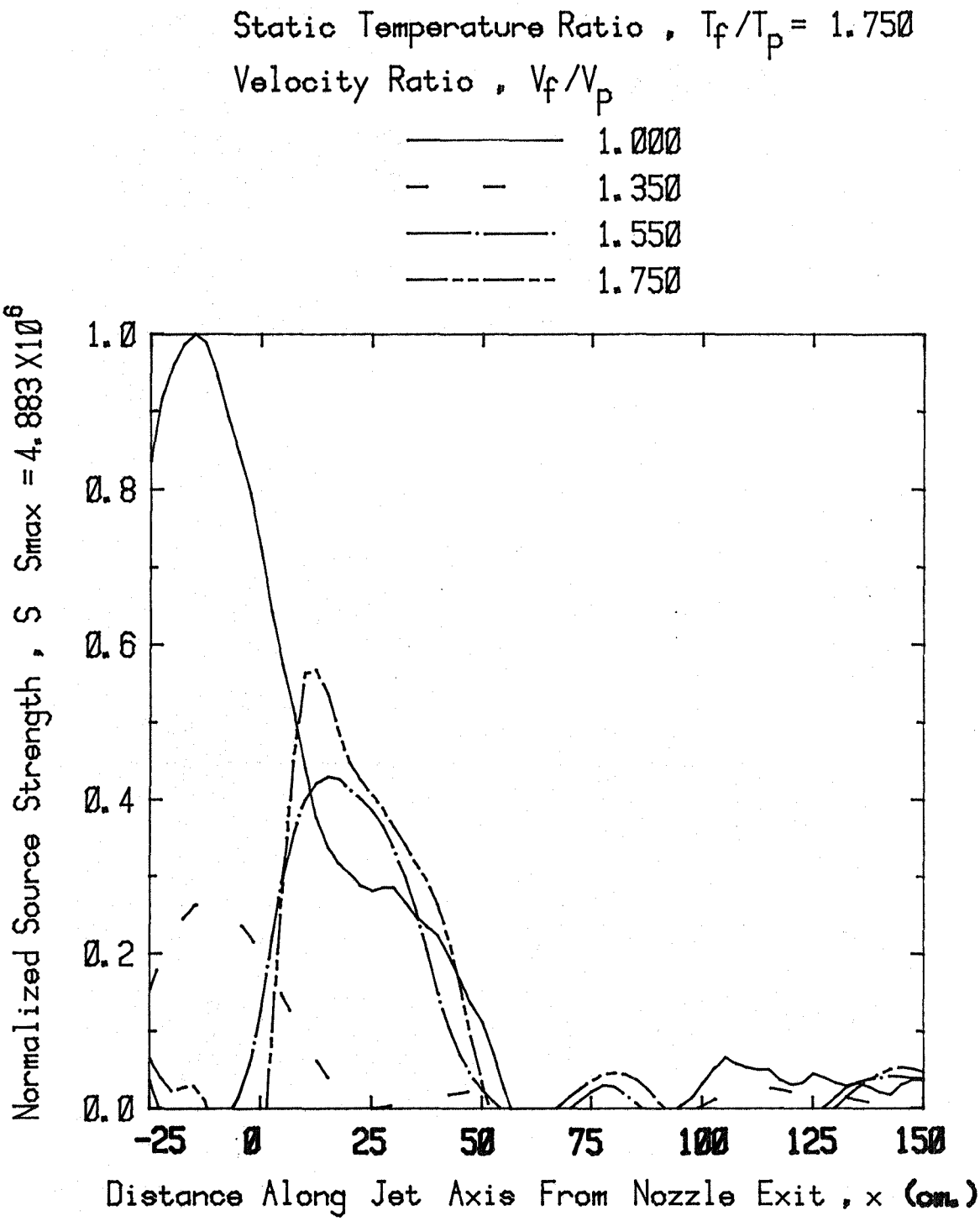

Coannular Jet - Source Distribution
(Frequency = 19.98 KHz)

Figure A2.17(g)

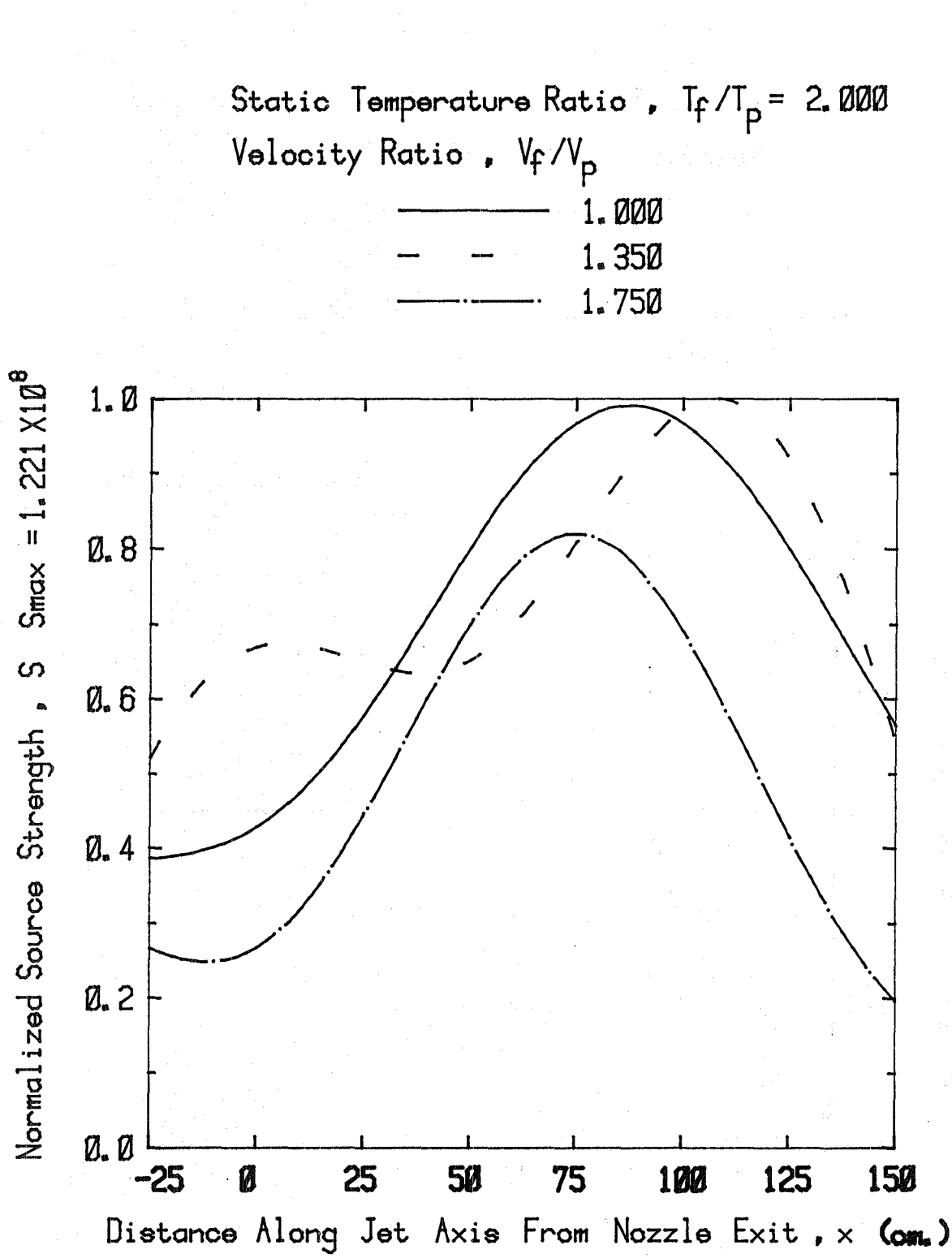

Coannular Jet - Source Distribution
(Frequency = 0.30 KHz)

Figure A2.18(a)

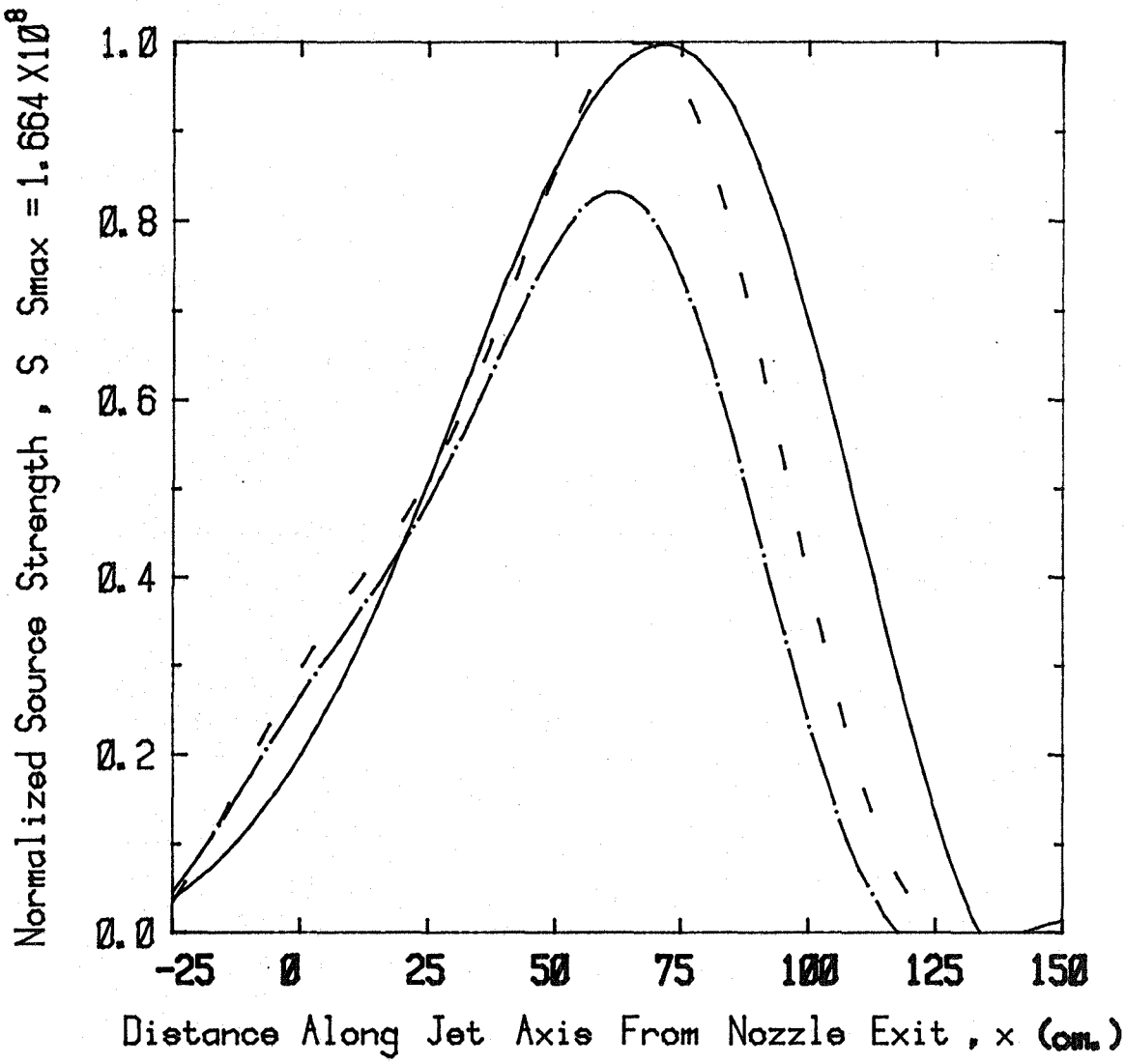

Coannular Jet - Source Distribution
(Frequency = 0.60 KHz)

Figure A2.18(b)

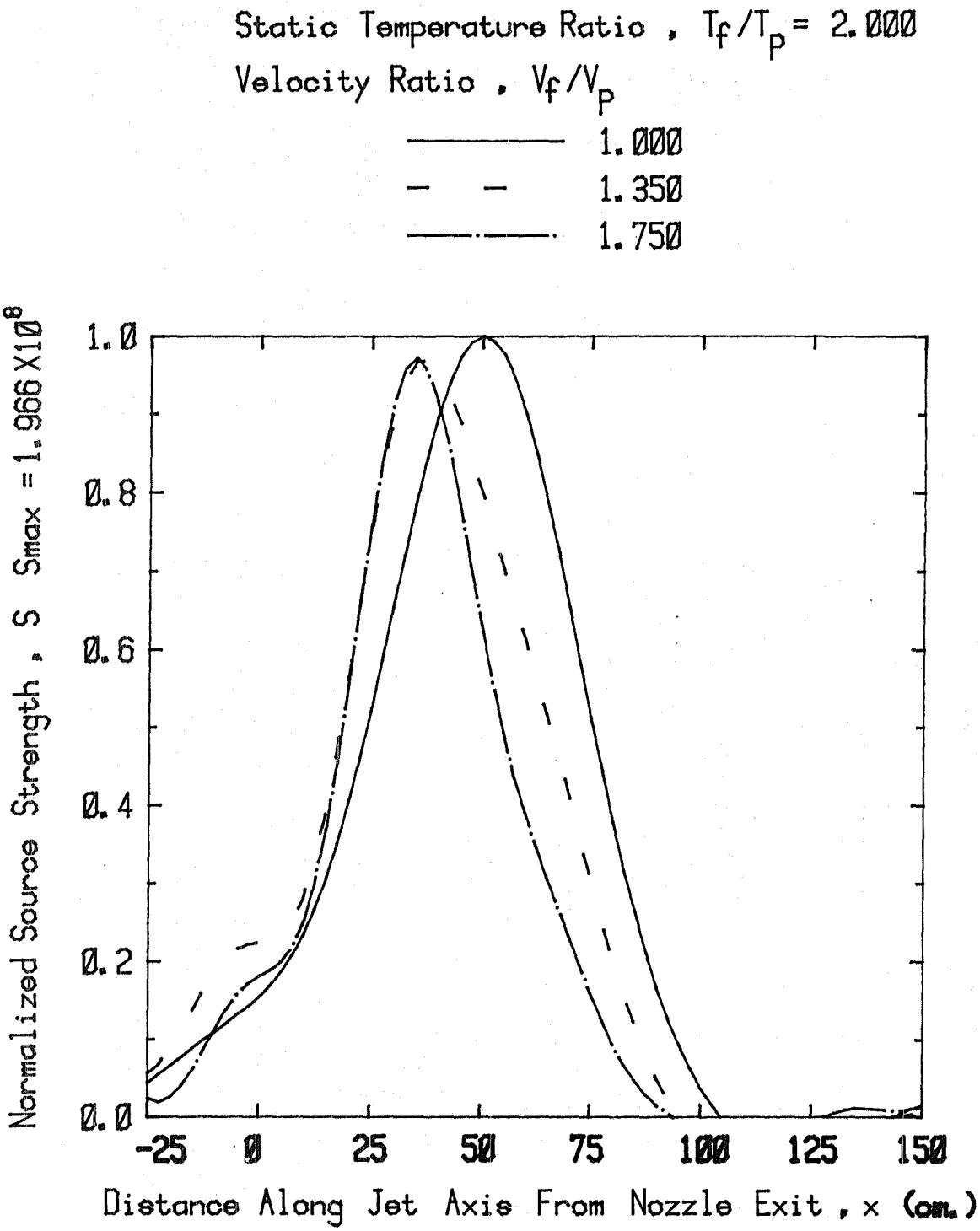

Coannular Jet - Source Distribution
(Frequency = 1.20 KHz)

Figure A2.18(c)

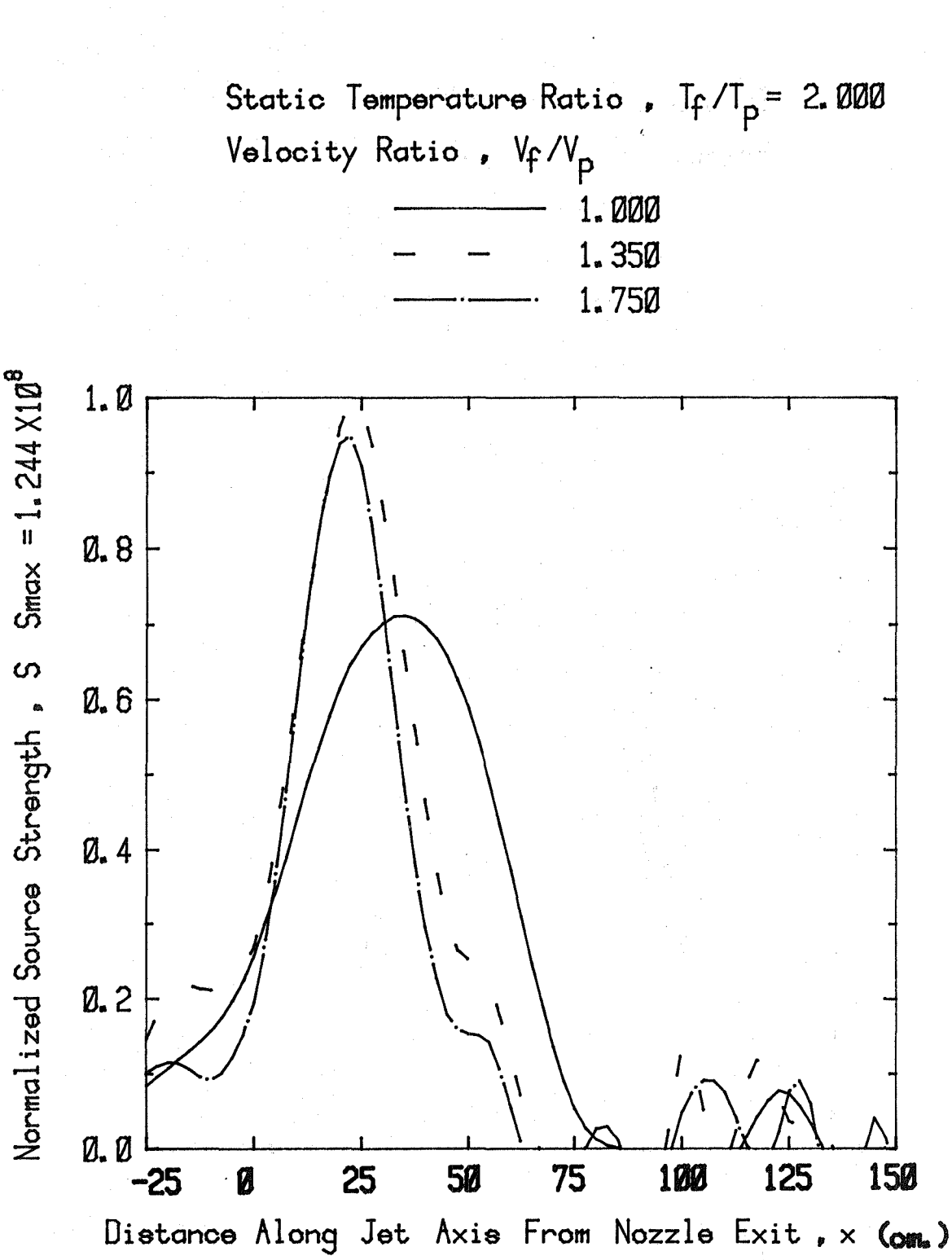

Coannular Jet - Source Distribution
(Frequency = 2.46 KHz)

Figure A2.18(d)

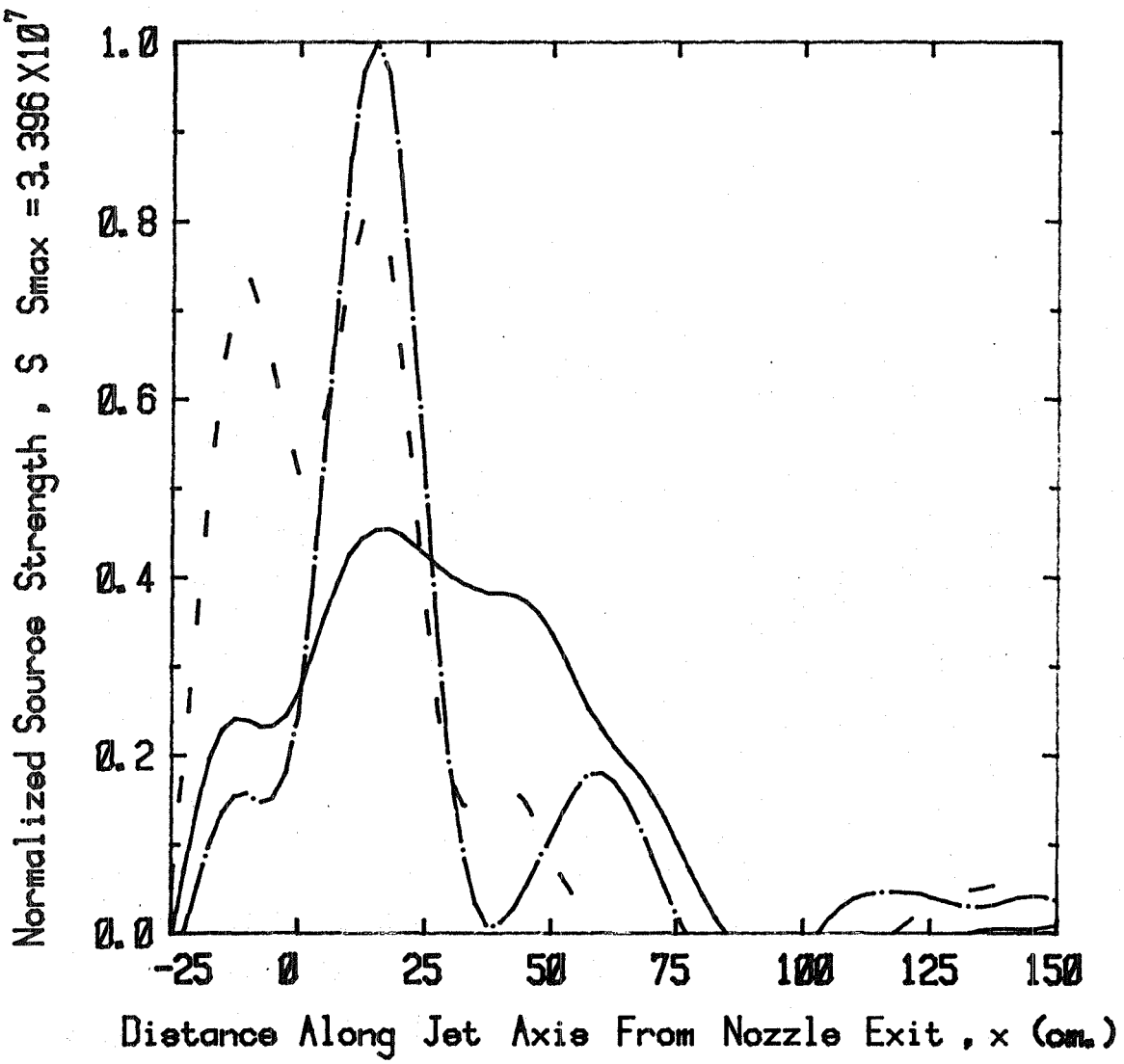

Coannular Jet - Source Distribution
(Frequency = 4.98 KHz)

Figure A2.18(e)

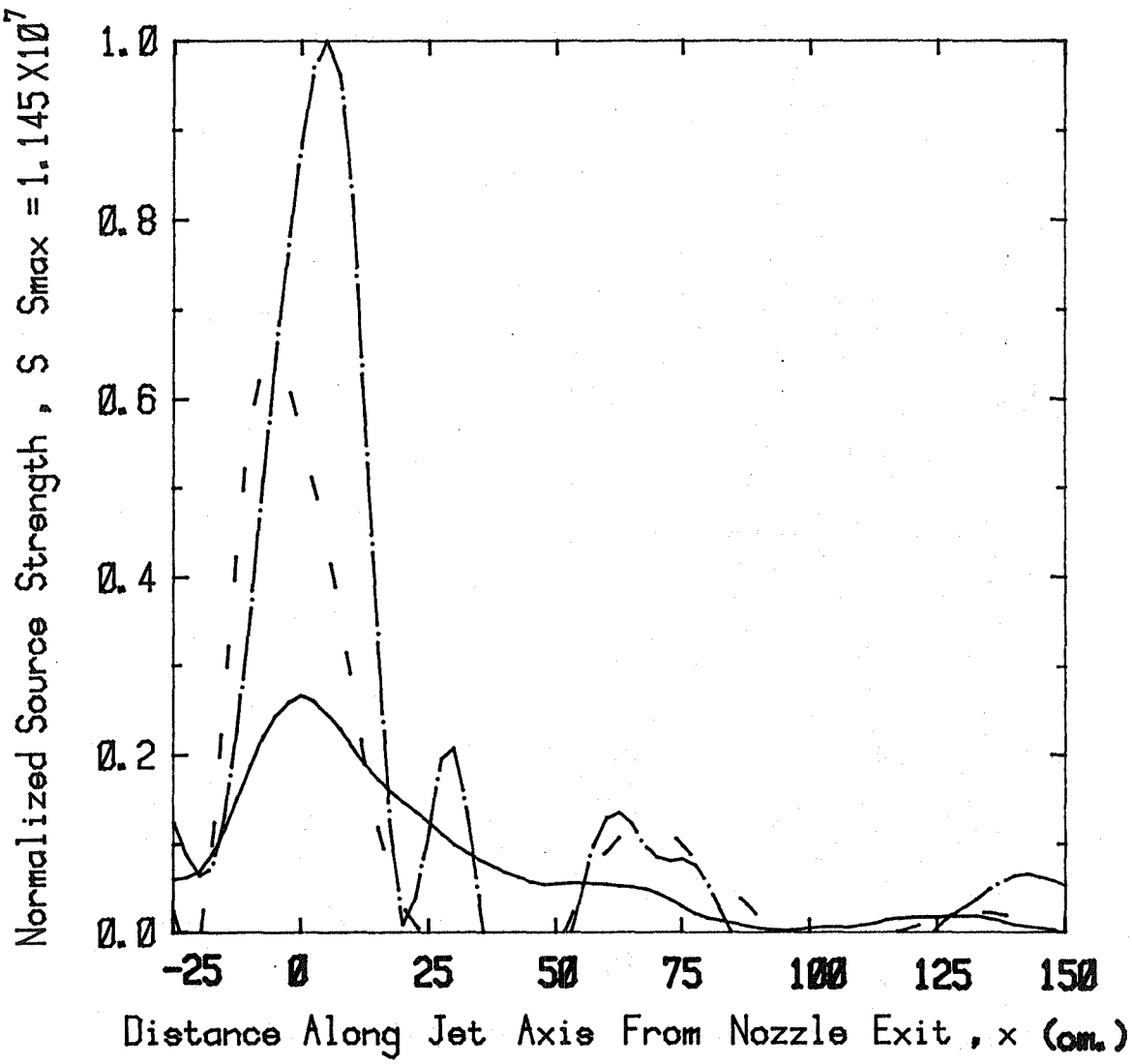

Coannular Jet - Source Distribution
(Frequency = 9.96 KHz)

Figure A2.18(f)

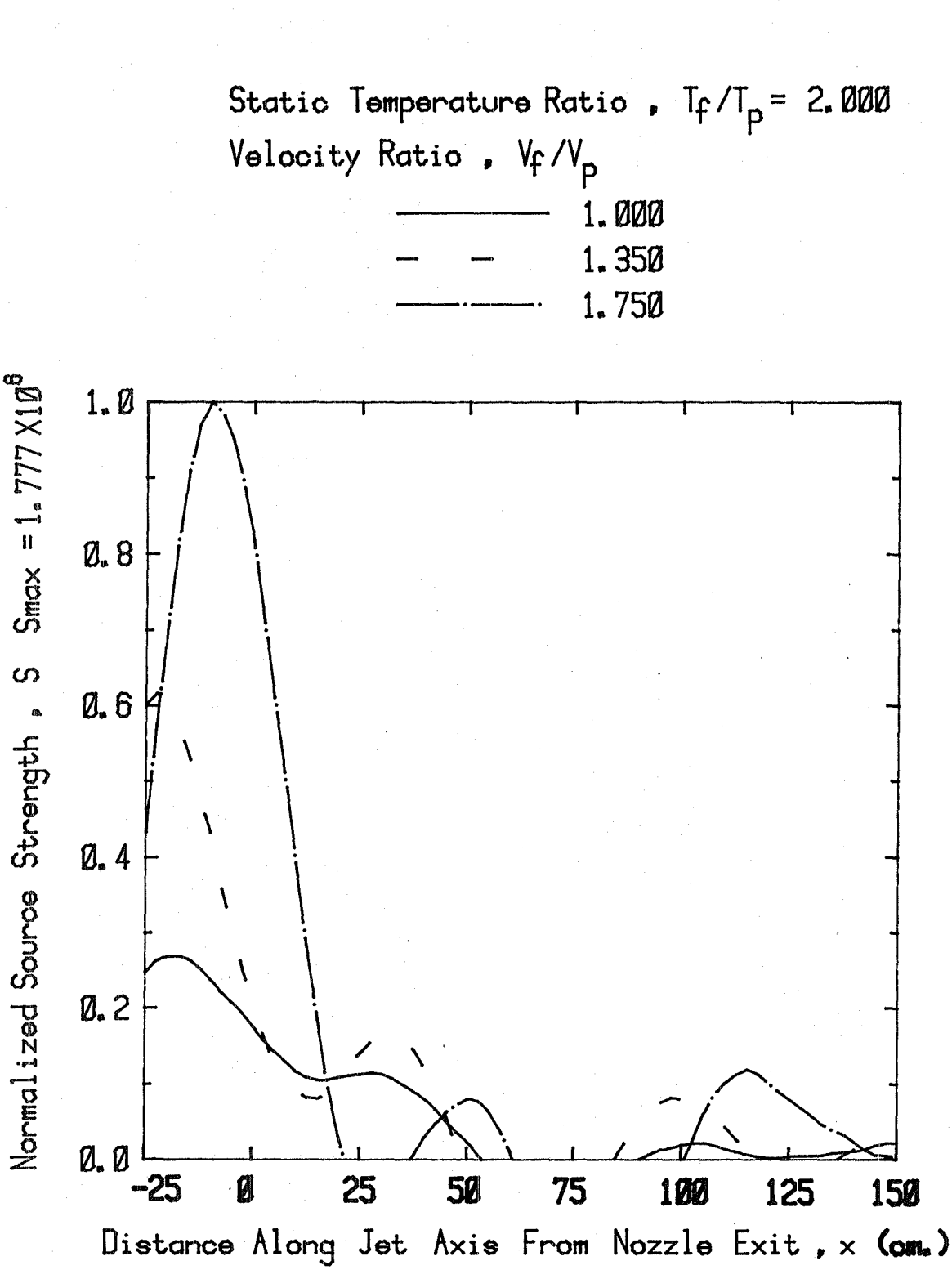

Coannular Jet - Source Distribution
(Frequency = 19.98 KHz)

Figure A2.18(g)

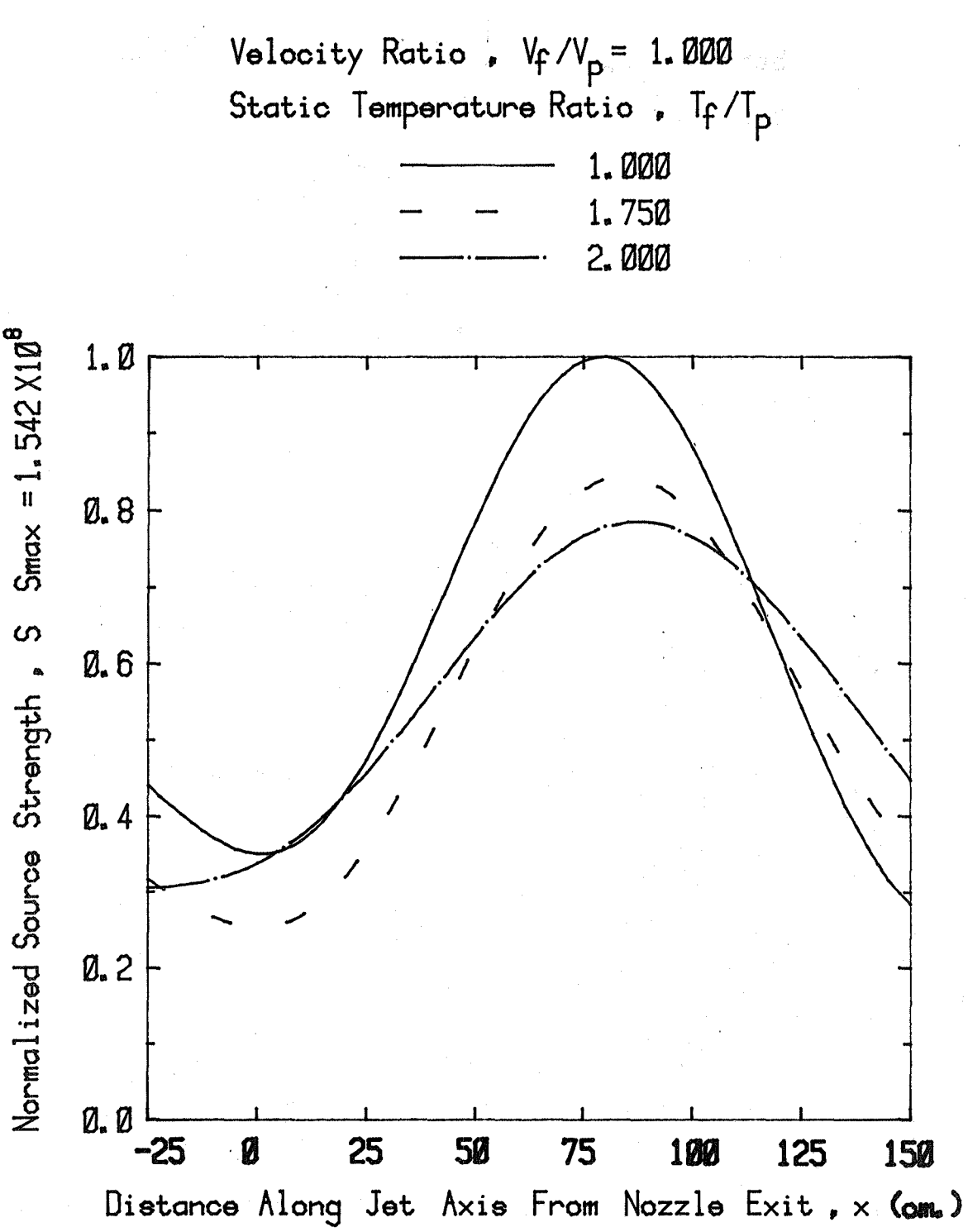

Coannular Jet - Source Distribution
(Frequency = 0.30 KHz)

Figure A2.19(a)

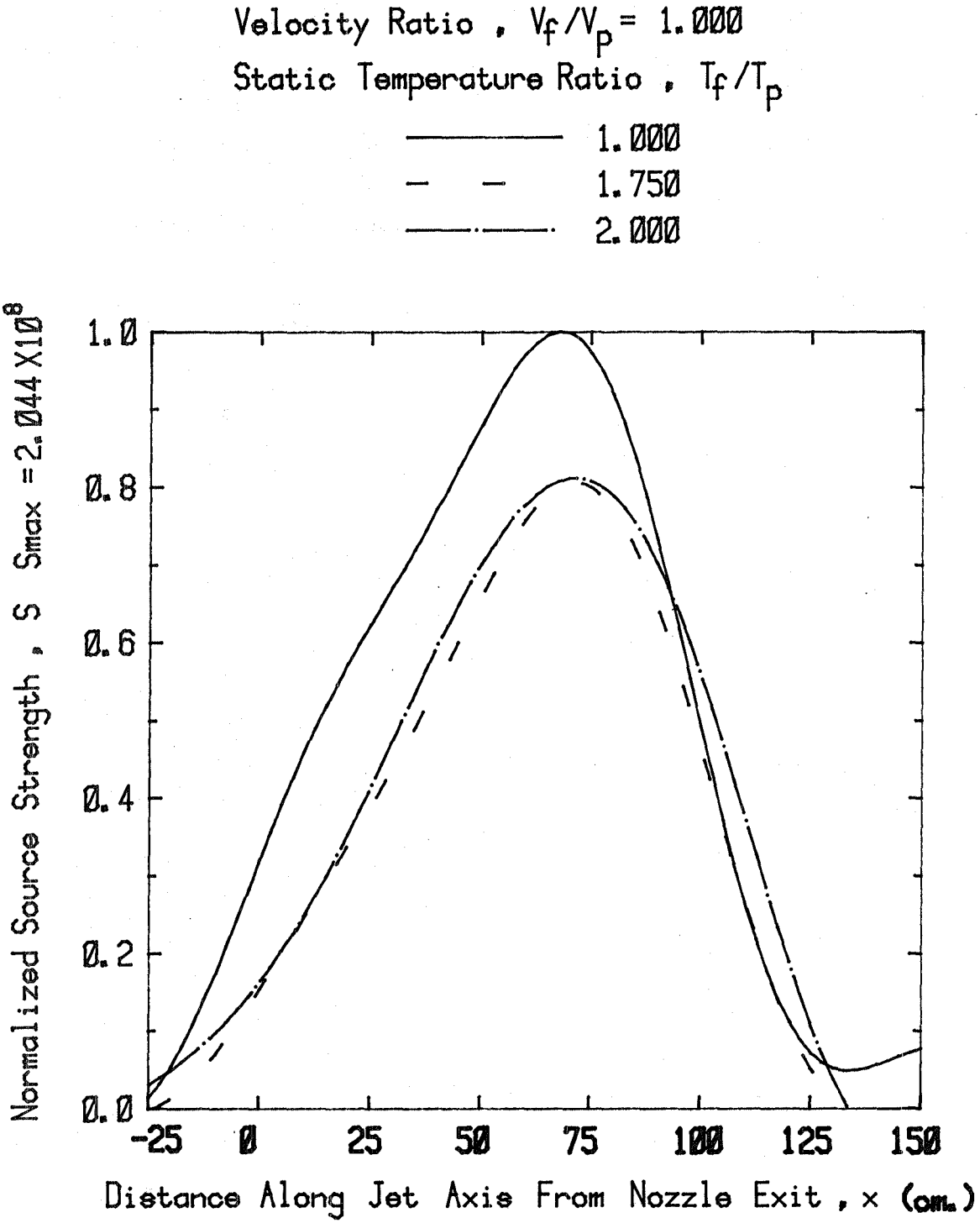

Coannular Jet - Source Distribution
(Frequency = 0.60 KHz)

Figure A2.19(b)

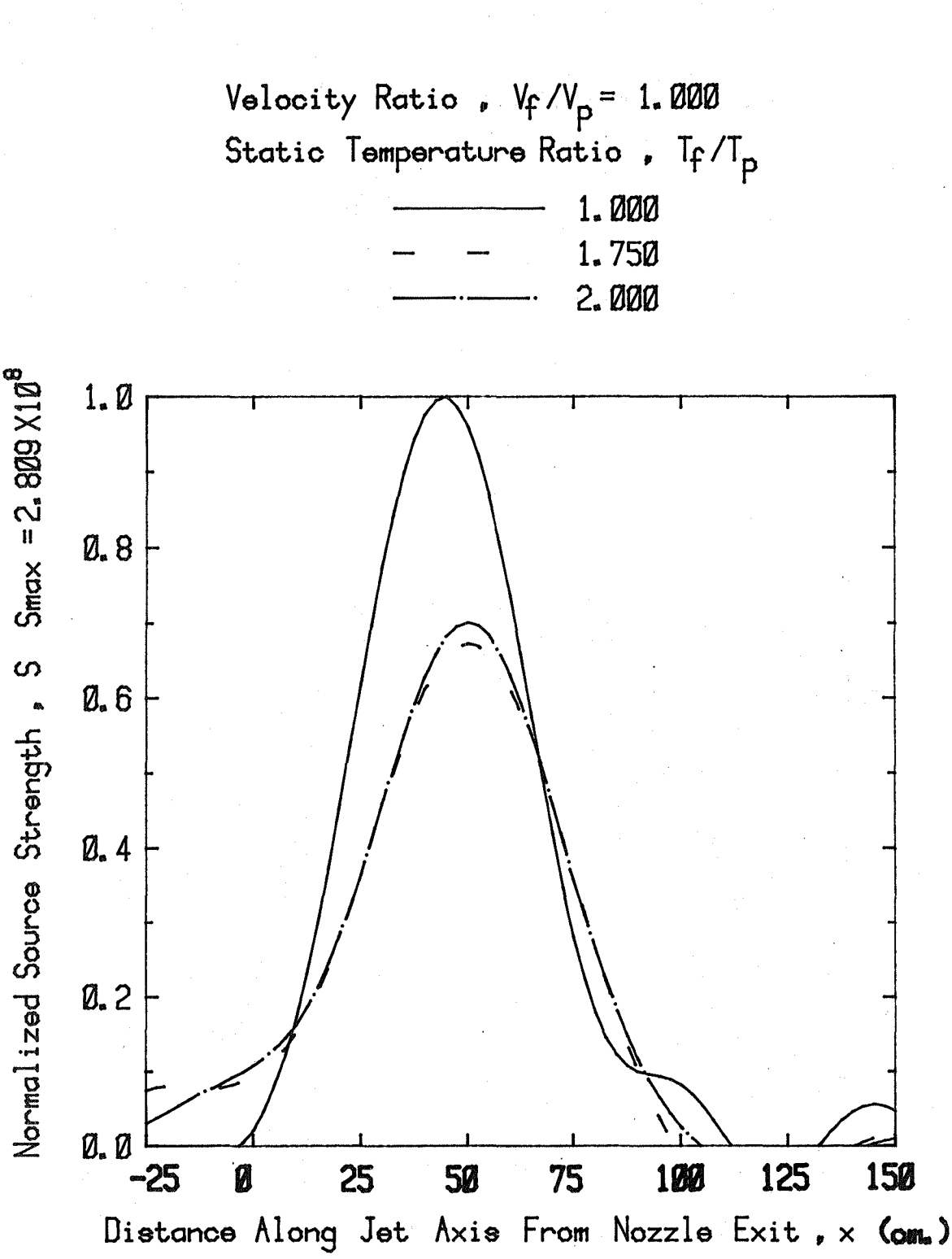

Coannular Jet - Source Distribution
(Frequency = 1.20 KHz)

Figure A2.19(c)

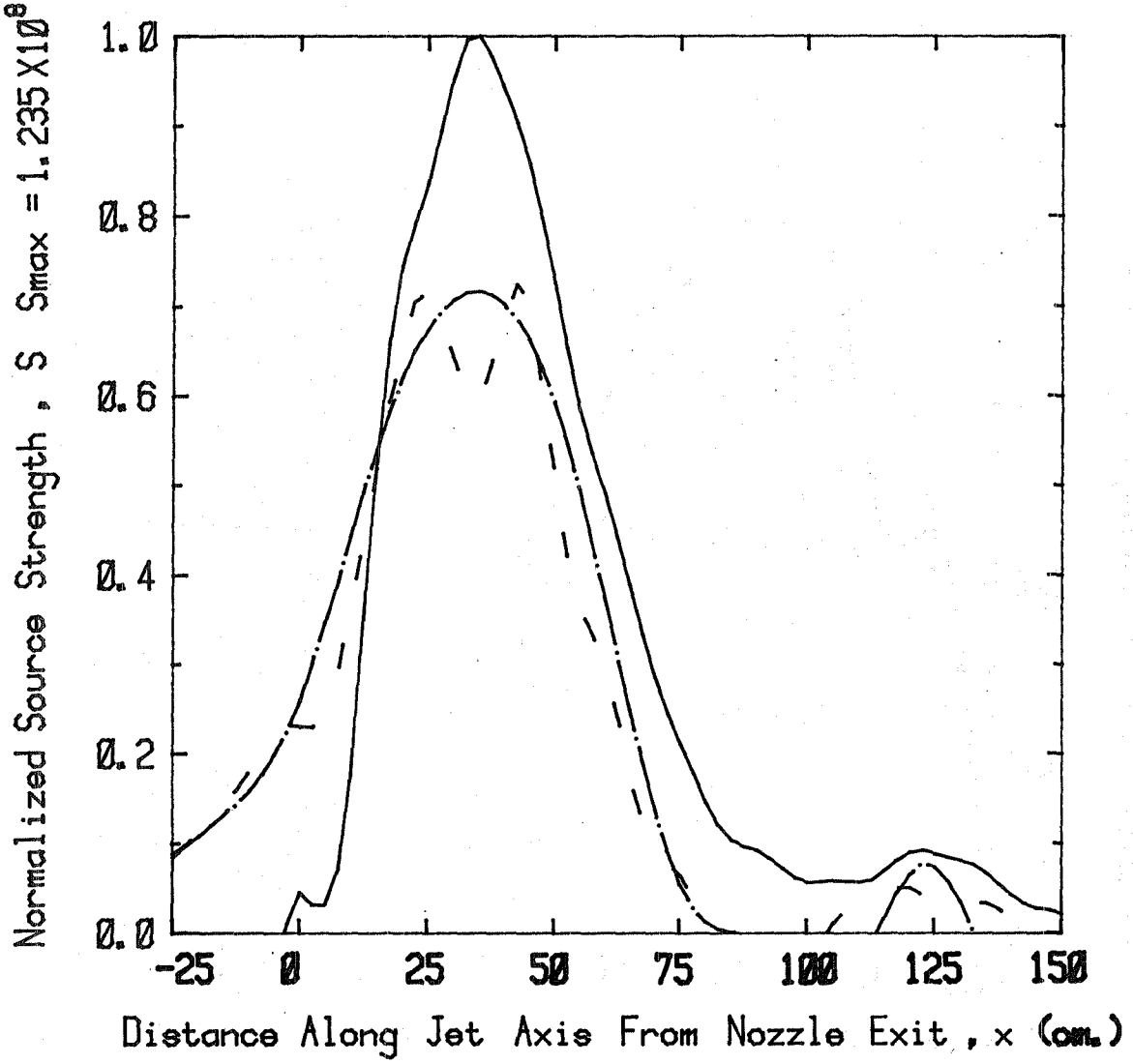

Coannular Jet - Source Distribution
(Frequency = 2.46 KHz)

Figure A2.19(d)

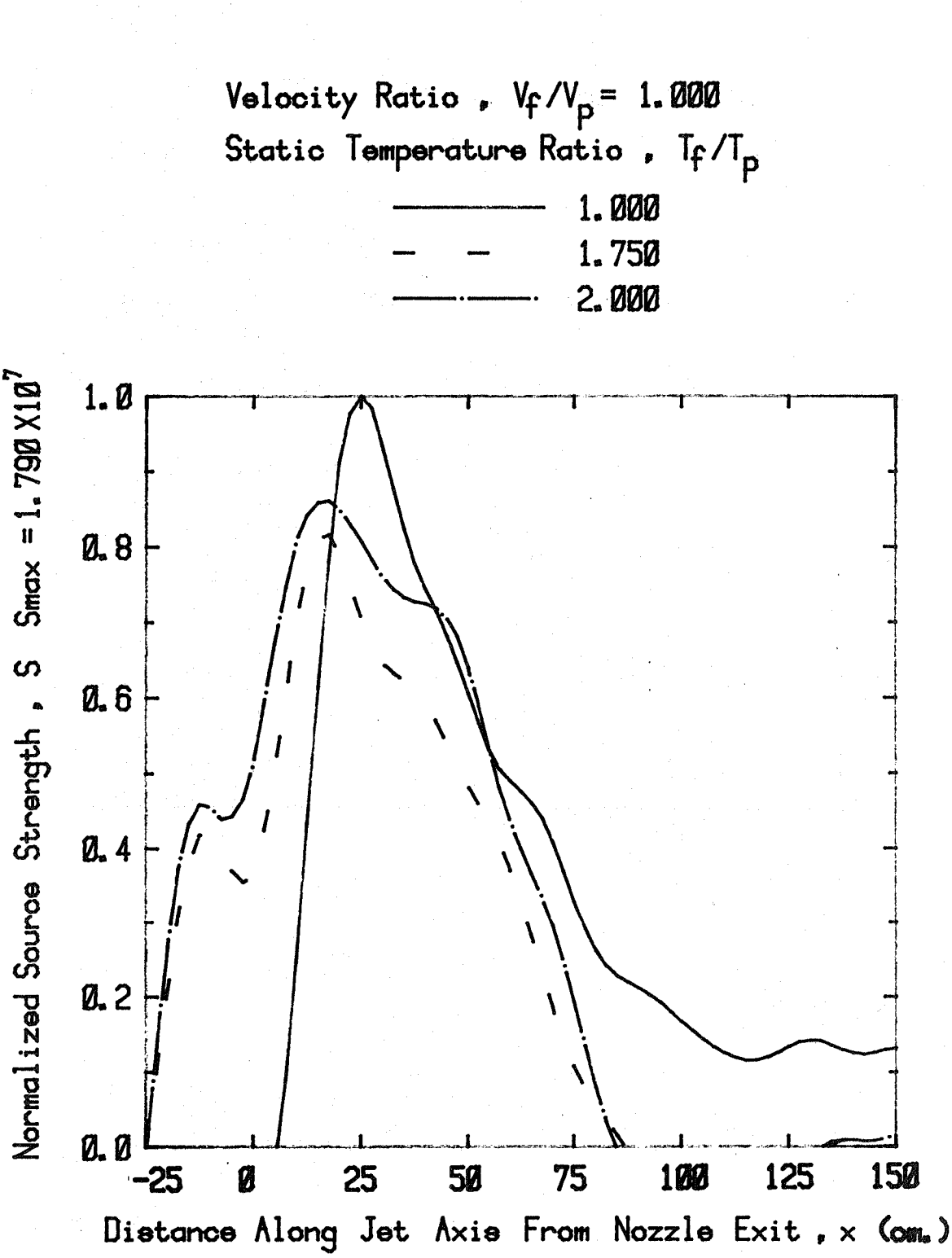

Coannular Jet - Source Distribution
(Frequency = 4.98 KHz)

Figure A2.19(e)

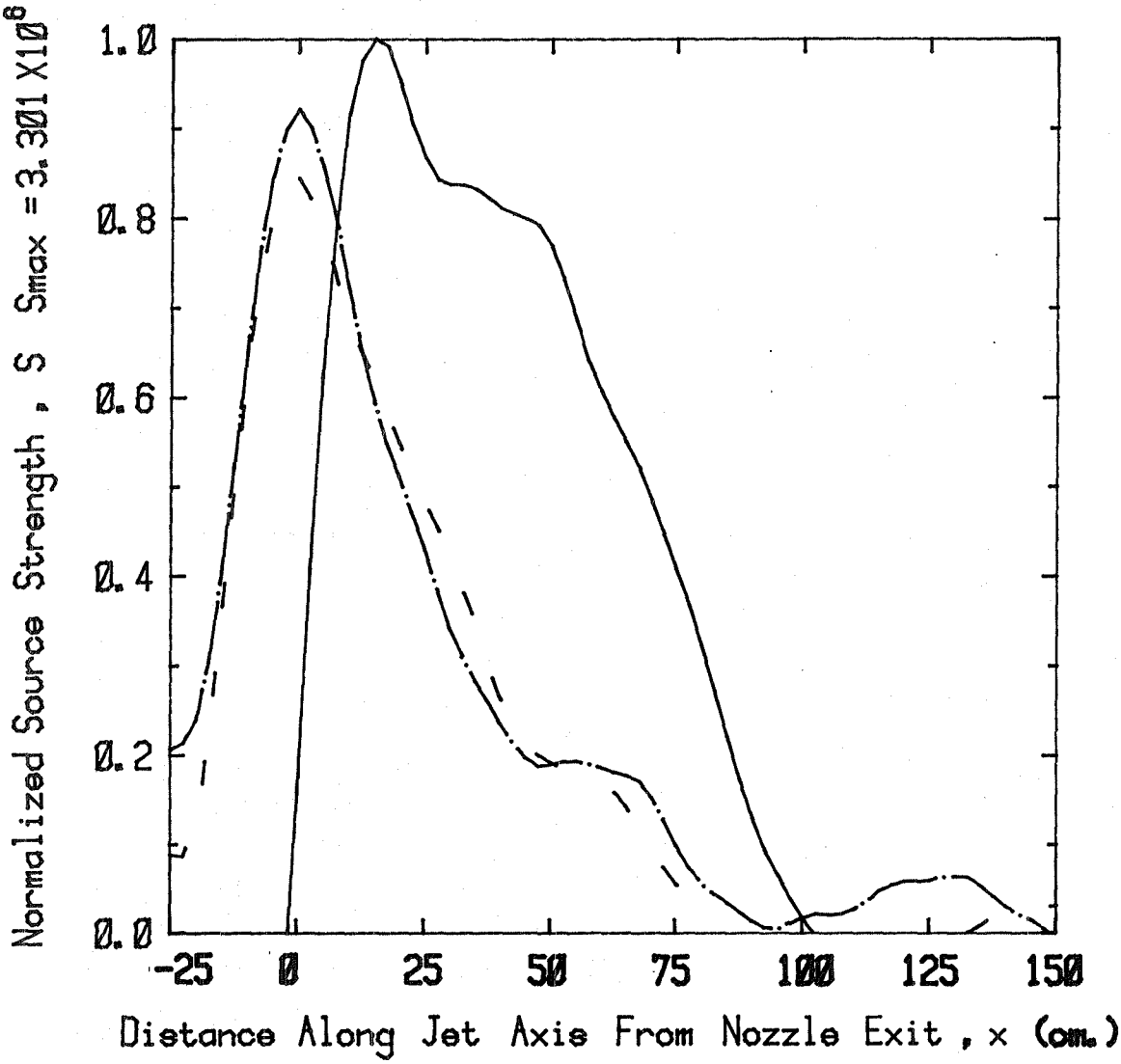

Coannular Jet - Source Distribution
(Frequency = 9.96 KHz)

Figure A2.19(f)

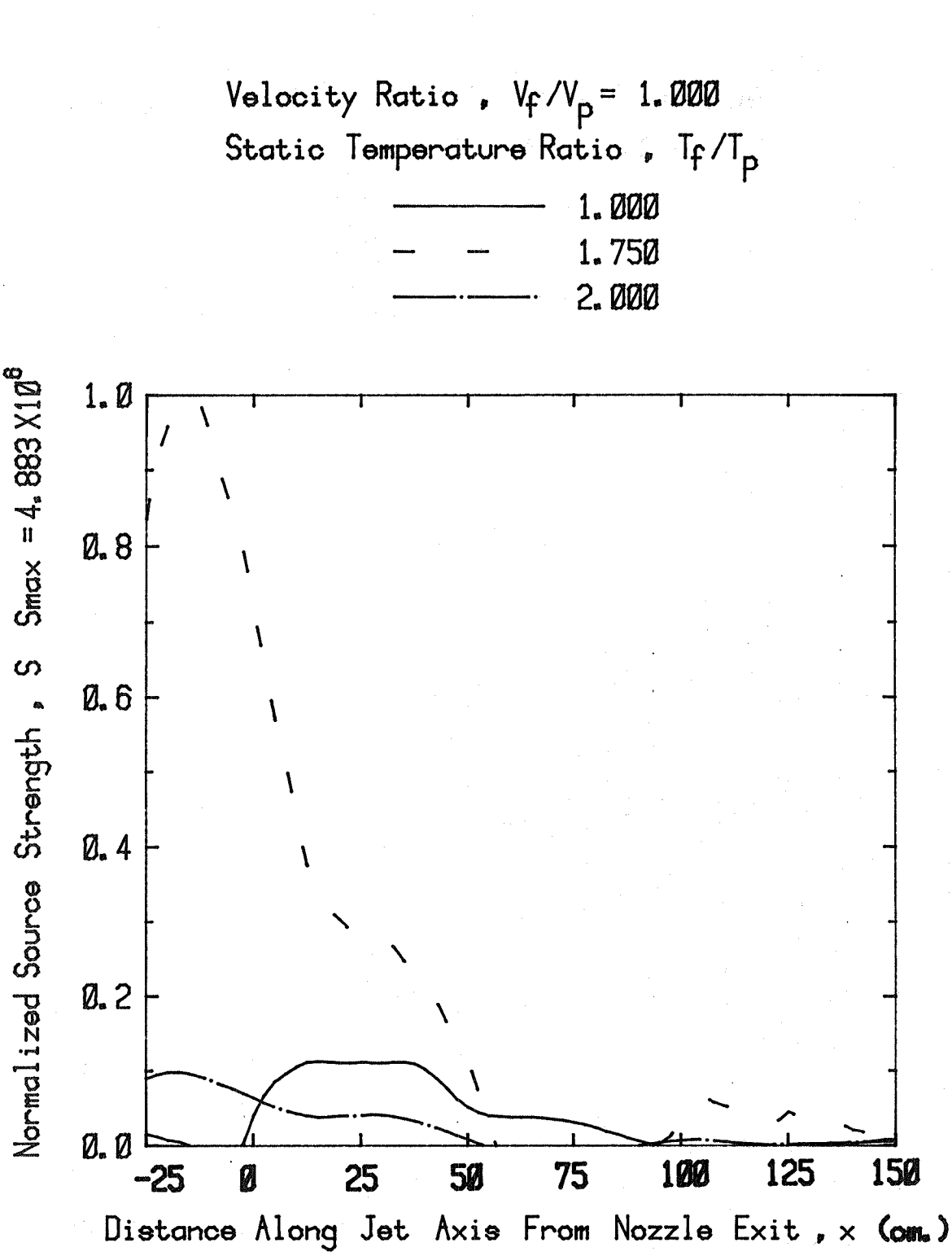

Coannular Jet - Source Distribution
(Frequency = 19.98 KHz)

Figure A2.19(g)

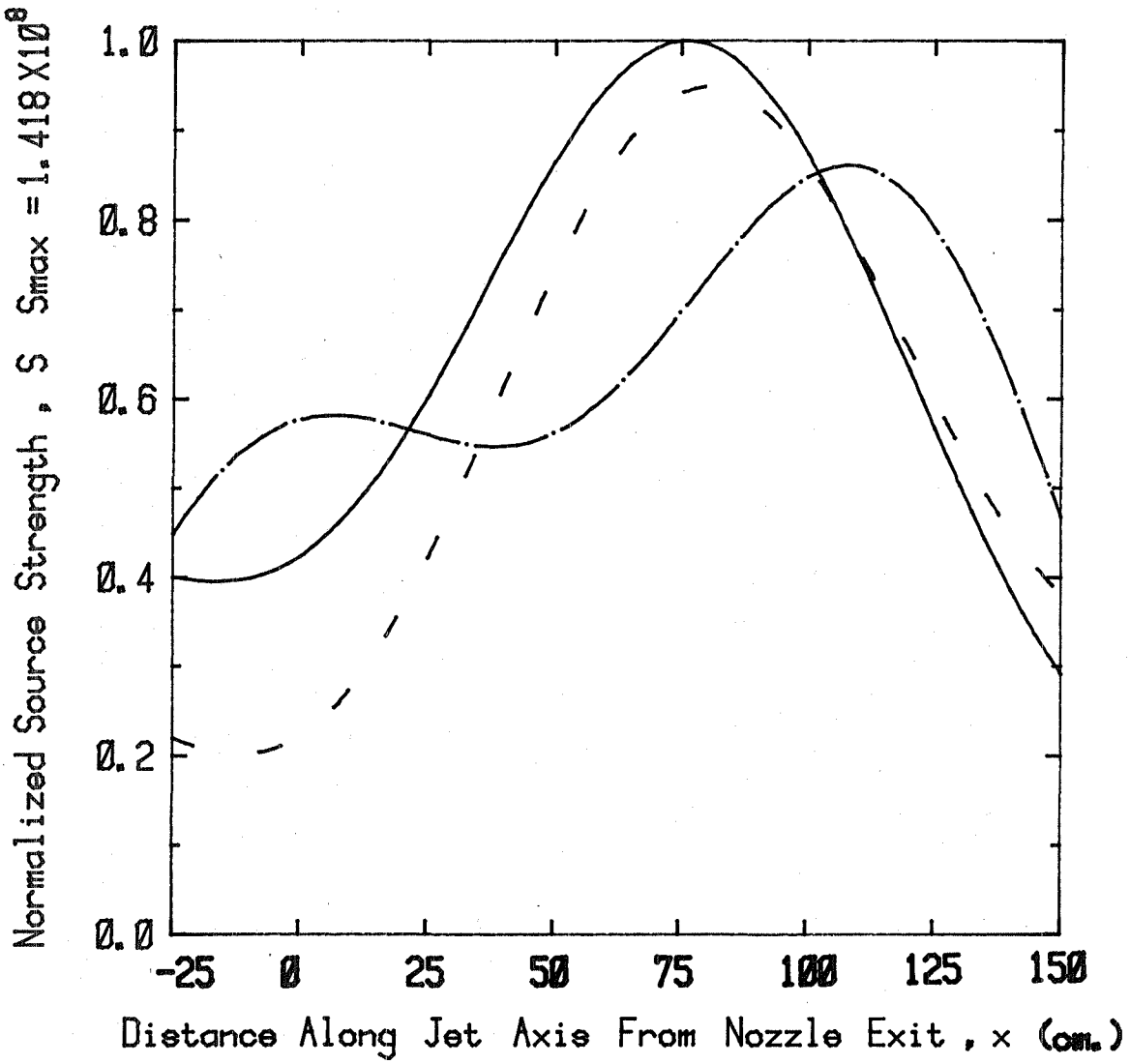

Coannular Jet - Source Distribution
(Frequency = 0.30 KHz)

Figure A2.20(a)

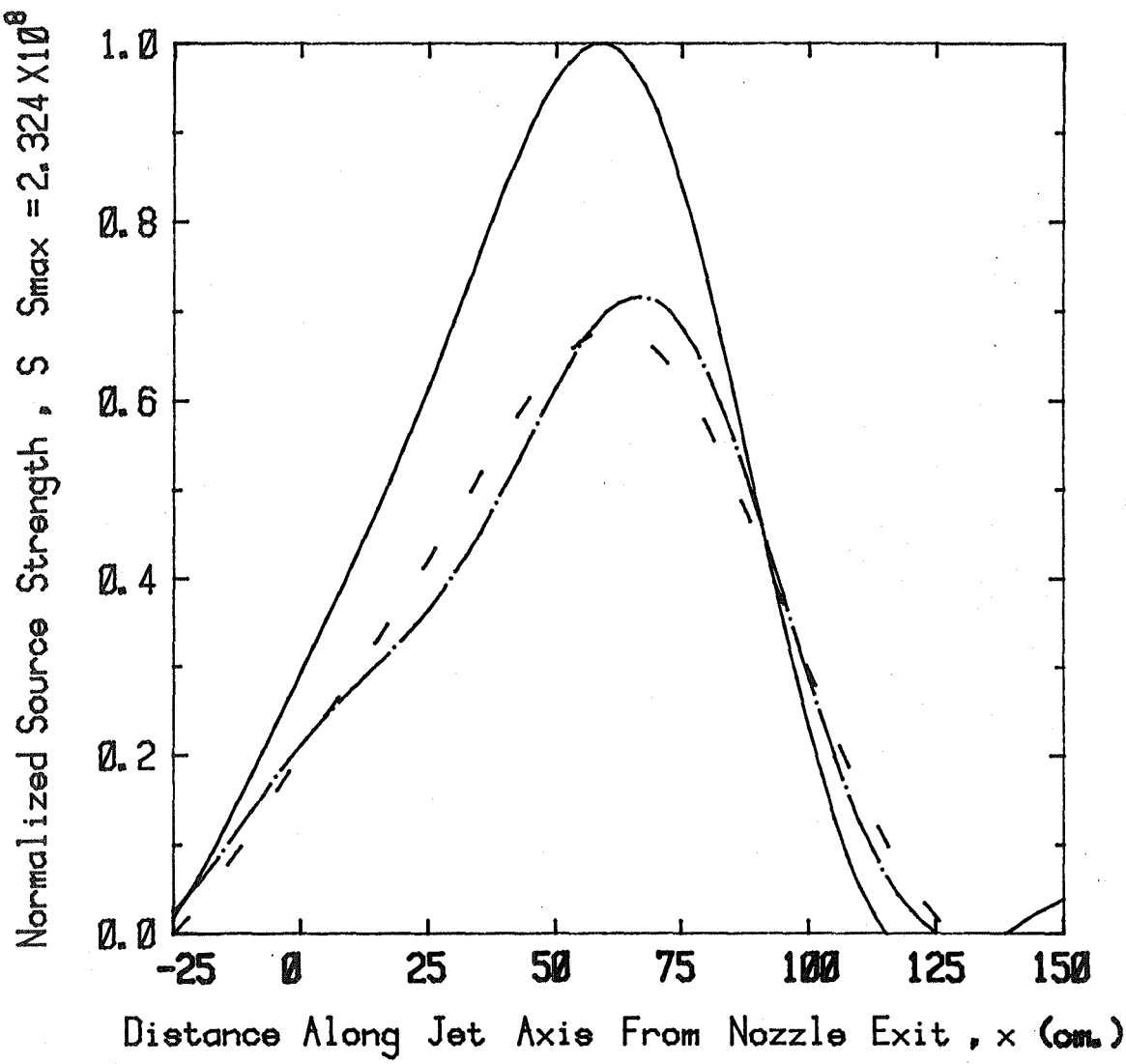

Coannular Jet - Source Distribution
(Frequency = 0.60 KHz)

Figure A2.20(b)

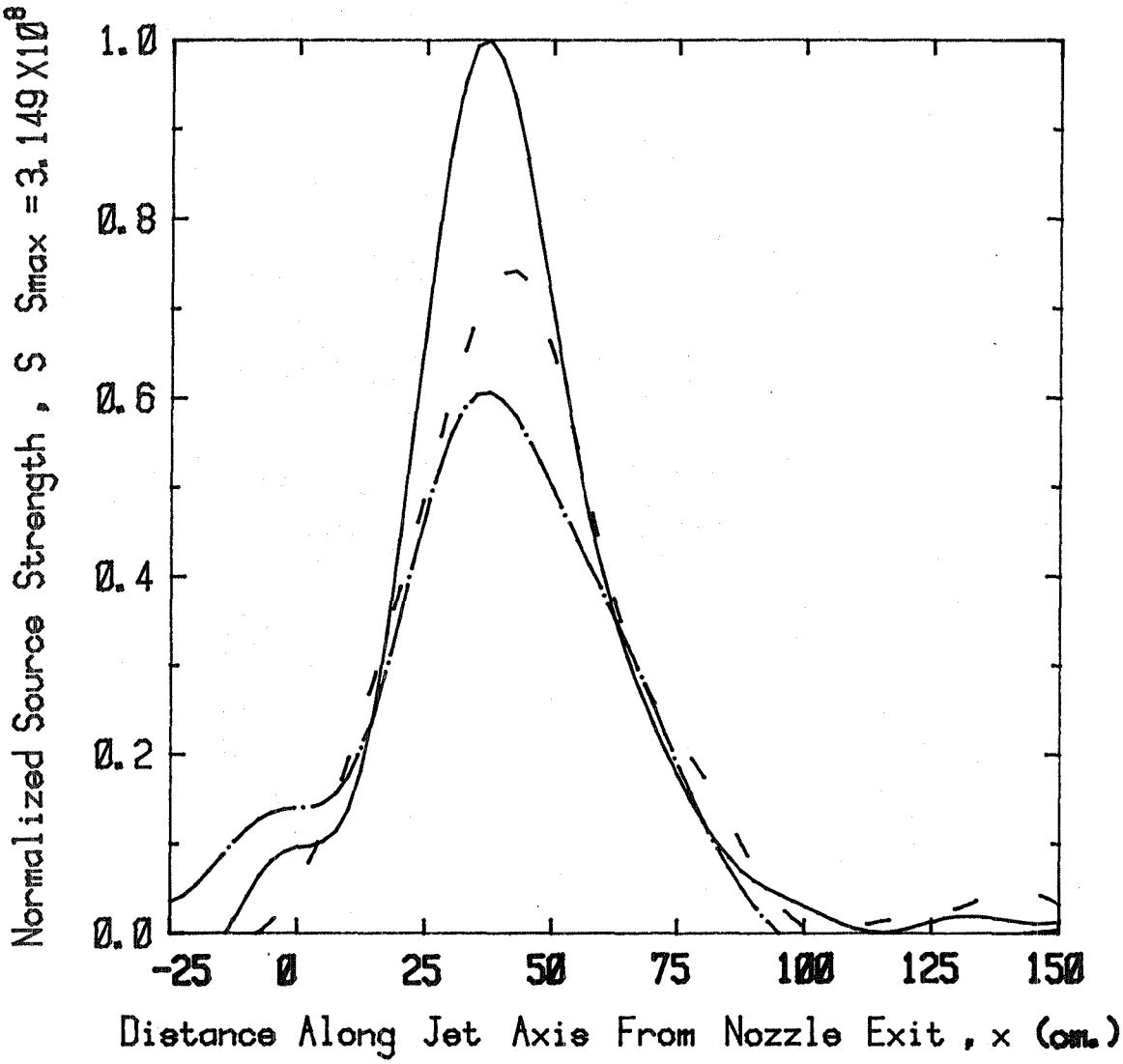

Coannular Jet - Source Distribution
(Frequency = 1.20 KHz)

Figure A2.20(c)

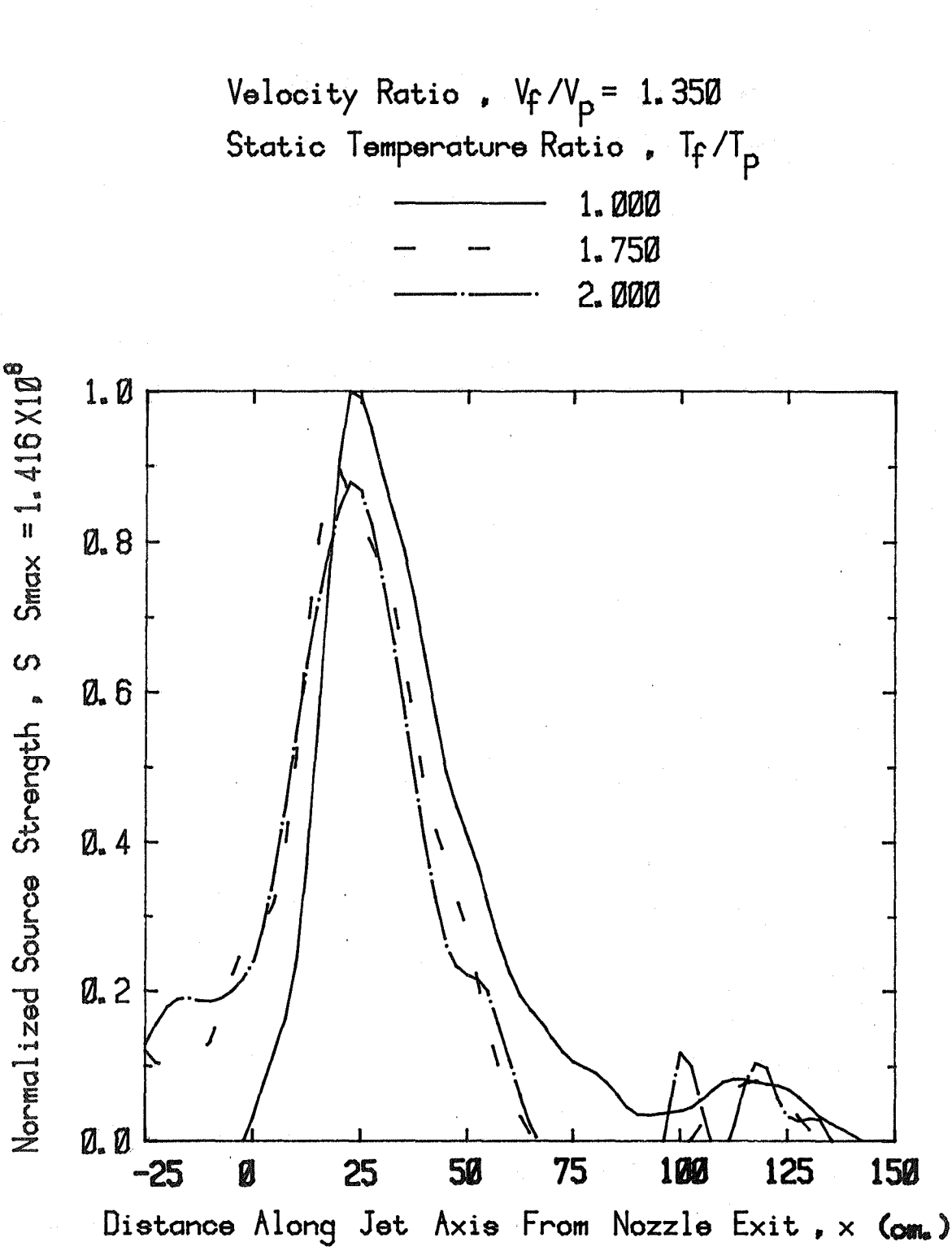

Coannular Jet - Source Distribution
(Frequency = 2.46 KHz)

Figure A2.20(d)

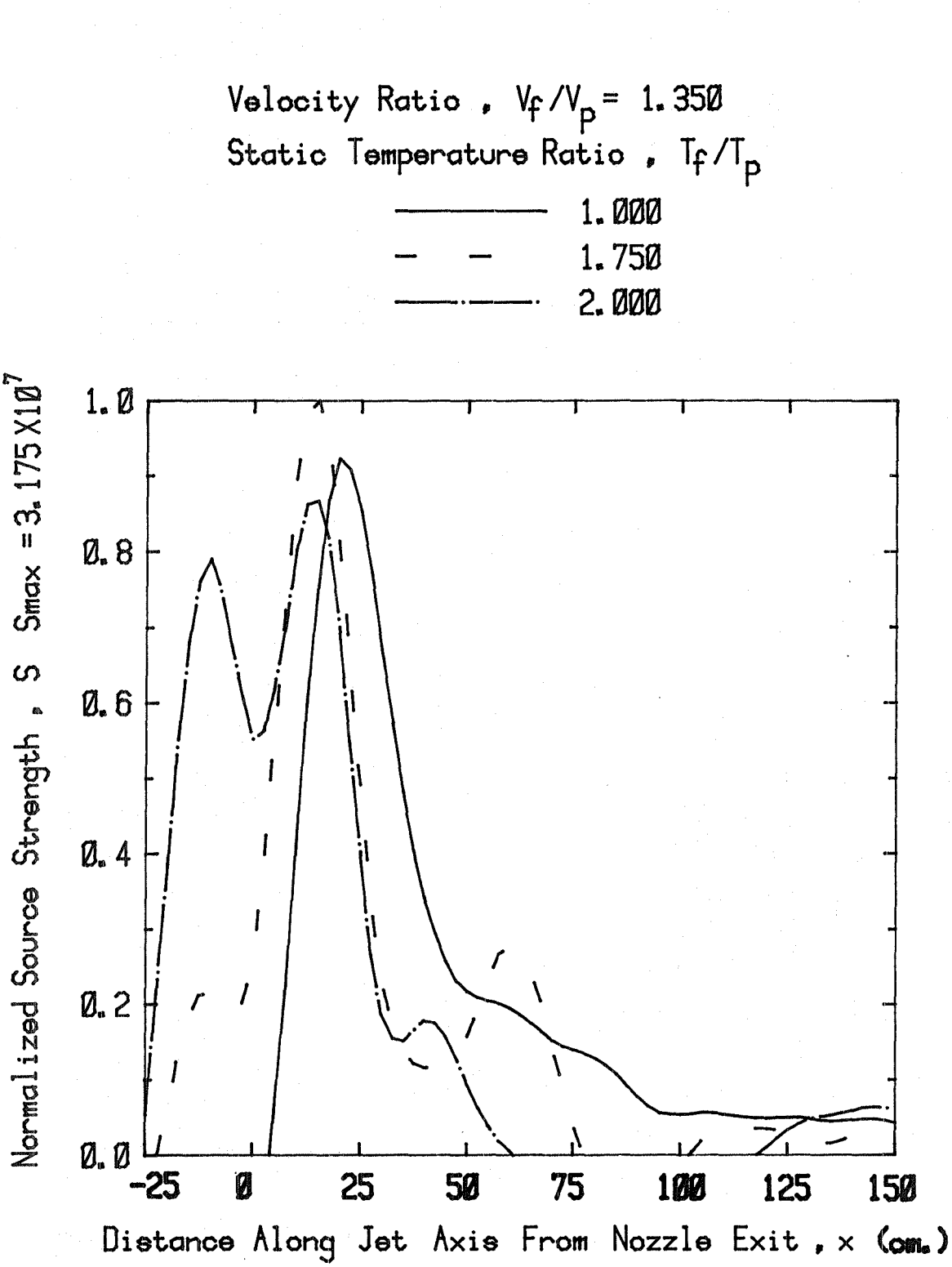

Coannular Jet - Source Distribution
(Frequency = 4.98 KHz)

Figure A2.20(e)

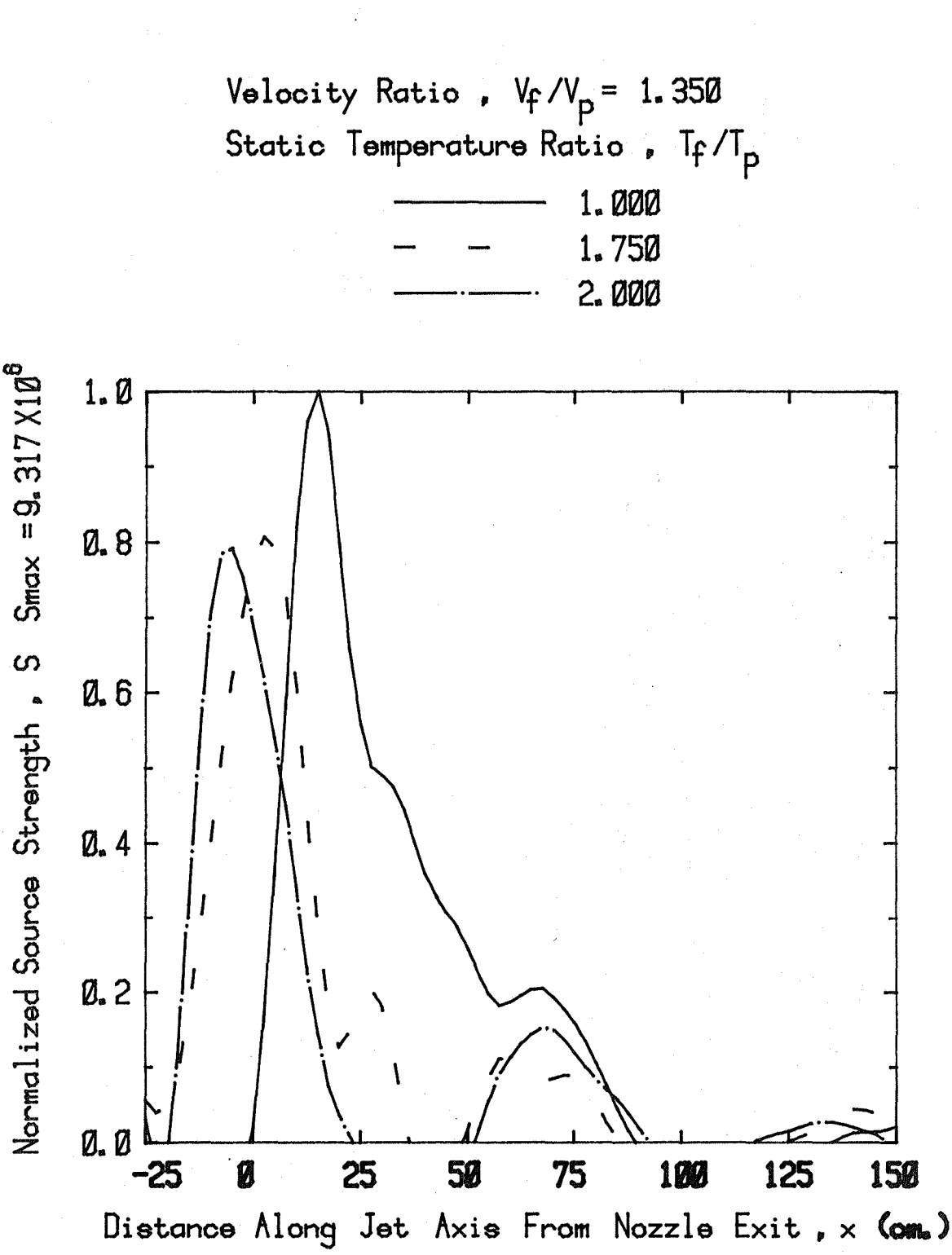

Coannular Jet - Source Distribution
(Frequency = 9.96 KHz)

Figure A2.20(f)

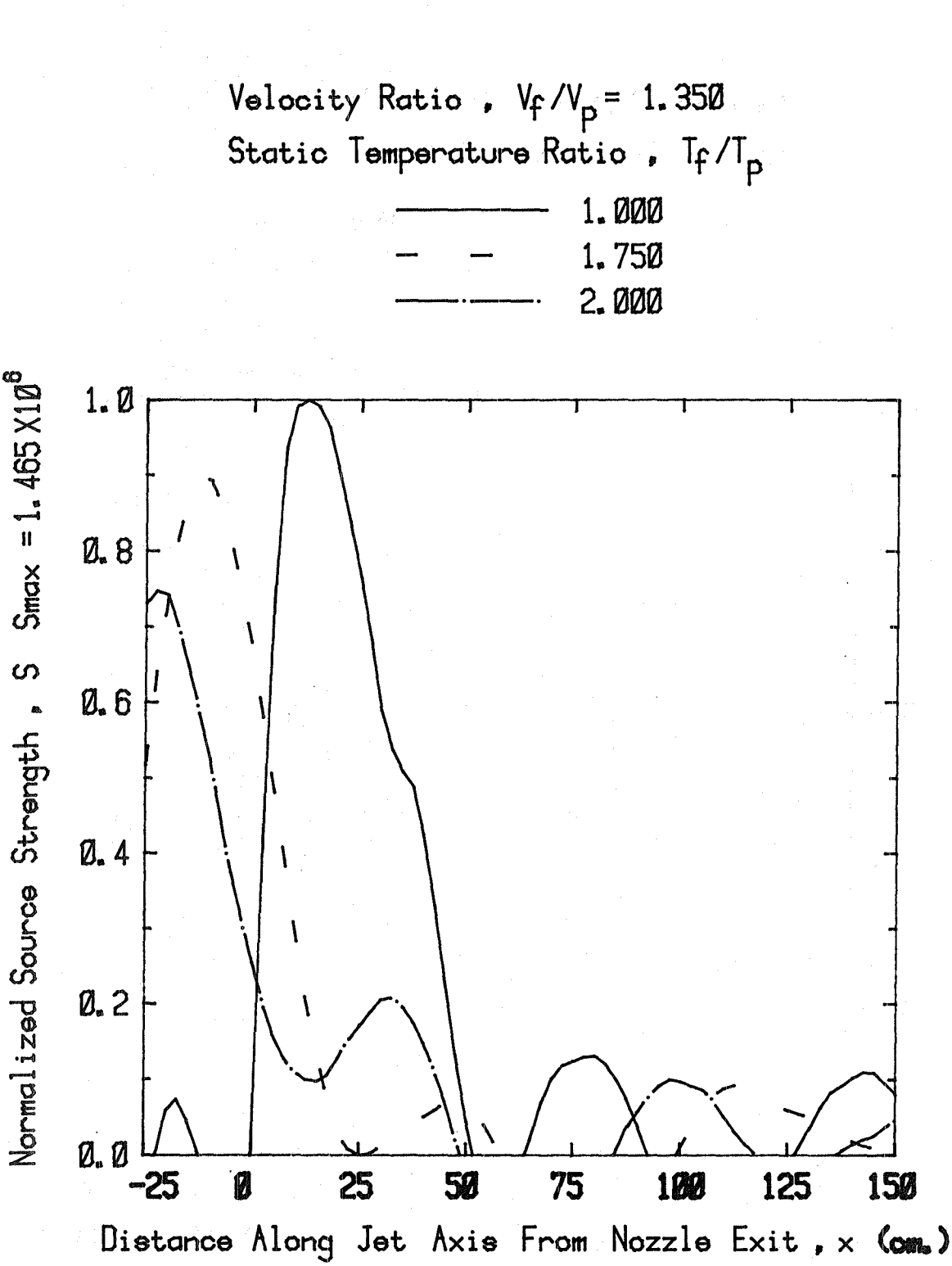

Coannular Jet - Source Distribution
(Frequency = 19.98 KHz)

Figure A2.20(g)

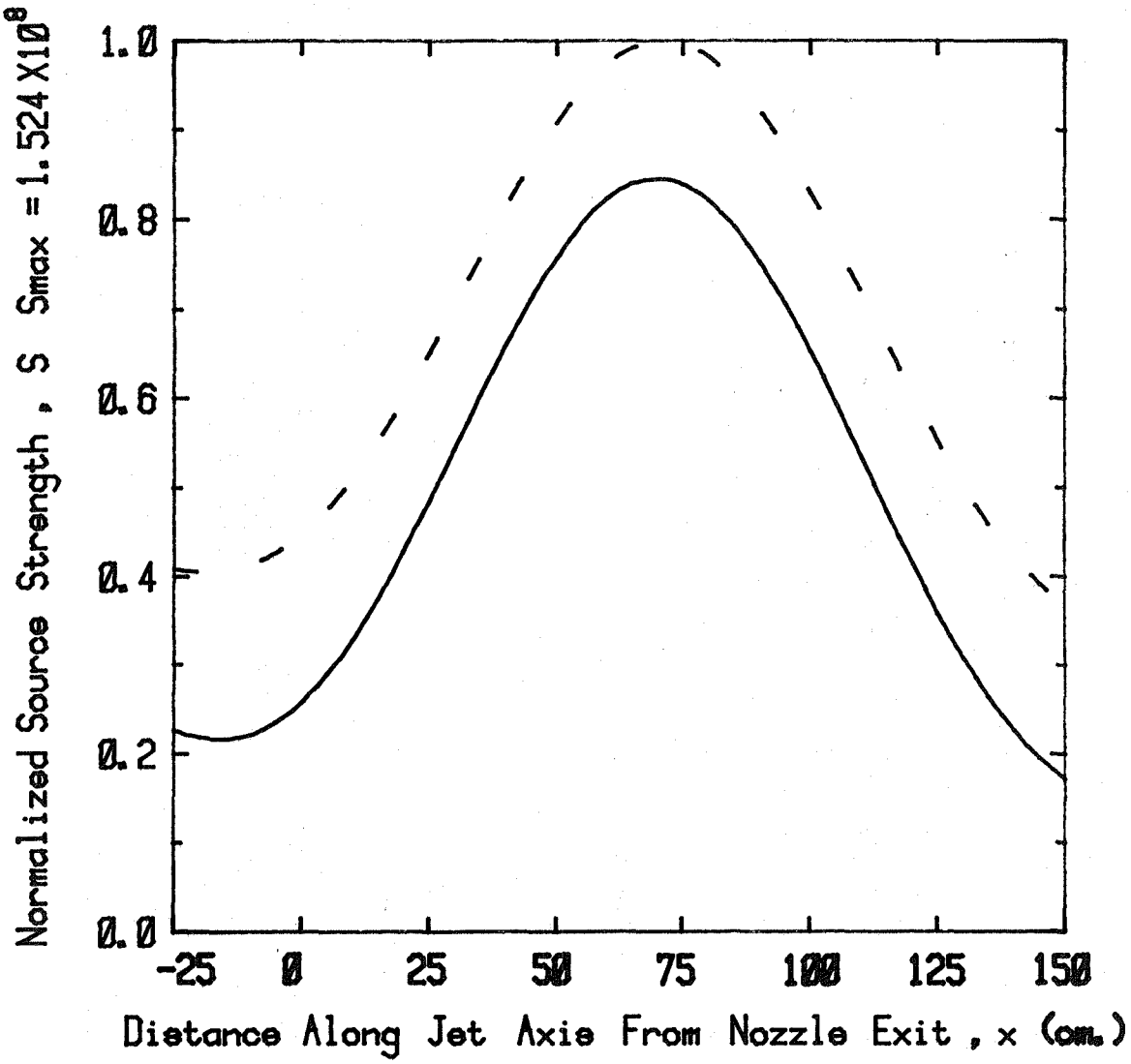

Coannular Jet - Source Distribution
(Frequency = 0.30 KHz)

Figure A2.21(a)

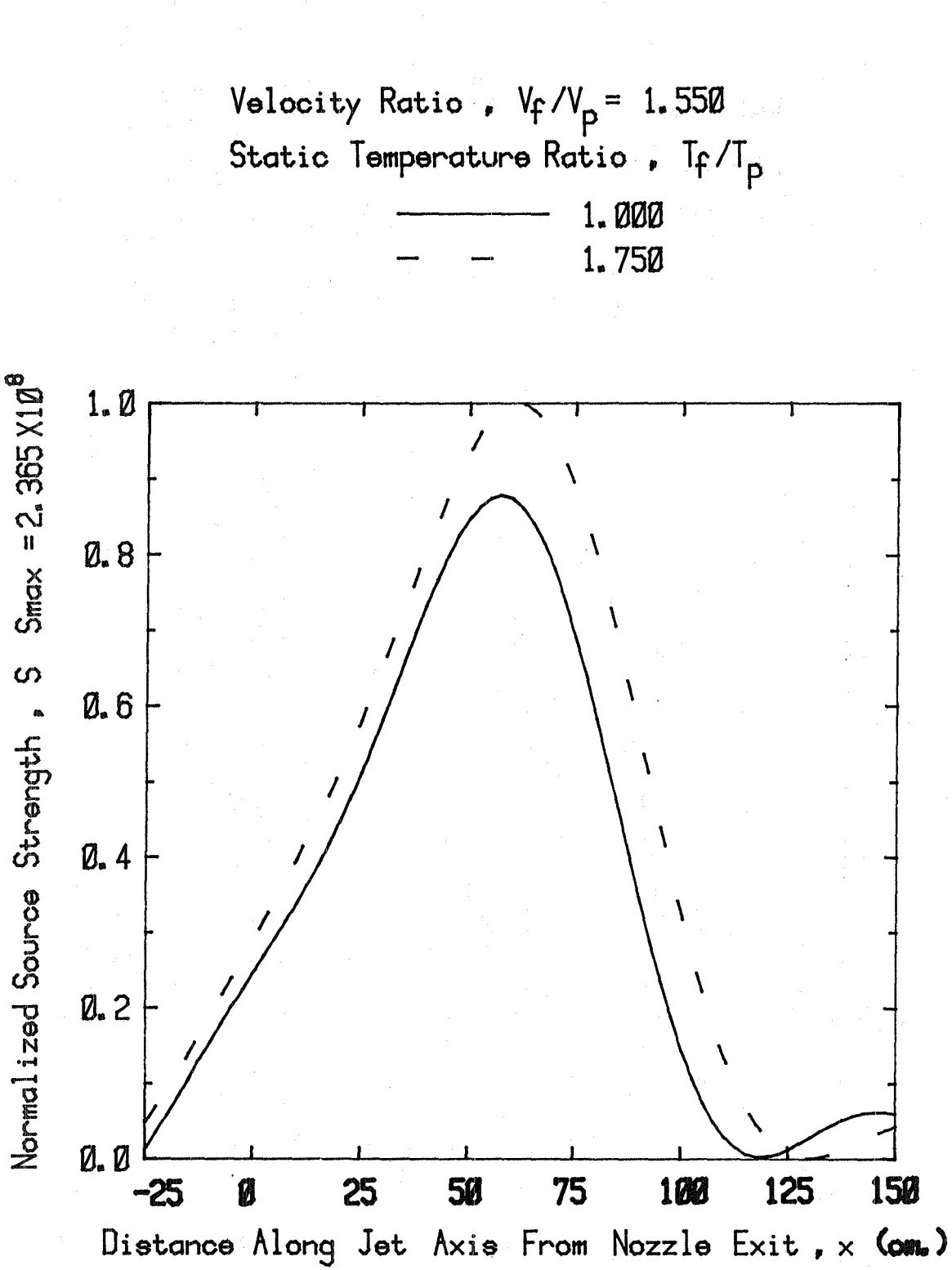

Coannular Jet - Source Distribution
(Frequency = 0.60 KHz)

Figure A2.21(b)

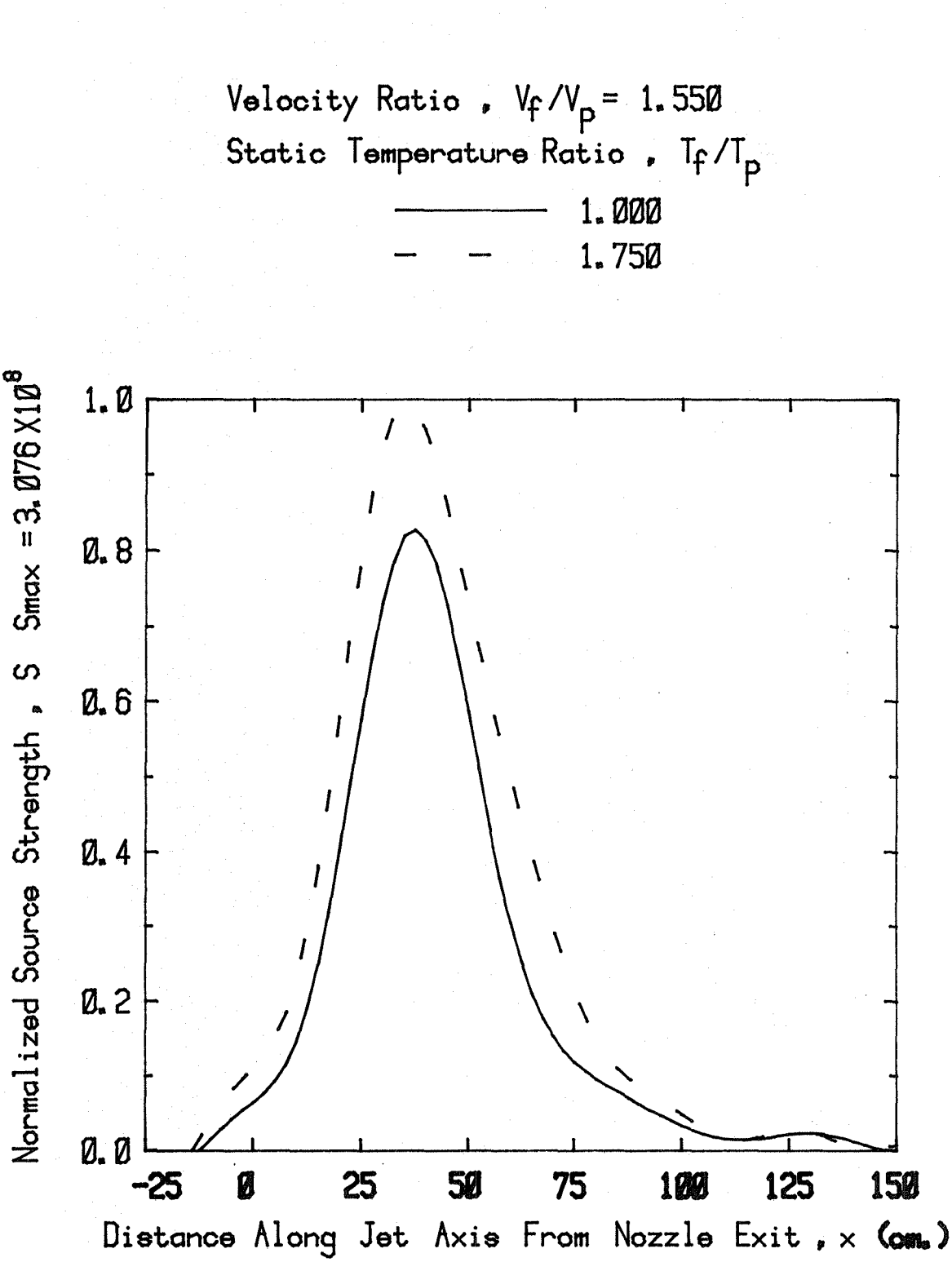

Coannular Jet - Source Distribution
(Frequency = 1.20 KHz)

Figure A2.21(c)

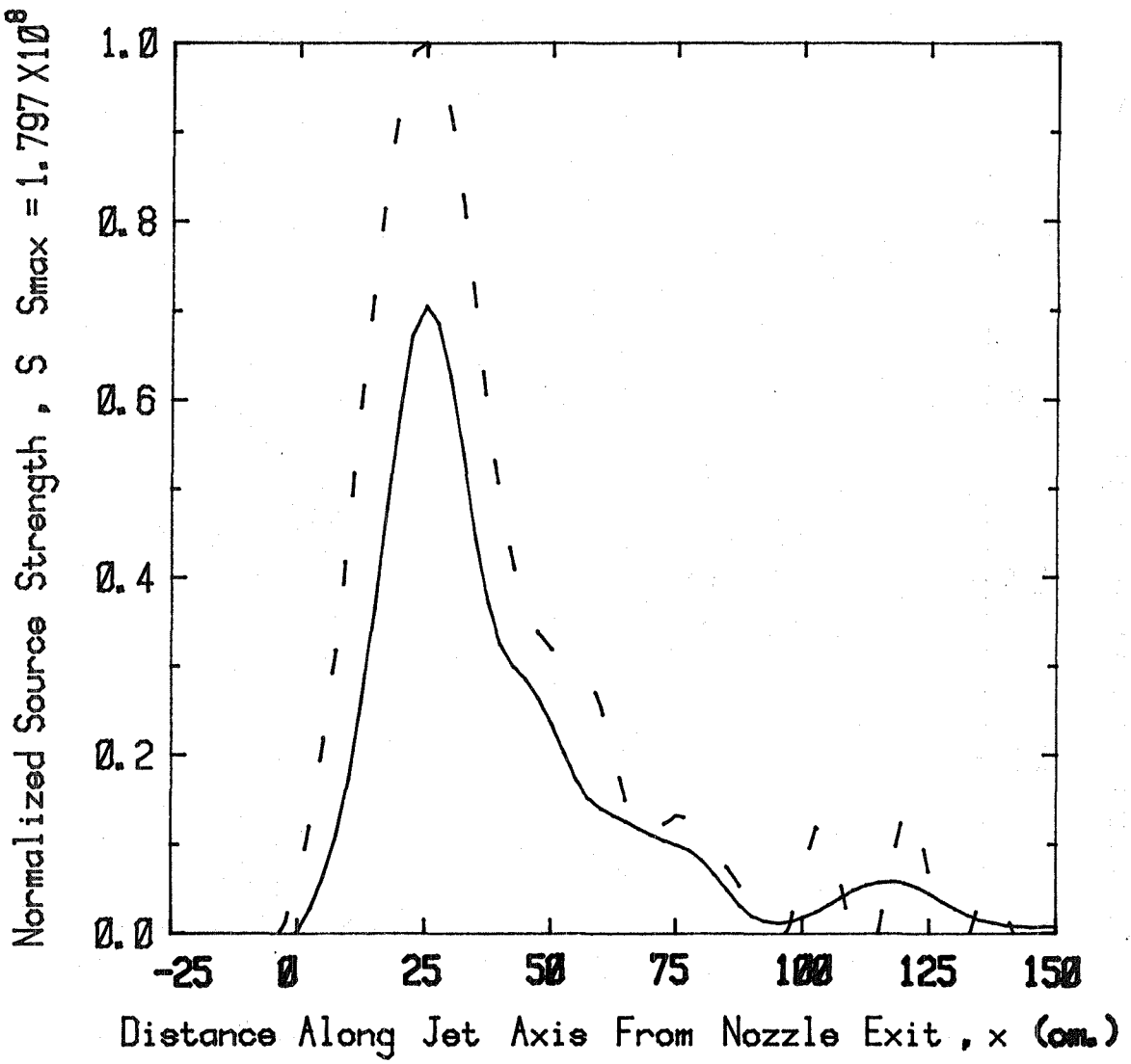

Coannular Jet - Source Distribution
(Frequency = 2.46 KHz)

Figure A2.21(d)

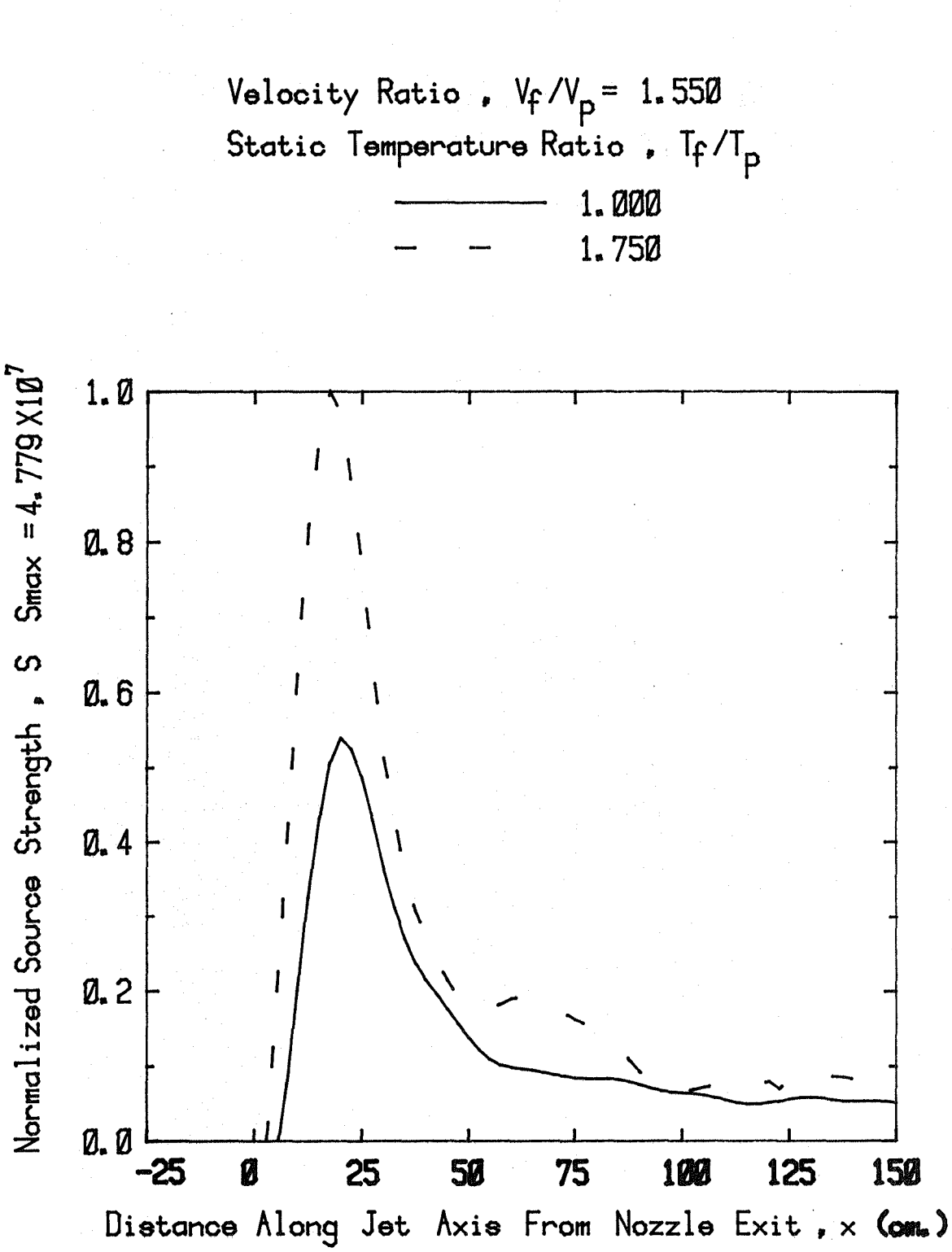

Coannular Jet - Source Distribution
(Frequency = 4.98 KHz)

Figure A2.21(e)

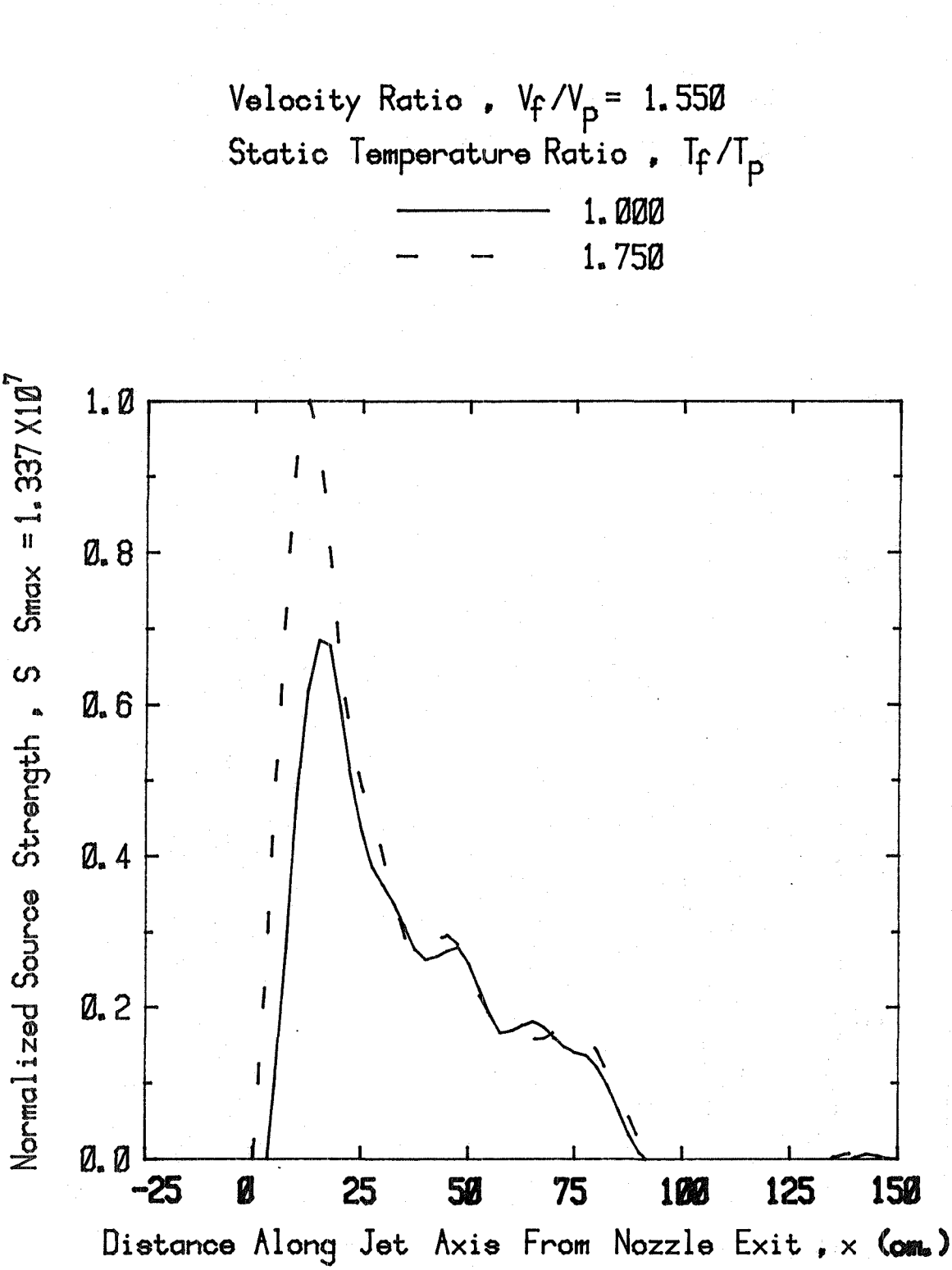

Coannular Jet - Source Distribution
(Frequency = 9.96 KHz)

Figure A2.21(f)

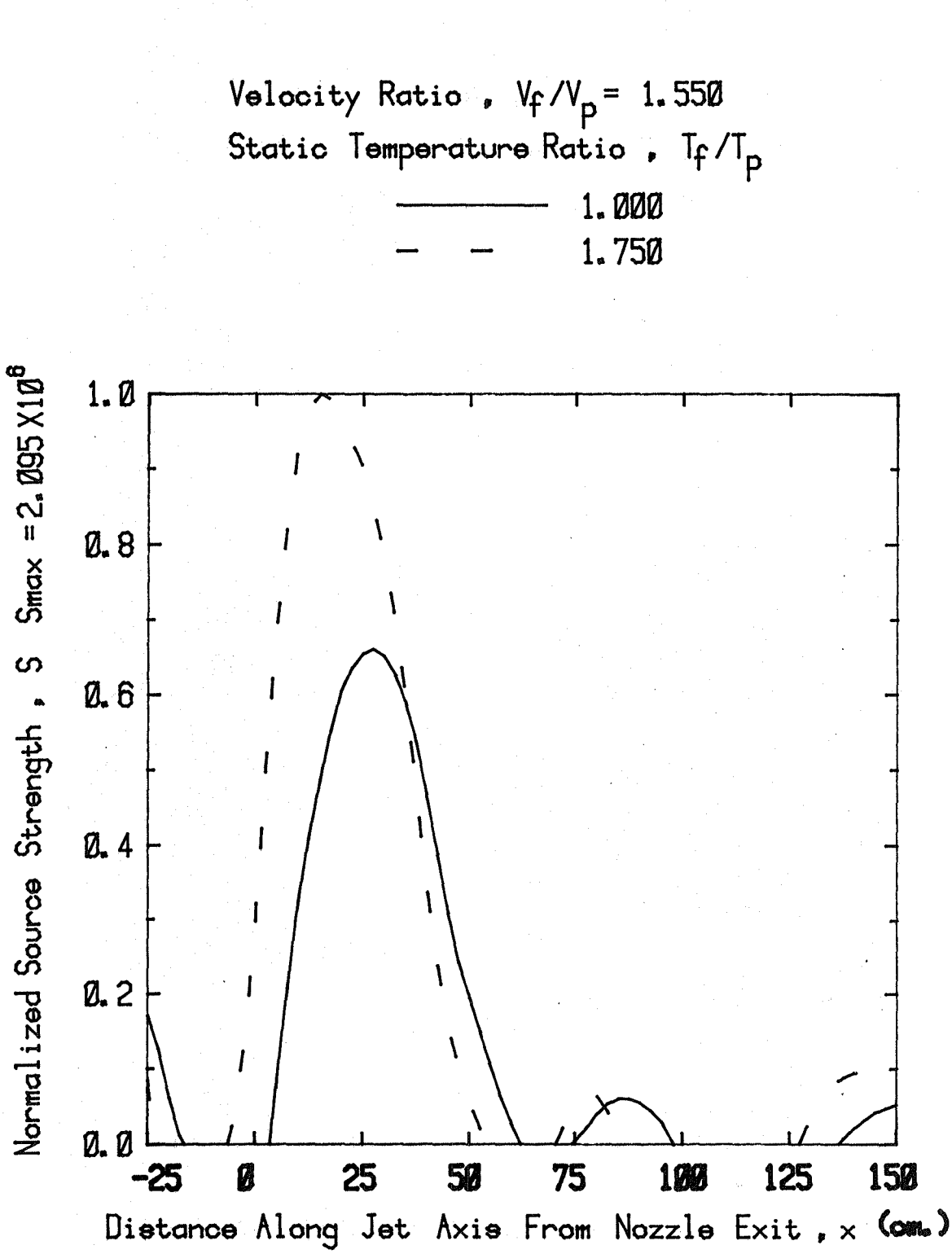

Coannular Jet - Source Distribution
(Frequency = 19.98 KHz)

Figure A2.21(g)

Velocity Ratio , V_f/V_p = 1.950

Static Temperature Ratio , T_f/T_p = 2.470

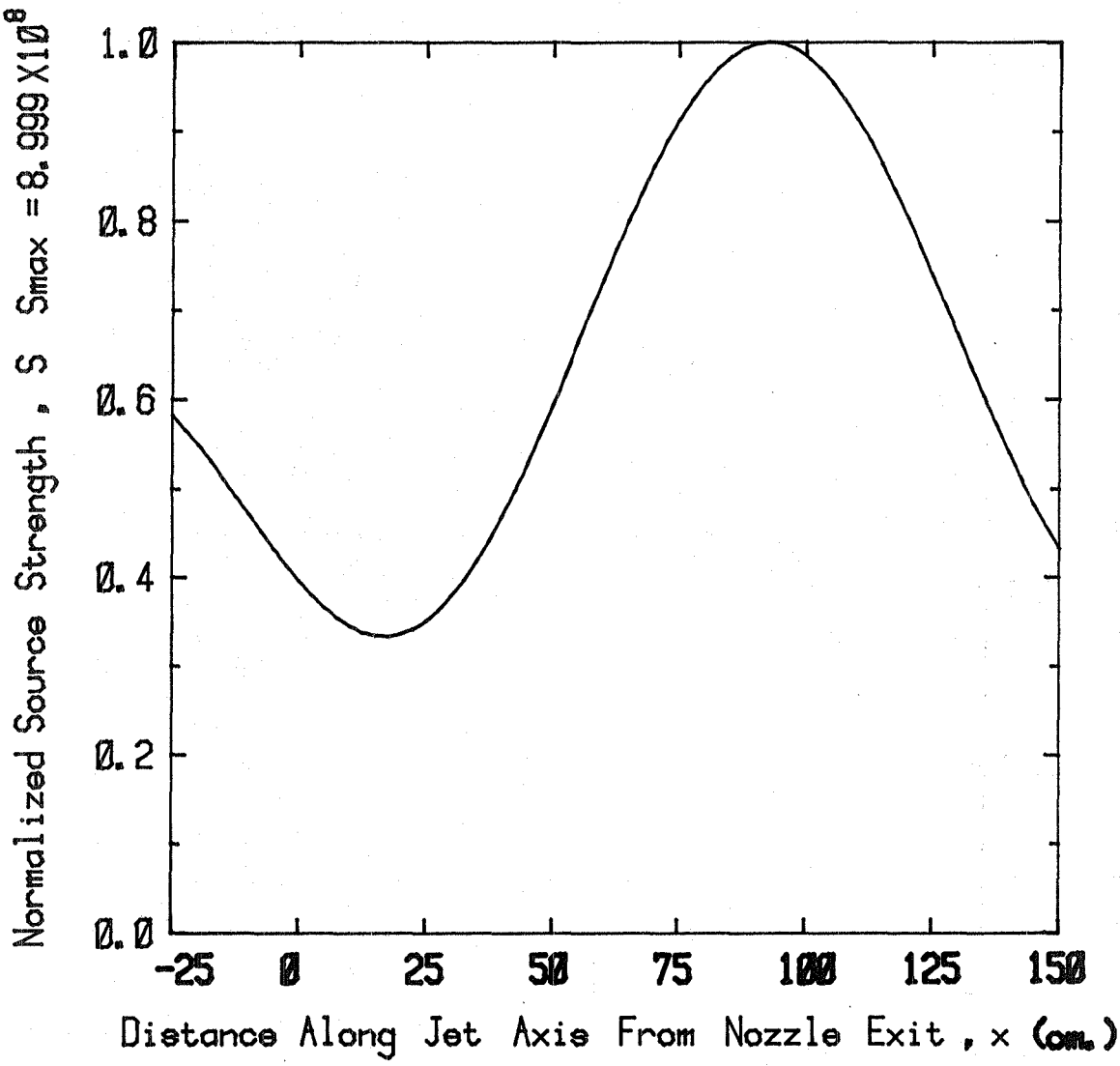

Coannular Jet - Source Distribution

(Frequency = 0.30 KHz)

Figure A2.22(a)

Velocity Ratio , V_f/V_p = 1.950

Static Temperature Ratio , T_f/T_p = 2.470

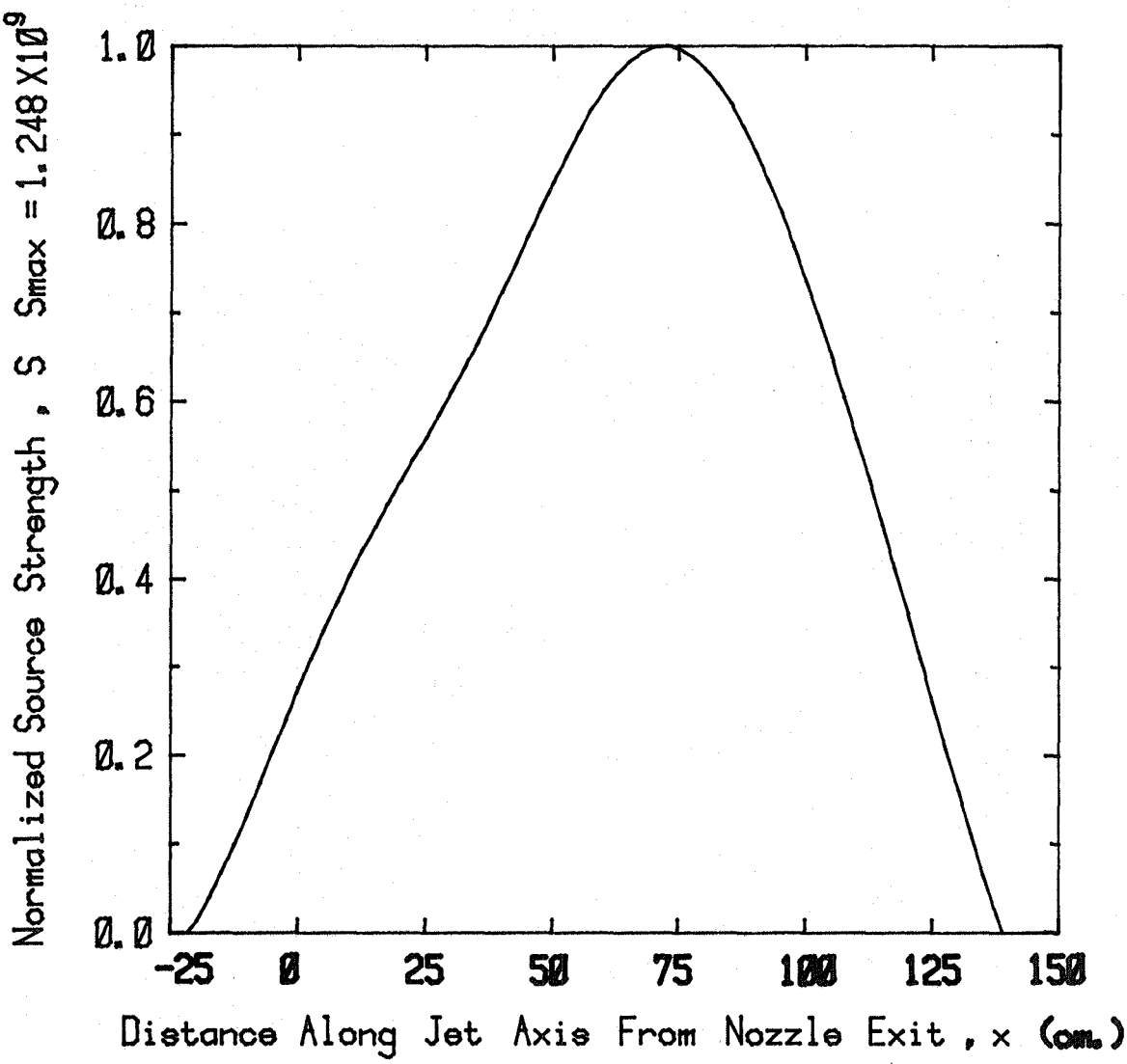

Coannular Jet - Source Distribution

(Frequency = 0.60 KHz)

Figure A2.22(b)

Velocity Ratio , V_f/V_p = 1.950

Static Temperature Ratio , T_f/T_p = 2.470

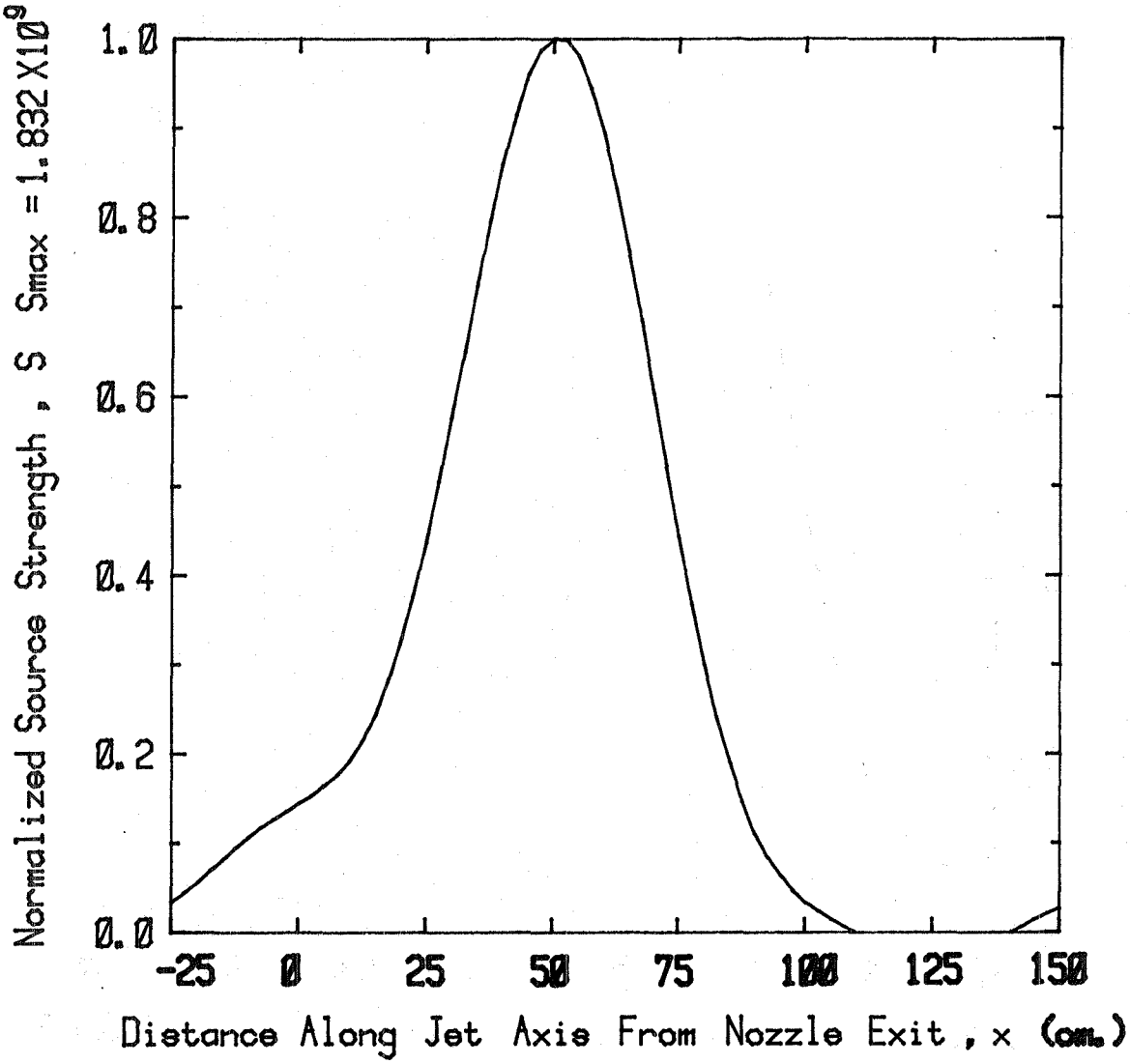

Coannular Jet - Source Distribution

(Frequency = 1.20 KHz)

Figure A2.22(c)

Velocity Ratio , V_f/V_p = 1.950

Static Temperature Ratio , T_f/T_p = 2.470

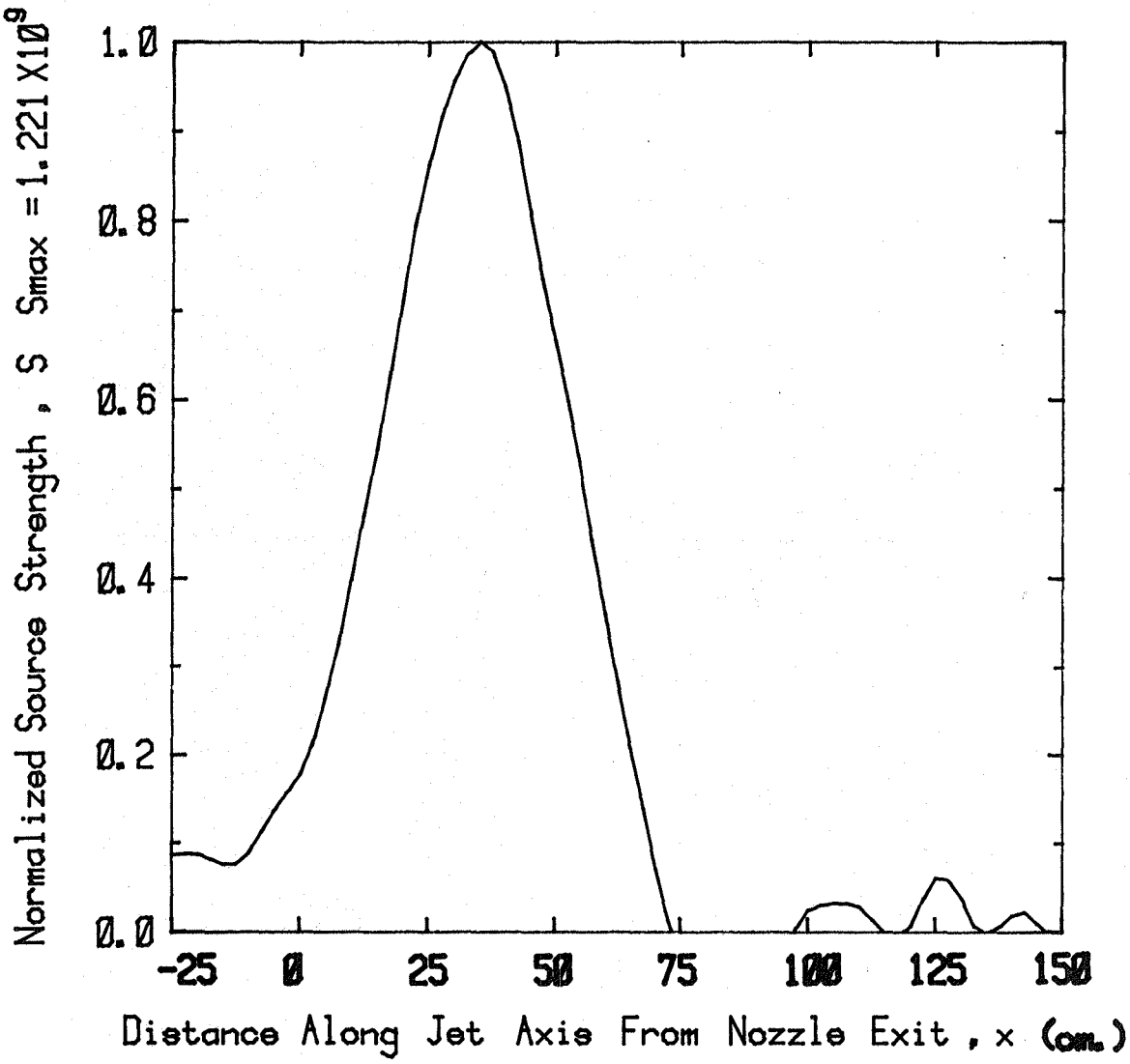

Coannular Jet - Source Distribution
(Frequency = 2.46 KHz)

Figure A2.22(d)

Velocity Ratio , V_f/V_p = 1.950

Static Temperature Ratio , T_f/T_p = 2.470

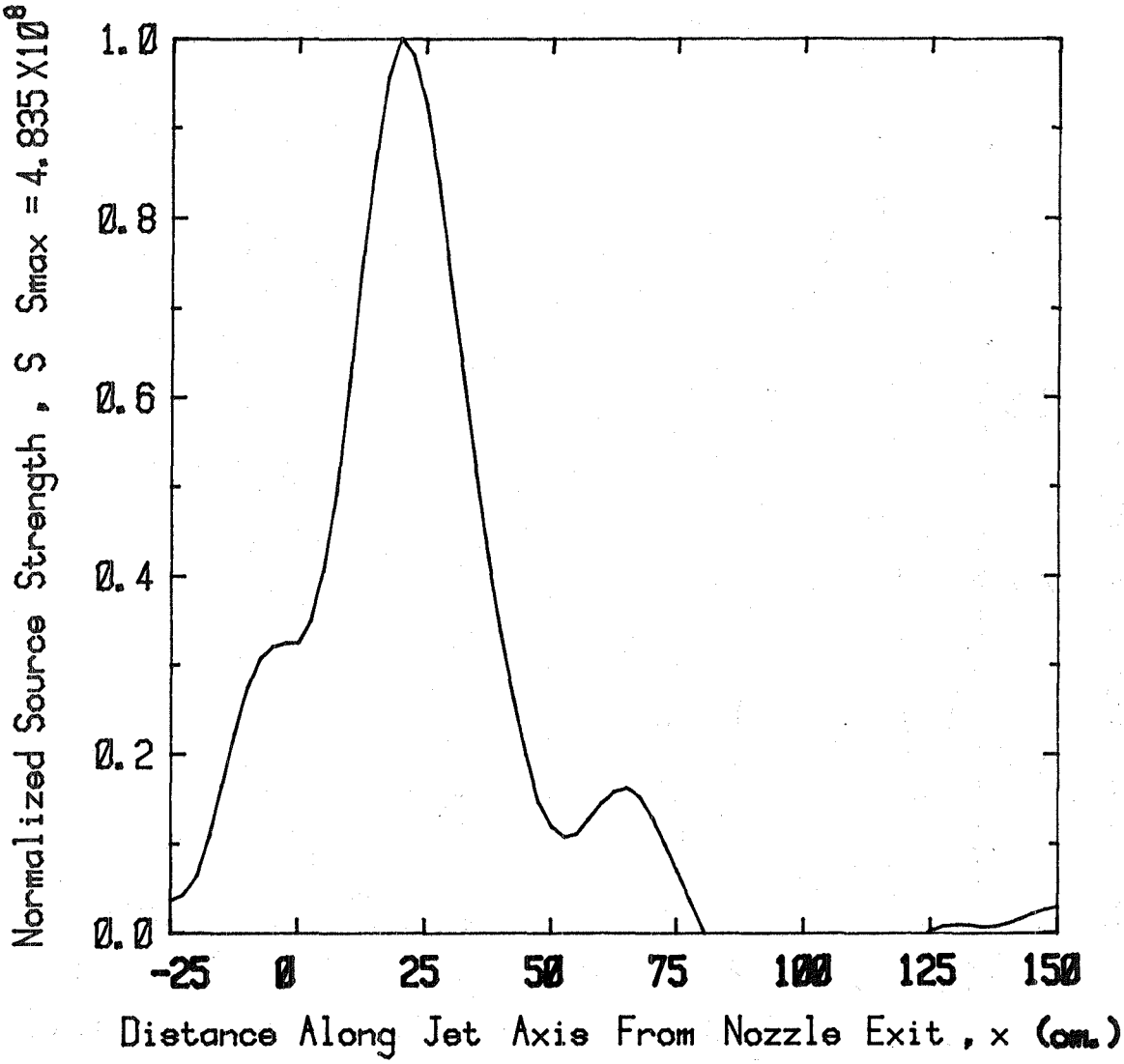

Coannular Jet - Source Distribution

(Frequency = 4.98 KHz)

Figure A2.22(e)

Velocity Ratio , V_f/V_p = 1.950

Static Temperature Ratio , T_f/T_p = 2.470

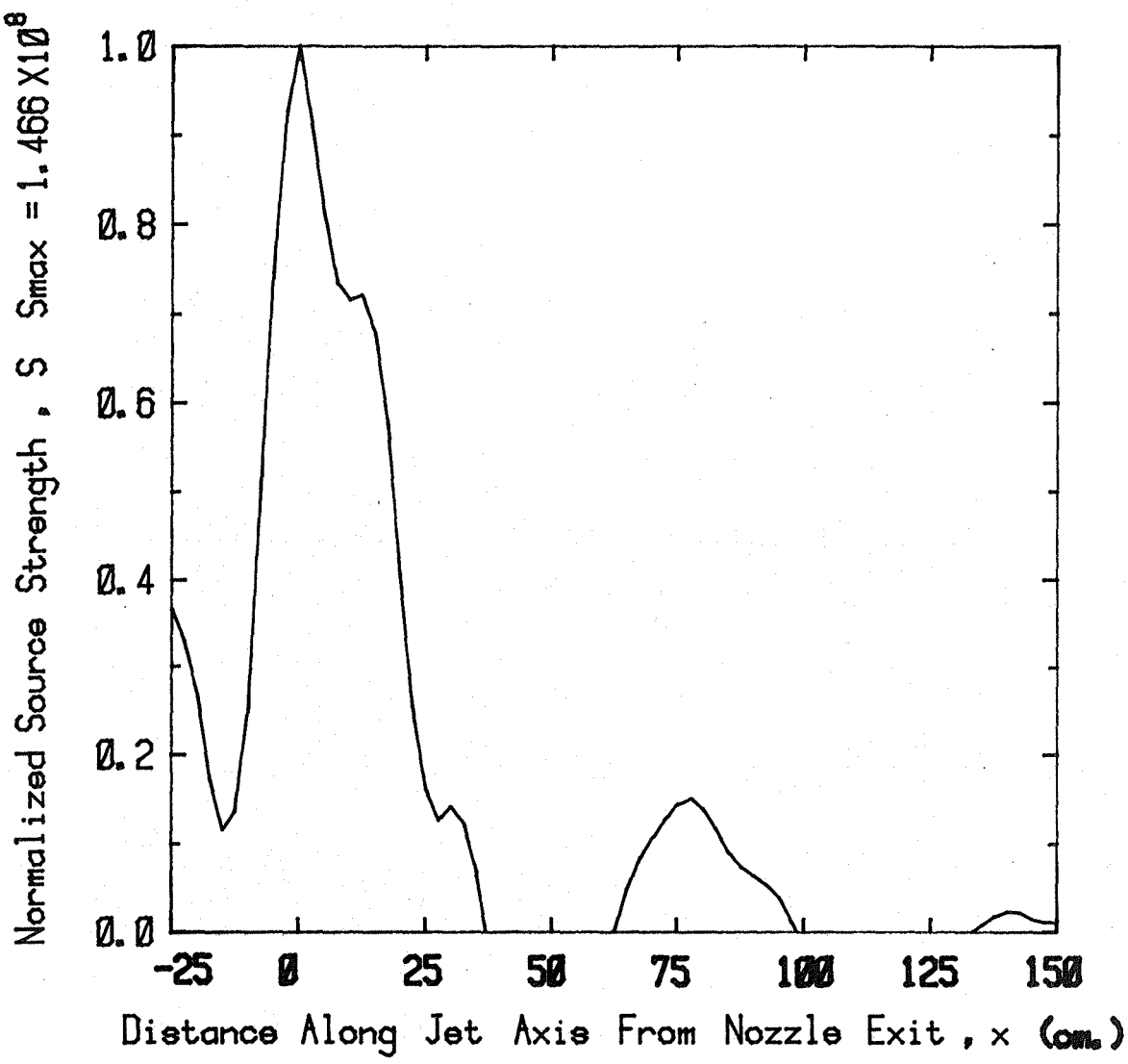

Coannular Jet - Source Distribution

(Frequency = 9.96 KHz)

Figure A2.22(f)

Velocity Ratio , V_f/V_p = 1.950

Static Temperature Ratio , T_f/T_p = 2.470

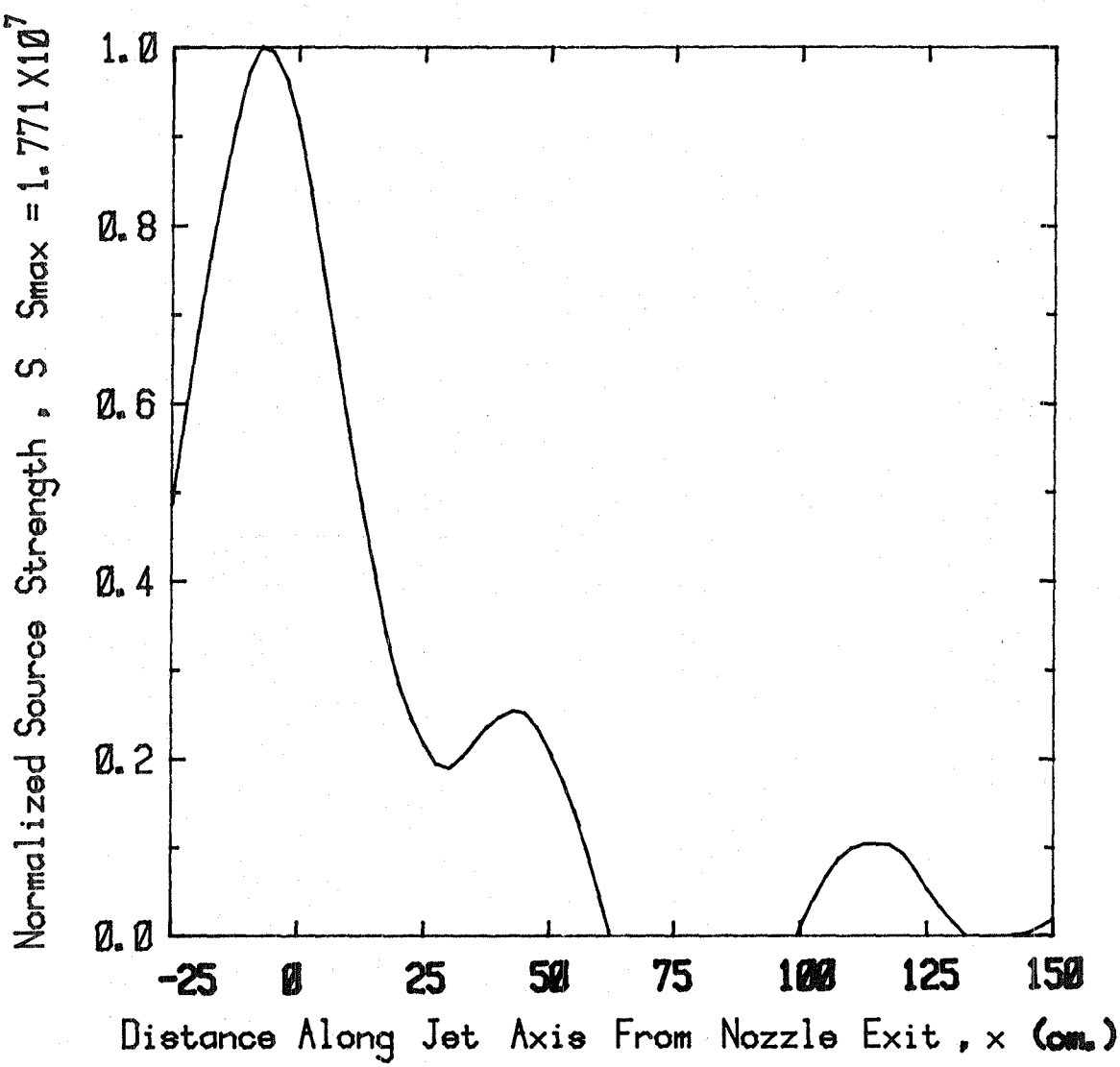

Coannular Jet - Source Distribution

(Frequency = 19.98 KHz)

Figure A2.22(g)

Velocity Ratio , V_f/V_p = 1.660

Static Temperature Ratio , T_f/T_p = 1.260

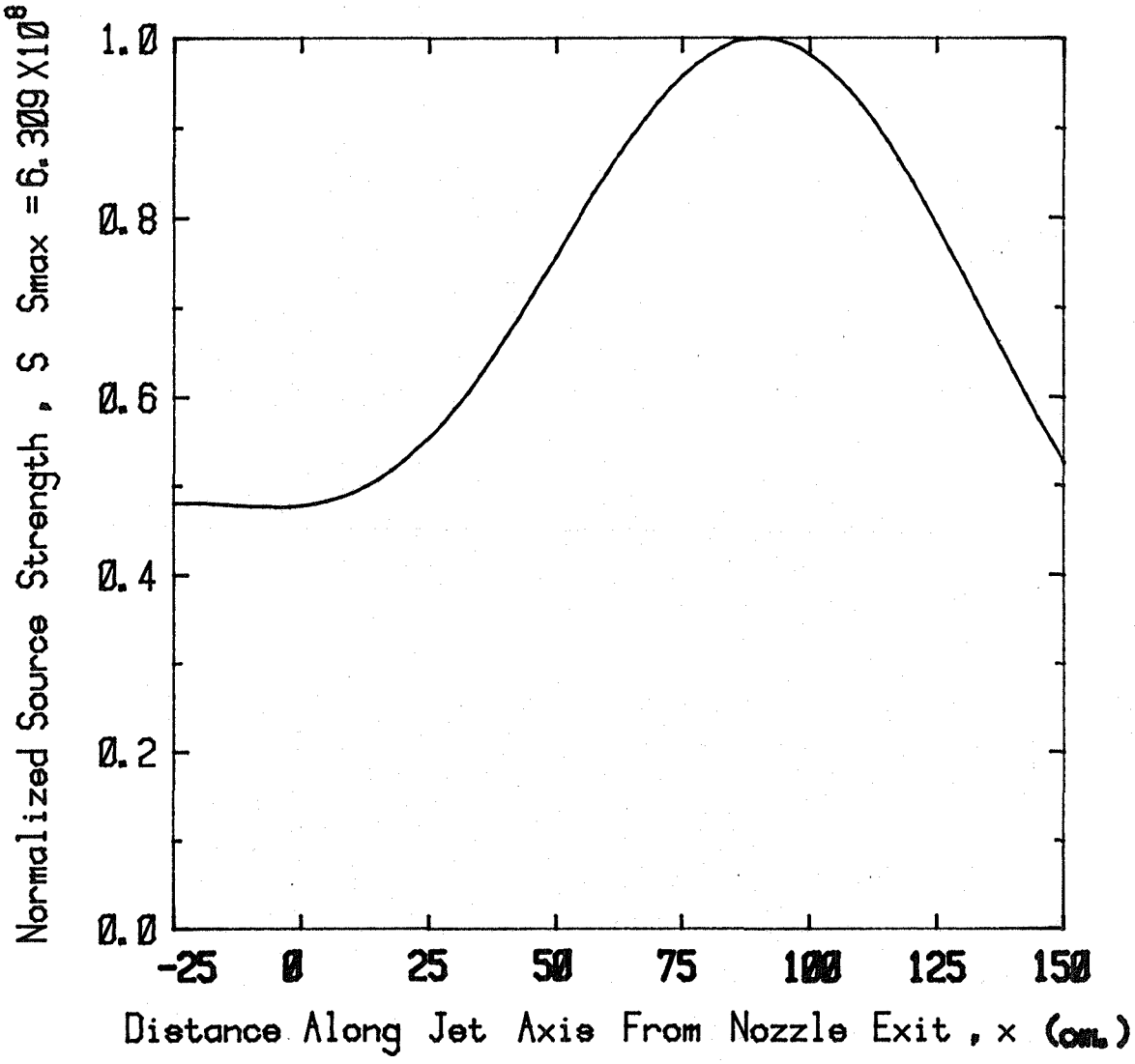

Coannular Jet - Source Distribution

(Frequency = 0.30 KHz)

Figure A2.23(a)

Velocity Ratio , V_f/V_p = 0.900

Static Temperature Ratio , T_f/T_p = 0.840

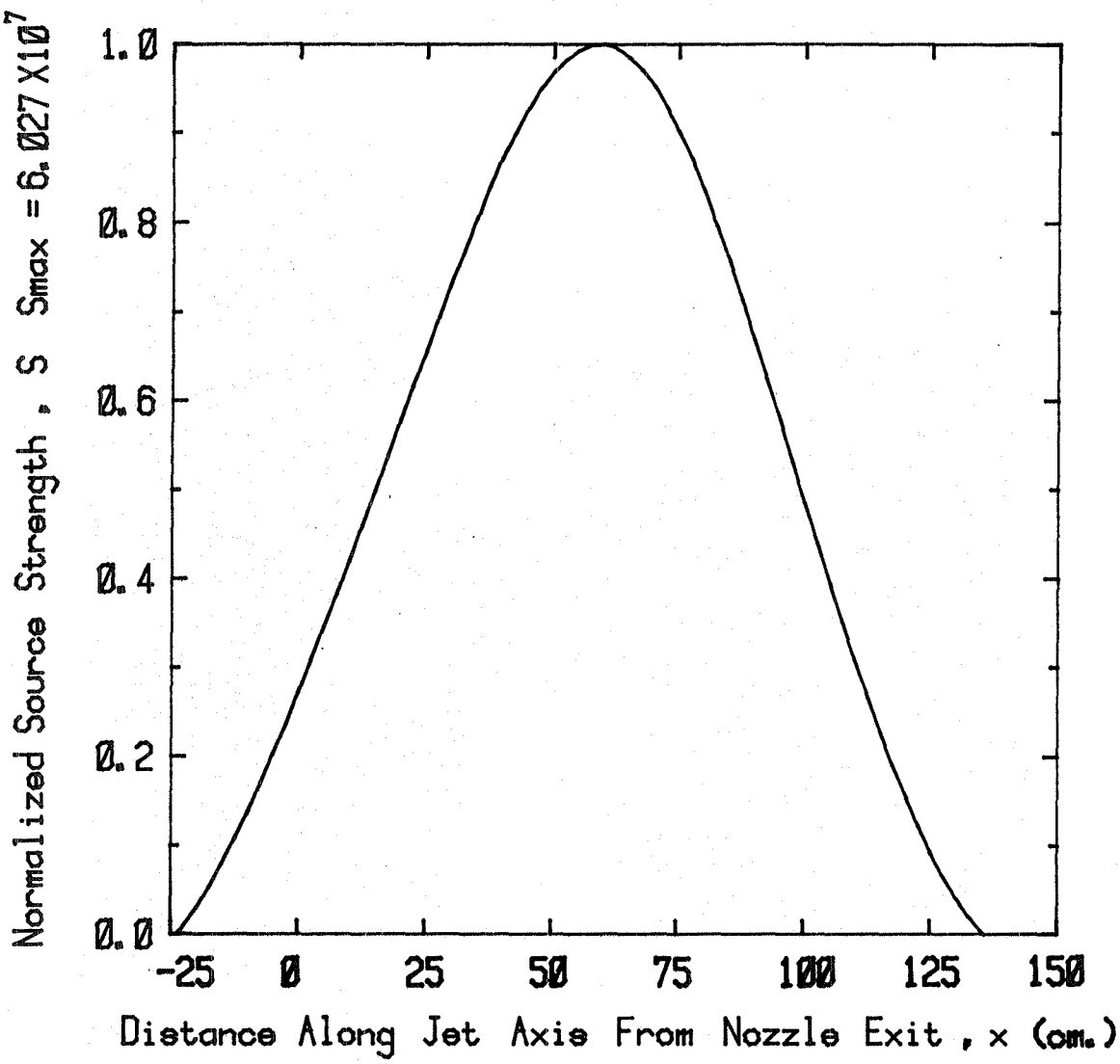

Coannular Jet - Source Distribution

(Frequency = 0.60 KHz)

Figure A2.24(b)

Velocity Ratio , V_f/V_p = 0.900

Static Temperature Ratio , T_f/T_p = 0.840

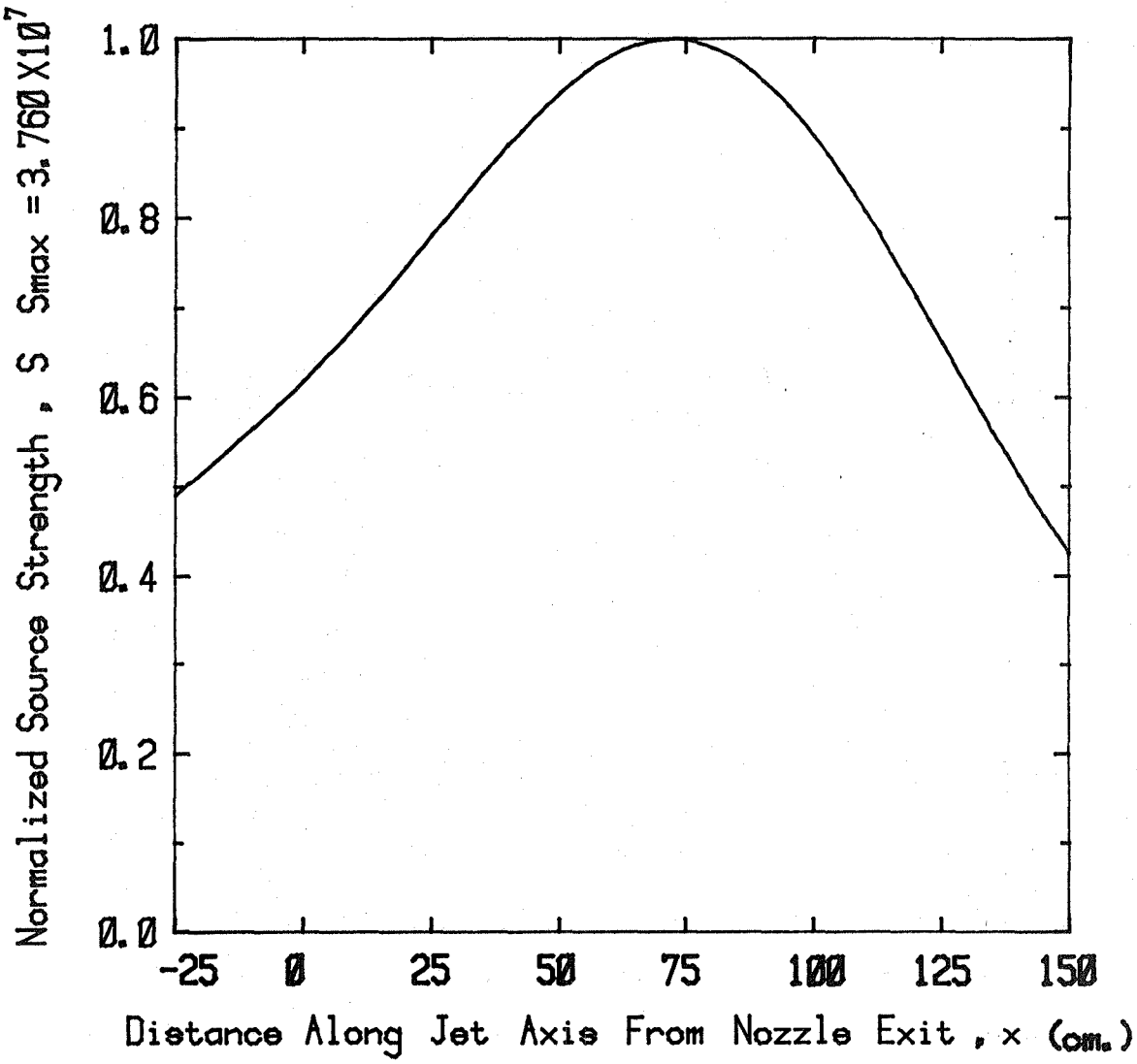

Coannular Jet - Source Distribution

(Frequency = 0.30 KHz)

Figure A2.24(a)

Velocity Ratio , V_f/V_p = 1.660

Static Temperature Ratio , T_f/T_p = 1.260

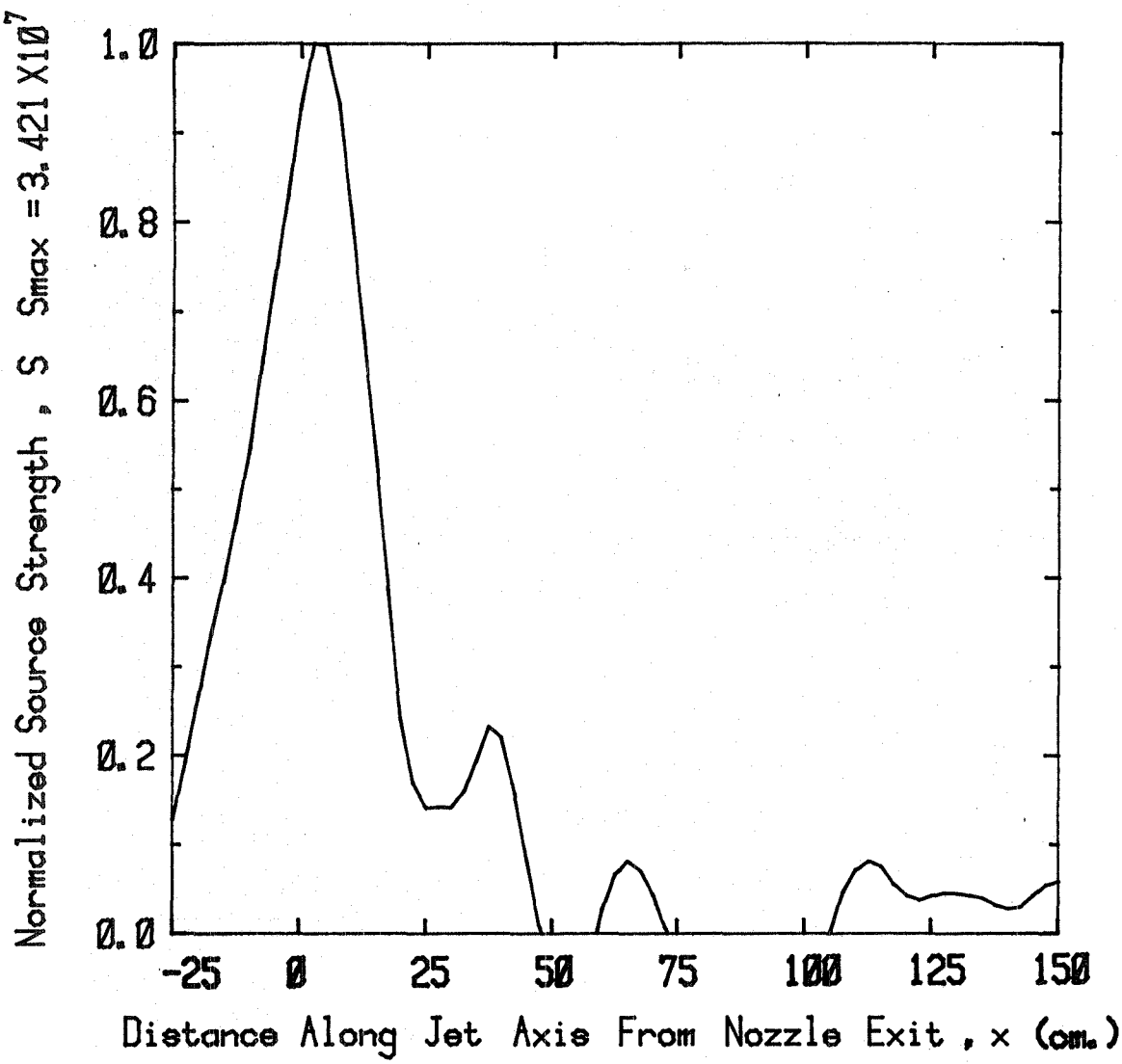

Coannular Jet - Source Distribution

(Frequency = 19.98 KHz)

Figure A2.23(g)

Velocity Ratio , V_f/V_p = 1.660

Static Temperature Ratio , T_f/T_p = 1.260

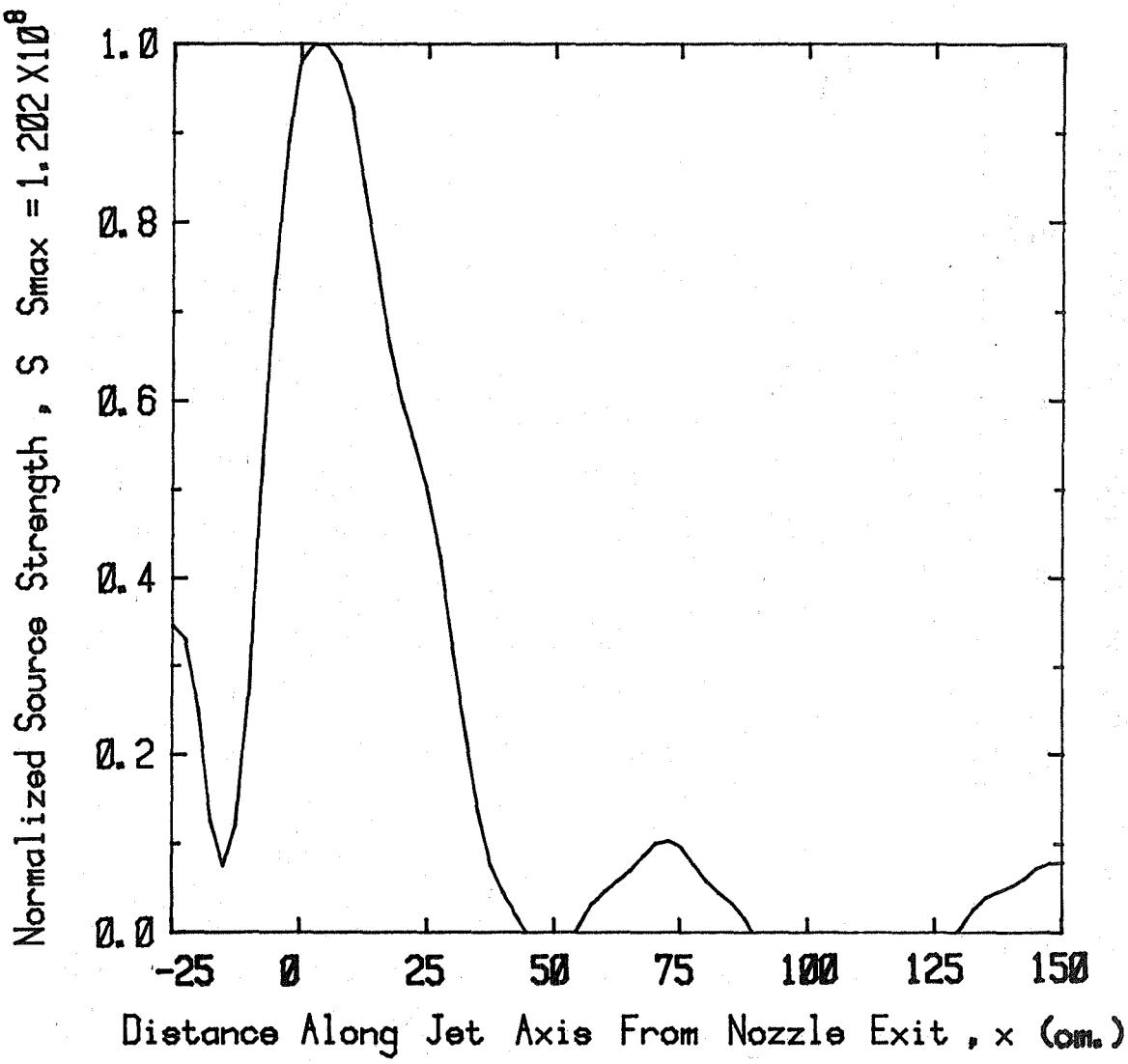

Coannular Jet - Source Distribution

(Frequency = 9.96 KHz)

Figure A2.23(f)

Velocity Ratio , V_f/V_p = 1.660

Static Temperature Ratio , T_f/T_p = 1.260

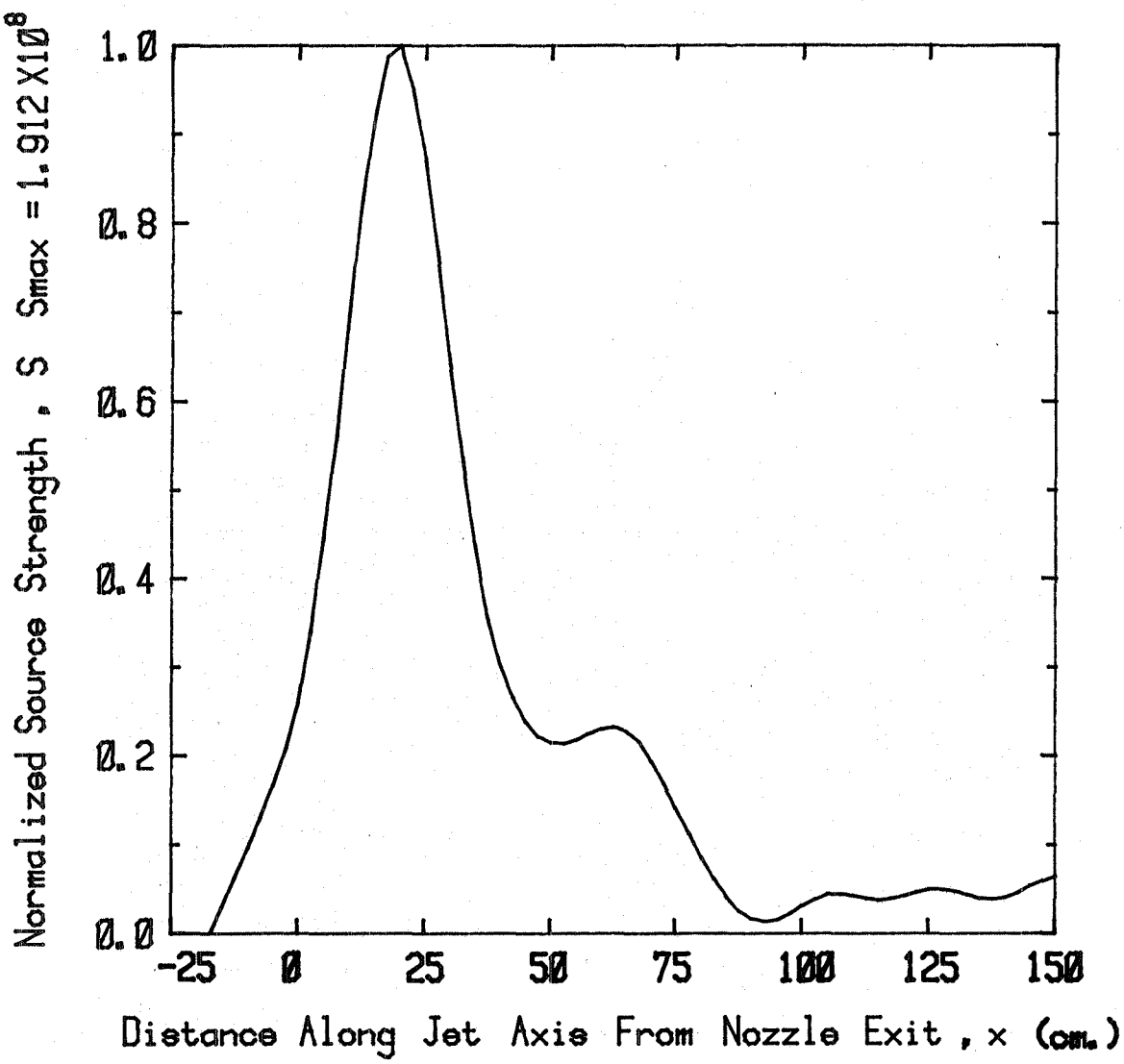

Coannular Jet - Source Distribution

(Frequency = 4.98 KHz)

Figure A2.23(e)

Velocity Ratio , V_f/V_p = 1.660

Static Temperature Ratio , T_f/T_p = 1.260

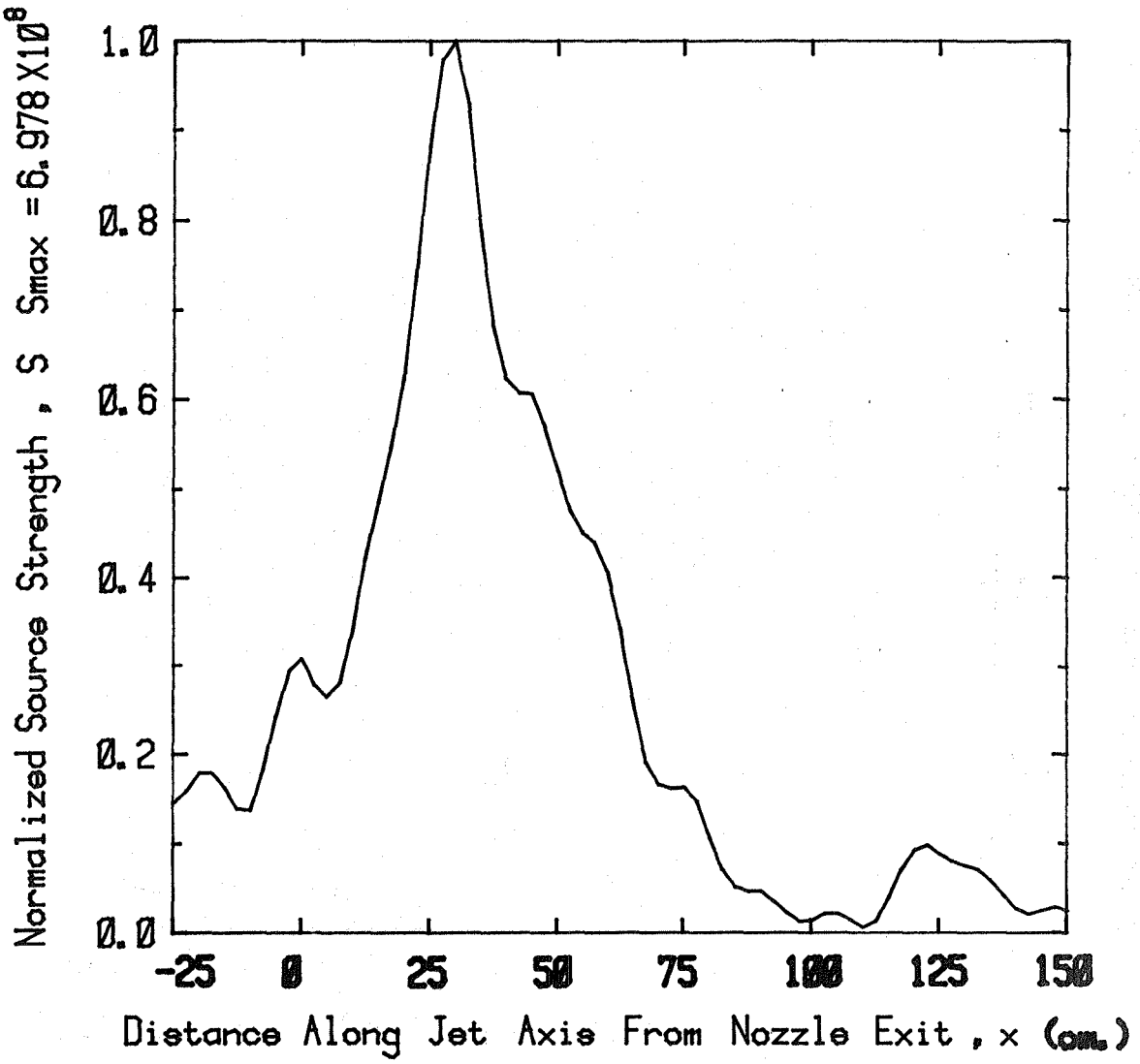

Coannular Jet - Source Distribution
(Frequency = 2.46 KHz)

Figure A2.23(d)

Velocity Ratio , V_f/V_p = 1.660

Static Temperature Ratio , T_f/T_p = 1.260

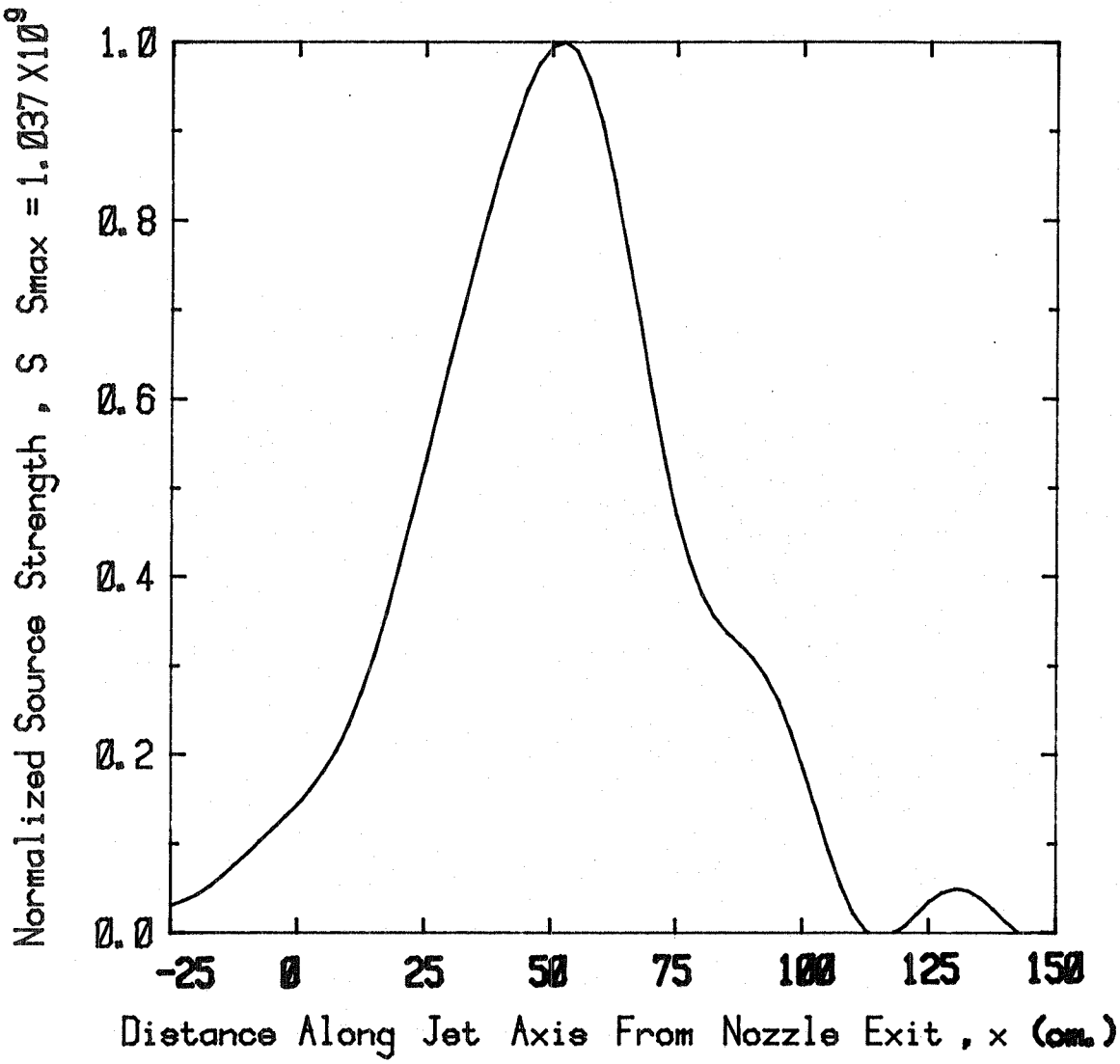

Coannular Jet - Source Distribution

(Frequency = 1.20 KHz)

Figure A2.23(c)

Velocity Ratio , V_f/V_p = 1.660

Static Temperature Ratio , T_f/T_p = 1.260

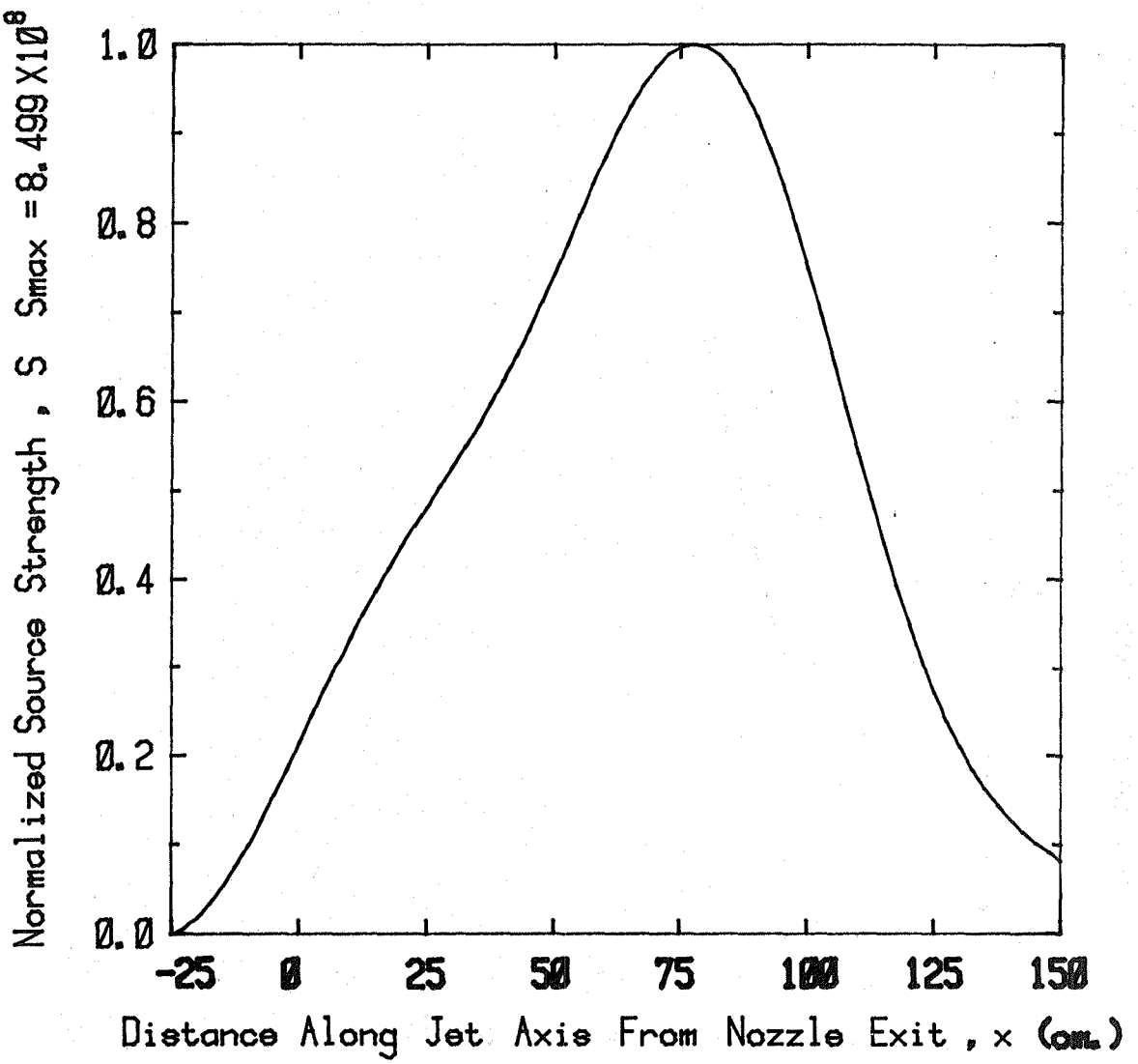

Coannular Jet - Source Distribution
(Frequency = 0.60 KHz)

Figure A2.23(b)

Velocity Ratio , V_f/V_p = 0.900

Static Temperature Ratio , T_f/T_p = 0.840

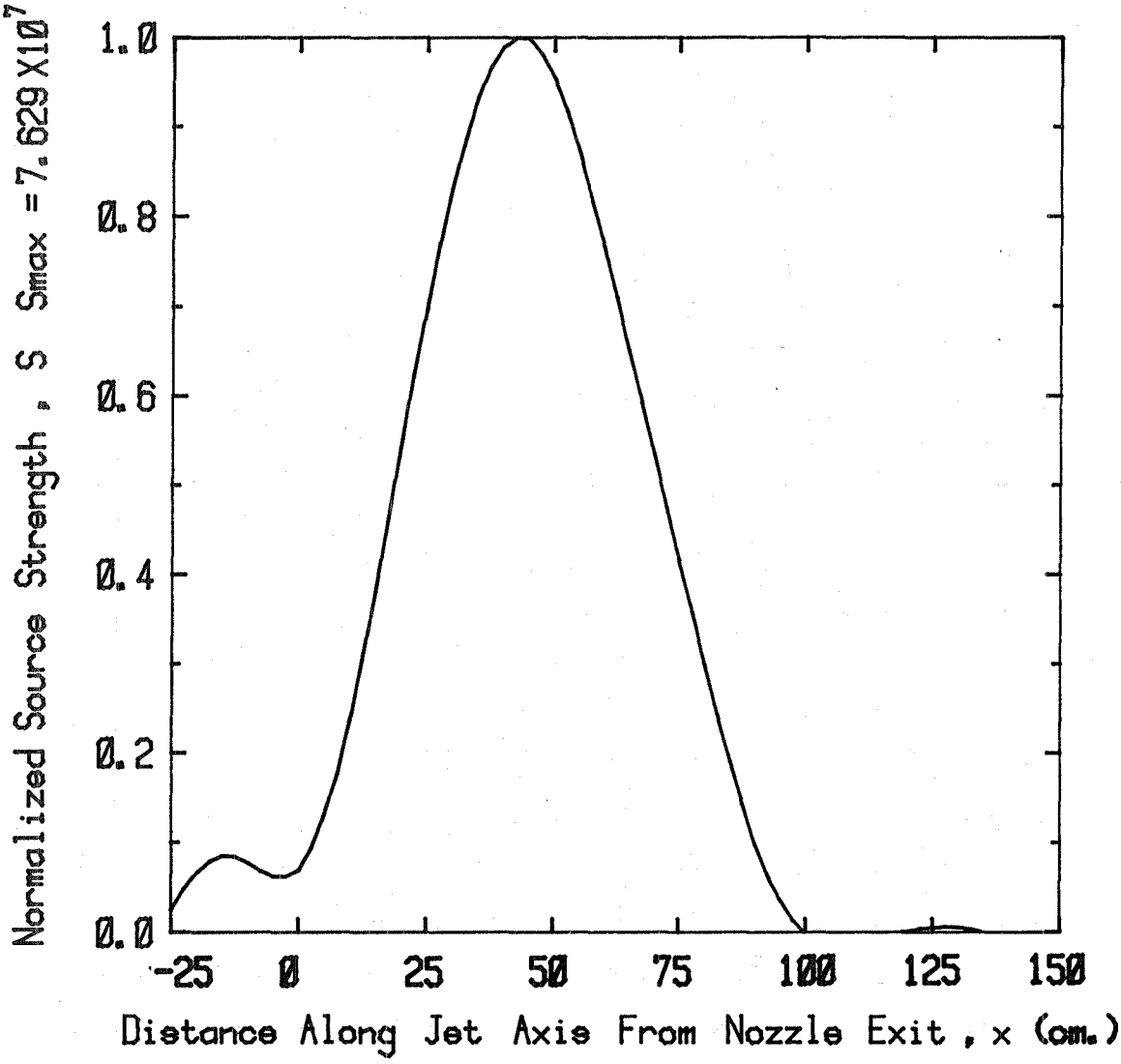

Coannular Jet - Source Distribution
(Frequency = 1.20 KHz)

Figure A2.24(c)

Velocity Ratio , V_f/V_p = 0.900

Static Temperature Ratio , T_f/T_p = 0.840

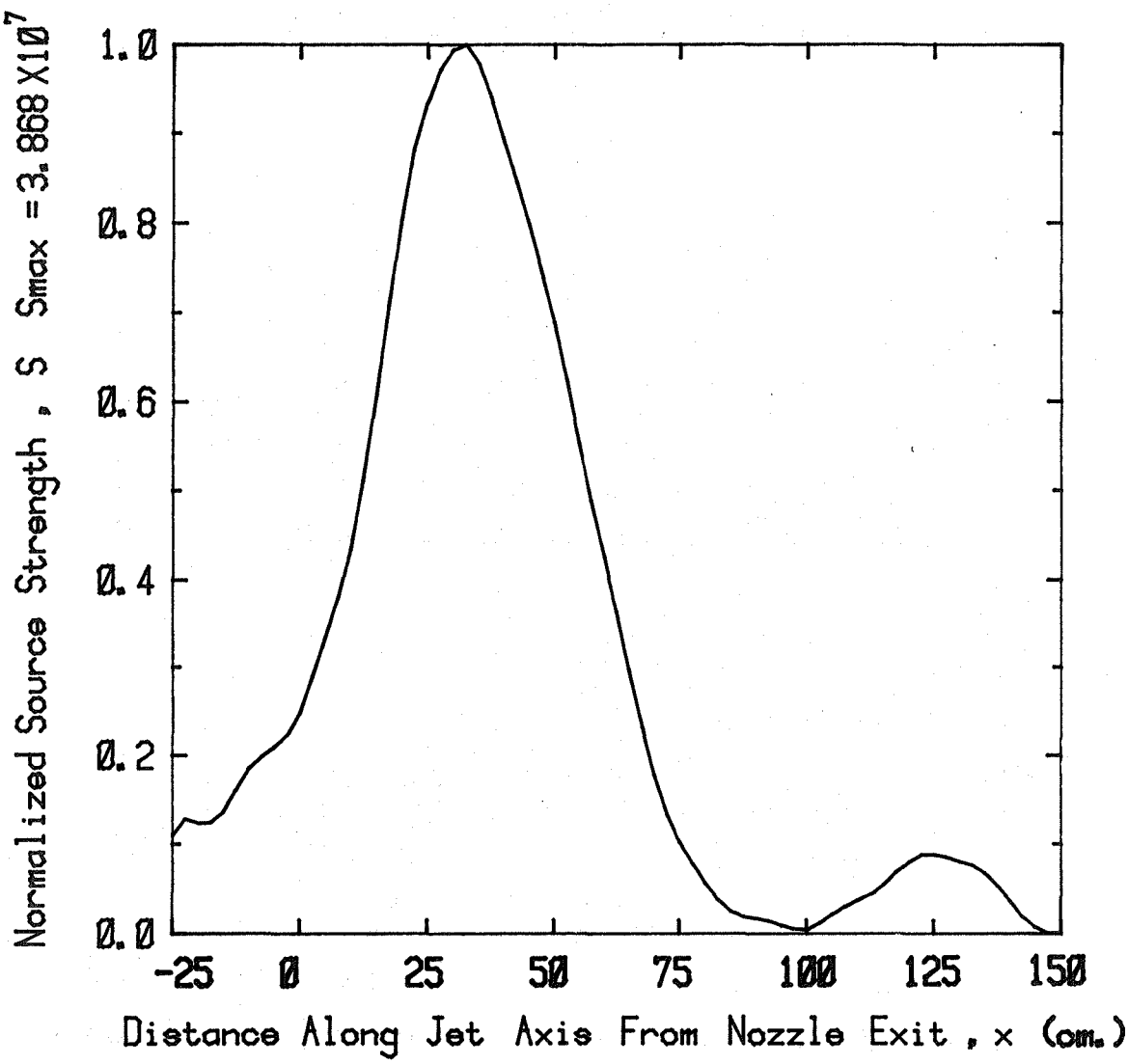

Coannular Jet - Source Distribution
(Frequency = 2.46 KHz)

Figure A2.24(d)

Velocity Ratio , V_f/V_p = 0.900

Static Temperature Ratio , T_f/T_p = 0.840

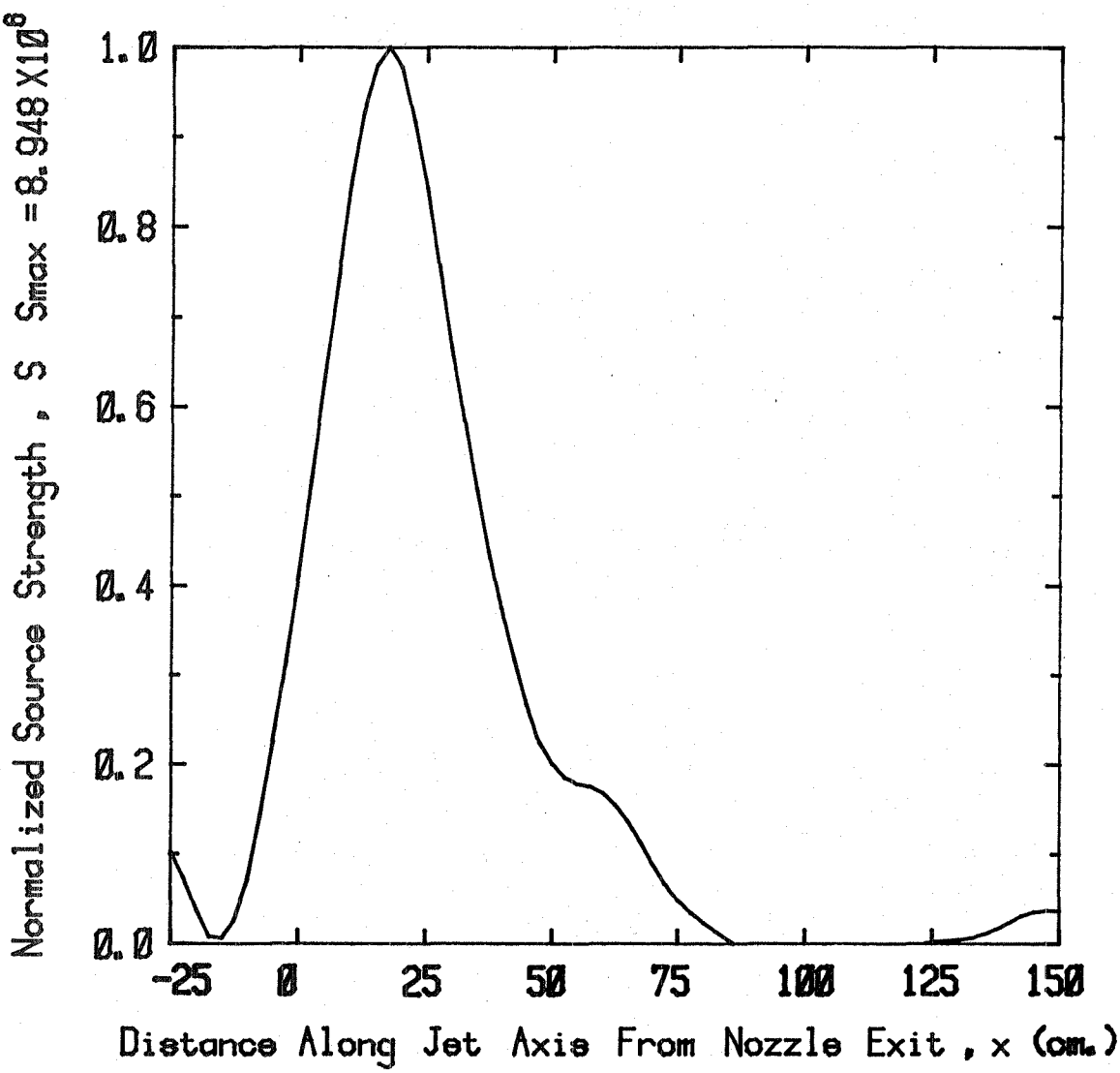

Coannular Jet - Source Distribution

(Frequency = 4.98 KHz)

Figure A2.24(e)

Velocity Ratio , V_f/V_p = 0.900

Static Temperature Ratio , T_f/T_p = 0.840

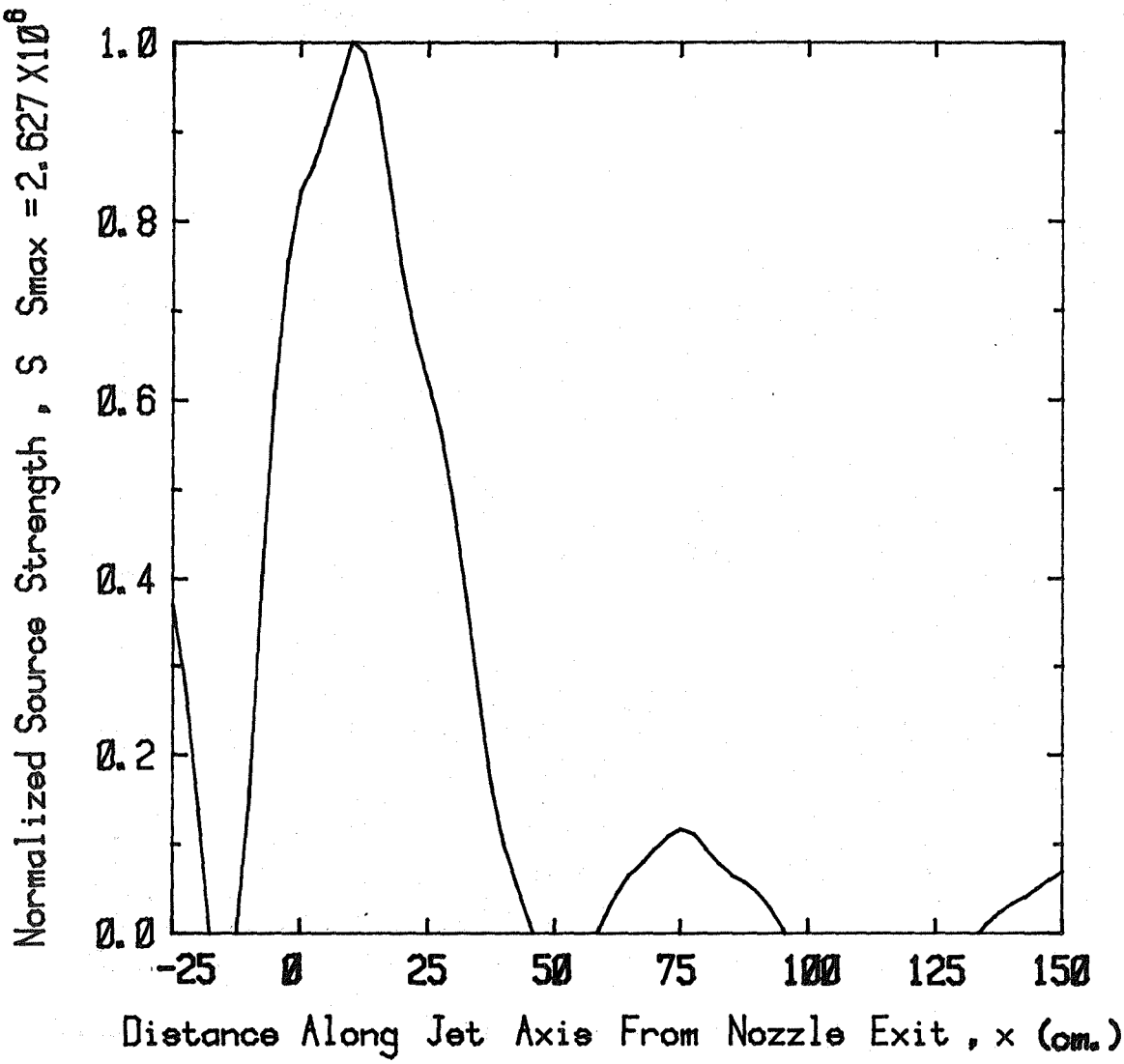

Coannular Jet - Source Distribution

(Frequency = 9.96 KHz)

Figure A2.24(f)

Velocity Ratio , V_f/V_p = 0.900

Static Temperature Ratio , T_f/T_p = 0.840

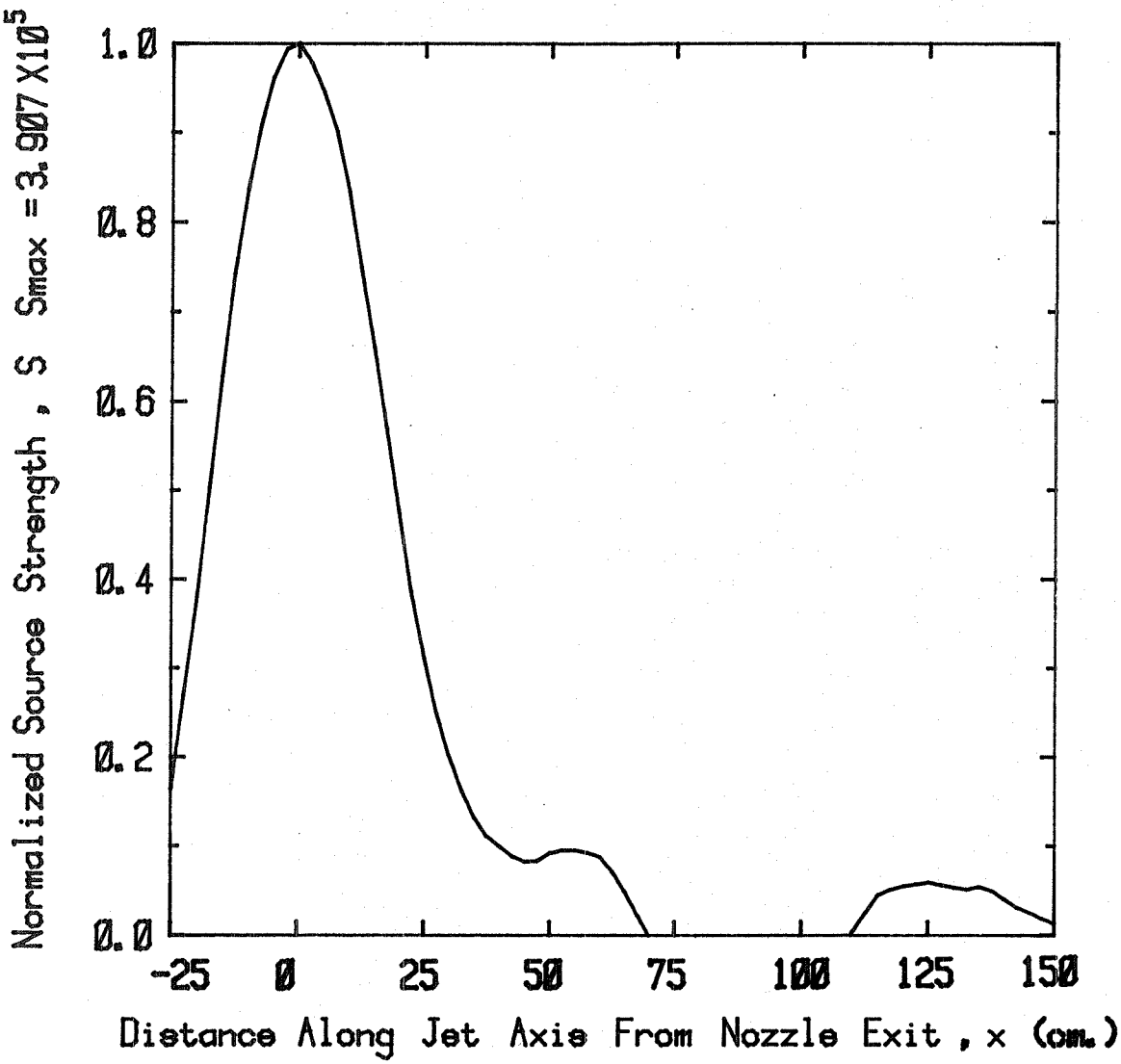

Coannular Jet - Source Distribution
(Frequency = 19.98 KHz)

Figure A2.24(g)

Velocity Ratio , V_f/V_p = 1.040

Static Temperature Ratio , T_f/T_p = 1.910

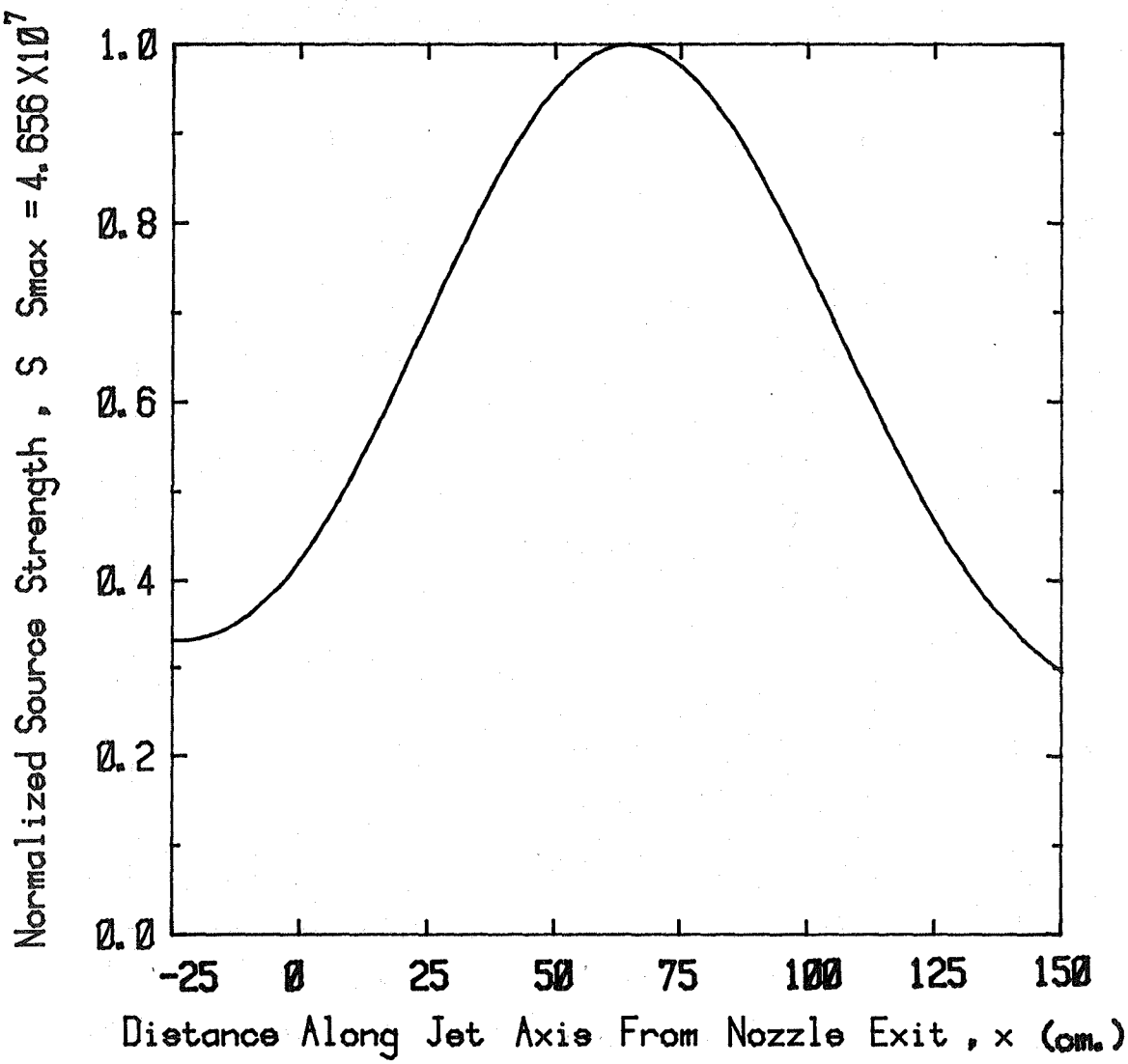

Coannular Jet - Source Distribution

(Frequency = 0.30 KHz)

Figure A2.25(a)

Velocity Ratio , V_f/V_p = 1.040

Static Temperature Ratio , T_f/T_p = 1.910

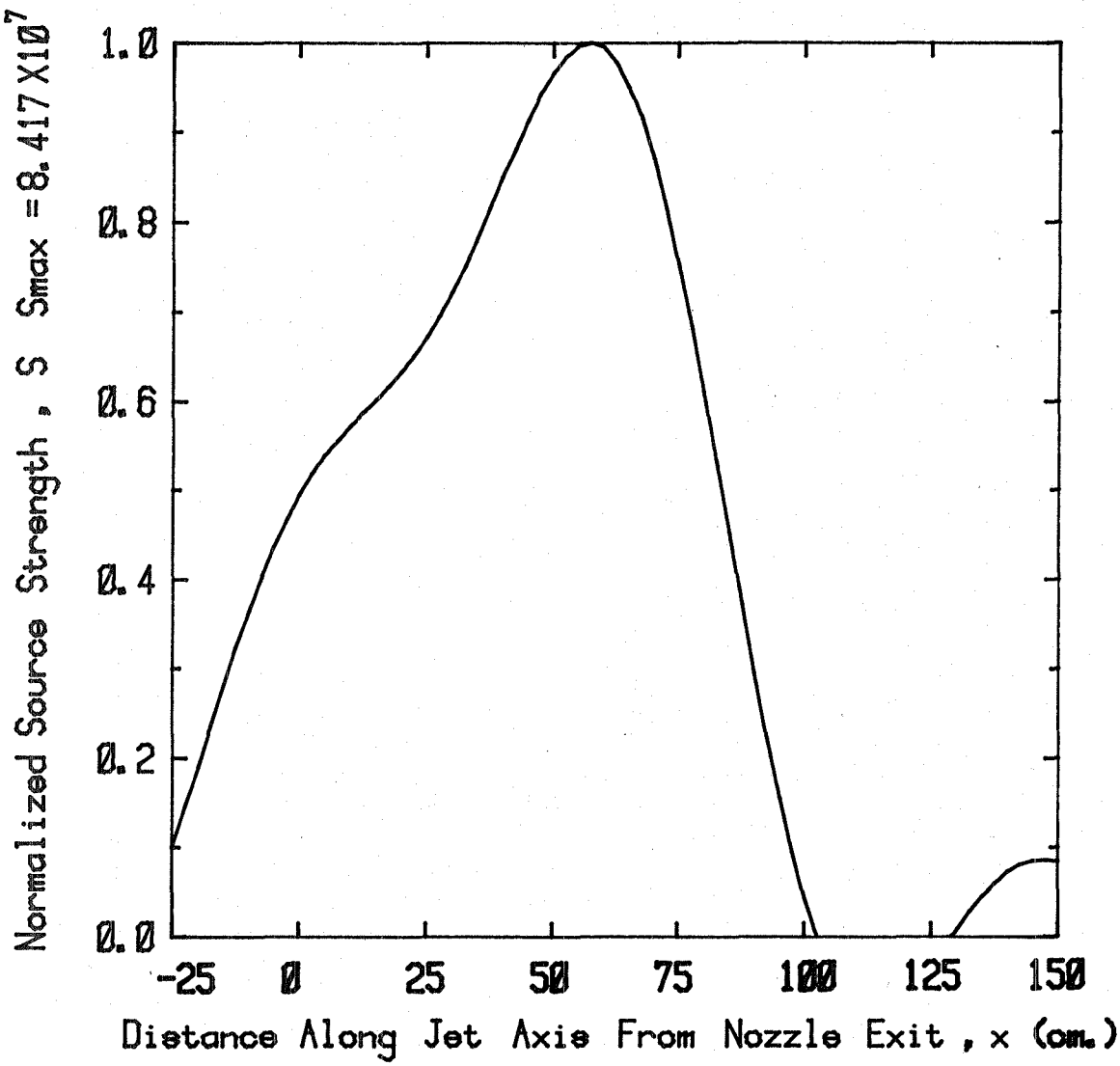

Coannular Jet - Source Distribution

(Frequency = 0.60 KHz)

Figure A2.25(b)

Velocity Ratio , V_f/V_p = 1.040

Static Temperature Ratio , T_f/T_p = 1.910

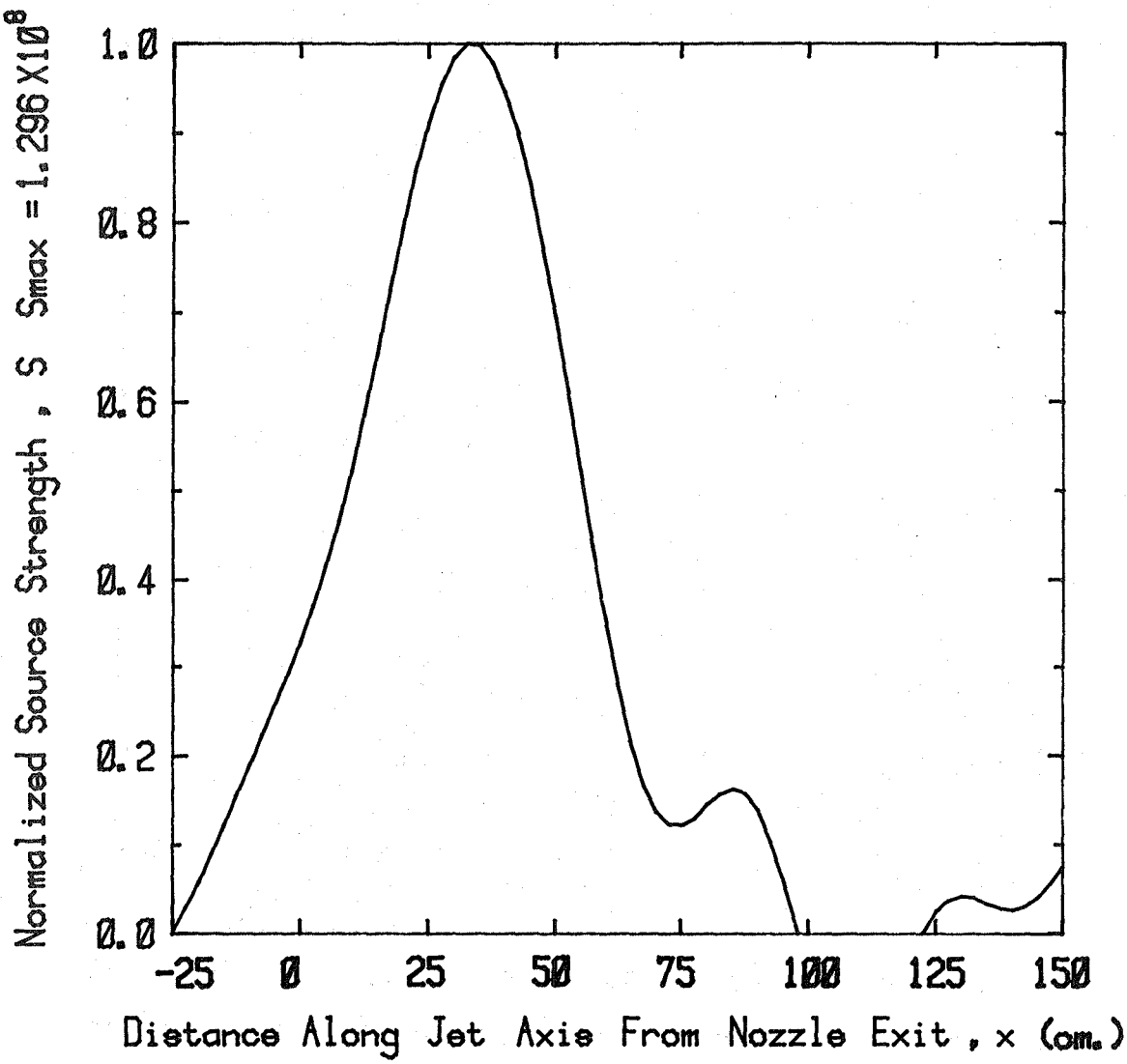

Coannular Jet - Source Distribution

(Frequency = 1.20 KHz)

Figure A2.25(c)

Velocity Ratio , V_f/V_p = 1.040

Static Temperature Ratio , T_f/T_p = 1.910

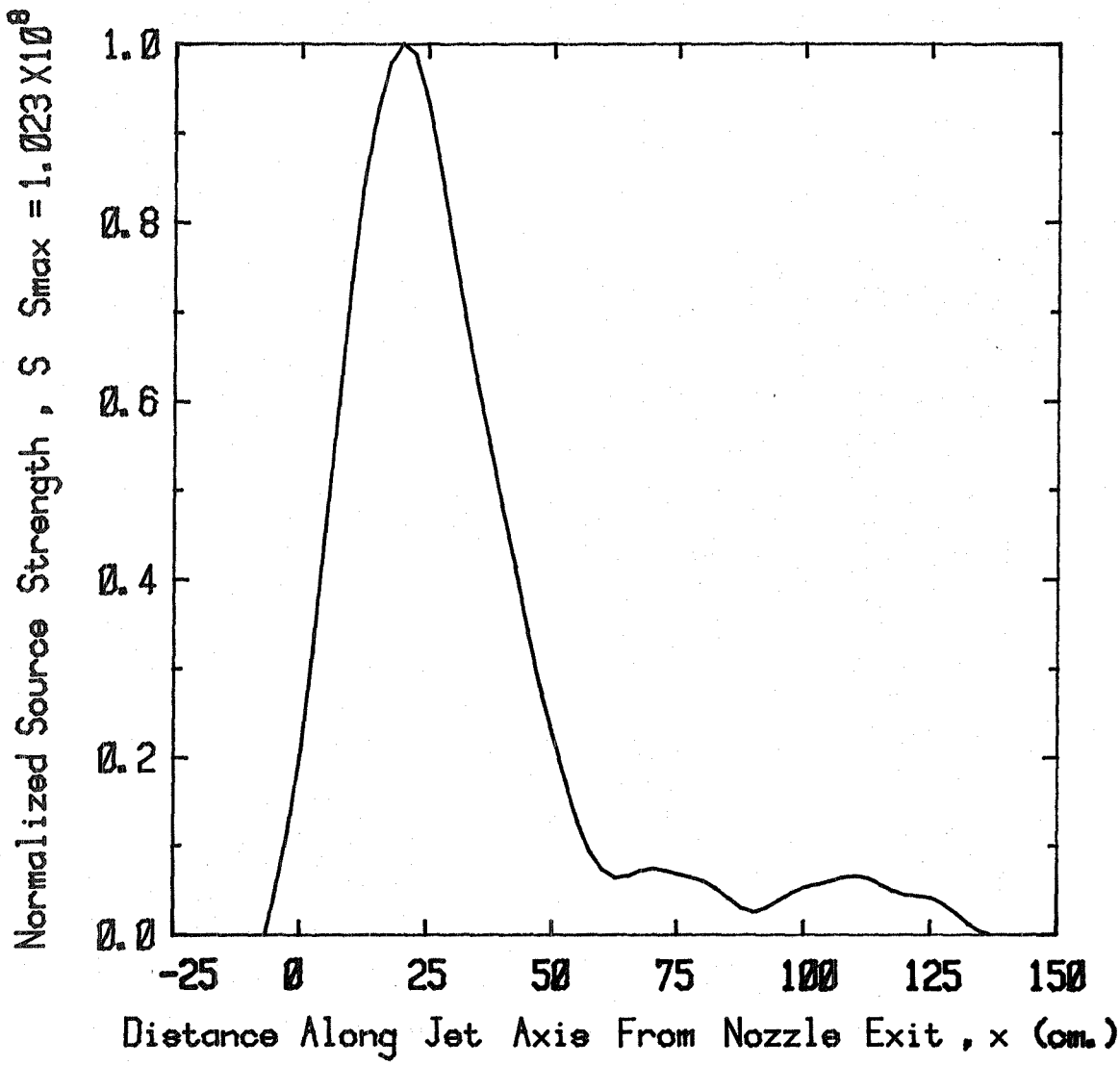

Coannular Jet - Source Distribution
(Frequency = 2.46 KHz)

Figure A2.25(d)

Velocity Ratio , V_f/V_p = 1.040

Static Temperature Ratio , T_f/T_p = 1.910

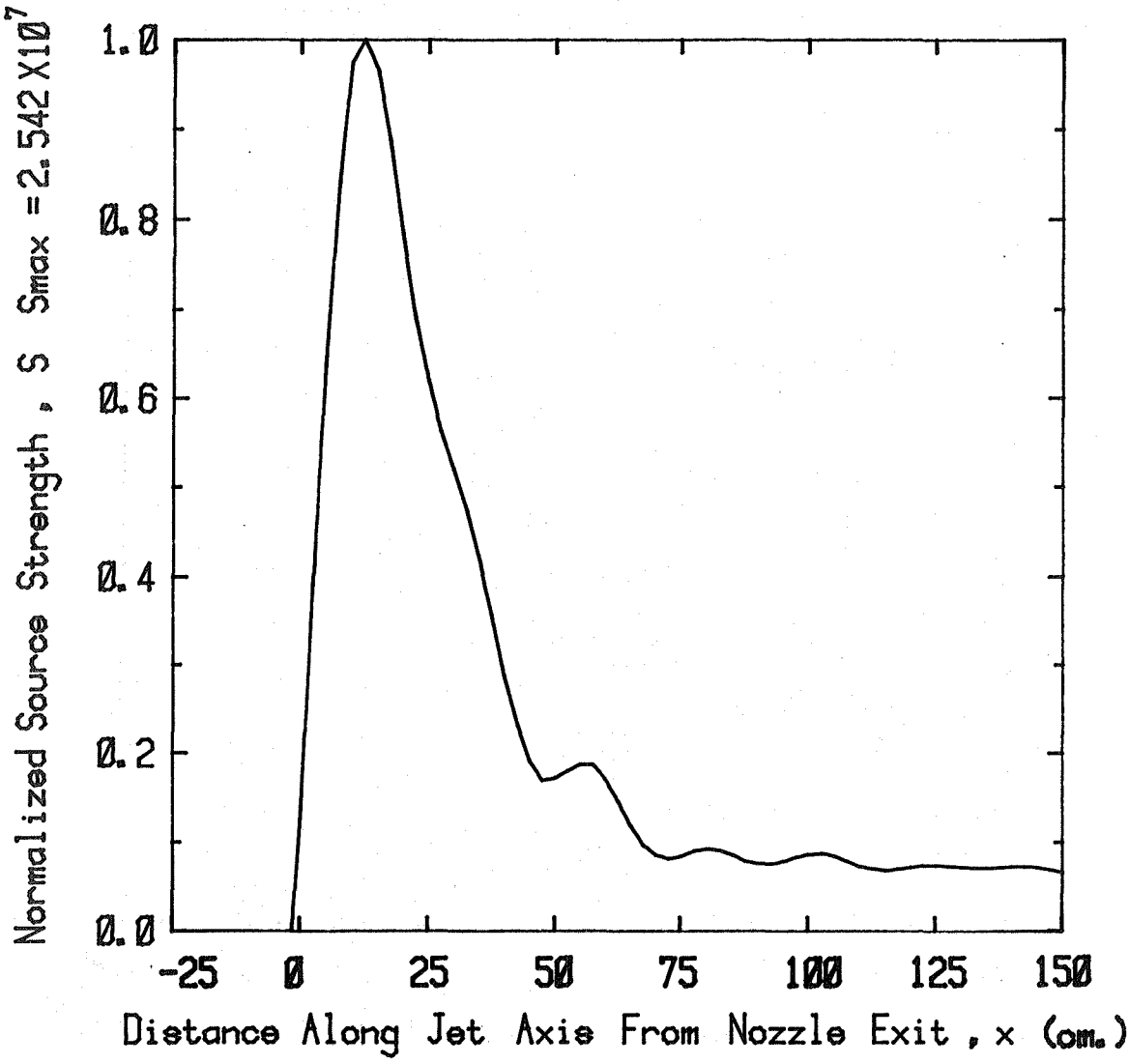

Coannular Jet - Source Distribution

(Frequency = 4.98 KHz)

Figure A2.25(e)

Velocity Ratio , V_f/V_p = 1.040

Static Temperature Ratio , T_f/T_p = 1.910

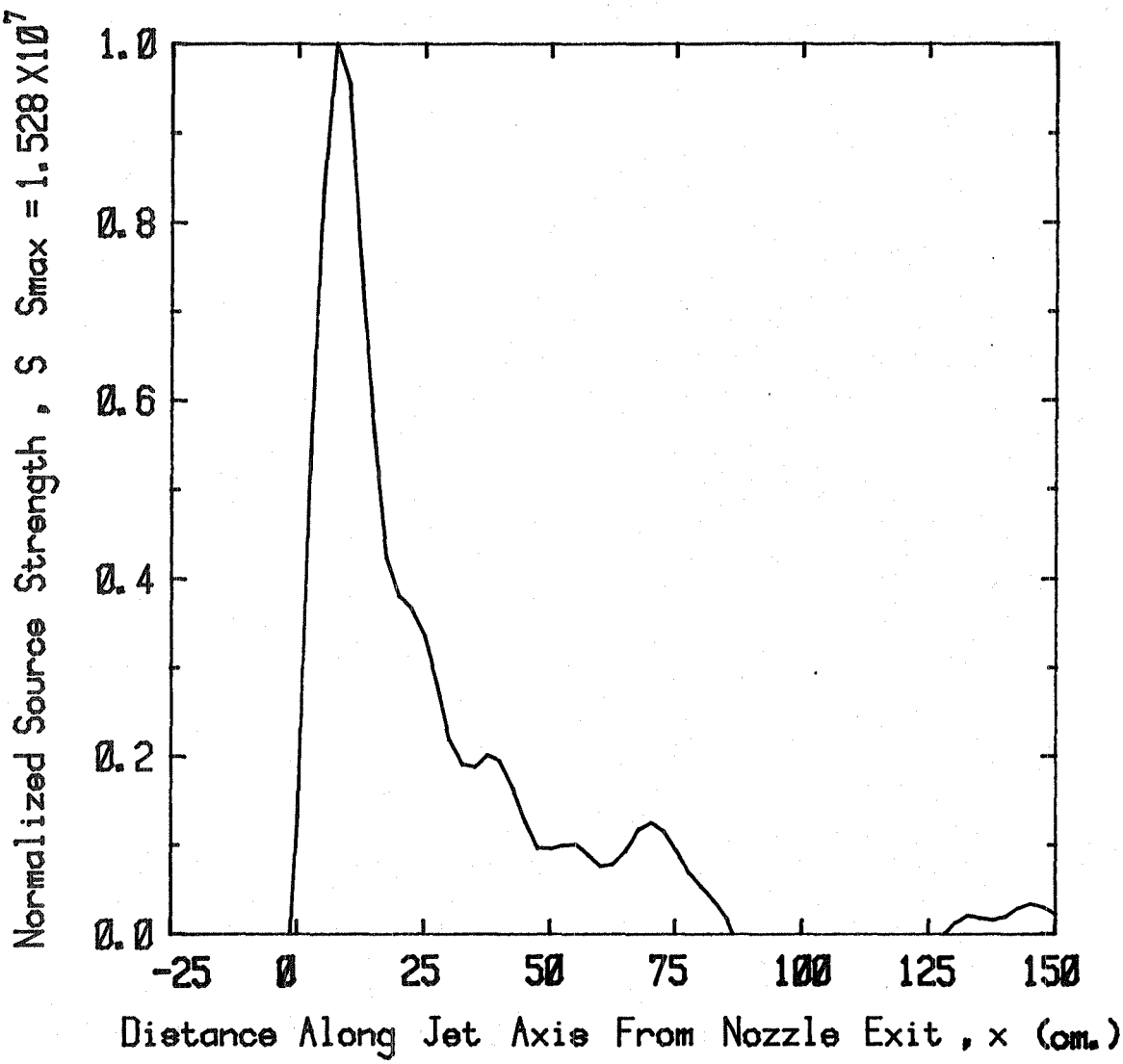

Coannular Jet - Source Distribution

(Frequency = 9.96 KHz)

Figure A2.25(f)

Velocity Ratio , V_f/V_p = 1.040

Static Temperature Ratio , T_f/T_p = 1.910

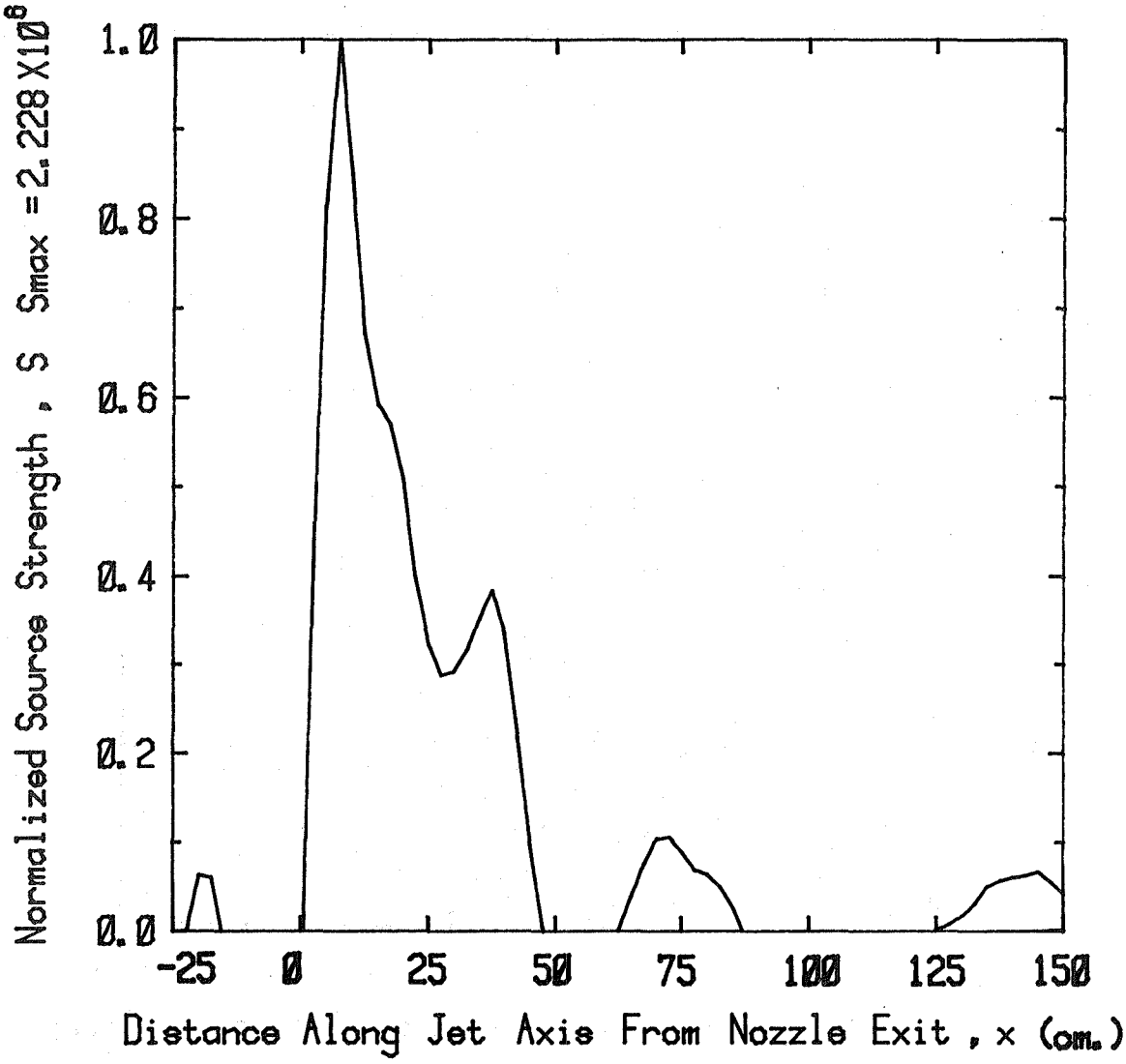

Coannular Jet - Source Distribution

(Frequency = 19.98 KHz)

Figure A2.25(g)

Velocity Ratio , V_f/V_p = 1.660

Static Temperature Ratio , T_f/T_p = 1.260

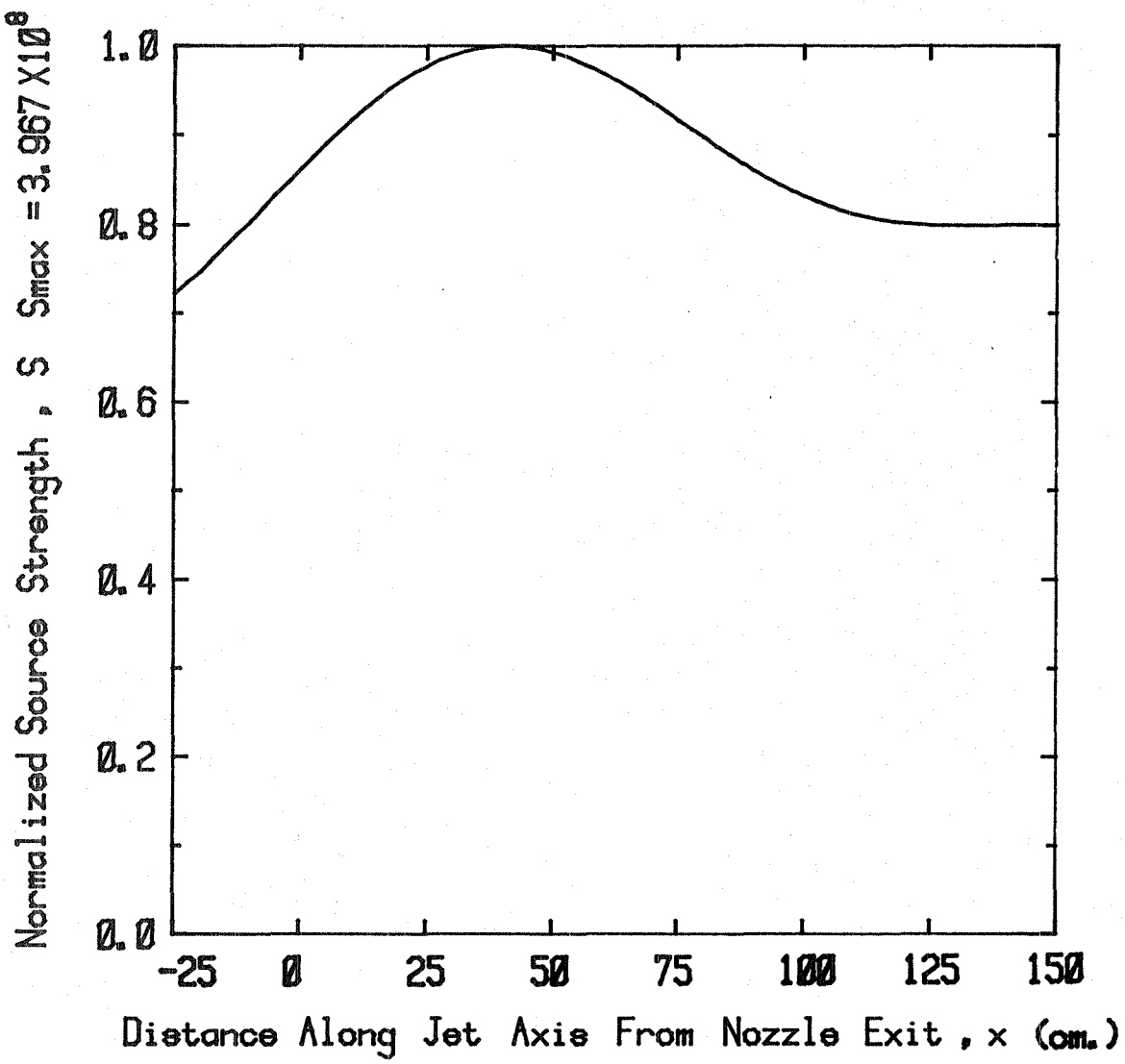

Coannular Jet - Source Distribution

(Frequency = 0.30 KHz)

Figure A2.26(a)

Velocity Ratio , V_f/V_p = 1.660

Static Temperature Ratio , T_f/T_p = 1.260

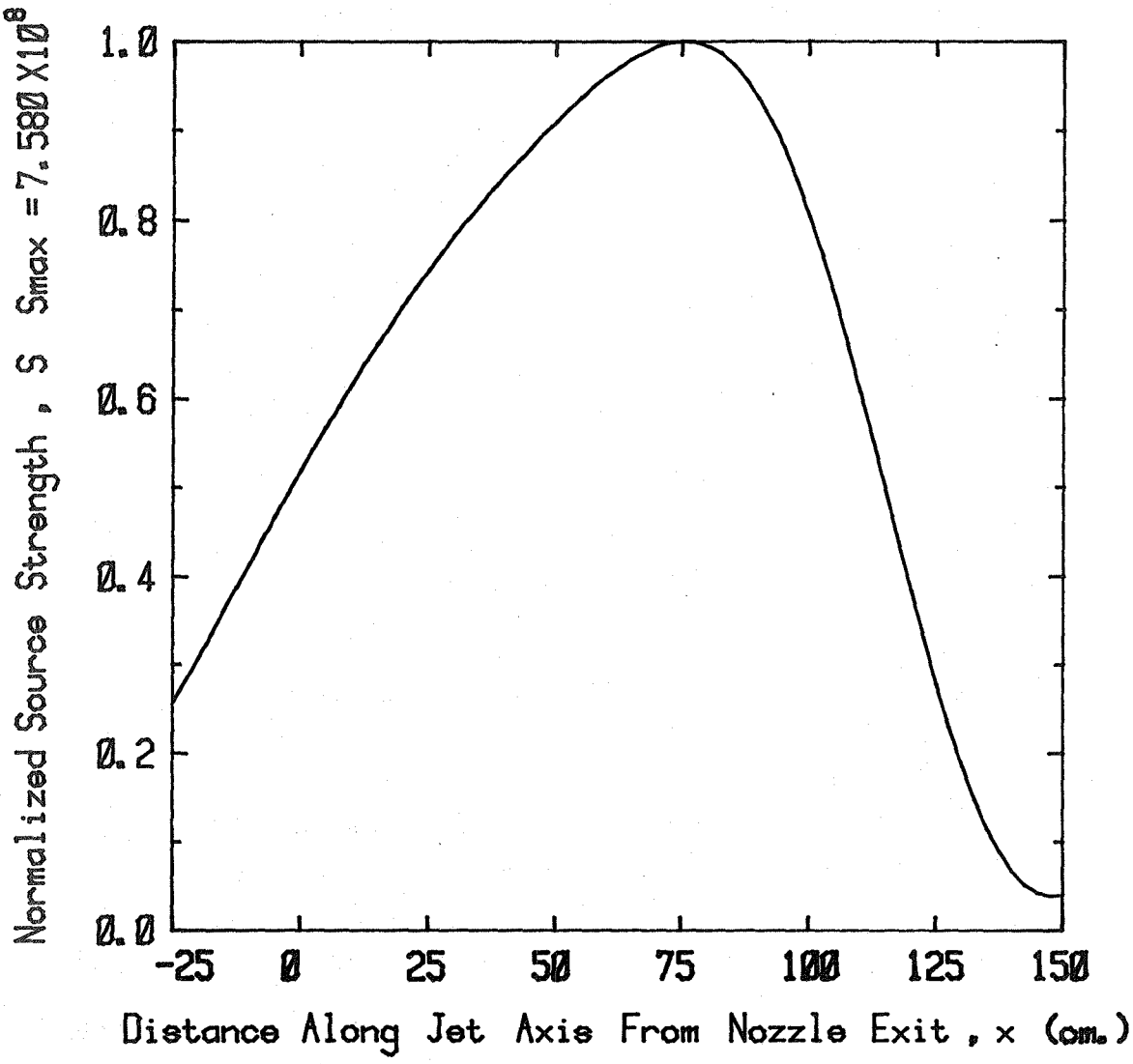

Coannular Jet - Source Distribution

(Frequency = 0.60 KHz)

Figure A2.26(b)

Velocity Ratio , V_f/V_p = 1.660

Static Temperature Ratio , T_f/T_p = 1.260

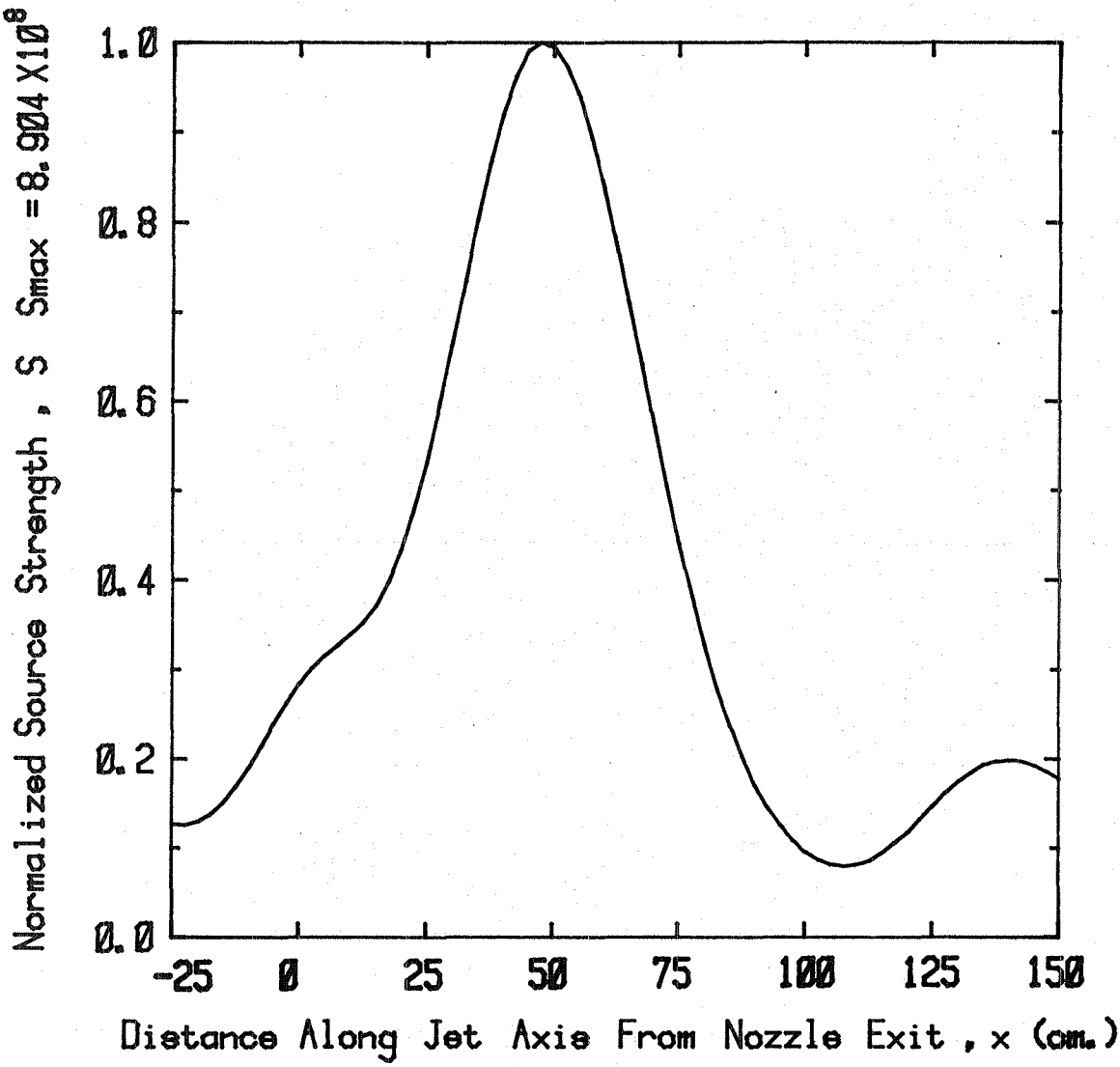

Coannular Jet - Source Distribution
(Frequency = 1.20 KHz)

Figure A2.26(c)

Velocity Ratio , V_f/V_p = 1.660

Static Temperature Ratio , T_f/T_p = 1.260

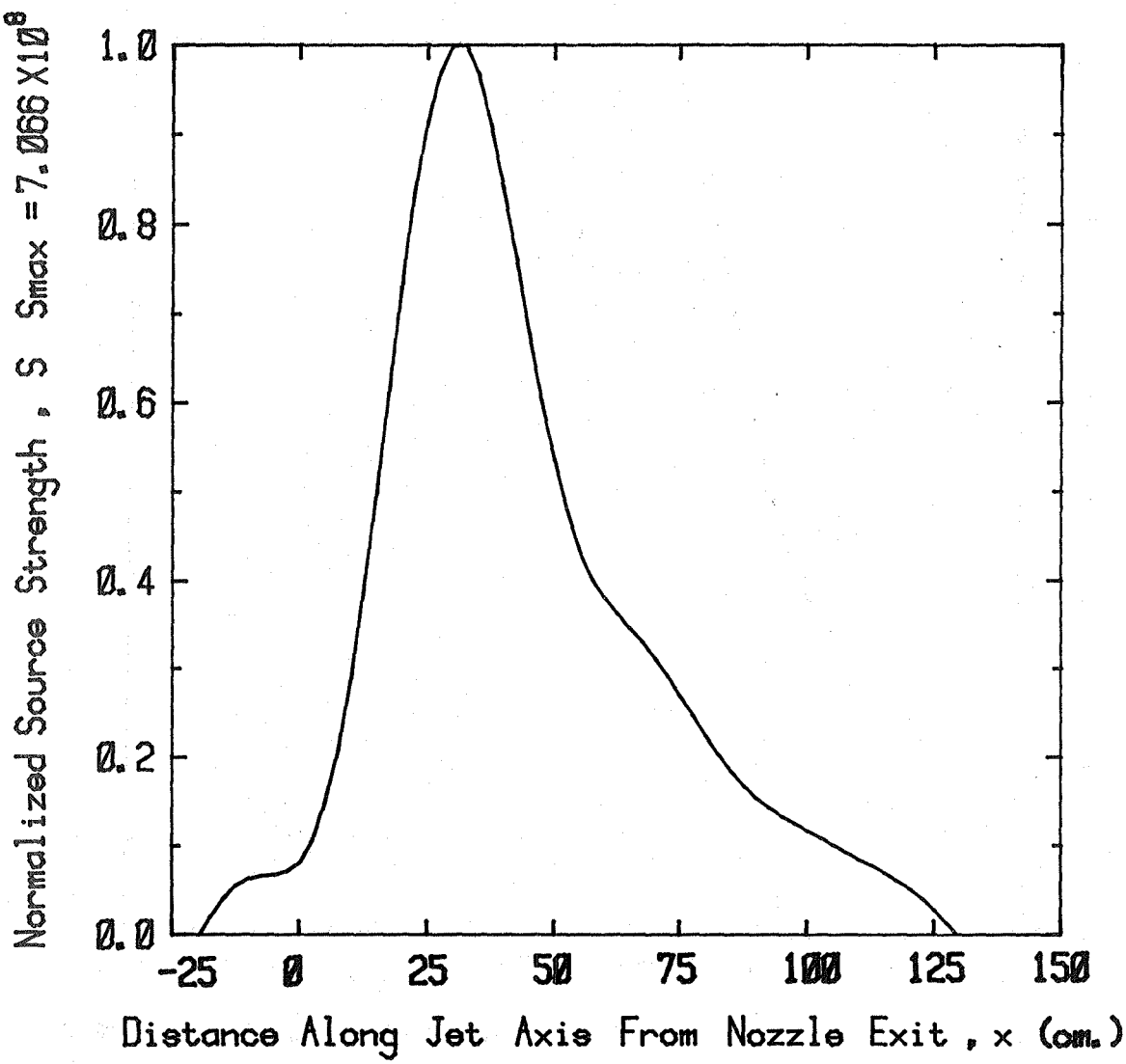

Coannular Jet - Source Distribution
(Frequency = 2.46 KHz)

Figure A2.26(d)

Velocity Ratio , V_f/V_p = 1.660

Static Temperature Ratio , T_f/T_p = 1.260

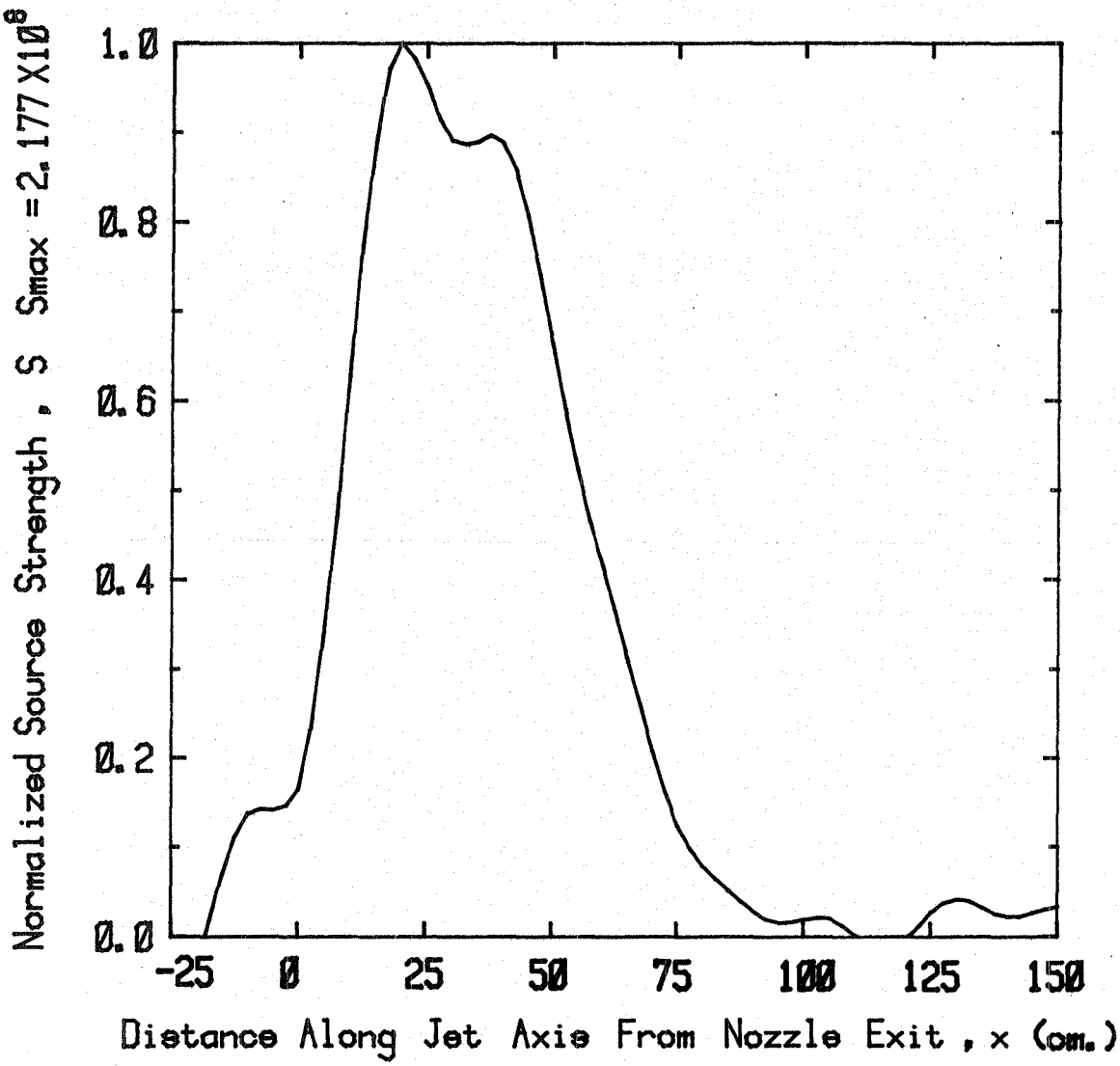

Coannular Jet - Source Distribution

(Frequency = 4.98 KHz)

Figure A2.26(e)

Velocity Ratio , V_f/V_p = 1.660

Static Temperature Ratio , T_f/T_p = 1.260

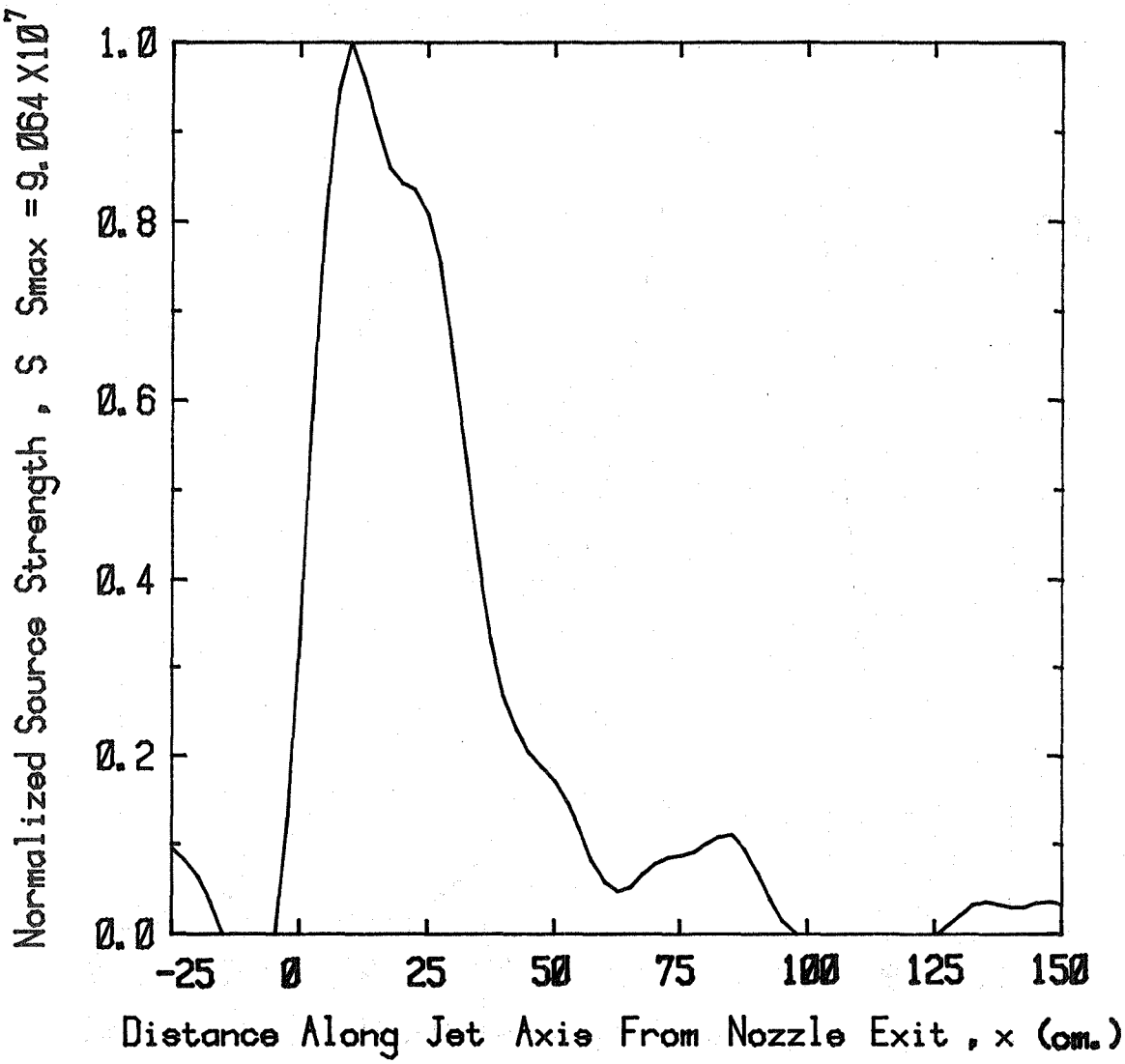

Coannular Jet - Source Distribution

(Frequency = 9.96 KHz)

Figure A2.26(f)

Velocity Ratio , V_f/V_p = 1.660

Static Temperature Ratio , T_f/T_p = 1.260

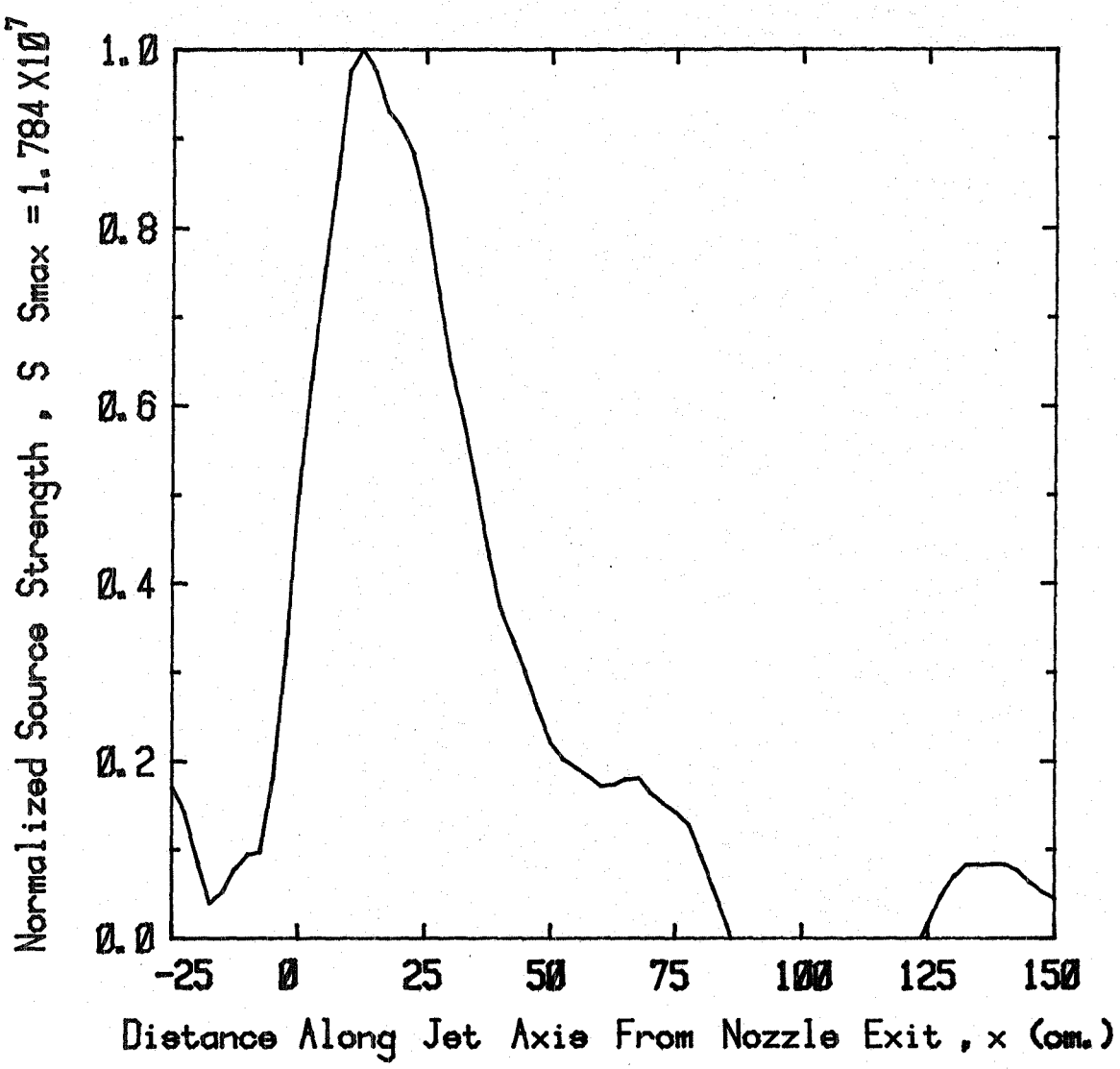

Coannular Jet - Source Distribution

(Frequency = 19.98 KHz)

Figure A2.26(g)

APPENDIX 3

MEAN FLOW DATA

The mean flow results obtained from the pressure/temperature surveys are documented in this Appendix. A figure index describing the various plots (96 in all) is given in Table 3A.1. The results are plotted in the form of radial profiles at several axial locations.† For each test point, four types of plots are presented: (i) mean velocity, (ii) Mach number, (iii) total temperature, and (iv) static temperature. For each of these four plot parameters, the figure is divided into three parts [i.e. (a), (b), and (c)]. The first part gives the profiles in the premerged region close to the nozzle exit ($x/D_{eq} \lesssim 1.5$), and the third part gives the profiles in the fully-developed region ($6 \lesssim x/D_{eq} \lesssim 20$). The middle part presents the profiles in the intermediate or transition region ($0 \lesssim x/D_{eq} \lesssim 9$) of the coannular jet flow.

†*The axial locations are given in terms of the axial distance x from the primary nozzle exit plane divided by the equivalent nozzle diameter. The symbols d or D_{eq} are used in the plots to denote the equivalent nozzle diameter.*

Table 3A.1 Figure index for mean flow data

TP	V_f/V_p	T_f/T_p	Plot Parameter	Figure Number	TP	V_f/V_p	T_f/T_p	Plot Parameter	Figure Number
1	1.00	1.00	Mean velocity	A3.1	5	1.00	1.75	Mean velocity	A3.17
↓	↓	↓	Mach number	A3.2	↓	↓	↓	Mach number	A3.18
↓	↓	↓	Total temperature	A3.3	↓	↓	↓	Total temperature	A3.19
↓	↓	↓	Static temperature	A3.4	↓	↓	↓	Static temperature	A3.20
2	1.35	1.00	Mean velocity	A3.5	6	1.35	1.75	Mean velocity	A3.21
↓	↓	↓	Mach number	A3.6	↓	↓	↓	Mach number	A3.22
↓	↓	↓	Total temperature	A3.7	↓	↓	↓	Total temperature	A3.23
↓	↓	↓	Static temperature	A3.8	↓	↓	↓	Static temperature	A3.24
3	1.55	1.00	Mean velocity	A3.9	7	1.55	1.75	Mean velocity	A3.25
↓	↓	↓	Mach number	A3.10	↓	↓	↓	Mach number	A3.26
↓	↓	↓	Total temperature	A3.11	↓	↓	↓	Total temperature	A3.27
↓	↓	↓	Static temperature	A3.12	↓	↓	↓	Static temperature	A3.28
4	1.75	1.00	Mean velocity	A3.13	8	1.75	1.75	Mean velocity	A3.29
↓	↓	↓	Mach number	A3.14	↓	↓	↓	Mach number	A3.30
↓	↓	↓	Total temperature	A3.15	↓	↓	↓	Total temperature	A3.31
↓	↓	↓	Static temperature	A3.16	↓	↓	↓	Static temperature	A3.32

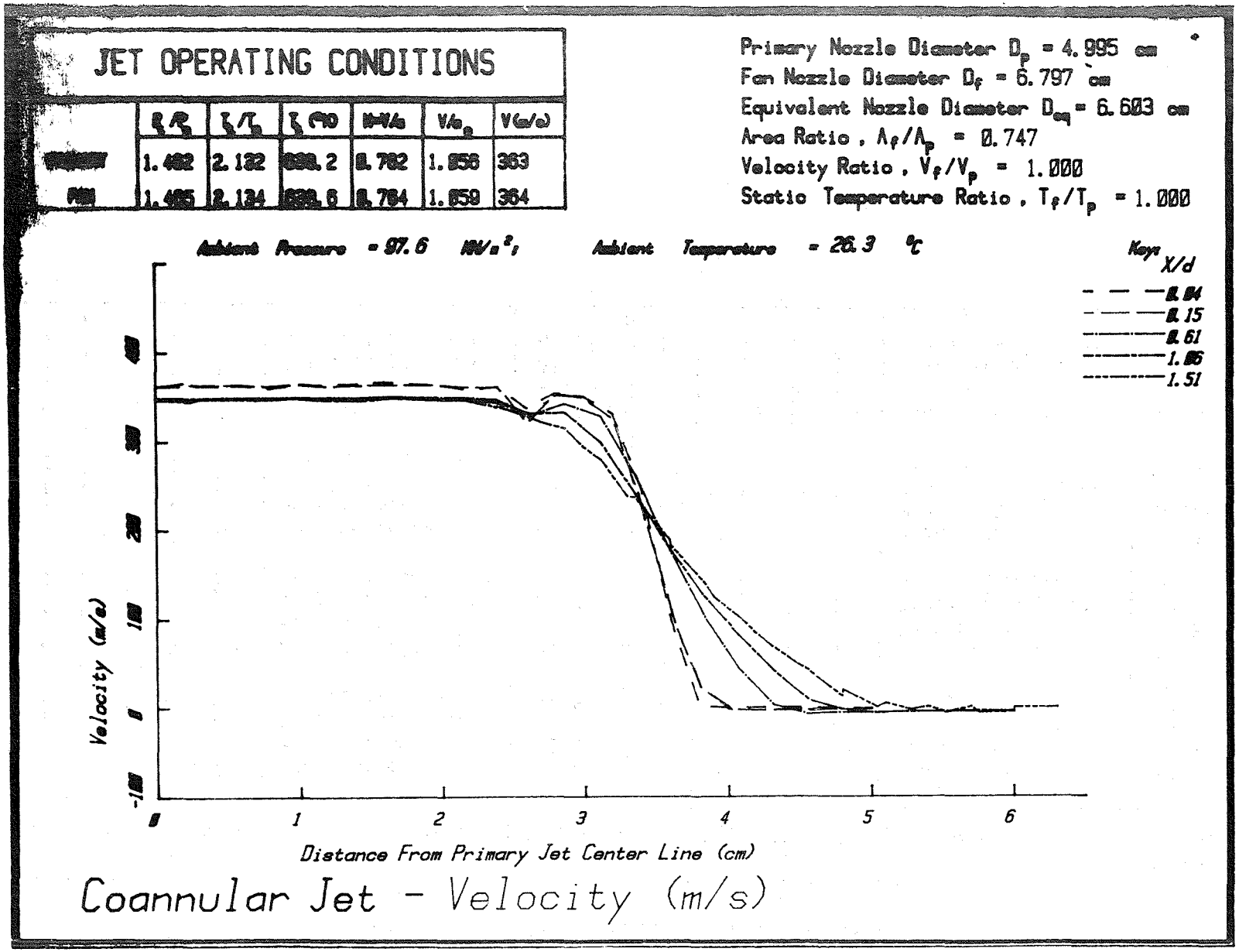
JET OPERATING CONDITIONS
1.492
2.132
1.858
363
1.495
2.134
1.859
364
Primary Nozzle Diameter D_p = 4.995 cm
Fan Nozzle Diameter D_f = 6.797 cm
Equivalent Nozzle Diameter D_{eq} = 6.603 cm
Area Ratio, A_f/A_p = 0.747
Velocity Ratio, V_f/V_p = 1.000
Static Temperature Ratio, T_f/T_p = 1.000
Ambient Pressure = 97.6 kN/m²; Ambient Temperature = 26.3 °C
Keys X/d
0.61
1.86
1.51
Velocity (m/s)
1
2
3
4
5
6
Distance From Primary Jet Center Line (cm)
Coannular Jet - Velocity (m/s)

Figure A3.1(a)

JET OPERATING CONDITIONS

	[illegible]	[illegible]	[illegible]	[illegible]	[illegible]	[illegible]
[illegible]	1.462	2.132	638.2	0.762	1.056	363
FAN	1.465	2.134	638.6	0.764	1.059	364

Primary Nozzle Diameter D_p = 4.995 cm
Fan Nozzle Diameter D_f = 6.797 cm
Equivalent Nozzle Diameter D_{eq} = 6.603 cm
Area Ratio , A_f/A_p = 0.747
Velocity Ratio , V_f/V_p = 1.000
Static Temperature Ratio , T_f/T_p = 1.000

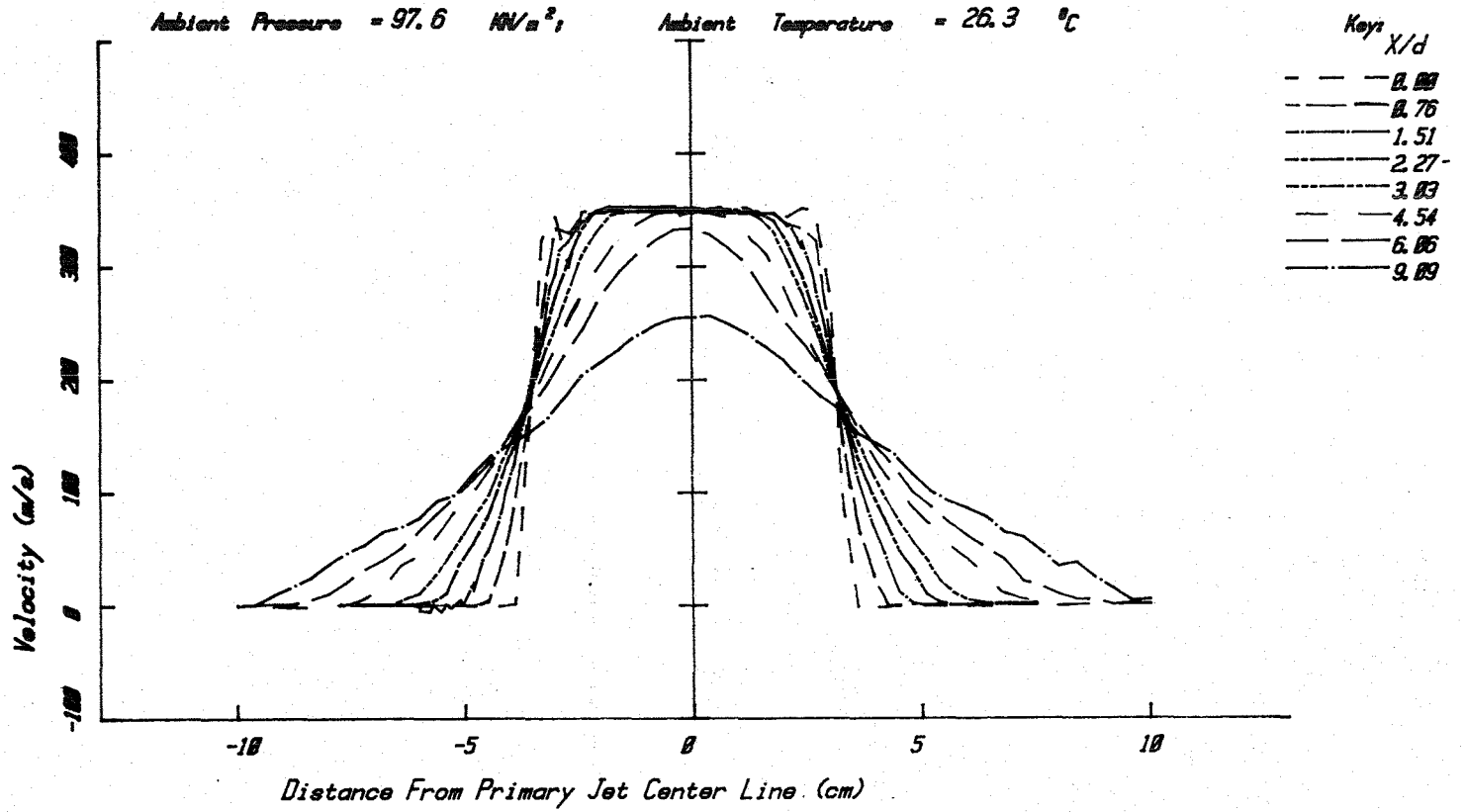

Coannular Jet - Velocity (m/s)

Figure A3.1(b)

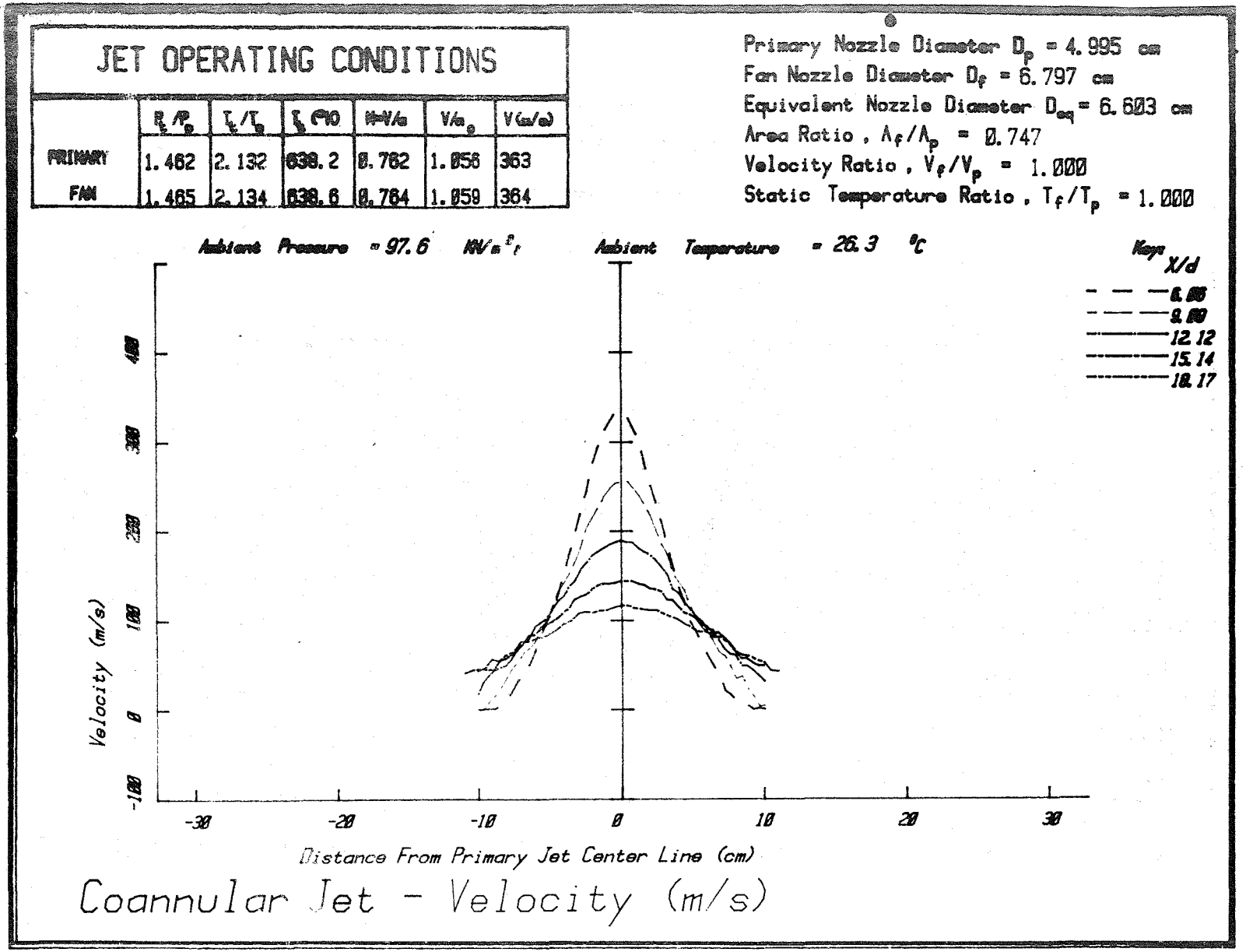
JET OPERATING CONDITIONS
PRIMARY
FAN
1.462
2.132
638.2
0.762
1.056
363
1.465
2.134
638.6
0.764
1.059
364
Primary Nozzle Diameter D_p = 4.995 cm
Fan Nozzle Diameter D_f = 6.797 cm
Equivalent Nozzle Diameter D_{eq} = 6.603 cm
Area Ratio , A_f/A_p = 0.747
Velocity Ratio , V_f/V_p = 1.000
Static Temperature Ratio , T_f/T_p = 1.000
Ambient Pressure = 97.6 KN/m²
Ambient Temperature = 26.3 °C
Keys X/d
6.05
9.09
12.12
15.14
18.17
Velocity (m/s)
400
300
200
100
0
-100
-30
-20
-10
0
10
20
30
Distance From Primary Jet Center Line (cm)
Coannular Jet - Velocity (m/s)

Figure A3.1(c)

JET OPERATING CONDITIONS

	P_t/P_o	T_t/T_o	T_t (°K)	M=V/a	V/a_o	V(m/s)
PRIMARY	1.462	2.132	638.2	0.762	1.056	363
FAN	1.465	2.134	638.6	0.764	1.059	364

Primary Nozzle Diameter D_p = 4.995 cm
Fan Nozzle Diameter D_f = 6.797 cm
Equivalent Nozzle Diameter D_{eq} = 6.603 cm
Area Ratio , A_f/A_p = 0.747
Velocity Ratio , V_f/V_p = 1.000
Static Temperature Ratio , T_f/T_p = 1.000

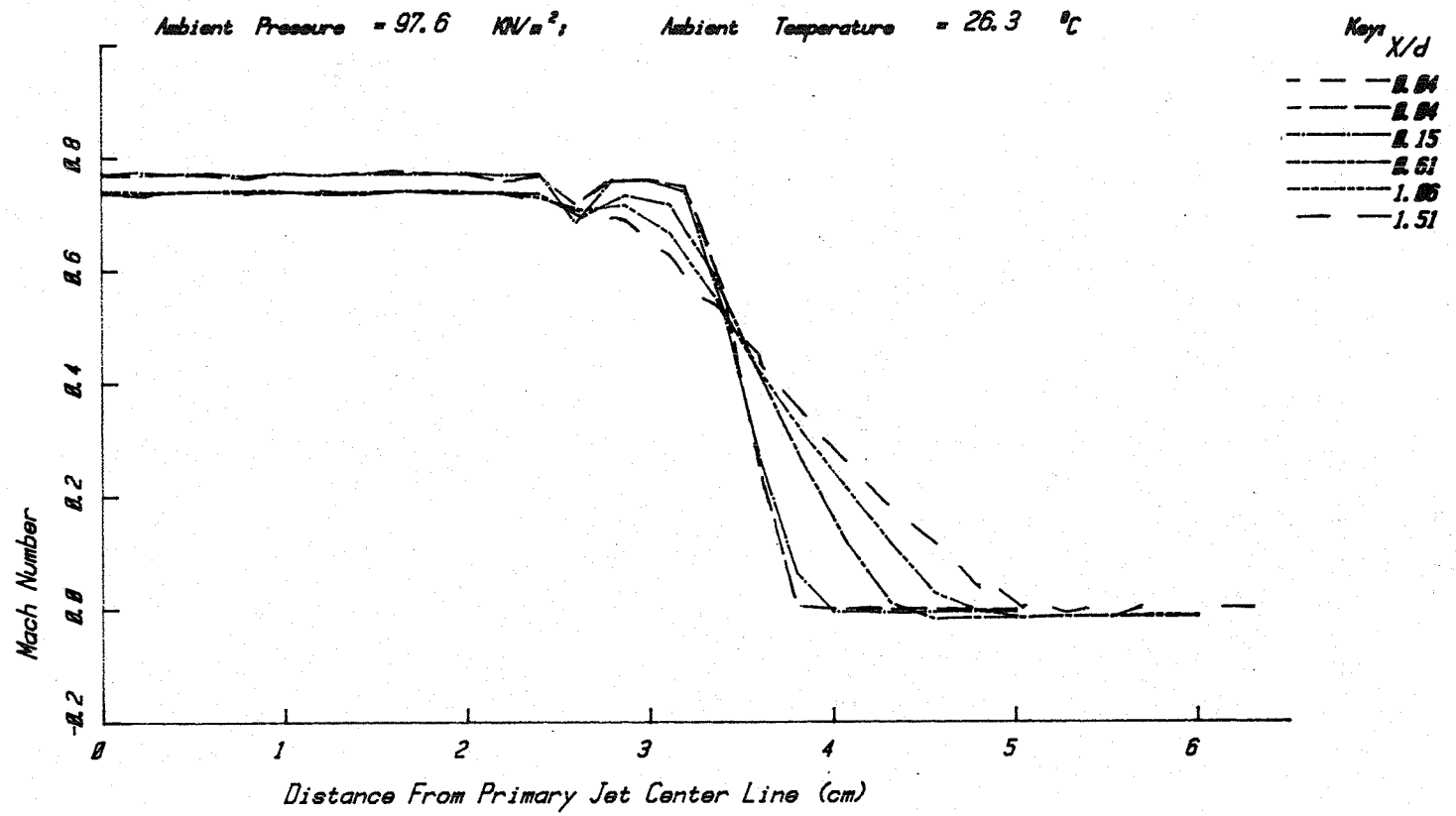

Coannular Jet - Mach Number

Figure A3.2(a)

JET OPERATING CONDITIONS

	P_t/P_o	T_t/T_o	T_t (°K)	M=V/a	V/a_o	V (m/s)
PRIMARY	1.462	2.132	638.2	0.762	1.056	363
FAN	1.465	2.134	638.6	0.764	1.059	364

Primary Nozzle Diameter D_p = 4.998 cm
Fan Nozzle Diameter D_f = 6.197 cm
Equivalent Nozzle Diameter D_{eq} = 6.603 cm
Area Ratio , A_f/A_p = 0.747
Velocity Ratio , V_f/V_p = 1.000
Static Temperature Ratio , T_f/T_p = 1.000

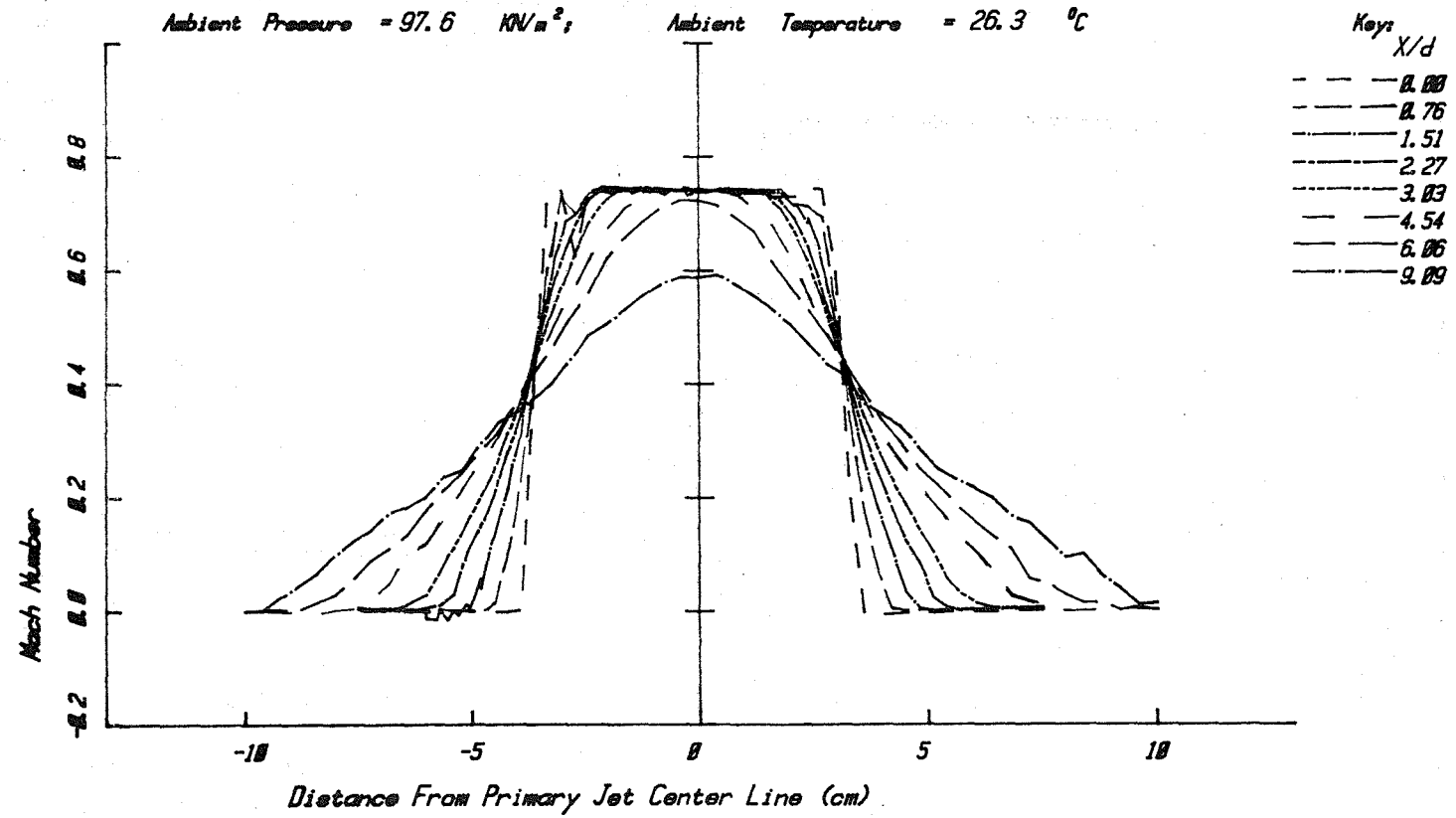

Coannular Jet - Mach Number

Figure A3.2(b)

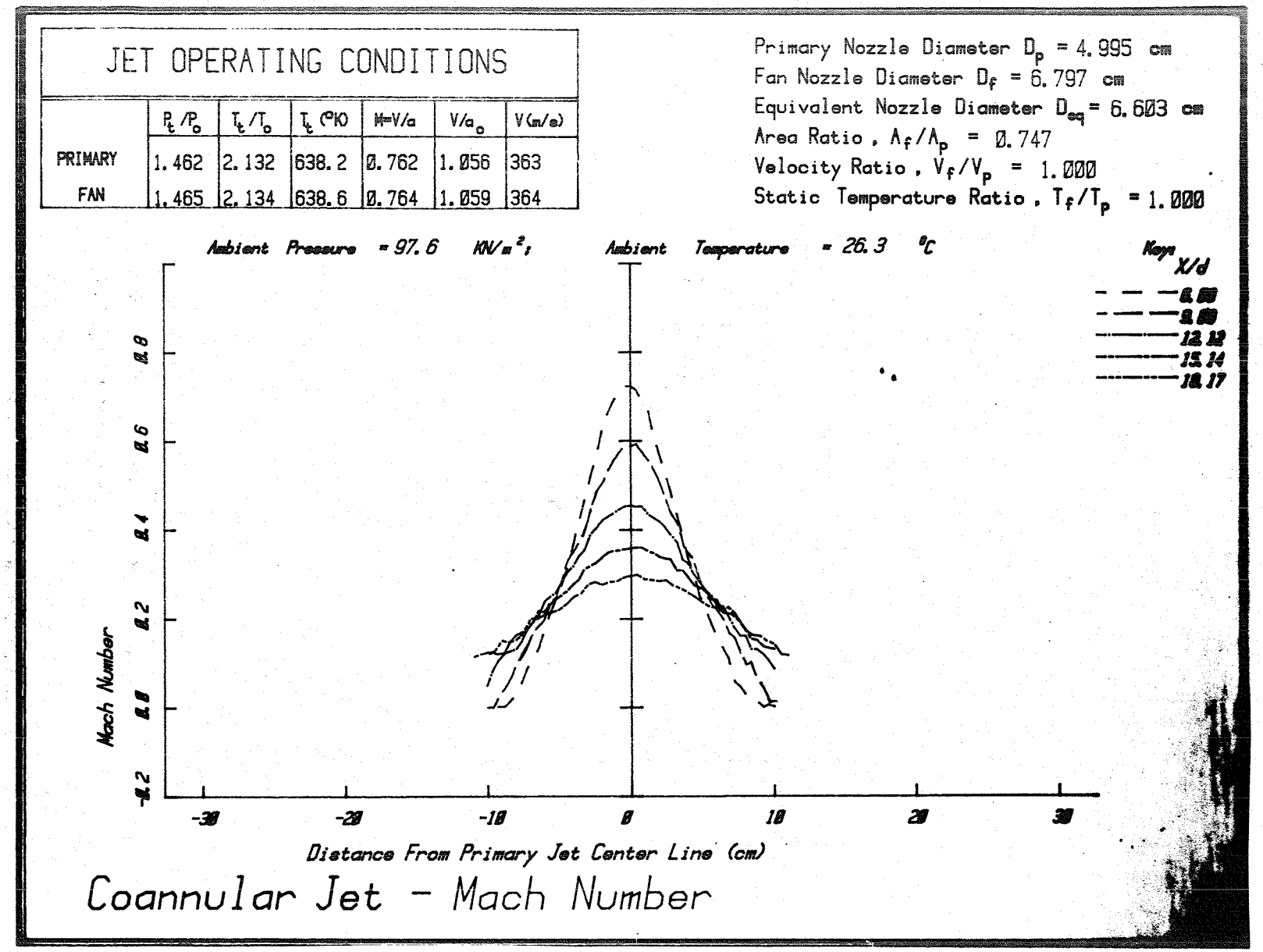
JET OPERATING CONDITIONS
PRIMARY
FAN
1.462
2.132
638.2
Ø.762
1.Ø56
363
1.465
2.134
638.6
Ø.764
1.Ø59
364
Primary Nozzle Diameter D_p = 4.995 cm
Fan Nozzle Diameter D_f = 6.797 cm
Equivalent Nozzle Diameter D_{eq} = 6.6Ø3 cm
Area Ratio , A_f/A_p = Ø.747
Velocity Ratio , V_f/V_p = 1.ØØØ
Static Temperature Ratio , T_f/T_p = 1.ØØØ
Ambient Pressure = 97.6 KN/m²;
Ambient Temperature = 26.3 °C
Keys X/d
Mach Number
Distance From Primary Jet Center Line (cm)
Coannular Jet - Mach Number

Figure A3.2(c)

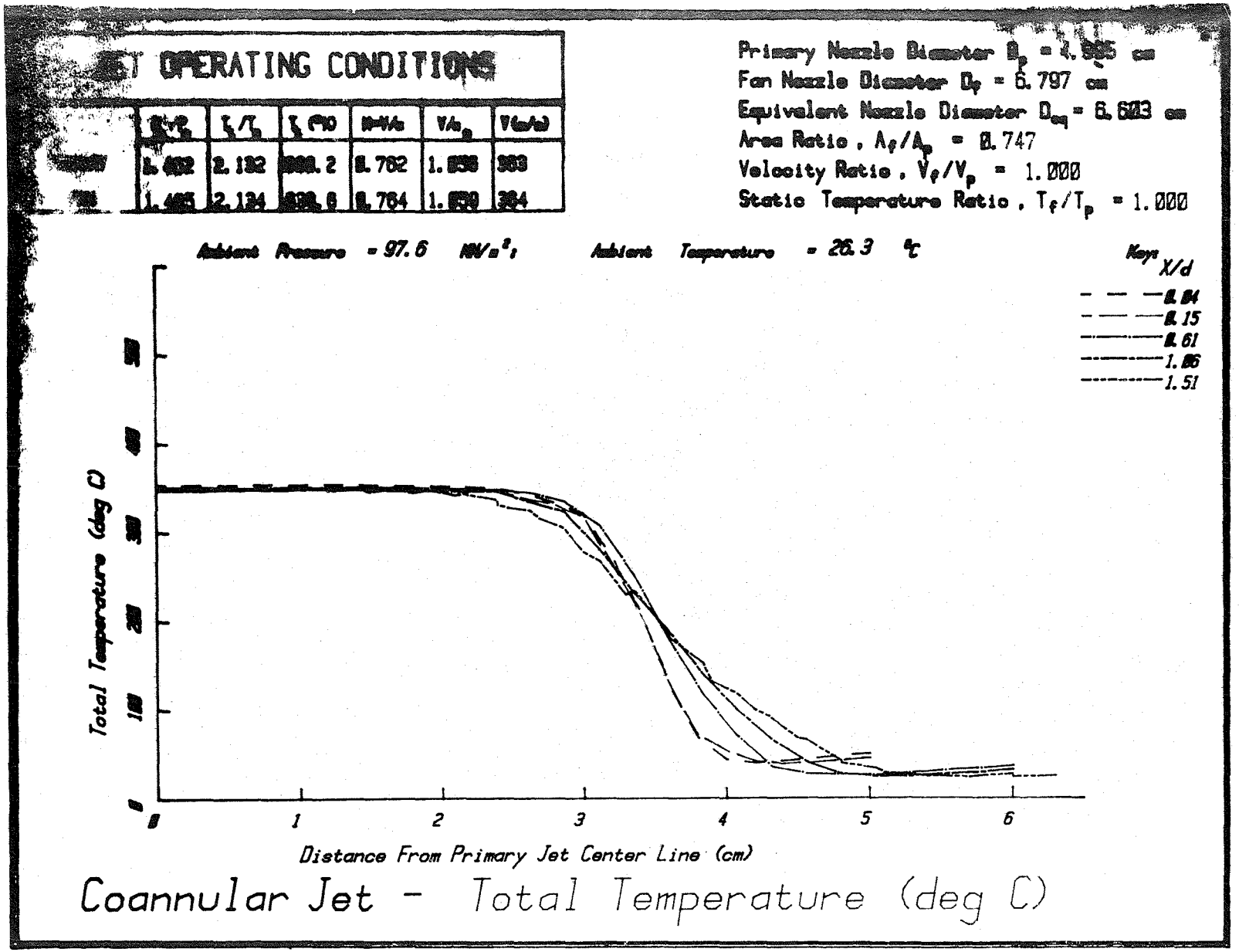
Primary Nozzle Diameter D_p = 4.995 cm
Fan Nozzle Diameter D_f = 6.797 cm
Equivalent Nozzle Diameter D_{eq} = 6.603 cm
Area Ratio, A_f/A_p = 0.747
Velocity Ratio, V_f/V_p = 1.000
Static Temperature Ratio, T_f/T_p = 1.000
Ambient Pressure = 97.6 kN/m²
Ambient Temperature = 26.3 °C
Keys X/d
0.84
0.15
0.61
1.06
1.51
Total Temperature (deg C)
Distance From Primary Jet Center Line (cm)
Coannular Jet - Total Temperature (deg C)

Figure A3.3(a)

JET OPERATING CONDITIONS

	P_t/P_0	T_t/T_0	T_t (°K)	M=V/a	V/a_0	V(m/s)
PRIMARY	1.462	2.132	638.2	0.762	1.056	363
FAN	1.465	2.134	638.6	0.764	1.059	364

Primary Nozzle Diameter D_p = 4.995 cm
Fan Nozzle Diameter D_f = 6.797 cm
Equivalent Nozzle Diameter D_{eq} = 6.603 cm
Area Ratio , A_f/A_p = 0.747
Velocity Ratio , V_f/V_p = 1.000
Static Temperature Ratio , T_f/T_p = 1.000

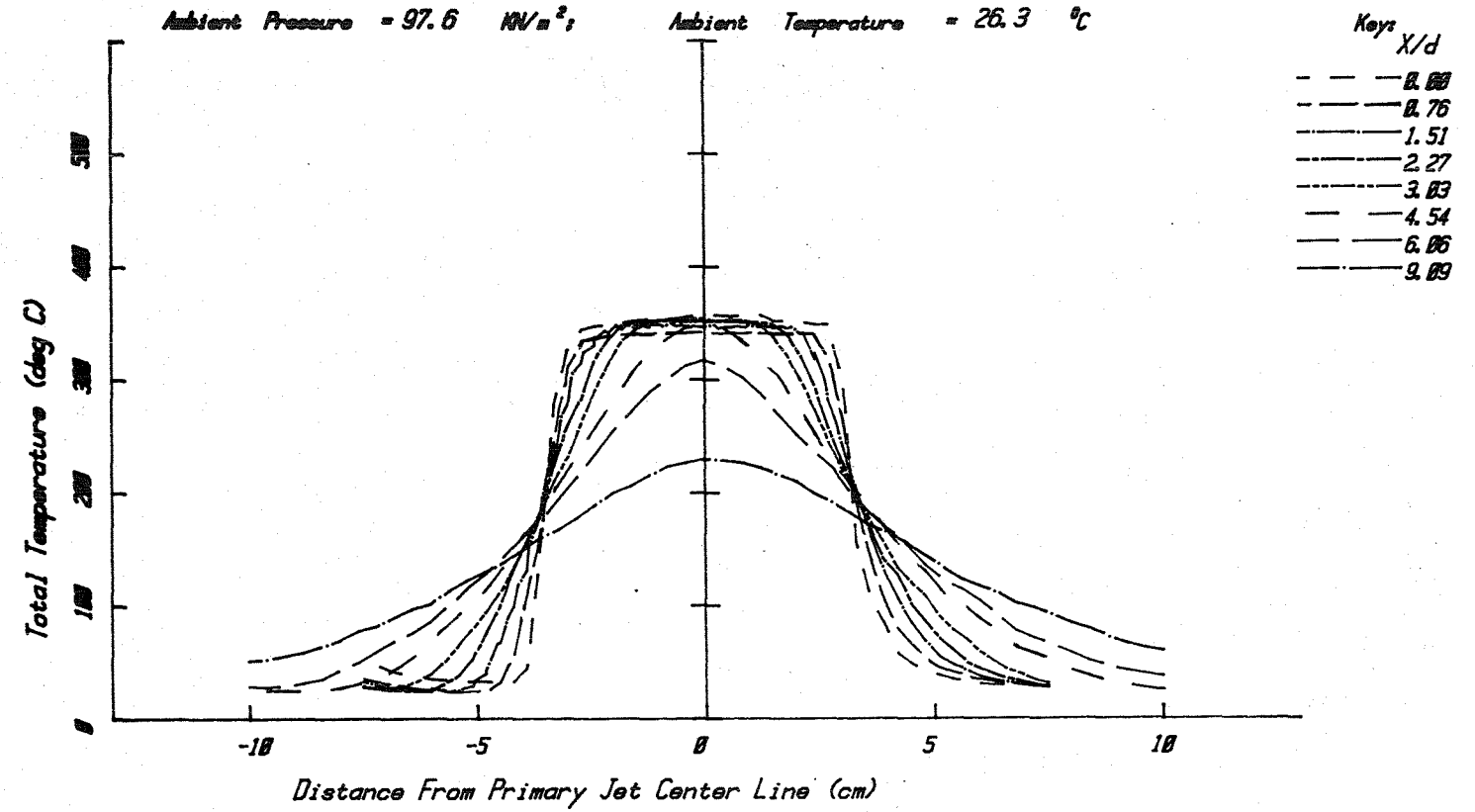

Coannular Jet - Total Temperature (deg C)

Figure A3.3(b)

JET OPERATING CONDITIONS

	P_t/P_o	T_t/T_o	T_t (°K)	M=V/a	V/a_o	V (m/s)
PRIMARY	1.462	2.132	638.2	0.762	1.056	363
FAN	1.465	2.134	638.6	0.764	1.059	364

Primary Nozzle Diameter D_p = 4.995 cm
Fan Nozzle Diameter D_f = 6.797 cm
Equivalent Nozzle Diameter D_{eq} = 6.603 cm
Area Ratio , A_f/A_p = 0.747
Velocity Ratio , V_f/V_p = 1.000
Static Temperature Ratio , T_f/T_p = 1.000

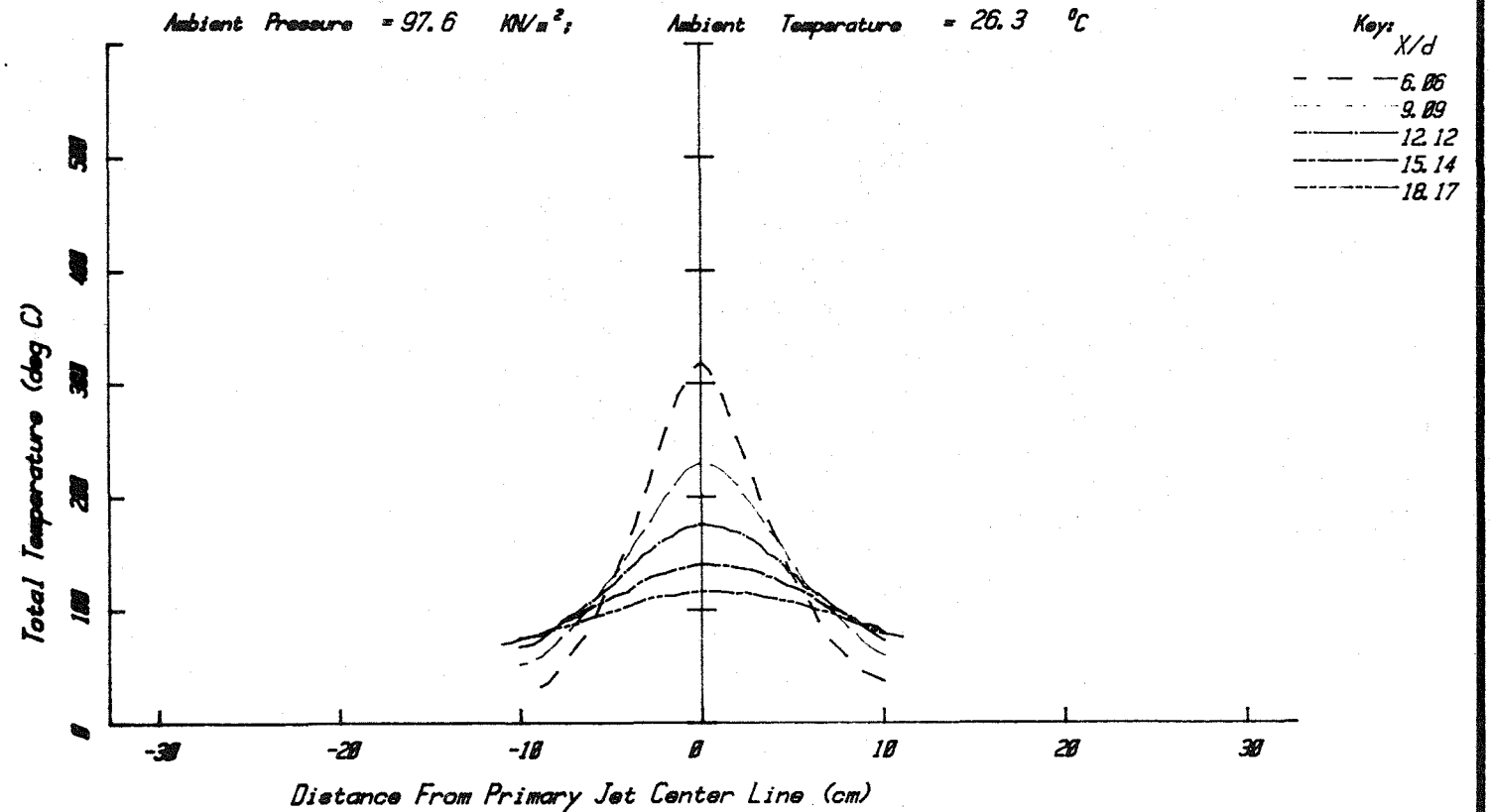

Coannular Jet - Total Temperature (deg C)

Figure A3.3(c)

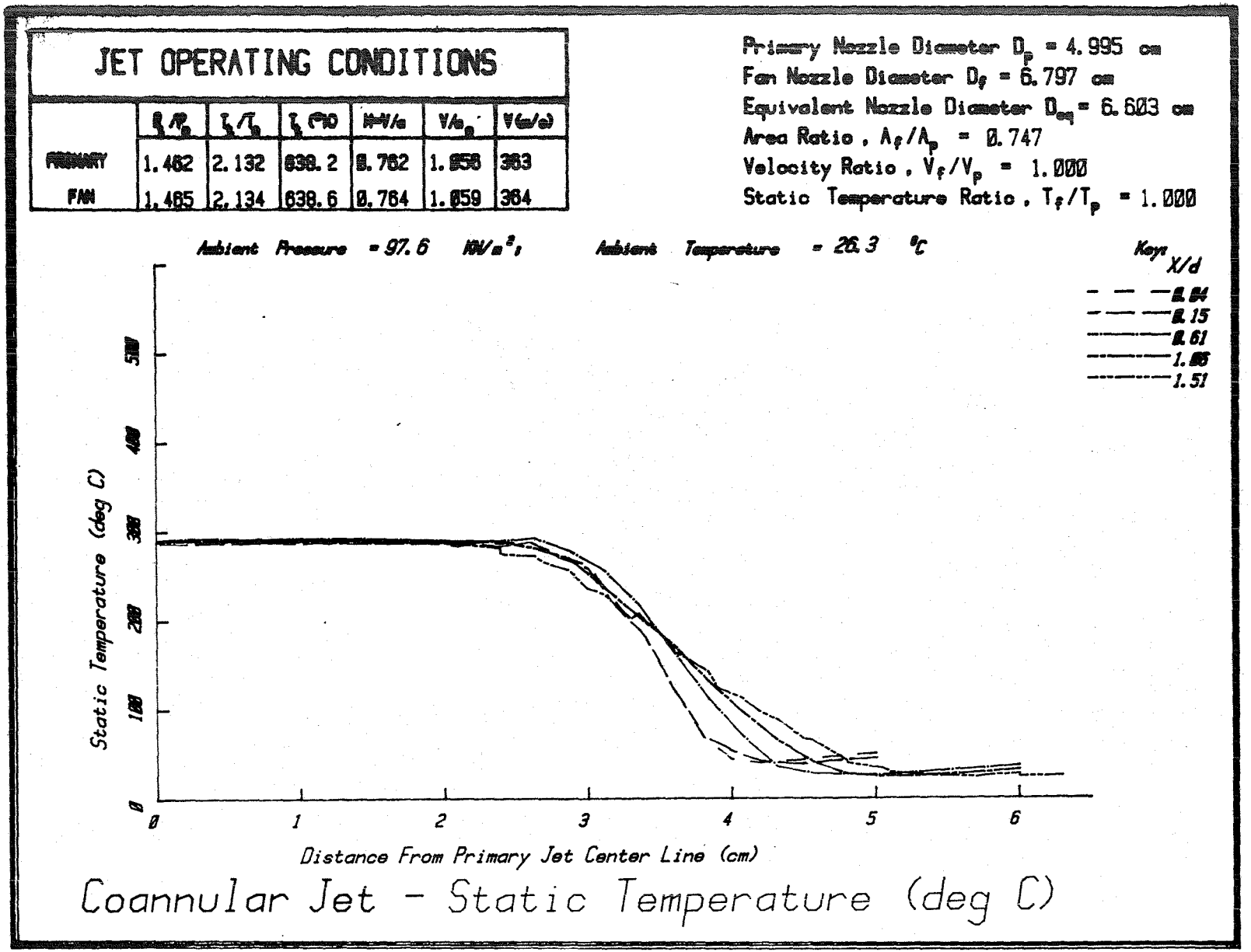
JET OPERATING CONDITIONS
PRIMARY 1.462 2.132 638.2 0.762 1.058 363
FAN 1.465 2.134 638.6 0.764 1.059 364
Primary Nozzle Diameter D_p = 4.995 cm
Fan Nozzle Diameter D_f = 6.797 cm
Equivalent Nozzle Diameter D_{eq} = 6.603 cm
Area Ratio , A_f/A_p = 0.747
Velocity Ratio , V_f/V_p = 1.000
Static Temperature Ratio , T_f/T_p = 1.000
Ambient Pressure = 97.6 kN/m², Ambient Temperature = 26.3 °C
Key X/d
0.84
1.15
1.61
1.95
1.51
Static Temperature (deg C)
0
100
200
300
400
500
0
1
2
3
4
5
6
Distance From Primary Jet Center Line (cm)
Coannular Jet - Static Temperature (deg C)

Figure A3.4(a)

JET OPERATING CONDITIONS

	P_t/P_o	T_t/T_o	T_t (°K)	M=V/a	V/a_o	V(m/s)
PRIMARY	1.462	2.132	638.2	0.762	1.056	363
FAN	1.465	2.134	638.6	0.764	1.059	364

Primary Nozzle Diameter D_p = 4.995 cm
Fan Nozzle Diameter D_f = 6.797 cm
Equivalent Nozzle Diameter D_{eq} = 6.603 cm
Area Ratio , A_f/A_p = 0.747
Velocity Ratio , V_f/V_p = 1.000
Static Temperature Ratio , T_f/T_p = 1.000

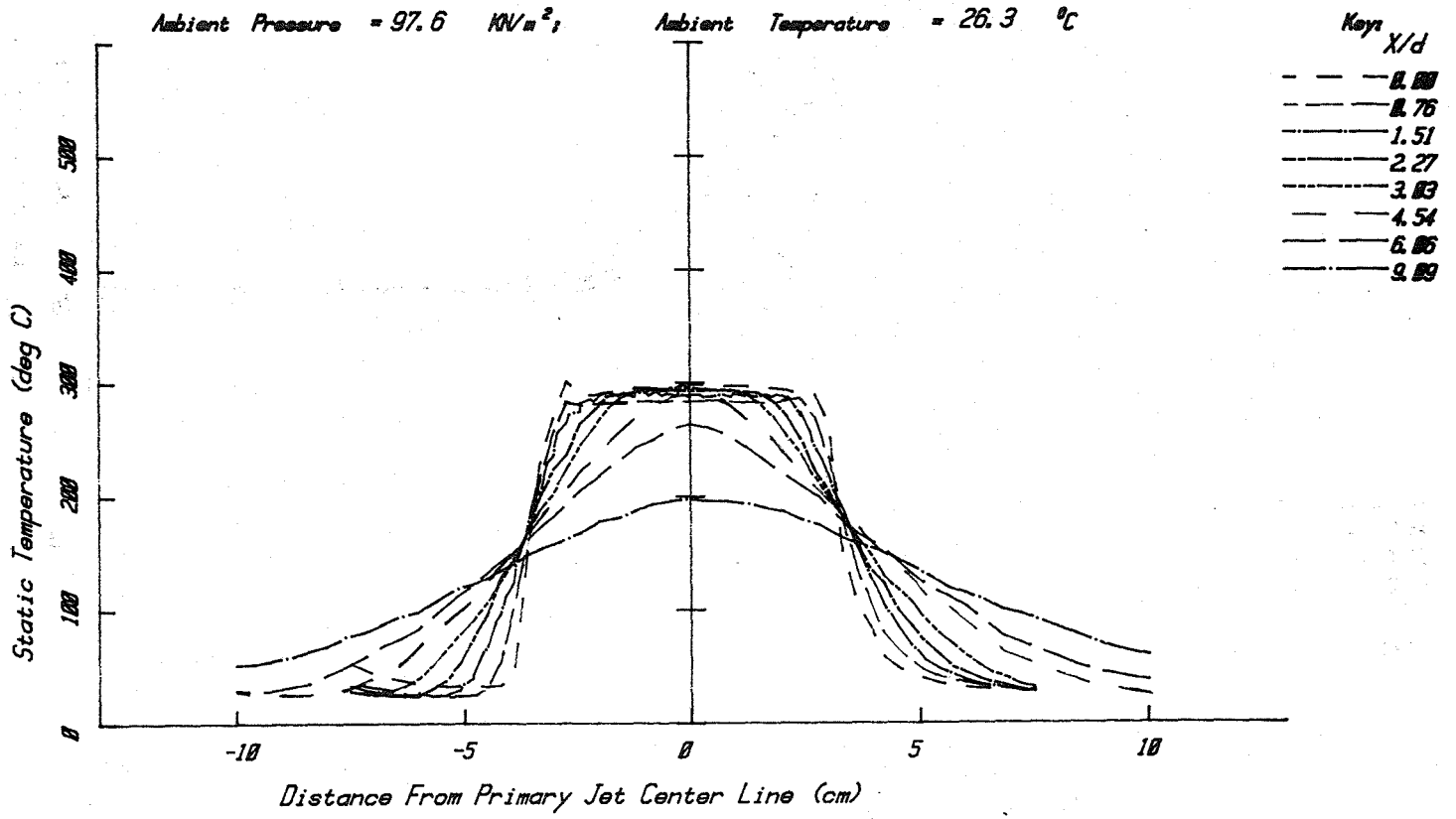

Coannular Jet - Static Temperature (deg C)

Figure A3.4(b)

JET OPERATING CONDITIONS

	P_t/P_o	T_t/T_o	T_t (°K)	M=V/a	V/a_o	V (m/s)
PRIMARY	1.462	2.132	638.2	Ø.762	1.Ø56	363
FAN	1.465	2.134	638.6	Ø.764	1.Ø59	364

Primary Nozzle Diameter D_p = 4.995 cm
Fan Nozzle Diameter D_f = 6.797 cm
Equivalent Nozzle Diameter D_{eq} = 6.6Ø3 cm
Area Ratio , A_f/A_p = Ø.747
Velocity Ratio , V_f/V_p = 1.ØØØ
Static Temperature Ratio , T_f/T_p = 1.ØØØ

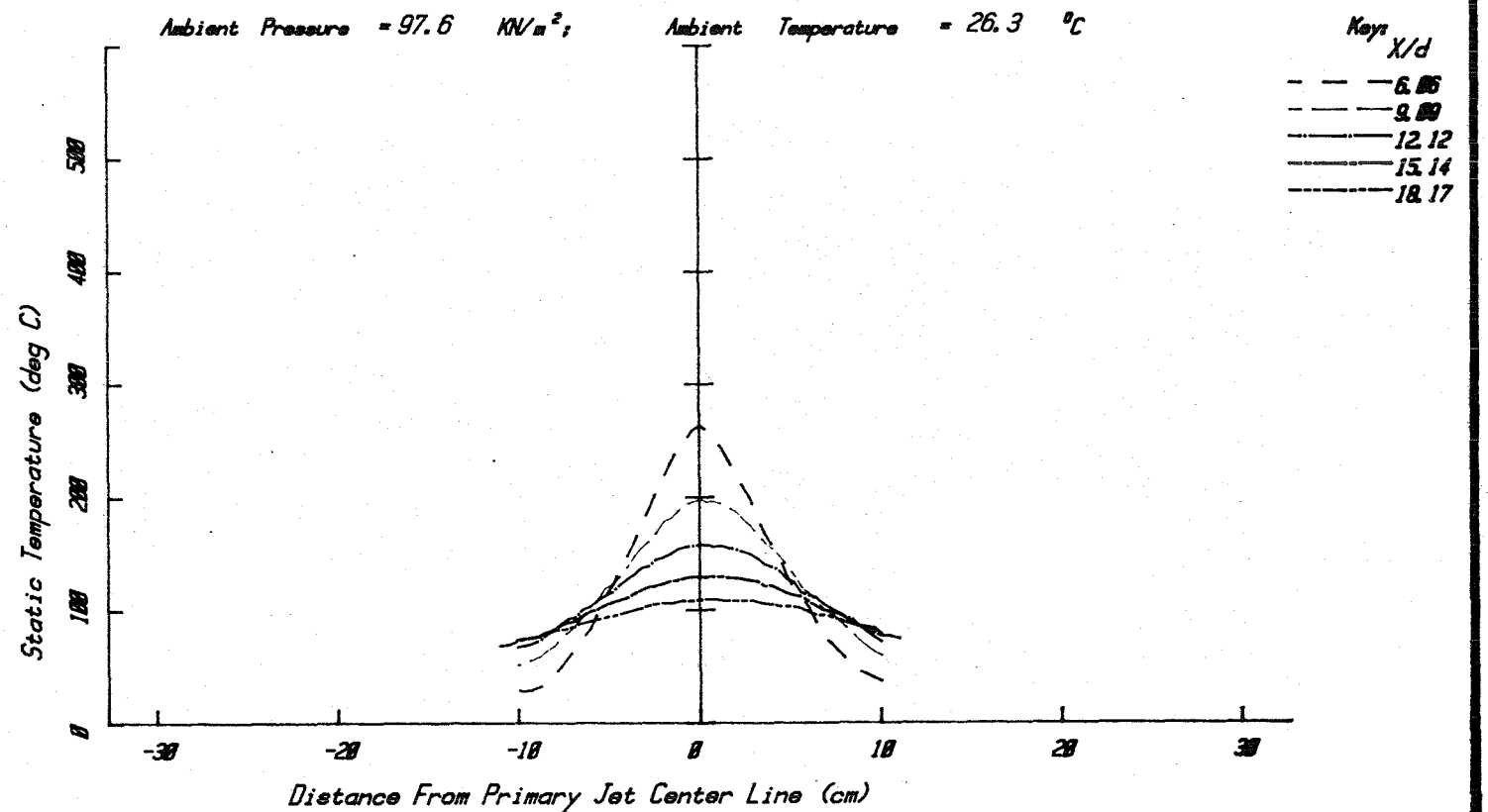

Coannular Jet - Static Temperature (deg C)

Figure A3.4(c)

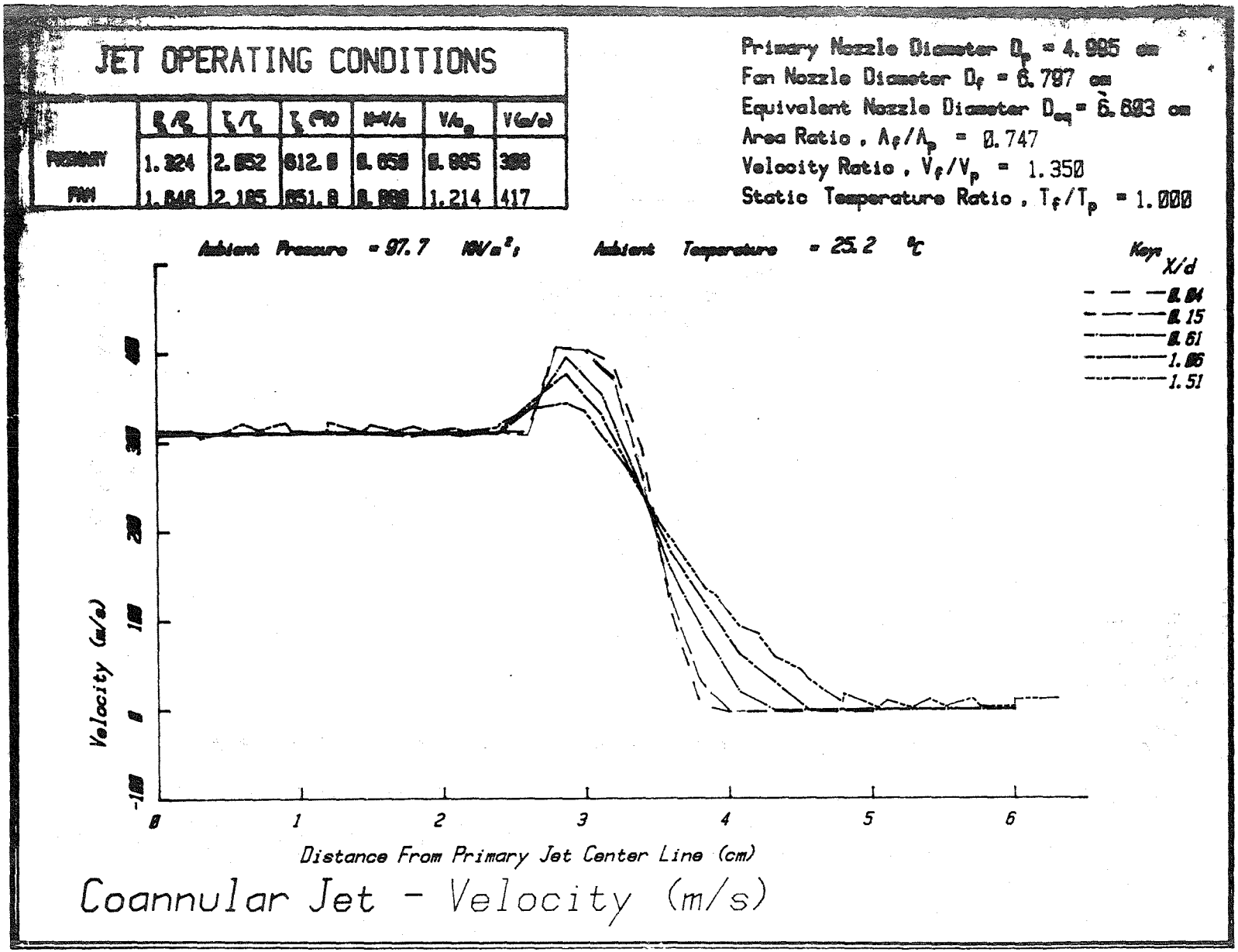
JET OPERATING CONDITIONS
PRIMARY
FAN
1.324
2.852
612.8
1.214
417
Primary Nozzle Diameter D_p = 4.985 cm
Fan Nozzle Diameter D_f = 6.797 cm
Equivalent Nozzle Diameter D_{eq} = 6.893 cm
Area Ratio, A_f/A_p = 0.747
Velocity Ratio, V_f/V_p = 1.350
Static Temperature Ratio, T_f/T_p = 1.000
Ambient Pressure = 97.7 kN/m²,
Ambient Temperature = 25.2 °C
Keys X/d
0.84
0.15
0.61
1.86
1.51
Velocity (m/s)
0
1
2
3
4
5
6
Distance From Primary Jet Center Line (cm)
Coannular Jet - Velocity (m/s)

Figure A3.5(a)

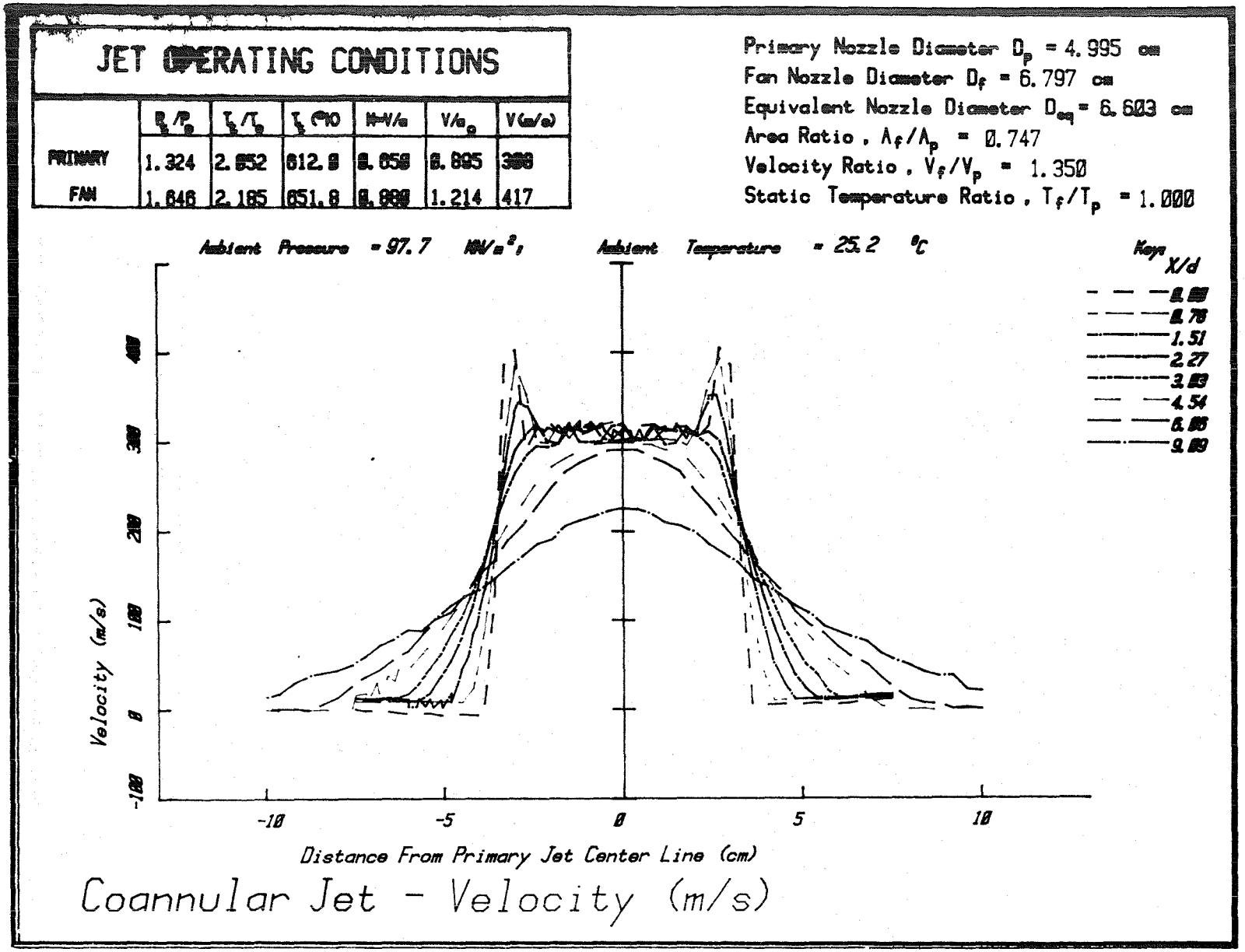
JET OPERATING CONDITIONS
PRIMARY
FAN
1.324
2.852
1.846
2.185
1.214
417
Primary Nozzle Diameter D_p = 4.995 cm
Fan Nozzle Diameter D_f = 6.797 cm
Equivalent Nozzle Diameter D_{eq} = 6.603 cm
Area Ratio , A_f/A_p = 0.747
Velocity Ratio , V_f/V_p = 1.350
Static Temperature Ratio , T_f/T_p = 1.000
Ambient Pressure = 97.7 kN/m²,
Ambient Temperature = 25.2 °C
Key X/d
1.51
2.27
4.54
Velocity (m/s)
-10
-5
0
5
10
Distance From Primary Jet Center Line (cm)
Coannular Jet - Velocity (m/s)

Figure A3.5(b)

JET OPERATING CONDITIONS

	P_t/P_o	T_t/T_o	T_t (°K)	M=V/a	V/a_o	V(m/s)
PRIMARY	1.324	2.052	612.0	0.650	0.895	308
FAN	1.646	2.185	651.8	0.880	1.214	417

Primary Nozzle Diameter D_p = 4.995 cm
Fan Nozzle Diameter D_f = 6.797 cm
Equivalent Nozzle Diameter D_{eq} = 6.603 cm
Area Ratio , A_f/A_p = 0.747
Velocity Ratio , V_f/V_p = 1.350
Static Temperature Ratio , T_f/T_p = 1.000

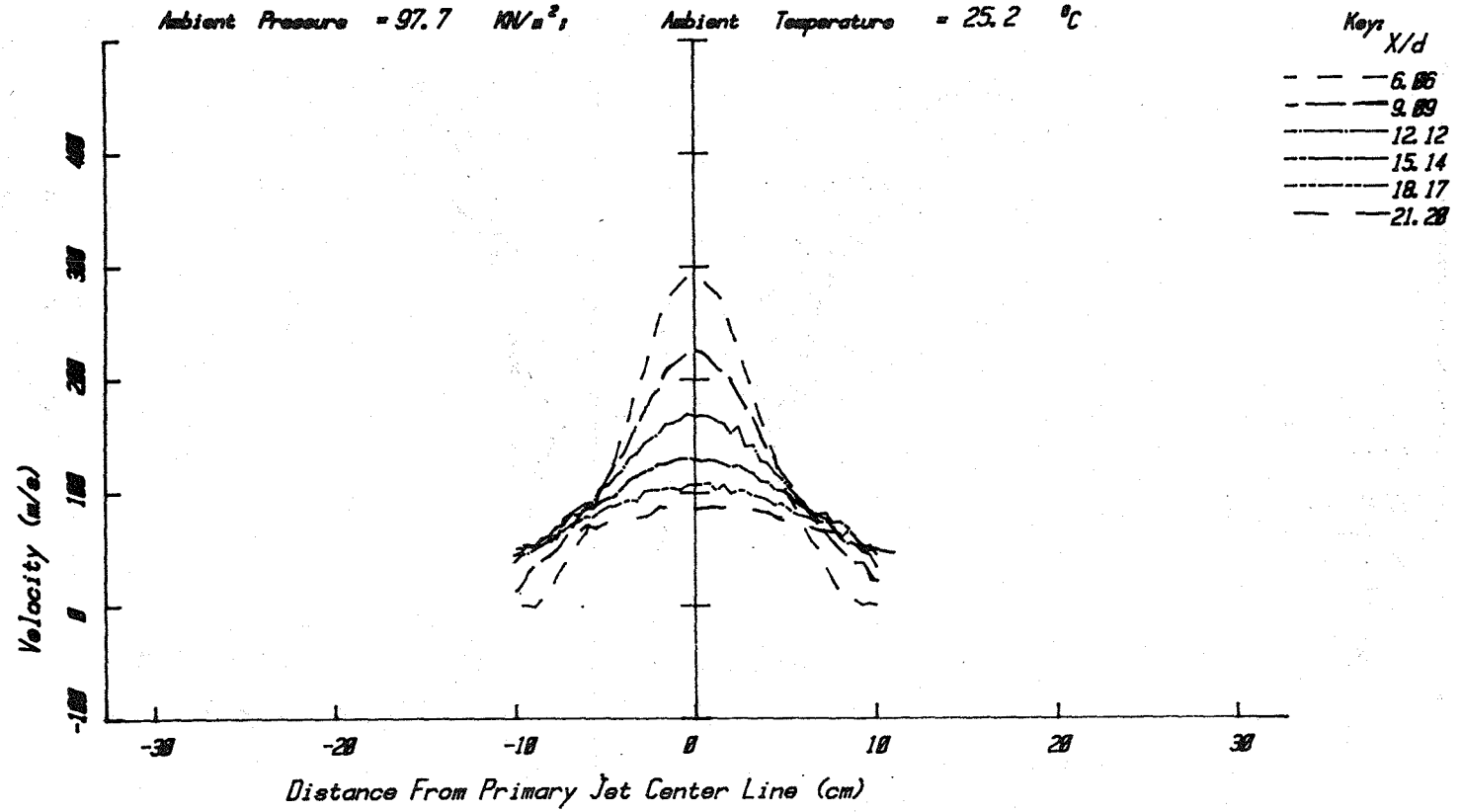

Coannular Jet - Velocity (m/s)

Figure A3.5(c)

JET OPERATING CONDITIONS

	P_t/P_o	T_t/T_o	T_t (°K)	M=V/a	V/a_o	V (m/s)
PRIMARY	1.324	2.052	612.0	0.650	0.895	308
FAN	1.646	2.185	651.8	0.880	1.214	417

Primary Nozzle Diameter D_p = 4.995 cm
Fan Nozzle Diameter D_f = 6.797 cm
Equivalent Nozzle Diameter D_{eq} = 6.603 cm
Area Ratio, A_f/A_p = 0.747
Velocity Ratio, V_f/V_p = 1.350
Static Temperature Ratio, T_f/T_p = 1.000

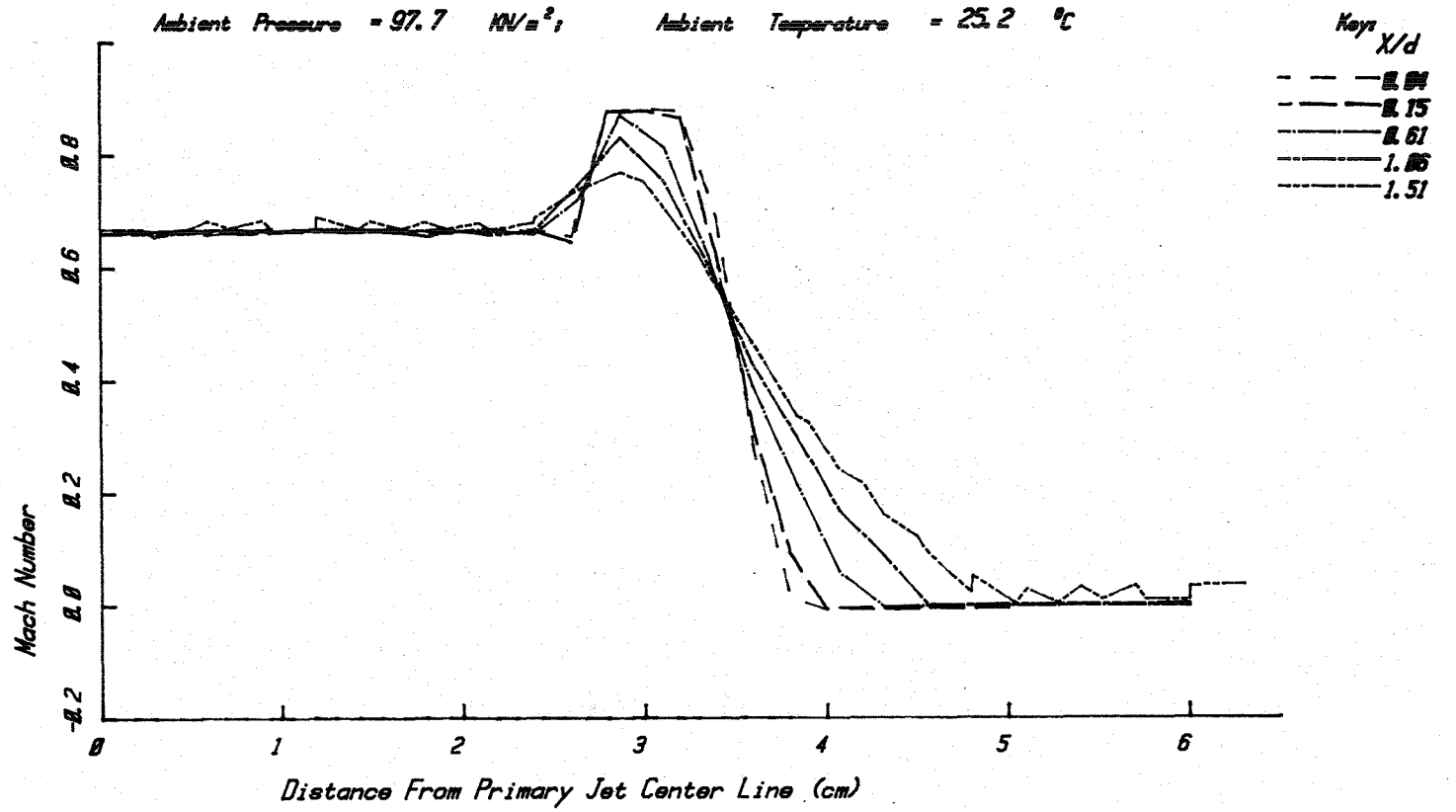

Coannular Jet - Mach Number

Figure A3.6(a)

JET OPERATING CONDITIONS

	P_t/P_o	T_t/T_o	T_t (°K)	M=V/a	V/a_o	V(m/s)
PRIMARY	1.324	2.052	612.0	0.650	0.895	308
FAN	1.646	2.185	651.8	0.880	1.214	417

Primary Nozzle Diameter D_p = 4.995 cm
Fan Nozzle Diameter D_f = 6.797 cm
Equivalent Nozzle Diameter D_{eq} = 6.603 cm
Area Ratio, A_f/A_p = 0.747
Velocity Ratio, V_f/V_p = 1.350
Static Temperature Ratio, T_f/T_p = 1.088

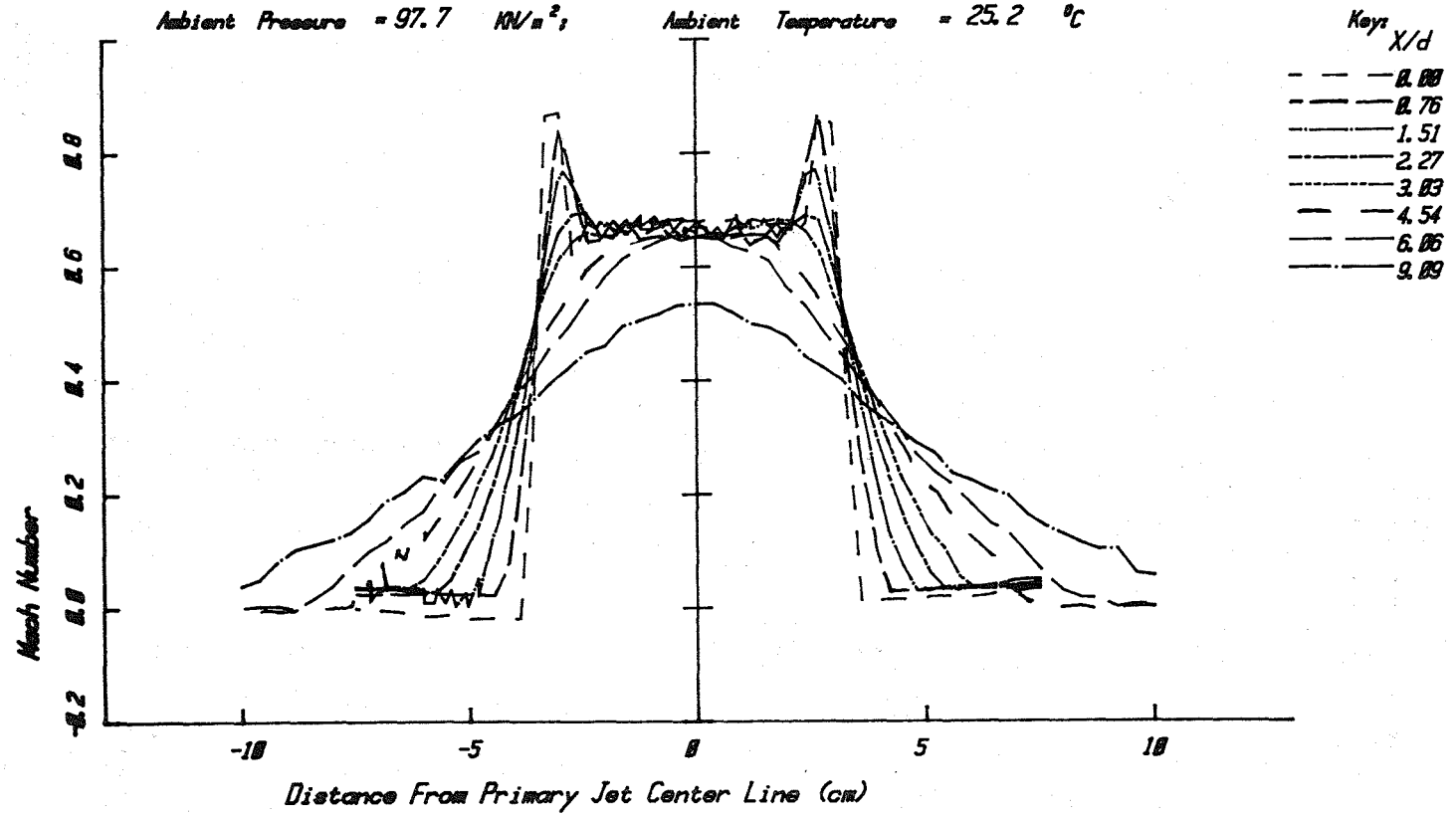

Coannular Jet - Mach Number

Figure A3.6(b)

JET OPERATING CONDITIONS

	P_t/P_o	T_t/T_o	T_t (°K)	M=V/a	V/a_o	V(m/s)
PRIMARY	1.324	2.052	612.0	0.650	0.895	308
FAN	1.646	2.185	651.8	0.880	1.214	417

Primary Nozzle Diameter D_p = 4.995 cm
Fan Nozzle Diameter D_f = 6.797 cm
Equivalent Nozzle Diameter D_{eq} = 6.603 cm
Area Ratio , A_f/A_p = 0.747
Velocity Ratio , V_f/V_p = 1.350
Static Temperature Ratio , T_f/T_p = 1.000

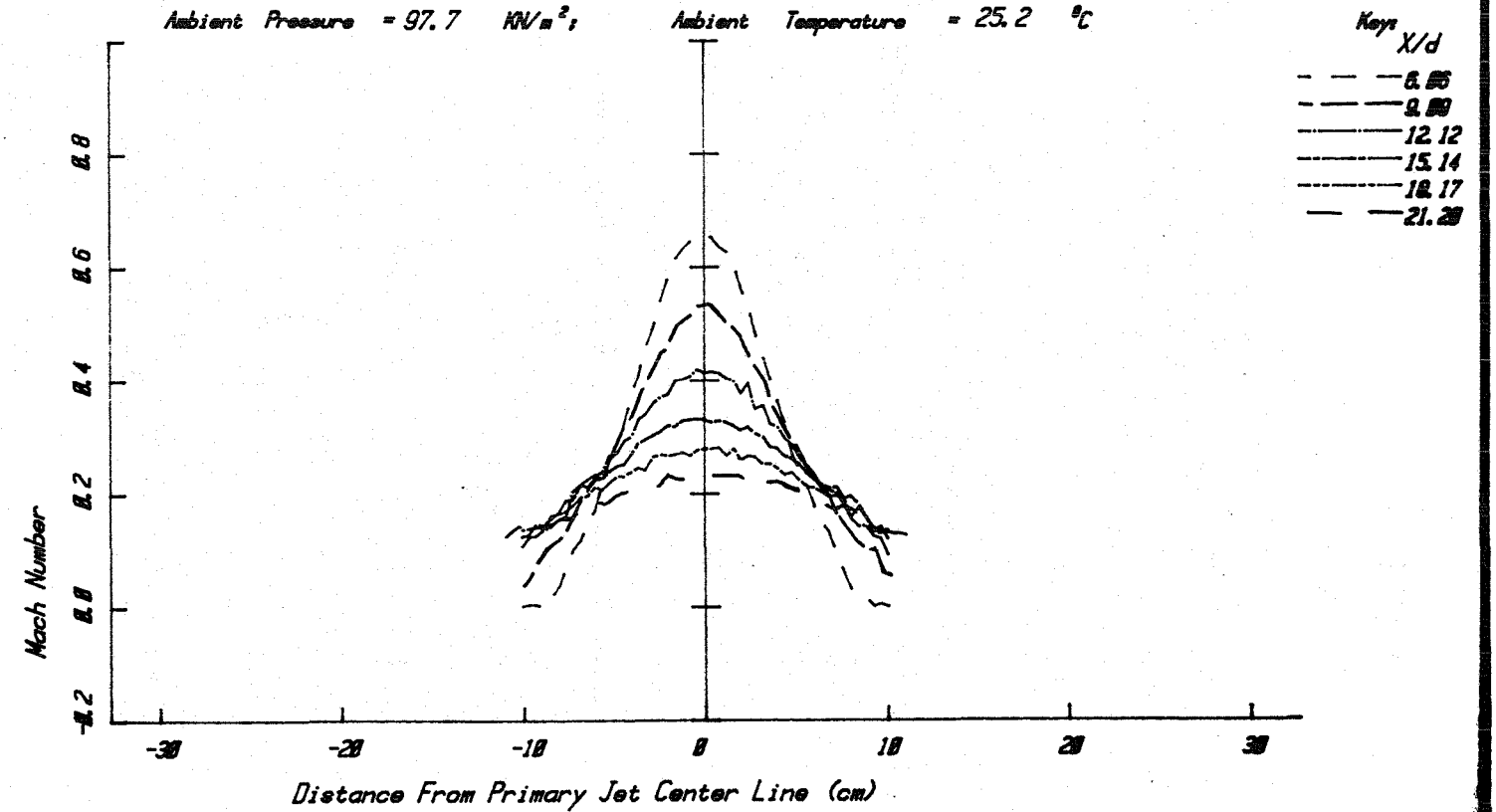

Coannular Jet - Mach Number

Figure A3.6(c)

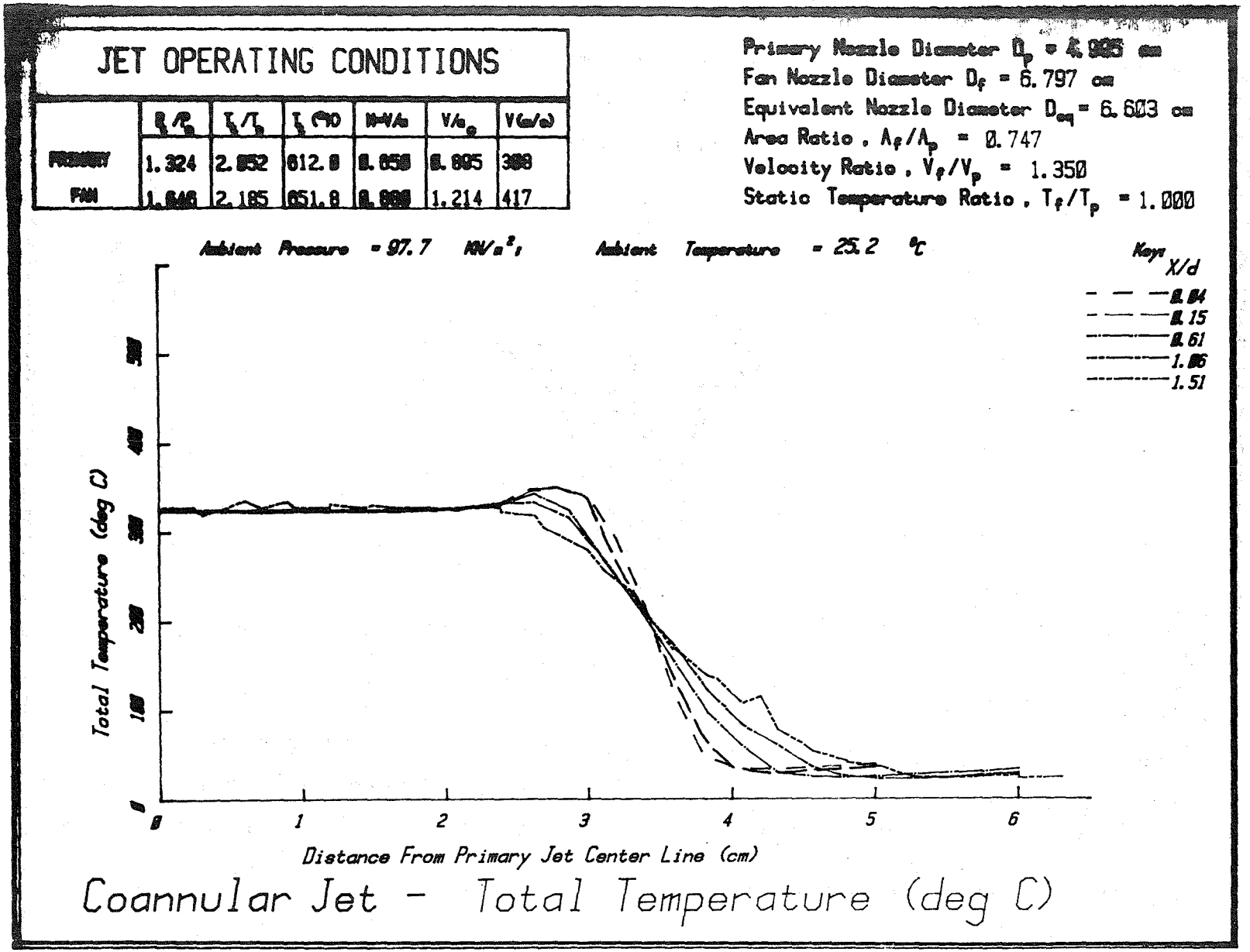
JET OPERATING CONDITIONS
Primary Nozzle Diameter D_p = 4.985 cm
Fan Nozzle Diameter D_f = 6.797 cm
Equivalent Nozzle Diameter D_{eq} = 6.603 cm
Area Ratio, A_f/A_p = 0.747
Velocity Ratio, V_f/V_p = 1.350
Static Temperature Ratio, T_f/T_p = 1.000
Ambient Pressure = 97.7 KN/m²,
Ambient Temperature = 25.2 °C
Key X/d
0.04
0.15
0.61
1.06
1.51
Total Temperature (deg C)
Distance From Primary Jet Center Line (cm)
Coannular Jet - Total Temperature (deg C)

Figure A3.7(a)

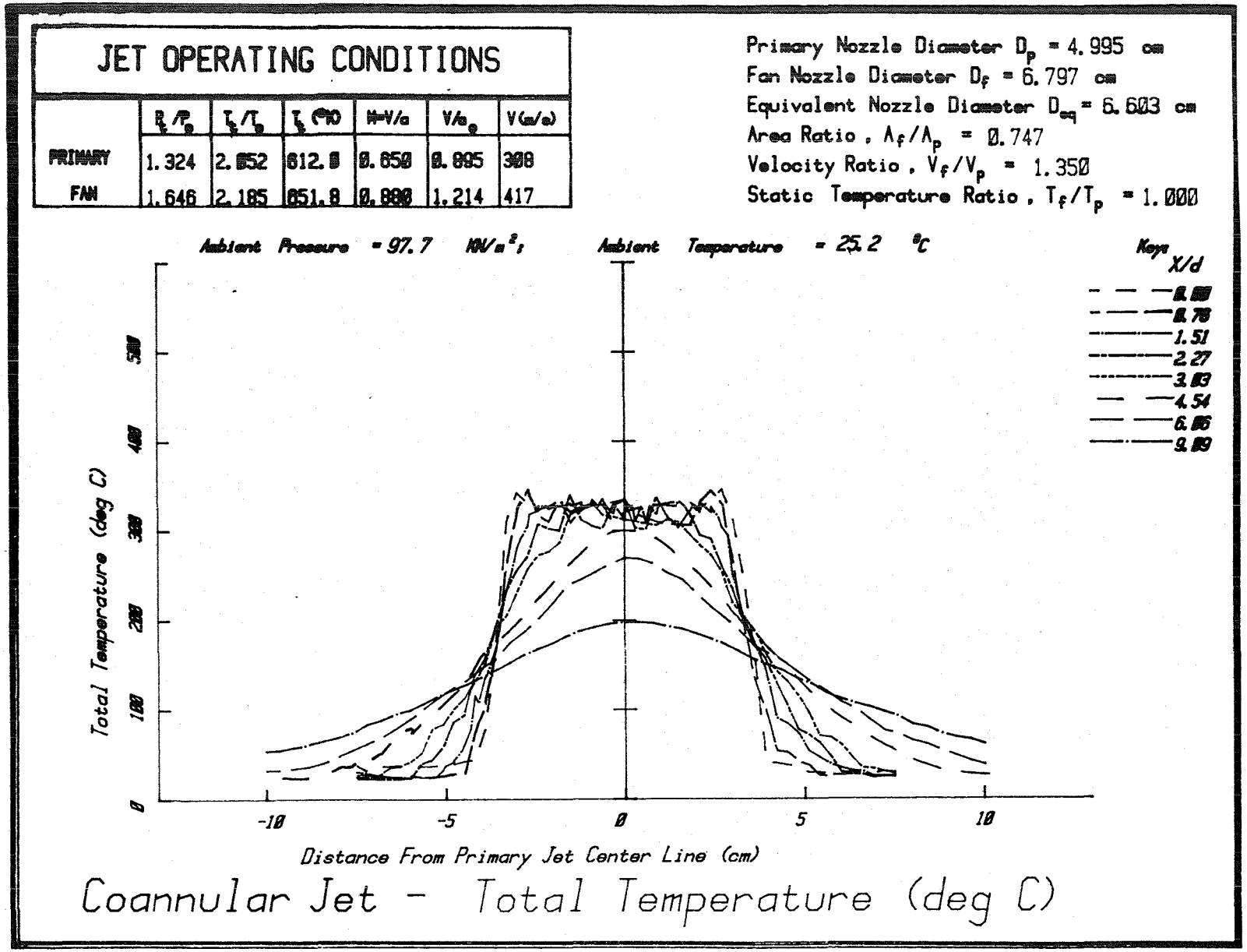
JET OPERATING CONDITIONS
PRIMARY 1.324 2.852 612.8 0.650 0.895 308
FAN 1.646 2.185 651.8 0.800 1.214 417
Primary Nozzle Diameter D_p = 4.995 cm
Fan Nozzle Diameter D_f = 6.797 cm
Equivalent Nozzle Diameter D_{eq} = 6.603 cm
Area Ratio , A_f/A_p = 0.747
Velocity Ratio , V_f/V_p = 1.350
Static Temperature Ratio , T_f/T_p = 1.000
Ambient Pressure = 97.7 KN/m²;
Ambient Temperature = 25.2 °C
Keys X/d
1.51
2.27
4.54
Total Temperature (deg C)
0
100
200
300
400
500
-10
-5
0
5
10
Distance From Primary Jet Center Line (cm)
Coannular Jet - Total Temperature (deg C)

Figure A3.7(b)

JET OPERATING CONDITIONS

	P_t/P_o	T_t/T_o	T_t (°K)	M=V/a	V/a_o	V(m/s)
PRIMARY	1.324	2.052	612.0	0.650	0.895	308
FAN	1.646	2.185	651.8	0.880	1.214	417

Primary Nozzle Diameter D_p = 4.995 cm
Fan Nozzle Diameter D_f = 6.797 cm
Equivalent Nozzle Diameter D_{eq} = 6.603 cm
Area Ratio , A_f/A_p = 0.747
Velocity Ratio , V_f/V_p = 1.358
Static Temperature Ratio , T_f/T_p = 1.000

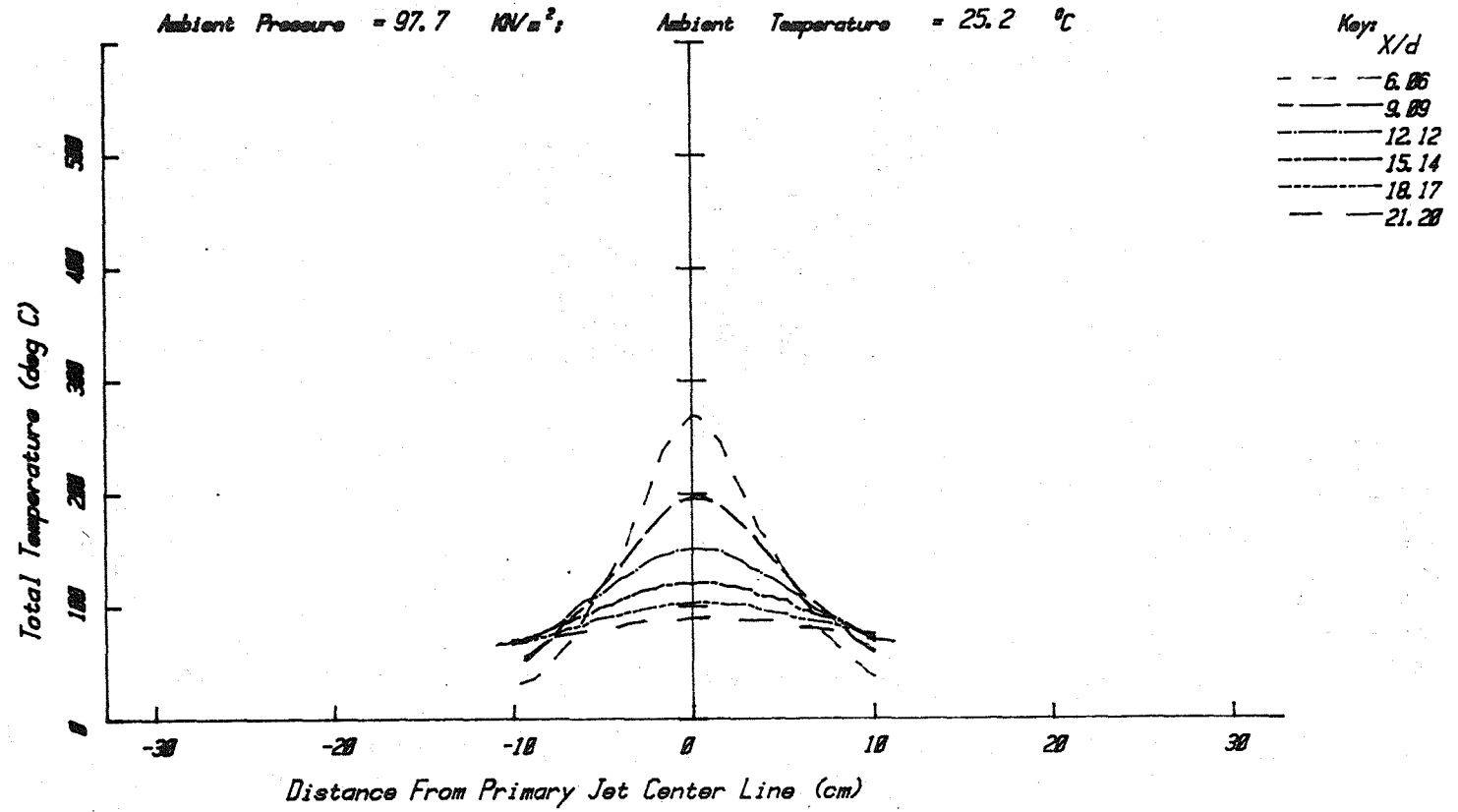

Coannular Jet - Total Temperature (deg C)

Figure A3.7(c)

JET OPERATING CONDITIONS

	P_t/P_o	T_t/T_o	T_t (°K)	M=V/a	V/a_o	V(m/s)
PRIMARY	1.324	2.052	612.0	0.650	0.895	308
FAN	1.646	2.185	651.8	0.880	1.214	417

Primary Nozzle Diameter D_p = 4.995 cm
Fan Nozzle Diameter D_f = 6.797 cm
Equivalent Nozzle Diameter D_{eq} = 6.603 cm
Area Ratio , A_f/A_p = 0.747
Velocity Ratio , V_f/V_p = 1.350
Static Temperature Ratio , T_f/T_p = 1.000

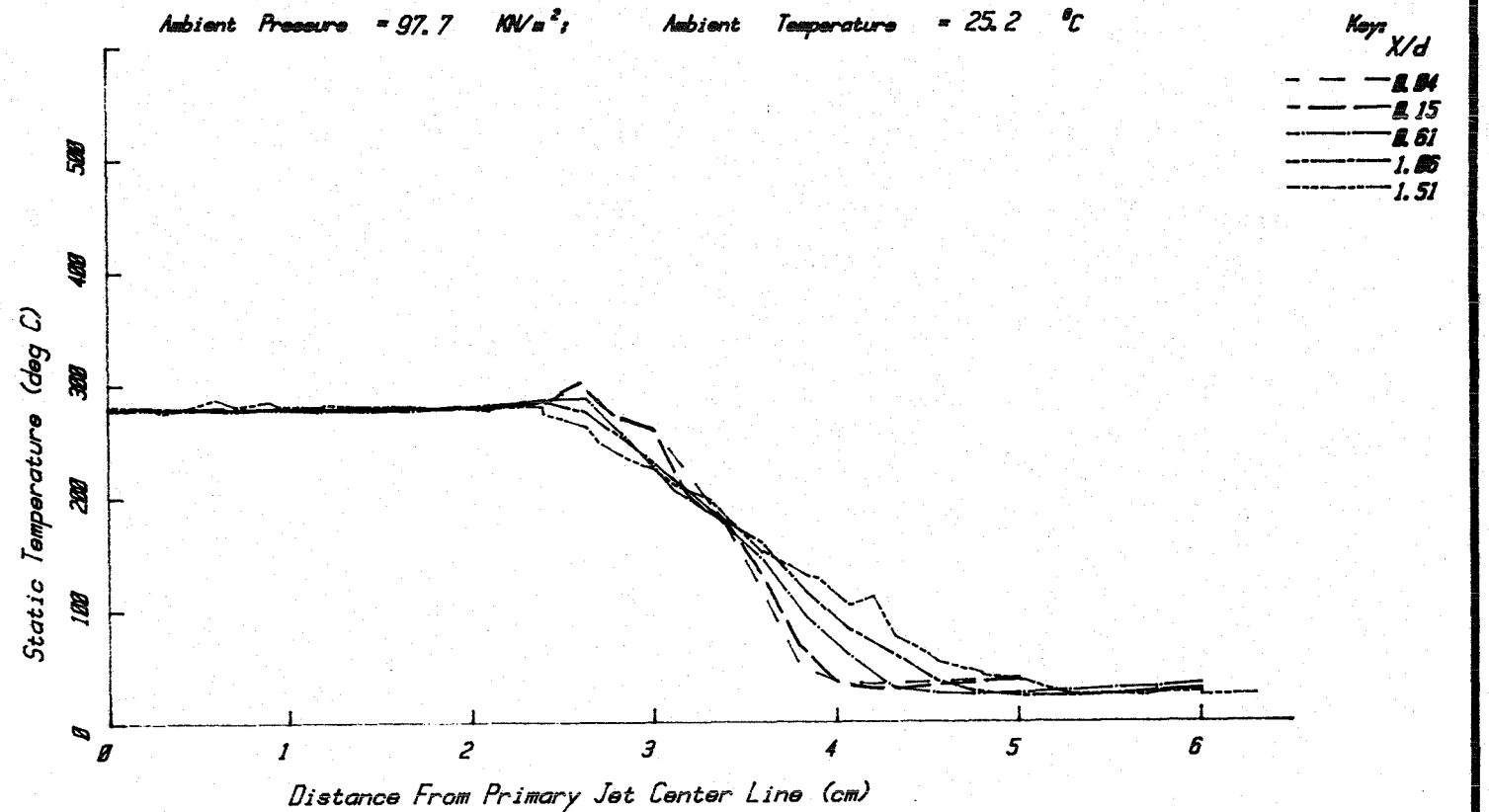

Coannular Jet - Static Temperature (deg C)

Figure A3.8(a)

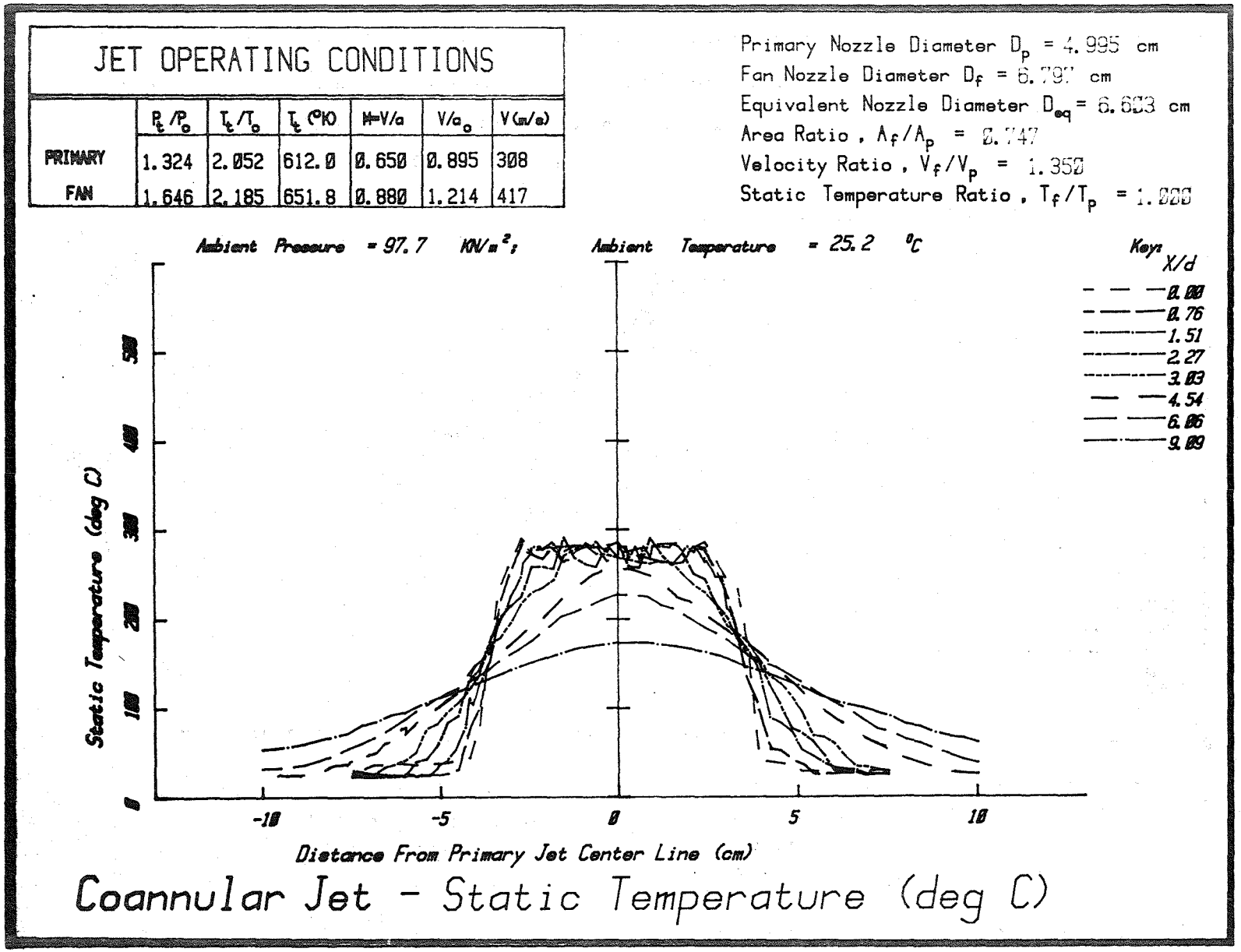

	P_t/P_o	T_t/T_o	T_t (°K)	M=V/a	V/a_o	V (m/s)
PRIMARY	1.324	2.052	612.0	0.650	0.895	308
FAN	1.646	2.185	651.8	0.880	1.214	417

Figure A3.8(b)

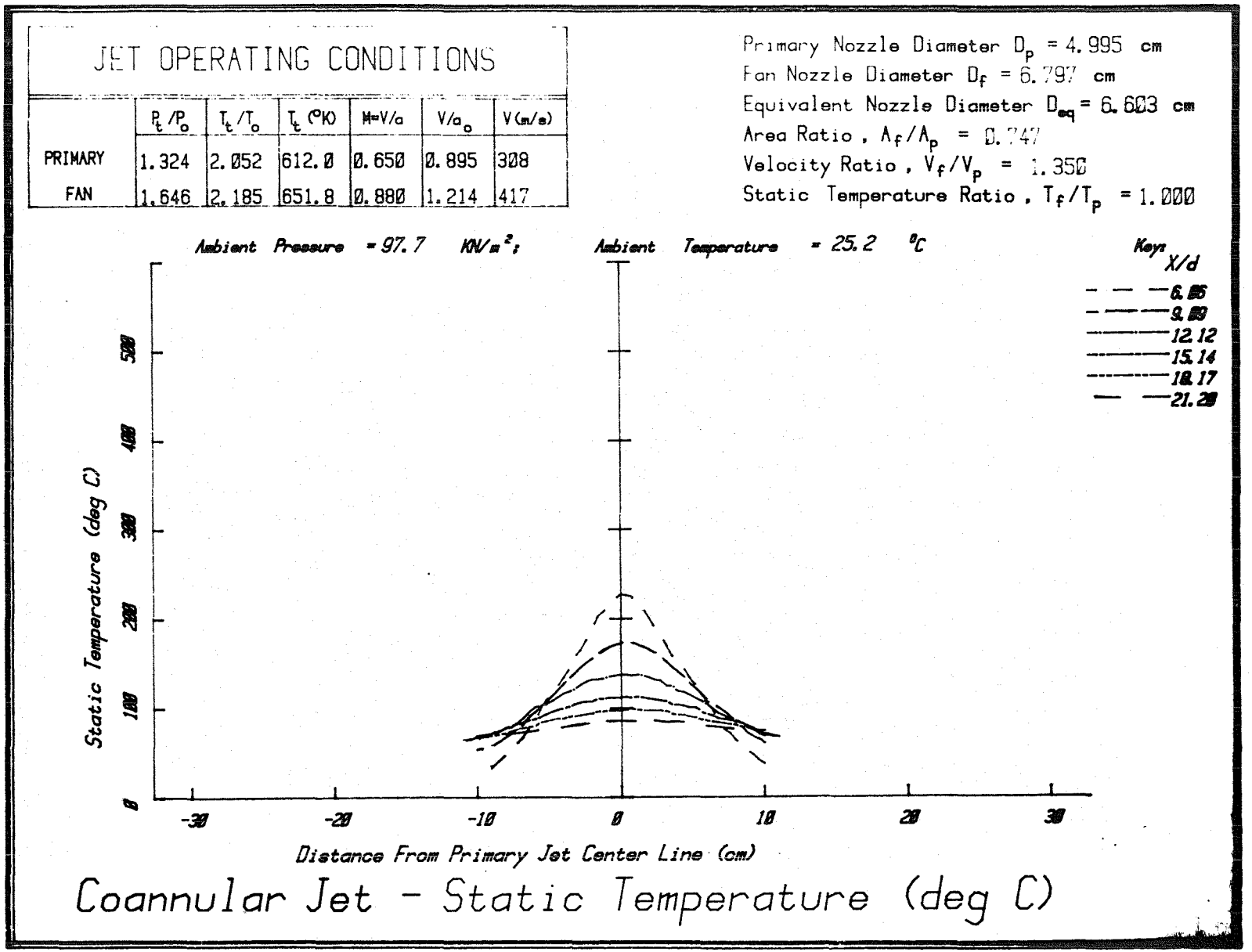

	P_t/P_o	T_t/T_o	T_t (°K)	M=V/a	V/a_o	V(m/s)
PRIMARY	1.324	2.052	612.0	0.650	0.895	308
FAN	1.646	2.185	651.8	0.880	1.214	417

Figure A3.8(c)

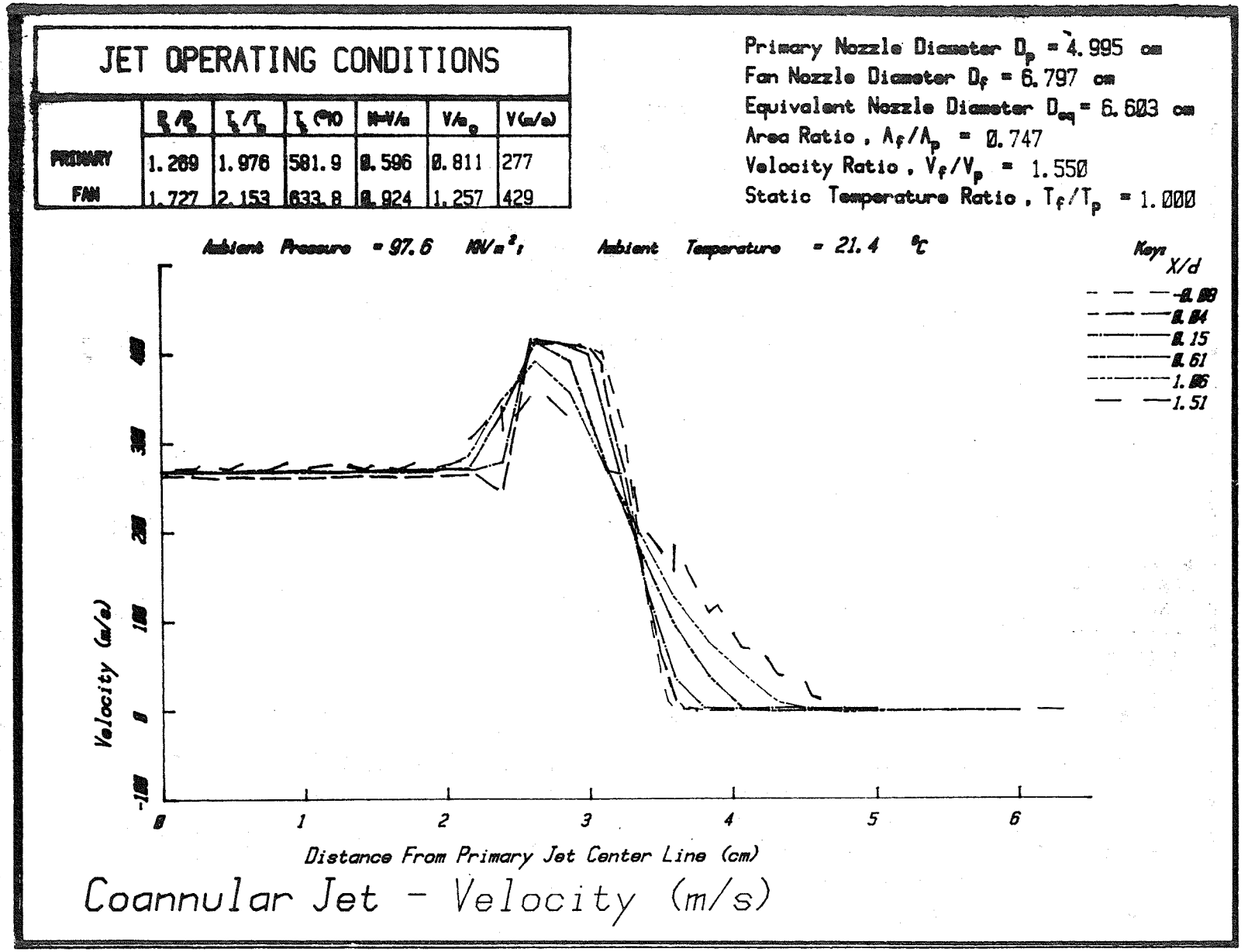
JET OPERATING CONDITIONS
PRIMARY
FAN
1.269
1.976
581.9
0.596
0.811
277
1.727
2.153
633.8
0.924
1.257
429
Primary Nozzle Diameter D_p = 4.995 cm
Fan Nozzle Diameter D_f = 6.797 cm
Equivalent Nozzle Diameter D_{eq} = 6.603 cm
Area Ratio, A_f/A_p = 0.747
Velocity Ratio, V_f/V_p = 1.550
Static Temperature Ratio, T_f/T_p = 1.000
Ambient Pressure = 97.6 KN/m²,
Ambient Temperature = 21.4 °C
Keys X/d
0.93
0.84
0.15
0.61
1.06
1.51
Velocity (m/s)
0
1
2
3
4
5
6
Distance From Primary Jet Center Line (cm)
Coannular Jet - Velocity (m/s)

Figure A3.9(a)

JET OPERATING CONDITIONS

	P_t/P_0	T_t/T_0	T_t (°K)	M=V/a	V/a_0	V (m/s)
PRIMARY	1.269	1.976	581.9	0.596	0.811	277
FAN	1.727	2.153	633.8	0.924	1.257	429

Primary Nozzle Diameter D_p = 4.995 cm
Fan Nozzle Diameter D_f = 6.797 cm
Equivalent Nozzle Diameter D_{eq} = 6.603 cm
Area Ratio , A_f/A_p = 0.747
Velocity Ratio , V_f/V_p = 1.550
Static Temperature Ratio , T_f/T_p = 1.000

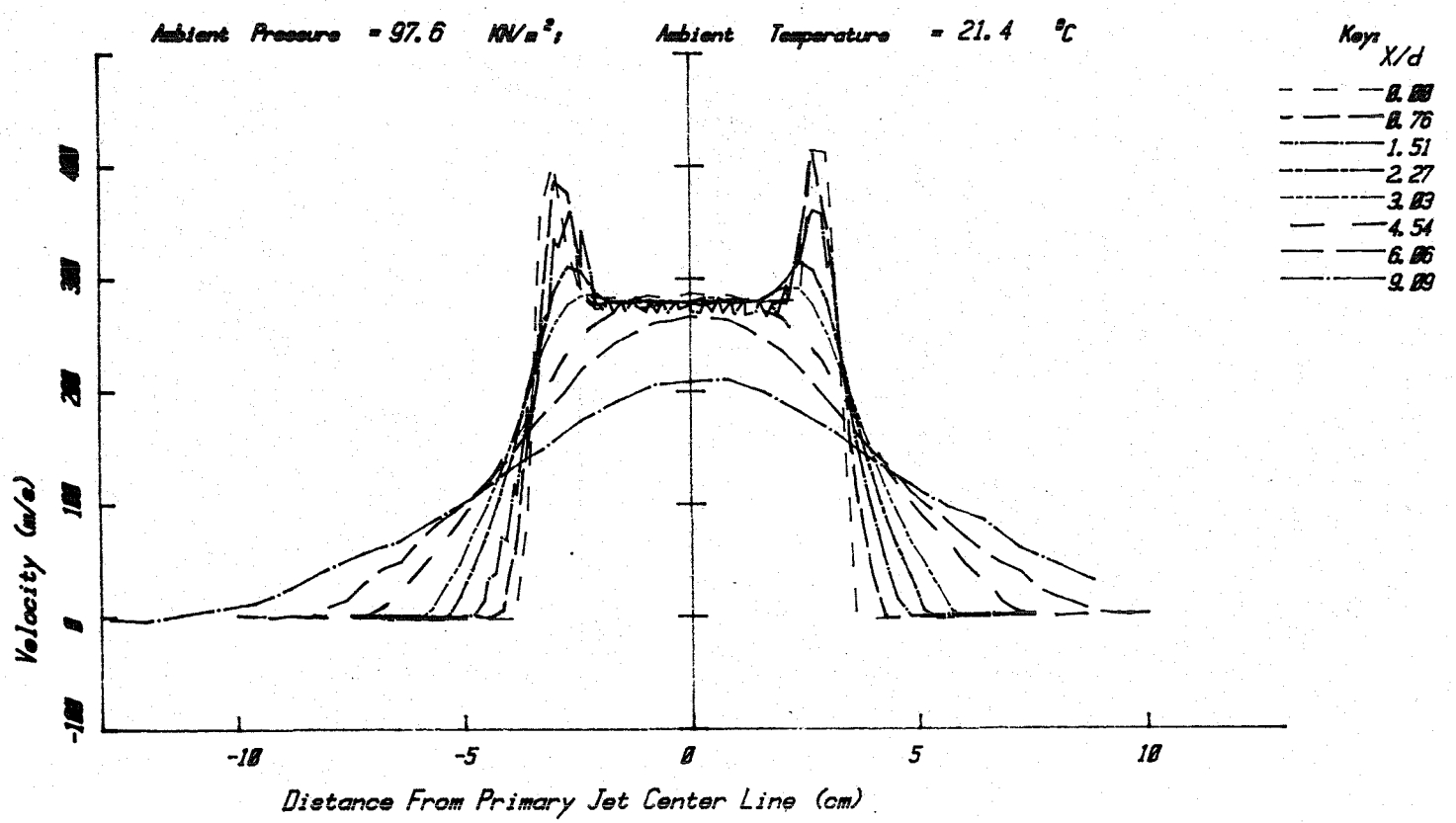

Coannular Jet - Velocity (m/s)

Figure A3.9(b)

JET OPERATING CONDITIONS

	P_t/P_o	T_t/T_o	T_t (°K)	M=V/a	V/a_o	V(m/s)
PRIMARY	1.269	1.976	581.9	0.596	0.811	277
FAN	1.727	2.153	633.8	0.924	1.257	429

Primary Nozzle Diameter D_p = 4.995 cm
Fan Nozzle Diameter D_f = 6.797 cm
Equivalent Nozzle Diameter D_{eq} = 6.603 cm
Area Ratio , A_f/A_p = 0.747
Velocity Ratio , V_f/V_p = 1.550
Static Temperature Ratio , T_f/T_p = 1.000

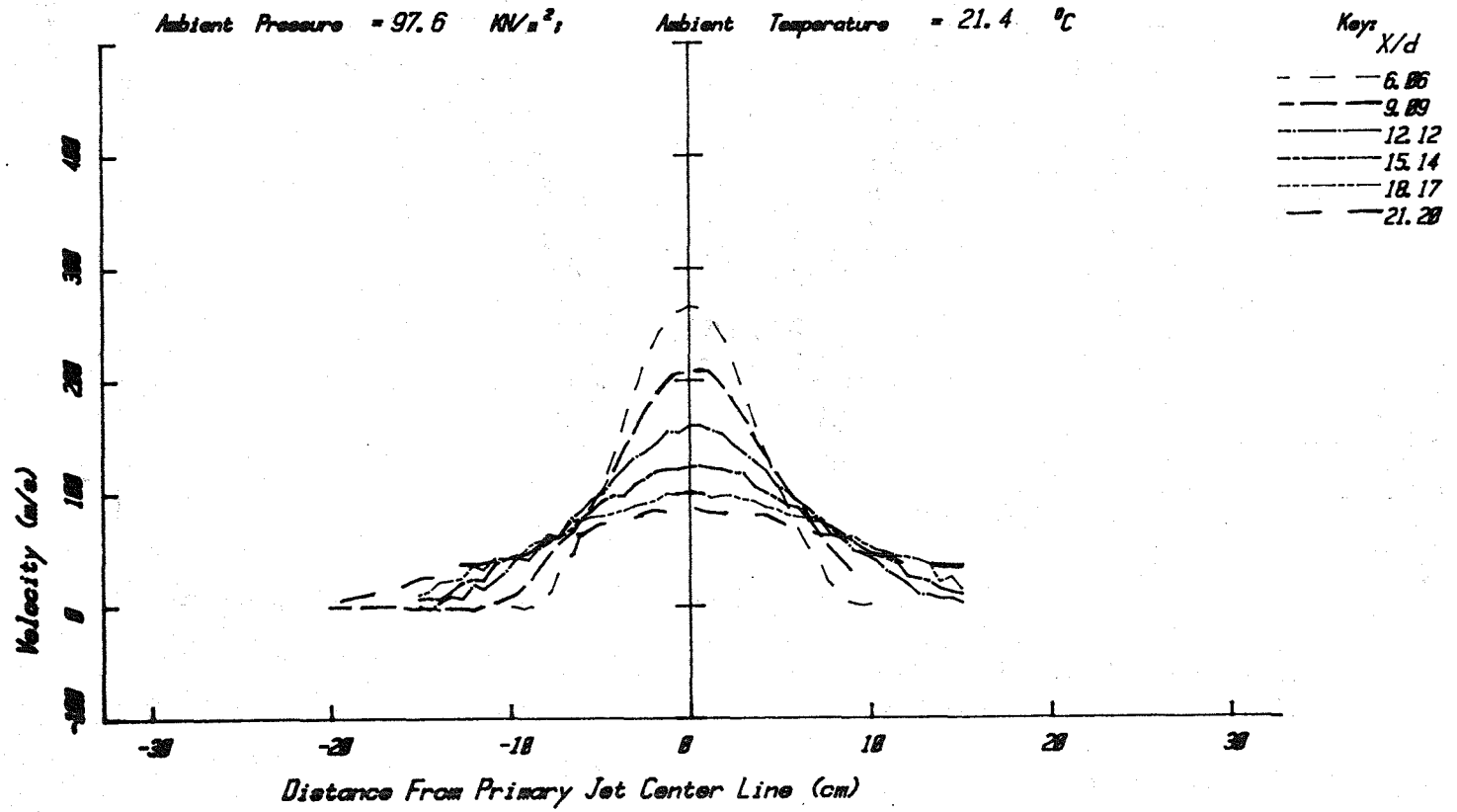

Coannular Jet - Velocity (m/s)

Figure A3.9(c)

JET OPERATING CONDITIONS

	P_t/P_0	T_t/T_0	T_t (°R)	$M=V/a$	V/a_0	V (m/s)
PRIMARY	1.269	1.976	581.9	0.596	0.811	277
FAN	1.727	2.153	633.8	0.924	1.257	429

Primary Nozzle Diameter D_p = 4.995 cm
Fan Nozzle Diameter D_f = 6.797 cm
Equivalent Nozzle Diameter D_{eq} = 6.603 cm
Area Ratio, A_f/A_p = 0.747
Velocity Ratio, V_f/V_p = 1.550
Static Temperature Ratio, T_f/T_p = 1.000

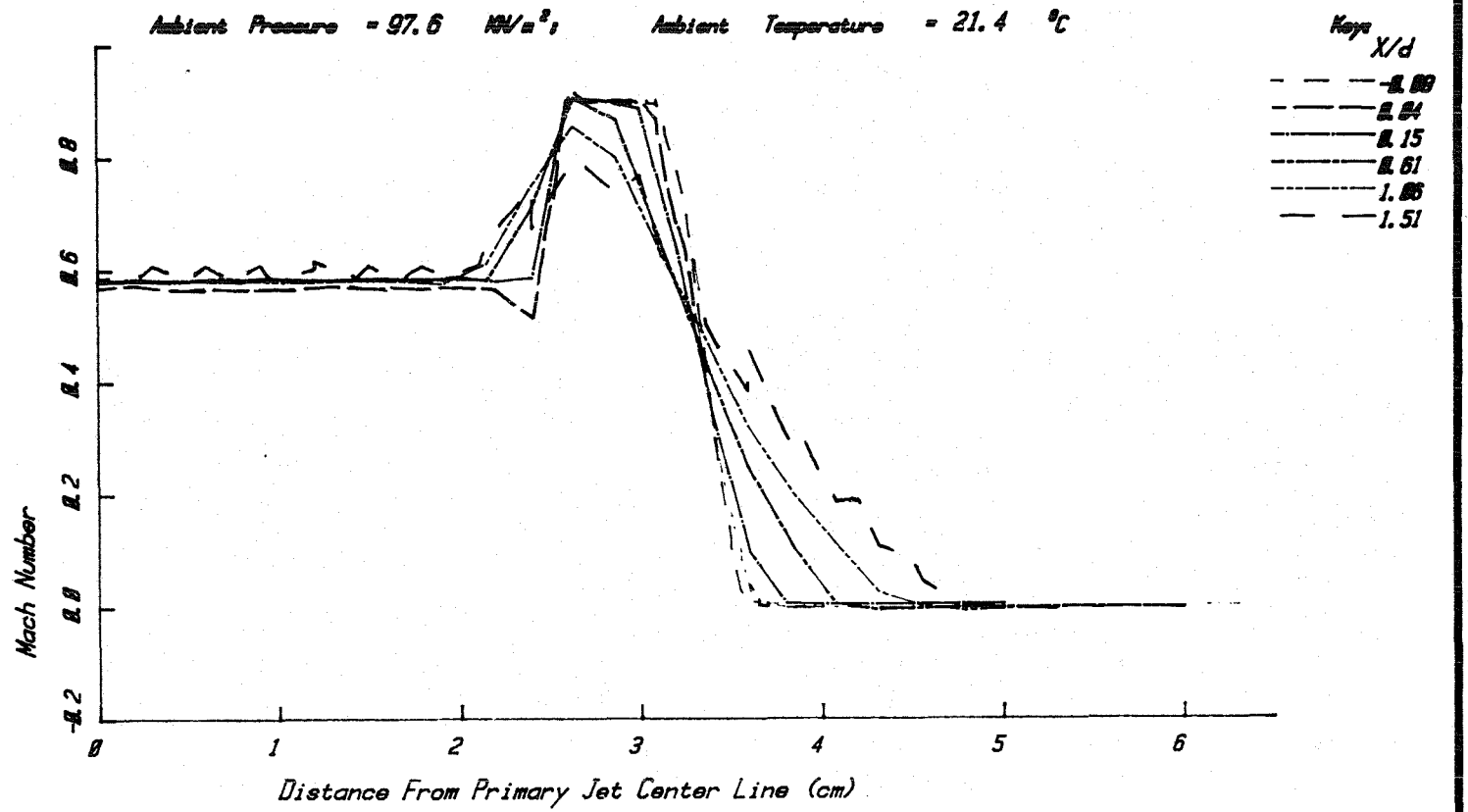

Coannular Jet - Mach Number

Figure A3.10(a)

JET OPERATING CONDITIONS

	P_t/P_o	T_t/T_o	T_t (°K)	M=V/a	V/a_o	V (m/s)
PRIMARY	1.269	1.976	581.9	Ø.596	Ø.811	277
FAN	1.727	2.153	633.8	Ø.924	1.257	429

Primary Nozzle Diameter D_p = 4.995 cm
Fan Nozzle Diameter D_f = 6.797 cm
Equivalent Nozzle Diameter D_{eq} = 6.603 cm
Area Ratio , A_f/A_p = Ø.747
Velocity Ratio , V_f/V_p = 1.55Ø
Static Temperature Ratio , T_f/T_p = 1.ØØØ

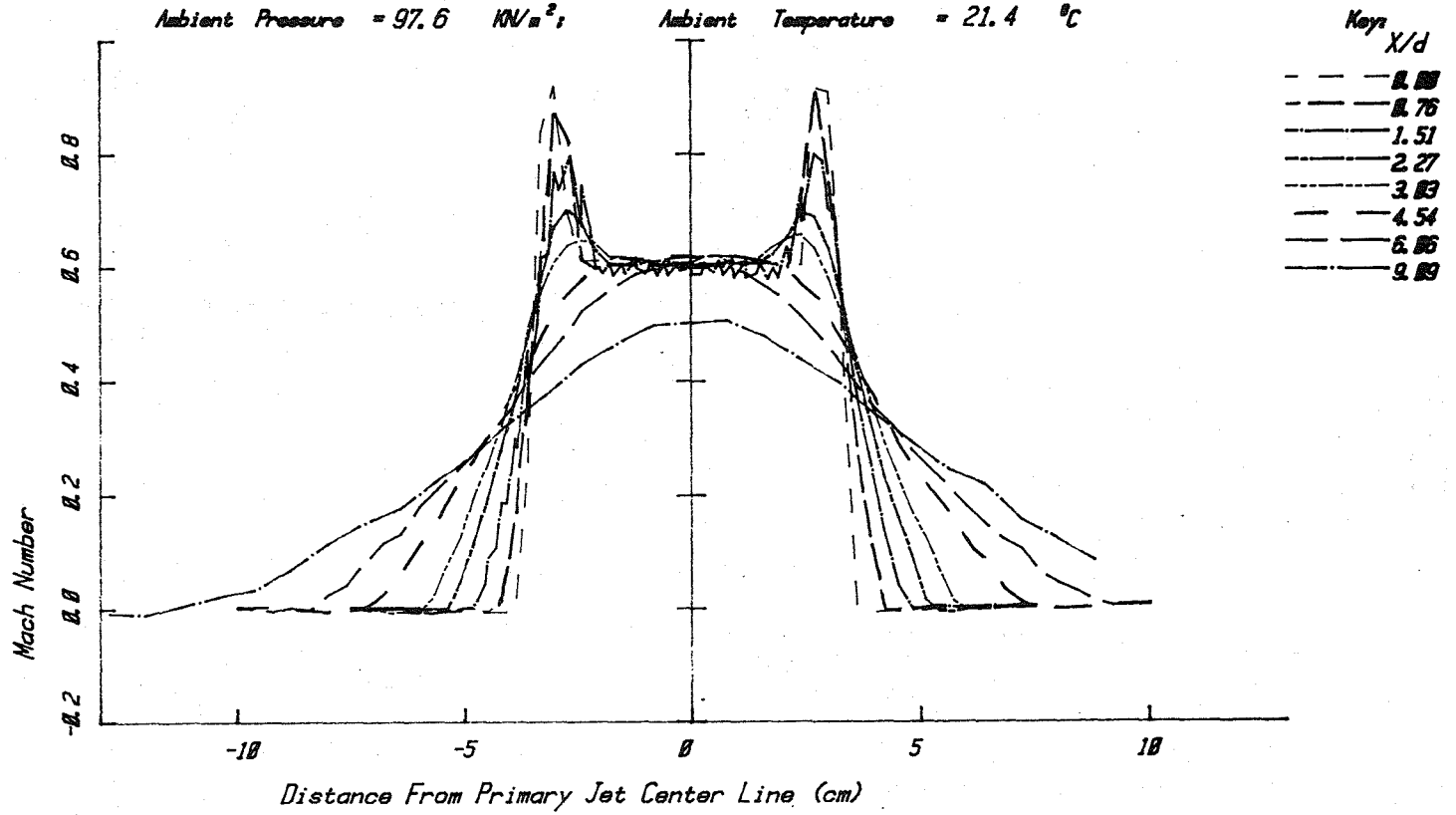

Coannular Jet - Mach Number

Figure A3.10(b)

JET OPERATING CONDITIONS

	P_t/P_o	T_t/T_o	T_t (°K)	M=V/a	V/a_o	V(m/s)
PRIMARY	1.269	1.976	581.9	0.596	0.811	277
FAN	1.727	2.153	633.8	0.924	1.257	429

Primary Nozzle Diameter D_p = 4.995 cm
Fan Nozzle Diameter D_f = 6.797 cm
Equivalent Nozzle Diameter D_{eq} = 6.603 cm
Area Ratio , A_f/A_p = 0.747
Velocity Ratio , V_f/V_p = 1.550
Static Temperature Ratio , T_f/T_p = 1.000

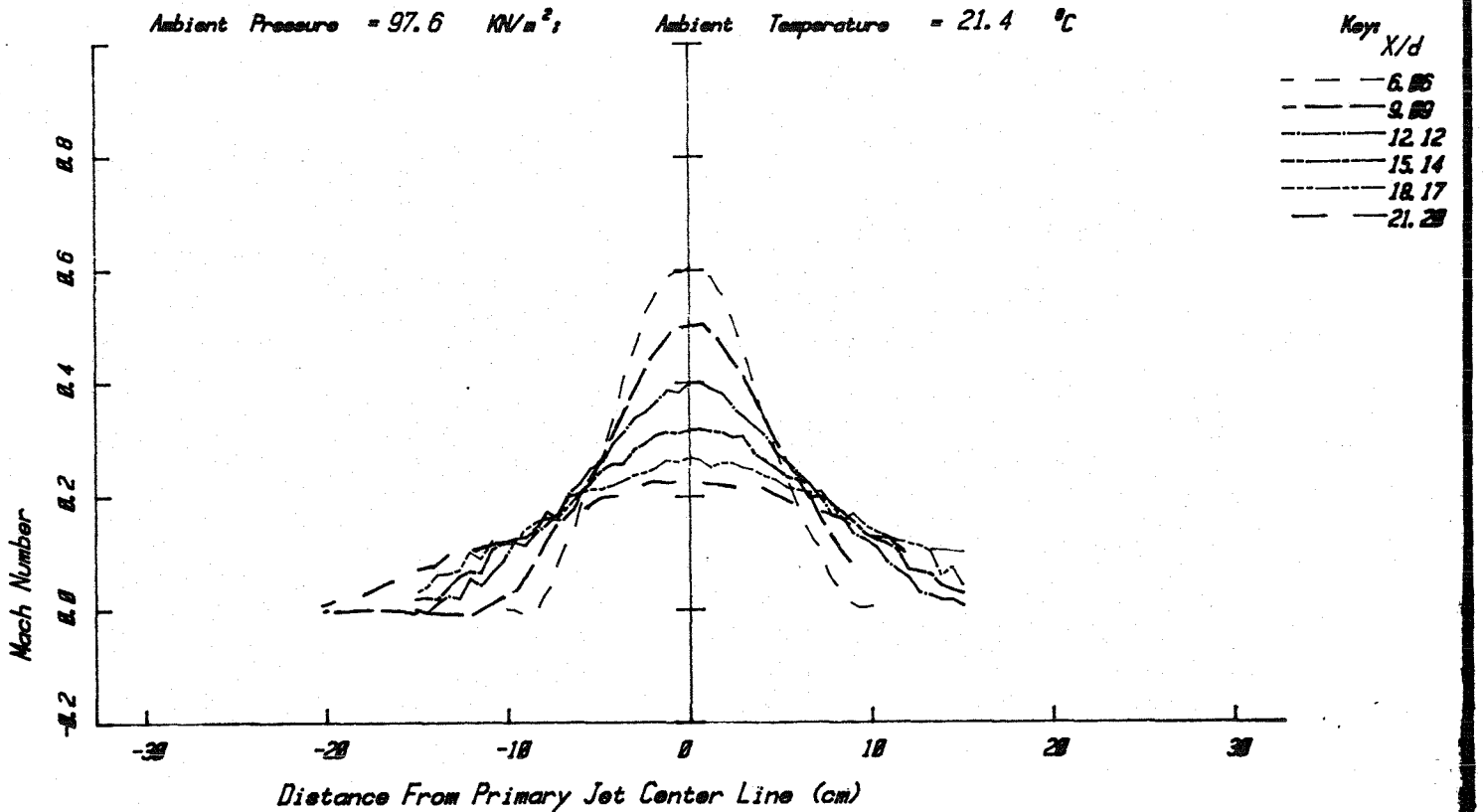

Coannular Jet - Mach Number

Figure A3.10(c)

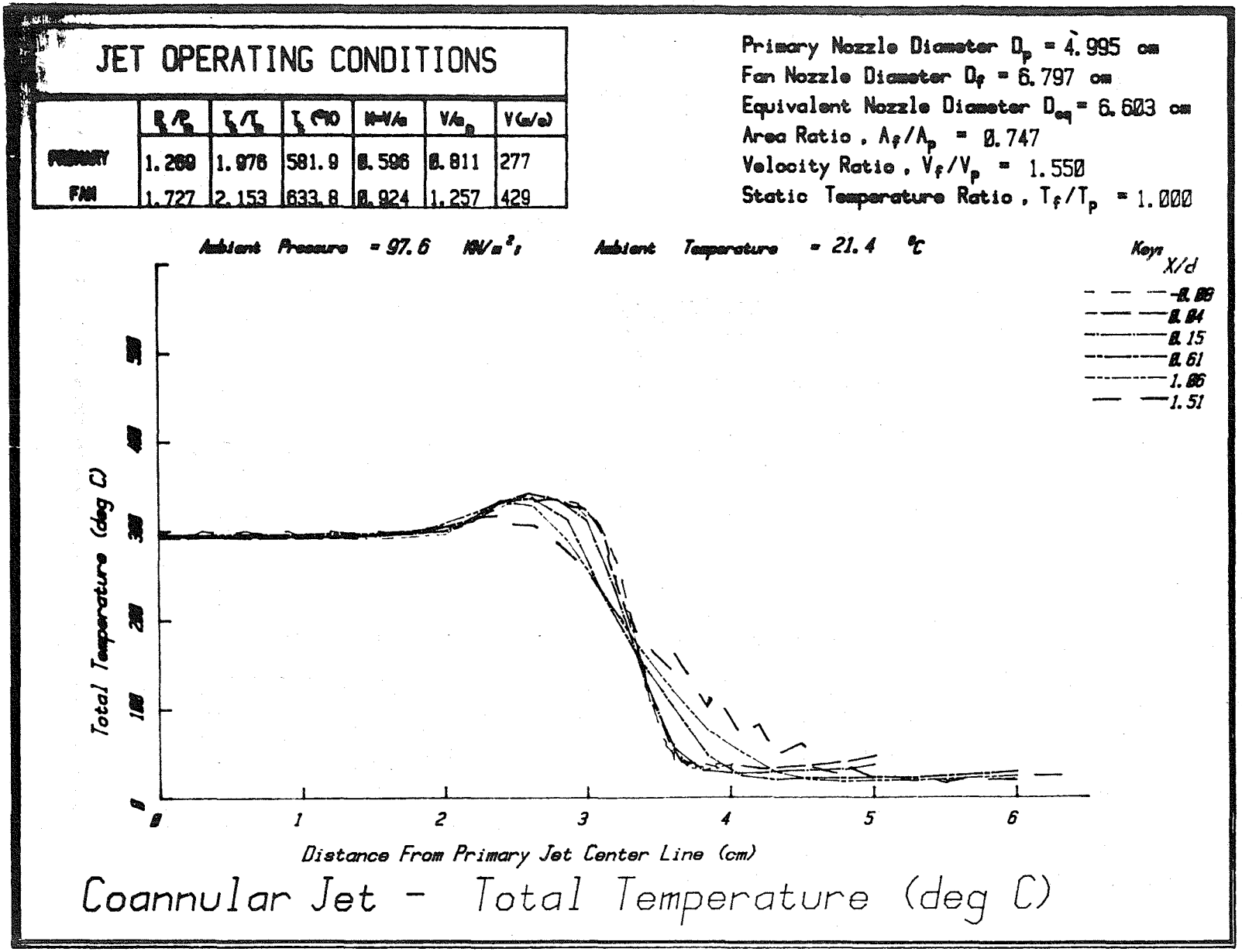

Figure A3.11(a)

JET OPERATING CONDITIONS

	P_t/P_o	T_t/T_o	T_t (°K)	M=V/a	V/a_o	V(m/s)
PRIMARY	1.269	1.976	581.9	Ø.596	Ø.811	277
FAN	1.727	2.153	633.8	Ø.924	1.257	429

Primary Nozzle Diameter D_p = 4.995 cm
Fan Nozzle Diameter D_f = 6.797 cm
Equivalent Nozzle Diameter D_{eq} = 6.6Ø3 cm
Area Ratio , A_f/A_p = Ø.747
Velocity Ratio , V_f/V_p = 1.55Ø
Static Temperature Ratio , T_f/T_p = 1.ØØØ

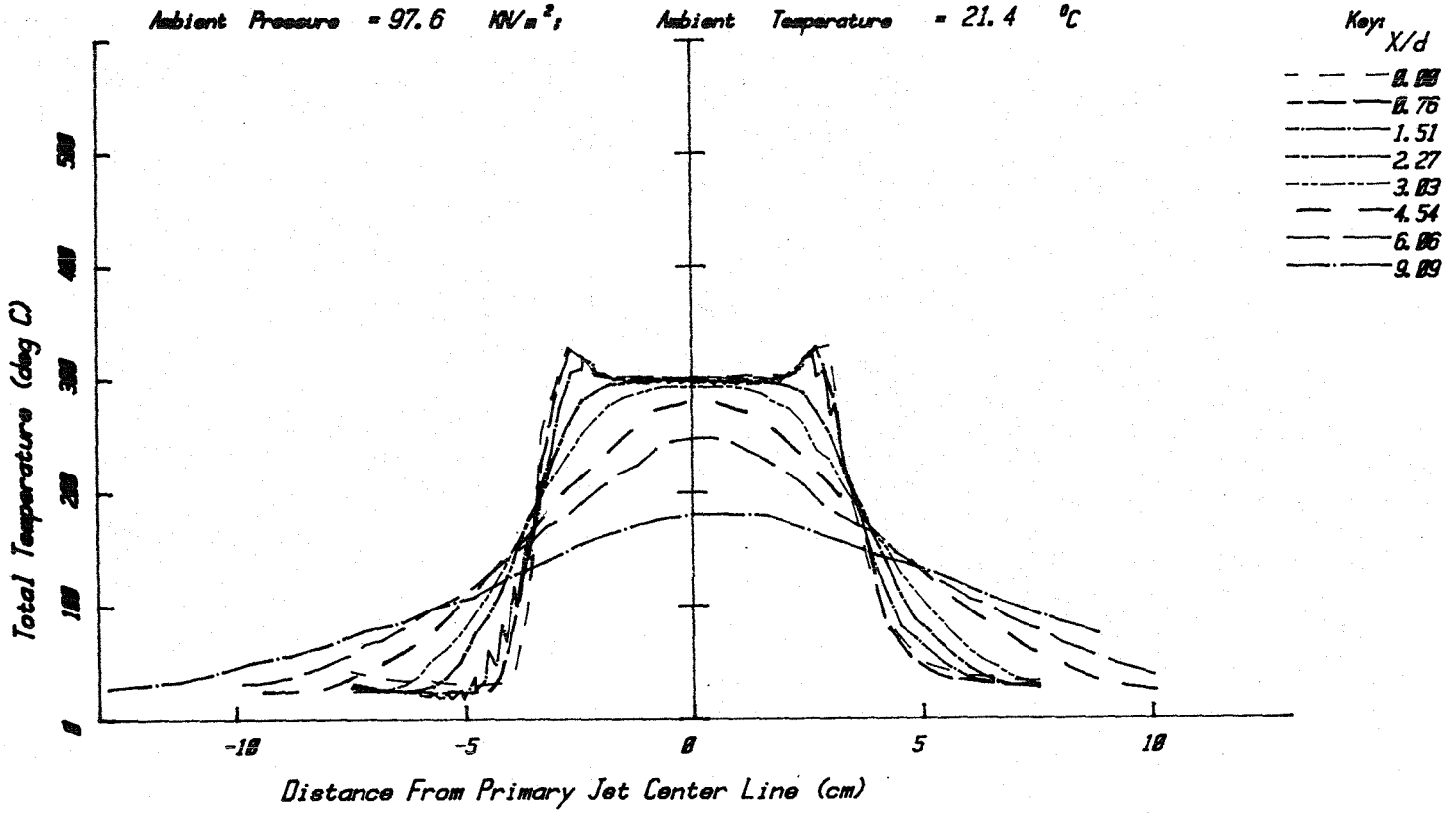

Coannular Jet - Total Temperature (deg C)

Figure A3.11(b)

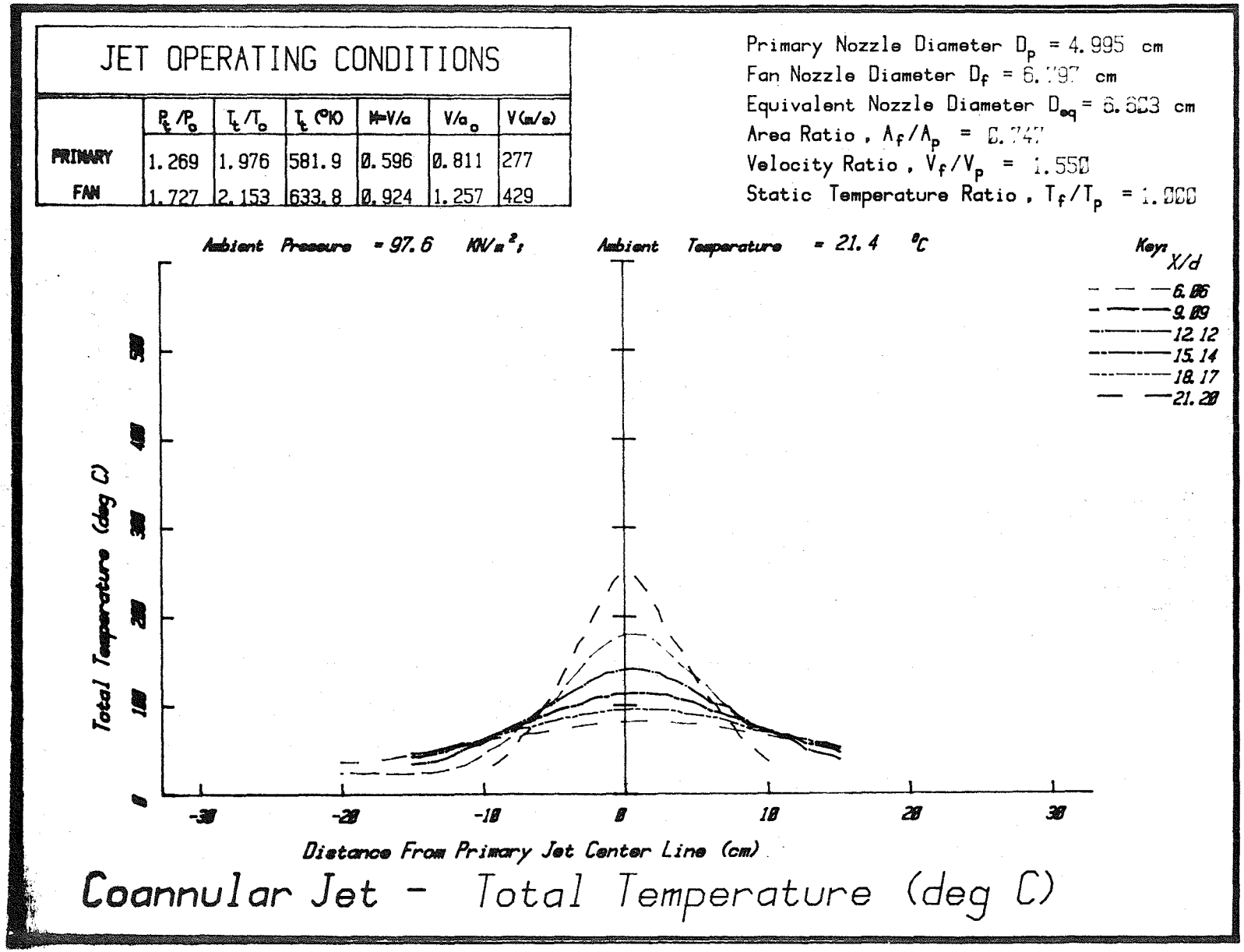

Figure A3.11(c)

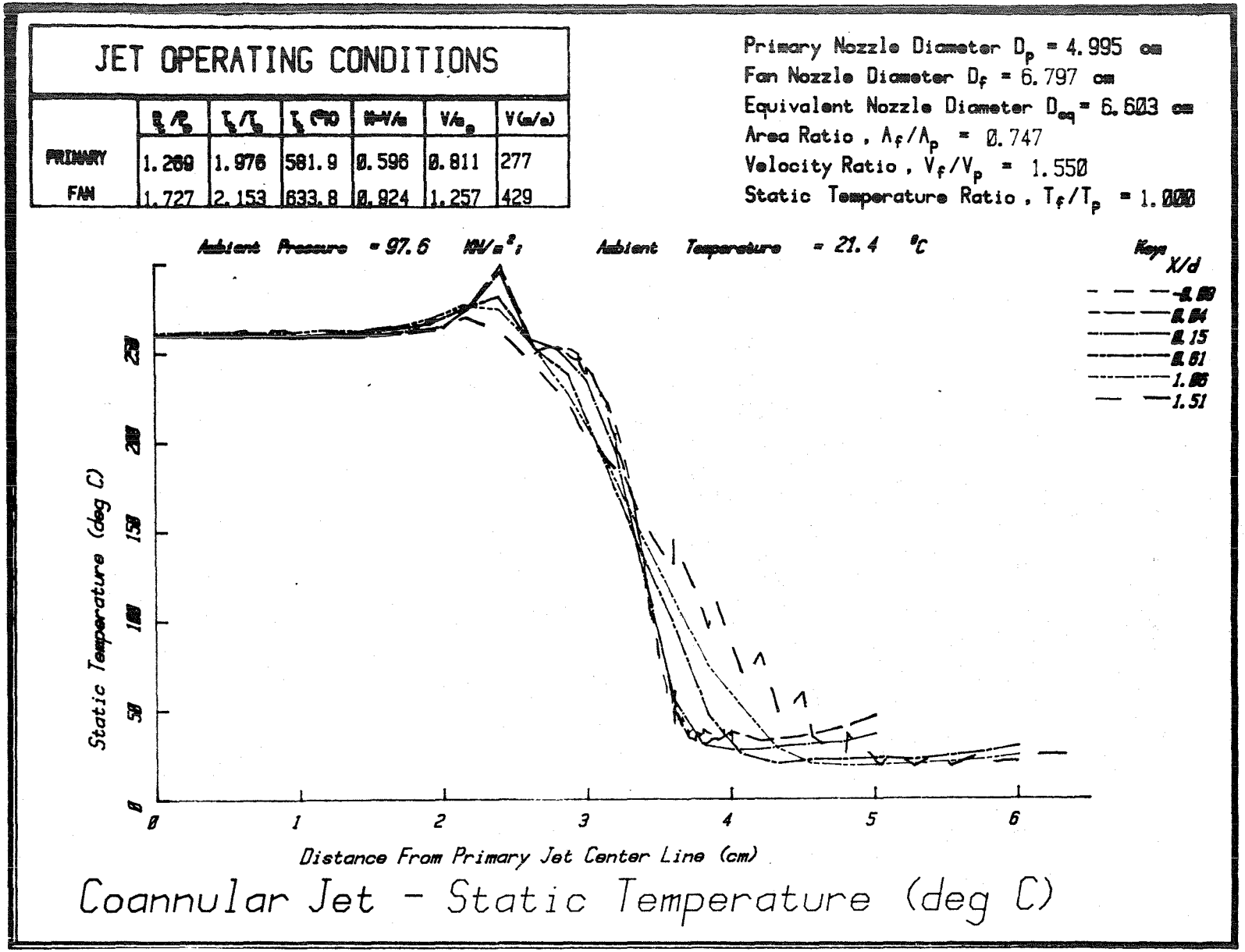

Figure A3.12(a)

JET OPERATING CONDITIONS

	P_t/P_o	T_t/T_o	T_t (°K)	M=V/a	V/a_o	V(m/s)
PRIMARY	1.269	1.976	581.9	0.596	0.811	277
FAN	1.727	2.153	633.8	0.924	1.257	429

Primary Nozzle Diameter D_p = 4.995 cm
Fan Nozzle Diameter D_f = 6.797 cm
Equivalent Nozzle Diameter D_{eq} = 6.603 cm
Area Ratio , A_f/A_p = 0.747
Velocity Ratio , V_f/V_p = 1.550
Static Temperature Ratio , T_f/T_p = 1.000

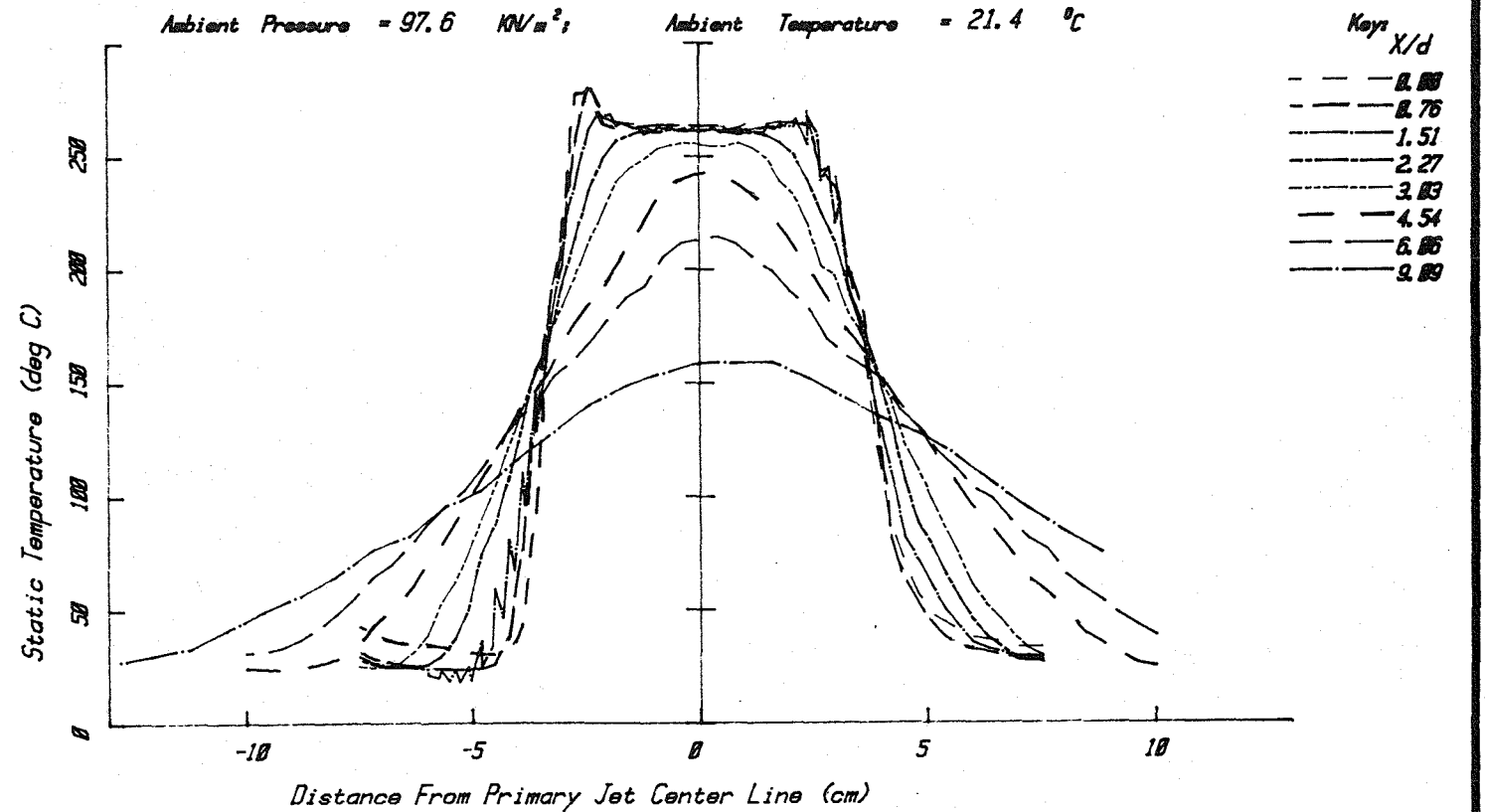

Coannular Jet - Static Temperature (deg C)

Figure A3.12(b)

JET OPERATING CONDITIONS

	P_t/P_o	T_t/T_o	T_t (°K)	M=V/a	V/a_o	V(m/s)
PRIMARY	1.269	1.976	581.9	Ø.596	Ø.811	277
FAN	1.727	2.153	633.8	Ø.924	1.257	429

Primary Nozzle Diameter D_p = 4.995 cm
Fan Nozzle Diameter D_f = 6.797 cm
Equivalent Nozzle Diameter D_{eq} = 6.603 cm
Area Ratio , A_f/A_p = Ø.747
Velocity Ratio , V_f/V_p = 1.55Ø
Static Temperature Ratio , T_f/T_p = 1.ØØØ

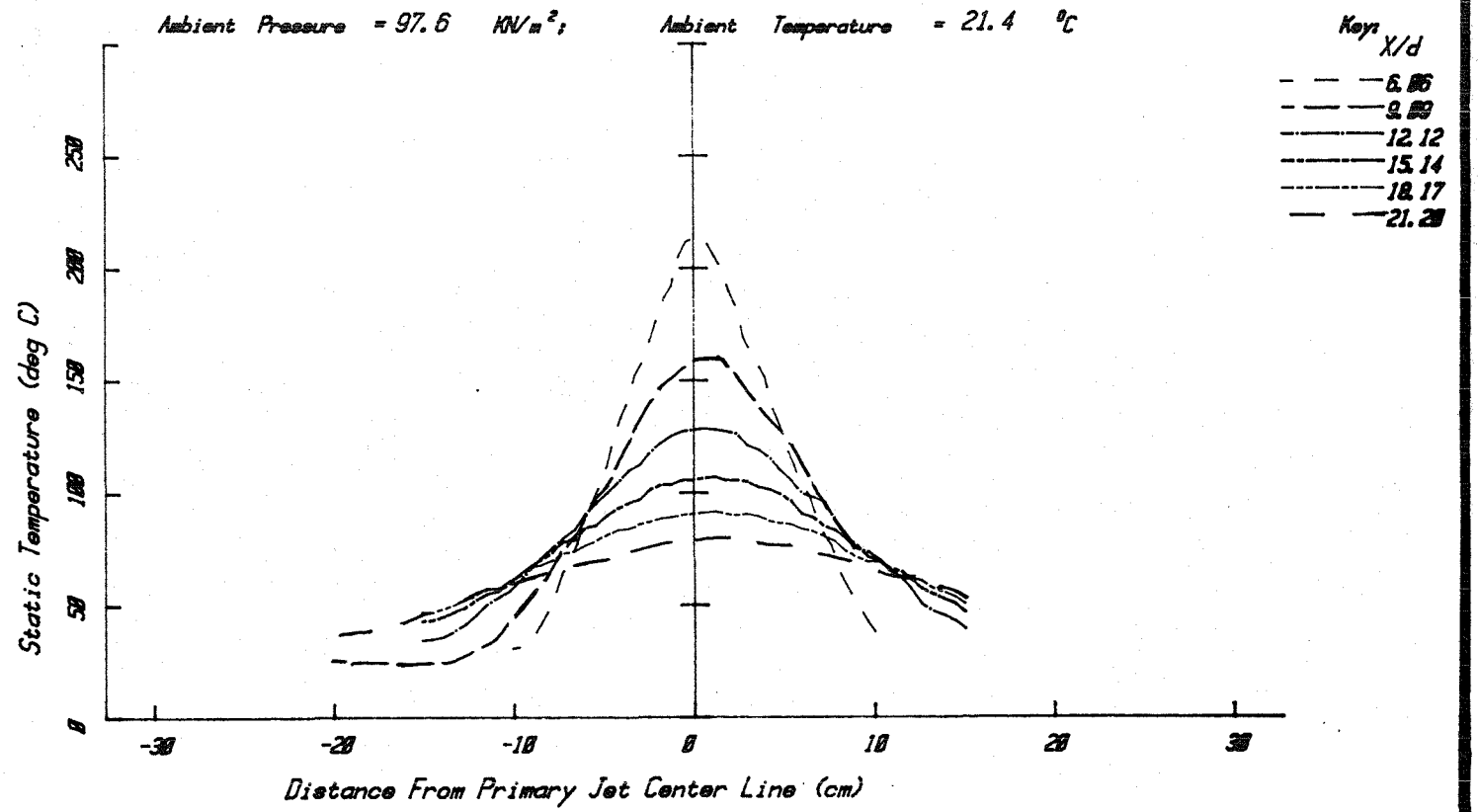

Coannular Jet - Static Temperature (deg C)

Figure A3.12(c)

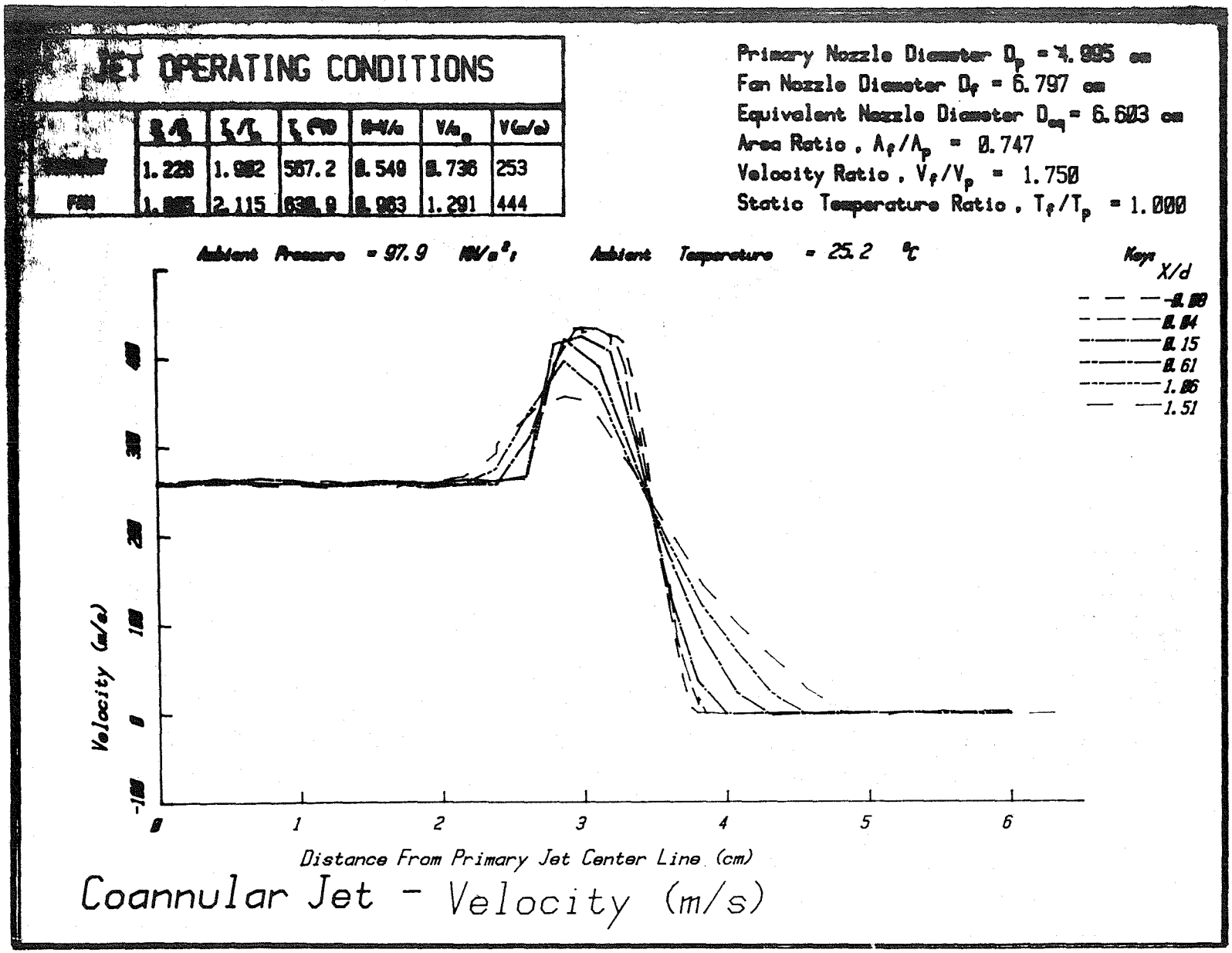

Figure A3.13(a)

JET OPERATING CONDITIONS

	P_t/P_0	T_t/T_0	T_t (°K)	M=V/a	V/a_0	V(m/s)
PRIMARY	1.226	1.902	567.2	0.549	0.736	253
FAN	1.805	2.115	630.9	0.963	1.291	444

Primary Nozzle Diameter D_p = 4.995 cm
Fan Nozzle Diameter D_f = 6.797 cm
Equivalent Nozzle Diameter D_{eq} = 6.603 cm
Area Ratio , A_f/A_p = 0.747
Velocity Ratio , V_f/V_p = 1.750
Static Temperature Ratio , T_f/T_p = 1.000

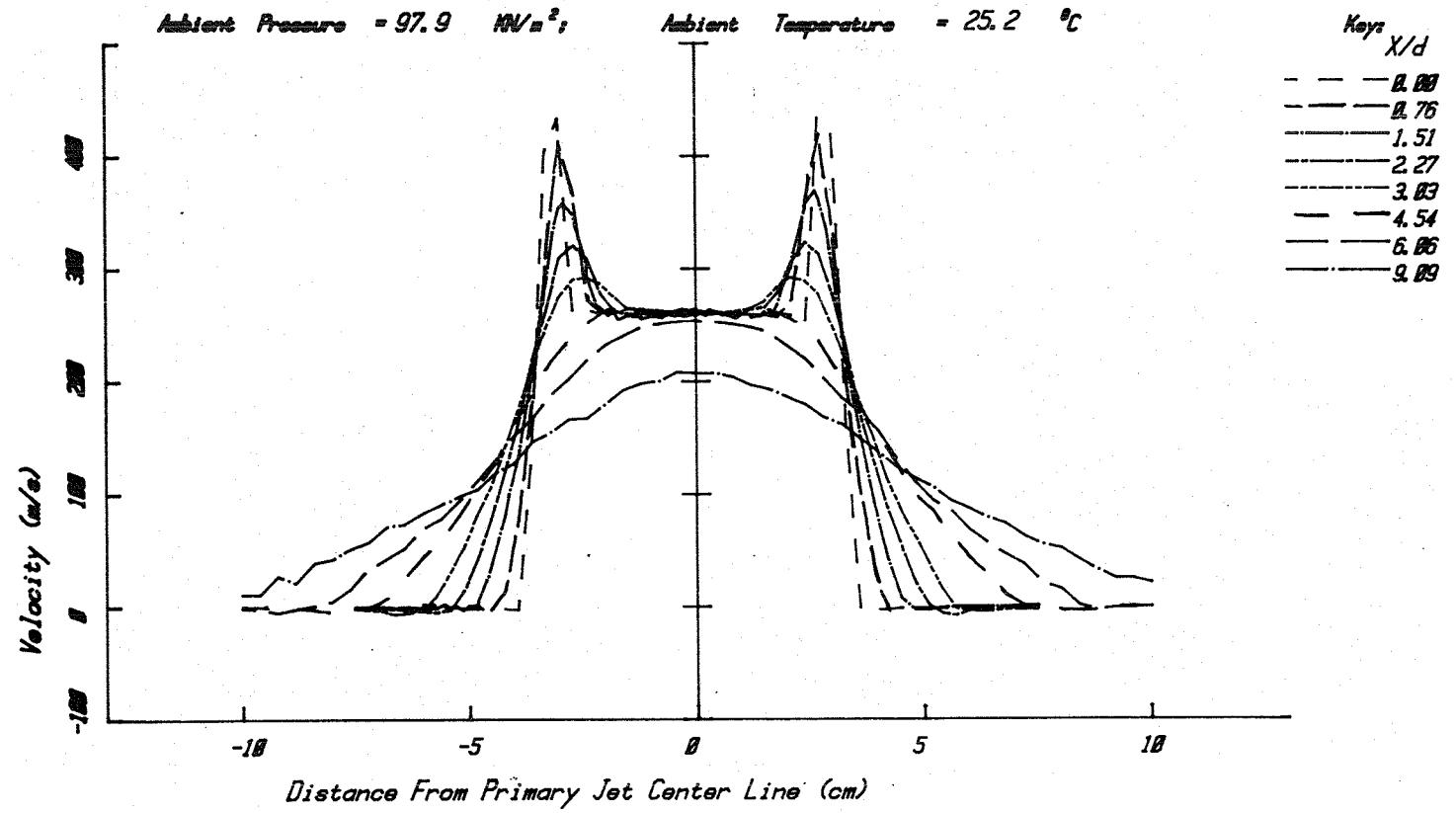

Coannular Jet - Velocity (m/s)

Figure A3.13(b)

JET OPERATING CONDITIONS

	P_t/P_o	T_t/T_o	T_t (°K)	M=V/a	V/a_o	V(m/s)
PRIMARY	1.226	1.902	567.2	0.549	0.736	253
FAN	1.805	2.115	630.9	0.963	1.291	444

Primary Nozzle Diameter D_p = 4.995 cm
Fan Nozzle Diameter D_f = 6.797 cm
Equivalent Nozzle Diameter D_{eq} = 6.603 cm
Area Ratio , A_f/A_p = 0.747
Velocity Ratio , V_f/V_p = 1.750
Static Temperature Ratio , T_f/T_p = 1.000

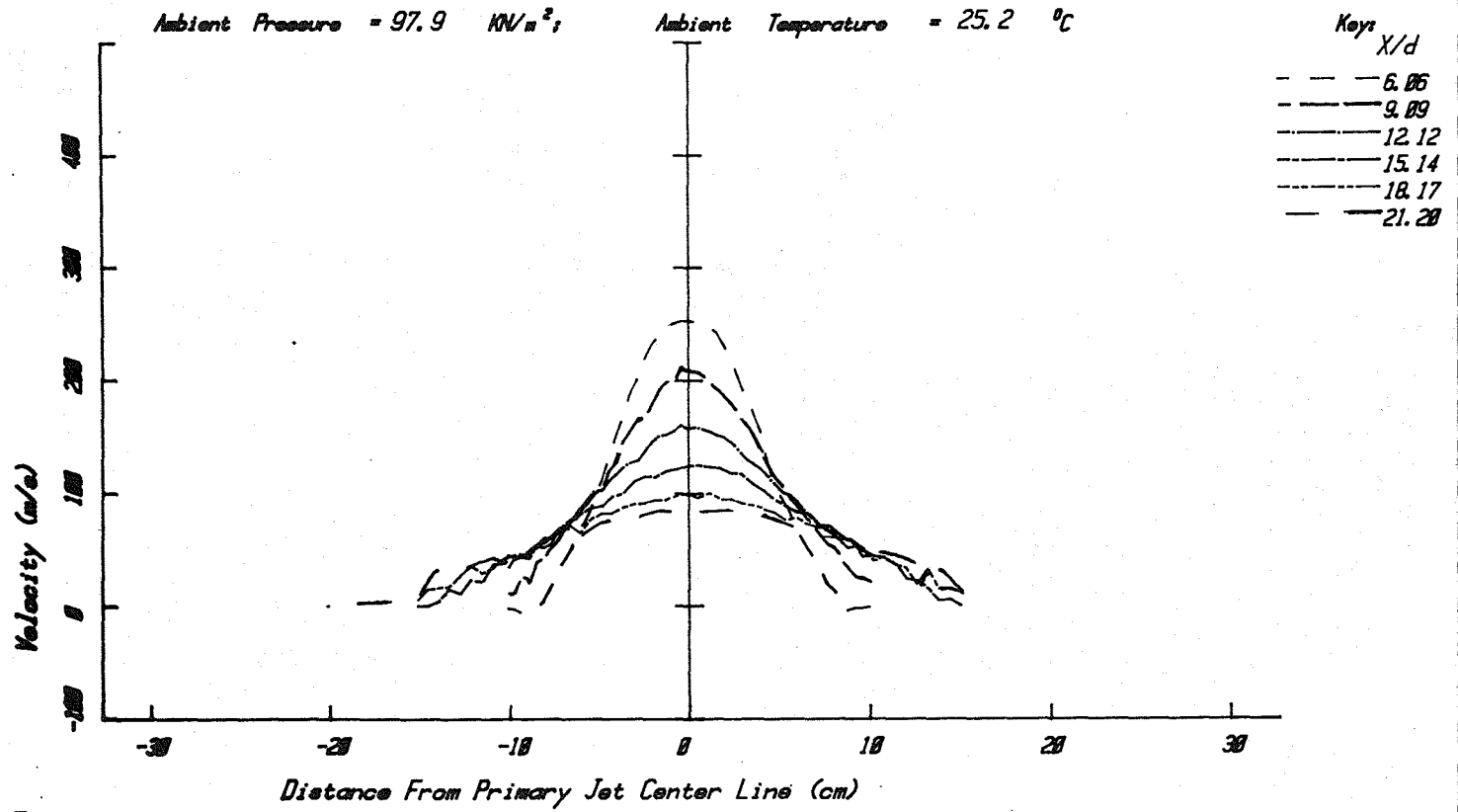

Coannular Jet - Velocity (m/s)

Figure A3.13(c)

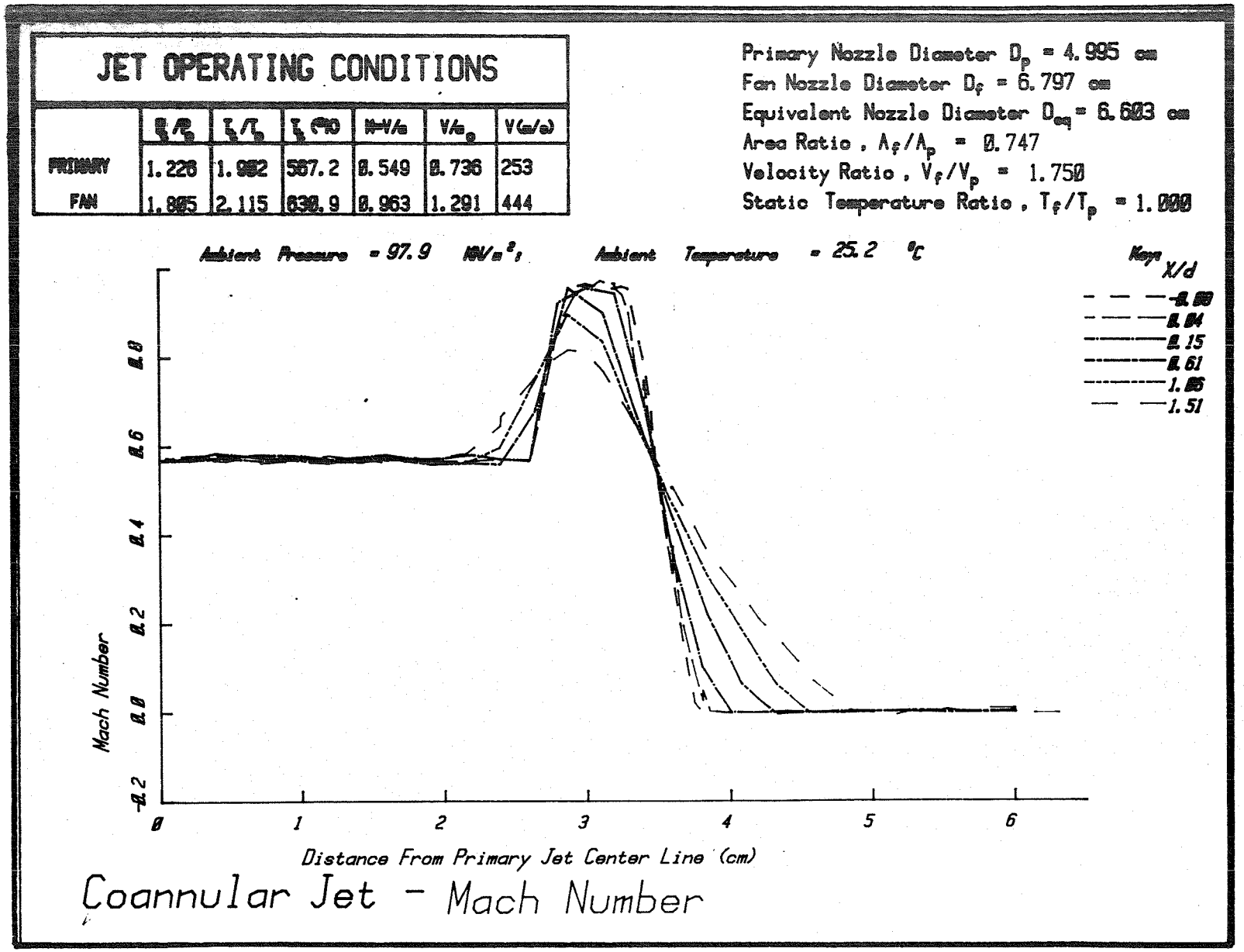

Figure A3.14(a)

JET OPERATING CONDITIONS

	P_t/P_o	T_t/T_o	T_t (°K)	M=V/a	V/a_o	V(m/s)
PRIMARY	1.226	1.902	567.2	0.549	0.736	253
FAN	1.805	2.115	630.9	0.963	1.291	444

Primary Nozzle Diameter D_p = 4.995 cm
Fan Nozzle Diameter D_f = 6.797 cm
Equivalent Nozzle Diameter D_{eq} = 6.603 cm
Area Ratio , A_f/A_p = 0.747
Velocity Ratio , V_f/V_p = 1.750
Static Temperature Ratio , T_f/T_p = 1.000

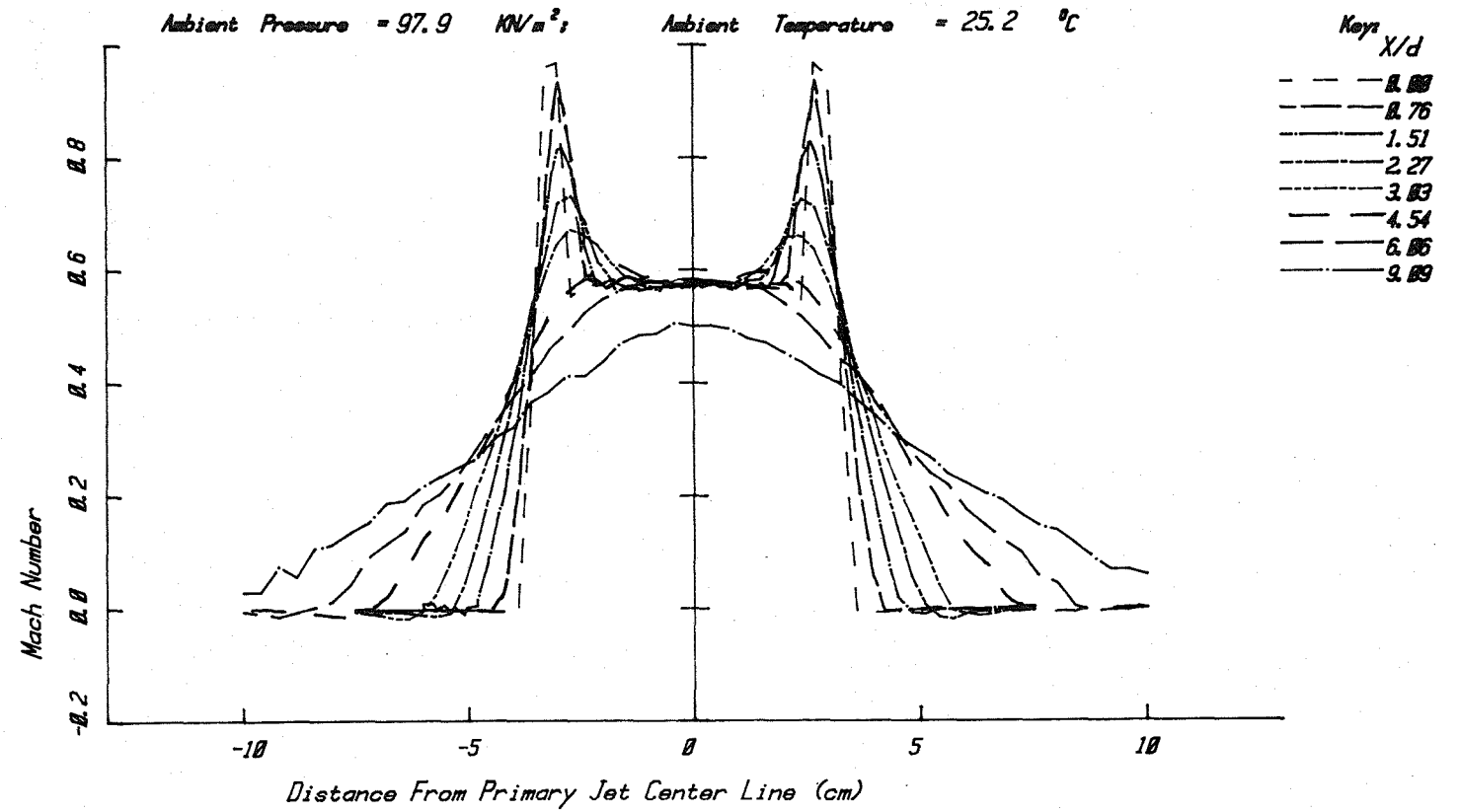

Coannular Jet - Mach Number

Figure A3.14(b)

JET OPERATING CONDITIONS

	P_t/P_o	T_t/T_o	T_t (°K)	M=V/a	V/a_o	V(m/s)
PRIMARY	1.226	1.902	567.2	0.549	0.736	253
FAN	1.805	2.115	630.9	0.963	1.291	444

Primary Nozzle Diameter D_p = 4.995 cm
Fan Nozzle Diameter D_f = 6.797 cm
Equivalent Nozzle Diameter D_{eq} = 6.603 cm
Area Ratio, A_f/A_p = 0.747
Velocity Ratio, V_f/V_p = 1.750
Static Temperature Ratio, T_f/T_p = 1.000

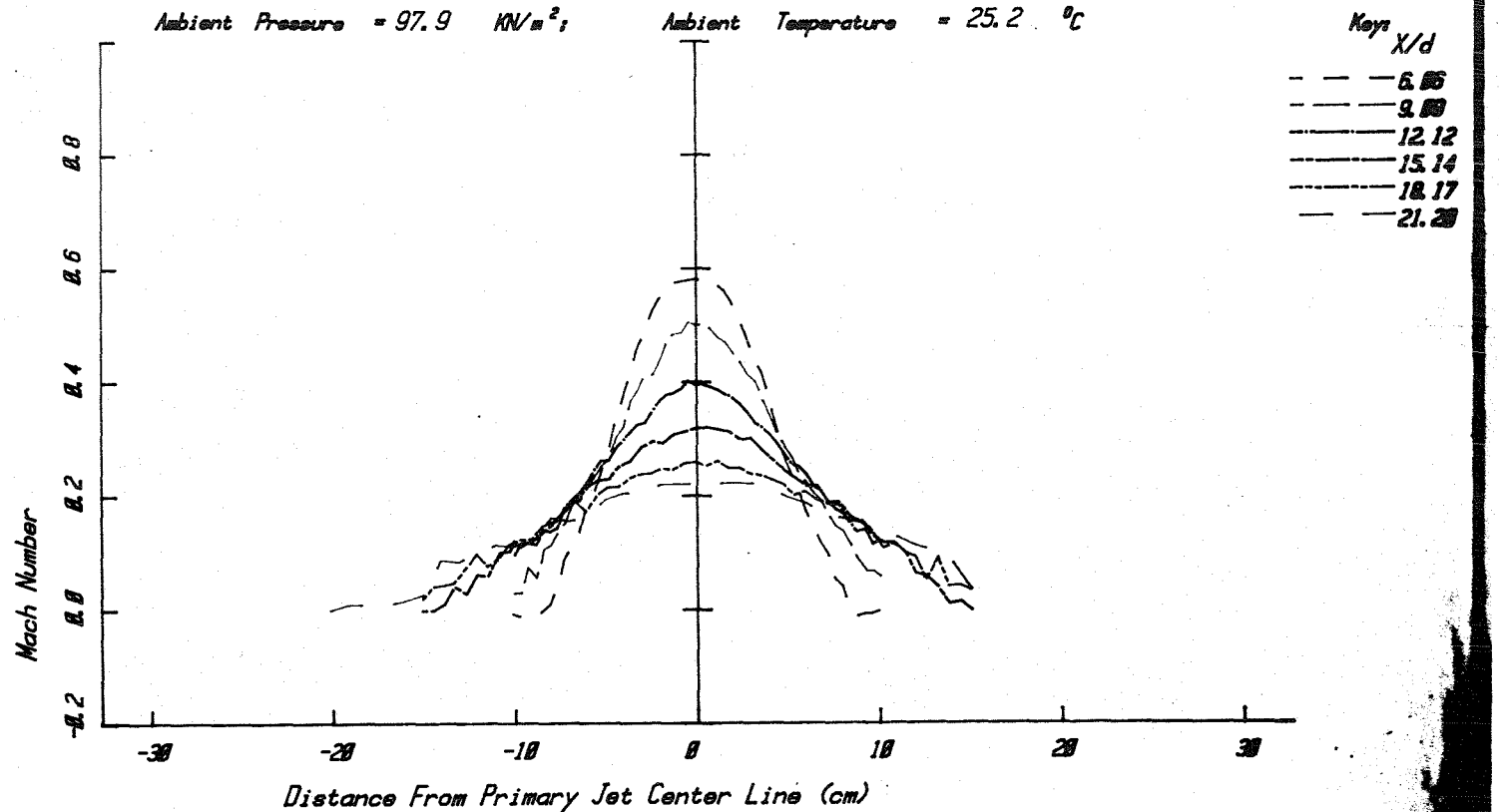

Coannular Jet - Mach Number

Figure A3.14(c)

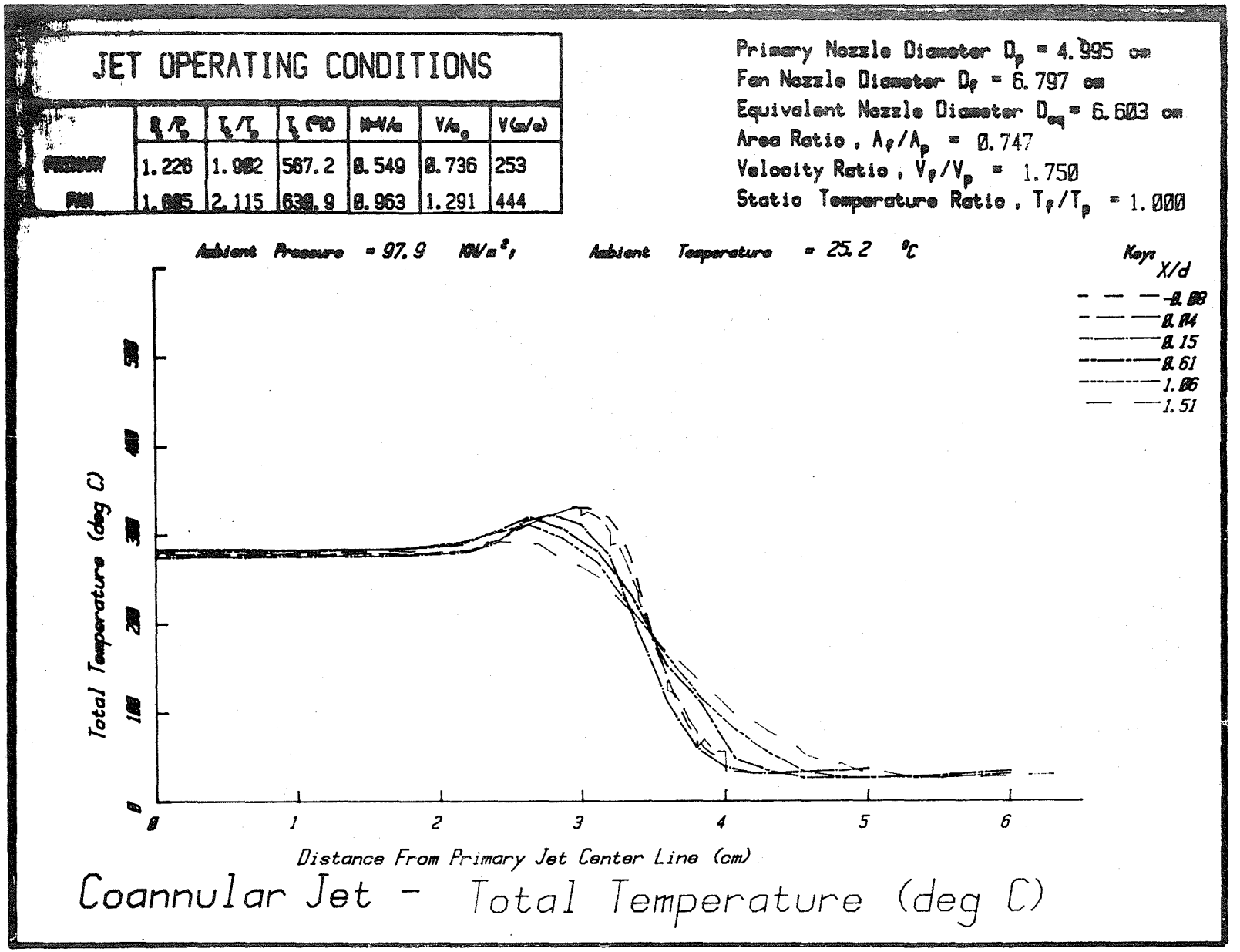

Figure A3.15(a)

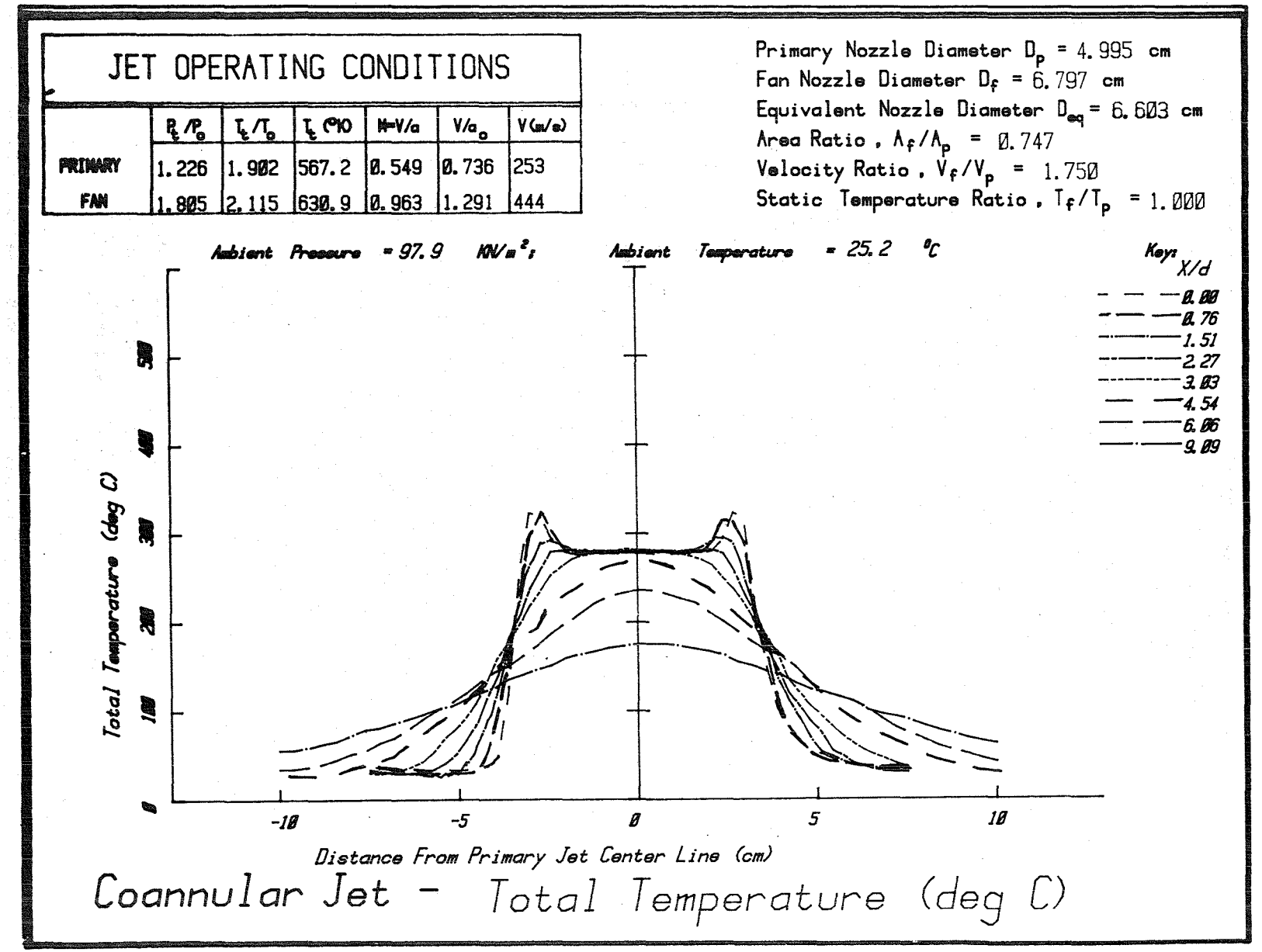

	P_t/P_o	T_t/T_o	T_t (°K)	M=V/a	V/a_o	V(m/s)
PRIMARY	1.226	1.902	567.2	0.549	0.736	253
FAN	1.805	2.115	630.9	0.963	1.291	444

Figure A3.15(b)

JET OPERATING CONDITIONS

	P_t/P_o	T_t/T_o	T_t (°K)	M=V/a	V/a_o	V(m/s)
PRIMARY	1.226	1.902	567.2	0.549	0.736	253
FAN	1.805	2.115	630.9	0.963	1.291	444

Primary Nozzle Diameter D_p = 4.995 cm
Fan Nozzle Diameter D_f = 6.797 cm
Equivalent Nozzle Diameter D_{eq} = 6.603 cm
Area Ratio , A_f/A_p = 0.747
Velocity Ratio , V_f/V_p = 1.750
Static Temperature Ratio , T_f/T_p = 1.000

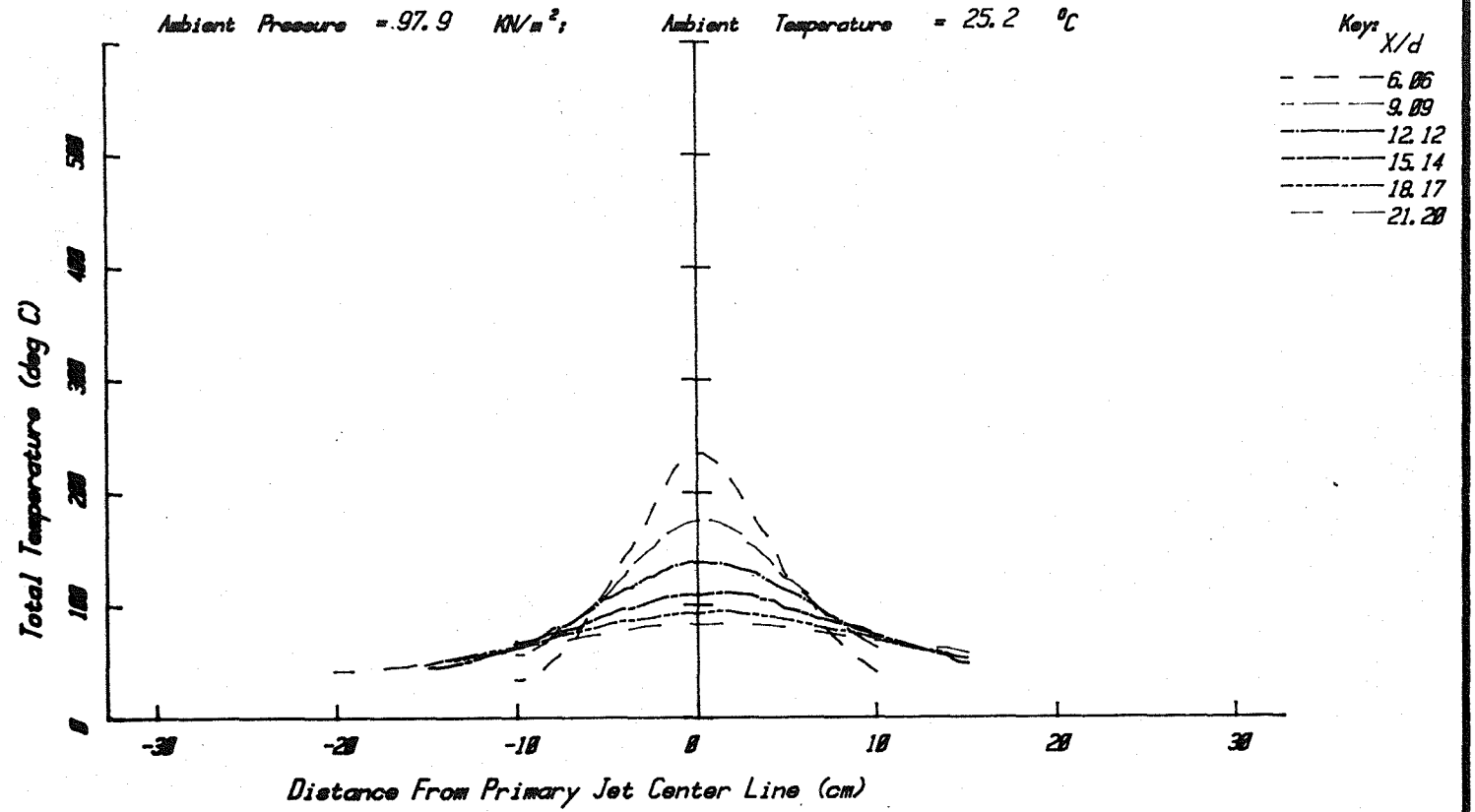

Coannular Jet - Total Temperature (deg C)

Figure A3.15(c)

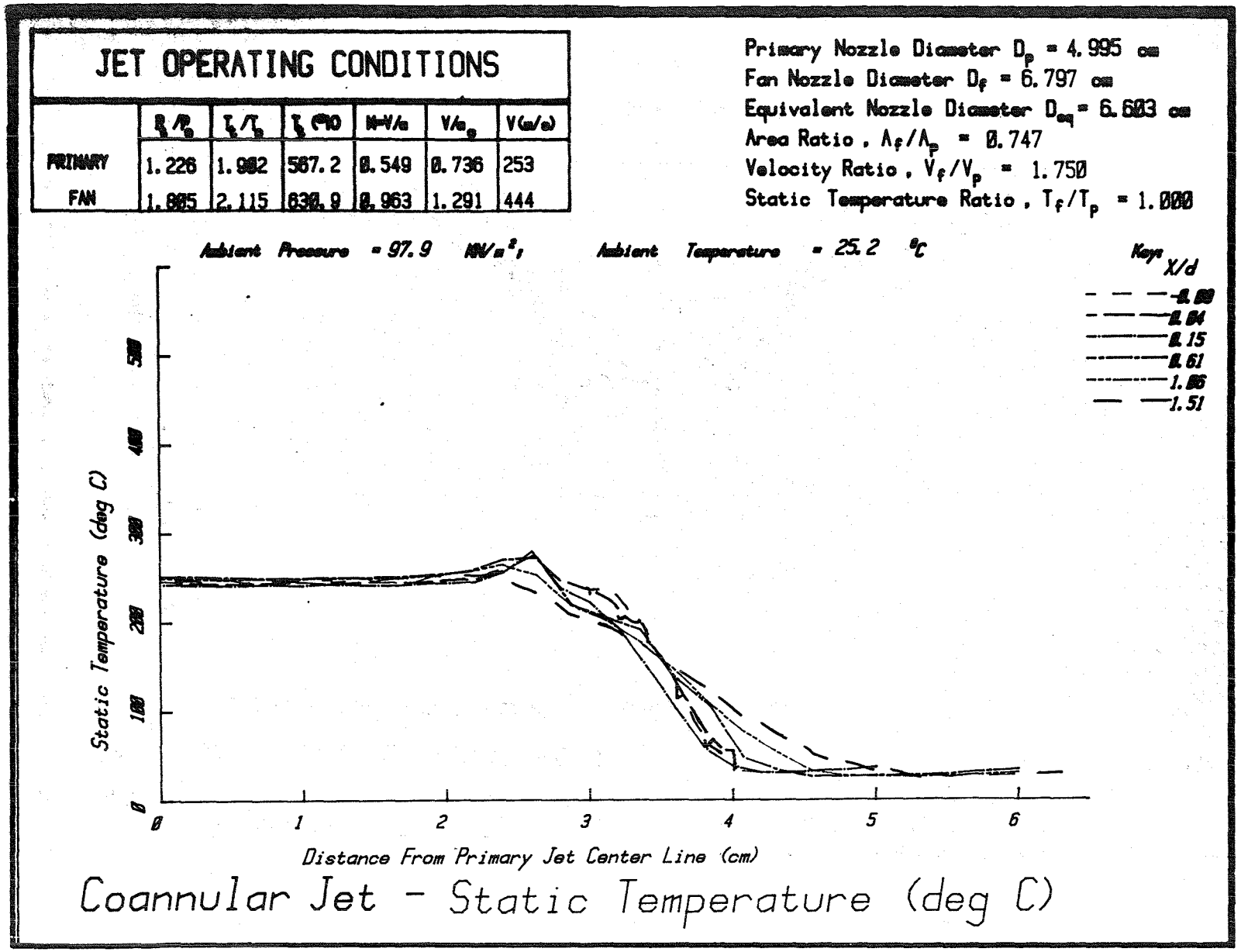

Figure A3.16(a)

JET OPERATING CONDITIONS

	P_t/P_o	T_t/T_o	T_t (°K)	M=V/a	V/a_o	V(m/s)
PRIMARY	1.226	1.902	567.2	0.549	0.736	253
FAN	1.805	2.115	630.9	0.963	1.291	444

Primary Nozzle Diameter D_p = 4.995 cm
Fan Nozzle Diameter D_f = 6.797 cm
Equivalent Nozzle Diameter D_{eq} = 6.603 cm
Area Ratio , A_f/A_p = 0.747
Velocity Ratio , V_f/V_p = 1.750
Static Temperature Ratio , T_f/T_p = 1.000

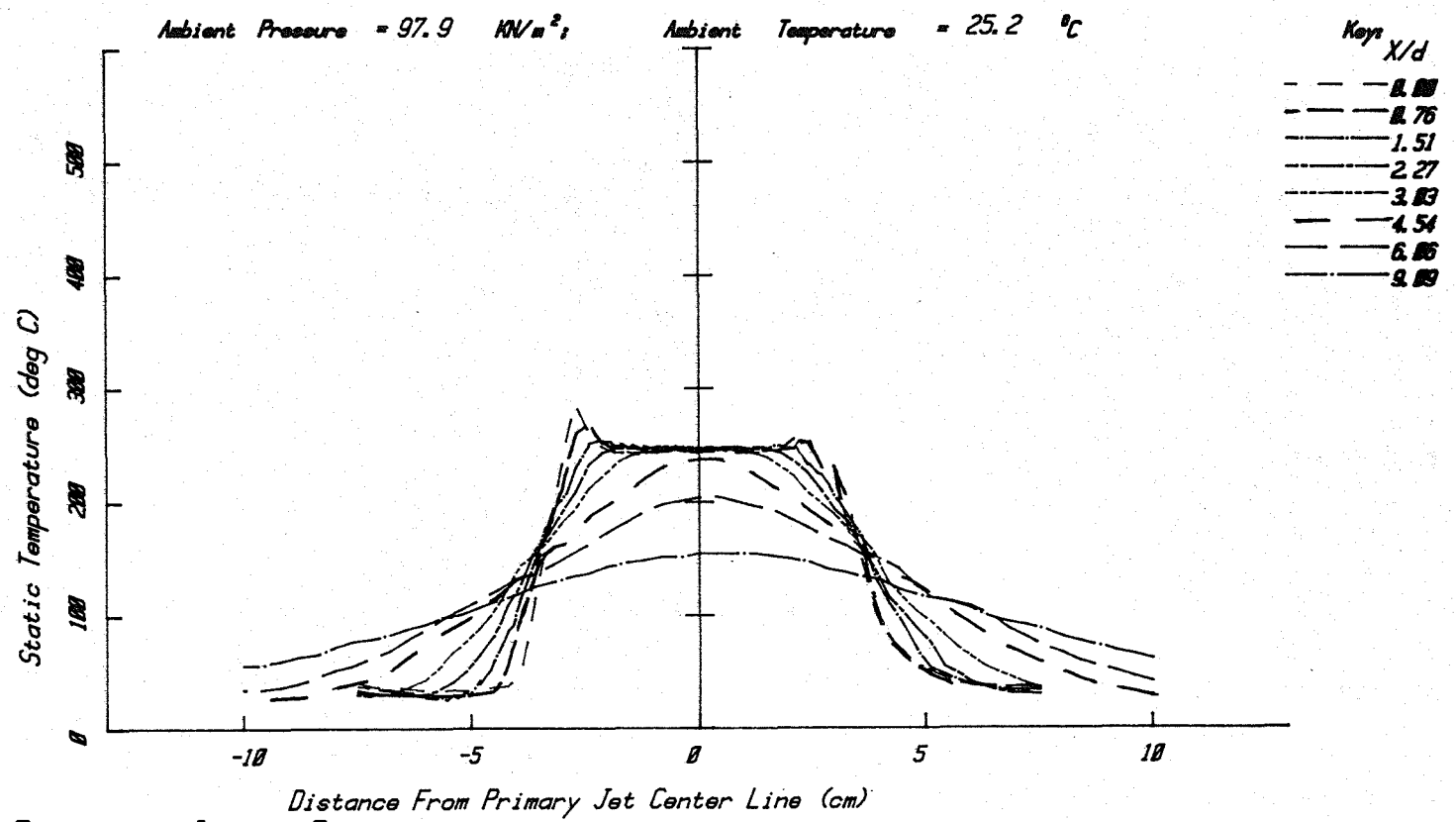

Coannular Jet - Static Temperature (deg C)

Figure A3.16(b)

JET OPERATING CONDITIONS

	P_t/P_o	T_t/T_o	T_t (°K)	M=V/a	V/a_o	V(m/s)
PRIMARY	1.226	1.902	567.2	0.549	0.736	253
FAN	1.805	2.115	630.9	0.963	1.291	444

Primary Nozzle Diameter D_p = 4.995 cm
Fan Nozzle Diameter D_f = 6.797 cm
Equivalent Nozzle Diameter D_{eq} = 6.603 cm
Area Ratio , A_f/A_p = 0.747
Velocity Ratio , V_f/V_p = 1.750
Static Temperature Ratio , T_f/T_p = 1.000

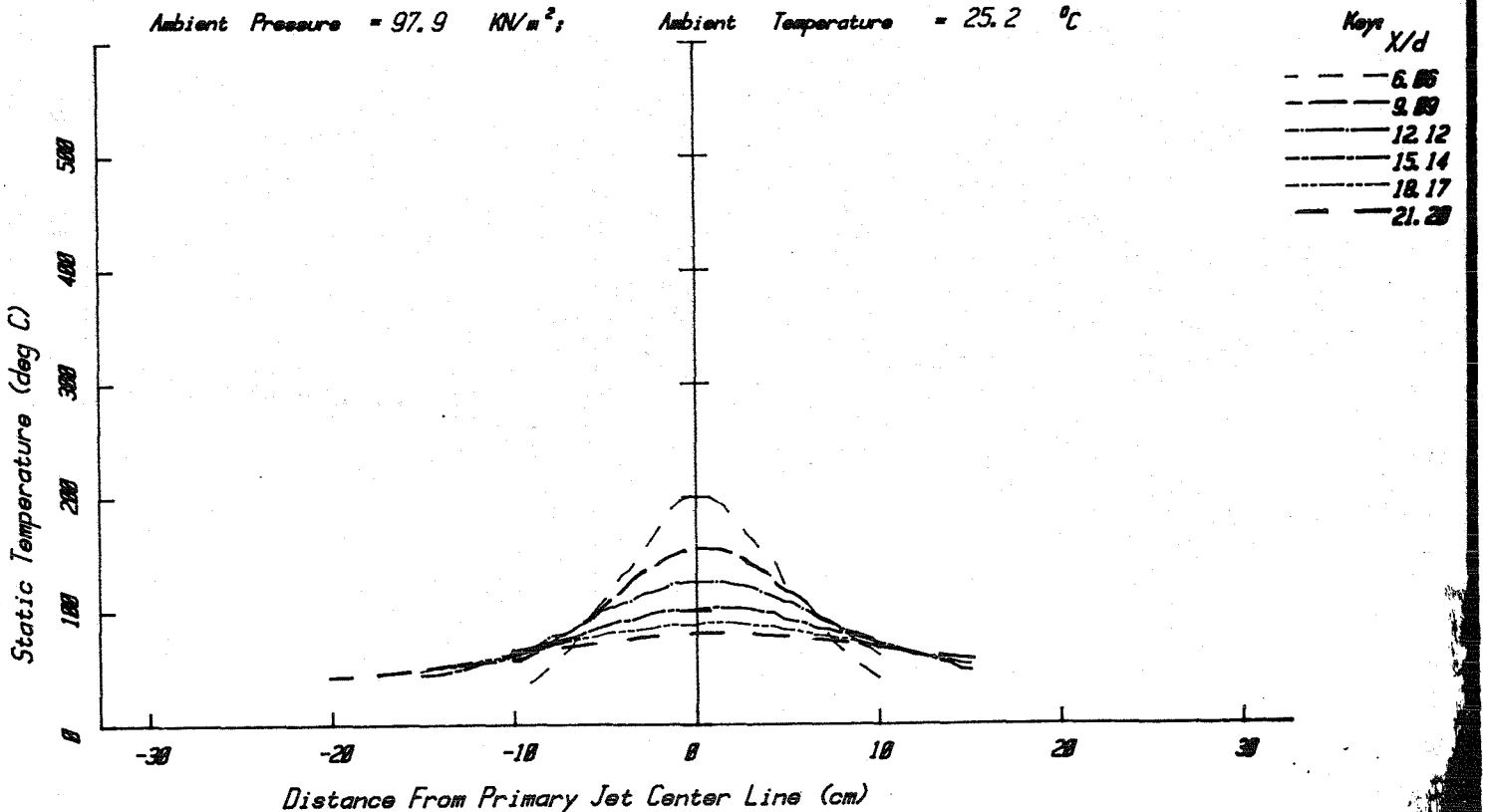

Coannular Jet - Static Temperature (deg C)

Figure A3.16(c)

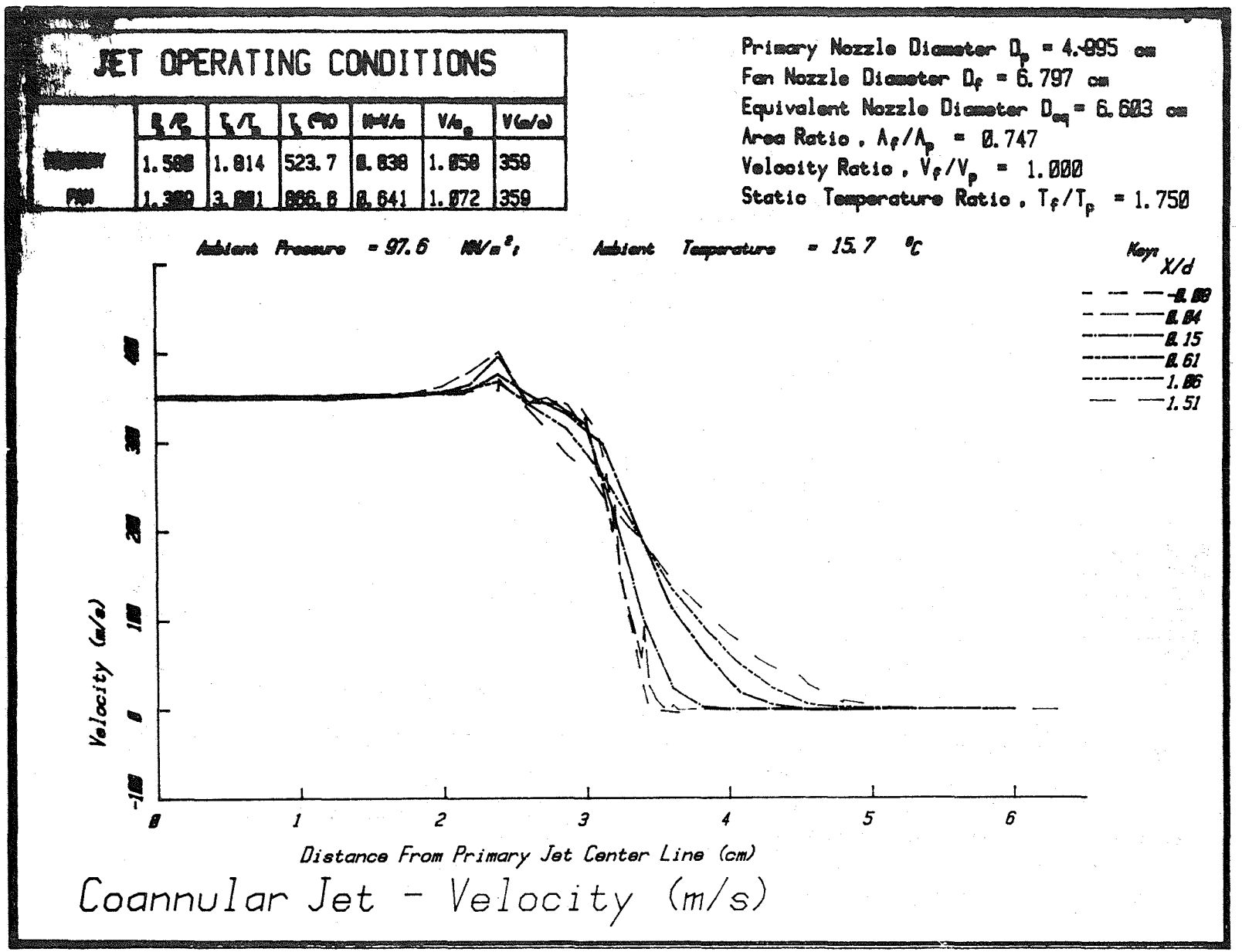

Figure A3.17(a)

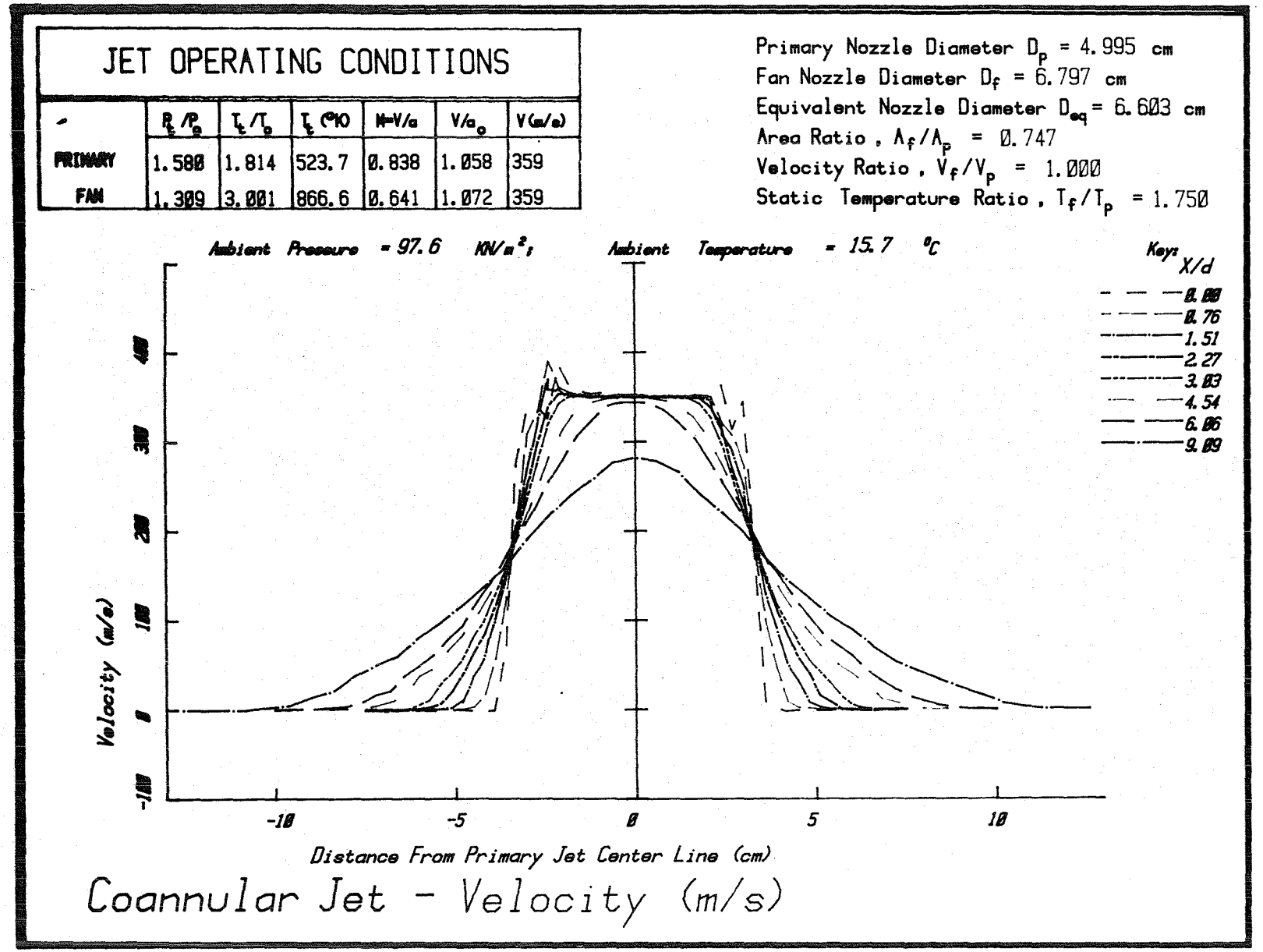

Figure A3.17(b)

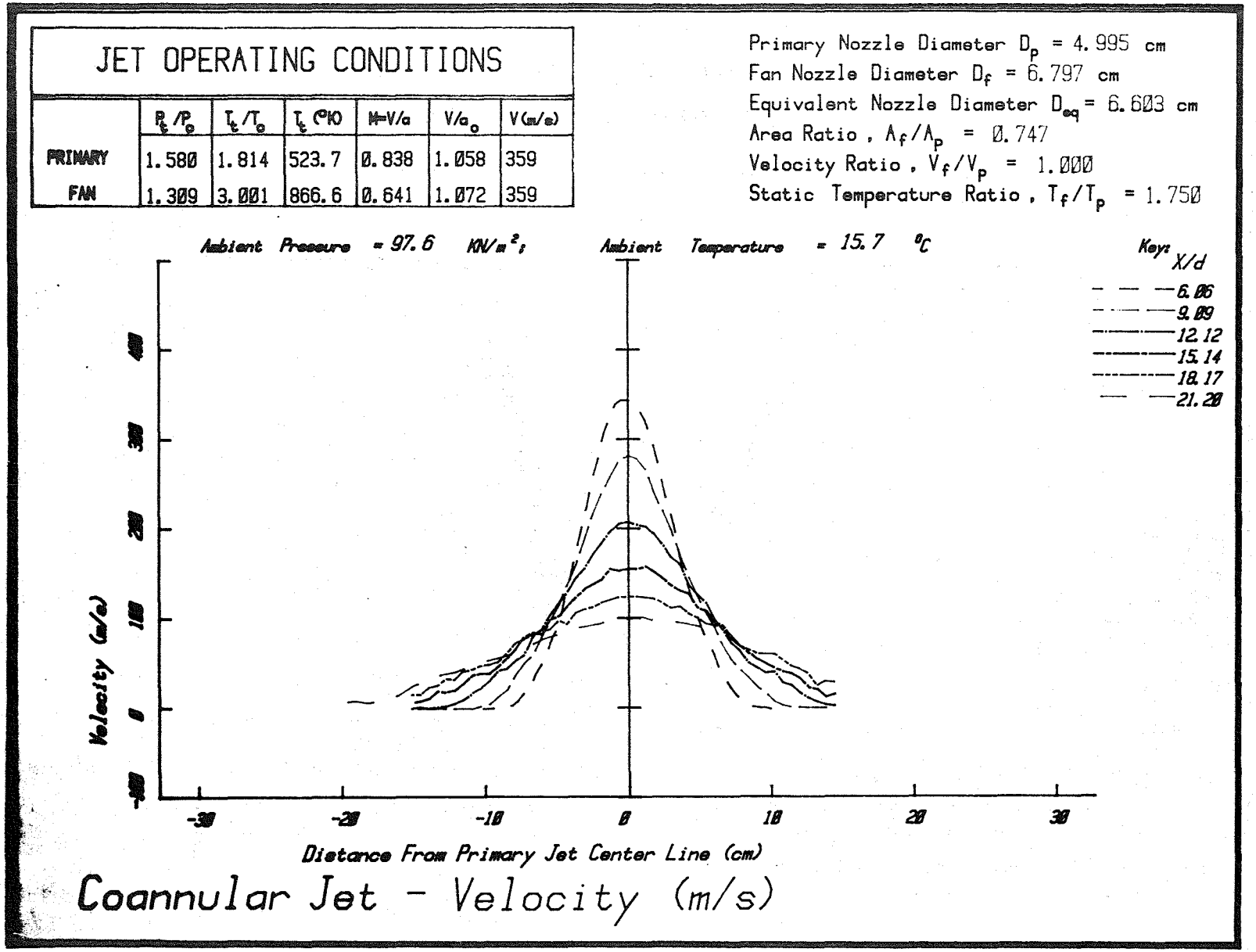

Figure A3.17(c)

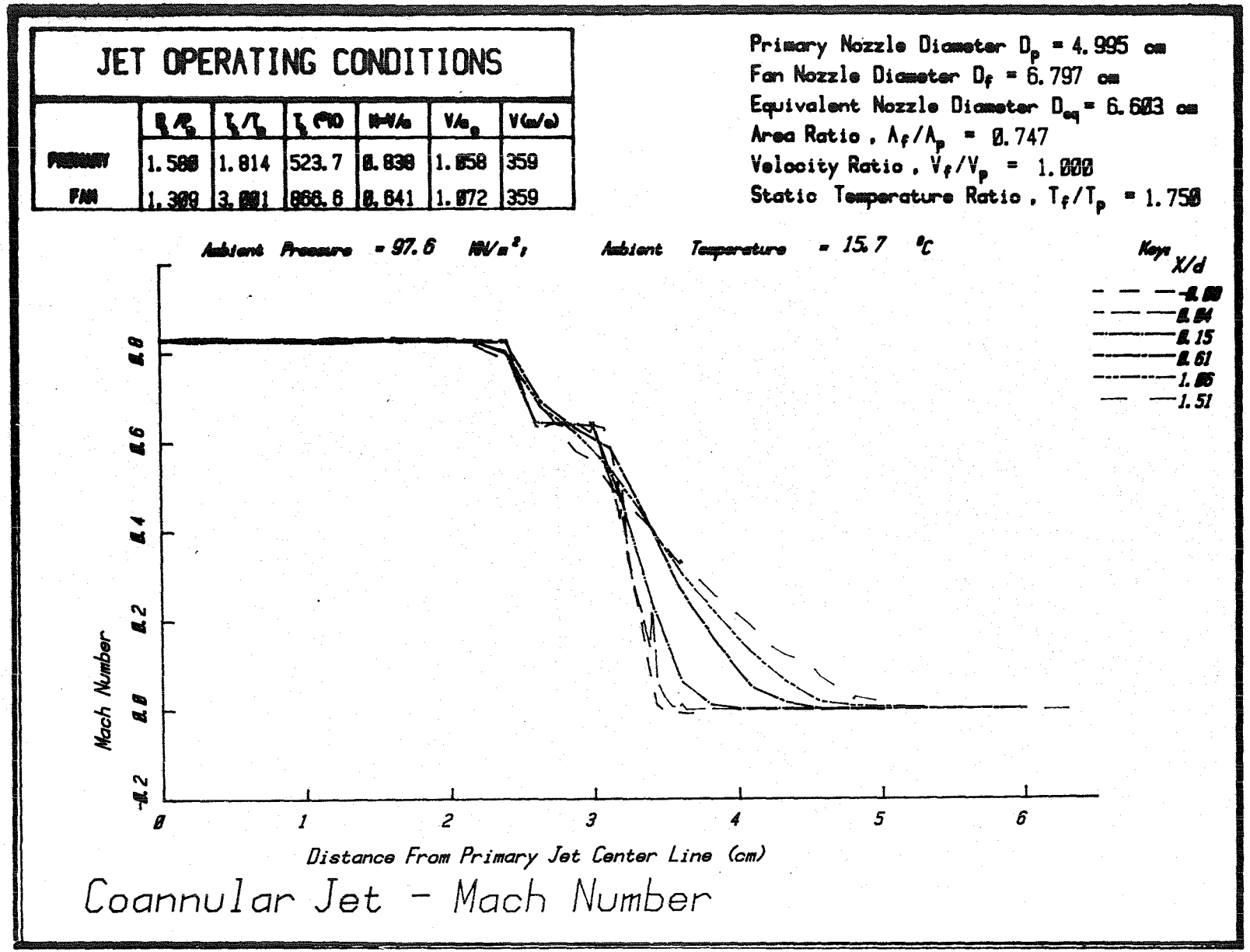

Figure A3.18(a)

JET OPERATING CONDITIONS

	P_t/P_o	T_t/T_o	T_t (°K)	M=V/a	V/a_o	V(m/s)
PRIMARY	1.580	1.814	523.7	0.838	1.058	359
FAN	1.309	3.001	866.6	0.641	1.072	359

Primary Nozzle Diameter D_p = 4.995 cm
Fan Nozzle Diameter D_f = 6.797 cm
Equivalent Nozzle Diameter D_{eq} = 6.603 cm
Area Ratio , A_f/A_p = 0.747
Velocity Ratio , V_f/V_p = 1.000
Static Temperature Ratio , T_f/T_p = 1.750

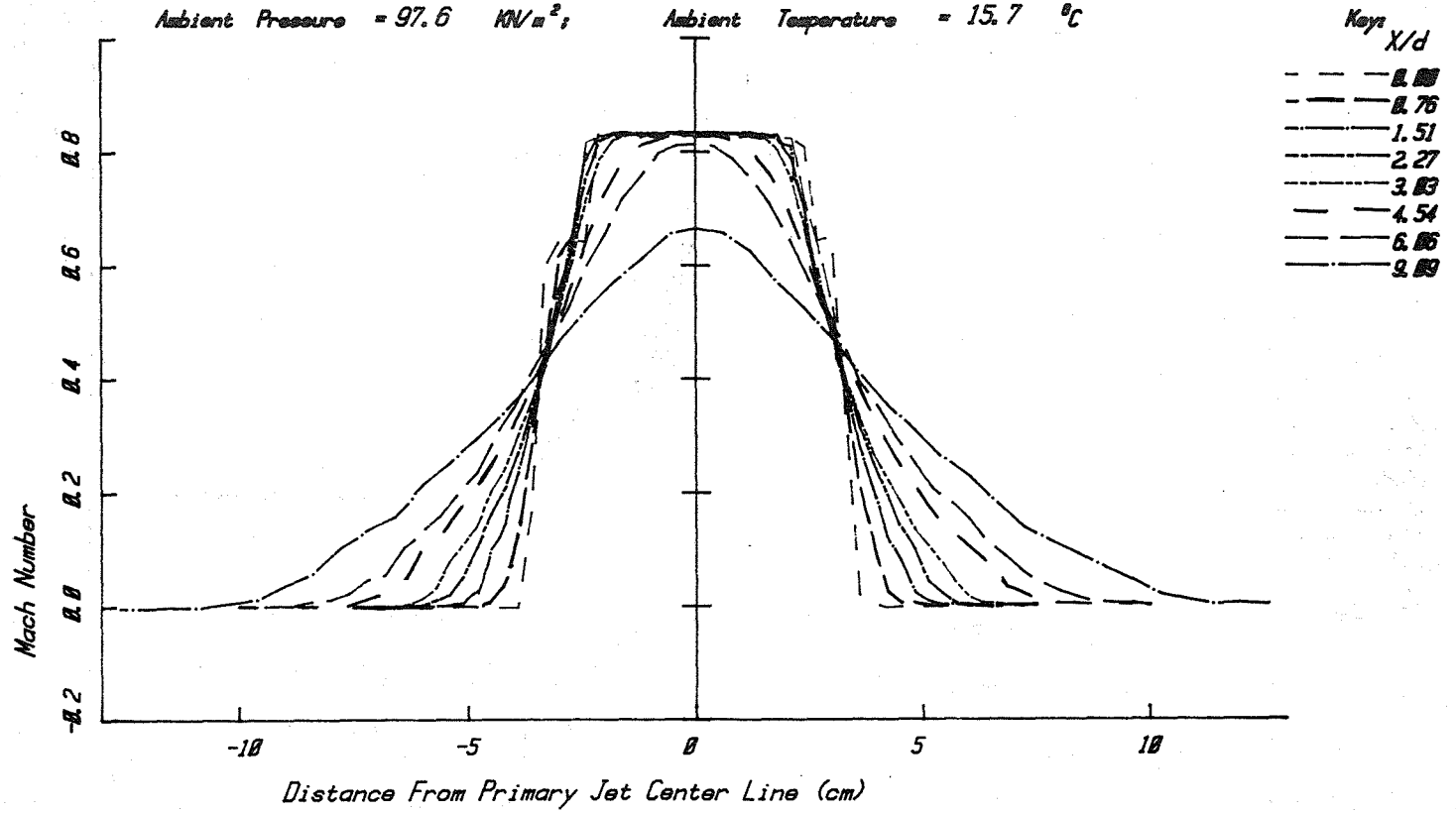

Coannular Jet - Mach Number

Figure A3.18(b)

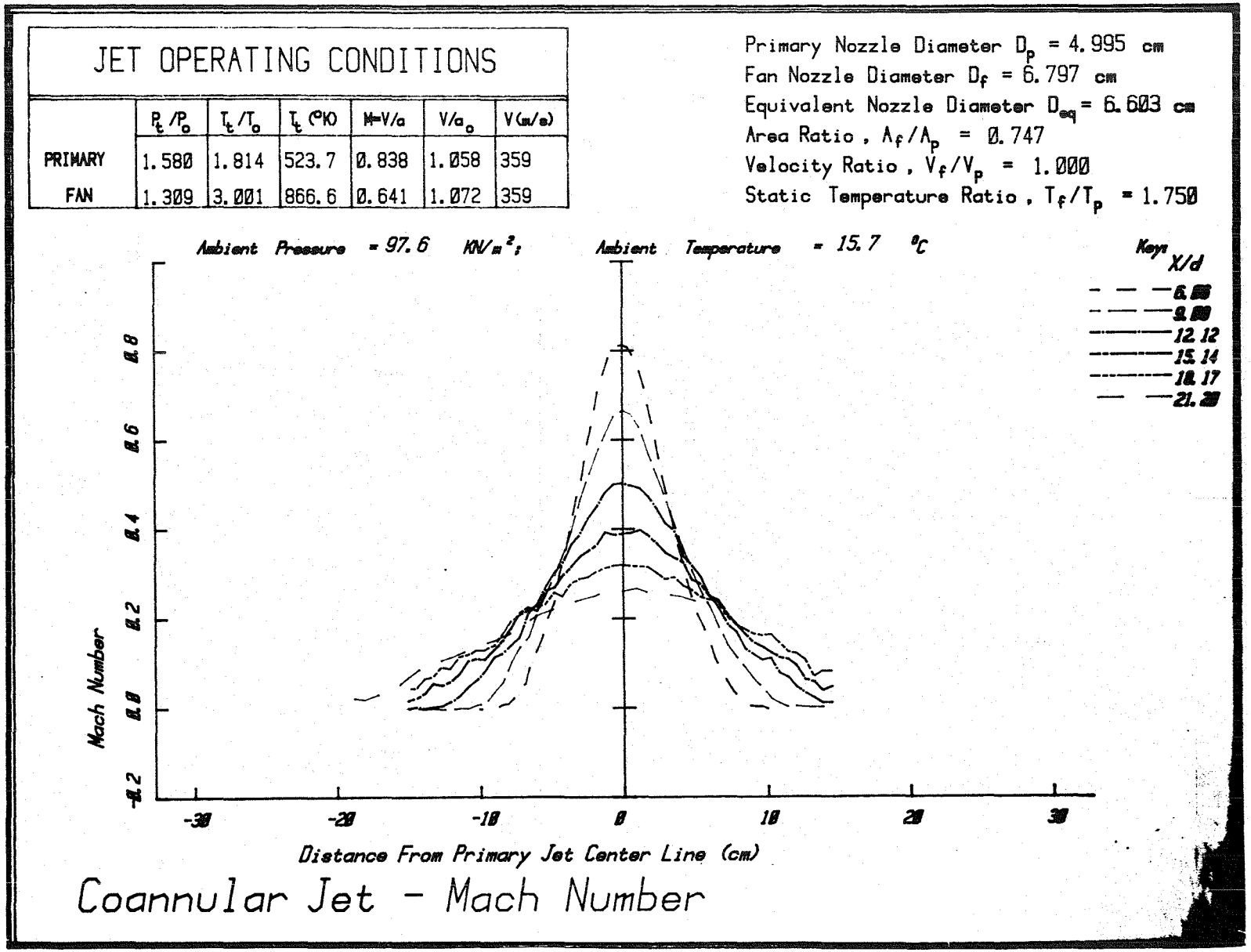

	P_t/P_o	T_t/T_o	T_t (°K)	M=V/a	V/a_o	V(m/s)
PRIMARY	1.580	1.814	523.7	0.838	1.058	359
FAN	1.309	3.001	866.6	0.641	1.072	359

Figure A3.18(c)

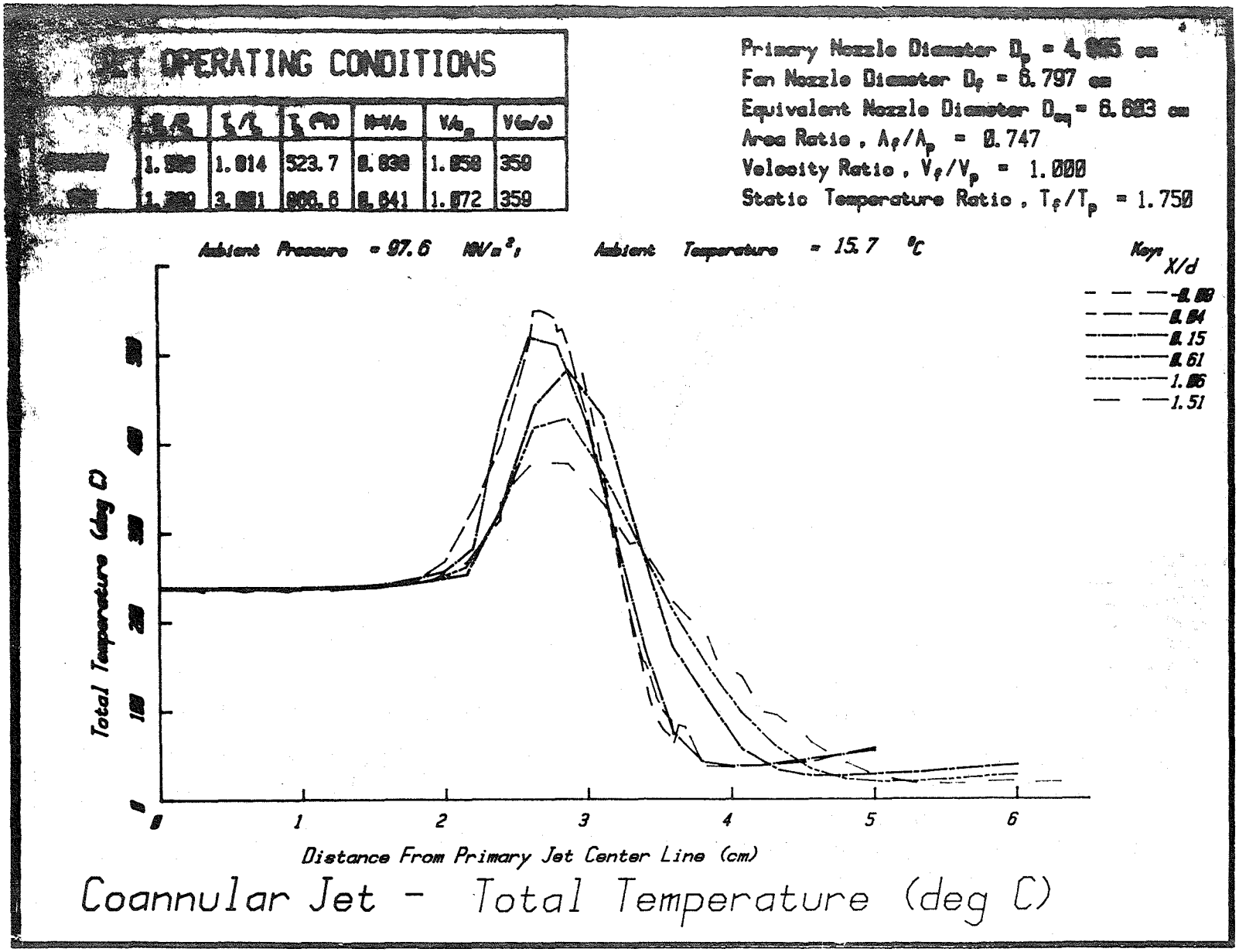

Figure A3.19(a)

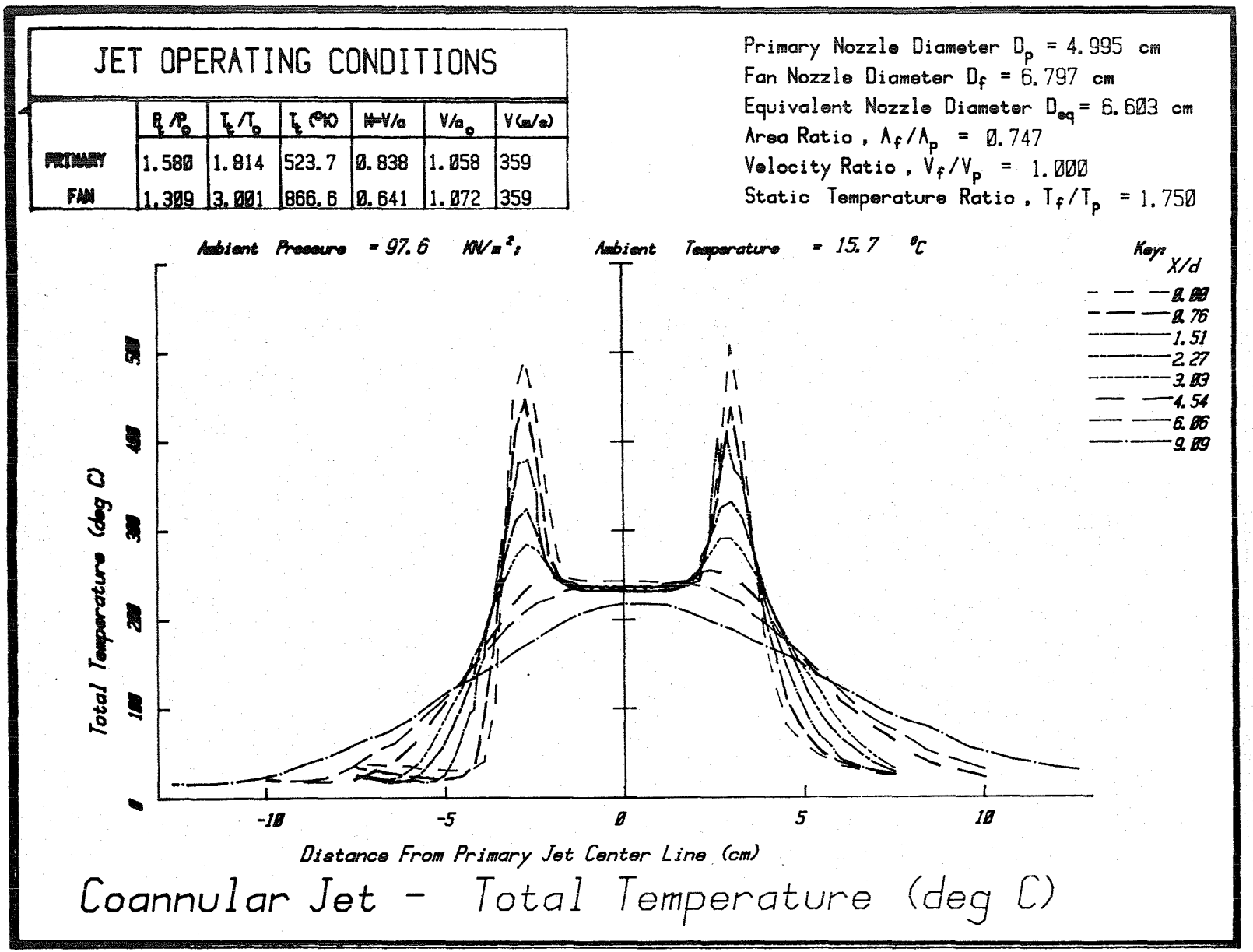

	P_t/P_0	T_t/T_0	T_t (°K)	M=V/a	V/a_0	V(m/s)
PRIMARY	1.580	1.814	523.7	0.838	1.058	359
FAN	1.309	3.001	866.6	0.641	1.072	359

Figure A3.19(b)

JET OPERATING CONDITIONS

	P_t/P_o	T_t/T_o	T_t °K	M=V/a	V/a_o	V (m/s)
PRIMARY	1.580	1.814	523.7	0.838	1.058	359
FAN	1.309	3.001	866.6	0.641	1.072	359

Primary Nozzle Diameter D_p = 4.995 cm
Fan Nozzle Diameter D_f = 6.797 cm
Equivalent Nozzle Diameter D_{eq} = 6.603 cm
Area Ratio , A_f/A_p = 0.747
Velocity Ratio , V_f/V_p = 1.000
Static Temperature Ratio , T_f/T_p = 1.750

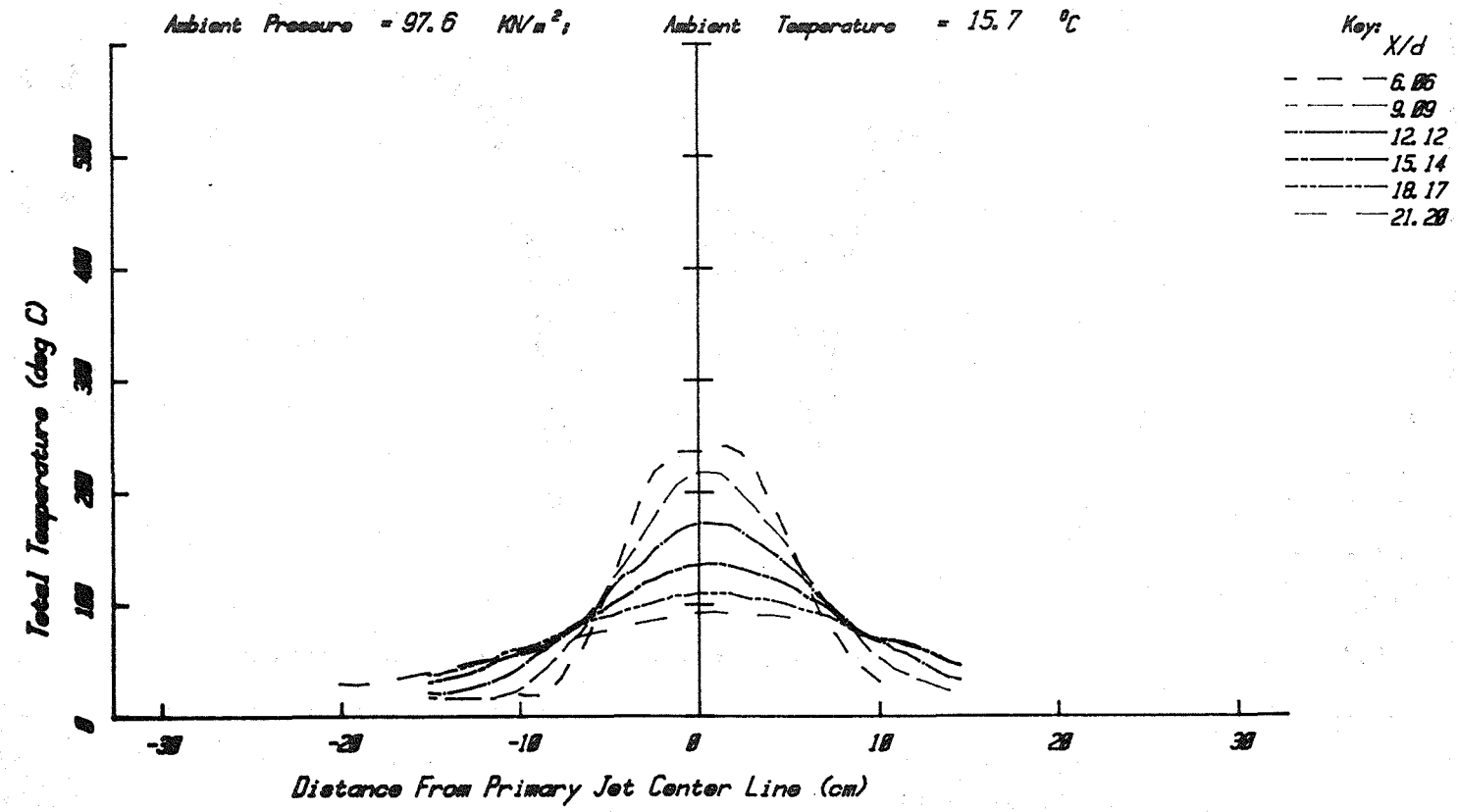

Coannular Jet - Total Temperature (deg C)

Figure A3.19(c)

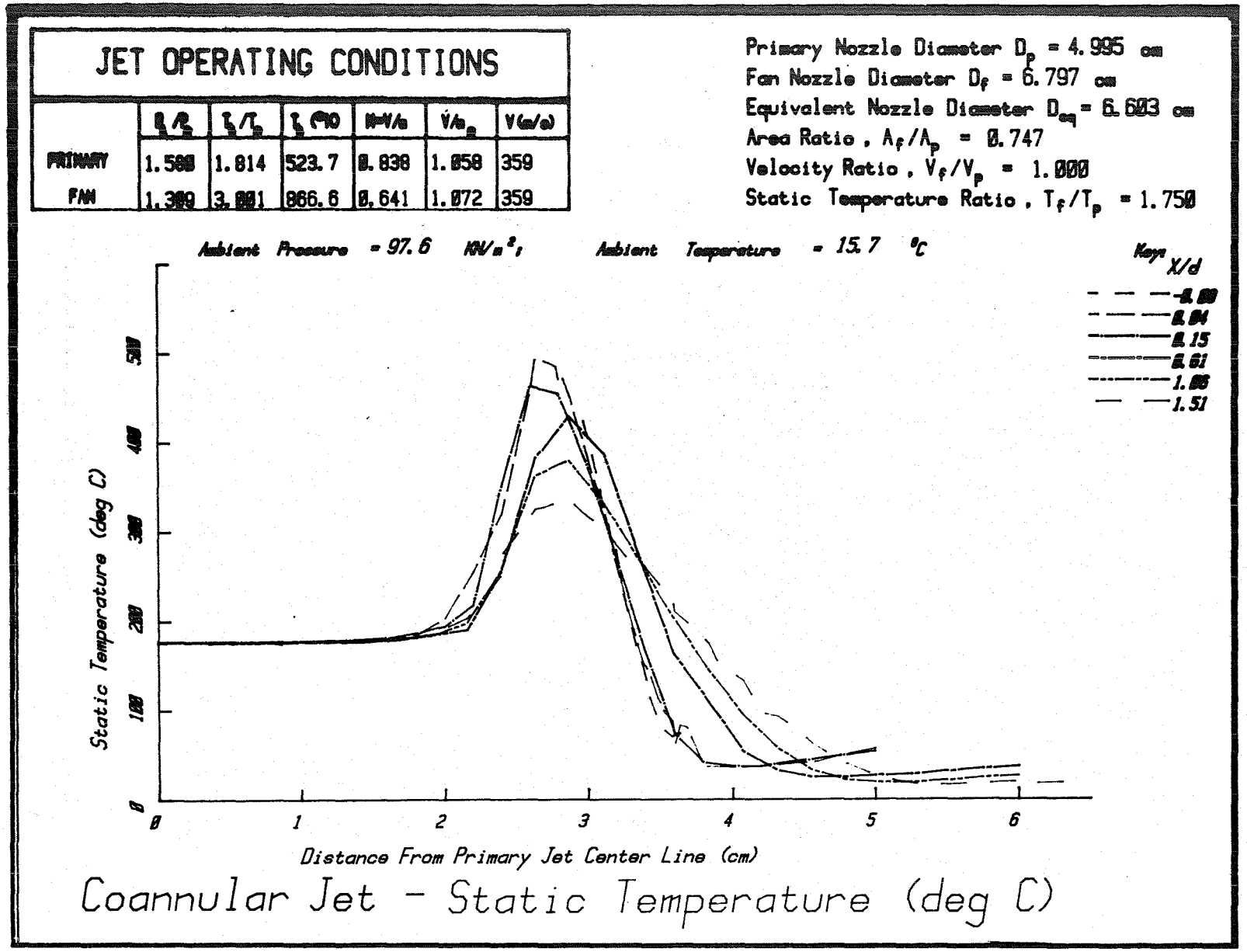

Figure A3.20(a)

JET OPERATING CONDITIONS

	P_t/P_o	T_t/T_o	T_t (°K)	M=V/a	V/a_o	V (m/s)
PRIMARY	1.580	1.814	523.7	0.838	1.058	359
FAN	1.309	3.001	866.6	0.641	1.072	359

Primary Nozzle Diameter D_p = 4.995 cm
Fan Nozzle Diameter D_f = 6.797 cm
Equivalent Nozzle Diameter D_{eq} = 6.603 cm
Area Ratio , A_f/A_p = 0.747
Velocity Ratio , V_f/V_p = 1.000
Static Temperature Ratio , T_f/T_p = 1.750

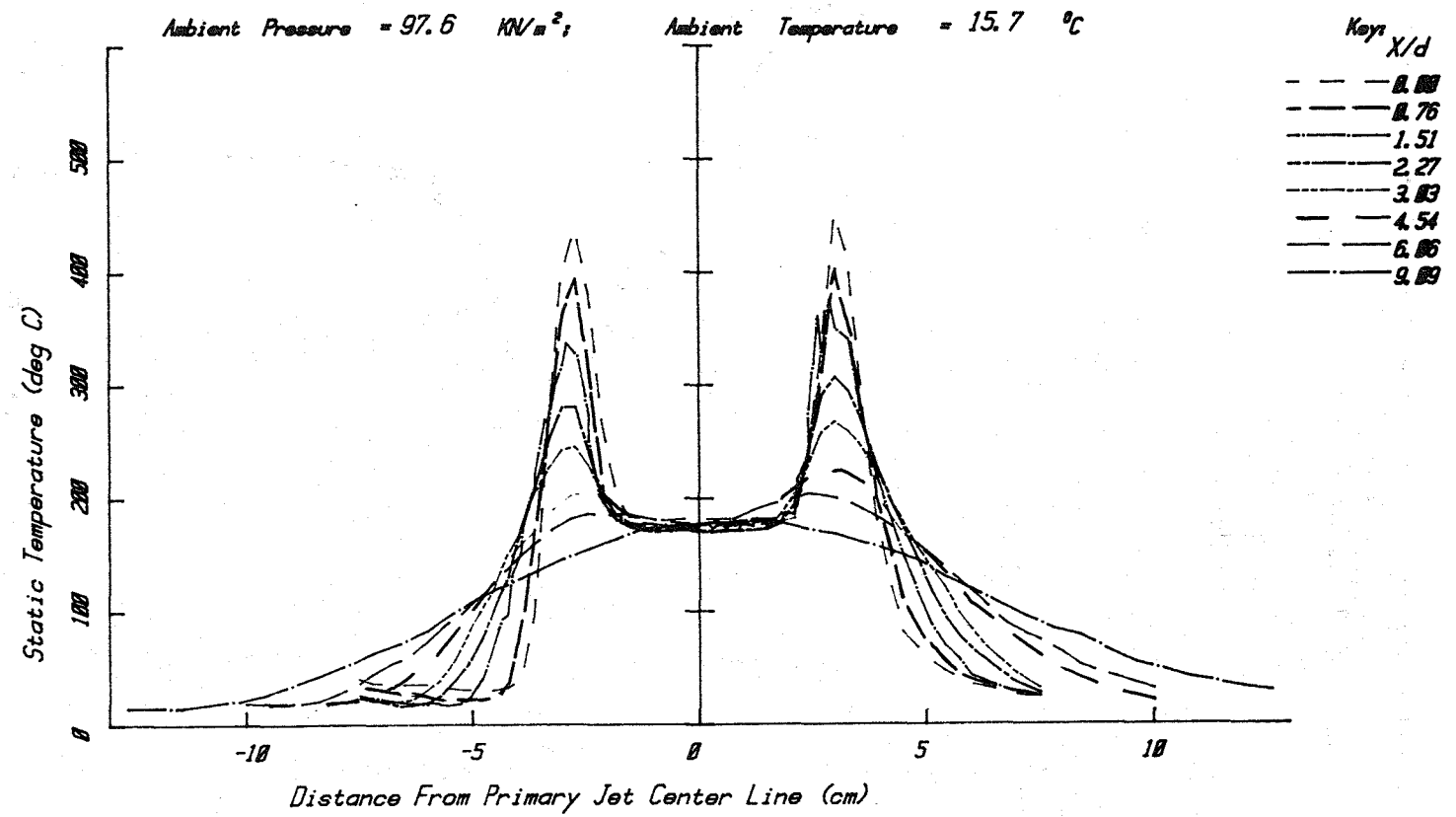

Coannular Jet - Static Temperature (deg C)

Figure A3.20(b)

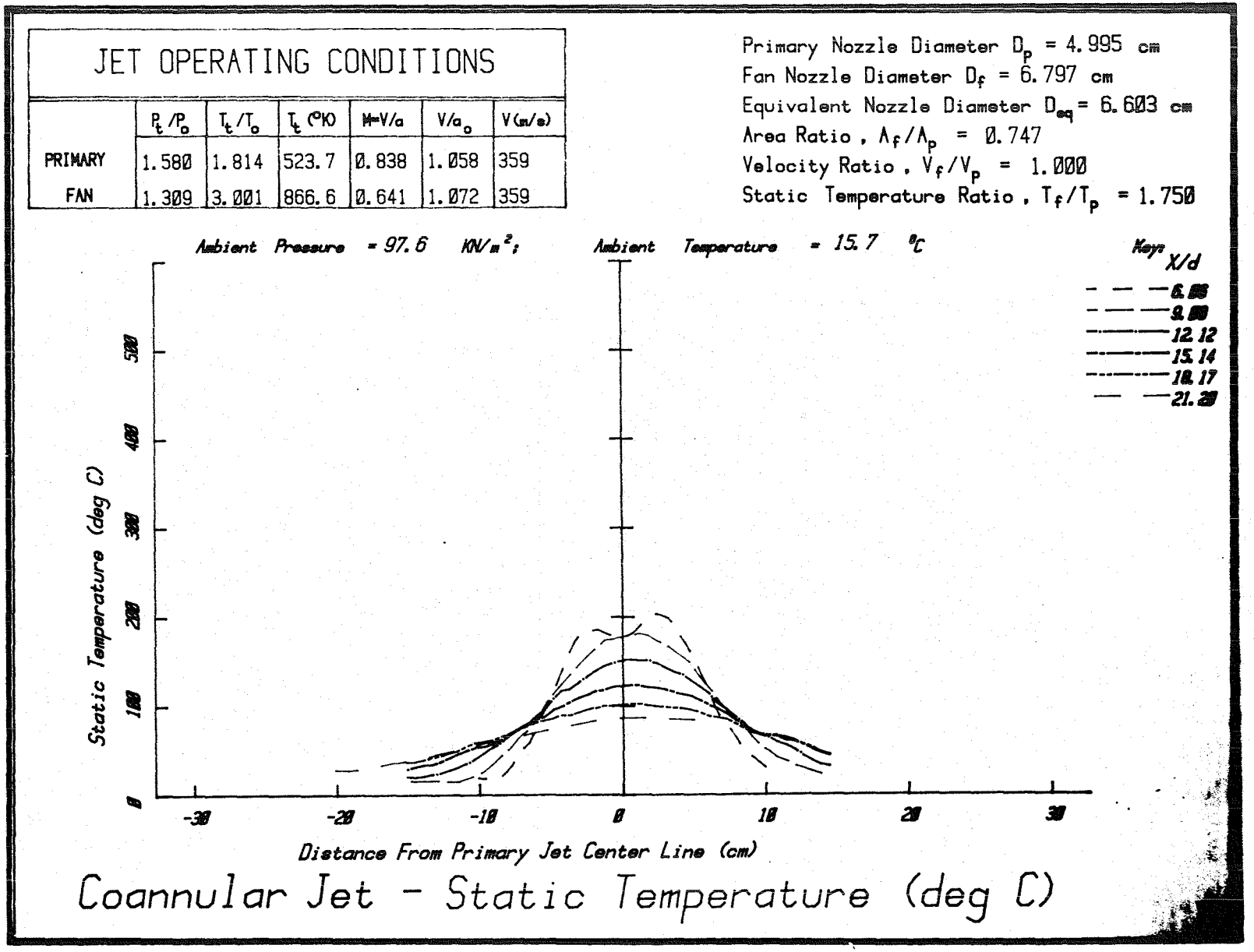

	P_t/P_o	T_t/T_o	T_t (°K)	M=V/a	V/a_o	V(m/s)
PRIMARY	1.580	1.814	523.7	0.838	1.058	359
FAN	1.309	3.001	866.6	0.641	1.072	359

Figure A3.20(c)

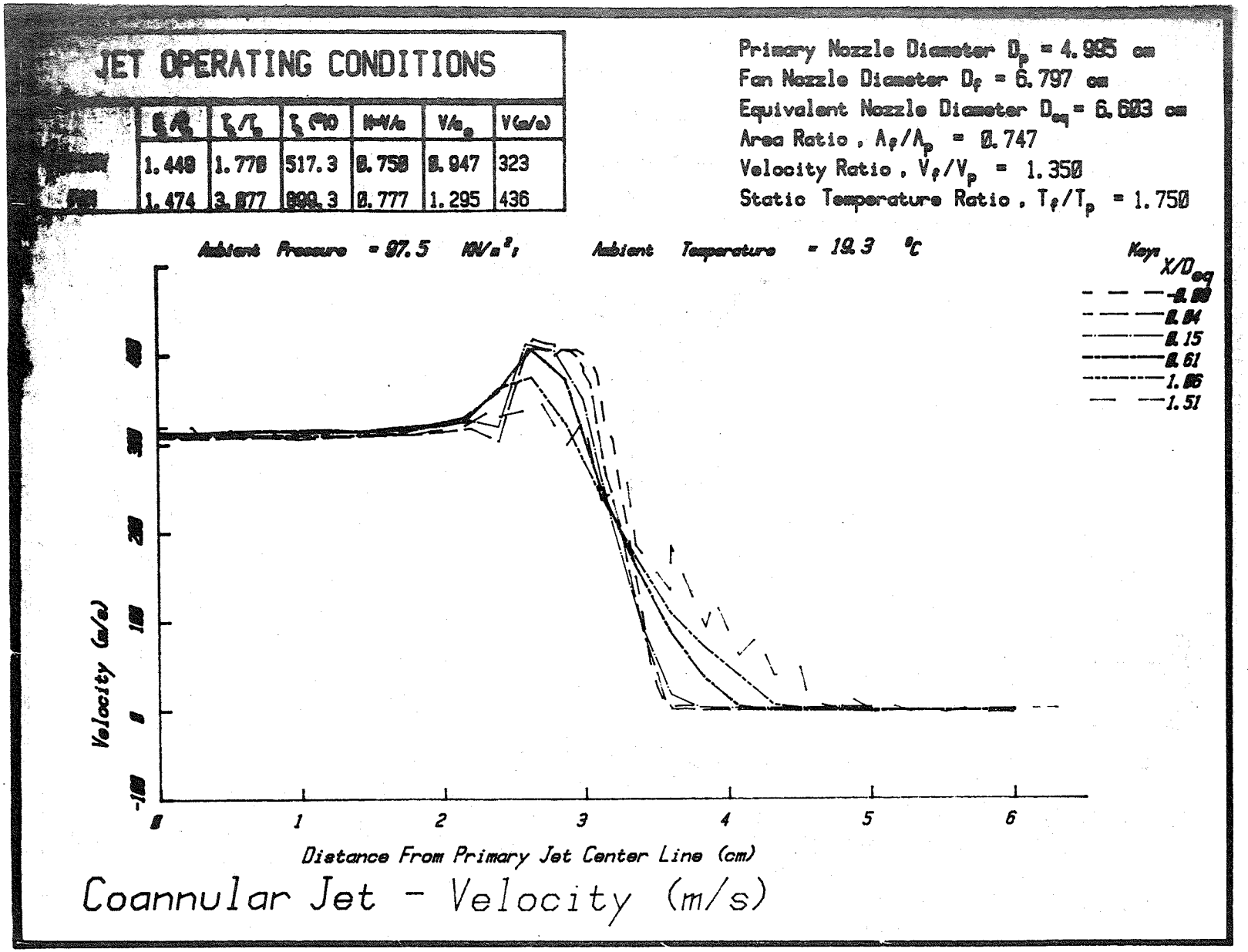

Figure A3.21(a)

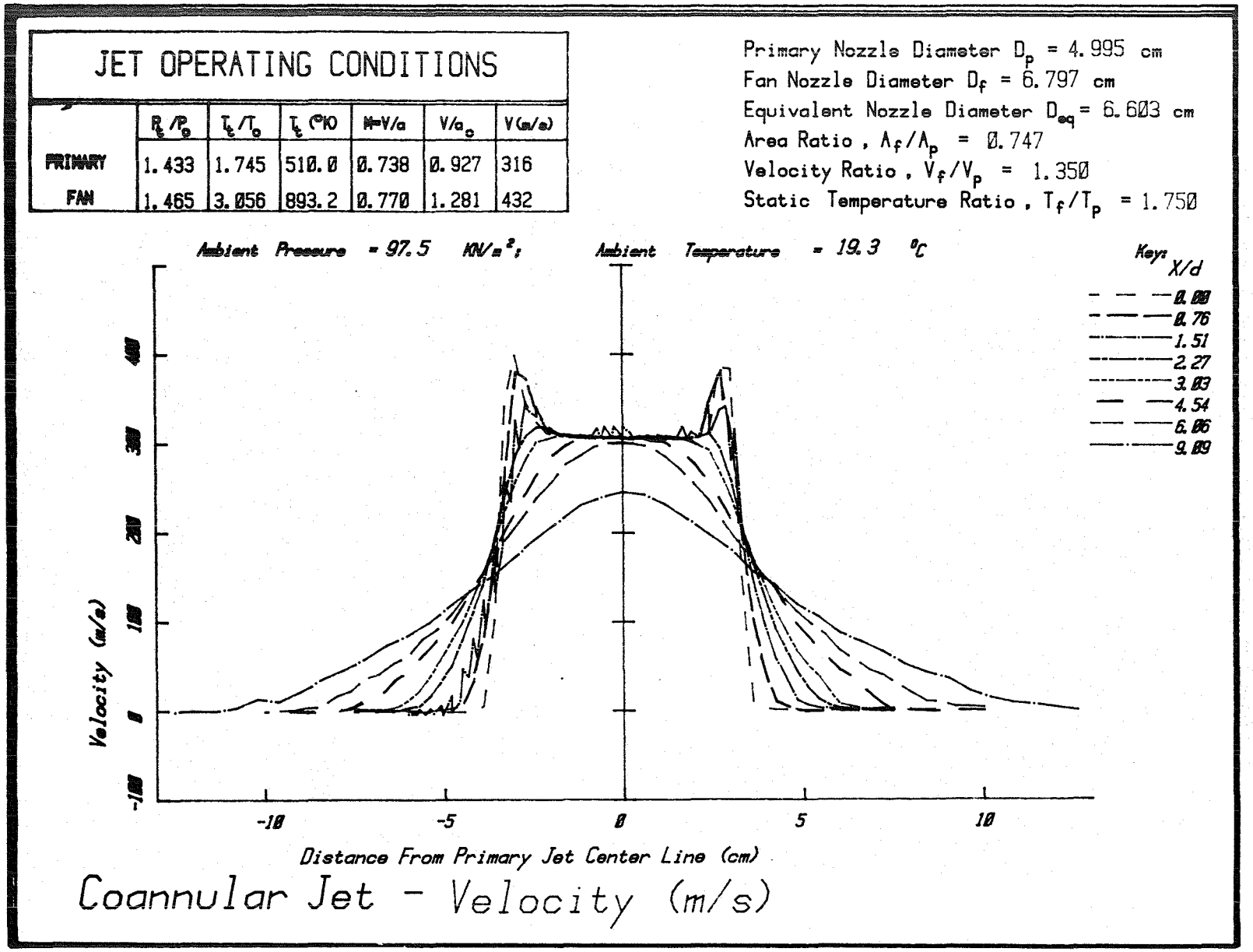

Figure A3.21(b)

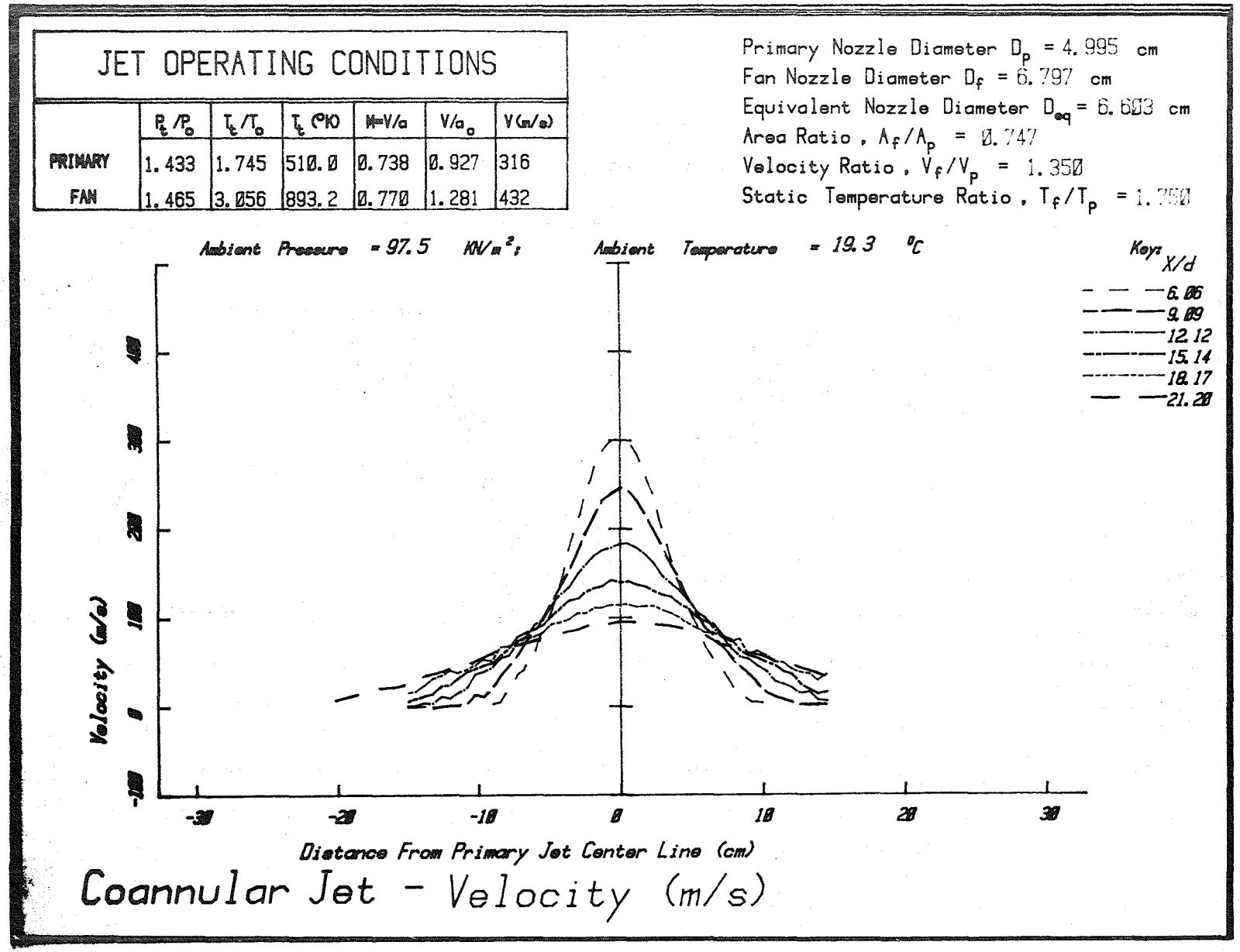

	P_t/P_o	T_t/T_o	T_t (°K)	M=V/a	V/a_o	V (m/s)
PRIMARY	1.433	1.745	510.0	0.738	0.927	316
FAN	1.465	3.056	893.2	0.770	1.281	432

Figure A3.21(c)

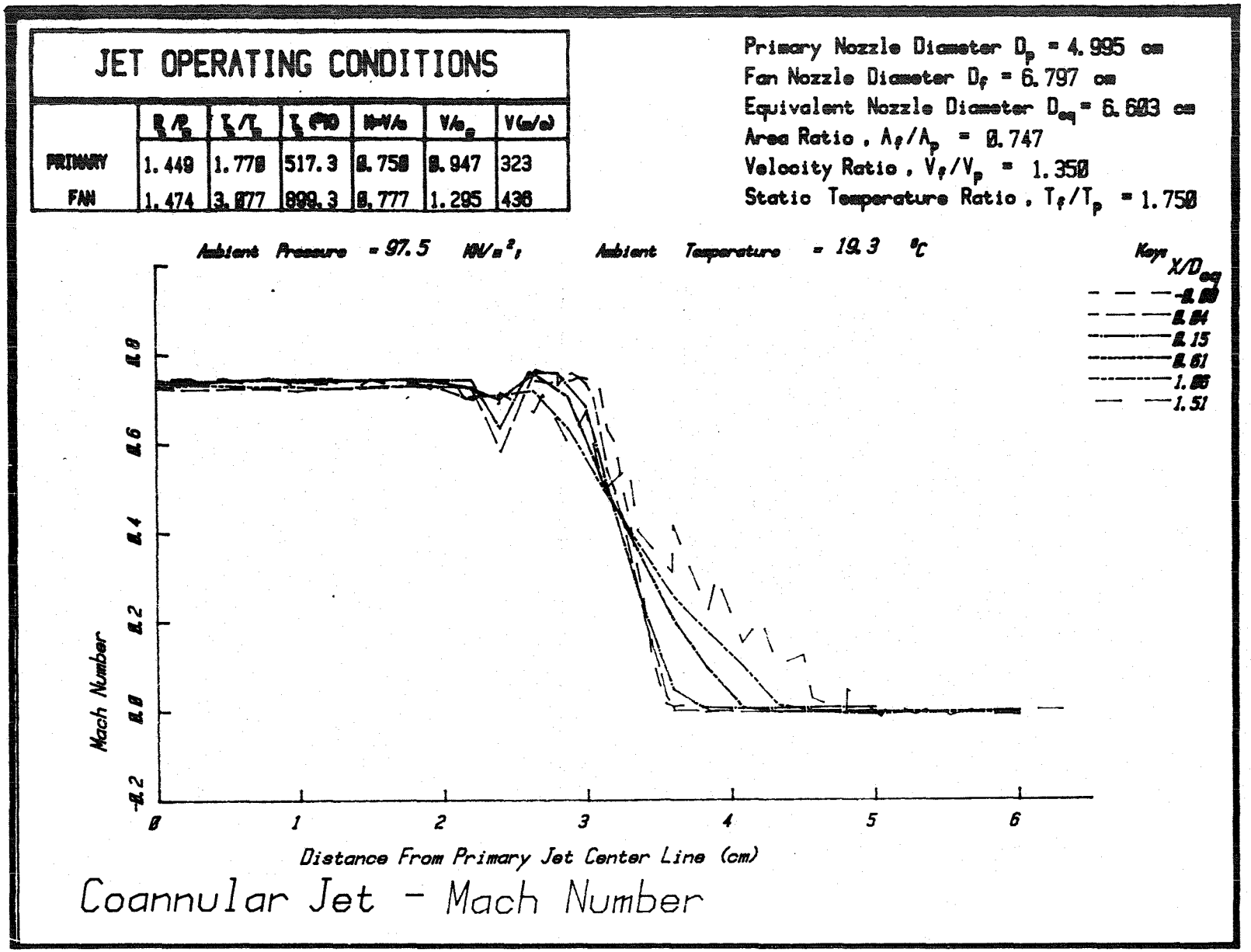

Figure A3.22(a)

JET OPERATING CONDITIONS

	P_t/P_o	T_t/T_o	T_t (°K)	M=V/a	V/a_o	V(m/s)
PRIMARY	1.433	1.745	510.0	0.738	0.927	316
FAN	1.465	3.056	893.2	0.770	1.281	432

Primary Nozzle Diameter D_p = 4.995 cm
Fan Nozzle Diameter D_f = 6.797 cm
Equivalent Nozzle Diameter D_{eq} = 6.603 cm
Area Ratio , A_f/A_p = 0.747
Velocity Ratio , V_f/V_p = 1.350
Static Temperature Ratio , T_f/T_p = 1.750

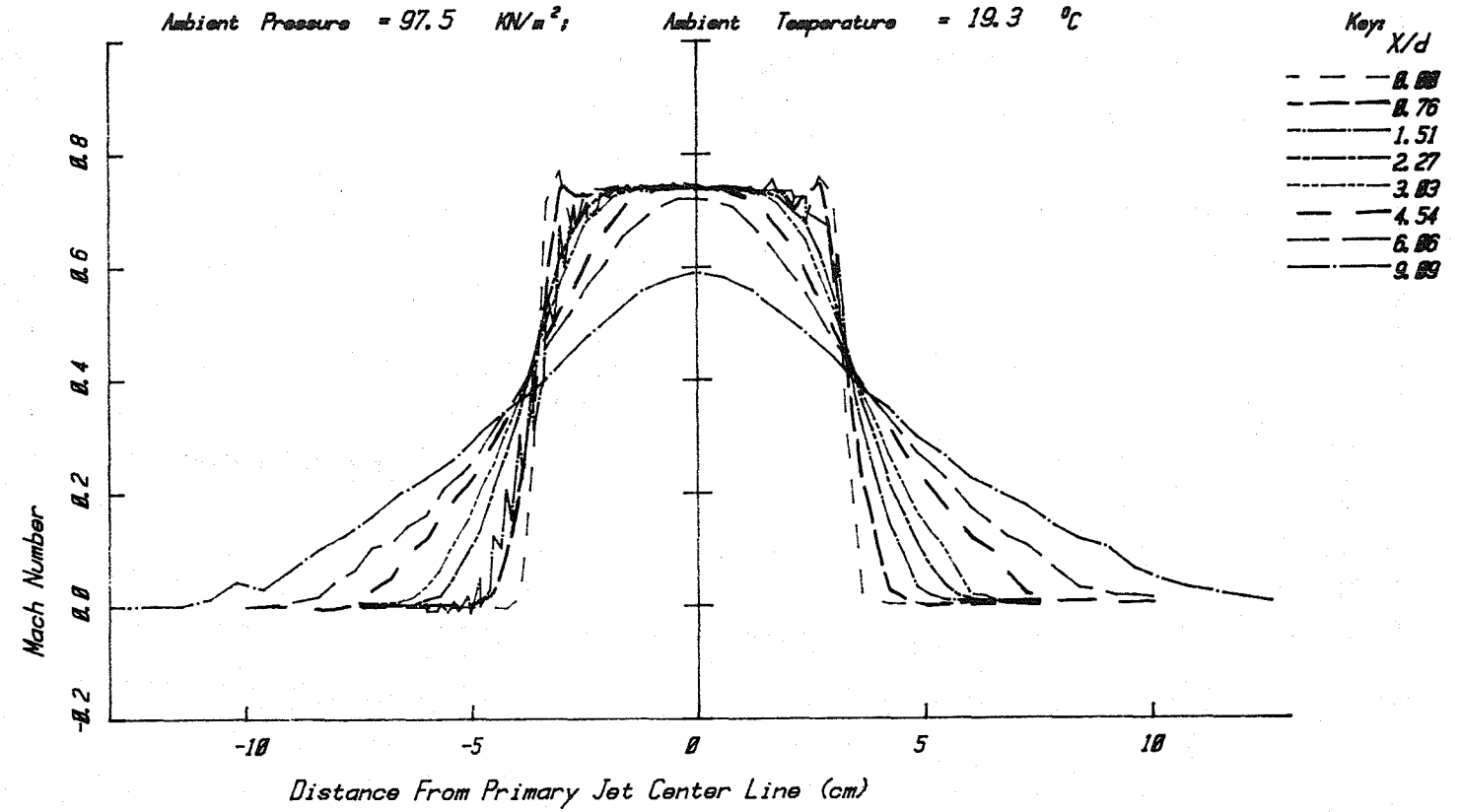

Coannular Jet - Mach Number

Figure A3.22(b)

JET OPERATING CONDITIONS

	P_t/P_o	T_t/T_o	T_t (°K)	M=V/a	V/a_o	V (m/s)
PRIMARY	1.433	1.745	510.0	0.738	0.927	316
FAN	1.465	3.056	893.2	0.770	1.281	432

Primary Nozzle Diameter D_p = 4.995 cm
Fan Nozzle Diameter D_f = 6.797 cm
Equivalent Nozzle Diameter D_{eq} = 6.603 cm
Area Ratio , A_f/A_p = 0.747
Velocity Ratio , V_f/V_p = 1.350
Static Temperature Ratio , T_f/T_p = 1.750

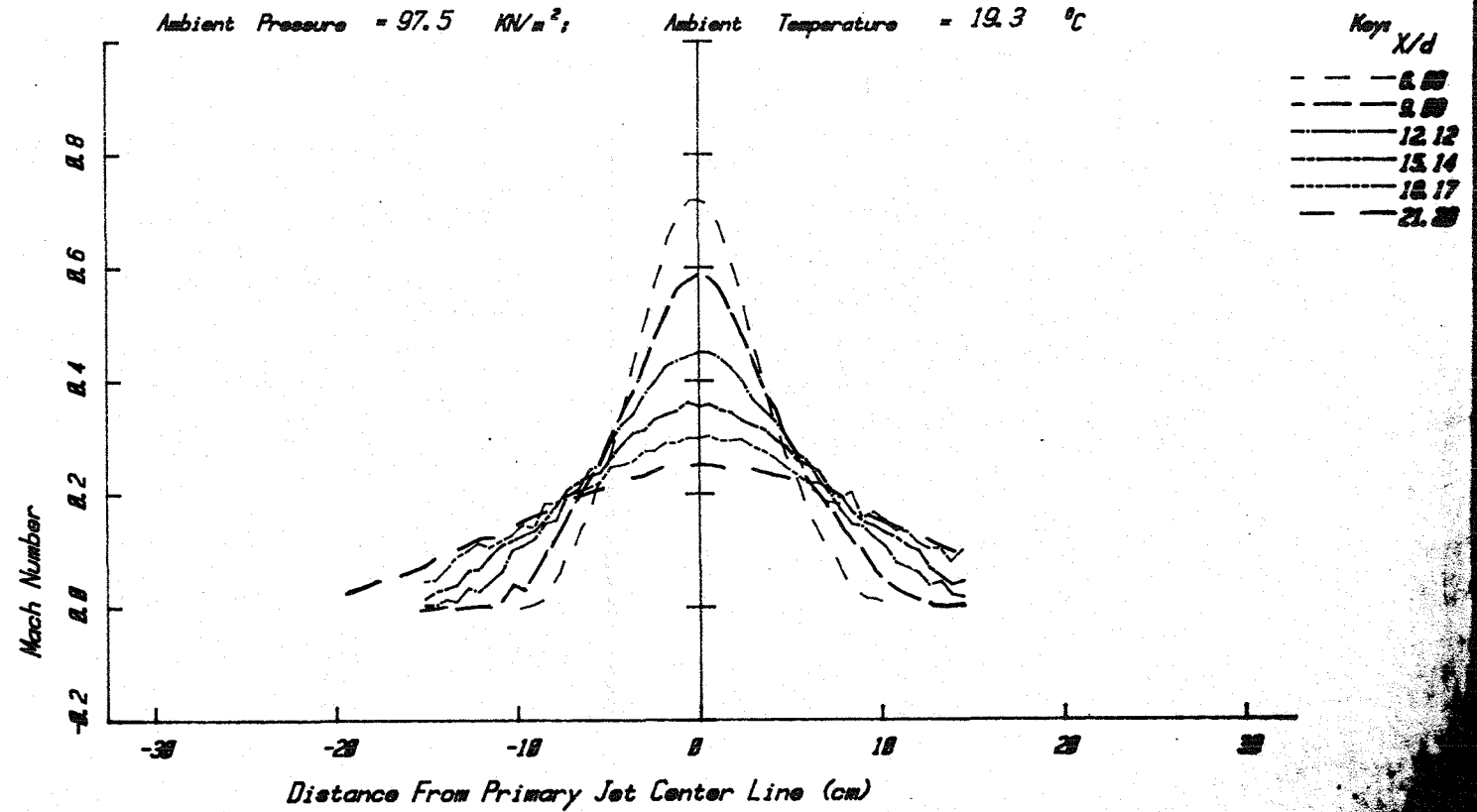

Coannular Jet - Mach Number

Figure A3.22(c)

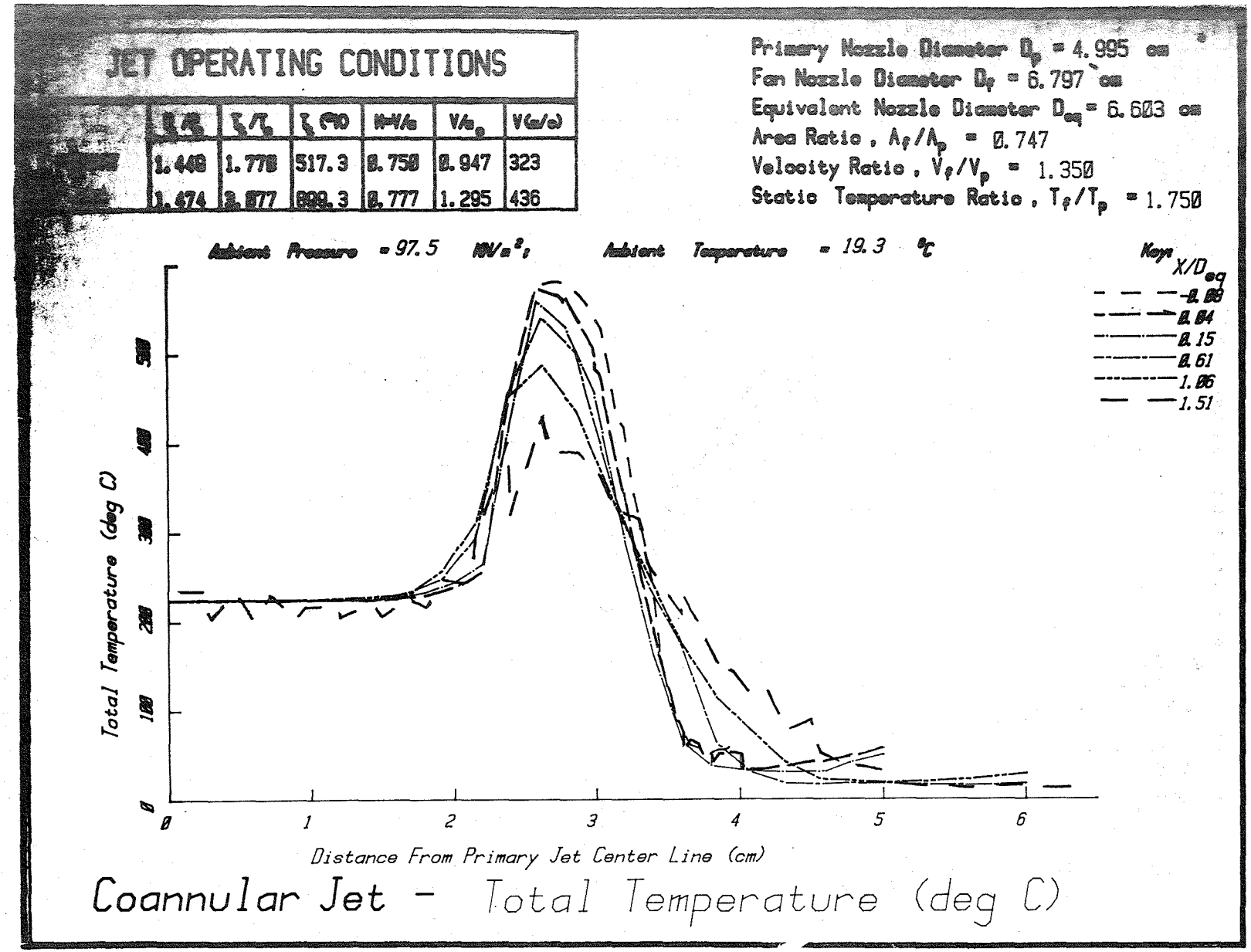

Figure A3.23(a)

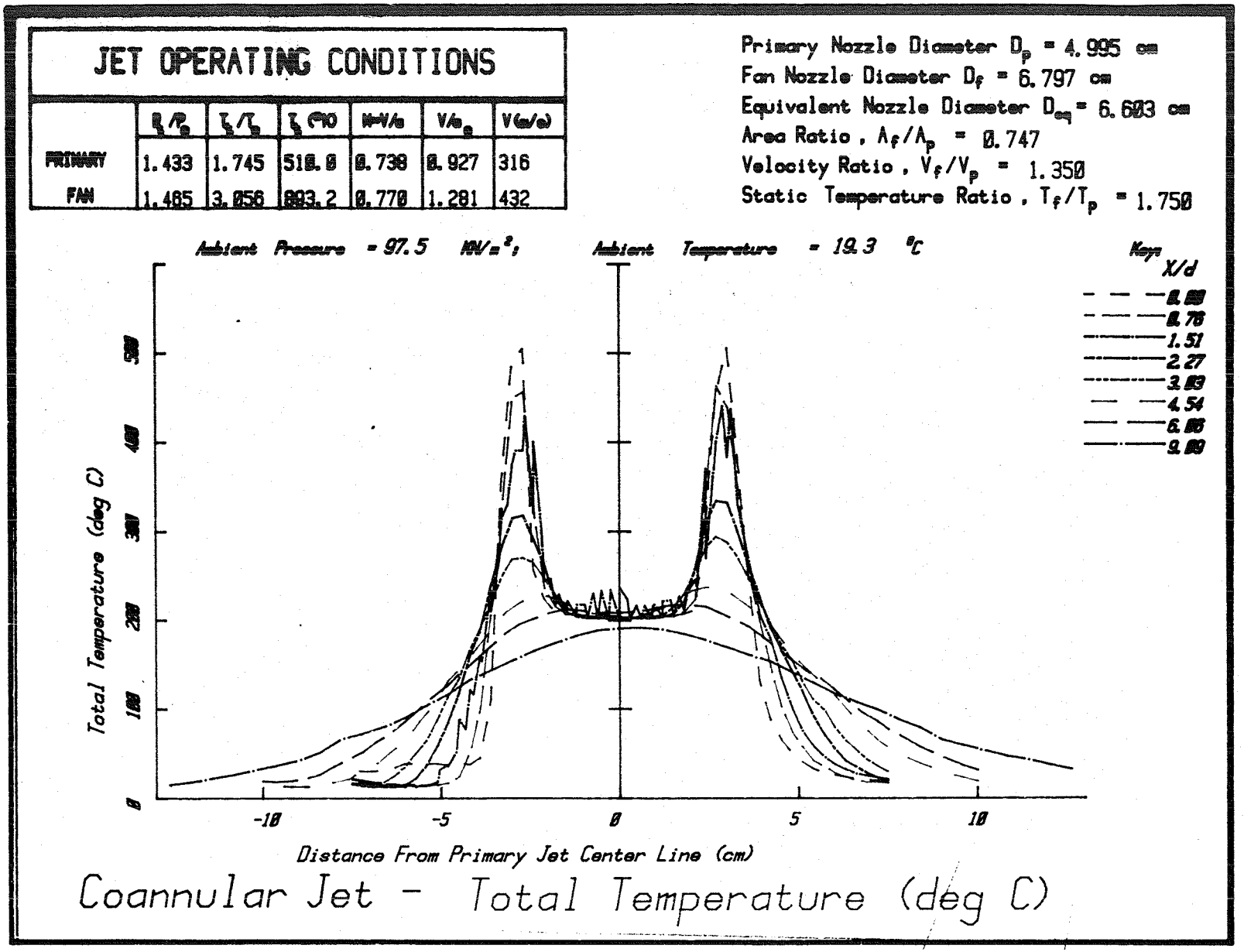

Figure A3.23(b)

JET OPERATING CONDITIONS

	P_t/P_o	T_t/T_o	T_t (°K)	M=V/a	V/a_o	V (m/s)
PRIMARY	1.433	1.745	510.0	0.738	0.927	316
FAN	1.465	3.056	893.2	0.770	1.281	432

Primary Nozzle Diameter D_p = 4.995 cm
Fan Nozzle Diameter D_f = 6.797 cm
Equivalent Nozzle Diameter D_{eq} = 6.603 cm
Area Ratio , A_f/A_p = 0.747
Velocity Ratio , V_f/V_p = 1.350
Static Temperature Ratio , T_f/T_p = 1.750

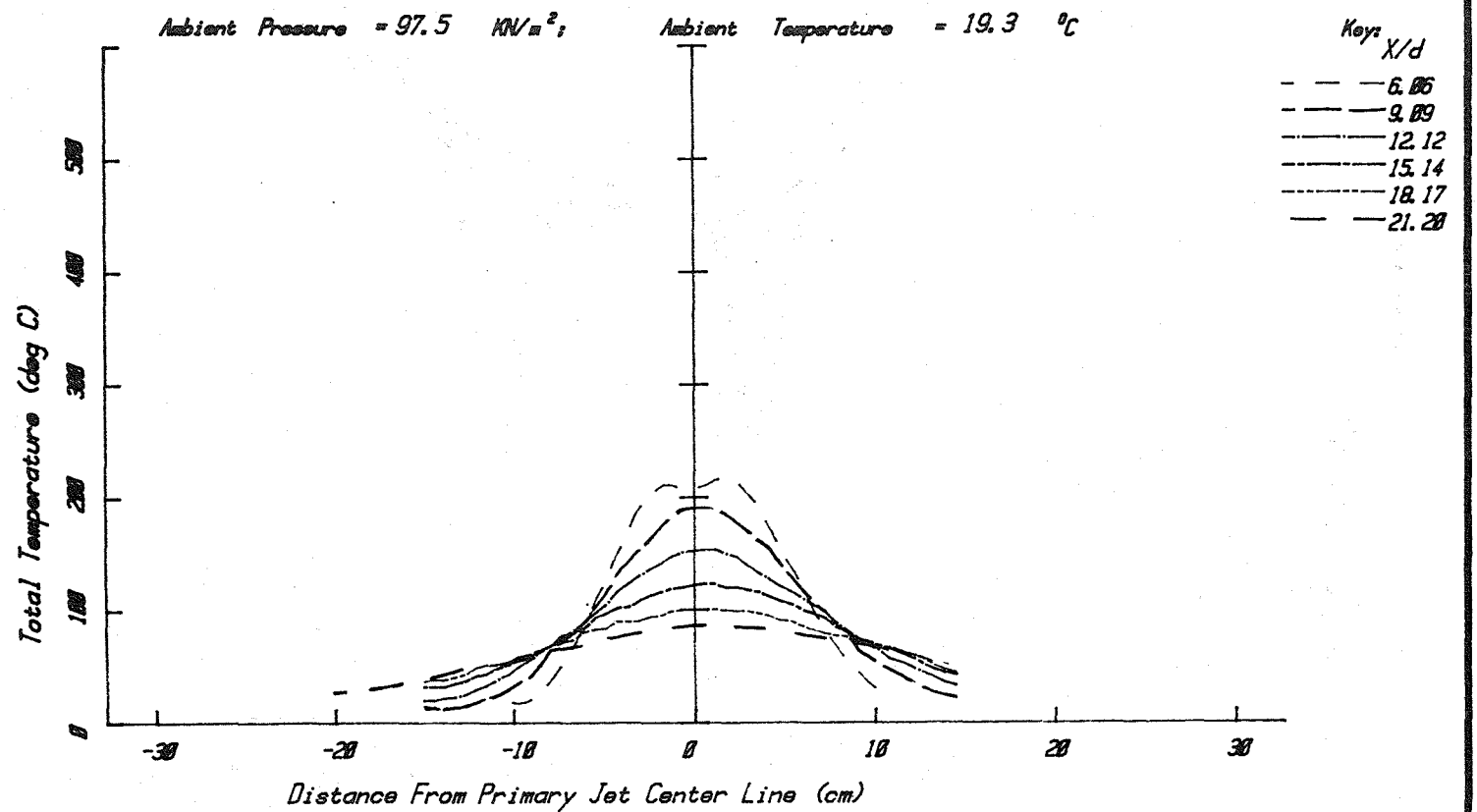

Coannular Jet - Total Temperature (deg C)

Figure A3.23(c)

JET OPERATING CONDITIONS

	P_t/P_o	T_t/T_o	T_t (°K)	M=V/a	V/a_o	V(m/s)
PRIMARY	1.449	1.770	517.3	0.750	0.947	323
FAN	1.474	3.077	899.3	0.777	1.295	436

Primary Nozzle Diameter D_p = 4.995 cm
Fan Nozzle Diameter D_f = 6.797 cm
Equivalent Nozzle Diameter D_{eq} = 6.603 cm
Area Ratio, A_f/A_p = 0.747
Velocity Ratio, V_f/V_p = 1.350
Static Temperature Ratio, T_f/T_p = 1.750

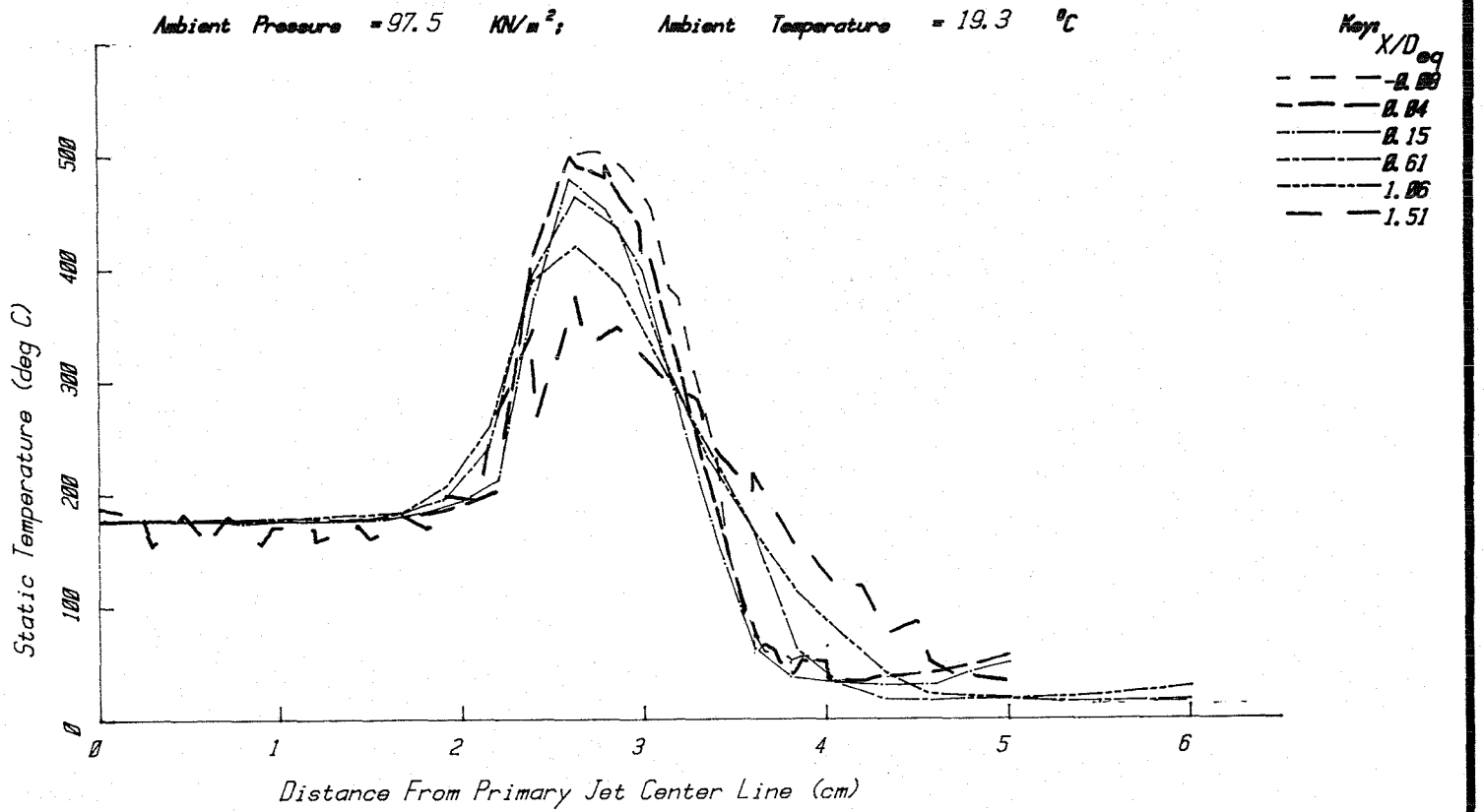

Coannular Jet - Static Temperature (deg C)

Figure A3.24(a)

JET OPERATING CONDITIONS

	P_t/P_o	T_t/T_o	T_t (°K)	M=V/a	V/a_o	V(m/s)
PRIMARY	1.433	1.745	510.0	0.738	0.927	316
FAN	1.465	3.056	893.2	0.770	1.281	432

Primary Nozzle Diameter D_p = 4.995 cm
Fan Nozzle Diameter D_f = 6.797 cm
Equivalent Nozzle Diameter D_{eq} = 6.603 cm
Area Ratio , A_f/A_p = 0.747
Velocity Ratio , V_f/V_p = 1.350
Static Temperature Ratio , T_f/T_p = 1.750

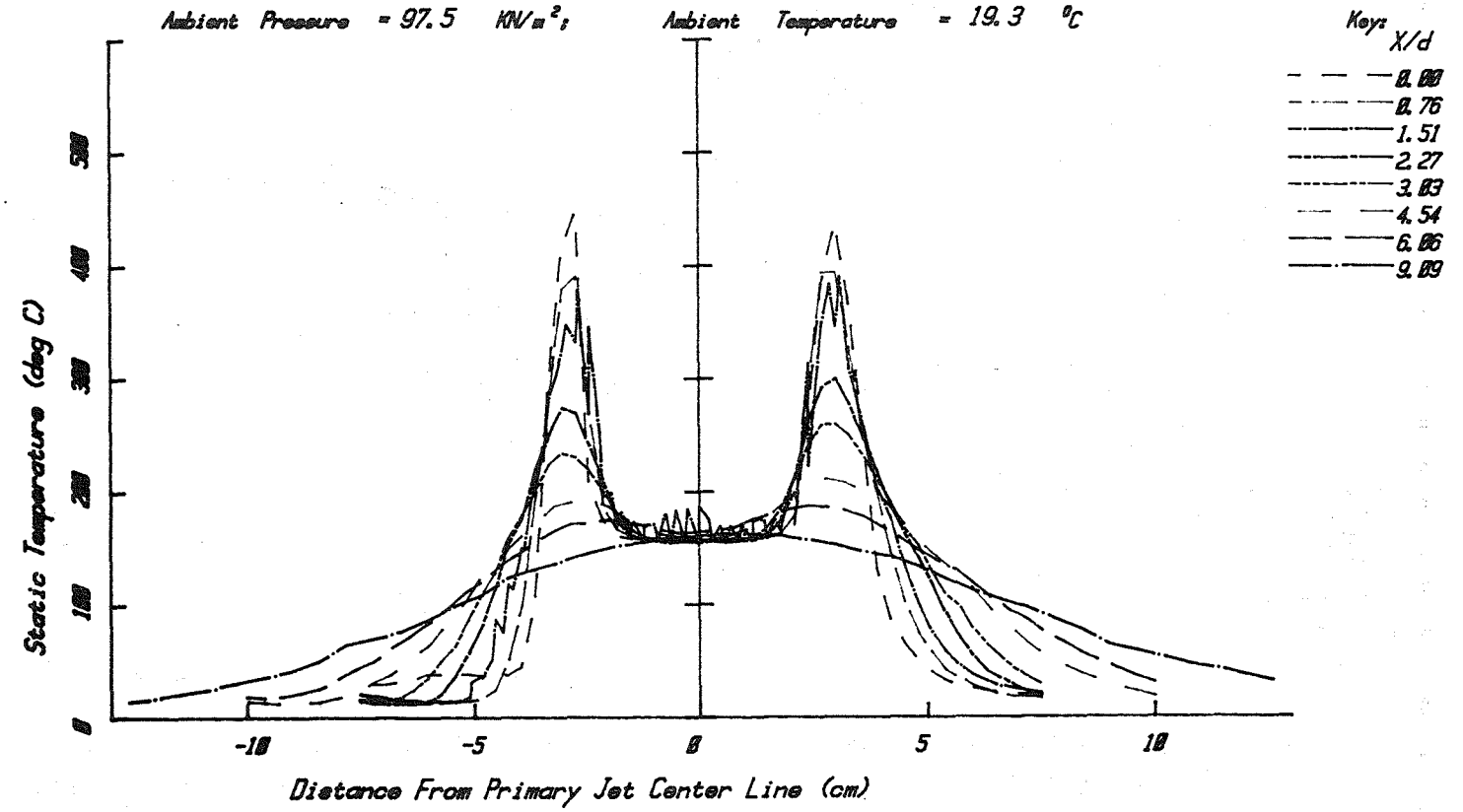

Coannular Jet - Static Temperature (deg C)

Figure A3.24(b)

JET OPERATING CONDITIONS

	P_t/P_o	T_t/T_o	T_t (°K)	M=V/a	V/a_o	V(m/s)
PRIMARY	1.433	1.745	510.0	0.738	0.927	316
FAN	1.465	3.056	893.2	0.770	1.281	432

Primary Nozzle Diameter D_p = 4.995 cm
Fan Nozzle Diameter D_f = 6.797 cm
Equivalent Nozzle Diameter D_{eq} = 6.603 cm
Area Ratio , A_f/A_p = 0.747
Velocity Ratio , V_f/V_p = 1.350
Static Temperature Ratio , T_f/T_p = 1.750

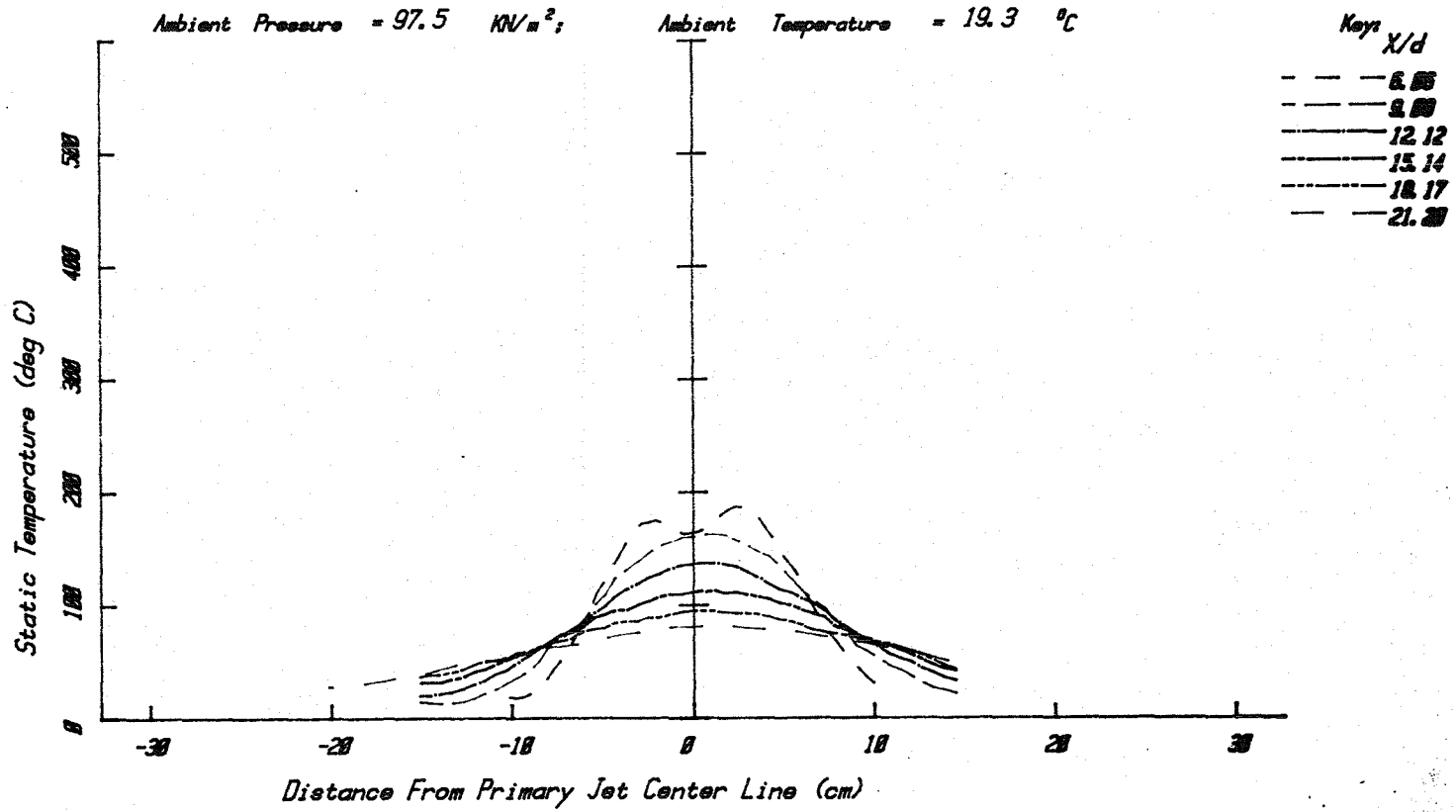

Coannular Jet - Static Temperature (deg C)

Figure A3.24(c)

JET OPERATING CONDITIONS

	P_t/P_0	T_t/T_0	T_t (°K)	M=V/a	V/a_0	V (m/s)
PRIMARY	1.385	1.638	490.3	0.700	0.856	296
FAN	1.558	2.957	885.2	0.833	1.351	461

Primary Nozzle Diameter D_p = 4.995 cm
Fan Nozzle Diameter D_f = 6.797 cm
Equivalent Nozzle Diameter D_{eq} = 6.603 cm
Area Ratio, A_f/A_p = 0.747
Velocity Ratio, V_f/V_p = 1.550
Static Temperature Ratio, T_f/T_p = 1.750

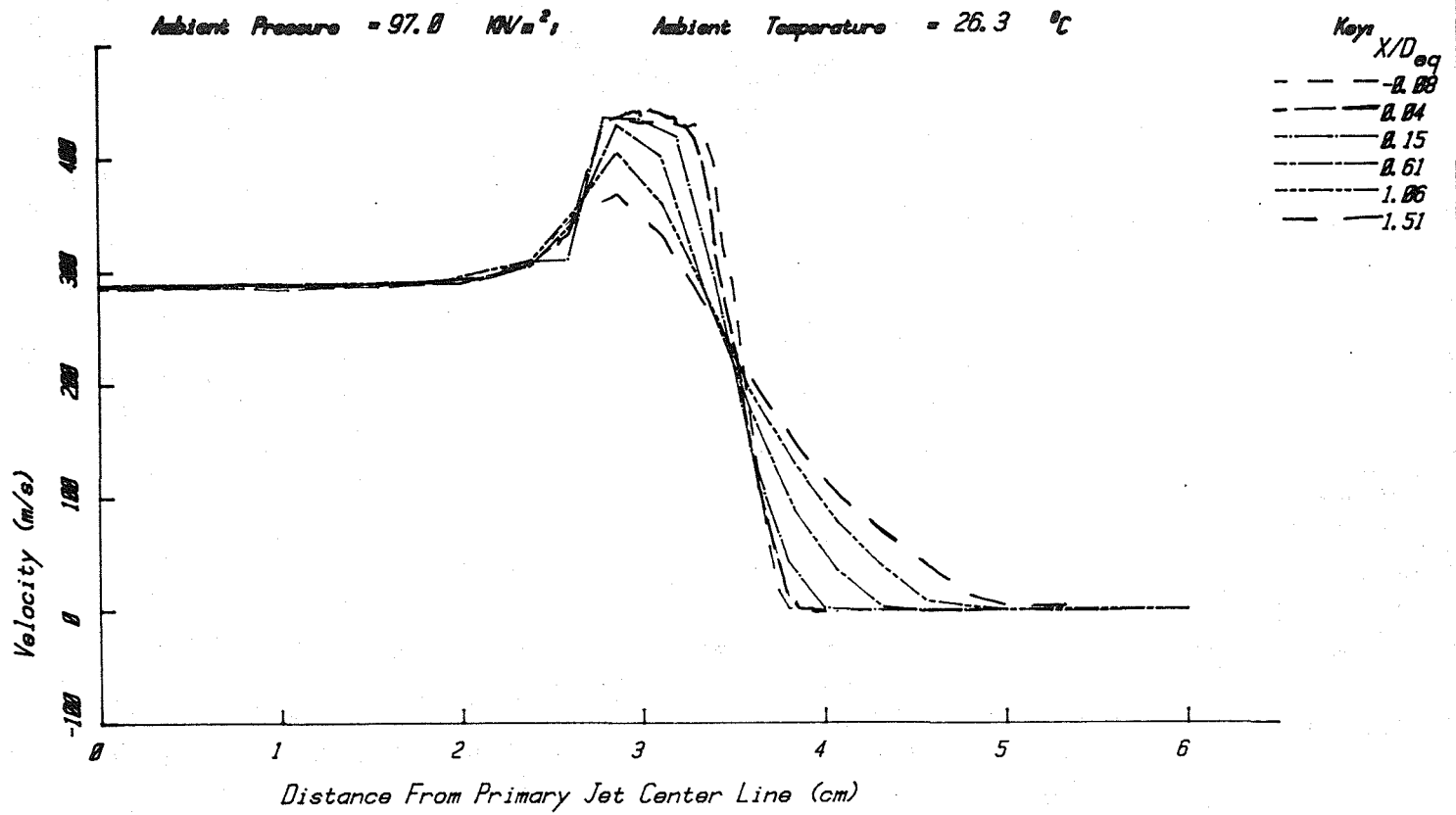

Coannular Jet - Velocity (m/s)

Figure A3.25(a)

JET OPERATING CONDITIONS

	P_t/P_o	T_t/T_o	T_t (°K)	M=V/a	V/a_o	V(m/s)
PRIMARY	1.385	1.638	490.3	0.700	0.856	296
FAN	1.558	2.957	885.2	0.833	1.351	461

Primary Nozzle Diameter D_p = 4.995 cm
Fan Nozzle Diameter D_f = 6.797 cm
Equivalent Nozzle Diameter D_{eq} = 6.683 cm
Area Ratio , A_f/A_p = 2.747
Velocity Ratio , V_f/V_p = 1.552
Static Temperature Ratio , T_f/T_p = 1.752

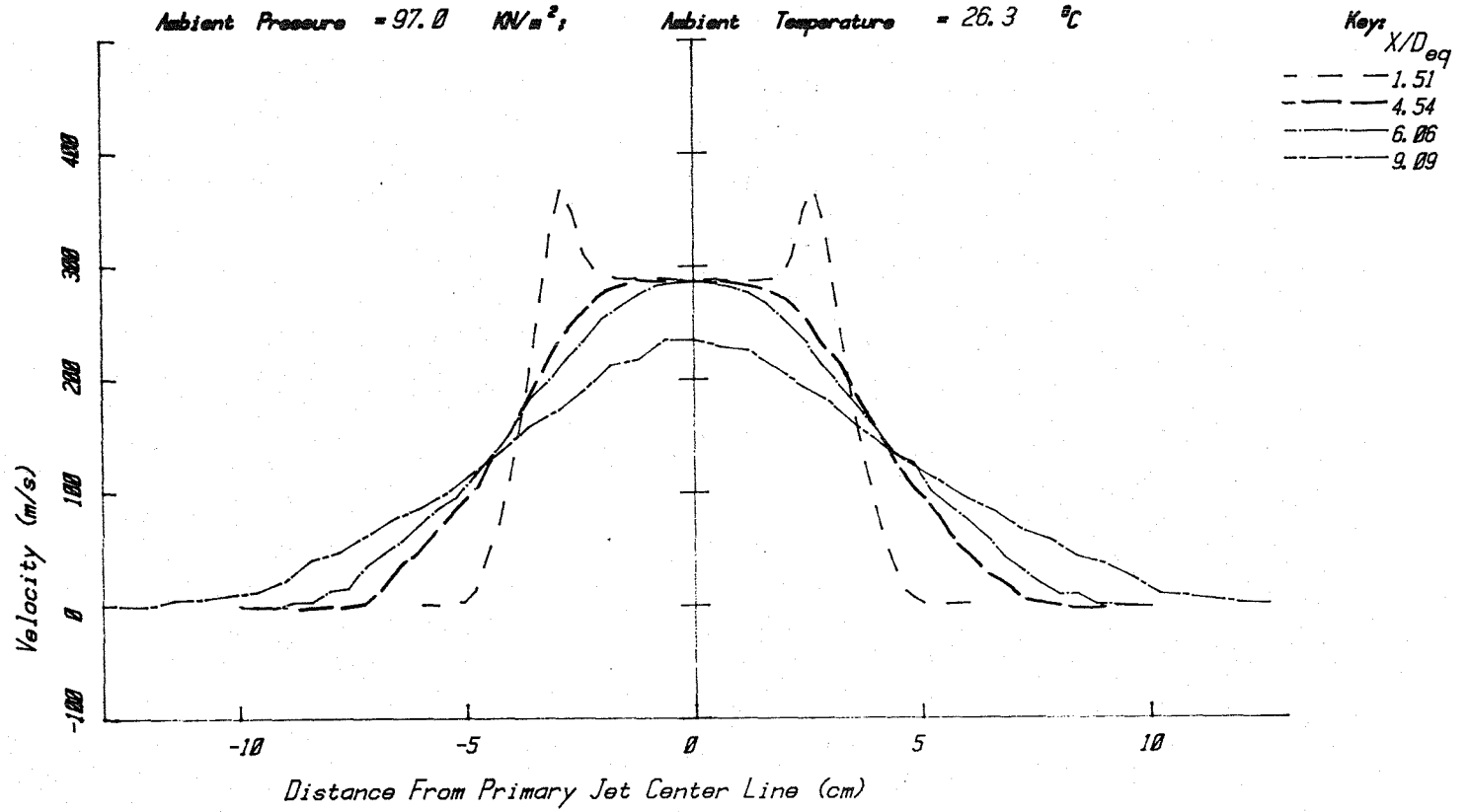

Coannular Jet - Velocity (m/s)

Figure A3.25(b)

JET OPERATING CONDITIONS

	P_t/P_o	T_t/T_o	T_t (°K)	M=V/a	V/a_o	V(m/s)
PRIMARY	1.385	1.638	490.3	0.700	0.856	296
FAN	1.558	2.957	885.2	0.833	1.351	461

Primary Nozzle Diameter D_p = [illegible] cm
Fan Nozzle Diameter D_f = [illegible] cm
Equivalent Nozzle Diameter D_{eq} = [illegible] cm
Area Ratio , A_f/A_p = [illegible]
Velocity Ratio , V_f/V_p = [illegible]
Static Temperature Ratio , T_f/T_p = [illegible]

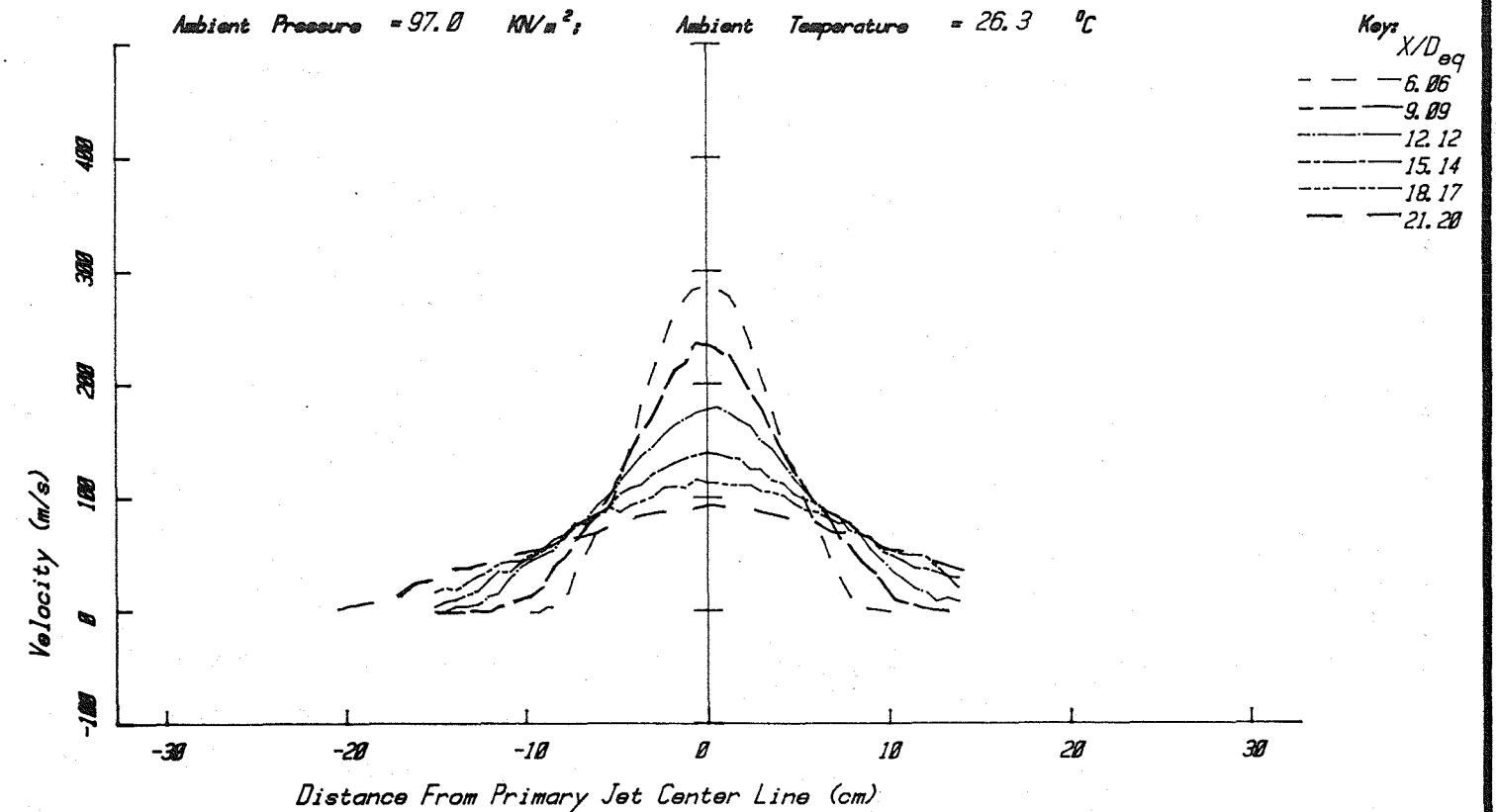

Coannular Jet - Velocity (m/s)

Figure A3.25(c)

JET OPERATING CONDITIONS

	P_t/P_o	T_t/T_o	T_t (°K)	M=V/a	V/a_o	V (m/s)
PRIMARY	1.385	1.638	490.3	0.700	0.856	296
FAN	1.558	2.957	885.2	0.833	1.351	461

Primary Nozzle Diameter D_p = 4.995 cm
Fan Nozzle Diameter D_f = 6.797 cm
Equivalent Nozzle Diameter D_{eq} = 6.603 cm
Area Ratio , A_f/A_p = 0.747
Velocity Ratio , V_f/V_p = 1.550
Static Temperature Ratio , T_f/T_p = 1.750

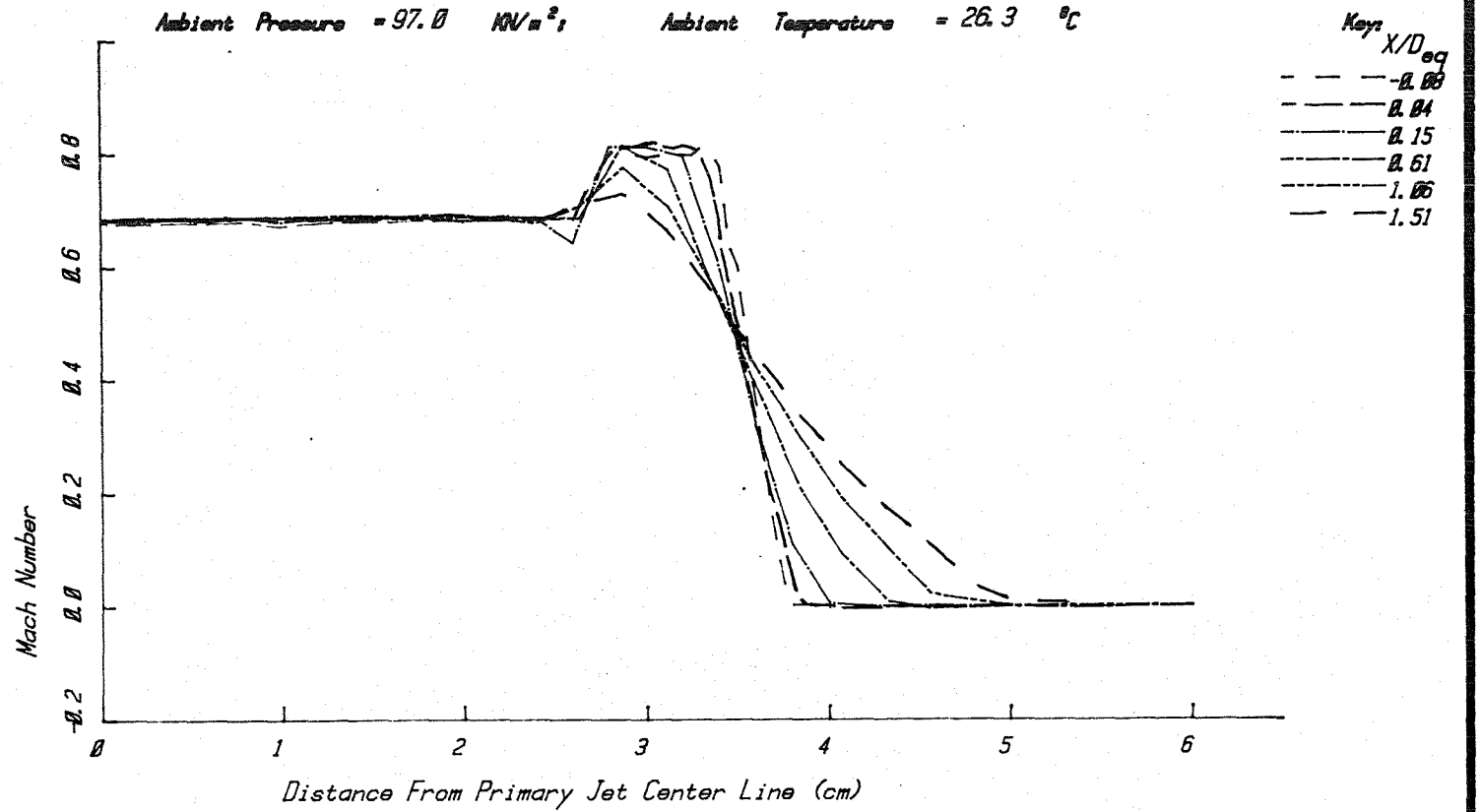

Coannular Jet - Mach Number

Figure A3.26(a)

JET OPERATING CONDITIONS

	P_t/P_o	T_t/T_o	T_t (°K)	M=V/a	V/a_o	V (m/s)
PRIMARY	1.385	1.638	490.3	0.700	0.856	296
FAN	1.558	2.957	885.2	0.833	1.351	461

Primary Nozzle Diameter D_p = 4.995 cm
Fan Nozzle Diameter D_f = 6.[illegible] cm
Equivalent Nozzle Diameter D_{eq} = 6.803 cm
Area Ratio , A_f/A_p = [illegible]
Velocity Ratio , V_f/V_p = [illegible]
Static Temperature Ratio , T_f/T_p = 1.[illegible]

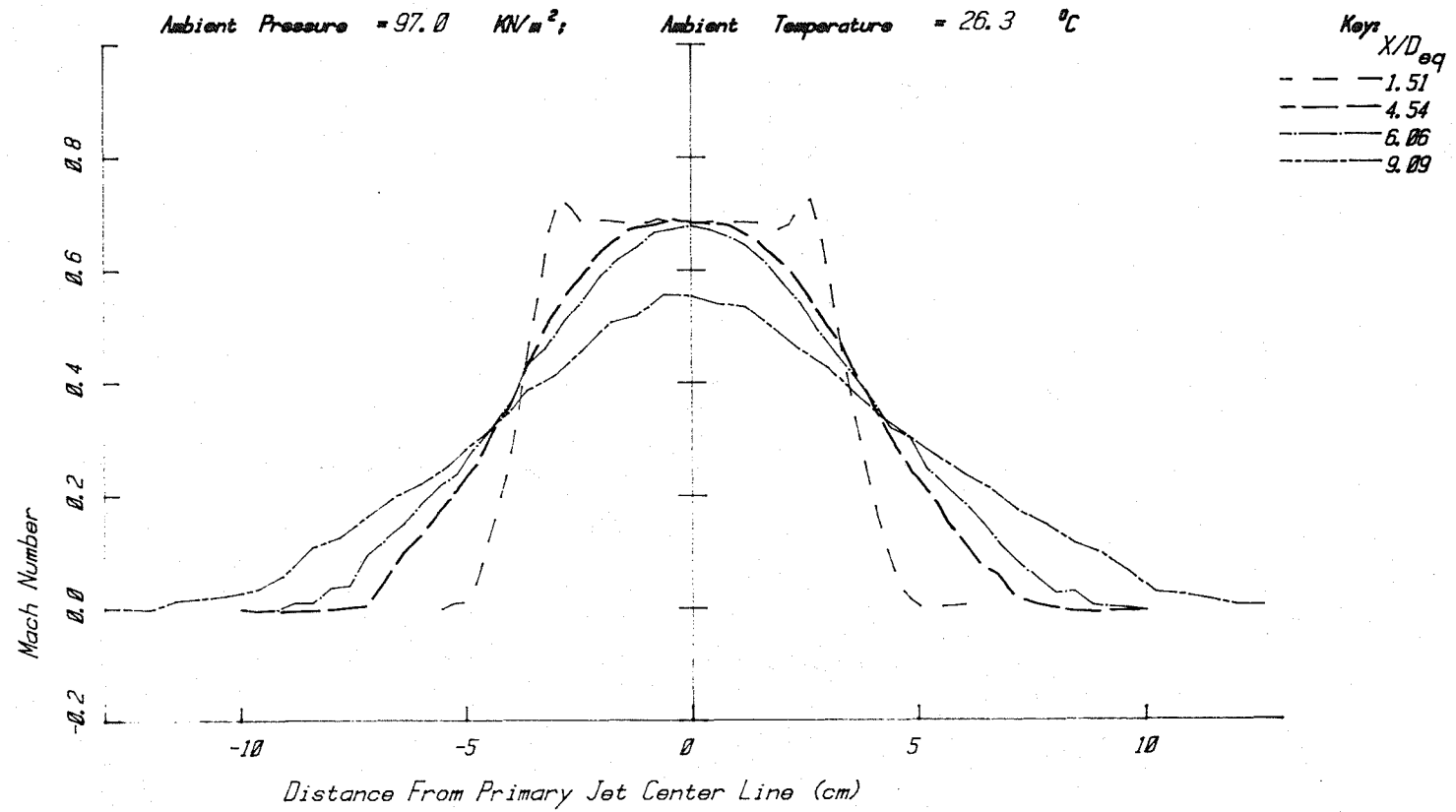

Coannular Jet - Mach Number

Figure A3.26(b)

JET OPERATING CONDITIONS

	P_t/P_o	T_t/T_o	T_t (°K)	M=V/a	V/a_o	V(m/s)
PRIMARY	1.385	1.638	490.3	0.700	0.856	296
FAN	1.558	2.957	885.2	0.833	1.351	461

Primary Nozzle Diameter D_p = 4.995 cm
Fan Nozzle Diameter D_f = 6.797 cm
Equivalent Nozzle Diameter D_{eq} = 6.603 cm
Area Ratio , A_f/A_p = 0.747
Velocity Ratio , V_f/V_p = 1.550
Static Temperature Ratio , T_f/T_p = 1.750

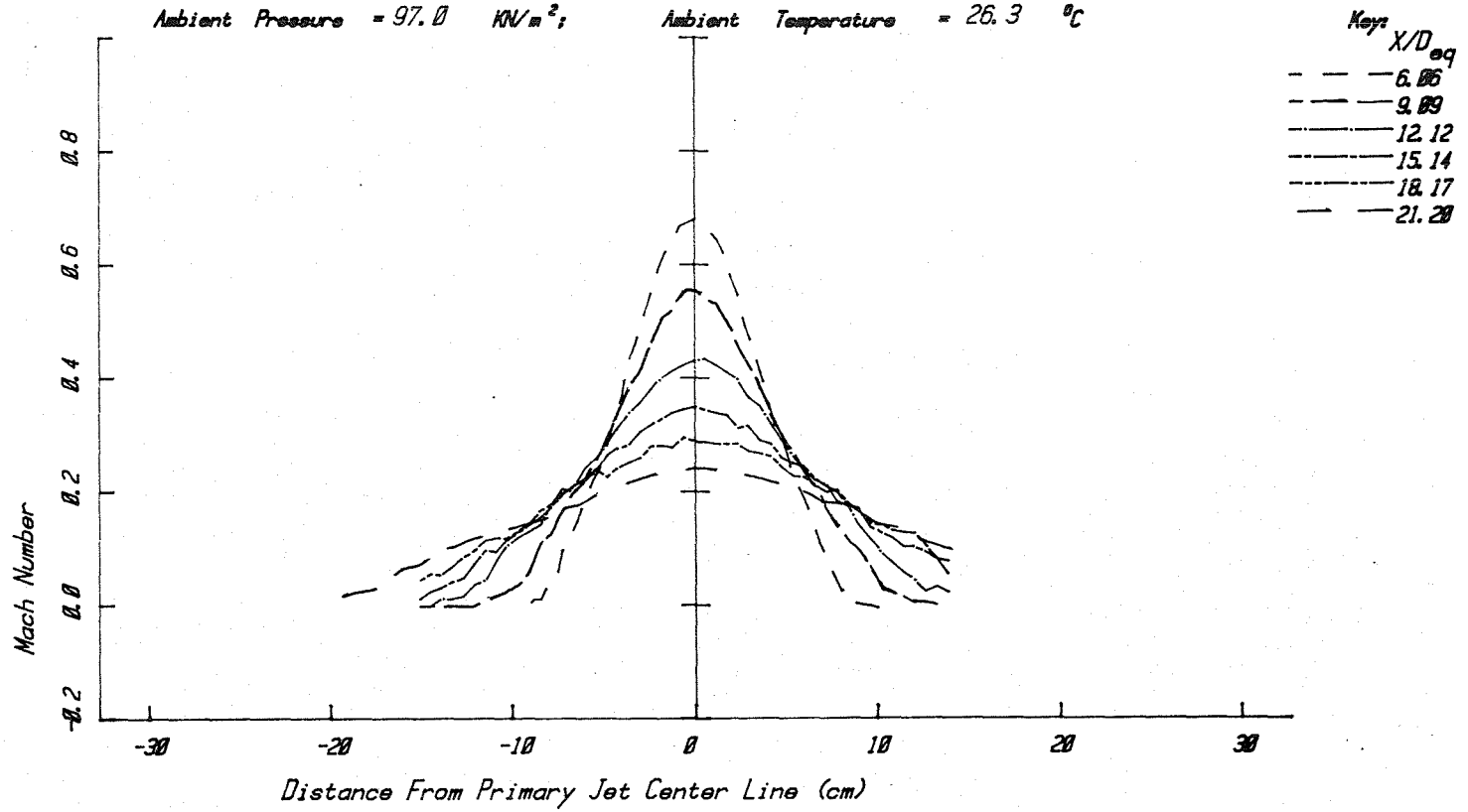

Coannular Jet - Mach Number

Figure A3.26(c)

JET OPERATING CONDITIONS

	P_t/P_∞	T_t/T_∞	T_t (°K)	M=V/a	V/a_∞	V(m/s)
PRIMARY	1.385	1.638	490.3	0.700	0.856	296
FAN	1.558	2.957	885.2	0.833	1.351	461

Primary Nozzle Diameter D_p = 4.995 cm
Fan Nozzle Diameter D_f = 6.797 cm
Equivalent Nozzle Diameter D_{eq} = 6.603 cm
Area Ratio, A_f/A_p = 0.747
Velocity Ratio, V_f/V_p = 1.550
Static Temperature Ratio, T_f/T_p = 1.750

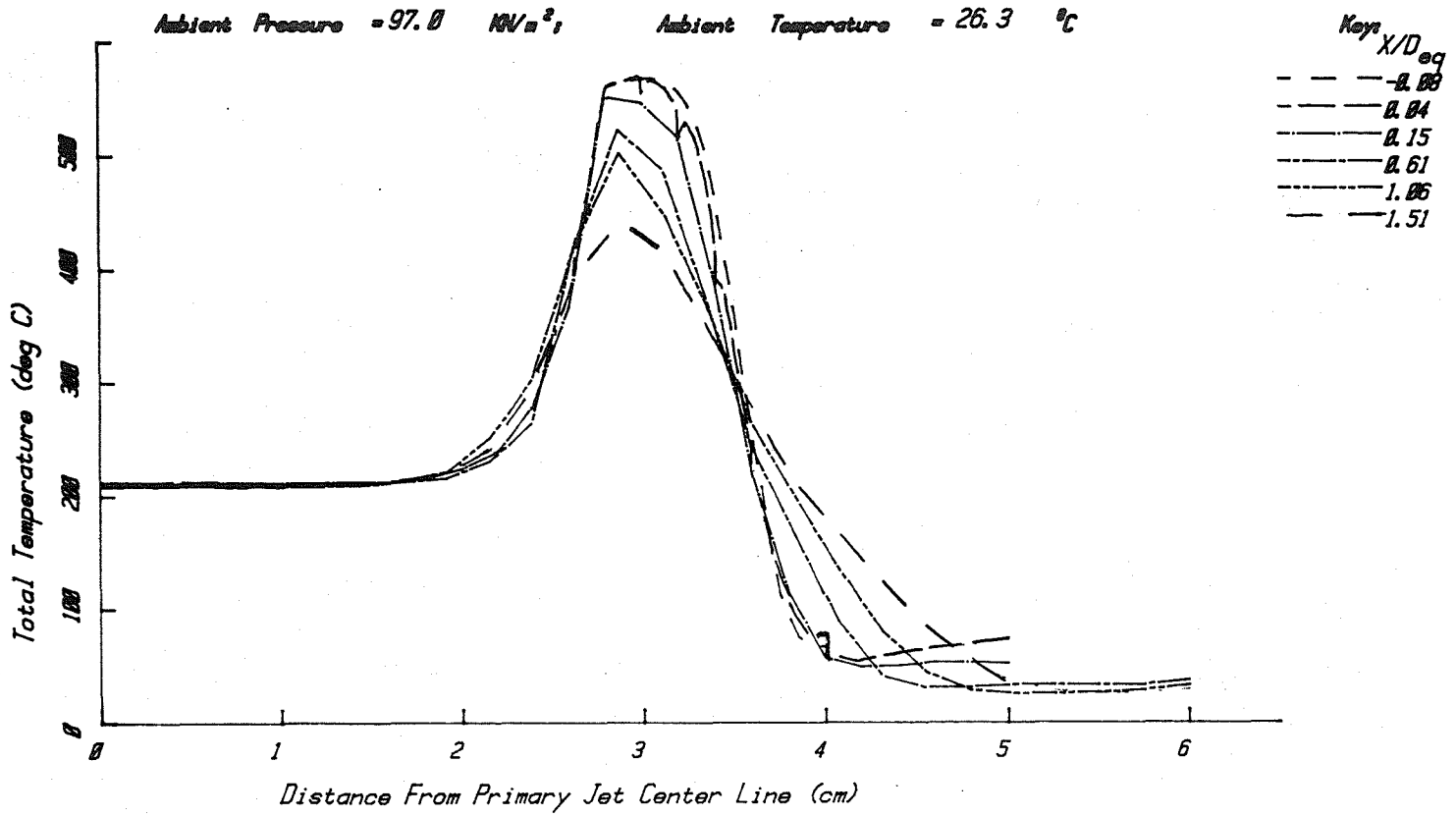

Coannular Jet - Total Temperature (deg C)

Figure A3.27(a)

JET OPERATING CONDITIONS

	P_t/P_o	T_t/T_o	T_t (°K)	M=V/a	V/a_o	V(m/s)
PRIMARY	1.385	1.638	490.3	0.700	0.856	296
FAN	1.558	2.957	885.2	0.833	1.351	461

Primary Nozzle Diameter D_p = 4.895 cm
Fan Nozzle Diameter D_f = 8.790 cm
Equivalent Nozzle Diameter D_{eq} = 8.803 cm
Area Ratio , A_f/A_p = 3.247
Velocity Ratio , V_f/V_p = 1.582
Static Temperature Ratio , T_f/T_p = 1.732

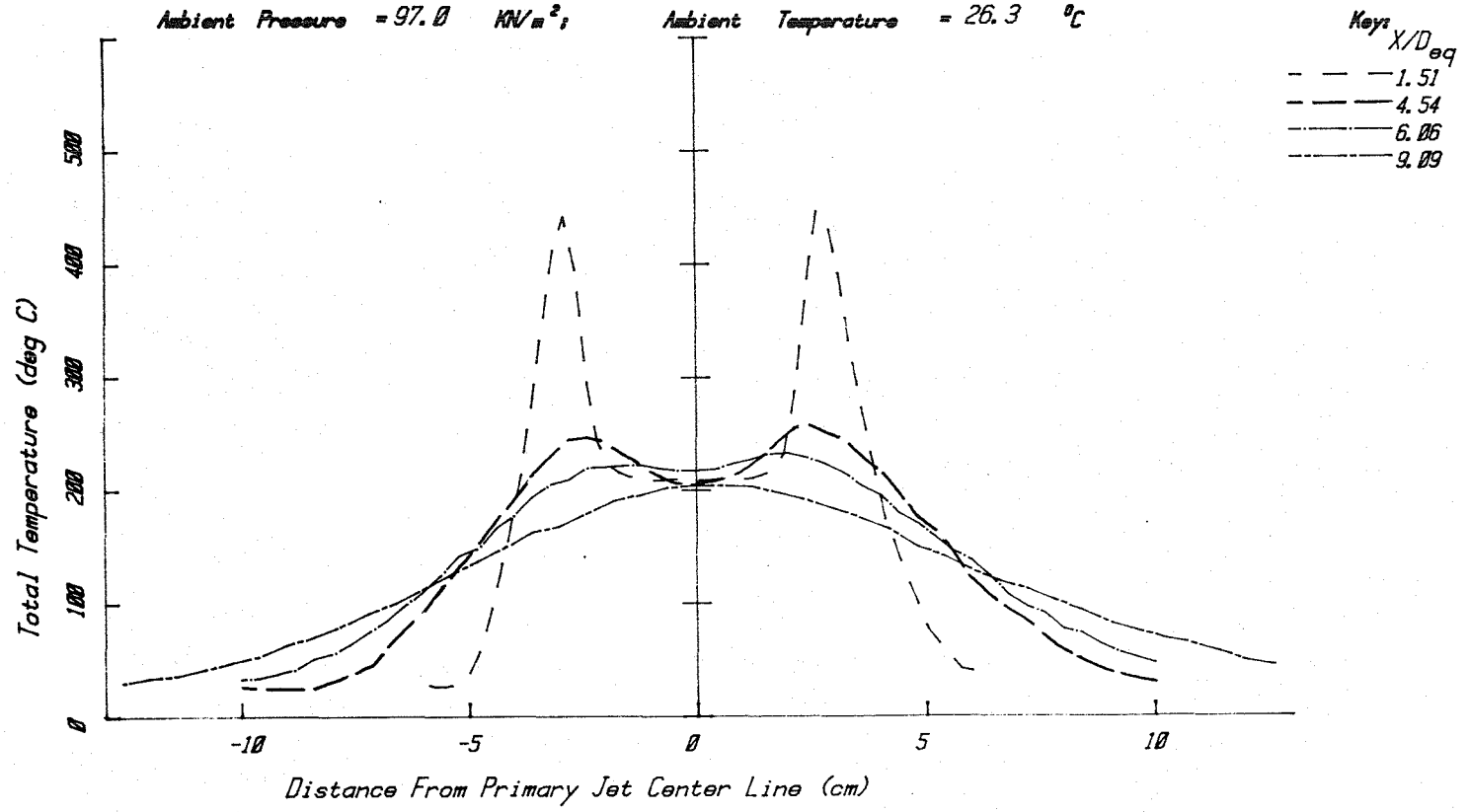

Coannular Jet - Total Temperature (deg C)

Figure A3.27(b)

JET OPERATING CONDITIONS

	P_t/P_o	T_t/T_o	T_t (°K)	M=V/a	V/a_o	V(m/s)
PRIMARY	1.385	1.638	490.3	0.700	0.856	296
FAN	1.558	2.957	885.2	0.833	1.351	461

Primary Nozzle Diameter D_p = [illegible] cm
Fan Nozzle Diameter D_f = [illegible] cm
Equivalent Nozzle Diameter D_{eq} = [illegible] cm
Area Ratio , A_f/A_p = [illegible]
Velocity Ratio , V_f/V_p = [illegible]
Static Temperature Ratio , T_f/T_p = [illegible]

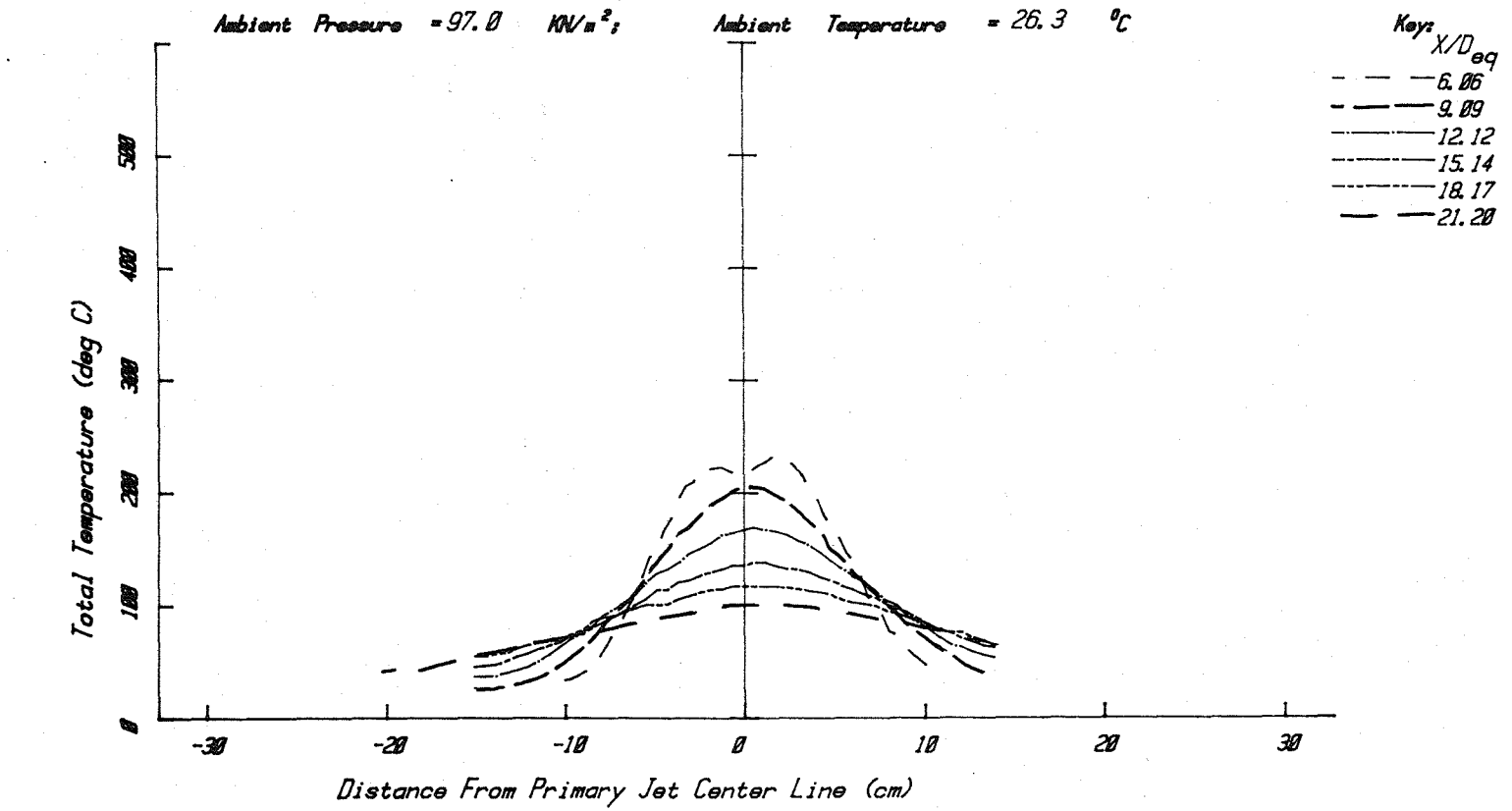

Coannular Jet - Total Temperature (deg C)

Figure A3.27(c)

JET OPERATING CONDITIONS

	P_t/P_o	T_t/T_o	T_t (°K)	M=V/a	V/a_o	V (m/s)
PRIMARY	1.385	1.638	490.3	0.700	0.856	296
FAN	1.558	2.957	885.2	0.833	1.351	461

Primary Nozzle Diameter D_p = 4.995 cm
Fan Nozzle Diameter D_f = 6.797 cm
Equivalent Nozzle Diameter D_{eq} = 6.603 cm
Area Ratio , A_f/A_p = 0.747
Velocity Ratio , V_f/V_p = 1.550
Static Temperature Ratio , T_f/T_p = 1.750

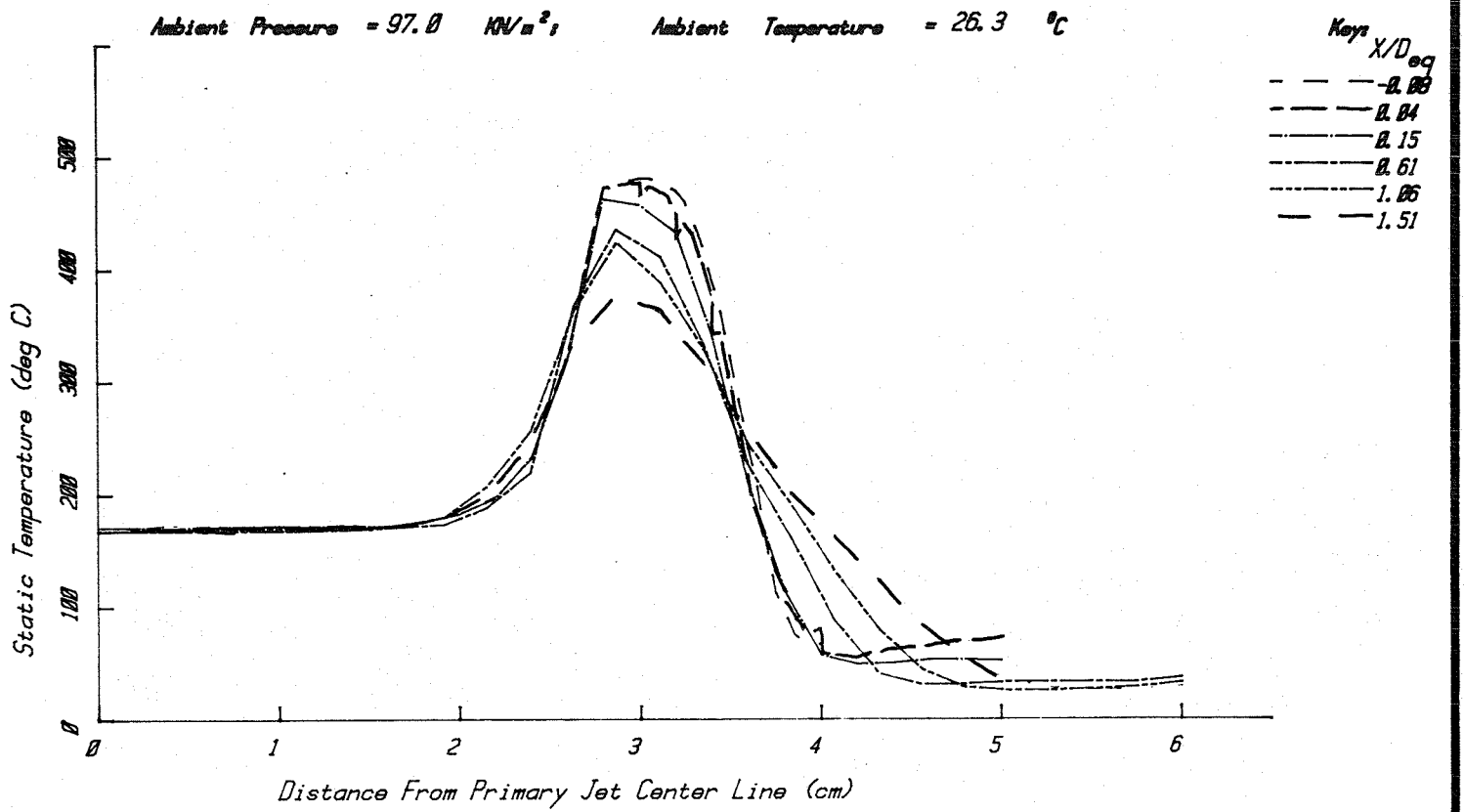

Coannular Jet - Static Temperature (deg C)

Figure A3.28(a)

JET OPERATING CONDITIONS

	P_t/P_o	T_t/T_o	T_t (°K)	M=V/a	V/a_o	V(m/s)
PRIMARY	1.385	1.638	490.3	0.700	0.856	296
FAN	1.558	2.957	885.2	0.833	1.351	461

Primary Nozzle Diameter D_p = 4.995 cm
Fan Nozzle Diameter D_f = 6.797 cm
Equivalent Nozzle Diameter D_{eq} = 6.603 cm
Area Ratio , A_f/A_p = 2.747
Velocity Ratio , V_f/V_p = 1.553
Static Temperature Ratio , T_f/T_p = 1.750

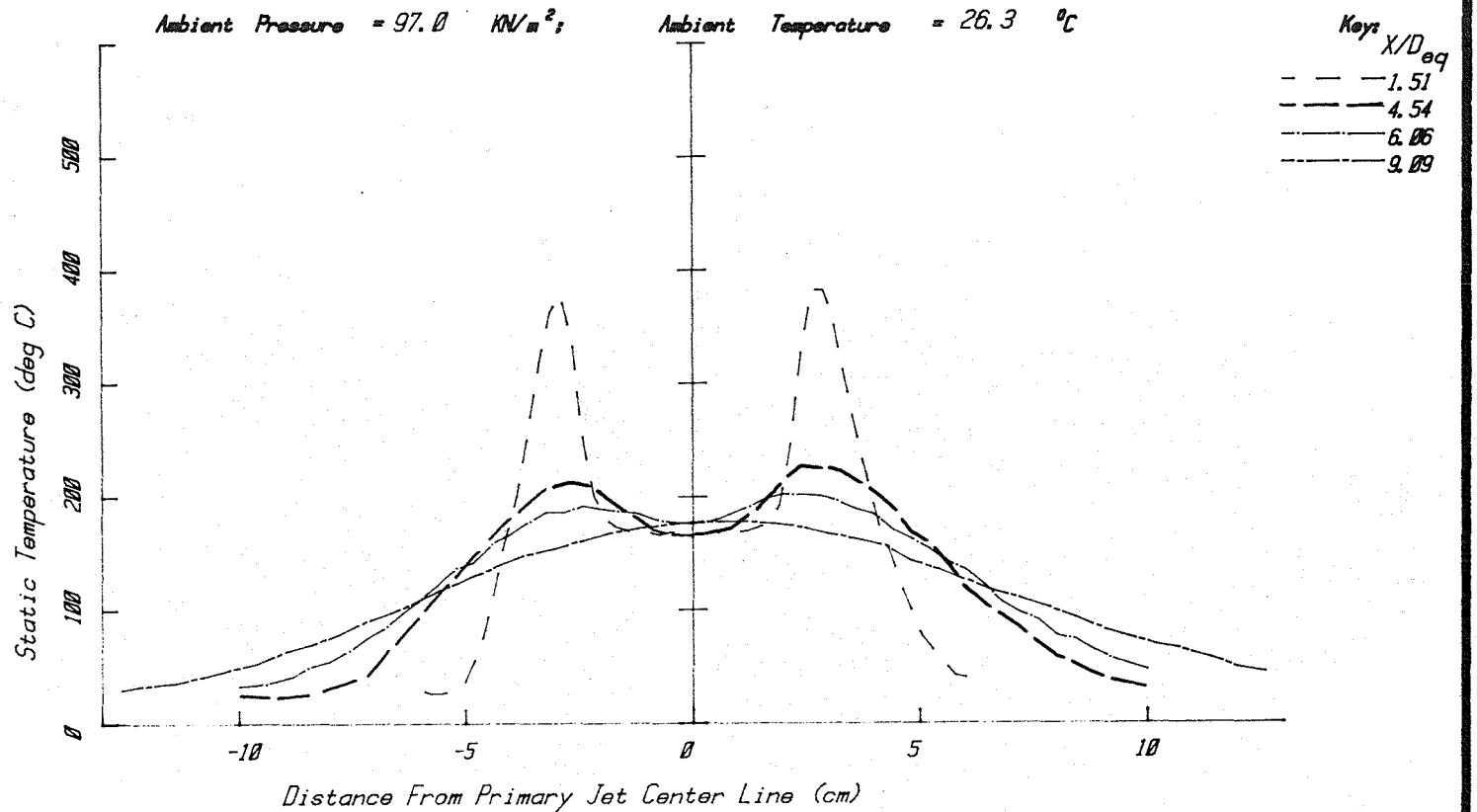

Coannular Jet - Static Temperature (deg C)

Figure A3.28(b)

JET OPERATING CONDITIONS

	P_t/P_o	T_t/T_o	T_t (°K)	M=V/a	V/a_o	V(m/s)
PRIMARY	1.385	1.638	490.3	0.700	0.856	296
FAN	1.558	2.957	885.2	0.833	1.351	461

Primary Nozzle Diameter D_p = 4.995 cm
Fan Nozzle Diameter D_f = 6.797 cm
Equivalent Nozzle Diameter D_{eq} = 6.603 cm
Area Ratio , A_f/A_p = 0.747
Velocity Ratio , V_f/V_p = 1.550
Static Temperature Ratio , T_f/T_p = 1.750

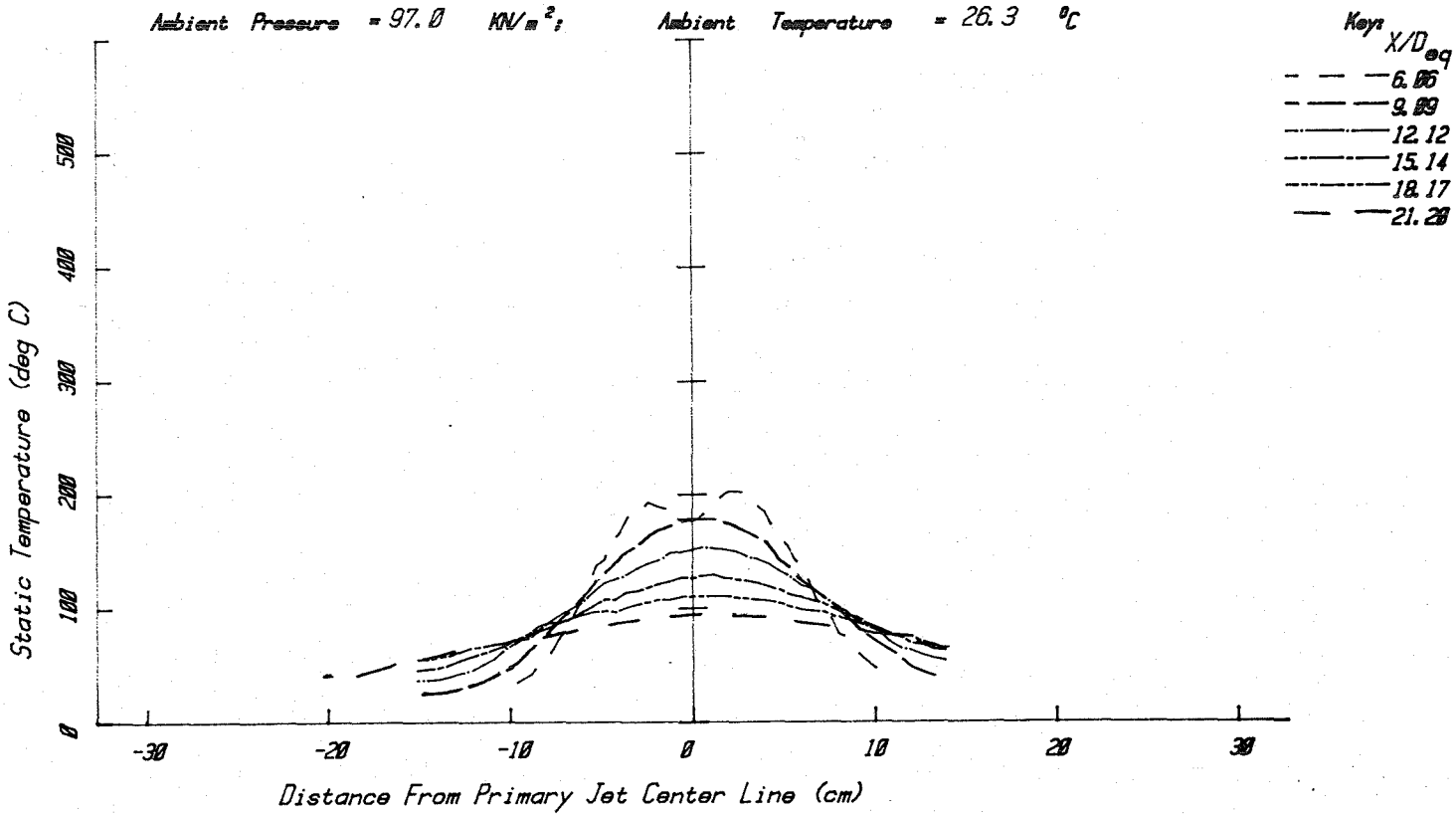

Coannular Jet - Static Temperature (deg C)

Figure A3.28(c)

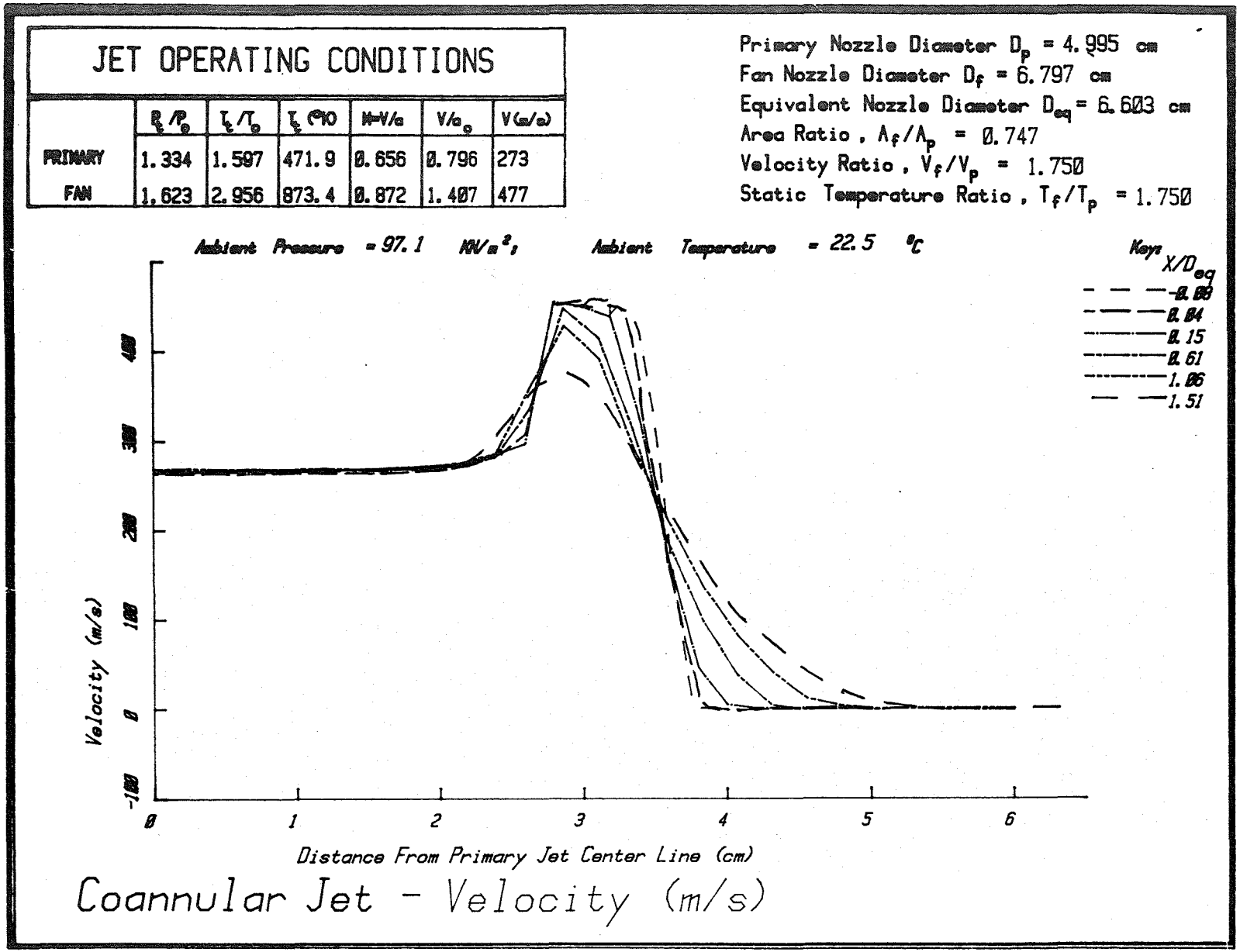

Figure A3.29(a)

JET OPERATING CONDITIONS

	P_t/P_o	T_t/T_o	T_t (°K)	M=V/a	V/a_o	V(m/s)
PRIMARY	1.334	1.597	471.9	0.656	0.796	273
FAN	1.623	2.956	873.4	0.872	1.407	477

Primary Nozzle Diameter D_p = 4.995 cm
Fan Nozzle Diameter D_f = 6.797 cm
Equivalent Nozzle Diameter D_{eq} = 6.883 cm
Area Ratio , A_f/A_p = 2.747
Velocity Ratio , V_f/V_p = 1.752
Static Temperature Ratio , T_f/T_p = 1.102

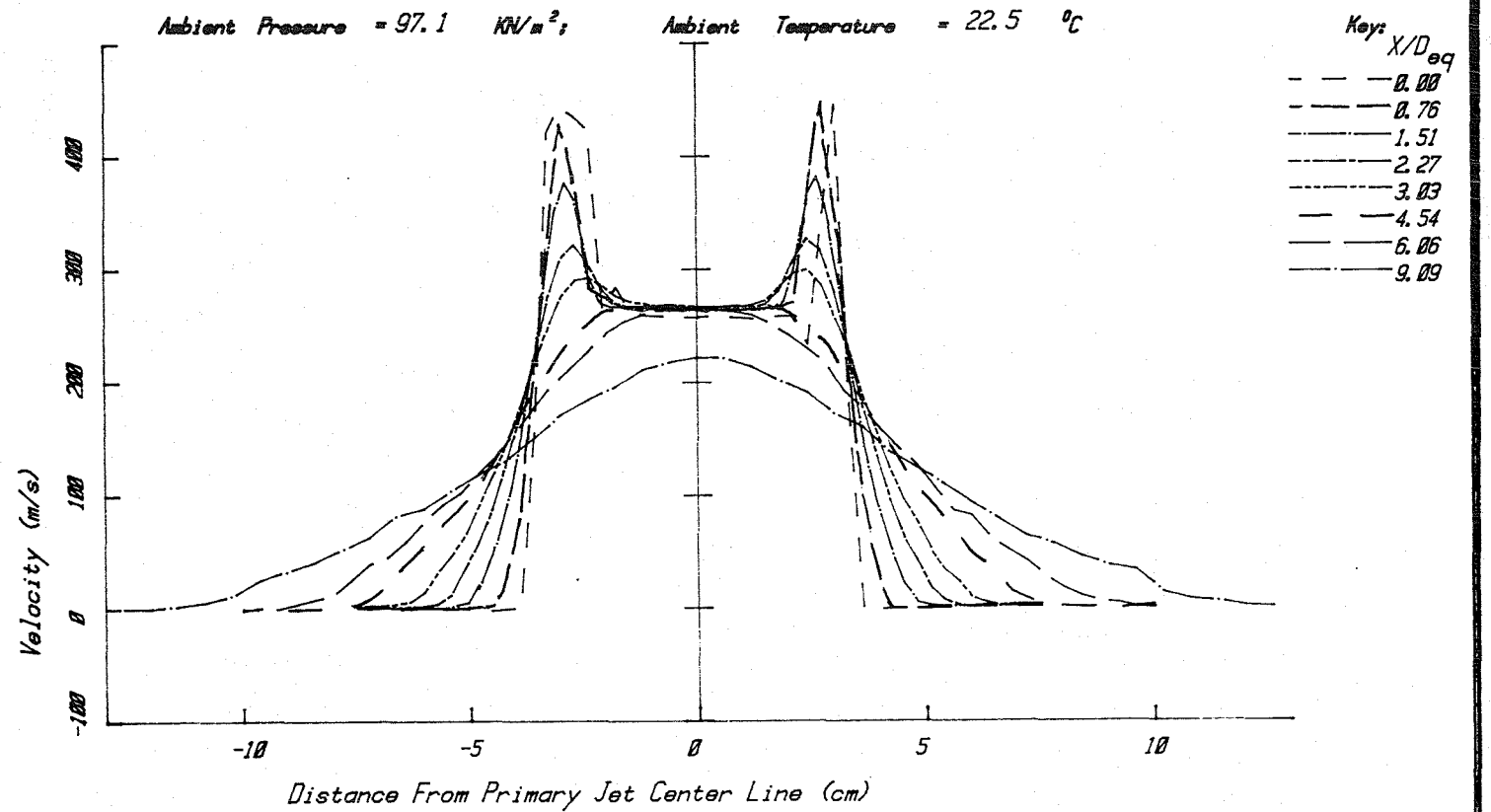

Coannular Jet - Velocity (m/s)

Figure A3.29(b)

JET OPERATING CONDITIONS

	P_t/P_o	T_t/T_o	T_t (°K)	M=V/a	V/a_o	V(m/s)
PRIMARY	1.334	1.597	471.9	Ø.656	Ø.796	273
FAN	1.623	2.956	873.4	Ø.872	1.4Ø7	477

Primary Nozzle Diameter D_p = [illegible] cm
Fan Nozzle Diameter D_f = [illegible] cm
Equivalent Nozzle Diameter D_{eq} = [illegible] cm
Area Ratio , A_f/A_p = [illegible]
Velocity Ratio , V_f/V_p = [illegible]
Static Temperature Ratio , T_f/T_p = [illegible]

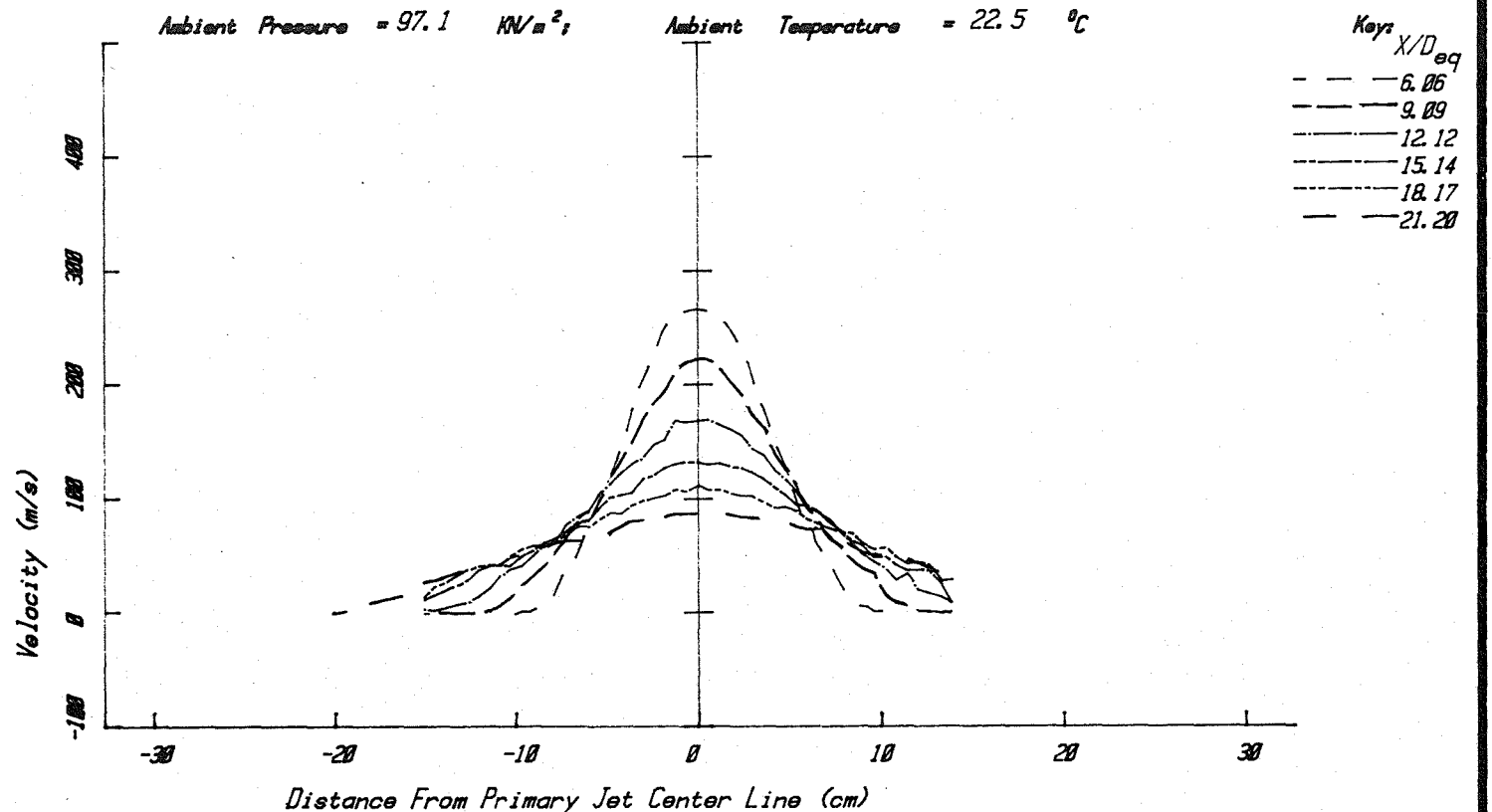

Coannular Jet - Velocity (m/s)

Figure A3.29(c)

JET OPERATING CONDITIONS

	P_t/P_0	T_t/T_0	T_t (°K)	M=V/a	V/a_0	V (m/s)
PRIMARY	1.334	1.597	471.9	Ø.656	Ø.796	273
FAN	1.623	2.956	873.4	Ø.872	1.4Ø7	477

Primary Nozzle Diameter D_p = 4.995 cm
Fan Nozzle Diameter D_f = 6.797 cm
Equivalent Nozzle Diameter D_{eq} = 6.6Ø3 cm
Area Ratio , A_f/A_p = Ø.747
Velocity Ratio , V_f/V_p = 1.75Ø
Static Temperature Ratio , T_f/T_p = 1.75Ø

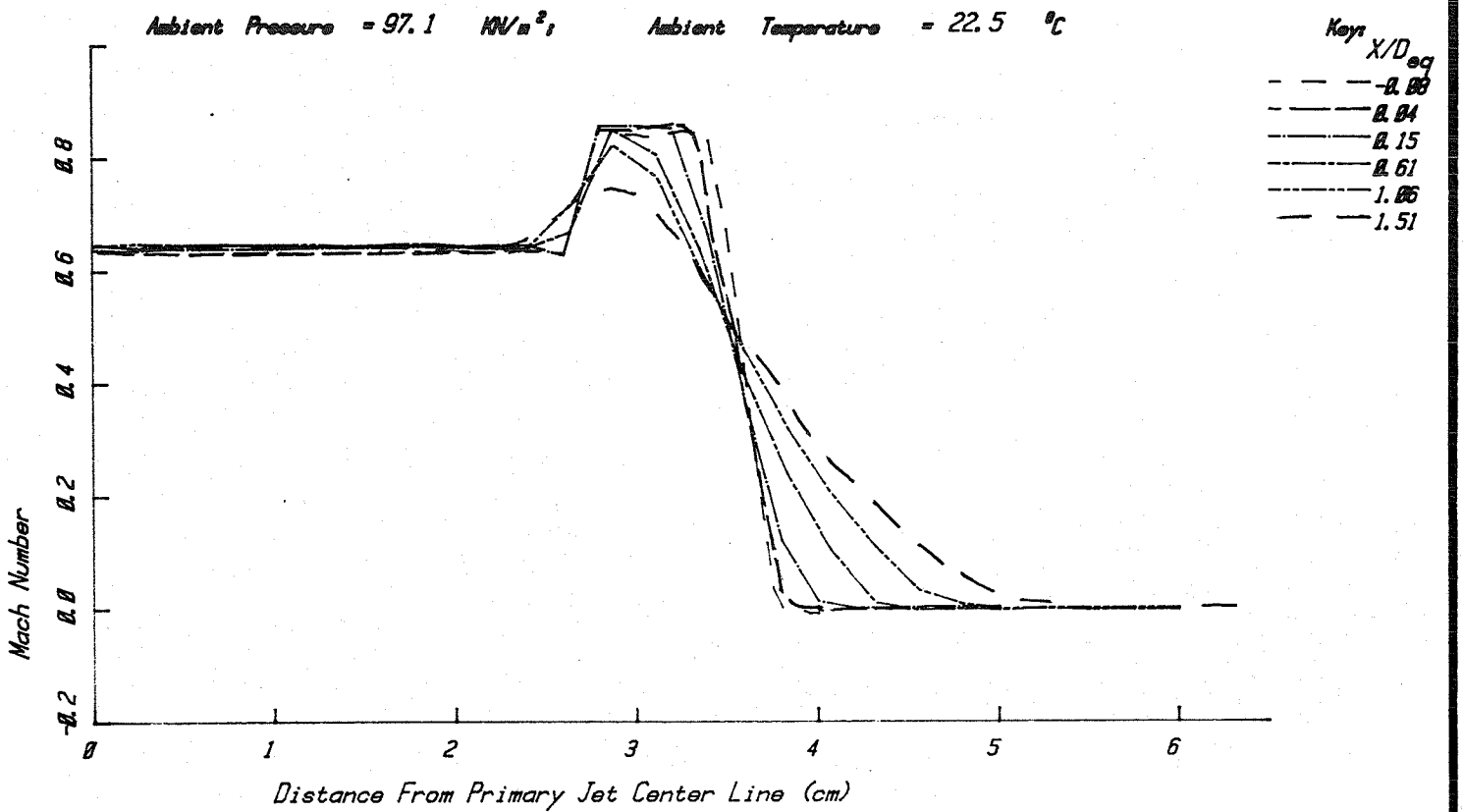

Coannular Jet - Mach Number

Figure A3.30(a)

JET OPERATING CONDITIONS

	P_t/P_o	T_t/T_o	T_t (°K)	M=V/a	V/a_o	V(m/s)
PRIMARY	1.334	1.597	471.9	0.656	0.796	273
FAN	1.623	2.956	873.4	0.872	1.407	477

Primary Nozzle Diameter D_p = 4.995 cm
Fan Nozzle Diameter D_f = 6.797 cm
Equivalent Nozzle Diameter D_{eq} = 6.683 cm
Area Ratio , A_f/A_p = 2.747
Velocity Ratio , V_f/V_p = 1.750
Static Temperature Ratio , T_f/T_p = 1.750

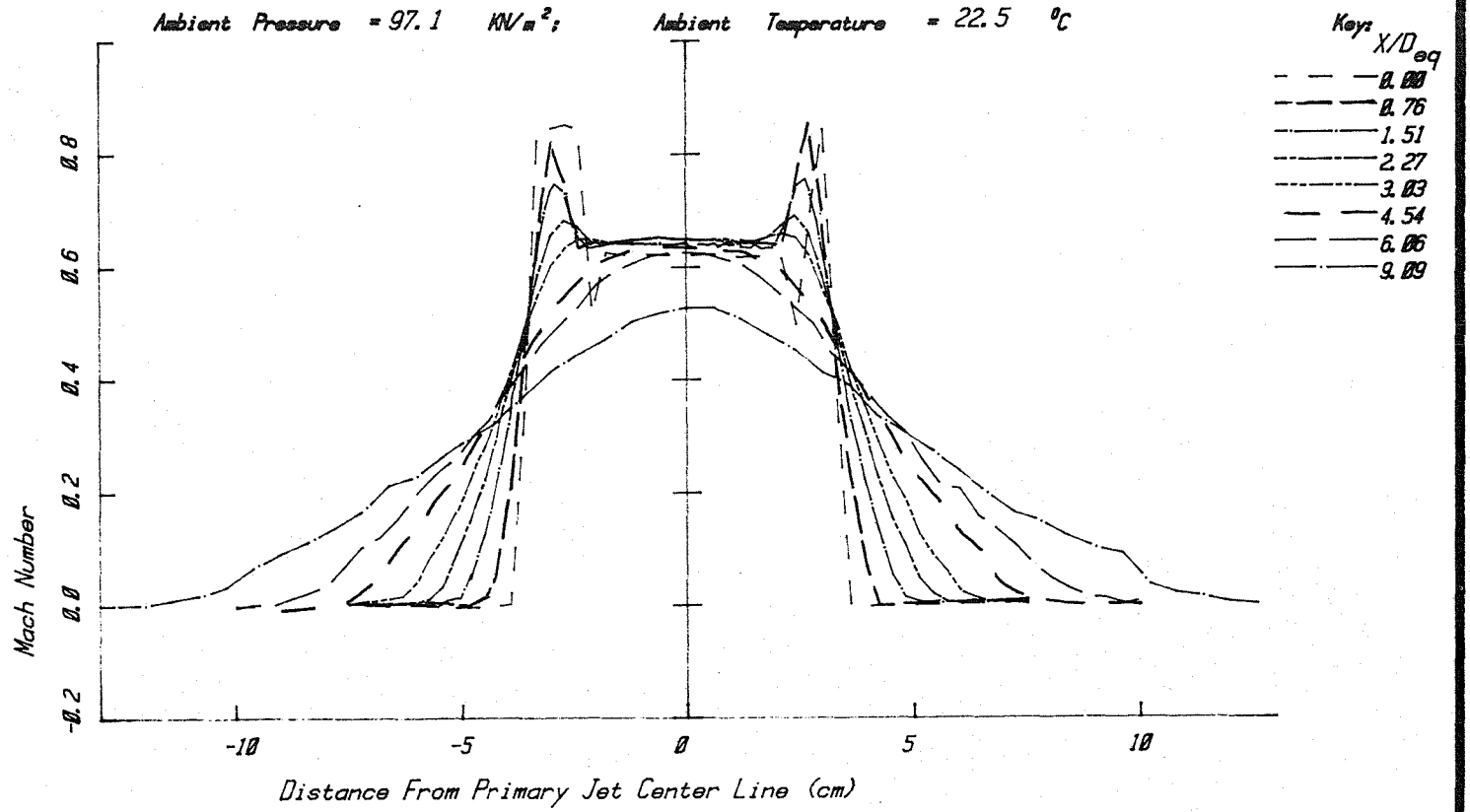

Coannular Jet - Mach Number

Figure A3.30(b)

JET OPERATING CONDITIONS

	P_t/P_o	T_t/T_o	T_t (°K)	M=V/a	V/a_o	V(m/s)
PRIMARY	1.334	1.597	471.9	Ø.656	Ø.796	273
FAN	1.623	2.956	873.4	Ø.872	1.4Ø7	477

Primary Nozzle Diameter D_p = 4.995 cm
Fan Nozzle Diameter D_f = 6.797 cm
Equivalent Nozzle Diameter D_{eq} = 6.6Ø3 cm
Area Ratio , A_f/A_p = Ø.747
Velocity Ratio , V_f/V_p = 1.75Ø
Static Temperature Ratio , T_f/T_p = 1.75Ø

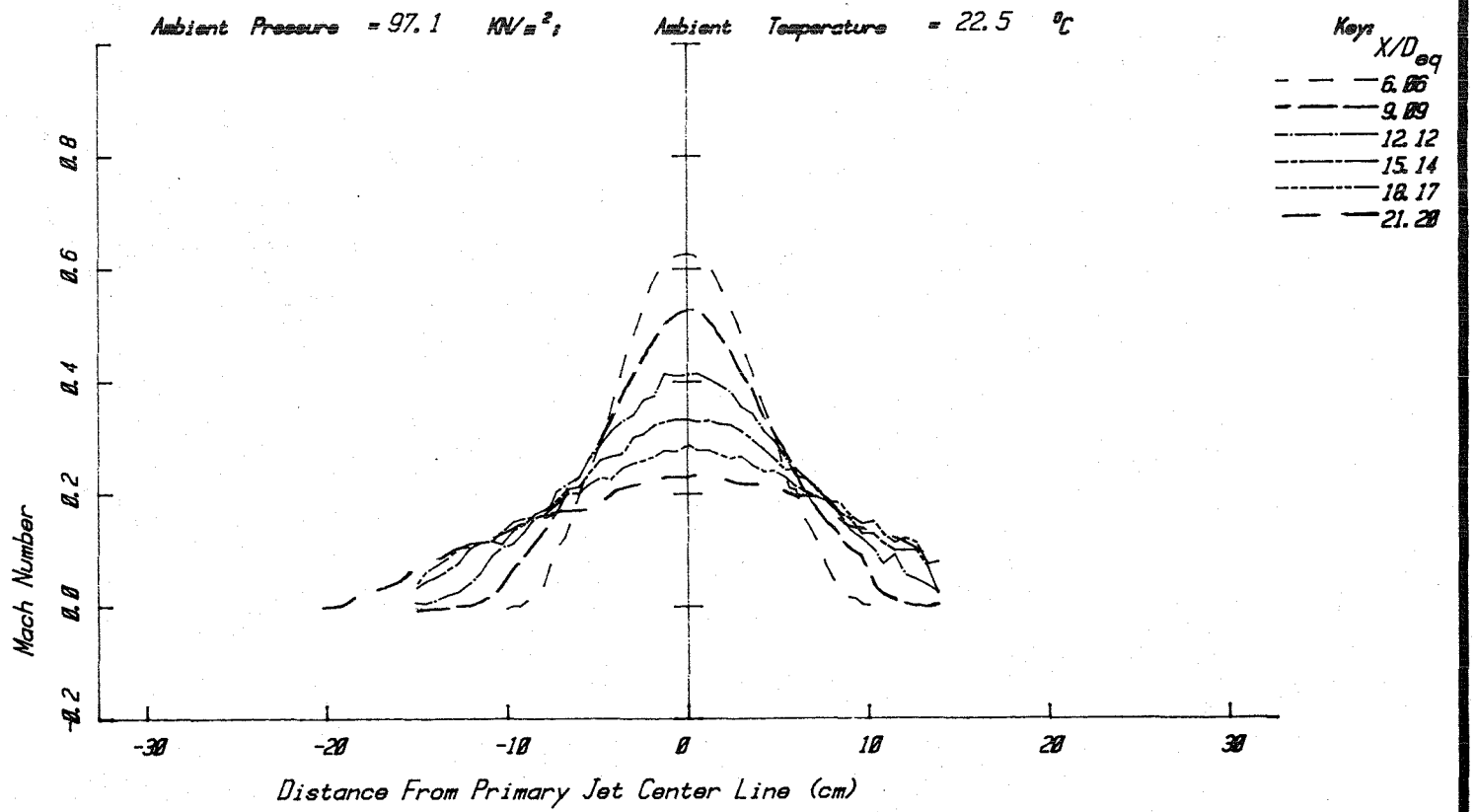

Coannular Jet - Mach Number

Figure A3.30(c)

JET OPERATING CONDITIONS

	P_t/P_0	T_t/T_0	T_t (°K)	M=V/a	V/a_0	V(a/s)
PRIMARY	1.334	1.597	471.9	0.656	0.796	273
FAN	1.623	2.956	873.4	0.872	1.407	477

Primary Nozzle Diameter D_p = 4.995 cm
Fan Nozzle Diameter D_f = 6.797 cm
Equivalent Nozzle Diameter D_{eq} = 6.603 cm
Area Ratio , A_f/A_p = 0.747
Velocity Ratio , V_f/V_p = 1.750
Static Temperature Ratio , T_f/T_p = 1.750

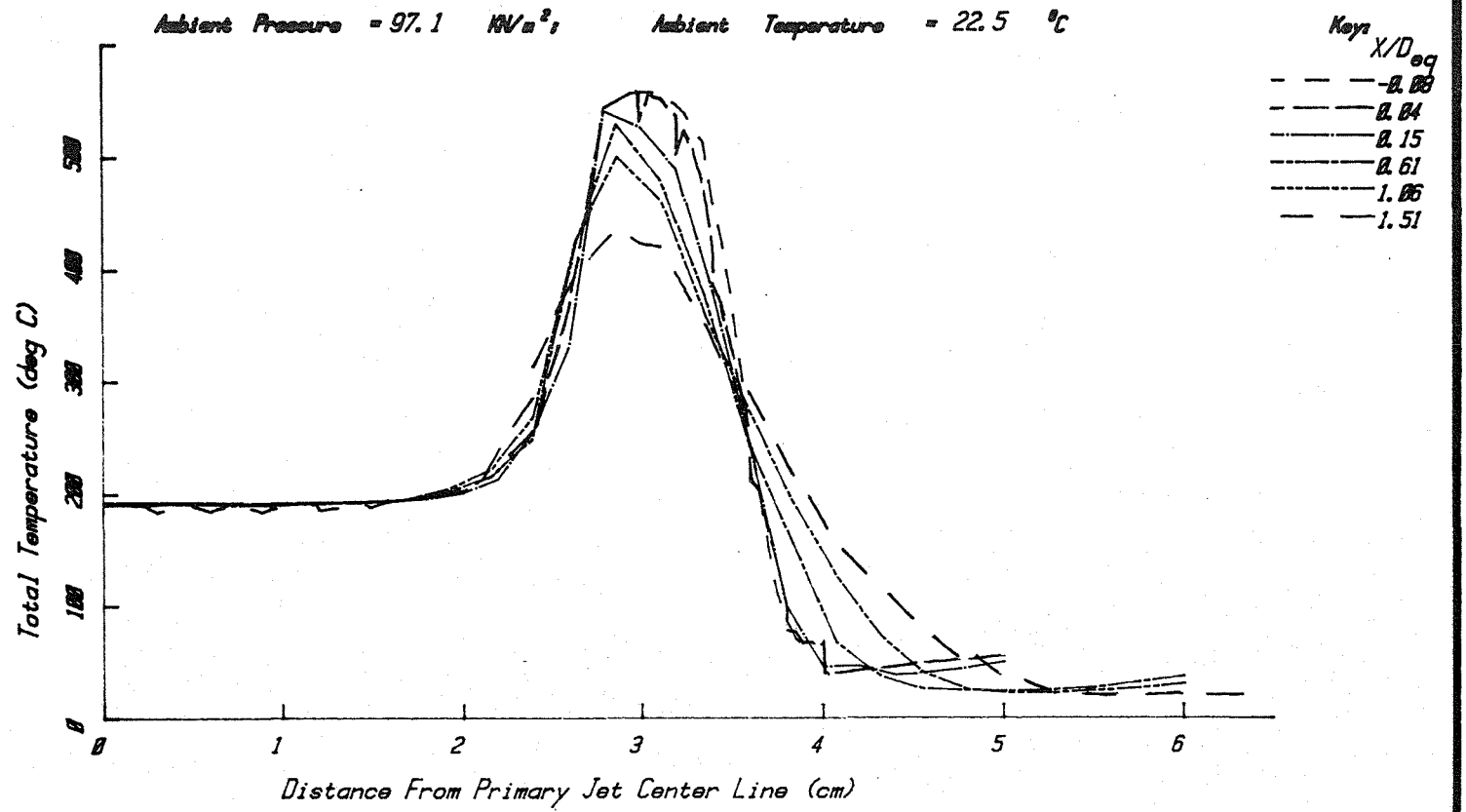

Coannular Jet - Total Temperature (deg C)

Figure A3.31(a)

JET OPERATING CONDITIONS

	P_t/P_o	T_t/T_o	T_t (°K)	M=V/a	V/a_o	V(m/s)
PRIMARY	1.334	1.597	471.9	0.656	0.796	273
FAN	1.623	2.956	873.4	0.872	1.407	477

Primary Nozzle Diameter D_p = 4.995 cm
Fan Nozzle Diameter D_f = 6.797 cm
Equivalent Nozzle Diameter D_{eq} = 6.803 cm
Area Ratio , A_f/A_p = 0.747
Velocity Ratio , V_f/V_p = 1.758
Static Temperature Ratio , T_f/T_p = 1.760

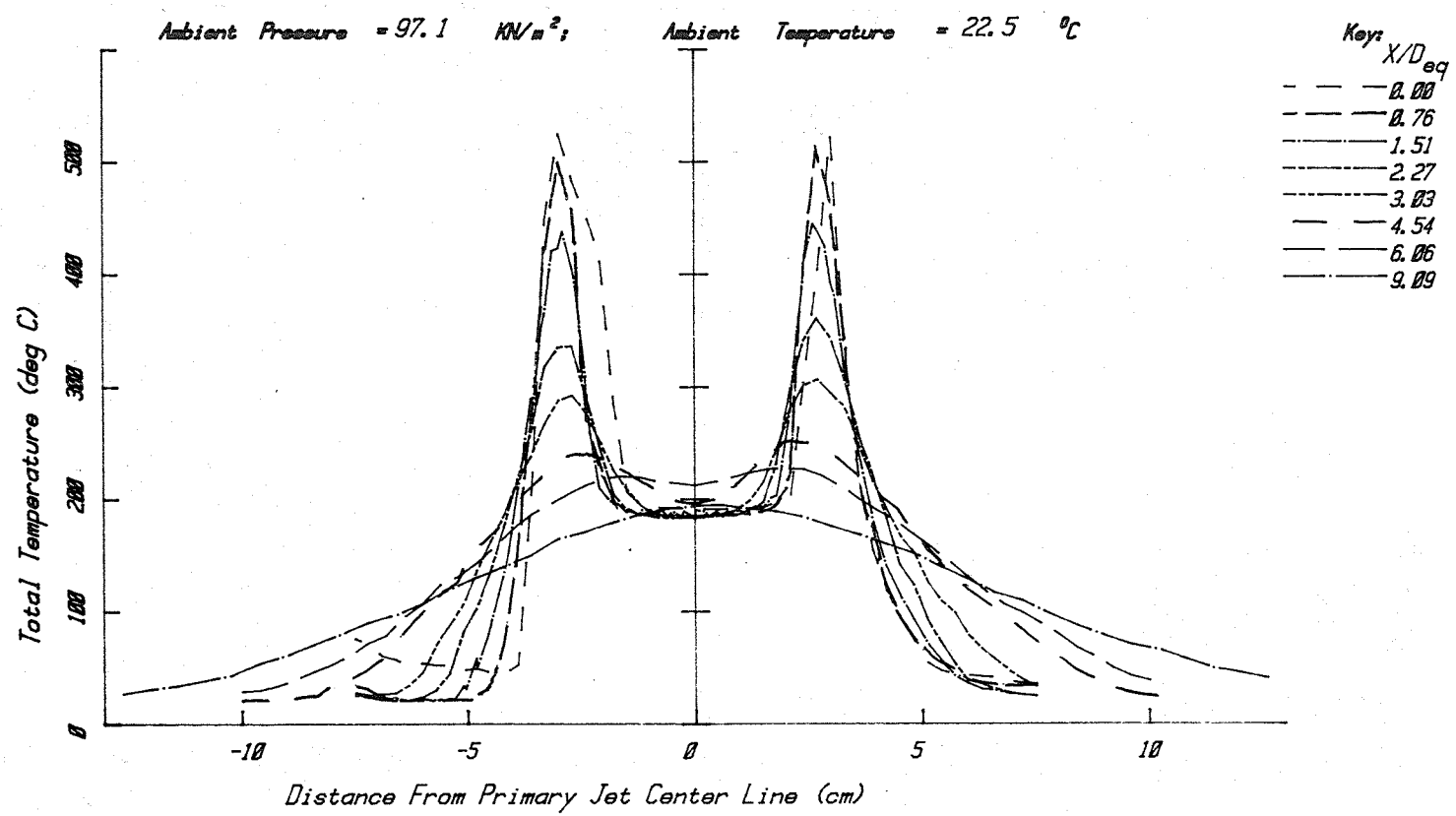

Coannular Jet - Total Temperature (deg C)

Figure A3.31(b)

JET OPERATING CONDITIONS

	P_t/P_o	T_t/T_o	T_t (°K)	M=V/a	V/a_o	V (m/s)
PRIMARY	1.334	1.597	471.9	0.656	0.796	273
FAN	1.623	2.956	873.4	0.872	1.407	477

Primary Nozzle Diameter D_p = 4.935 cm
Fan Nozzle Diameter D_f = 8.[illegible] cm
Equivalent Nozzle Diameter D_{eq} = 6.883 cm
Area Ratio , A_f/A_p = [illegible]
Velocity Ratio , V_f/V_p = [illegible]
Static Temperature Ratio , T_f/T_p = [illegible]

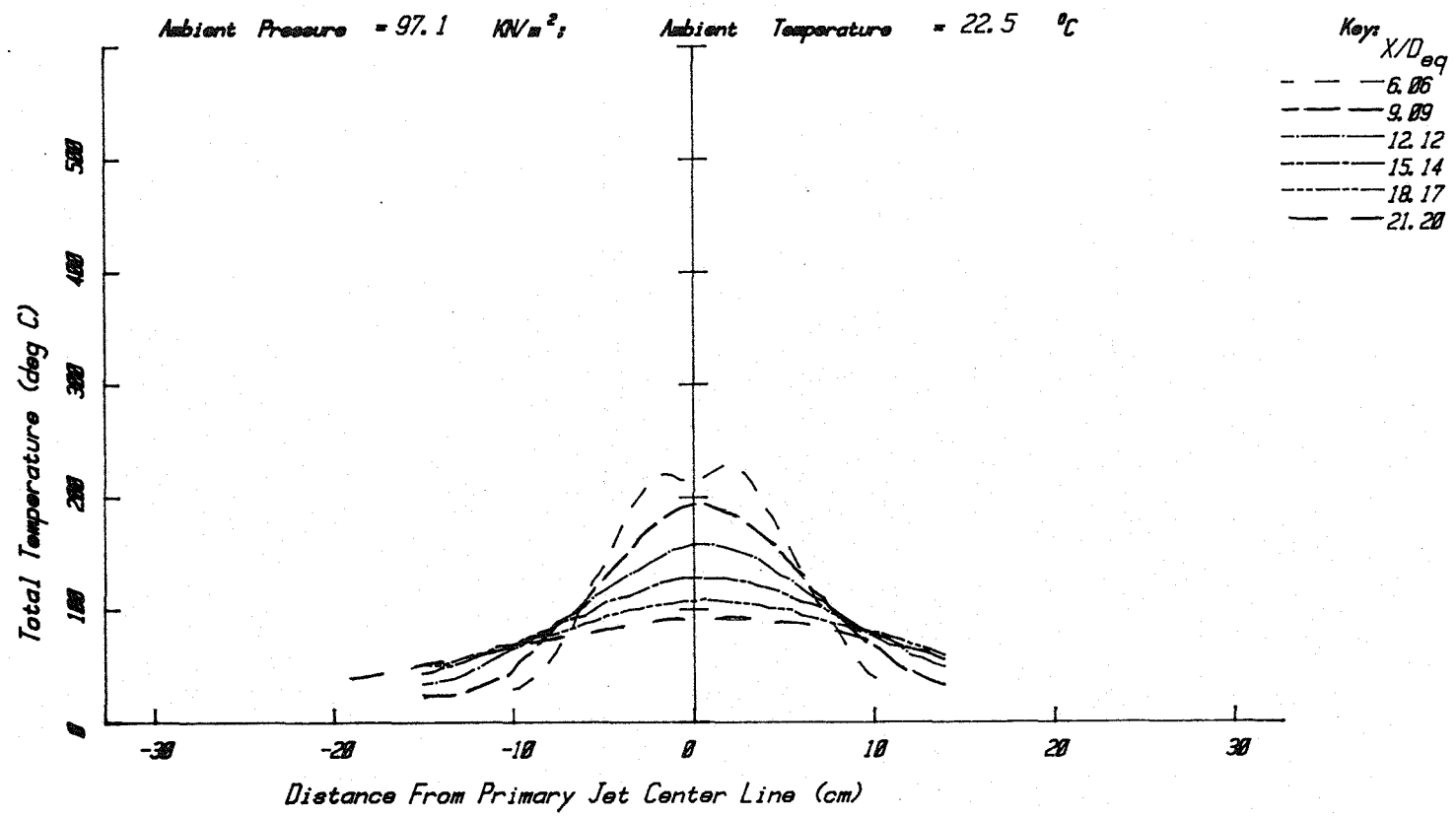

Coannular Jet - Total Temperature (deg C)

Figure A3.31(c)

JET OPERATING CONDITIONS

	P_t/P_o	T_t/T_o	T_t (°K)	M=V/a	V/a_o	V (m/s)
PRIMARY	1.334	1.597	471.9	0.656	0.796	273
FAN	1.623	2.956	873.4	0.872	1.407	477

Primary Nozzle Diameter D_p = 4.995 cm
Fan Nozzle Diameter D_f = 6.797 cm
Equivalent Nozzle Diameter D_{eq} = 6.603 cm
Area Ratio , A_f/A_p = 0.747
Velocity Ratio , V_f/V_p = 1.750
Static Temperature Ratio , T_f/T_p = 1.750

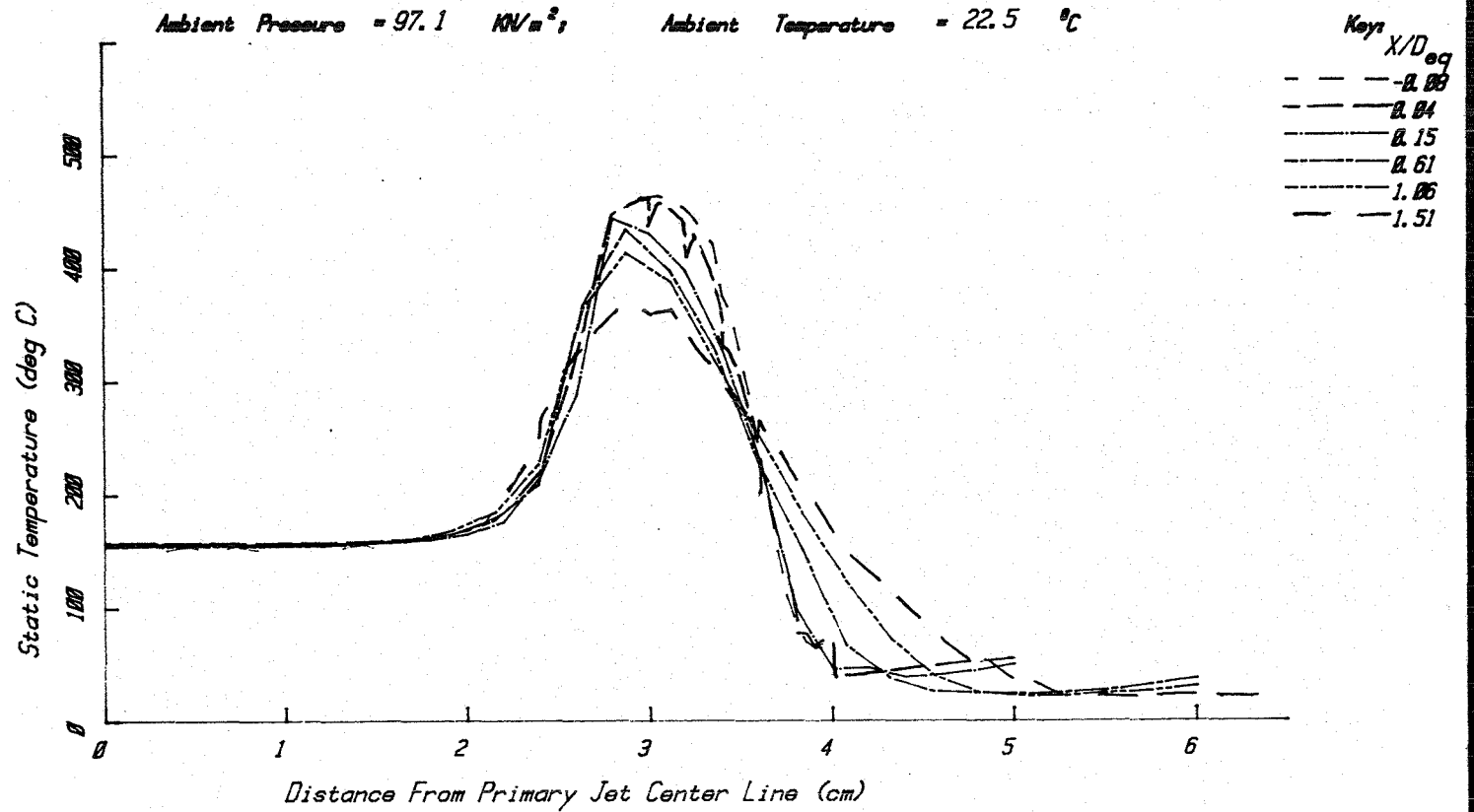

Coannular Jet - Static Temperature (deg C)

Figure A3.32(a)

JET OPERATING CONDITIONS

	P_t/P_o	T_t/T_o	T_t (°K)	M=V/a	V/a_o	V(m/s)
PRIMARY	1.334	1.597	471.9	0.656	0.796	273
FAN	1.623	2.956	873.4	0.872	1.407	477

Primary Nozzle Diameter D_p = 4.995 cm
Fan Nozzle Diameter D_f = 6.797 cm
Equivalent Nozzle Diameter D_{eq} = 6.603 cm
Area Ratio , A_f/A_p = 0.747
Velocity Ratio , V_f/V_p = 1.750
Static Temperature Ratio , T_f/T_p = 1.750

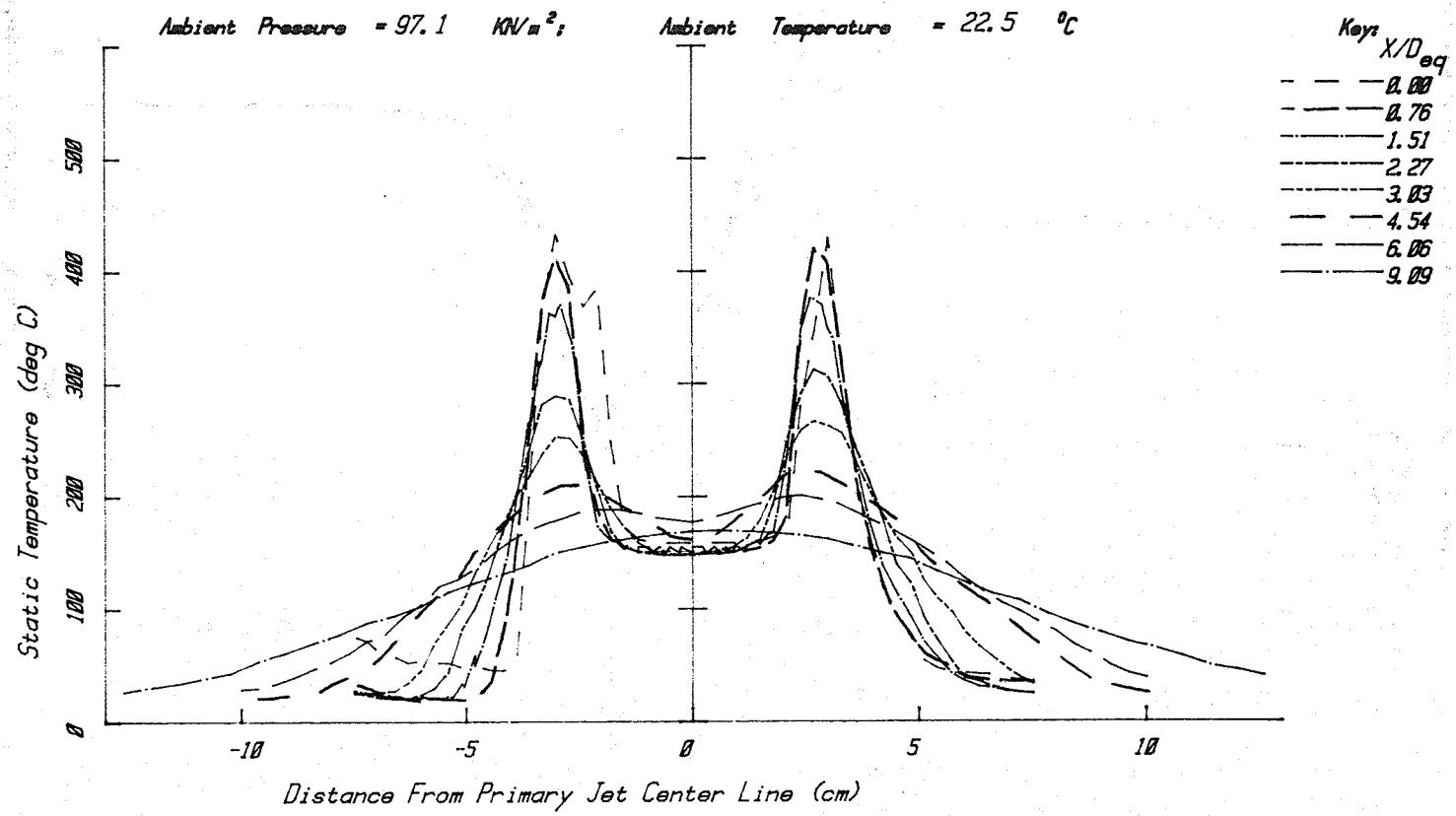

Coannular Jet - Static Temperature (deg C)

Figure A3.32(b)

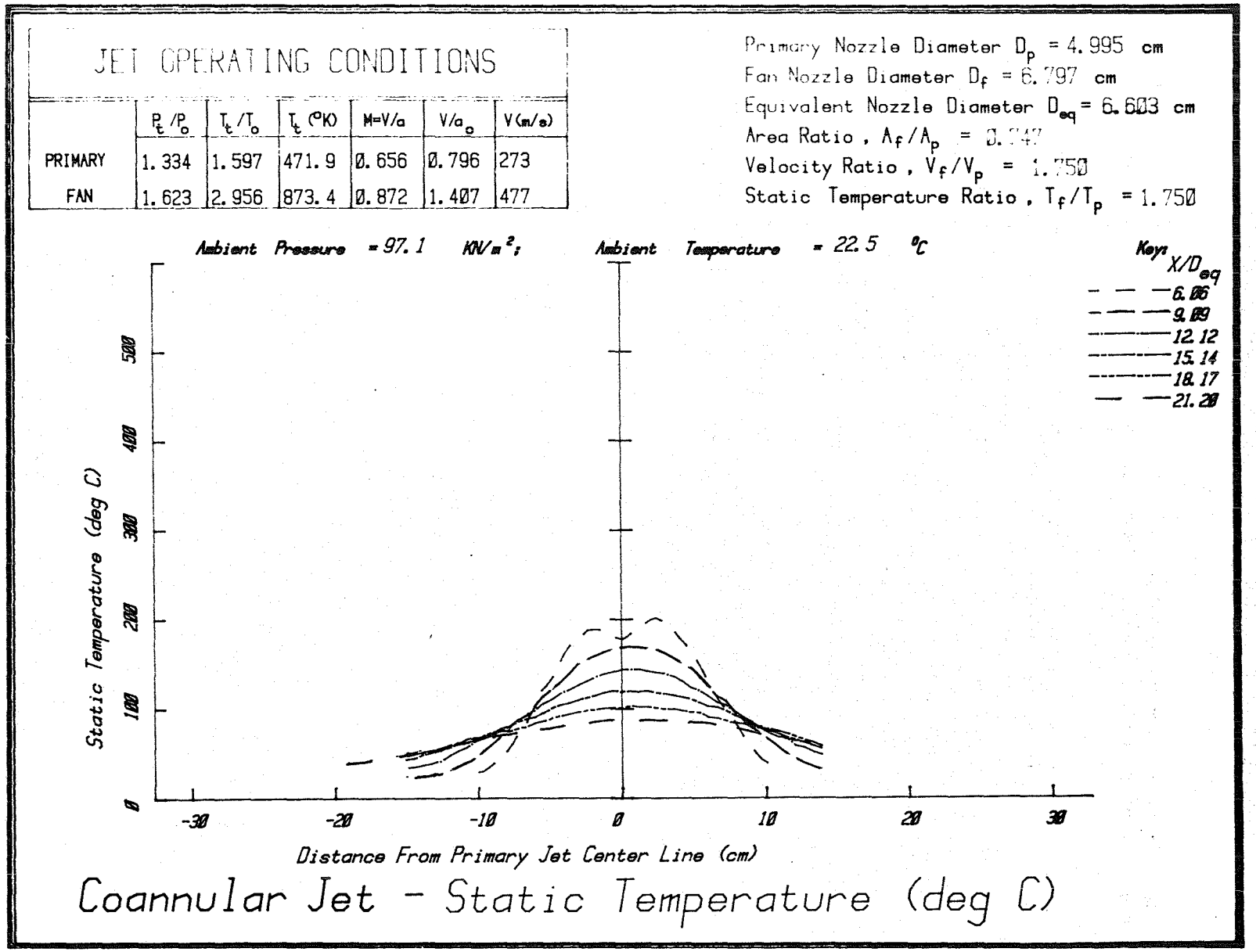

Figure A3.32(c)

APPENDIX 4

COMPARISON BETWEEN LV AND PROBE MEASUREMENTS

Representative comparisons of mean flow distributions obtained with the laser velocimeter and the pressure-temperature probe are presented in this appendix.

Figure A4.1 shows the radial distributions of the axial mean velocity obtained under varying test conditions. Both the LV and the pressure-temperature probe results are obtained at an axial station close to the nozzle exit plane, with the LV measurement plane located marginally upstream of the probe measurement plane. The results obtained by the two measuring techniques show good agreement, and in particular, it may be seen that in Figure A4.1(c), the peak velocity in the annular flow region is reproduced faithfully by the two methods. The LV data, however, tend to indicate a greater gradient within the outer shear layer in general and may be attributed to the fact that the LV measurements are obtained at a station closer to the nozzle.

Figure A4.2 shows the same kind of comparison made at a station substantially downstream of the nozzle ($x/D_{eq} \cong 12$). The two sets of results are obtained at axial stations which are practically identical, and they agree very well.

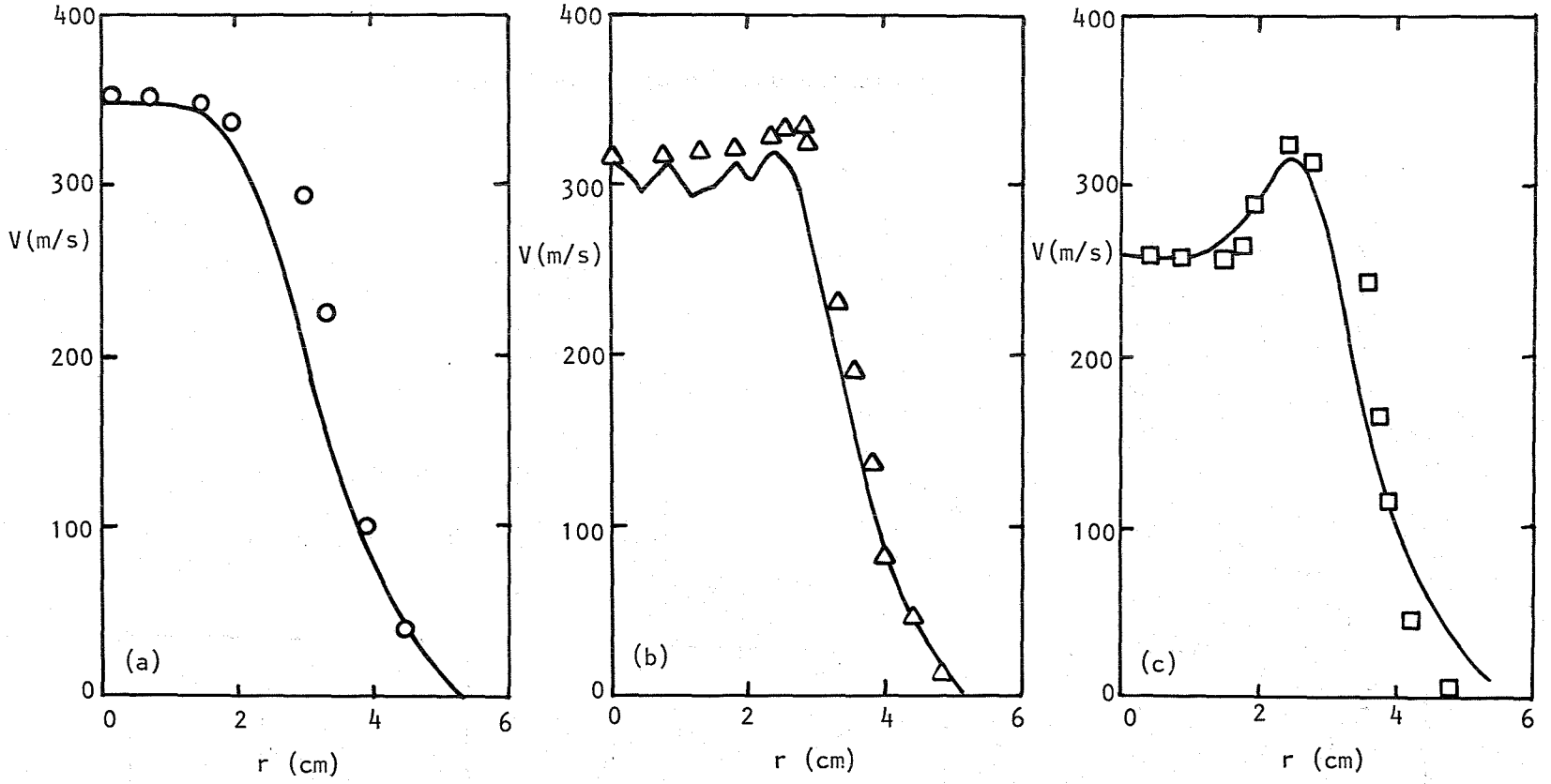

		x/D_{eq}
O, Δ, □	LV	2.00
———	PROBE	2.27

	V_f/V_p	T_f/T_p	TP
(a)	1.00	1.00	1
(b)	1.35	1.00	2
(c)	1.75	1.00	4

Figure 4A.1 Comparison between LV and probe data.

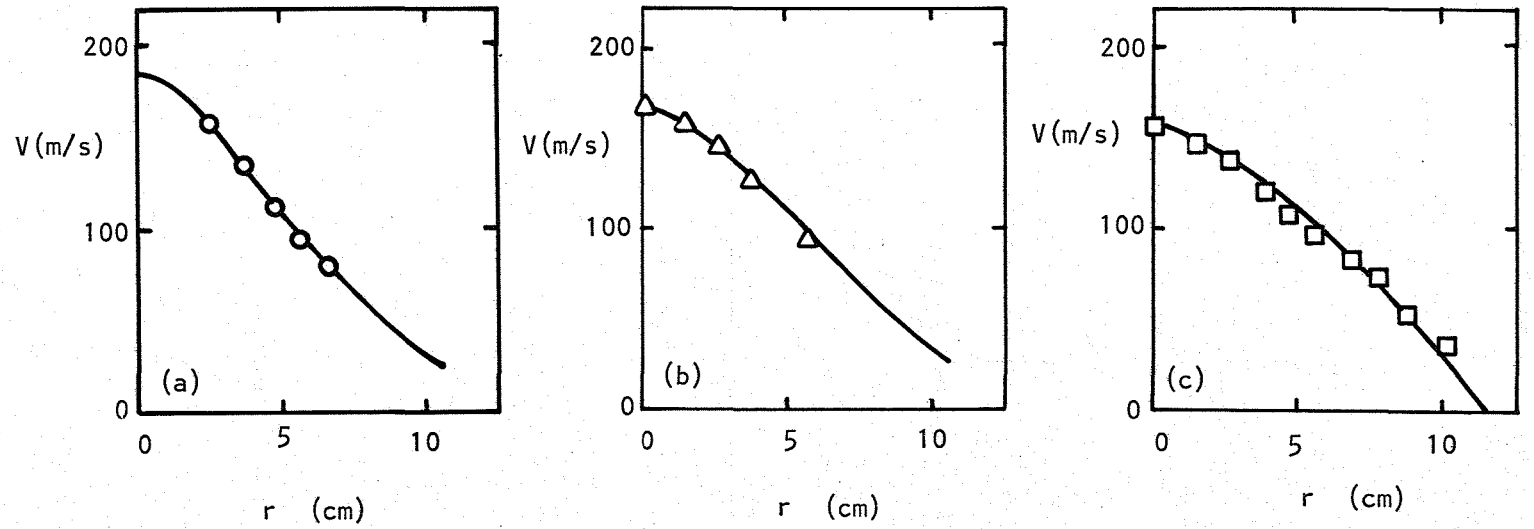

		x/D_{eq}
○, △, □	LV	12.00
———	PROBE	12.12

	V_f/V_p	T_f/T_p	TP
(a)	1.00	1.00	1
(b)	1.35	1.00	2
(c)	1.75	1.00	4

Figure 4A.2 Comparison between LV and probe data.

APPENDIX 5

ON THE RADIATION OF NOISE BY THE LARGE-SCALE STRUCTURE OF TURBULENT COAXIAL JETS

In this discussion the noise radiation process will only be outlined for flows in which some component of the jet exit velocity, either the fan or the primary stream, is supersonic. This limitation has to be imposed at this stage since the role of the large-scale structure in the generation of noise at subsonic velocities is still a matter of considerable debate. However, some of the observed structure of subsonic coaxial jets is likely to be exhibited at supersonic conditions so subsonic observations will be described.

The measurements of Ko and Kwan (ref. A5.1) and Kwan and Ko (ref. A5.2) indicate a distinct coherent structure in normal-velocity-profile coaxial jets (i.e. $V_f < V_p$). These coherent structures consist of two arrays of vortex rings in the primary and secondary mixing regions of the coaxial jet. The convection velocity of the outer vortex rings was approximately 0.6 times the fan velocity and that of the inner rings was $0.6\ (V_p - V_f) + V_f$ where V_p is the primary jet velocity and V_f is the fan jet velocity. Downstream of the end of the inner and outer potential cores, the characteristics more closely resemble those of a single jet. Thus, in the initial region the two annular mixing regions apparently behave independently. The degree of independence is crucial if the noise radiation is to be calculated, especially in the case of inverted profiles.

The mechanism by which the large-scale components of the jet structure radiate noise has been described by Tam and Morris (ref. A5.3) and Tester et al. (ref. A5.4). It is now generally recognized that the gross features of the large-scale structure may be described by linear stability theory. In this analysis the structure is modelled by an instability wave propagating in the basic turbulent mean flow. In the initial region of the jet, disturbances of almost all frequencies are unstable and so the coherent structure grows in amplitude. Further downstream the wave of a given frequency will no longer be unstable and starts to decay. Thus, each frequency component undergoes a process of growth and decay. The phase velocity of a given frequency wave also varies, fairly slowly, as a function of axial distance. Associated with each frequency component will be a wavenumber component spectrum, being the Fourier transform of the wave's axial variation in amplitude and phase. For the case of a constant amplitude and phase velocity wave, the wavenumber component spectrum consists of a delta function at a wavenumber given by $k_o = \omega/c_o$ where c_o is the constant phase velocity. However, since neither the amplitude nor the phase velocity of the wave are constant, there is a spreading of the wavenumber component spectrum about k_o which could be regarded as the average local wavenumber given by local stability calculations. Some of the resulting wavenumber components will lie in the range $-\omega M \leq k \leq \omega M$ where ω and k are the suitably nondimensionalized frequency and wavenumber and M is the ratio of the velocity scale, i.e. the primary jet exit velocity, to the ambient speed of sound. In this range the wave has sonic velocity components to some direction in the ambient medium and hence, in principle, can radiate noise. The analysis

which describes this process is described by Tam and Morris (ref. 5A.3). The agreement between prediction and experiment, given in Tester et al. (ref. 5A.4) is very encouraging.

With the mechanism of noise radiation by the large-scale structure now defined, we must consider how the differences between the coaxial and single jets might affect this component of the total noise generation. Firstly, we would anticipate that any modifications would be only observable at small angles to the jet axis since the coherent structure's noise radiation dominates in this region. In order to proceed further, we must examine the stability characteristics of coaxial jets to determine whether:

(i) the typical phase velocity of the disturbances alters with velocity ratio, or

(ii) the growth of disturbances is altered.

If the latter were the case, then the maximum amplitude of the pressure fluctuations in the near field might be reduced. This in turn, depending on the phase velocity of the disturbances, might lead to a corresponding reduction in noise radiation. There are some indications from preliminary calculations that the phase velocity of waves in a coaxial jet with an inverted profile are less than those in a single jet with the same maximum velocity. This would lead to a reduction in the radiation efficiency of the large-scale structure. However, it should be remembered that the disturbances would have to be modelled, in the simplest case, as a wave with constant phase velocity across the jet which is in disagreement with the experimental observations discussed above. If account were taken of the axial variation of the mean velocity by using, for example, the method of multiple scales, radial variations in phase velocity could be predicted.

Thus, the role of the large-scale structure in coaxial jet noise radiation is still unclear, though some possible effects have been noted. It remains to be seen, from a complete stability analysis and noise calculation program, whether these hypothesized changes really exist in coaxial jets.

APPENDIX 6
LIST OF SYMBOLS

a_o	ambient speed of sound
A	nozzle exhaust area
D	nozzle diameter
f	frequency
M	Mach number
P_o	ambient pressure
P_t	total (or reservoir) pressure
r	radial distance from jet centerline
S	Strouhal number
T	static temperature
T_o	ambient temperature
T_t	total temperature
TP	test point
$\tilde{u}$	axial turbulence level
$\tilde{v}$	radial turbulence level
V	axial mean velocity
V_c	eddy convection velocity
V_s	fluid velocity in source region
x	axial distance from primary nozzle exit plane
x_c	potential core length
x_s	axial location of peak in source distribution
β	area ratio A_f/A_p (Section 5)
η^*	$= (r - r_{0.5})/x$, where $r_{0.5}$ is the value of r at which V/V_p or V/V_f equals 0.5.

$\eta^{*'}$	$= (r - r'_{0.5})/x$, where $r'_{0.5}$ is the value of r at which $(V - V_p)/(V_f - V_p)$ equals 0.5.
θ	observer angle relative to downstream jet axis
λ	velocity ratio V_f/V_p (Section 5)
ξ	nozzle pressure ratio
τ	time delay

Subscripts

a, $\mathfrak{L}$	value along jet centerline
eq	equivalent single jet exit conditions
f	fan (or secondary) jet exit conditions
J	single jet exit conditions
o	ambient conditions
p	primary jet exit conditions[†]

[†]*In Section 5, the subscript p is also used to denote the peak value of turbulence.*

REFERENCES

2.1. Kozlowski, H.; and Packman, A. B.: Aero-Acoustic Tests of Duct-Burning Turbofan Exhaust Nozzles. NASA CR-2628, 1976.

2.2. Knott, P. R.; Stringas, E. J.; Brausch, J. F.; Staid, P. S.; Heck, P. H.; and Latham, D.: Acoustic Tests of Duct-Burning Turbofan Jet Noise Simulation. NASA CR-2966, 1978.

2.3. Ahuja, K. K.: Noise Studies of Cold and Heated Model Jets at Supersonic and High Subsonic Speeds with Particular Reference to Noise Reduction. Ph.D. Dissertation, Syracuse University, 1976.

2.4. Burrin, R. H.; and Tanna, H. K.: The Lockheed-Georgia Coannular Jet Research Facility. Lockheed-Georgia Company Report No. LG77ER0243, 1977.

2.5. Shields, F. D.; and Bass, H. E.: Atmospheric Absorption of High Frequency Noise and Application to Fractional-Octave Bands. NASA CR-2760, 1977.

3.1. Fisher, M. J.; Harper-Bourne, M.; and Glegg, S. A. L.: Jet Engine Noise Source Location: The Polar Correlation Technique. *J. Sound Vib.*, Vol. 51, No. 1, 1977, pp. 23-54.

3.2. Fuchs, H. V.: On the Application of Acoustic "Mirror", "Telescope" and "Polar Correlation" Techniques to Jet Noise Source Location. *J. Sound Vib.*, Vol. 58, No. 1, 1978, pp. 117-126.

3.3. Tester, B. J.; Morris, P. J.; Lau, J. C.; and Tanna, H. K.: The Generation, Radiation and Prediction of Supersonic Jet Noise. AFAPL-TR-78-85, Vol. I, 1978.

3.4. Grosche, F. R.: Distributions of Sound Source Intensities in Subsonic and Supersonic Jets. AGARD CP-131, Noise Mechanisms (see also AIAA Paper No. 73-989), 1973.

3.5. Laufer, J.; Kaplan, R. E.; and Chu, W. T.: On Noise Produced by Subsonic Jets. Proceedings of the Second Interagency Symposium on University Research in Transportation Noise, Vol. 1, 1974, pp. 50-58.

3.6. Fisher, M. J.: Personal Communication, 1978.

5.1. Willis, D. R.; and Glassman, I.: The Mixing of Unbounded Coaxial Compressible Streams. *Jet Propulsion*, Vol. 27, 1957, pp. 1241-1248.

5.2. Chigier, N. A.; and Beer, J. M.: The Flow Region Near the Nozzle in Double Concentric Jets. *J. Basic Eng.*, Vol. 86, 1964, pp. 797-804.

5.3. Williams, T. J.; Ali, M.R.M.H.; and Anderson, J. S.: Noise and Flow Characteristics of Coaxial Jets. *J. Mech. Eng. Sc.*, Vol. 11, 1969, pp. 133-142.

5.4. Durão, D.; and Whitelaw, J. H.: Turbulent Mixing in the Developing Region of Coaxial Jets. ASME Paper No. 73-FE-19, 1973.

5.5. Ko, N. W. M.; and Kwan, A. S. H.: The Initial Region of Subsonic Coaxial Jets. *J. Fluid Mech.*, Vol. 13, 1976, pp. 305-332.

5.6. Forstall, W. Jr.; and Shapiro, A. H.: Momentum and Mass Transfer in Coaxial Gas Jets. *J. Appl. Mech.*, Vol. 10, 1950, pp. 399-408.

5.7. Antonia, R. A.; and Bilger, R. W.: The Heated Round Jet in a Coflowing Stream. *AIAA Journal*, Vol. 14, 1976, pp. 1541-1547.

5.8. Morris, P. J.: Turbulence Measurements in Subsonic and Supersonic Axisymmetric Jets in a Parallel Stream. *AIAA Journal*, Vol. 14, 1976, pp. 1468-1475.

5.9. Barnett, D. O.; and Giel, T. V. Jr.: Application of a Two-Component Bragg-Diffracted Laser Velocimeter to Turbulence Measurements in a Subsonic Jet. Arnold Eng. Dev. Center Rep. No. AEDC TR-76-36, 1976.

5.10. Lau, J. C.; Morris, P. J.; and Fisher, M. J.: Turbulence Measurements in Subsonic and Supersonic Jets Using a Laser Velocimeter. AIAA Paper No. 76-348, 1976.

5.11. Whiffen, M. C.; Lau, J. C.; and Smith, D. M.: Design of LV Experiments for Turbulence Measurements. Proc. Third International Workshop on Laser Velocimetry, Purdue Univ., 1978.

5.12. Lau, J. C.: Mach Number and Temperature Effects on Jets. AIAA Paper No. 78-1152, 1978.

5.13. Witze, P. O.: Centerline Velocity Decay of Compressible Free Jets. *AIAA Journal*, Vol. 12, 1974, pp. 417-418.

5.14. Kleinstein, G.: An Approximation Solution for the Axisymmetric Jet of a Laminar Compressible Fluid. *Quart. J. Appl. Math.*, Vol. 20, 1962, pp. 49-54.

5.15. Tester, B. J.; Morris, P. J.; Lau, J. C.; and Tanna, H. K.: The Generation, Radiation and Prediction of Supersonic Jet Noise. AFAPL-TR-78-85, Vol. I, 1978.

5.16. Bradshaw, P.; Ferris, D. H.; and Johnson, R. H.: Turbulence in the Noise Producing Region of a Circular Jet. *J. Fluid Mech.*, Vol. 19, 1964, pp. 591-624.

5.17. Davies, P. O. A. L.: Turbulence Structure in Free Shear Layers. *AIAA Journal*, Vol. 4, 1966, pp. 1971-1978.

5.18. Lau, J. C.; Fisher, M. J.; and Fuchs, H. V.: The Intrinsic Structure of Turbulent Jets. *J. Sound and Vib.*, Vol. 22, 1972, pp. 379-406.

6.1. American Society of Mechanical Engineers. Supplement to Power Test Codes: Flow Measurement. ASME PTC 19.5; 4, 1959.

A5.1. Ko, N. W. M.; and Kwan, A. S. H.: The Initial Region of Subsonic Coaxial Jets. *J. Fluid Mech.*, Vol. 73, pp. 305-332, 1976.

A5.2. Kwan, A. S. H.; and Ko, N. W. M.: Coherent Structures in Subsonic Coaxial Jets. *J. Sound Vib.*, Vol. 48, pp. 203-219, 1976.

A5.3. Tam, C. K. W.; and Morris, P. J.: The Radiation of Sound by Instability Waves of Compressible Plane Turbulent Shear Layer. To be published, *J. Fluid Mech.*, 1978.

A5.4. Tester, B. J.; Morris, P. J.; Lau, J. C.; and Tanna, H. K.: The Generation, Radiation and Prediction of Supersonic Jet Noise. AFAPL-TR-78-85, Vol. I, 1978.

1. Report No.	2. Government Accession No.	3. Recipient's Catalog No.
NASA CR-158995		

4. Title and Subtitle	5. Report Date
THE NOISE AND FLOW CHARACTERISTICS OF INVERTED-PROFILE COANNULAR JETS	February 1979
	6. Performing Organization Code

7. Author(s)	8. Performing Organization Report No.
H. K. Tanna, B. J. Tester and J. C. Lau	
	10. Work Unit No.

9. Performing Organization Name and Address	11. Contract or Grant No.
Lockheed-Georgia Company Marietta, Georgia 30063	NAS1-15018
	13. Type of Report and Period Covered
12. Sponsoring Agency Name and Address	Contractor Report
National Aeronautics and Space Administration Washington, D. C. 20546	14. Sponsoring Agency Code

15. Supplementary Notes

Final Report. Technical Monitor, S. P. Pao, Acoustics and Noise Reduction Division, NASA-Langley Research Center, Hampton, Virginia. Lockheed Program Manager, H. E. Plumblee, Jr.; Principal Investigator, H. K. Tanna.

16. Abstract

The work described in this report is conducted to obtain a basic understanding of the noise reduction mechanisms in shock-free inverted-velocity-profile coannular jets. Acoustic measurements are first conducted in an anechoic facility to isolate the effects of "inverted velocity" and "inverted temperature" for coannular jets having constant total thrust, mass flow rate and exit area. To obtain physical explanations of the measured noise changes (i.e. reductions or increases), several types of experiments are conducted. These include (i) source location experiments using the "polar correlation technique", (ii) mean flow surveys using a combination pressure/temperature probe, and (iii) detailed mean flow and turbulence measurements using a two-point four-channel laser velocimeter. The results from these experiments are presented and discussed in detail. Finally, the measured variations of coannular jet mixing noise with fan-to-primary velocity ratio and static temperature ratio are interpreted by utilizing the results from the various experimental phases in conjunction with the existing Lockheed single jet noise prediction model.

17. Key Words (Suggested by Author(s))	18. Distribution Statement
Coannular Jets, Coaxial Jets, Jet Noise, Jet Flow, Turbulence, Laser Velocimeter, Aircraft Noise Reduction, Noise Generation, Shock Structure	Unclassified - Unlimited

19. Security Classif. (of this report)	20. Security Classif. (of this page)	21. No. of Pages	22. Price*
UNCLASSIFIED	UNCLASSIFIED	375	

* For sale by the National Technical Information Service, Springfield, Virginia 22161

End of Document